ISSN 1816-5230

НАНОСИСТЕМИ, НАНОМАТЕРІАЛИ, НАНОТЕХНОЛОГІЇ

Nanosistemi, Nanomateriali, Nanotehnologii

ЗБІРНИК НАУКОВИХ ПРАЦЬ

ТОМ 24, ВИПУСК 1, 2026

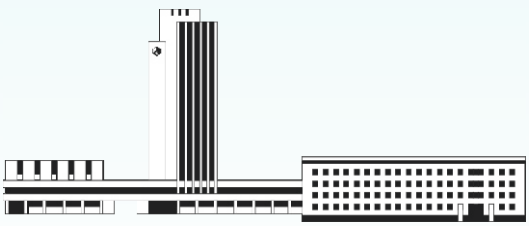

НАЦІОНАЛЬНА АКАДЕМІЯ НАУК УКРАЇНИ

НАНОСИСТЕМИ
НАНОМАТЕРІАЛИ
НАНОТЕХНОЛОГІЇ

NANOSYSTEMS
NANOMATERIALS
NANOTECHNOLOGIES

Засновник: Інститут металофізики ім. Г. В. Курдюмова НАН України
Видавець: Інститут металофізики ім. Г. В. Курдюмова НАН України

«Наносистеми, наноматеріали, нанотехнології» ♦ 'Nanosistemi, Nanomateriali, Nanotehnologii'
Щоквартальний збірник наукових праць ◊ Quarterly Collected Scientific Transactions

НАЦІОНАЛЬНА АКАДЕМІЯ НАУК УКРАЇНИ
Інститут металофізики ім. Г. В. Курдюмова

НАНОСИСТЕМИ, НАНОМАТЕРІАЛИ, НАНОТЕХНОЛОГІЇ

ЗБІРНИК НАУКОВИХ ПРАЦЬ

ТОМ 24, ВИПУСК 1

РВВ ІМФ
КИЇВ — 2026

УДК 536:669

НАНОСИСТЕМИ, НАНОМАТЕРІАЛИ, НАНОТЕХНОЛОГІЇ / Щоквартальний збірник наукових праць / Том 24, вип. 1. — Київ: РВВ ІМФ, 2026. — XVIII с. + 326 с.

У збірнику наведено оригінальні та оглядові статті за результатами робіт, виконаних у рамках досліджень за напрямом «Перспективні фундаментальні дослідження та інноваційні розробки наноматеріалів і нанотехнологій для потреб промисловості, охорони здоров'я та сільського господарства». Основну увагу приділено розгляду проблемних питань нанофізики, наноелектроніки, особливостей будови наноструктурованих матеріялів, з'ясуванню їхніх електричних, термічних, механічних, реологічних і хемічних властивостей, поверхневих явищ і самоорганізації. Представлено результати фабрикації, оброблення, тестування й аналізування нанорозмірних частинок, наномасштабних структур і багатофункціональних наноматеріялів технічного та біомедичного призначення в умовах впливу зовнішніх чинників. Розглянуто особливості технологій одержання, діягностики та характеризації наносистем.

Статті друкуються мовами оригіналів.

Збірник розраховано на наукових працівників, інженерів, викладачів ЗВО, аспірантів і студентів відповідних спеціяльностей.

ISSN 1816-5230

НАЦІОНАЛЬНА АКАДЕМІЯ НАУК УКРАЇНИ ● ІНСТИТУТ МЕТАЛОФІЗИКИ ім. Г. В. Курдюмова

НАНОСИСТЕМИ, НАНОМАТЕРІАЛИ, НАНОТЕХНОЛОГІЇ

ЗБІРНИК НАУКОВИХ ПРАЦЬ
ЗАСНОВАНИЙ У ЖОВТНІ 2003 р.

Том 24, вип. 1; 2026 р.

ЗМІСТ

Науковий редактор випуску — *В. А. Татаренко*
Відповідальний секретар редакційної колеґії — *В. В. Лізунов*
Редактори-коректори: *І. О. Головашич, Д. С. Леонов, Н. А. Леонова*
Технічні редактори: *І. М. Заболотний, Д. С. Леонов*
Оригінал-макет для прямого репродукування виготовлено комп'ютеризованою групою РВВ Інституту металофізики ім. Г. В. Курдюмова НАН України
Друкується за постановою редакційної колеґії збірника англійською або українською мовами
Затверджено до друку вченою радою ІМФ ім. Г. В. Курдюмова НАН України
Свідоцтво суб'єкта видавничої справи серії ДК № 5875 від 13.12.2017 р.
Рішення Національної ради України з питань телебачення і радіомовлення № 907 від 21.03.2024 р. про суб'єкт у сфері друкованих медіа (ідентифікатор медіа R30-03169)
Підп. до друку 26.03.2026 р. Формат 70×100/16. Гарн. SchoolBookC. Папір офсет. № 1. Друк різограф.
Адреса редакції «ННН»: Інститут металофізики ім. Г. В. Курдюмова НАН України, бульв. Акад. Вернадського, 36, каб. 210; 03142 Київ, Україна
Тел.: +380 44 4241221, +380 44 4249042; факс: +380 44 4242561
Ел. пошта: tatar@imp.kiev.ua, dsleonov@gmail.com
Надруковано в РВВ ІМФ ім. Г. В. Курдюмова НАН України.
бульв. Акад. Вернадського, 36; 03142 Київ, Україна. Тел.: +380 44 4240236
Зав. поліграфічно-розмножувальної групи — *Л. І. Малініна*

NATIONAL ACADEMY OF SCIENCES OF UKRAINE ● G. V. KURDYUMOV INSTITUTE FOR METAL PHYSICS

COLLECTED SCIENTIFIC TRANSACTIONS

NANOSISTEMI, NANOMATERIALI, NANOTEHNOLOGII

FOUNDED IN OCTOBER, 2003

Volume 24, Issue 1 (2026)

CONTENTS

Scientific Editor of the Issue—*V. A. Tatarenko*
Executive Managing Editor—*V. V. Lizunov*
Technical Editors—*D. S. Leonov, I. M. Zabolotnyy*
Editorial-Publishing Department, G. V. Kurdyumov Institute for Metal Physics, N.A.S. of Ukraine
State Registration Certificate of the Printed Mass Medium: Media Identifier R30-03169

Editorial Office: 36 Academician Vernadsky Boulevard, UA-03142 Kyyiv, Ukraine
Telephone: +380 44 4241221, +380 44 4249042. Fax: +380 44 4242561
E-mail: tatar@imp.kiev.ua, dsleonov@gmail.com

ІНФОРМАЦІЯ ДЛЯ ПЕРЕДПЛАТНИКІВ

Редакція щоквартального збірника наукових праць
«НАНОСИСТЕМИ, НАНОМАТЕРІАЛИ, НАНОТЕХНОЛОГІЇ»
(CODEN: NNNAAT; ISSN (Print): 1816-5230, ISSN (Online): 2617-3794;
у «Каталозі медіа України «Преса поштою»» передплатний індекс: **94919**)
повідомляє про передплату (починаючи з поточного кварталу випуску).
Рекомендуємо оформити передплату безпосередньо перерахуванням оплати

у гривнях:
«Отримувачу»: Інститут металофізики ім. Г. В. Курдюмова НАН України
на розрахунковий рахунок № UA058201720313291001201001901 в банку ГУДКСУ в м. Києві
код банку 820172
код ЗКПО: 05417331
для «Постачальника» — Інституту металофізики ім. Г. В. Курдюмова НАН України
Свідоцтво платника податку № 36283185
ІПН 054173326066
Код призначення платежу: 25010100
Призначення платежу: за збірник «Наносистеми, наноматеріали, нанотехнології» для РВВ ІМФ НАНУ
Підстава: передоплата 100%

в іноземній валюті (доларах США, євро) через відповідні банки-кореспонденти АТ «Державний експортно-імпортний банк України»:
«Отримувачу»: Філія АТ «Державний експортно-імпортний банк України» в м. Києві (Україна, 04053 Київ, вул. Бульварно-Кудрявська, 11[б])
на розрахунковий рахунок № UA603223130000025308000000067
МФО 322313
для «Постачальника» — Інституту металофізики ім. Г. В. Курдюмова НАН України
Призначення платежу: за збірник «Наносистеми, наноматеріали, нанотехнології» для РВВ ІМФ НАНУ
Підстава: передоплата 100%

За цього способу передплати необхідно сповістити редакцію збірника за поштовою адресою:
РВВ (№ 83) ІМФ НАНУ,
бульв. Акад. Вернадського, 36,
03142 Київ, Україна

e-mail: **tatar@imp.kiev.ua**; факс: +380 44 4242561; телефон: +380 44 4241221, +380 44 4249042

дату сплати, назву установи або найменування передплатника, адресу для поштової доставки, а за потреби — свої реквізити для податкової накладної.

Періодичність — том з 4 випусків у рік.

Із врахуванням поштової пересилки
для передплатників в Україну передплатна ціна: одного примірника випуску — 390 грн., тому — 1560 грн.;
для іноземних передплатників передплатна ціна: одного примірника випуску — 40 US$ (37 EUR), тому — 160 US$ (148 EUR).

✂ *Зразок для оплати річної передплати*

Рахунок-фактура

«Постачальник»: Інститут металофізики ім. Г. В. Курдюмова НАН України
«Отримувач»: Філія АТ «Державний експортно-імпортний банк України» в м. Києві
(Україна, 04053 Київ, вул. Бульварно-Кудрявська, 11[б])
на розрахунковий рахунок № UA603223130000025308000000067, МФО 322313
Призначення платежу: за збірник «Наносистеми, наноматеріали, нанотехнології» для ІМФ НАНУ
«Платник»: .....
.....
Підстава: передоплата 100%

№	Назва	Од. вим.	Кількість	Ціна	Сума
1	збірник «Наносистеми, наноматеріали, нанотехнології» (включаючи доставку поштою)	прим.	4	40 US$	160 US$
	Сума до сплати				160 US$

INFORMATION FOR SUBSCRIBERS

Editorial Board of Quarterly Collected Scientific Transactions
'NANOSISTEMI, NANOMATERIALI, NANOTEHNOLOGII'
(*i.e.* 'NANOSYSTEMS, NANOMATERIALS, NANOTECHNOLOGIES')
(CODEN: NNNAAT; ISSN (Print): 1816-5230, ISSN (Online): 2617-3794)
advertises the subscription on an annual basis for this year.

Orders should be placed through one of the methods described below.

Besides the subscription *via* the Private limited company **'PresCentr Kyiv'** / **«ПресЦентр Київ»** (with address: UA-01019 Kyiv, Ukraine, P.B. 185, tel./fax: +380 44 5361180 / 44 5361175, and e-mails: **podpiska1@prescentr.kiev.ua**, **market7@prescentr.kiev.ua**, **ksl1@prescentr.kiev.ua**) or *via* Internet: **http://www.prescentr.kiev.ua/index.php?route=product/category&path=332_252_266**, as well as besides the subscription *via* **Subscription agency 'Mercury' / «Меркурій»** (with juridical address: UA-49000 Dnipro, 10 Slobozhansky Ave., Bldg. 2, apt. 51, postal address in Kyiv: UA-03056 Kyiv, 27 Vadym Hetman Str., tel.: +380 93 3935740 / 44 2210557, e-mails: **podpiska@mercury.net.ua**, **l.podbereznaja.mercury@gmail.com**), the Editorial Board will take orders sent directly to the Editorial Board. To obtain our edition, the persons and institutions, interested in this title, should made the definite payment sent, according to the order, to the account of the Publisher—Institute for Metal Physics of the N.A.S. of Ukraine.

This edition frequency is 4 issues per year. The annual subscription rate for 'Nanosistemi, Nanomateriali, Nanotehnologii' is of **160** US$ (or 148 EUR), including airmail postage, packing and handling charges. All other currency payments should be made using the current conversion rate set by the Publisher (subscribers should contact the Editorial Board).

Subscription is valid after obtaining by the Editorial Board of banker's order. Banker's order should be sent to the address:

G. V. Kurdyumov Institute for Metal Physics, N.A.S. of Ukraine,
currency account No. UA603223130000025308000000067, MFO 322313
in the Kyiv's Branch of JSC 'The State Export-Import Bank of Ukraine'
(Joint Stock Company 'Ukreximbank')
(11[b] Bulvarno-Kudriavska Str., UA-04053 Kyiv, Ukraine)

simultaneously with written notice providing the Editorial Board with a copy of banker's order for subscription and detailed address for mailing.

Address of the Editorial Board Office:

G. V. Kurdyumov Institute for Metal Physics, N.A.S. of Ukraine,
36 Academician Vernadsky Blvd.,
UA-03142 Kyiv, Ukraine.
E-mail: **tatar@imp.kiev.ua** (with subject beginning by word 'nano').
Fax: +380 44 4242561.

After receiving of banker's order, the Editorial Board will send the guarantee letter to the subscriber's address for mailing the collected scientific transactions for a corresponding term.

Editorial Board of this edition hopes for effective co-operation with its present and future readers and asks to promote the maximum information about its contents to persons, institutions and organizations concerned.

ИНФОРМАЦИЯ ДЛЯ АВТОРОВ

Сборник научных трудов «*Наносистеми, наноматеріали, нанотехнології*» (ННН) публикует ещё неопубликованные и не находящиеся на рассмотрении для опубликования в иных изданиях научные обзоры и оригинальные статьи, содержащие и характеризующие результаты экспериментальных и теоретических исследований в области физики, химии, биологии, техники, методов синтеза, обработки и диагностики наноразмерных систем и наномасштабных материалов: кластеров, наночастиц, нанотрубок, нанокристаллов и наноструктур (апатитоподобных и др. биосистем, аморфных и коллоидных наноразмерных систем, наноструктурных плёнок и покрытий, нанопорошков и т.д.).

Сборник ННН не публикует: статьи полемические, классификационные и узкоспециальные, содержащие решения стандартных задач; статьи описательные и методические (если метод не является принципиально новым); статьи, в которых излагаются отдельные этапы исследования или материал, разделённый на несколько последовательных публикаций; статьи о рядовых исследованиях, не представляющих общего интереса и не содержащих значимых выводов.

Статьи публикуются на одном из двух языков: **английском** или **украинском**.

Статьи, в оформлении которых не соблюдены следующие правила для публикации в ННН, возвращаются авторам без рассмотрения по существу. (Датой поступления считается день повторного представления статьи после соблюдения указанных ниже правил.)

1. Статья должна быть подписана всеми авторами (с указанием их адресов электронной почты); **следует указать** фамилию, имя и отчество автора, с которым редакция будет вести переписку, его почтовый адрес, номер телефона (факса), адрес электронной почты.

2. Изложение должно быть ясным, **структурированным** (разделами **«1. Вступ»**, **«2. Експериментальна/Теоретична методика»**, **«3. Результати та їх обговорення»**, **«4. Висновки»**, **«Внески співавторів»**, **«Цитована література»**), сжатым, без длинных введений, отступлений, повторов, дублирования в тексте данных таблиц, рисунков, подписей к ним. Аннотация и раздел **«Висновки»** должны не дублировать друг друга. Числовые данные следует приводить в общепринятых единицах.

3. Объём статьи должен быть не более 5000 слов (с учётом основного текста, таблиц, подписей к рисункам, списка литературы) и 10 рисунков. Вопросы, связанные с публикацией научных обзоров (не более 22000 слов и 60 рисунков), решаются редколлегией ННН на основании предварительно предоставленной авторами расширенной аннотации работы.

4. В редакцию обязательно предоставляется по **e-mail** (или на компакт-диске) файл рукописи статьи (с иллюстративным материалом), набранный в текстовом редакторе Microsoft Word 2003, 2007 или 2010 с названием, состоящим из фамилии первого автора (латиницей), например, Smirnov.doc.

5. Электронная версия рукописи должна содержать **аннотацию** (200–250 слов) статьи (вместе с **5–6 ключевыми словами**) и **5–7 индексов PACS** (в последней редакции 'Physics and Astronomy Classification Scheme 2010'—http://publishing.aip.org/publishing/pacs/pacs-2010-regular-edition; см. **PACS numbers (imp.kiev.ua)**). Тексты украиноязычных статей должны также содержать заглавие статьи (вместе со списком авторов и адресами соответствующих учреждений), расширенную аннотацию (300–350 слов), ключевые слова, заголовки таблиц и подписи к рисункам на **английском языке**. Кроме того, содержания аннотаций на украинском и английском языках должны быть идентичными по смыслу.

7. Рисунки (цветные, черно-белые или полутоновые с градацией серого) должны быть представлены в виде отдельных файлов (предпочтительно в **графических форматах TIFF**, **EPS** или **JPEG**) с названиями, состоящими из фамилии первого автора (латиницей) и номера рисунка, например, Smirnov_fig2a.tiff. Качество **иллюстраций** (в том числе полутоновых) должно обеспечивать их воспроизведение с разрешением 300–600 точек на дюйм. Дополнительно рисунки предоставляются в формате программы, в которой они создавались.

8. Надписи на рисунках (особенно полутоновых) надо по возможности заменить буквенными обозначениями (набранными на контрастном фоне), а кривые обозначить цифрами или различного типа линиями/маркерами, разъясняемыми в подписях к рисункам или в тексте. На графиках все линии/маркёры должны быть чёрного цвета и достаточных толщин/размеров для качественного воспроизведения в уменьшенном в 2–3 раза виде (рекомендуемая ширина рисунка — 12,7 см). Снимки должны быть чёткими и контрастными, а надписи и обозначения должны не закрывать существенные детали (для чего можно использовать стрелки). Вместо указания в подтекстовке увеличения при съёмке желательно проставить масштаб (на контрастном фоне) на одном из идентичных снимков. На графиках подписи к осям, **выполненные на языке статьи**, должны содержать обозначения (или наименования) откладываемых величин и через запятую их единицы измерения.

9. Формулы в текст необходимо вставлять с помощью редактора формул MathType, полностью совместимого с MS Office 2003, 2007, 2010.

10. Рисунки, а также **таблицы** и подстрочные **примечания (сноски)** должны иметь сплошную нумерацию по всей статье.

11. Ссылки на литературные источники следует давать в виде порядкового номера, напечатанного в строку в квадратных скобках. Список литературы составляется в порядке первого упоминания источника. Примеры оформления ссылок приведены ниже; просим обратить внимание на порядок следования инициалов и фамилий авторов, библиографических сведений и на разделительные знаки, а также на необходимость указания **всех** соавторов цитированной работы и (в конце

каждой ссылки) её **цифрового идентификатора DOI**, если таковой имеется у соответствующей публикации (и указан на её интернет-странице издательства):

1. T. M. Radchenko and V. A. Tatarenko, *Usp. Fiz. Met.*, **9**, No. 1: 1 (2008) (in Ukrainian); https://doi.org/10.15407/ufm.09.01.001
2. T. M. Radchenko, A. A. Shylau, and I. V. Zozoulenko, *Phys. Rev. B*, **86**: 035418 (2012); https://doi.org/10.1103/PhysRevB.86.035418
3. A. Meisel, G. Leonhardt, und R. Szargan, *Röntgenspektren und Chemische Bindung* [X-Ray Spectra and Chemical Bond] (Leipzig: Akademische Verlagsgesellschaft Geest & Portig K.-G.: 1977) (in German).
4. J. M. Ziman, *Printsipy Teorii Tvyordogo Tela* [Principles of the Theory of Solids] (Moskva: Mir: 1974) (Russian translation).
5. M. A. Stucke, D. M. Dimiduk, and D. M. Hazzledine, *High Temperature Ordered Intermetallic Alloys. V* (Eds. I. Baker and R. Darolia) (Pittsburgh, PA, USA: MRS: 1993), p. 471.
6. *Handbook of Mathematical Functions with Formulas, Graphs and Mathematical Tables* (Eds. M. Abramowitz and I. A. Stegun), Nat'l Bureau of Standards. Appl. Math. Ser. Vol. **55** (Washington, D.C.: U.S. Govt. Printing Office: 1964).
7. B. B. Karpovych and O. B. Borovkoff, *Proc. of Symp. 'Micromaterials Engineering' (Dec. 25–31, 1999)* (Kyiv: RVV IMF: 2000), vol. **2**, p. 113 (in Ukrainian).
8. T. M. Radchenko, *Vplyv Uporiadkuvannya Defektnoyi Struktury на Transportni Vlastyvosti Zmishanykh Krystaliv* [Influence of Ordering of the Defect Structure on Transport Properties of the Mixed Crystals] (Thesis of Disser. for Dr. Phys.-Math. Sci.) (Kyiv: G. V. Kurdyumov Institute for Metal Physics, N.A.S.U.: 2015) (in Ukrainian).
9. E. M. Gololobov, V. B. Shipilo, N. I. Sedrenok, and A. I. Dudyak, *Sposob Polucheniya Karbonitridov Metallov* [Production Method of Metal Carbonitrides], Authors' Certificate 722341 SSSR (Published November 21, 1979) (in Russian).
10. V. G. Trubachev, K. V. Chuistov, V. N. Gorshkov, and A. E. Perekos, *Sposob Polucheniya Metallicheskikh Poroshkov* [The Technology of Metallic Powder Production]: Patent 1639892 SU. MKI, B22 F9/02, 9/14 (Otkrytiya i Izobreteniya, **34**, No. 13: 11) (1991) (in Russian).
11. Yu. M. Koval' and V. V. Nemoshkalenko, *O Prirode Martensitnykh Prevrashchenij* [On the Nature of Martensitic Transformations] (Kyiv: 1998) (Prepr./N.A.S. of Ukraine. Inst. for Metal Physics. No. 1, 1998) (in Russian).

Следует применять общепринятые сокращения названий журналов и сборников трудов: http://www.cas.org/content/references/corejournals; http://rmp.aps.org/files/rmpguapb.pdf; http://images.webofknowledge.com/WOK46P9/help/WOS/A_abrvjt.html; http://www.ams.org/msnhtml/serials.pdf.

Обязательным требованием является предоставление дополнительного списка цитированной литературы (**References**) в **латинской транслитерации** (система **BGN/PCGN**; рекомендуемые транслитераторы: http://www.slovnyk.ua/services/translit.php; http://ru.translit.net/?account=bgn). После транслитерированных названий книг, диссертаций, патентов и пр. надо приводить в квадратных скобках их англоязычный перевод. При транслитерации статей из ННН надо использовать написание Ф.И.О. авторов, приведённое **только** в англоязычном оглавлении соответствующего выпуска, и **официальное** транслитерированное название сборника (см. также сайт).

12. Корректура авторам может быть выслана электронной почтой в виде pdf-файла. На проверку корректуры авторам отводятся 5 рабочих дней, начиная со дня, следующего за датой отправки корректуры. По истечении указанного срока статья автоматически направляется в печать. Исправления следует отметить и прокомментировать в самом pdf-файле либо оформить в виде перечня исправлений и переслать (от имени уполномоченного представителя коллектива авторов) по электронной почте в адрес редакции.

Рукописи можно направлять непосредственно в редакцию ННН по почтовому адресу: **бульвар Акад. Вернадского, 36, каб. 210; 03142 Киев, Украина** либо члену редакционной коллегии (состав редколлегии указан на 2-й странице обложки). Электронный вариант статьи направляется по e-mail: **tatar@imp.kiev.ua** (с темой, начинающейся словом 'nano').

В соответствии с договорённостью между редакцией ННН и учредителями сборника, редакция считает, что авторы, посылая ей рукопись статьи, передают учредителям и редколлегии право опубликовать эту рукопись на **английском (украинском)** языке, и просит авторов сразу прикладывать к рукописи подписанное авторами «Соглашение о передаче авторского права»:

Угода про передачу авторського права

Ми, що нижче підписалися, автори рукопису «.....», передаємо засновникам і редколегії збірника наукових праць «*Наносистеми, наноматеріали, нанотехнології*» право опублікувати цей рукопис англійською (чи то українською) мовою. Ми підтверджуємо, що ця публікація **не** порушує авторського права інших осіб, установ або організацій.
Підписи авторів: ..... (ПРІЗВИЩЕ Ім'я, дата, адреса, № телефону, e-mail)

При этом за авторами сохраняются все остальные права как собственников этой рукописи. Авторы могут получить опубликованный выпуск со своей статьёй в редакции сборника по вышеуказанному адресу (тел. №№: **+380 44 4241221**, **+380 44 4249042**), а также загрузить pdf-файл статьи с сайта сборника: http://www.imp.kiev.ua/nanosys/ru/articles/index.html.

INFORMATION FOR CONTRIBUTORS

Submission of Manuscripts: Papers should be sent to the Executive Managing Editor, Editorial Office, Institute for Metal Physics, N.A.S.U., 36 Academician Vernadsky Boulevard, UA-03142 Kyiv, Ukraine. Manuscripts may also be submitted to a member of the Editorial Advisory Board or to the appropriate Editorial Board Member who is familiar with the research presented.

Submission of a paper to '*Nanosistemi, Nanomateriali, Nanotehnologii*' (i.e., 'Nanosystems, Nanomaterials, Nanotechnologies') will be taken to imply that it represents original work not previously published, it is not being considered for publication elsewhere, and if accepted for publication, it will not be published in the same language without the consent of the Editors and Publisher. It is a condition of acceptance by the Editor of a typescript for publication that the Publishers acquire automatically the copyright in the typescript throughout the world.

Scope of the Collected Scientific Transactions: '*Nanosistemi, Nanomateriali, Nanotehnologii*' (i.e., 'Nanosystems, Nanomaterials, Nanotechnologies'—NNN) is the quarterly multidisciplinary peer-reviewed collected scientific transactions, which publish high-quality work on all aspects of nanoscience and nanotechnology. Currently, transactions stand alone in serving the 'nano' community in providing up-to-date information on all developments and progresses being made in nanoscience and nanotechnology and the future predictions for this extraordinary technology. The topics covered by the transactions relate to all 'nano' related areas of the latest research and recent development works including nanomaterials, characterization tools, fabrication methods, numerical simulation, and theory as well as discussions in the field of nanoscience and technology ranging from basic aspects of the science of nanoscale systems and materials to practical applications of such systems and materials ranging from civil engineering to advanced molecular electronics so promising to transform our everyday technology as well as basic economics. The subjects covered include the following: 1. physical sciences; 2. chemical sciences; 3. life sciences; 4. theoretical and computational science and engineering.

The Transactions does not publish: articles, which are polemical and classifying, have a restricted meaning, or contain the solutions of standard problems; descriptive and methodical articles (if the method is not basically new); articles presenting separate stages of studies or the material divided into several parts for subsequent publications; articles with trivial results, which are not of general interest and do not contain significant conclusions.

Language: The language of publication may be English or Ukrainian.

Abstract: Each paper requires an English abstract of 200–250 words summarizing the significant coverage and findings.

Keywords and PACS numbers: Up to six keywords and PACS numbers reflecting the content of the contribution should be supplied (see 'Physics and Astronomy Classification Scheme 2010' at http://publishing.aip.org/publishing/pacs/pacs-2010-regular-edition or **PACS numbers (imp.kiev.ua)**).

Manuscript Preparation: Papers should be typed with double spacing and wide margins on camera-ready pages of A4 size. The length of original contributions should not in general exceed 5000 words and 10 figures, and subject review articles should not exceed 22000 words and 60 figures, including tables and diagrams. Authors are urged to arrange the subject matter clearly under headings such as 1. Introduction, 2. Experimental/Theoretical Details, 3. Results, 4. Discussion, 5. Conclusion(s), Acknowledgement(s) (if any), Authors' Contributions (obligatory, if there is more than one), References. Subsections should be identified with section and subsection numbers (such as 6.1. Second-Value Subheading).

References and Notes: Notes are indicated in the text by consecutive superior Arabic numbers (without parentheses). References should be numbered consecutively (in square brackets) throughout the text. The full list should be collected and typed at the end of the paper in numerical order. Listed references should be completed in all details including **DOI** (if available) but excluding article titles in journals. All authors' initials should precede their surnames. Examples of references preparation:

1. T. M. Radchenko and V. A. Tatarenko, *Usp. Fiz. Met.*, **9**, No. 1: 1 (2008) (in Ukrainian); https://doi.org/10.15407/ufm.09.01.001
2. T. M. Radchenko, A. A. Shylau, and I. V. Zozoulenko, *Phys. Rev. B*, **86**: 035418 (2012); https://doi.org/10.1103/PhysRevB.86.035418
3. A. Meisel, G. Leonhardt, und R. Szargan, *Röntgenspektren und Chemische Bindung* [X-Ray Spectra and Chemical Bond] (Leipzig: Akademische Verlagsgesellschaft Geest & Portig K.-G.: 1977) (in German).
4. J. M. Ziman, *Printsipy Teorii Tvyordogo Tela* [Principles of the Theory of Solids] (Moskva: Mir: 1974) (Russian translation).
5. M. A. Stucke, D. M. Dimiduk, and D. M. Hazzledine, *High Temperature Ordered Intermetallic Alloys. V* (Eds. I. Baker and R. Darolia) (Pittsburgh, PA, USA: MRS: 1993), p. 471.
6. *Handbook of Mathematical Functions with Formulas, Graphs and Mathematical Tables* (Eds. M. Abramowitz and I. A. Stegun), Nat'l Bureau of Standards. Appl. Math. Ser. Vol. **55** (Washington, D.C.: U.S. Govt. Printing Office: 1964).
7. B. B. Karpovych and O. B. Borovkoff, *Proc. of Symp. 'Micromaterials Engineering' (Dec. 25–31, 1999)* (Kyiv: RVV IMF: 2000), vol. **2**, p. 113 (in Ukrainian).
8. T. M. Radchenko, *Vplyv Uporyadkuvannya Defektnoyi Struktury на Transportni Vlastyvosti*

Zmishanykh Krystaliv [Influence of Ordering of the Defect Structure on Transport Properties of the Mixed Crystals] (Thesis of Disser. for Dr. Phys.-Math. Sci.) (Kyiv: G. V. Kurdyumov Institute for Metal Physics, N.A.S.U.: 2015) (in Ukrainian).
9. E. M. Gololobov, V. B. Shipilo, N. I. Sedrenok, and A. I. Dudyak, *Sposob Polucheniya Karbonitridov Metallov* [Production Method of Metal Carbonitrides], Authors' Certificate 722341 SSSR (Published November 21, 1979) (in Russian).
10. V. G. Trubachev, K. V. Chuistov, V. N. Gorshkov, and A. E. Perekos, *Sposob Polucheniya Metallicheskikh Poroshkov* [The Technology of Metallic Powder Production]: Patent 1639892 SU. MKI, B22 F9/02, 9/14 (Otkrytiya i Izobreteniya, **34**, No. 13: 11) (1991) (in Russian).
11. Yu. M. Koval' and V. V. Nemoshkalenko, *O Prirode Martensitnykh Prevrashchenij* [On the Nature of Martensitic Transformations] (Kyiv: 1998) (Prepr./N.A.S. of Ukraine. Inst. for Metal Physics. No. 1, 1998) (in Russian).

Journal title abbreviations should conform to generally accepted styles:
http://www.cas.org/content/references/corejournals; http://rmp.aps.org/files/rmpguapb.pdf;
http://images.webofknowledge.com/WOK46P9/help/WOS/A_abrvjt.html;
http://www.ams.org/msnhtml/serials.pdf.

Equations and Formulae: Formulas in the text should be inserted by MathType Editor, which is fully compatible with MS Office 2003, 2007, 2010. (Word's formula editor is undesirable for typing them!)

Tables: Number tables consecutively with Arabic numerals and give a clear descriptive caption at the top.

Figures: All figures should be numbered with consecutive Arabic numerals, have descriptive captions and be mentioned in the text. Keep figures separate at the end of the text and clearly label each figure with author's name and figure number. The labels at axis should contain the designation (or notation) of quantities and their units.

Preparation: Figures submitted (black-and-white or greyscale recommended) must be of a high enough standard for reproduction with 300–600 dpi resolution (including half-tone illustrations). Redrawing or retouching of unusable figures will be charged to the authors.

Colour Plates: Whenever the use of colour is an integral part of the research, or where the work is generated in colour, the Transactions will insert the colour illustrations into the PDF version of the article published on the Editorial Office site. (Reprints in colour will carry a surcharge. Please write to the Publisher for details.)

Submission of Electronic Text with Figures: Authors should submit papers (with figures) by e-mail (**tatar@imp.kiev.ua**) or on a CD. The file should be saved in the native formats of the Microsoft Word 2003, 2007 or 2010 with a name consisting of the name of the first author, for example, Smirnov.doc. The electronic form of figures (graphics files in TIFF, EPS or JPEG formats preferably and with name consisting the name of the first author also, for example, Smirnov_fig2a.tiff) should be planned so that they reduce to 12.7 cm column width (or less), and keep them separate from the text file. It is necessary to submit additionally all the **figures** within the format of the program, in which they were created.

Proofs: In a special emergency, contributors may receive page proofs for correction by e-mail as a PDF document. In that case, these must be returned to Kyiv office (**tatar@imp.kiev.ua**) with subject beginning by word 'nano' within 120 hours of receipt.

Page Charges: There are no page charges to individuals or institutions.

Reprints: Hard-copy reprints provided to the first-named author of each paper may be ordered by completing the appropriate form sent with proofs. Authors can de-archive a PDF version of their published article from the Editorial Office site: http://www.imp.kiev.ua/nanosys/ru/articles/index.html.

Further Information: All questions arising after the acceptance of manuscripts, especially those relating to reprints, should be directed to Executive Managing Editor, Editorial Office, G. V. Kurdyumov Institute for Metal Physics, N.A.S.U., 36 Academician Vernadsky Blvd., UA-03142 Kyiv, Ukraine.
Fax: +380 44 4242561, e-mail: **tatar@imp.kiev.ua** (with subject beginning by word 'nano').
We ask the authors to apply with their manuscript

Copyright Transfer Agreement

We, the undersigned authors of the manuscript '_____', transfer to the founders and the Editorial Board of the Collected Scientific Transactions 'Nanosistemi, Nanomateriali, Nanotehnologii' the right to publish this manuscript in English language (or in the Ukrainian translation). We confirm that publication of this manuscript will not infringe a copyright of other persons, institutions or organizations.

Author(s):_____
(Last Name, First Name, Affiliation)

Authors' contributions to the article:_____
(Please specify the contribution of each author, if there is more than one.)

Correspondence Address:_____
Phone and e-mail: _____

_____ _____
(Signature) *(Date)*

ВИДАВНИЧА ЕТИКА

ТА ЗАПОБІГАННЯ НЕСУМЛІННІЙ ПРАКТИЦІ ПУБЛІКАЦІЙ

Редакційна колеґія збірника наукових праць «Наносистеми, наноматеріали, нанотехнології» дотримується етичних норм, прийнятих міжнародним науковим співтовариством, і робить усе для запобігання будь-яким порушенням їх. У своїй діяльності редакція спирається на рекомендації Комітету з етики наукових публікацій (http://publicationethics.org).

Обов'язки редакції

- Всі представлені статті рецензуються експертами в даній області.
- Під час розгляду статті враховуються її відповідність предметній області, обґрунтованість, значимість, ориґінальність, читабельність і мова (правопис).
- За результатами рецензування стаття може бути прийнята до опублікування без доробки, прийнята з доробкою або відхилена.
- Відхилені статті повторно не рецензуються.
- Статті можуть бути відхилені без рецензії, якщо вони очевидним чином не підходять для публікації.
- Редакція ухвалює рішення щодо публікації, керуючись політикою збірника, з урахуванням діючого законодавства в області авторського права.
- Не допускається до публікації інформація, якщо є достатньо підстав уважати, що вона є плаґіятом.

За наявности яких-небудь конфліктів інтересів (фінансових, академічних, особистих) всі учасники процесу рецензування повинні сповістити про це редколеґії. Всі спірні питання розглядаються на засіданні редколеґії.

Прийняті до опублікування статті розміщаються у відкритому доступі на сайті збірника; авторські права зберігаються за авторами.

Етичні принципи в діяльності рецензентів

- Рецензенти оцінюють статті за їхнім вмістом, безвідносно до національности, статі, сексуальної орієнтації, релігійних переконань, етнічної приналежности або політичних переконань авторів.
- Співробітники редакції не повинні повідомляти яку-небудь інформацію про статті, що надійшли, особам, які не є рецензентами, авторами, співробітниками редакції та видавництва.
- Рецензування повинне бути проведено об'єктивно. Персональна критика автора неприпустима. Рецензенти зобов'язані обґрунтовувати свою точку зору чітко й об'єктивно.
- Рецензування допомагає видавцеві приймати рішення та за допомогою співробітництва з рецензентами й авторами поліпшити статтю.
- Матеріяли, отримані для рецензії, є конфіденційними документами та рецензуються анонімно.
- Рецензент також зобов'язаний звертати увагу редактора на істотну або часткову подібність представленої статті з якою-небудь іншою роботою, з якою рецензент безпосередньо знайомий.

Принципи, якими повинні керуватися автори наукових публікацій

- Автори статей повинні надавати точний звіт про виконану роботу й об'єктивне обговорення її значимости.
- Автори статті повинні надавати достовірні результати проведеного огляду й аналізи досліджень. Свідомо помилкові або сфальсифіковані твердження неприйнятні.
- Стаття повинна містити достатню кількість інформації для перевірки та повторення експериментів або розрахунків іншими дослідниками. Шахрайські або свідомо неправдиві заяви прирівнюються до неетичного поводження і є неприйнятними.
- Автори можуть надавати ориґінальні реґулярні й оглядові роботи. За використання текстової або графічної інформації, отриманої з робіт інших осіб, обов'язково необхідні посилання на відповідні публікації або письмовий дозвіл їхніх авторів.
- Подача статті більш ніж в один журнал розцінюється як неетичне поводження і є неприйнятною.
- Авторство повинне бути обмежене тими, хто зробив значний внесок у концепцію, розробку, виконання або інтерпретацію заявленого дослідження.
- Джерела фінансової підтримки дослідження, що публікується, можуть бути зазначені.

PUBLICATION ETHICS

AND MALPRACTICE STATEMENT

The Editorial Board of the Collected Scientific Transactions '*Nanosistemi, Nanomateriali, Nanotehnologii*' (i.e., 'Nanosystems, Nanomaterials, Nanotechnologies') follows ethics norms accepted by international scientific community and makes every endeavour to prevent any infringements of the norms. The Editorial Board follows the guidelines of the Committee on Publication Ethics (http://publicationethics.org).

Duties of Editors

- All submitted papers are subject to strict peer-review process by reviewers that are experts in the area of the particular paper.
- The factors, which are taken into account in reviewing process, are relevance, soundness, significance, originality, readability, and quality of language.
- The possible decisions include acceptance, acceptance with revisions, or rejection.
- If authors are encouraged to revise and resubmit a submission, there is no guarantee that the revised submission will be accepted.
- Rejected articles will not be re-reviewed.
- Articles may be rejected without review, if they are obviously not suitable for publication.
- The paper acceptance is constrained by such legal requirements as shall then be in force regarding libel, copyright infringement, and plagiarism.

When a conflict of interests arising, all the participants of reviewing process should inform the Editorial Board. All the contentions questions are considered in the Board meeting.

The accepted papers are allocated in open access on the journal site; copyrights reserved.

Duties of Reviewers

- The reviewers evaluate manuscripts for their intellectual content without regard to race, gender, sexual orientation, religious belief, ethnic origin, citizenship, or political philosophy of the authors.
- The staff must not disclose any information about a submitted manuscript to anyone other than the corresponding author, reviewers, other editorial advisers, and the Publisher, as appropriate.
- Reviews should be conducted objectively. Personal criticism of the author is inappropriate. Referees should express their views clearly with supporting arguments.
- Peer review assists the Publisher in making editorial decisions and through the editorial communications with the experts from the scientific board and the author may assist the author in improving the paper.
- Manuscripts received for review are treated as confidential documents and are reviewed by anonymous staff.
- A reviewer should also call to the Publisher's attention any substantial similarity or overlap between the manuscript under consideration and any other published paper of which they have personal knowledge.

Duties of Authors

- Authors of contributions and studies research should present an accurate account of the work performed as well as an objective discussion of its significance.
- A paper should contain sufficient details and references to permit others to replicate the work. Fraudulent or knowingly inaccurate statements constitute unethical behaviour and are unacceptable.
- The authors should ensure that they have written original regular or entirely review works, if the authors have used the work and/or words of others that this has been obligatory and appropriately cited or quoted.
- Submitting the same manuscript to more than one publication concurrently constitutes unethical publishing behaviour and is unacceptable.
- Authorship should be limited to those who have made a significant contribution to the conception, design, execution, or interpretation of the reported study.
- Sources of financial support for the reported results can be specified.

Наносистеми, наноматеріали, нанотехнології
Nanosistemi, Nanomateriali, Nanotehnologii
2026, т. 24, № 1, сс. 1–16
https://doi.org/10.15407/nnn.24.01.0001

PACS numbers: 71.10.Pm, 71.45.Lr, 73.22.Lp, 73.43.Lp, 75.30.Fv, 75.47.Lx

Formation of Bosons in $SmMnO_{3+}$ as 1*D* Charge/Spin Density Waves Caused by Confinement of Spinon Pairs in a System of AFM Spin Chains; Step-Like Quantum Hall Effect for Massless Dirac Fermions

F. M. Bukhanko

Donetsk Institute for Physics and Engineering Named after O. O. Galkin, N.A.S. of Ukraine,
46 Nauky Ave.,
UA-03028 Kyiv, Ukraine

As shown, the appearance of two unusual peak features of isotherms 1 and 2 of the magnetization reversal of $SmMnO_{3+\delta}$ near zero magnetic field is a natural consequence of the spin–charge separation characteristic of the previously well-studied theoretically one-dimensional Mott insulator in the state of a quantum Luttinger liquid. Attention is drawn to the difference between the two peak features of isotherms 1 and 2 of the magnetization reversal near $H = 0$ Oe, which depends on the direction of growth of the external magnetic-field strength. We believe that such behaviour of magnetization in the low-temperature region is caused by the fact that the transverse component of the external magnetic field closes the spinon gap Δ_s in $SmMnO_{3+\delta}$. A characteristic feature of this state is the spatial separation of charge and spin excitations. According to these studies, even a weak increase in the transverse component of the external magnetic field can lead to further confinement of spinon pairs, which is accompanied by the appearance of gapless modes of natural longitudinal oscillations of the spin chain system. We assume that the step-like features of field dependences of magnetization of $SmMnO_{3+\delta}$ at temperature $T = 0.6$ K are similar to characteristics of step-like quantum Hall effect for massless Dirac fermions in graphene.

Показано, що поява двох незвичайних пікових особливостей ізотерм 1 і 2 перемагнетування $SmMnO_{3+\delta}$ поблизу нульового магнетного поля є природнім наслідком характеристики розділення спін-зарядів раніше добре вивченого теоретично одновимірного Моттового ізолятора у стані квантової Латтинжерової рідини. Звертається увага на ріжницю між двома піковими особливостями ізотерм 1 і 2 перемагнетування поблизу $H = 0$ Е, яка залежить від напрямку зростання напруженості зовніш-

нього магнетного поля. Ми вважаємо, що таку поведінку намагнетованости в області низьких температур зумовлено тим, що поперечна складова зовнішнього магнетного поля закриває спінонну щілину Δ_s у $SmMnO_{3+\delta}$. Характерною особливістю цього стану є просторове розділення зарядових і спінових збуджень. Згідно з цими дослідженнями, навіть слабке збільшення поперечної складової зовнішнього магнетного поля може привести до подальшого обмеження спінонних пар, що супроводжується появою безщілинних мод власних поздовжніх коливань системи спінового ланцюга. Ми припускаємо, що ступінчасті особливості польових залежностей намагнетованости $SmMnO_{3+\delta}$ за температури $T = 0{,}6$ К є подібними до характеристик ступінчастого квантового Голлового ефекту для безмасових Діракових ферміонів у графені.

Key words: quantum Luttinger liquid, 1*D* charge–spin density waves, confinement of spinon pairs, step-like quantum Hall effect for massless Dirac fermions.

Ключові слова: Латтинжерова квантова рідина, одновимірні хвилі зарядово-спінової густини, обмеження спінонних пар, ступінчастий квантовий Голлів ефект для безмасових Діракових ферміонів.

(Received 4 September, 2025)

1. INTRODUCTION

In Refs. [1, 2], a Luttinger exactly soluble model of a one-dimensional many-fermion system is discussed. The model has a fairly realistic interaction between pairs of fermions. An exact calculation of the momentum distribution in the ground state is given. As shown, there is no discontinuity in the momentum distribution in this model at the Fermi surface, but that the momentum distribution has infinite slope there. Comparison with the results of perturbation theory for the same model is also presented, and it is shown that, for this case at least, the perturbation and exact answers behave qualitatively alike. Finally, the response of the system to external fields is also discussed. As shown, he did not solve his model properly because of the paradoxical fact that the density operator commutators, which always vanish for any finite number of particles, no longer vanish in the field-theoretic limit of a filled Dirac sea. In fact, the operators define a boson field, which is *ipso facto* associated with the Fermi–Dirac field. This observation to solve the model was used and was obtained the exact (and now nontrivial) spectrum, free energy, and dielectric constant. This was also extended to interactions, which are more realistic. According to Ref. [3], one powerful approach to 1*D*-lattice fermion systems is to utilize a particular continuum limit to derive a low-energy effective

model that can be solved analytically. For the simplest case of spinless fermions with local interactions away from half-filling, this approach leads to the so-called Luttinger model [1], which can be solved exactly using bosonization [2].

Exact solubility means a lot in this case: not only the partition function, but also all Green's functions of the Luttinger model can be computed exactly by analytical methods. This method can be generalized to 1*D* Hubbard-like systems and is the basis of a paradigm for 1*D* interacting fermion systems. In Ref. [3], a detailed derivation of a two dimensional (2*D*) low energy effective model for spinless fermions on a square lattice with local interactions is given. This derivation utilizes a particular continuum limit that is justified by physical arguments. It is shown that the effective model thus obtained can be treated by exact bosonization methods. It is also discussed how this effective model can be used to obtain physical information about the corresponding lattice fermion system.

According to Ref. [11], the problem of interacting fermions simplifies in one dimension. In a pioneering paper, Tomonaga treated the case of a two-body interaction, which is long ranged in real space. He showed that the low-energy excitations of the noninteracting as well as the interacting system can be described in terms of noninteracting bosons. The important idea to solve the case of interacting fermions was the observation that a long-range interaction in real space is short ranged in momentum space and therefore only particles and holes in the vicinity of the Fermi points are involved in the interacting ground state and states with low excitation energy. To obtain his results, Tomonaga linearized the energy dispersion around the two Fermi points $\pm k_F$. Luttinger later used a model with strictly linear energy dispersions, which is closely related to the massless Thirring's model. A very elegant method to calculate correlation functions for the model is the bosonization of the fermion field operator. The exponents of the anomalous power law decay of various correlation functions are determined by the anomalous dimension, which can be calculated explicitly for the Tomonaga–Luttinger (TL) model. It was an important observation of Haldane that the low-energy physics of the exactly solvable TL-model provides the generic scenario for one-dimensional fermions with repulsive interactions. Like in the Landau's Fermi-liquid picture, a few parameters completely determine the low energy physics.

Generally, they are as difficult to calculate as the Landau parameters. In contrast to the higher dimensional case, there are additional exactly solvable models, for which Haldane's Luttinger liquid scenario can be tested and the parameters determining the anomalous dimension can be calculated using the Bethe-ansatz technique. Another important manifestation of Luttinger liquids is called

spin–charge separation, *i.e.*, for low energy excitations, the charge and spin degrees are completely decoupled. This shows up, for example, in the spectral function of the one-particle Green's function, which largely determines the photoemission spectrum. Recent high-resolution photoemission experiments on quasi-one-dimensional organic conductors have been interpreted to show Luttinger-liquid behaviour.

In Ref. [12], it was investigated the electronic band structure of Pt-induced nanowires on Ge(001) [Pt/Ge(001) NWs] by angle-resolved photoelectron spectroscopy at 6 K. Single-domain samples of Pt/Ge(001) NWs were prepared on vicinal Ge(001) substrates. One of the bands disperses only in the nanowire direction, and its Fermi surface consists of strictly straight lines, indicating that it is an ideal one-dimensional metallic state. An energy distribution curve of the one-dimensional band is explained by a Fermi–Dirac-type spectral shape, which is against both a Luttinger liquid and Peierls instability schemes. In Ref. [13], dispersing 1D bands have been observed for the first time in an organic conductor by high-resolution photoemission experiments on TTFTCNQ (tetrathiafulvalene tetracyanoquinodimethane). Their properties are extremely unusual: the bandwidth is much larger than traditional estimates, and the quasi-particle states are strongly renormalized, with no weight at the chemical potential. A deep pseudogap around the Fermi energy persists, and even increases, up to room temperature. Also was reported a direct determination of k_F in this material, and the observation of the opening of a Peierls gap in the low-temperature charge-density wave phase. In Ref. [14], it was presented that the Luttinger liquids are paramagnetic one-dimensional metals without Landau quasi-particle excitations. The elementary excitations are collective charge and spin modes, leading to charge–spin separation. Correlation functions exhibit power-law behaviour. All physical properties can be calculated, *e.g.*, by bosonization, and depend on three parameters only: the renormalized coupling constant K_ρ, and the charge and spin velocities.

Also it was discussed the stability of Luttinger liquids with respect to temperature, interchain coupling, lattice effects and phonons, and list important open problems. In Ref. [15], it was compute mean field phase diagrams of two closely related interacting fermion models in two spatial dimensions (2D). The first is the so-called 2D t–t'–V model describing spinless fermions on a square lattice with local hopping and density–density interactions. The second is the so-called 2D Luttinger model that provides an effective description of the 2D t–t'–V model, and in which parts of the fermion degrees of freedom are treated exactly by bosonization. In mean-field theory, both models have a charge-density-wave (CDW) insta-

bility making them gapped at half-filling. The 2*D* $t-t'-V$ model has a significant parameter regime away from half-filling, where neither the CDW nor the normal states are thermodynamically stable. It was shown that the 2*D* Luttinger model allows obtaining more detailed information about this mixed region. In this work, the confinement of low-energy thermal excitations of spinons in $SmMnO_{3+\delta}$ was found in the form of excitations of the type of nanofragments of 1*D* charge and spin-density waves, characteristic for low-energy excitations of a metallic one-dimensional quantum Luttinger liquid.

2. MATERIAL AND METHODS

Samples of self-doped manganites $SmMnO_{3+\delta}$ ($\delta \cong 0.1$) were obtained from high-purity oxides of lanthanum, samarium and electrolytic manganese, taken in a stoichiometric ratio. The synthesized powder was pressed under pressure of 10 kbar into discs of 6 mm in diameter, 1.2 mm thick and sintered in air at a temperature of 1170°C for 20 h followed by cooling at a rate of 70°C/h. The resulting tablets were a single-phase ceramic according to x-ray data. X-ray studies were carried out with 300 K on DRON-1.5 diffractometer in radiation $NiK_{\alpha 1+\alpha 2}$. Symmetry and crystal lattice parameters were determined by the position and character splitting reflections of the perovskite-type pseudocubic lattice. Temperature and field dependences of dc magnetization were measured using a VSM EGG (Princeton Applied Research) vibrating magnetometer and a nonindustrial magnetometer in ZFC and FC modes. When measuring the temperature dependences of the magnetization $M(T)$ in the ZFC mode, the sample was first cooled to 4.2 K in a zero external magnetic field, followed by an increase in temperature to the required value. In the FC mode for measuring the magnetization $M(T)$, the sample was first cooled to 4.2 K in magnetic fields of various strengths, followed by heating. The field dependences of the magnetization $M(H)$ were measured during sample remagnetization at a temperature of 4.2 K in a wide range of magnetic fields in the ZFC and FC measurement modes.

3. EXPERIMENTAL RESULTS AND DISCUSSION

In this work, the field dependences of $SmMnO_{3+\delta}$ magnetization were investigated in the ZFC and FC measurement mode in the magnetic field range of ±5000 Oe (Figs. 1–4). The confinement of low-energy thermal excitations of spinons in $SmMnO_{3+\delta}$ was found in the form of excitations of the type of nanofragments of 1*D* charge and spin density waves, characteristic of low-energy excita-

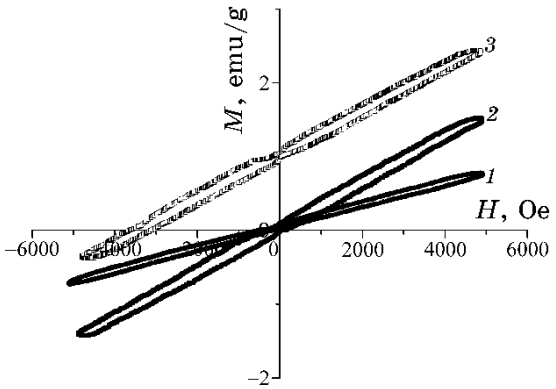

Fig. 1. Field dependences of magnetization of $SmMnO_{3+\delta}$ in the ZFC measurement mode in the form of isotherms of magnetization reversal of samples with different directions of growth of the external magnetic-field strength at $T = 0.6$ K (*1*) and $T = 4.2$ K (*2*). Field dependences of magnetization of $SmMnO_{3+\delta}$ at $T = 4.2$ K in the FC measurement mode (*3*).

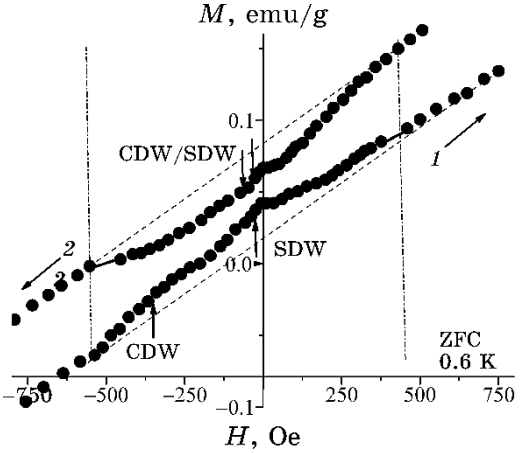

Fig. 2. Field dependences of magnetization of $SmMnO_{3+\delta}$ at $T = 0.6$ K in the ZFC measurement mode in the form of isotherms 1 and 2 of magnetization reversal of samples with different directions of growth of the external magnetic-field strength. As can be seen in this figure, during the magnetization reversal of the sample in the ZFC measurement mode, two peak features of magnetization are formed near $H = 0$ Oe in the range of magnetic fields of ±500 Oe.

tions of a metallic one-dimensional quantum Luttinger liquid.

With an increase in the external magnetic-field strength, a second-order quantum phase transition of the QSL to the Luttinger liquid state occurs, induced by an increase in the external magnetic-

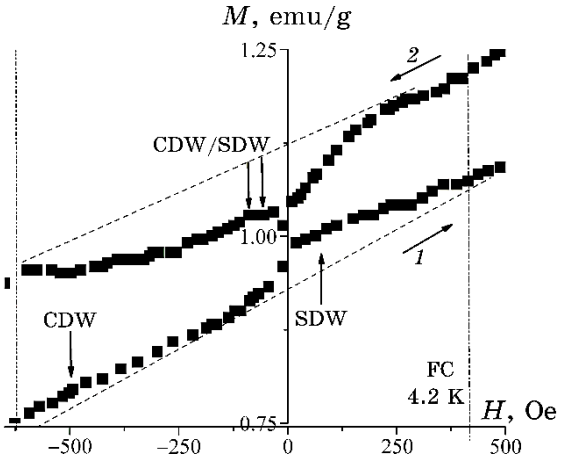

Fig. 3. Field dependences of magnetization of $SmMnO_{3+\delta}$ at $T = 4.2$ K in FC measurement mode in the form of isotherms 1 and 2 of magnetization reversal of samples with different directions of growth of the external magnetic-field strength. During the magnetization reversal of the sample in FC measurement mode, two peak features of magnetization are formed near $H = 0$ Oe in the magnetic-field range of ±500 Oe.

field strength. As a result of this transition, near $H = 0$ Oe, peak features of 'supermagnetization' are formed with varying degrees of their overlap, characteristic of the excitation of gapless decoupled charge and spin density waves in a Luttinger liquid. As can be seen in these figures, during the magnetization reversal in two measurement modes, two peak features of the magnetization $M(H)$ near $H = 0$ Oe are formed in the range of magnetic fields of ±500 Oe (Figs. 2, 3).

The difference between the two peak features of isotherms 1 and 2 of the magnetization reversal near $H = 0$ Oe, which depends on the direction of growth of the external magnetic-field strength, is noteworthy. As can be seen in Figs. 3 and 4, with an increase in the magnetic field in the positive direction (isotherm 1), separate CDW and SDW states are realized, which are not related to each other. At the same time, when the sign of the field growth changes to the opposite (isotherm 2), we observe near $H = 0$ Oe related CDW/SDW states that stimulates the transition of the system of zigzag AFM spin chains weakly coupled by the exchange interaction into a state similar to a metallic Luttinger liquid.

We believe that such behaviour of the magnetization in the low-temperature region is caused by the fact that the transverse component of the external magnetic field closes the spinon gap Δ_s for $SmMnO_{3+\delta}$. A characteristic feature of this state is the spatial sepa-

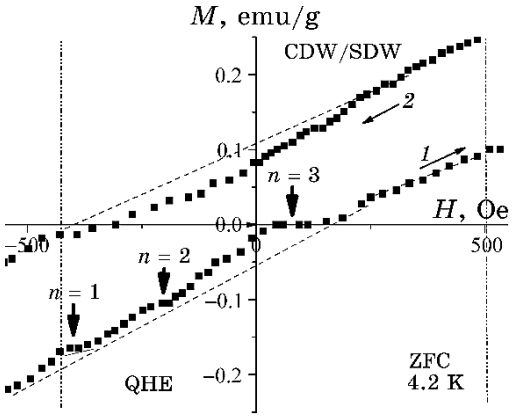

Fig. 4. Field dependences of magnetization of $SmMnO_{3+\delta}$ at $T = 4.2$ K in the ZFC measurement mode in the form of isotherms 1 and 2 of magnetization reversal of samples with different directions of growth of the external magnetic-field strength. As can be seen in the figure, during the magnetization growth of the sample in the ZFC measurement mode, three unusual step-like features of magnetization $M(H)$ are formed near $H = 0$ Oe that characteristic for forming of Landau bands in a Luttinger liquid. We explain the formation of a wide dip in magnetization near zero external magnetic field in isotherm 2 with the decay of the bound state of charge/spin density waves (CDW/SDW) during the process of sample demagnetization.

ration of charge and spin excitations. In this quasi-one-dimensional state, multiparticle excitations in the form of 1*D* charge and spin density waves, which obey the Bose statistics, dominate and largely replace elementary excitations in the form of spinon pairs. Of interest is the result that decoupled charge/spin density waves are formed in isotherms 1, whereas coupled 1*D* CDW/SDW collective excitation of the quantum spin liquid arises in isotherms 2 near zero magnetic field. Excitation of such 1*D* collective states in an external magnetic field was observed earlier in systems of weakly-coupled exchange Heisenberg and Ising AFM spin chains with different configurations and degrees of anisotropy. According to these studies, even a weak increase in the transverse component of the external magnetic field can lead to further confinement of spinon pairs, which is accompanied by the appearance of gapless modes of natural longitudinal oscillations of the spin chain system.

According to Ref. [6], in the limit of low excitation energies of a one-dimensional Mott dielectric, spin–charge separation occurs, which made it possible to accurately calculate their dynamic spectral function of charge density and spin $A(\omega, k_F+q)$. It was found that, in a one-dimensional Mott dielectric at a temperature $T = 0$ K,

the excitation and annihilation operators of an ensemble of fermions with left and right directions of motion separate them into separate charge and spin regions as a result of bosonization in the form of fragments of separated one-dimensional charge density waves (CDW) and spin density waves incommensurate with the crystal lattice. We believe that the appearance of two unusual peak features of isotherms 1 and 2 of the magnetization reversal of $SmMnO_{3+\delta}$ near zero magnetic field are a natural consequence of the spin–charge separation characteristic of the previously well-studied theoretically one-dimensional Mott insulator in the state of a quantum Luttinger liquid [6, 7]. Attention is drawn to the difference between the two peak features of isotherms 1 and 2 of the magnetization reversal near $H = 0$ Oe, which depends on the direction of growth of the external magnetic-field strength. As can be seen in Figs. 2, 3, with the increase of the magnetic field in the positive direction (isotherm 1), separate CDW and SDW states are realized, which are not related to each other. At the same time, when the sign of the field growth changes to the opposite (isotherm 2), we observe near $H = 0$ Oe the CDW/SDW states related to each other that stimulates the transition of the system of zigzag AFM spin chains weakly coupled by the exchange interaction to a state similar to the metallic Luttinger liquid. We believe that such behaviour of magnetization in the low-temperature region is caused by the fact that the transverse component of the external magnetic field closes the spinon gap Δ_s for $SmMnO_{3+\delta}$. A characteristic feature of this state is the spatial separation of charge and spin excitations.

In this quasi-one-dimensional state, multiparticle excitations in the form of 1*D* charge and spin density waves, which obey the Bose statistics, dominate and largely replace elementary excitations in the form of spinon pairs. Of interest is the result that decoupled charge/spin density waves are formed in isotherms 1, whereas coupled 1*D* CDW/SDW collective excitation of the quantum spin liquid arises in isotherms 2 near zero magnetic field. Excitation of such 1*D* collective states in an external magnetic field was observed earlier in systems of weakly-coupled exchange Heisenberg and Ising AFM spin chains with different configurations and degrees of anisotropy. According to these studies, even a weak increase in the transverse component of the external magnetic field can lead to further confinement of spinon pairs, which is accompanied by the appearance of gapless modes of natural longitudinal oscillations of the spin chain system.

Field dependences of magnetization $M(H)$ of $SmMnO_{3+\delta}$ at $T = 4.2$ K in the ZFC measurement mode (Fig. 4) differ greatly from the graphs presented in Figs. 2, 3. As can be seen in these figures, during the magnetization of the sample in the ZFC measurement mode,

three step-like features of magnetization are formed near $H = 0$ Oe in the range of magnetic fields of ±500 Oe (isotherm 1). During the process of demagnetization of the sample (isotherm 2) in the magnetic-field range of ±500 Oe, a wide dip is formed with an extreme drop in the magnetization of the sample $M(H)$ near the zero field. We explain the formation of a wide dip in magnetization near zero external magnetic field in isotherm 2 with the decay of the bound state of charge/spin density waves (CDW/SDW) during the process of sample demagnetization.

We assume that step-like features of field dependences of magnetization of $SmMnO_{3+\delta}$ (Fig. 4) are similar characteristic of quantum Hall effect for massless Dirac fermions in graphene [16–18]. In Ref. [16], it first was reported a condensed matter system, where electron transport is essentially governed by the Dirac equation and charge carriers mimic relativistic particles with zero mass and an effective 'speed of light' $c^* \approx 10^6$ m/s. The unusual response of massless fermions to magnetic field is highlighted further by their behaviour in the high-field limit, where there is the quantum Hall effect (QHE). It was shown the Hall conductivity σ_{xy} of graphene plotted as a function of electron and hole concentrations in a constant field **B**. Pronounced QHE plateaux are clearly seen but, surprisingly, they do not occur in the expected sequence $\sigma_{xy} = (4e^2/h)N$, where N is integer. On the contrary, the plateaux correspond to half-integer ν, so that the first plateau occurs at $2e^2/h$ and the sequence is $(4e^2/h)(N + 1/2)$. Note that the transition from the lowest hole (ν $-1/2$) to lowest electron ($\nu = +1/2$) Landau level (LL) in graphene requires the same number of carriers ($\Delta n = 4B/\varphi_0 \approx 1.2 \cdot 10^{12}$ cm^{-2}) as the transition between other nearest levels (cf. distances between minima in ρ_{xx}).

This one results in a ladder of equidistant steps in σ_{xy}, which are not interrupted, when passing through zero. To emphasize this highly unusual behaviour, it was shown that σ_{xy} for a graphite film consisting of only two graphene layers, where the sequence of plateaux returns to normal and the first plateau is at $4e^2/h$, as in the conventional QHE. It was attributed this qualitative transition between graphene and its two-layer counterpart to the fact that fermions in the latter exhibit a finite mass near $n \cong 0$ (as found experimentally and to be published elsewhere) and can no longer be described as massless Dirac particles. These studies of graphene have revealed a variety of unusual phenomena characteristic of two-dimensional ($2D$) Dirac fermions. In particular, it was observed that: a) the integer quantum Hall effect in graphene is anomalous in that it occurs at half-integer filling factors; b) graphene conductivity never falls below a minimum value corresponding to the conductance quantum e^2/h, even when carrier concentrations tend to

zero; c) the cyclotron mass m_c of massless carriers with energy E in graphene is described by equation $E = m_c c_*^2$; d) Shubnikov–de Haas oscillations in graphene exhibit a phase shift of π due to Berry's phase. As can be seen in Fig. 4 in this work, during the magnetization growth of the sample in the ZFC measurement mode, three step-like features of magnetization $M(H)$ are formed near $H = 0$ Oe that is characteristic for forming three Landau bands in a Luttinger liquid.

According to Ref. [17], when electrons are confined in two-dimensional (2*D*) materials, quantum-mechanically enhanced transport phenomena, as exemplified by the quantum Hall effect, can be observed. Graphene, an isolated single atomic layer of graphite, is an ideal realization of such a 2*D* system. The low-energy band structure of graphene can be approximated as cones located at two inequivalent Brillouin-zone corners. In these cones, the 2*D* energy dispersion relation is linear and the electron dynamics can be treated as 'relativistic,' where the Fermi velocity v_F of the graphene plays the role of the speed of light. In particular, at the apex of the cones (termed Dirac point), electrons and holes (particles and antiparticles) are degenerate. Landau level (LL) formation for electrons in such a system under a perpendicular magnetic field, **B**, has been studied theoretically using an analogy to the $2 + 1$ dimensional quantum electrodynamics. The exceptionally high-mobility graphene samples allow investigating transport phenomena in the extreme magnetic quantum limit, such as the QHE. In this work, the overall positive R_{xy} indicates that the contribution is mainly from electrons. At high external magnetic fields $B \cong 1–8$ T, $R_{xy}(B)$ exhibits step-like features (plateaus), and R_{xx} is vanishing, which are the hallmark of the QHE. At least two well-defined plateaus are observed before the QHE features transform into Shubnikov–de Haas oscillations at lower magnetic field. The quantization of R_{xy} for these first two plateaus is better than 1 part in 10^4, precise within the instrumental uncertainty.

In Ref. [18], the quantum Hall effect with a Berry's phase of π is demonstrated on a single graphene layer grown on the *C*-face of 4*H* silicon carbide. The mobility is of $\cong 20000$ cm^2/(V·s) at 4 K and 15000 cm^2/(V·s) at 300 K despite contamination and substrate steps. This is comparable to the best-exfoliated graphene flakes on SiO_2 and an order of magnitude larger than Si-face epitaxial graphene monolayers. The QHE is well resolved in this sample, which shows quantum Hall plateaus in the magnetic-field dependence of the Hall resistance, as first observed in exfoliated graphene flakes on SiO_2. The Hall plateaus correspond to transverse resistances $\rho_{xy} = (h/4e^2)/(n + 1/2)$ for $n = 0$ to 3, where n is the Landau level index, which establishes the nontrivial Berry's phase of π. The longi-

tudinal resistivity ρ_{xx} shows the characteristic Shubnikov–de Haas (SdH) oscillations (SdHOs), in which Landau levels from $n = 0$ up to $n = 8$ are easily recognized. The SdHOs develop into the QHE in high fields, manifested by characteristic zero resistance minima and Hall plateaus.

According to Ref. [19], the electronic properties of a graphite monolayer have attracted theoretical interest due to a Dirac-type spectrum of charge carriers in this gapless semiconductor. Recently, Novoselov *et al.* fabricated ultra-thin graphitic devices including monolayer structures. This was followed by further observations of the classical and quantum Hall effects in such systems confirming the expectations of an unusual phase of Shubnikov–de Haas oscillations and QHE plateaus sequencing, as manifestations of a peculiar magneto-spectrum of chiral Dirac-type quasi-particles containing a Landau level at zero energy. In Ref. [19], it was studied an effective two-dimensional Hamiltonian to describe the low-energy electronic excitations of a graphite bilayer, which correspond to chiral quasi-particles with a parabolic dispersion exhibiting Berry's phase of 2π. Its high-magnetic-field Landau level spectrum consists of almost equidistant groups of four-fold degenerate states at finite energy and eight zero-energy states. This can be translated into the Hall conductivity dependence on carrier density, $\sigma_{xy}(N)$, which exhibits plateaus at integer values of $4e^2/h$ and has a 'double' $8e^2/h$ step between the hole and electron gases across zero density, in contrast to $(4n + 2)e^2/h$ sequencing in a monolayer.

According to Ref. [20], the half-integer quantum Hall effect in single-layer graphene (SLG) 1, 2 and the unconventional quantum Hall effect in bilayer graphene (BLG) 3 reveal spin- and valley-degenerate relativistic Landau levels. Due to the extremely large Landau-level splitting, completely-resolved levels can be observed up to room temperature. However, even at very high perpendicular magnetic fields, the Zeeman splitting within one Landau level is negligible smaller compared to the Landau-level splitting and, more importantly, the Landau-level width generally exceeds the spin splitting. Exceptionally, the zeroth Landau level in SLG becomes extremely narrow at magnetic fields $B > 20$ T that allows an experimental observation of a spin-related gap opening at magnetic fields $B > 20$ T. Another observation of a spin degeneracy lifting with an effective g factor $g^* = 2$ was reported for $\nu = \pm 4$ in SLG for magnetic fields $B > 30$ T, combined with lifting the valley degeneracy at $\nu = \pm 1$. In Ref. [20], it was determined the spin splitting of broadened Landau levels for SLG and BLG by measuring SdH oscillations in tilted magnetic fields. This technique allows adjusting the ratio between the spin splitting and the Landau-level splitting by controlling the ratio between a total magnetic field and a component per-

pendicular to a two-dimensional graphene flake. Using the well-established Lifshitz–Kosevich formula, it was determined the product of the effective g factor and cyclotron mass m^*g^* from the angular dependence of the SdH amplitudes, and it was found that g^* is enhanced compared to the free-electron value.

Similar stepwise oscillations of magnetization were previously discovered by us for $SmMnO_{3+\delta}$ in the temperature dependences of $M(T)$ [21]. According to Ref. [21], quantum oscillations of the temperature dependence $M(T)$ of the magnetization of $SmMnO_{3+\delta}$ (QHE) measured in the strong magnetic field $H = 3.5$ kOe in the temperature range 4.2–12 K have an unusual form. With an increase in the field to $H = 3.5$ kOe, a step-like quantization of the spinon spectrum appeared in the form of the formation of threshold features of magnetization in the Landau bands $n = 1$, $n = 2$, and $n = 3$ in the kind of steps (plateaus) corresponding to the integer filling of three Landau bands with a finite gap by spinons. As the temperature rises, the height of the thresholds and the width of the steps increase. Emergence of new quantum oscillations of the magnetization temperature dependences in the strong field regime of measurements is caused by the Landau quantization by the gauge field of the spinon gas with a fractional spin $S = 1/2$, moving on circular orbits in the direction transverse to the direction of the 'magnetic' component B of the gauge field.

4. CONCLUSIONS

According to the theory, in the limit of low excitation energies of a one-dimensional Mott dielectric, spin–charge separation occurs, which made it possible to accurately calculate their dynamic spectral function of charge density and spin $A(\omega, k_F + q)$. It was found that in a one-dimensional Mott dielectric at a temperature $T = 0$ K, the excitation and annihilation operators of an ensemble of fermions with left and right directions of motion separate them into separate charge and spin regions as a result of bosonization in the form of fragments of separated one-dimensional charge density waves (CDW) and spin density waves incommensurate with the crystal lattice. We believe that the appearance of two unusual peak features of isotherms 1 and 2 of the magnetization reversal of $SmMnO_{3+\delta}$ near zero magnetic field are a natural consequence of the spin–charge separation characteristic of a quantum Luttinger liquid. Attention is drawn to the difference between the two peak features of isotherms 1 and 2 of the magnetization reversal near $H = 0$ Oe, which depends on the direction of growth of the external magnetic-field strength. As can be seen in Figs. 2, 3, with the increase of the magnetic field in the positive direction (isotherm 1) separate

CDW and SDW states are realized, which are not related to each other. At the same time, when the sign of the field growth changes to the opposite (isotherm 2), we observe near $H = 0$ Oe the CDW/SDW states related to each other that stimulates the transition of the system of zigzag AFM spin chains weakly coupled by the exchange interaction to a state similar to the metallic Luttinger liquid. We believe that such behaviour of magnetization in the low-temperature region is caused by the fact that the transverse component of the external magnetic field closes the spinon gap Δ_s in $SmMnO_{3+\delta}$. A characteristic feature of this state is the spatial separation of charge and spin excitations.

In this quasi-one-dimensional state, multiparticle excitations in the form of $1D$ charge and spin density waves, which obey the Bose statistics, dominate and largely replace elementary excitations in the form of spinon pairs. Of interest is the result that decoupled charge/spin density waves are formed in isotherms 1, whereas coupled $1D$ CDW/SDW collective excitation of the quantum spin liquid arises in isotherms 2 near zero magnetic field. Excitation of such $1D$ collective states in an external magnetic field was observed earlier in systems of weakly-coupled exchange Heisenberg and Ising AFM spin chains with different configurations and degrees of anisotropy. According to these studies, even a weak increase in the transverse component of the external magnetic field can lead to further confinement of spinon pairs, which is accompanied by the appearance of gapless modes of natural longitudinal oscillations of the spin chain system.

We assume that step-like features of field dependences of magnetization of $SmMnO_{3+\delta}$ at temperature $T = 0.6$ K are similar characteristic of quantum Hall effect for massless Dirac fermions in graphene. In these works, it was firstly observed a condensed matter system, where electron transport is essentially governed by the Dirac equation and charge carriers mimic relativistic particles with zero mass and an effective 'speed of light' $c^* \cong 10^6$ m/s. These studies of graphene have revealed a variety of unusual phenomena characteristic of two-dimensional ($2D$) Dirac fermions. In particular, it was observed that: a) the step-like quantum Hall effect in graphene is anomalous in that it occurs at half-integer filling factors; b) graphene conductivity never falls below a minimum value corresponding to the conductance quantum e^2/h, even when carrier concentrations tend to zero; c) the cyclotron mass m_c of massless carriers with energy E in graphene is described by equation $E = m_c c^{*2}$; d) Shubnikov–de Haas oscillations in graphene exhibit a phase shift of π due to Berry's phase. During the magnetization growth of the sample in the ZFC measurement mode, three step-like features of magnetization $M(H)$ are formed near $H = 0$ Oe that is characteristic

for forming three Landau bands in a Luttinger liquid.

The low-energy band structure of graphene can be approximated as cones located at two inequivalent Brillouin-zone corners. In these cones, the 2*D* energy dispersion relation is linear and the electron dynamics can be treated as 'relativistic', where the Fermi velocity v_F of the graphene plays the role of the speed of light. In particular, at the apex of the cones (termed Dirac point), electrons and holes (particles and antiparticles) are degenerate. Landau level (LL) formation for electrons in such system under a perpendicular magnetic field, **B**, has been studied theoretically using an analogy to the $2+1$ dimensional quantum electrodynamics. The exceptionally high-mobility graphene samples allow investigating transport phenomena in the extreme magnetic quantum limit, such as the QHE. It was shown the overall positive R_{xy} that indicates the contribution from electrons mainly. At high external magnetic fields $B \cong 1{-}8$ T, $R_{xy}(B)$ exhibits step-like features (plateaus), and R_{xx} is vanishing, which are the hallmark of the QHE. At least two well-defined plateaus are observed before the QHE features transform into Shubnikov–de Haas oscillations at lower magnetic field. The quantization of R_{xy} for these first two plateaus is better than 1 part in 10^4, precise within the instrumental uncertainty.

REFERENCES

1. J. M. Luttinger, *J. Math. Phys.*, **4**: 1154 (1963); https://doi.org/10.1063/1.1704046
2. D. C. Mattis and E. H. Lieb, *J. Math. Phys.*, **6**: 304 (1965); doi:10.1063/1.1704281
3. E. Langmann, *arXiv:0903.0055v3 [math-ph]* 14 Apr 2010.
4. U. Ledermann, A dissertation submitted to the ETH Zürich for the degree of the Doctor of Natural Sciences (2001).
5. E. Langmann, *arXiv:math-ph/0606041v3* 14 Apr 2010.
6. J. Voit, *arXiv:cond-mat/9510014v1* 29 Sep 1995.
7. F. D. M. Haldane, *J. Phys. C*, **14**: 2585 (1981); doi:10.1088/0022-3719/14/19/010
8. J.-S. Caux and C. M. Smith, *arXiv:1702.03735v1 [cond-mat.str-el]* 13 Feb 2017.
9. J. Liang and J. Hu, *Quantum Frontiers*, **4**: 1 (2025); https://doi.org/10.3389/fphy.2025.1541888
10. S. Rao and D. Sen, *arXiv:cond-mat/0005492v2* 6 Jul 2001.
11. K. Schönhammer and V. Meden, *arXiv:cond-mat/9606018v1* 5 Jun 1996.
12. K. Yaji, I. Mochizuki, S. Kim, Y. Takeichi, A. Harasawa, Y. Ohtsubo, P. Le Fèvre, F. Bertran, A. Taleb-Ibrahimi, A. Kakizaki, and F. Komori, *Phys. Rev. B*, **87**: 241413(R) (2013); https://doi.org/10.1103/PhysRevB.87.241413
13. F. Zwick, D. Jérome, G. Margaritondo, M. Onellion, J. Voit, and M. Grioni, *Phys. Rev. Lett.*, **81**: 2974 (1998);

https://doi.org/10.1103/PhysRevLett.81.2974
14. J. Voit, *arXiv:cond-mat/0005114v1 [cond-mat.str-el]* 5 May 2000.
15. J. de Woul and E. Langmann, *arXiv:0907.1277v2 [math-ph]* 16 Apr 2010.
16. K. S. Novoselov, A. K. Geim, S. V. Morozov, D. Jiang, M. I. Katsnelson, I. V. Grigorieva, S. V. Dubonos, and A. A. Firsov, *Nature (London)*, **438**: 197 (2005); https://doi.org/10.1038/nature04233438
17. Y. Zhang, Y.-W. Tan, H. Stormer, and P. Kim, *Nature (London)*, **438**: 201 (2005); https://doi.org/10.1038/nature04235
18. X. Wu, Y. Hu, M. Ruan, N. K. Madiomanana, J. H. Hankinson, M. Sprinkle, C. Berger, and W. A. de Heer, *Applied Physics Letters*, **95**, No. 22: 223108 (2009); doi:10.1063/1.3266524. hal-01002933
19. E. McCann and V. I. Fal'ko, *arXiv:cond-mat/0510237v2 [cond-mat.mes-hall]* 3 Mar 2006.
20. E. V. Kurganova, H. J. van Elferen, A. McCollam, L. A. Ponomarenko, K. S. Novoselov, A. Veligura, B. J. van Wees, J. C. Maan, and U. Zeitler, *Phys. Rev. B*, **84**: 121407(R) (2011); doi:10.1103/PhysRevB.84.121407
21. F. N. Bukhanko and A. F. Bukhanko, *Low Temp. Phys.*, **47**: 937 (2021); https://doi.org/10.1063/10.0006569

Наносистеми, наноматеріали, нанотехнології
Nanosistemi, Nanomateriali, Nanotehnologii
2026, т. 24, № 1, сс. 17–31
https://doi.org/10.15407/nnn.24.01.0017

PACS numbers: 03.65.Ta, 03.65.Yz, 03.67.-a, 03.67.Lx, 73.21.La, 85.25.Am, 85.35.Be

Quantum Fisher Information Tensor and Diagnostic Metrics for Qubit Architectures: Towards Informational Nanotechnologies at the Nanoscale

G. P. Chuiko, Y. S. Darnapuk, and P. K. Kravchenko

Petro Mohyla Black Sea National University,
10, 68-Desantnykiv Str.,
UA-54009 Mykolaiv, Ukraine

Quantum computing is increasingly regarded as a part of information nanotechnology, where reliable diagnostics under realistic noise conditions are crucial. Depolarization channels are commonly used as a fundamental model of quantum noise, but systematic diagnostic frameworks are still underdeveloped. We introduce a structured approach as to computational methods for depolarization channels, establish formal criteria such as metric reliability, and develop diagnostic maps and quantum Fisher information (QFI) tensors. Symbolic modelling of density matrices under noise allows for the analytical calculation of QFI components, revealing the isotropy and degeneracy of tensors at the critical point of Bloch-sphere collapse. Comparing quantum metrics, including purity, entropy, accuracy, Bloch norm, and Bloch-angle deviation (BAD), uncovers different sensitivities. Notably, purity and entropy reach their extremes with minimal uncertainty, while the Bloch norm and BAD quickly detect orientation loss and the inversion of the Bloch vector. The classification of subcritical Bloch-sphere compression, critical collapse, and supercritical inversion is validated, with BAD serving as an operational boundary marker. Potential applications include reliability testing in quantum processors, decoherence diagnostics in nanoscale devices, and benchmarking quantum gates. In Ukraine, this work is among the first systematic studies of a depolarizing quantum-noise channel, enhancing national expertise in diagnostic tools for quantum nanotechnology.

Квантові обчислення все частіше розглядають як частину інформаційних нанотехнологій, де надійна діягностика в реалістичних умовах шуму є критично важливою. Канали деполяризації зазвичай використовують як фундаментальний модель квантового шуму, але систематичні діягностичні рамки все ще недостатньо розроблено. Ми впроваджуємо структурований підхід щодо обчислювальних методів для каналів деполяризації, встановлюємо формальні критерії, такі як метрична на-

дійність, і розробляємо діягностичні карти та тензори квантової інформації за Фішером (КІФ). Символічне моделювання матриць густини в умовах шуму уможливлює аналітично розраховувати компоненти КІФ, виявляючи ізотропію та виродження тензорів у критичній точці колапсу Блохової сфери. Порівняння квантових метрик, включаючи чистоту, ентропію, точність, Блохову норму та девіяцію Блохового кута (ДБК), виявляє різну чутливість. Примітно, що чистота й ентропія сягають своїх крайнощів з мінімальною невизначеністю, тоді як Блохова норма та ДБК швидко виявляють втрату орієнтації й інверсію Блохового вектора. Класифікацію субкритичного стиснення Блохової сфери, критичного колапсу та надкритичної інверсії підтверджено, причому ДБК служить операційним граничним маркером. Потенційні застосування включають тестування надійности квантових процесорів, діягностику декогеренції в нанорозмірних пристроях і порівняльну аналізу квантових вентилів. Ця робота є одним з перших в Україні систематичних досліджень деполяризувального квантового шумового каналу, що розширює національну експертизу в діягностичних інструментах для квантових нанотехнологій.

Key words: quantum nanotechnology, depolarization channel, quantum Fisher information, Bloch-sphere collapse, diagnostic metrics, Bloch-angle deviation.

Ключові слова: квантова нанотехнологія, канал деполяризації, квантова інформація за Фішером, колапс Блохової сфери, діягностичні метрики, девіяція Блохового кута.

(Received 12 January, 2026)

1. INTRODUCTION

Quantum computing is increasingly seen as a specialized area of information nanotechnology for three main reasons. First, it utilizes qubits, nanoscale devices developed through nanotechnology. Second, qubit behaviour and information processing are governed by quantum physics, including superposition, entanglement, and decoherence. Finally, quantum computing introduces a novel method of processing information at the quantum nanoscale, positioning it as an innovative tool for data management.

The intersection of quantum computing and nanotechnology presents significant potential, as quantum computation depends on nanoscale precision and materials [1]. Nanoscale materials are crucial for advancing quantum technologies, including computation and sensing [2]. Moreover, nanotechnology is essential for the creation and control of qubits, where quantum effects exclusively emerge at the nanoscale [3].

Therefore, quantum computing should no longer be viewed mere-

ly as a technology that utilizes quantum phenomena; it should be regarded as informational nanotechnology.

Despite advancements in quantum computing and nanotechnology for qubit design, there is a lack of robust diagnostic frameworks for assessing qubit stability and reliability under realistic noise conditions. It often leaves a gap between theoretical research and practical engineering applications in quantum processors.

Although the depolarization channel is widely recognized as a fundamental model for quantum noise [4], there is a lack of understanding of how to systematically quantify and diagnose quantum information loss at the device level. Current methods do not fully utilize quantum Fisher information and related tensor-based metrics to evaluate the informativeness and robustness of qubit states against environmental disturbances.

The depolarization channel is an essential model of quantum noise that explains how quantum information is lost due to environmental disturbances. In this channel, a quantum state is randomly affected by one of the Pauli operators, leading to increased mixedness and a loss of coherence. Superconducting qubits, with short coherence times and strong environmental coupling, are especially vulnerable to this noise [5–7].

This work addresses this gap by developing a comprehensive, computation-based diagnostic framework that links quantum information theory with engineering practice.

By introducing formal criteria like metric validity and self-boundedness and by automating the creation of diagnostic maps and quantum Fisher information tensors, this research provides new tools for real-time evaluation and optimization of nanoscale quantum architectures.

The authors connect quantum information theory with engineering models and analyse quantum channels affected by depolarizing noise [5, 8]. Key aspects include critical points for orientation loss, criteria for metric usability, and self-boundedness for evaluating quantum states in single-shot measurements.

This study advances quantum diagnostics by providing a framework for nanoscale quantum structures in informational nanotechnology [9, 10].

2. SYMBOLIC MODELLING METHODS

Our approach is based on a fundamental concept in quantum mechanics, namely, the density matrix. The density matrix describes the complete statistical state of a quantum system. It extends the idea of a state vector, allowing us to explain both coherent and incoherent superpositions (*i.e.*, mixed states) arising from uncertainty

or environmental factors. This framework enables us to calculate expectation values, entropies, and diagnostic metrics, including quantum Fisher information (QFI), purity, and fidelity [10].

Let the density matrix of a pure state of a qubit be ρ. Then, one can write down the standard expression for the matrix of a noisy state [5]:

$$\rho_n = (1-p)\rho + \frac{p}{3}(X\rho X + Y\rho Y + Z\rho Z)\,. \tag{1}$$

In this context, X, Y, and Z represent the well-known Pauli matrices associated with the corresponding quantum gates, while p indicates the depolarization rate [5]. This demonstrates that there is a $(1-p)$ probability that the qubit state remains unchanged. Conversely, there p is a probability that the qubit experiences an equal mixture of three errors.

If one chooses the initial pure state of a qubit in the form

$$|\psi\rangle = \cos\left(\frac{\theta}{2}\right)^2 |0\rangle + \exp(-i\varphi)\sin\left(\frac{\theta}{2}\right)^2 |1\rangle\,, \tag{2}$$

where θ, φ are the quantum state angular co-ordinates on the Bloch-sphere surface, then, Eq. (1) is as follows:

$$\rho_n = \begin{pmatrix} \dfrac{1+\lambda\cos(\theta)}{2} & \dfrac{\lambda\sin(\theta)}{2}\exp(i\varphi) \\ \dfrac{\lambda\sin(\theta)}{2}\exp(-i\varphi) & \dfrac{1-\lambda\cos(\theta)}{2} \end{pmatrix}, \tag{3}$$

where $\lambda = 1 - 4p/3$. If one sets $\lambda = 1$ (that is, $p = 0$), then, they get the density matrix ρ for a pure initial state.

A couple of essential nuances must be addressed before proceeding with the analysis.

Second, the admissible range of the Bloch-sphere shrink parameter λ requires clarification. In the standard formulation, one typically defines: Then the Kraus probability parameter range is $p \in [0, 3/4]$.

However, several sources [8–11] extend the range to $\lambda \in [-1/3, 1]$. This broader interval arises naturally when the Kraus parameter is interpreted as a probability ($p \in [0,1]$), and it still preserves the channel's entirely positive, trace-preserving (CPTP) character. The extended range allows one to analyse both the critical point (with the collapse of the Bloch sphere at $p = 3/4$) and the overcritical regime, where the Bloch sphere inverts for the noisy state.

In the following sections, we accept the expanded range [8–11] for λ, as it offers a more symmetric and metrically meaningful

framework for quantum metrological diagnostics.

Quantum Fisher Information (QFI) is a key concept in quantum metrology, because it defines the ultimate limit on the accuracy of parameter estimation [10]. Often called a monotonic measure, QFI functions as the quantum equivalent of classical Fisher Information (CFI) [12]. While CFI measures how a statistical probability distribution changes with parameter variations, QFI shows how a quantum state responds to tiny changes in a selected parameter.

The Quantum Fisher Information (QFI) is specifically defined for a quantum state with respect to a particular parameter. It quantifies the sensitivity of that state to changes in the parameter through the geometry of quantum statistical manifolds. In this way, QFI establishes a practical connection between the structure of quantum states and the maximum measurement precision achievable [10].

The calculation of QFI using symmetric logarithmic derivatives (SLDs) is explained in Ref. [12] and clarified further in Ref. [13]. In this study, we adopt the methods described in those sources. While the approaches in Refs. [12] and [13] offer analytical formulas for the components of the QFI metric tensor in simple quantum systems, it is essential to note that 'standard numerical procedures based on eigen decomposition quickly become impractical with increasing system size' [10].

The noisy density matrix (3) depends on three parameters: either (λ, θ, φ) or equivalent (p, θ, φ), with the Kraus probability (p) offering the more straightforward physical interpretation. Consequently, the quantum Fisher information (QFI) metric tensor is defined as a 3×3 matrix

$$\mathbf{F}(p,\theta,\varphi) = \begin{pmatrix} F_{pp} & F_{p\theta} & F_{p\varphi} \\ F_{\theta p} & F_{\theta\theta} & F_{\theta\varphi} \\ F_{\varphi p} & F_{\kappa\theta} & F_{\varphi\varphi} \end{pmatrix}. \quad (4)$$

Similarly, any quantum metric (m) derived from the density matrix can be expressed as a function $m(p, \theta, \varphi)$.

The quantum Cramér–Rao bound (QCRB) establishes the minimal achievable variance of an unbiased estimator for a single-shot measurement and is a cornerstone of quantum metrology [14, 15]. For a scalar metric observable, the bound is expressed in terms of the gradient and the inverse of the QFI matrix:

$$\Delta_m = \nabla m(p,\theta,\varphi)^{\dagger} \cdot \mathbf{F}^{-1}(p,\theta,\varphi) \cdot \nabla m(p,\theta,\varphi). \quad (5)$$

The QFI matrix defines the geometry of the quantum statistical manifold, while the gradient maps the metric's dependence on this

geometry. In turn, quadratic form (5) provides the tightest lower bound on the variance of the single-shot estimation for the metric.

Let us consider the Bloch vector of a noisy state, for example,

$$\mathbf{b}_n = \begin{pmatrix} Tr(\rho_n X) \\ Tr(\rho_n Y) \\ Tr(\rho_n Z) \end{pmatrix} = \begin{pmatrix} \lambda \sin(\theta)\cos(\varphi) \\ -\lambda \sin(\theta)\sin(\varphi) \\ \lambda \cos(\theta) \end{pmatrix}. \quad (6)$$

The Euclidean norm of this vector, which is clearly equal to the absolute value of λ, can serve as a scalar measure that depends solely on the Kraus parameter, since λ is defined as $(1 - 4p/3)$. This scalar captures the isotropic compression of the Bloch sphere caused by the depolarizing noise channel. At the critical point ($p = 3/4$ and $\lambda = 0$), the Bloch vector completely collapses, and for $\lambda < 0$, it inverts, marking the transition into the overcritical regime.

Additionally, one can calculate the variance (or its square root, called uncertainty) of this measure, if the quantum Fisher information tensor (QFI) is known. This is especially relevant for p-intervals, where the uncertainty of a single test does not surpass the metric. As a result, repeated measurements are unnecessary, saving resources, particularly, time, which is often the most valuable.

3. RESULTS AND DISCUSSION

Let the indices α and β range over all pairs from the set of parameters (p, θ, φ). Then, the elements of the QFI metric tensor (**F**) can be expressed as follows:

$$F_{\alpha\beta} = \left(\frac{1}{2}\right) Tr\left(\rho_n \left\{L_\alpha, L_\beta\right\}\right). \quad (7)$$

Here, $\left\{L_\alpha, L_\beta\right\}$ is the anticommutator of the two SLD matrices mentioned above. The following matrix equation defines them [14, 15]:

$$\frac{\partial \rho_n}{\partial x_\alpha} = \left(\frac{1}{2}\right)\left\{\rho_n, L_\alpha\right\}\left(x_\alpha \in (p, \theta, \varphi)\right). \quad (8)$$

The main computational challenge arises from the fact that the dimensions of all matrices in the system grow exponentially as 2^n, where n is the number of qubits [15]. However, for a single qubit ($n = 1$), there are no significant issues, and the analytic forms of the three operators $\mathbf{L}_\alpha$ are provided in Table 1.

Considering these and the expression (7), $\mathbf{F}(p, \theta, \varphi)$ can be uttered in the following form:

TABLE 1. Analytic expressions for symmetrical logarithmic derivatives (SLDs).

Parameter	$\mathbf{L}_\alpha$
Kraus parameter, p	$\frac{3}{4p(p-3/2)}\begin{pmatrix}\cos(\theta)-1+4p/3 & \sin(\theta)\exp(i\varphi)\\ \sin(\theta)\exp(-i\varphi) & -\cos(\theta)-1+4p/3\end{pmatrix}$
Polar angle, θ	$(4p/3-1)\begin{pmatrix}\sin(\theta) & -\cos(\theta)\exp(i\varphi)\\ -\cos(\theta)\exp(-i\varphi) & -\sin(\theta)\end{pmatrix}$
Azimuthal angle, φ	$(4p/3-1)\sin(\theta)\begin{pmatrix}0 & -\exp(i\varphi)\\ \exp(-i\varphi) & 0\end{pmatrix}$

$$\mathbf{F}=\begin{pmatrix}\frac{2}{p(3-2p)} & 0 & 0\\ 0 & (1-4p/3)^2 & 0\\ 0 & 0 & (1-4p/3)^2\sin(\theta)^2\end{pmatrix}. \tag{9}$$

A diagonality in the QFI (Quantum Fisher Information) metric tensor shows that the parameters (p, θ, φ) are statistically independent directions in quantum information geometry. Since there are no cross-terms (covariances) between these parameters, their sensitivities to changes can be measured separately. In other words, estimating p does not affect the analysis of θ or φ, and *vice versa*.

QFI metric tensor is invertible almost everywhere, excepting the critical point $p = 3/4$. It means that the quantum Cramér–Rao bound (QCRB; see expression (5)) is well defined. Thus, the tensor provides a valid Riemannian metric on the parameter space; so, the geometry is non-degenerate.

At $p = 3/4$, the Bloch sphere collapses to a single point ($\mathbf{b}_n = \mathbf{0}$). The angular part of the QFI tensor (related to θ and φ) becomes degenerate because angles lose meaning, when the Bloch-vector length drops to zero. However, the radial component (the p-direction) remains well defined, so estimating the noise strength is still feasible. Physically, this means that, once the state is maximally mixed, one cannot extract orientation information, *i.e.*, the system carries no angular information.

This interesting observation was previously noted in Refs. [16, 17]. They highlighted that the channel's spherical symmetry causes all angular information to disappear once the Bloch sphere shrinks to the maximally mixed state. As a result, the QFI tensor becomes degenerate in its angular block at the critical point. At the same

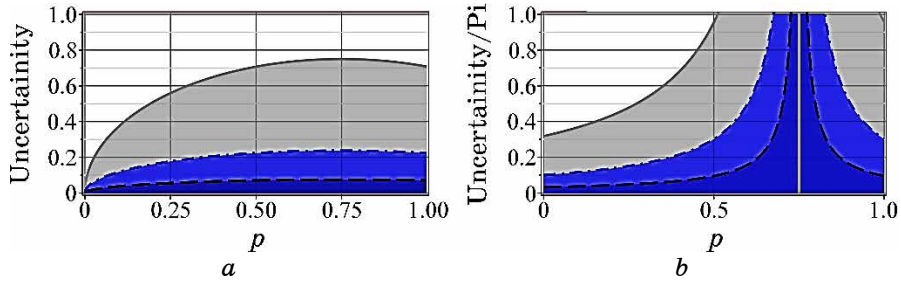

Fig. 1. Displaying the uncertainties (standard deviations) for two parameters: *a*) the Kraus parameter (p), which represents the noise strength, and *b*) the polar angle (θ), which defines the quantum-state position on the Bloch sphere (these uncertainties are normalized to π). The top edges of the shaded regions depict the uncertainties as functions of p across different scenarios: at a single-shot trial ($N = 1$; grey solid line); after $N = 10$ measurements (dark dash-dot line); after $N = 100$ measurements (dashed line).

time, the radial component related to the noise strength stays finite and can still be estimated.

The diagonality and invertibility of the QFI metric tensor (9) indicate that the depolarizing channel maintains isotropy, meaning the informational geometry is separable. At the critical point, only angular information is lost, while scalar metrics depending solely on the Kraus parameter p remains unaffected. Even when the Bloch sphere collapses and orientation information cannot be obtained, it is still possible to estimate the noise parameter p.

The uncertainty in the Kraus parameter (p) shows a local maximum of 3/4 at the critical point, indicating that a single estimate near collapse is unreliable. This highlights the need for repeated measurements to ensure accuracy, reflecting the complex interplay between isotropy, tensor degeneracy, and operational sensitivity.

Using Eqs. (5) and (9), we determine the minimum uncertainties for p and θ. Figures 1, *a* and *b* display these uncertainties for both single-shot and repeated measurements as functions of noise strength p. In single-shot scenarios, uncertainties stay significant across most of the p range, making repeated measurements more effective for achieving reasonable precision.

Note that Fig. 1, *b* also shows the minimal uncertainties of the azimuthal angle φ, observed at $\theta = \pi/2$, which is on the equator of the Bloch sphere. The uncertainties of the Kraus parameter vary smoothly, with a local maximum at the critical point ($p = 3/4$). In contrast, the angular uncertainties exhibit a singularity there, reflecting the geometric loss of orientation information at maximal mixing, as mentioned above.

Quantum metrics are mathematical tools used to measure changes in quantum states, especially, the decoherence, caused by noise. The selection of appropriate quantum metrics to describe a specific noise channel, such as depolarizing noise, is not strictly fixed. Instead, it depends on expert judgment influenced by two main factors.

Contextual Relevance. The chosen metric must align with the researcher's physical intuition and the operational goals of the analysis, whether it is tracking coherence loss, estimating parameters, or benchmarking quantum operations.

Channel Behaviour Specificity. Some metrics are selectively sensitive to certain types of noise. For example, purity might be particularly useful for decoherence, while fidelity is often favoured as a measure of quantum gate performance.

Our short list of metrics, which is presented in Table 2 in a bit of detail, of quantum metrics for depolarizing includes several essential measures: the Quantum Fisher Information (QFI) mentioned earlier, purity, the Bloch-vector norm, von Neumann entropy, fidelity, and a less common but specific metric: the angle between pure and noisy Bloch vectors.

In a depolarizing channel, the qubit's action is isotropic, causing uniform contraction of the Bloch sphere by a factor represented by the Kraus parameter, which indicates noise strength. This contrac-

TABLE 2. List of quantum metrics for the depolarizing noise channel.

Metric	Definition	Operational Role	Sensitivity
Quantum Fisher Information (QFI)	Derived from derivatives of the density matrix with respect to parameters (see Eq. (9))	Precision bounds for parameter estimation	Sensitive to parameter changes (*e.g.*, Kraus parameter p)
Purity	$Tr\left(\rho_n^2\right)$	Tracks decoherence strength	Decreases monotonically with noise
Bloch-vector norm	$\|\mathbf{b}_n\|$	Geometric measure of coherence	Shrinks isotropically under depolarization
von Neumann entropy	$-Tr\left(\rho_n \log_2 \rho_n\right)$	Quantifies disorder and information loss	Increases with mixing
Fidelity	$\left(Tr\sqrt{\sqrt{\rho}\rho_n\sqrt{\rho}}\right)^2$	Benchmarking gate/channel performance	Sensitive to overlap with the target state
Bloch-angle deviation	Angle between pure and noisy Bloch vectors	Diagnosis of angular information collapse	Sensitive to orientation loss and inversion

tion affects scalar metrics such as those in Table 2 making them dependent solely on the noise strength and ignoring angular orientation. In contrast, Quantum Fisher Information (QFI) involves derivatives of the density matrix, making it sensitive to both angular and radial variables. This difference allows QFI to detect directional degeneracies at critical points.

Figure 2 shows the results of calculations for quantum metrics along with their uncertainties, presented as scalar functions of the Kraus parameter. The critical point manifests differently across these metrics: purity and von Neumann entropy show extrema indicating maximum mixing; the Bloch-vector norm exhibits a distinct corner, signalling collapse and reversal of orientation; while fidelity, relative to the input pure state, remains smooth and unaffected by the criticality, as it depends only on overlap and not on orientation. Together, these results highlight the selective sensitivities of scalar metrics some directly capture the collapse of coherence, while others are unaffected by the geometric singularity.

Uncertainties in quantum metrics respond to the critical point in two diverse ways. Fidelity and the Bloch-vector norm show local maxima, indicating instability in single-shot estimation near the

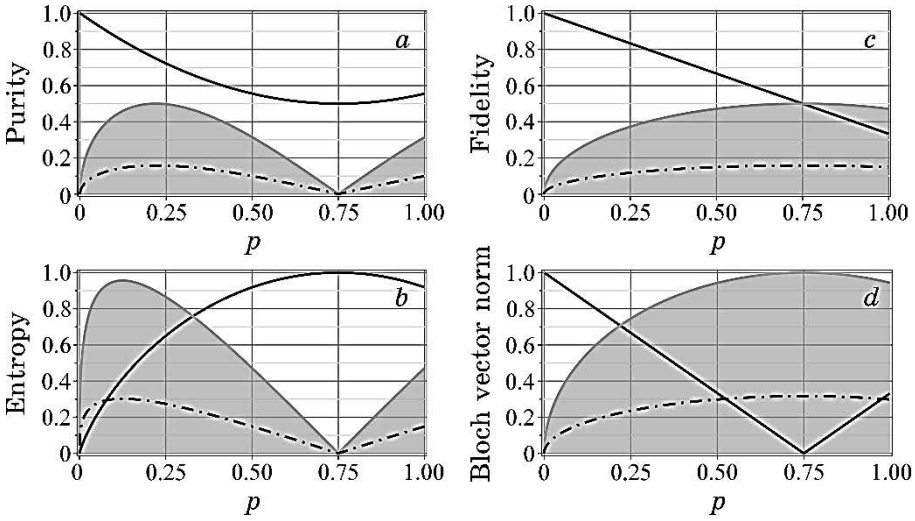

Fig. 2. Presenting various metrics along with their uncertainties (standard deviations) plotted against the Kraus parameter p. The metrics displayed include (*a*) purity, (*b*) fidelity, (*c*) entropy, and (*d*) Bloch-vector norm. The solid black lines represent the metrics themselves, while the solid gray lines and shaded areas indicate the uncertainties for a single-shot measurement ($N = 1$). Additionally, the dash-dot lines represent the uncertainties after conducting $N = 10$ measurements.

collapse point. In contrast, purity and von Neumann entropy have sharp corners, where uncertainty drops to zero. This dichotomy highlights the operational trade-offs: single-shot trials are feasible for purity, but they remain difficult for the Bloch-vector norm, except in a narrow low-noise regime. Additionally, the extreme values of purity and entropy at the critical point coincide with the minimum uncertainty, suggesting that these metrics can serve as reliable probes for quantum metrology in depolarizing channels. Therefore, the collapse point is not just a singularity in geometry but also a region of improved diagnostic precision for specific scalar measures.

The concept of Bloch-sphere collapse at the dephasing channel's critical point suggests that the norm of the Bloch vector can be measured directly; however, this is impractical. Uncertainty dominates near the crucial point, making it impossible to pinpoint the moment of collapse due to statistical fluctuations. Thus, the zero norm serves as a geometric indicator rather than a measurable quantity. This emphasizes the need to focus on other diagnostics, like purity or entropy, which offer more practical insights into depolarizing dynamics with a less uncertainty at critical points.

The Bloch-angle deviation (BAD) normalized by π exhibits a Heaviside step function dependent on the Kraus parameter p. At the critical point, the Bloch vector collapses, and BAD undergoes a discontinuous jump. Consequently, the derivative of BAD with respect to p is the Dirac delta function: identically zero across the entire domain except at the critical point, where it diverges to infinity. This singular derivative defines the uncertainty of BAD, which remains negligible everywhere except precisely at the collapse.

Operationally, this behaviour indicates that BAD can be measured with nearly zero uncertainty on either side of the critical point, but not precisely at the point itself. In metrological terms, one can 'capture' use brackets around the collapse measurement from both directions a strategy like the artillerymen's phrase 'into a fork', where the target is localized by bounding shots from opposite sides. This property makes BAD a uniquely precise diagnostic: it remains insensitive to criticality yet maximally discriminates between states before and after collapse. In this way, BAD provides a sharp operational boundary marker for the depolarizing channel, complementing scalar metrics that smooth over the transition.

It is worthwhile revisiting the discussion of parameter ranges for the depolarizing channel introduced in Sec. 2. For the Kraus parameterization, the contraction factor takes values, with representative noise strength. Within this framework, the channel exhibits a distinct internal structure.

Subcritical mode ($1 \geq \lambda > 0$ *and* $1 \geq p > 3/4$). The Bloch sphere under-

goes isotropic shrinkage and the normalized BAD remains zero, indicating that the orientation of the Bloch vector is preserved.

Critical point ($\lambda = 0$ *and* $p = 3/4$). The Bloch sphere collapses, and BAD becomes undefined. This marks the singular transition between depolarizing and repolarizing behaviour.

Overcritical mode ($0 > \lambda \geq -1/3$ *and* $3/4 < p \leq 1$). The Bloch sphere reverts to its original size, but is flipped in orientation, with BAD set to 1. This flip corresponds to a repolarizing regime, where states are mapped to their antipodes.

The internal structure of the depolarizing noise channel, described here as the taxonomy of subcritical contraction, critical collapse, and overcritical inversion, has been well supported by academic literature for the last two decades. This structure can be divided into three types: subcritical contraction, critical collapse, and overcritical inversion. Early research in Ref. [18] has expanded the Kraus representation of the depolarizing channel to include memory effects, noting that the contraction factor λ can take negative values. This suggests an inversion of the Bloch-vector direction. Such results confirm the existence of an overcritical regime, where the Bloch sphere not only recovers its magnitude, but also reverses its orientation. Pang and co-workers in Ref. [19] experimentally demonstrate that even fully depolarized channels (zero capacity, collapsed Bloch sphere) can regain operational utility. This aligns with our interpretation of the post-collapse regime, in which diagnostic strategies such as BAD bracketing (‘taking into account’) can extract information despite the collapse.

Recent studies reinforce the distinction between metrics at key points. The authors of Ref. [20] highlight singularities and unstable trajectories in depolarizing maps, indicating that geometric measures, such as the Bloch-vector norm, show significant uncertainty near collapse. Furthermore, Ref. [21] demonstrated that entropy-based diagnostics enter ‘absolute regimes’ under depolarizing conditions, serving as reliable markers with minimal uncertainty. The paper [22] emphasizes that fidelity is smooth and insensitive to collapse, which aligns with our finding that fidelity does not distinguish between regimes. Burrell extends the geometric analysis of generalized depolarizing channels, confirming that contraction factors crossing zero correspond to an inversion of orientation [23].

4. CONCLUSIONS

In conclusion, the depolarizing channel has a complex internal structure that a single diagnostic cannot fully capture. While traditional measures such as purity, entropy, and fidelity track behaviour across noise regimes, geometric diagnostics like the Bloch-

vector norm and BAD more clearly illustrate singular collapse and inversion. To synthesize these findings, Table 3 summarizes the behaviour and uncertainty of each metric across the subcritical, critical, and overcritical regimes, providing the reader with a clear operational map of the channel's diagnostic landscape.

In computer engineering, the taxonomy of depolarizing noise channel regimes and the uncertainty analysis can enhance reliability modelling and error-aware scheduling in quantum processors. This ensures that nanosystems avoid unstable operating points that could lead to collapse. In the realm of informational nanotechnologies, metrics such as purity and entropy, which maintain minimal uncertainty at the critical point, serve as robust indicators for controlling decoherence in nanoscale devices, ranging from spintronic circuits to quantum dots. In quantum computing, BAD can be a precise diagnostic tool for benchmarking channels and gates, comple-

TABLE 3. Comparative synthesis of the behaviour and uncertainty of key quantum metrics across the subcritical, critical, and overcritical regimes of the depolarizing channel.

Metric	Subcritical mode	Critical point	Overcritical mode	Uncertainty behaviour
Purity	Smoothly decreases with p; coherence is gradually lost	Minimum value at the collapse point	Increases with p; symmetric about the critical point	Corner with minimal uncertainty at the collapse point; feasible single-shot estimation
Entropy	Increases with p; mixing grows	Maximum entropy (maximally mixed state)	Decreases with p; symmetric behaviour	Corner with minimal uncertainty at the collapse point; strong metrological probe
Bloch vector norm	Shrinks isotopically	Zero (Bloch sphere collapses to a point)	Continues decreasing; unaffected by inversion	Local maximum in uncertainty; insensitive to collapse but noisy near criticality
Fidelity	Decreases linearly with p	Smooth, no singularity	Continues decreasing; unaffected by inversion	Local maximum in uncertainty; insensitive to collapse but noisy near criticality
BAD (Bloch Angle Deviation)	0 (orientation preserved)	Undefined (collapse)	1 (orientation flipped to antipode)	Zero uncertainty everywhere except a Dirac- delta spike at collapse; measurable 'fork' strategy available

menting fidelity measurements by distinguishing between depolarizing and repolarizing regimes. Additionally, the 'fork' strategy for measuring BAD near the point of collapse suggests new methods for single-shot estimation in quantum metrology. Furthermore, identifying overcritical inversion is linked to recent experimental advances in zero-capacity recovery through channel superposition [19].

These opportunities highlight both the innovative ideas and practical uses of the proposed diagnostic framework. By combining geometric representations, uncertainty analysis, and metrological feasibility, this study lays a foundation for future work in quantum information science and engineering. A clear understanding of qubit behaviour at critical points is crucial for both theoretical and practical progress in these areas.

Despite extensive literature on quantum noise, the authors found limited publications by Ukrainian researchers on depolarizing channels in quantum nanosystems. This does not reflect a lack of interest; active research continues in related fields. Our study aims to be among the first systematic investigations in Ukraine focused on quantum metrology of noise channels, contributing to the global dialogue on quantum information geometry and advancing quantum computing and nanotechnology research in Ukraine.

This study introduces BAD as a new diagnostic tool and presents one of the First systematic uncertainty analyses of scalar and geometric measures of depolarizing noise. While the current research focuses on single-qubit channels, future studies should expand to include multi-qubit systems and incorporate correlated noise to improve applicability. By identifying which metrics remain dependable near the point of collapse, this framework will support the development of robust quantum metrology protocols. Additionally, it will be valuable for fault-tolerant architectures and diagnostic tools essential for scalable quantum nanotechnologies.

REFERENCES

1. M. Nayak and S. K. Moharana, *NanoMind: Exploring Synergies in Nanotechnology and Machine Learning*, **27**: 197 (2025); https://doi.org/10.1007/978-3-031-77296-2_9
2. Q. Dai, C.-Y. Lu, and Z. Sun, *Nanoscale*, **15**, Iss. 26: 10858 (2023); https://doi.org/10.1039/D3NR90099A
3. Talha Nadeem, Tariq Rafique, Waseem Khan, Sahadat Khandakar, Ahmad Alkhayyat, Mahesh Lohith K S, Zemate Achraf Abdelghafour, and Sedra Moulay Brahim, *Nanotechnology Perceptions*, **20**: Iss. 15: 248 (2024). https://doi.org/10.62441/nano-ntp.vi.3463
4. M. Urbanek, B. Nachman, V. R. Pascuzzi, A. He, C. W. Bauer, and W. A. de Jong. *Phys. Rev. Lett.*, **127**, Iss. 27: 270502 (2021); https://doi.org/10.1103/PhysRevLett.127.270502

5. B. Khanal and P. Rivas, *Mathematics*, **12**, Iss. 9: 1385 (2024); https://doi.org/10.3390/math12091385
6. A. Blais, A. L. Grimsmo, S. M. Girvin, and A. Wallraff, *Reviews of Modern Physics*, **93**, Iss. 2: 025005 (2021); https://doi.org/10.1103/RevModPhys.93.025005
7. A. Somoroff, Q. Ficheux, R. A. Mencia, H. Xiong, R. Kuzmin, and V. E. Manucharyan. *Phys. Rev. Lett,* **130**, Iss. 26: 267001 (2023); https://doi.org/10.1103/PhysRevLett.130.267001
8. E. Martinez, A. deMarti iOlius, and P. M. Crespo, *Phys. Rev. A*, **108**, Iss. 3: 032602 (2023); https://doi.org/10.1103/PhysRevA.108.032602
9. S. L. Braunstein and C. M. Caves, *Phys. Rev. Lett*, **72**, Iss. 22: 3439 (1994); https://doi.org/10.1103/PhysRevLett.72.3439
10. G. Wyjtowicz, S. F. Huelga, M. M. Rams, and M. B. Plenio, *Phys. Rev. A*, **112**, Iss. 5: 052410 (2025); https://doi.org/10.1103/xjln-7ddy
11. M. A. Nielsen and I. L. Chuang, *Quantum Computation and Quantum Information: 10th Anniversary Edition* (Cambridge Univ. Press: 2010).
12. P. Denes and C. G. Ghinea, *Quantum Probability and Related Topics. Proceedings of the 30th Conference (23–28 November, 2009)* (Eds. Rolando Rebolledo and Miguel Orszag) (Santiago, Chile: 2011), p. 261–281; https://doi.org/10.1142/9789814338745_0015
13. M. Yu, D. Li, J. Wang, Y. Chu, P. Yang, M. Gong, N. Goldman, and J. Cai, *Phys. Rev. Research*, **3**, Iss. 4: 043122 (2021); https://doi.org/10.1103/PhysRevResearch.3.043122
14. M. Hayashi and Y. Ouyang, *Quantum*, **9**: 1806 (2025); https://doi.org/10.22331/q-2025-07-22-1806
15. J. R. Hervas, A. Z. Goldberg, A. S. Sanz, Z. Hradil, J. Reháček, and L. L. Sánchez-Soto, *Phys. Rev. Lett*, **134**, Iss. 1: 010804 (2025); https://doi.org/10.1103/PhysRevLett.134.010804
16. J. Liu, H. Yuan, X.-M. Lu, and X. Wang, *Journal of Physics A: Mathematical and Theoretical*, **53**: 023001 (2019); https://doi.org/10.1088/1751-8121/ab5d4d
17. F. Albarelli, M. G. Genoni, M. A. C. Rossi, and D. Tomaselli, *Quantum*, **2**: 110 (2018); https://doi.org/10.22331/q-2018-12-03-110
18. S. Daffer, K. Wydkiewicz, J. D. Cresser, and J. K. McIver, *Phys. Rev. A*, **70**, Iss. 1: 010304R (2004); https://doi.org/10.1103/PhysRevA.70.010304
19. A. O. T. Pang, N. Lupu-Gladstein, H. Ferretti, Y. B. Yilmaz, A. Brodutch, and A. M. Steinberg, *Quantum*, **7**: 1125 (2023); https://doi.org/10.22331/q-2023-10-03-1125
20. A. Abu-Nada, S. Banerjee, and A. Sabale, *Phys. Rev. A*, **110**, Iss. 5: 052209 (2024); https://doi.org/10.1103/PhysRevA.110.052209
21. T. Patro, K. Mukherjee, and N. Ganguly, *Quantum Inf. Process.*, **23**: 228 (2024); https://doi.org/10.1007/s11128-024-04439-1
22. B. Khanal and P. Rivas, *Mathematics*, **12**, Iss. 9: 1385 (2024); https://doi.org/10.3390/math12091385
23. C. K. Burrell, *Phys. Rev. A*, **80**, Iss. 4: 042330 (2009); https://doi.org/10.1103/PhysRevA.80.042330

Наносистеми, наноматеріали, нанотехнології
Nanosistemi, Nanomateriali, Nanotehnologii
2026, т. 24, № 1, сс. 33–52
https://doi.org/10.15407/nnn.24.01.0033

PACS numbers: 03.67.-a, 07.50.Ek, 73.21.-b, 73.63.-b, 84.30.Bv, 85.35.Be, 85.40.Bh

A Study on 2-Dimensional 4-Dot 2-Electron QCA-Based Reversible-Circuit Design with Energy Dissipation Analysis

Md. Abdullah-Al-Shafi

University of Development Alternative (UODA),
80, Satmosjid Road,
Dhanmondi, Dhaka, Bangladesh

Since the scaling of archetypal transistors has extended its lowest point, the rational substitute for the complementary metal-oxide semiconductor (CMOS) technology to attain advance improvements in the circuits on the criterions of size, low power, and device density usage has turned into an imperative essential. In an extremely rapid expansion of VLSI technology, it is the requirement of the era to reach a consistent model with area and low-power consumption. Quantum-dot cellular automata (QCA) are a prospective nanotech archetype, which performs as a different resolution to regular CMOS that has several physical limitations and sets of circuits' bounds. QCA is an enticing nanotechnological paradigm because of its better switching frequency and faster-performing speed besides it comprise a novel approach for information transformation. This paper illustrates a new design of XNOR, TR, BVF gates, and 1-bit comparator by Feynman gate based on the QCA and CMOS technology, which is well organized compared with the earlier outline. To computer simulate and confirm the suggested gate, QCA designer and Microwind Lite engines are utilized. The quantum costs of the proposed typical circuits and their QCA designs are computed and compared that confirms that the proposed QCA designs have extremely low quantum cost compared to typical layouts. The power dissipation by the designs is estimated that confirms the prospect of QCA nanodevice performing as a substitute stage for the implementation of reversible circuits. The firmness of the proposed designs under thermal randomness is analysed, presenting the functioning efficacy of the designs. The designs have a propitious future in forming of nanoscopic-scale low-power consumption information transforming scheme and can be motivated advanced digital functions in QCA.

Оскільки масштабування архетипових транзисторів досягло свого найнижчого рівня, раціональна заміна технології виготовлення комплементарних інтеґральних схем типу метал–оксид–напівпровідник (КМОНп) для досягнення передових удосконалень у схемах за критеріями розмі-

ру, низького енергоспоживання та щільности використання пристроїв стала надзвичайно важливою. В умовах надзвичайно швидкого розвитку технології виготовлення надвеликих інтеґральних схем (НВІС) вимогою епохи є досягнення узгодженого моделю із площею та низьким енергоспоживанням. Клітинний автомат на квантових цятках (ККА) — це перспективний нанотехнологічний архетип, який має відмінну роздільчу здатність щодо звичайної КМОНп, але має й кілька фізичних обмежень і наборів меж контурів. ККА є привабливою нанотехнологічною парадигмою завдяки кращій частоті перемикання та швидшій роботі, а також представляє собою новий підхід щодо перетворення інформації. У цій статті проілюстровано нові конструкції логічних вентилів типу «виключне АБО–НЕ», «TR (Thapliyal–Ranganathan)», «BVF (межове векторне поле)» й 1-бітного компаратора за Фейнмановим вентилем на основі технології ККА та КМОНп, яка є добре організованою порівняно з попереднім планом. Для комп'ютерного моделювання та підтвердження запропонованого вентиля використовуються конструктор ККА та механізми Microwind Lite. Розраховано та порівняно квантові витрати стосовно запропонованих типових схем та їхніх конструкцій ККА, які підтверджують, що запропоновані конструкції ККА мають надзвичайно низькі квантові витрати порівняно з типовими схемами. Оцінено розсіяння потужности конструкціями, що підтверджує перспективність використання нанопристроїв ККА як заміни для реалізації оборотніх схем. Проаналізовано стійкість запропонованих конструкцій щодо теплової випадковости, що представляє ефективність функціонування конструкцій. Конструкції мають сприятливе майбутнє у формуванні схем перетворення інформації наноскопічного масштабу з низьким енергоспоживанням і можуть бути ініційовані розширеними цифровими функціями в ККА.

Key words: quantum-dot cellular automata, XNOR gate, TR gate, BVF gate, 1-bit Feynman gate comparator, power dissipation.

Ключові слова: клітинний автомат на квантових цятках, вентиль виключне АБО–НЕ, вентиль TR, вентиль BVF, 1-бітний компаратор за Фейнмановим вентилем, розсіяння потужности.

(Received 6 September, 2024)

1. INTRODUCTION

CMOS technology has been dominant the roost for several times and currently it is the reasonable technology in the microelectronic area. In current period, the goal is to scaling down to scheme a combined circuit, specifically rising the thickness of the circuit and thus it is essential to change from transistor to transistor less circuit. Nanotech has been the attentions of a widespread explore to replace the estimated restrictions of regular CMOS at the edge of the roadmap [1]. Moore's law expresses that the escalation of com-

bined circuits is at the level of $2X$ per each 18 months, where X denotes the number of transistors per entity area [2]. As the manifested restrictions of this technology, *i.e.*, fault analysis complications, speed, oxide thickness, and extent overhead; enlarged with the better circuit intricacy as shift to an advanced stage of system unification, the effective substitute for the CMOS has grown into an instant requirement. Quantum-dot cellular automata [3, 4] that has currently been identified as one of the elites arising technologies with conceivable applications in imminent computing [5, 6] for its specific speed, smaller space, and very low power utilization in different computational functions [3]. Quantum dots are small elements generally (2–10 nm) composed from semiconductor resources, which show microelectronic properties. Their lesser size denotes that electrons do not have to move as far as equated with higher particles; so, electronic tools conceived by quantum dots can perform swifter. Logic circuits created from quantum dots is one of the utmost contemporary technologies that is being scrutinized and circuits occupied in quantum-based computers can be obtained from the quantum dot circuits. This technology is an assuring computing concept which has huge applications in evolving technologies, *e.g.*, quantum computing, optical information handling, digital signal processing, optical computing, DNA computing, *etc.* [7–9].

In information-lossless circuit, the input vector is produced from each output vector, and vice versa. It has presented [10] that the cost of each bit of information depletes the energy of $kT\ln 2$ [J], where k is Boltzmann's constant and T is the pure temperature. At room temperature, the extent of heat produced because of a single bit of information loss is minor, that is estimated as $2.9 \cdot 10^{-21}$ J, but it is not insignificant. Later, it is indicated [11] that the energy falls could be avoidable, if the computation is carried out with no cost of information. Molecular QCA can function at room temperature [12] and an amount of QCA based circuits have been suggested based on QCA wires, inverter and majority gate. Several QCA occupying combinational [13–18] and sequential [19–22] designs have been projected in recent times, though, reversible circuit form [23–28] in QCA are still uncharted research field. In this paper, three inventive QCA circuit models and comparator have been proposed that is more effectual in terms of total cell numbers, space and complexity corresponding to the earlier design [40–42] and their performance has been tested using the QCADesigner and Microwind. Besides, analyses of the proposed reversible circuits and their corresponding QCA designs are presented based on quantum cost and the heat-energy dissipation as well as the output polarization and consistency of the designs is measured under thermal randomness.

This article is organized in six sections. Section 1 presents the introduction of QCA. Section 2 discusses a concise synopsis of the

QCA structures. In section 3, the approach and urged layout of the proposed design in QCA are discussed. The simulation outcomes as regards different characteristics of these shown designs are described in section 4. Section 5 describes the quantum cost and power dissipation of proposed QCA layout. Lastly, section 6 concludes this analysis with imminent work.

2. QUANTUM-DOT CELLULAR AUTOMATA

All QCA provisions logic cases not as voltage phases but rather based on the point of separate electrons. The central QCA features are QCA wire, inverter and majority gates. Cells are the elementary entities of QCA based circuit and they are usually constituted of four quantum dots positioned at the corners of a square pattern. Each cell is charged with two supplementary electrons, which channel from one low-potential state to another across a high-potential direction and a back plane voltage switches the cell occupancy.

The electrons will be located in transversely to each other owing to reciprocal repulsive electrostatic power, possessing the utmost distance between them. A remote cell may be in one of two corresponding energy positions. These positions are called cell polarizations $P = +1.00$ and $P = -1.00$ as shown in Fig. 1, *a*. $P = 0$ denotes an unpolarised cell, which covers no information. A cell polarization P is -1, if the electrons are involved the locus 2 and 4; in the same way, a cell polarization P is $+1$, if electrons are involved the position 1 and 3. The cell-polarization equation [29] is presented below:

$$P = \frac{(\rho_2 + \rho_4) - (\rho_1 + \rho_3)}{(\rho_1 + \rho_2 + \rho_3 + \rho_4)}, \tag{1}$$

where the charge at dot i denoted by ρ_i. QCA wire encompasses of series of cells, where the cells are united one after another [26, 27]. QCA wire is employed to transfer signal from one position to another in a circuit. Logical charges are moved from cell to cell because of the Coulomb contacts. There are two modes of alignments in a QCA wire namely binary wire and inverter chain. QCA wires can be either originated up of 45° cells or 90° cells as shown in Fig. 1, *b*. In case of inverter, if two cells point at 45° with regard to each other, their contact will be reverse and, for that, these cells are mostly employed for coplanar wire crossings.

The inverter is a pattern of cells that reverse the input topology from one logic to another. Usually, two categories of inverter are applied [28] that has been operated for the realization of several structures as an essential cell [14], [16], [28], [31]. The inverter can be designed by fixing QCA cells at 45° position [31] as appeared in

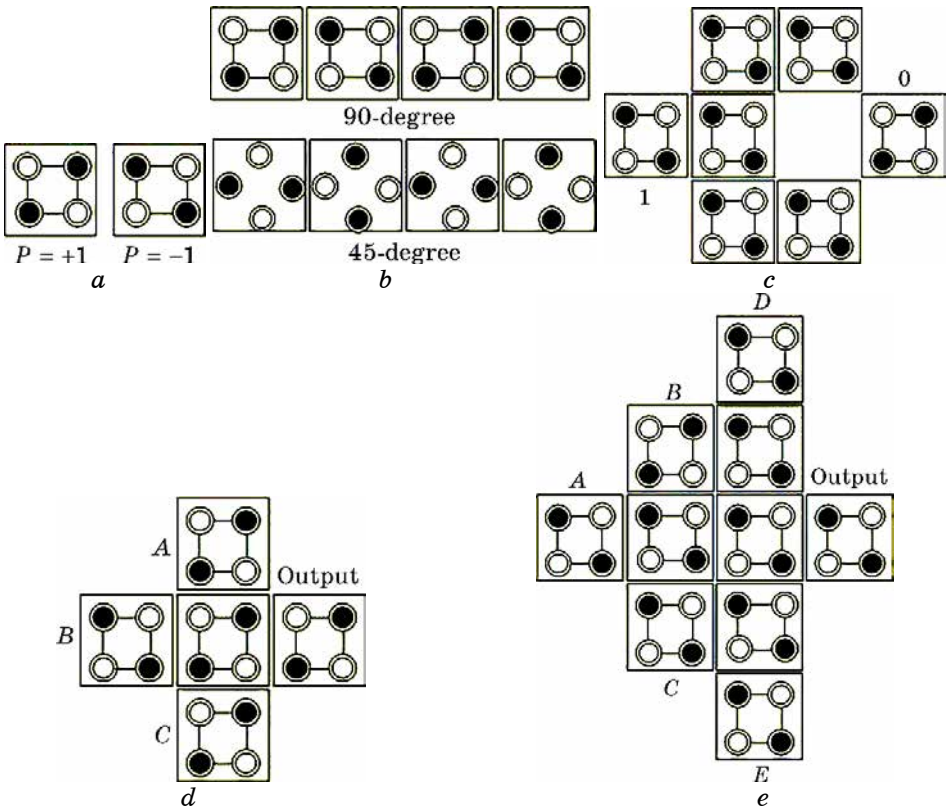

Fig. 1. QCA logical designs: *a*—plain cell; *b*—wires; *c*—potent inverter; *d*—3-input majority gate; *e*—5-input majority gate.

Fig. 1, *c*, which is potent and mostly used in circuit design. The logic values 0 and 1 transformed to 1 and 0 because of electrostatic repulsion. Binary wire transfers signal with similar polarity from one place to another, while inverter chain reverses the input cell polarity when odd figures of cells are employed in it. Majority gate is assembled of five QCA cells; a central cell, one output, and three inputs. Polarity of the middle cell, as identified as device cell, is imposed by the Coulomb repulsion to be equivalent to the output cell. The device cell at the centre of the gate has its least energy, when it accepts the polarization of the majority of the three input cells, since this is the formation, where the repulsion between the electrons in the three inputs cells and the electrons in the device cell is lowest.

Table 1 presents the output and input cells arrangements; '1' signifies logic '1' and '0' implies logic '0' in Table 1. So, an arrangement of inverter and majority voter is appropriate to con-

TABLE 1. Truth table of three input majority gate.

A	*B*	*C*	Output
0	0	0	0
0	0	1	0
0	1	0	0
0	1	1	1
1	0	0	0
1	0	1	1
1	1	0	1
1	1	1	1

struct an extensive logic set for scheming of any circuit.

Majority voter can operate as AND or OR logic gate depending on the static polarity of the third input of the majority voter as presented in Fig. 1, *d*. The logical equation of the 3-input majority gate can be stated as follows:

$$MV(A, B, C) = AB + BC + AC. \quad (2)$$

Logical 2-input AND and 2-input OR functions can be executed using majority voter by putting one input cell to binary '0' and '1', subsequently. Equations (3) and (4) express the 'AND' and 'OR' gate process, while $C = 0$ and $C = 1$:

$$MV(A, B, 1) = A + B, \quad (3)$$

$$MV(A, B, 0) = AB. \quad (4)$$

The satisfying attainment of realizing a 3-input majority voter with five QCA cells inspired the analysts to hypothesize an inventive configuration for 5-input majority voter. Later, a specific layer [30] 5-input majority voter utilizing ten cells executed in a precise cell layout, which is displays in Fig. 1, *e*. The logic equation of the 5-input majority voter can be expressed as follows:

$$MV(A, B, C, D, E) = ABC + ABD + ABE + ACD + ACE + \\ + ADE + BCD + BCE + BDE + CDE. \quad (5)$$

To form more complicated QCA devices, the location of QCA cell is not only essential also needs to coordinate the information, so that evade having a signal extending a logic gate and proliferating before the other inputs move the gate. This specific characteristic is particularly imperative in QCA circuits, ensuring its accurate function, and this aspect is attained by QCA clock. The clock is an elec-

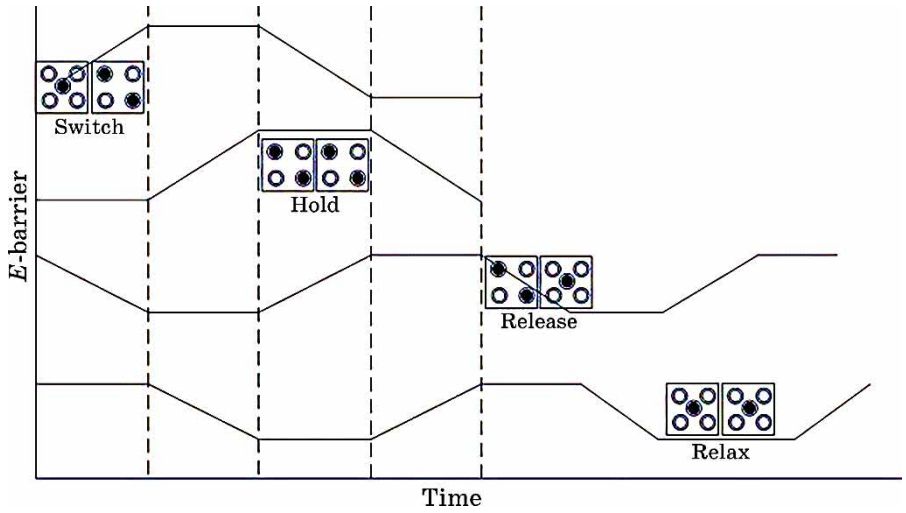

Fig. 2. QCA switching between four stage clocking.

trical region that switches the channelling barriers within the cell, therefore, retaining control, when a cell may or may not be polarized. QCA clocking is produced of four periods lagging by $\pi/2$ [32, 33] (see Fig. 2) that generates an innovative way to conceive nanocircuits distinct from the regular CMOS circuits [34]. In each region, a certain potential can adjust the barriers between the dots, and the organization of clock zones allows a group of QCA cells to construct a particular calculation; then, its positions are stationary and its outputs can be applied as inputs to the following clock zone.

Switch period: the barrier between dots of QCA cell is elevated and the dots are motivated by the electron of its adjoining as well as electron begins channelling between dots; thus, the cell turns into polarized. *Hold period*: cell barrier stays high and electron cannot channel between dots, and the cell keeps its existing position. *Release period*: barrier between dots is decreased, the electron can channel within dots and cell comes to be unpolarised. *Relax period*: barrier remains at lowered and cell stays in unpolarised position.

3. METHODOLOGY AND PROPOSED DESIGN

An assay is fulfilled to acquire the required devices and selected to realize the suggested design. The composition level is permitted applying a number of approximate simulators as the nonlinear approximation methods and bistable simulation device. However, these approximate do not develop the specified measures because these methods are iterative. In time, the QCA designer is preferred and

this simulation tool is demonstrated [35]. The bistable simulation tool has been occupied in the simulation interface between cells; clearly, the contact force linking two cells decomposes contrariwise with the fifth power of the length untangling them. During this estimation, not all the cells impact is counted and cells within the radius of R are being measured. For i-th cell, the scientific pattern is depicted by the following Hamiltonian:

$$H_i = \sum_j \begin{pmatrix} -\frac{1}{2} P_j E_{i,j}^k & -\gamma \\ -\gamma & \frac{1}{2} P_j E_{i,j}^k \end{pmatrix}, \tag{6}$$

where P_j is the polarization for cell j, $E_{i,j}^k$ is the kink energy between the cells (i and j), and γ is the channelling energy. For every cell i, the amount of the Hamiltonian is over all cells (*viz.*, j) in its radius of effect, R. The Jacobi algorithm has been utilized to obtain the eigenvectors and eigenvalues of the Hamiltonian. At the layout level, small QCA block is designed and simulated for analysis of its precision. Later, these QCA blocks are unified together through QCA wire to manage the proposed composition. Finally, the consistency of the design is surveyed by the QCA designer. The simulation outcome the essential waveform for the logical circuit and during simulation, it created few criterions that contains default standards as the cell size, layer separation, relative permittivity, samples number, *etc*. The proposed design in CMOS is formulated and simulated using Microwind [36] tool. This engine is standard and appropriate to achieve the surface of the diverse logic circuit. In this paper, the waveform of the proposed layout seamlessly fits the logical input and output.

A gate is identified information-lossless or reversible, if there is a one-to-one correspondence between its number of output and input assignments. Information-lossless circuit stimulates a certain set of input vector for each set of the output vector and it accomplished common attention since their possibility to subside the dissipation of power. In this paper, a significant layout of BVF and XNOR circuits is organized. The XNOR gate (also denoted as ENOR or Exclusive NOR) is a digital logic gate with two or more inputs and one output, which presents logical equivalence. The result of an XNOR gate is valid, when all of its inputs are false or all inputs are true. If certain of its inputs are true and others are false, then, the outcome of the gate is false. Two input XNOR gate can be achieved by an inverter and three majority gates as presented in Fig. 3.

Among these majority voters, two majority gates are effected to perform like OR gates by making one input equivalent to '1' and

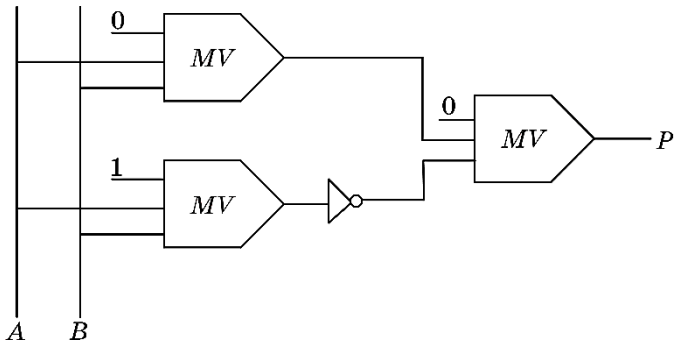

Fig. 3. Proposed layout of XNOR gate in QCA.

the last majority gate is effected to perform like an AND gate by composing the third input equivalent to '0'. The logical equation of XNOR gate is as follows:

$$P = (AB) + (A + B)' = AB + A'B'. \tag{7}$$

The TR gate (also familiar as Thapliyal and Ranganathan gate) [37] is a 3-input and 3-output reversible gate shown in Fig. 4. The

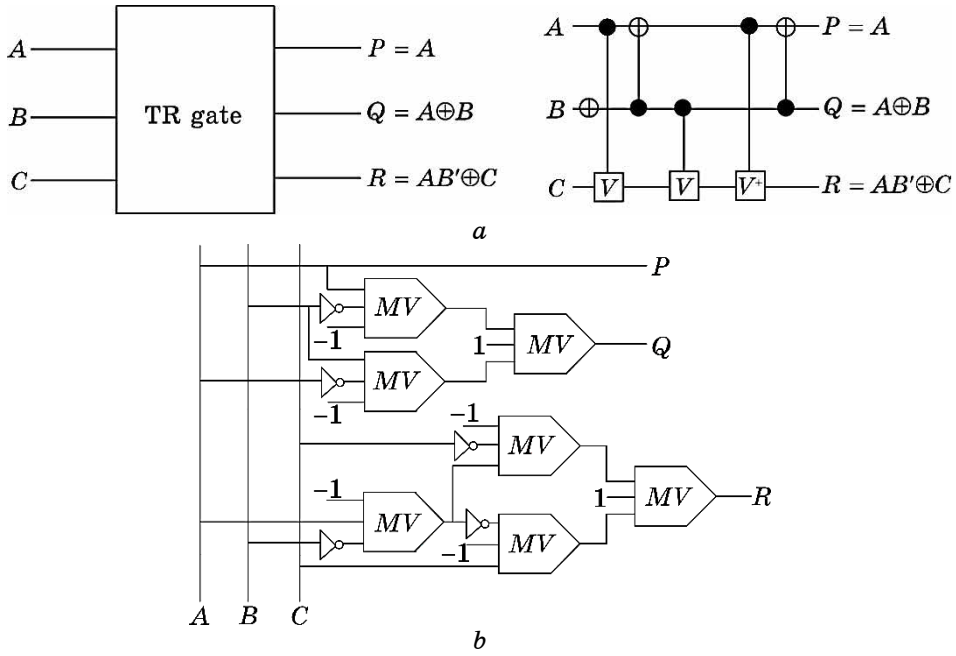

Fig. 4. Block diagram of (*a*) TR gate; (*b*) proposed layout of TR gate in QCA.

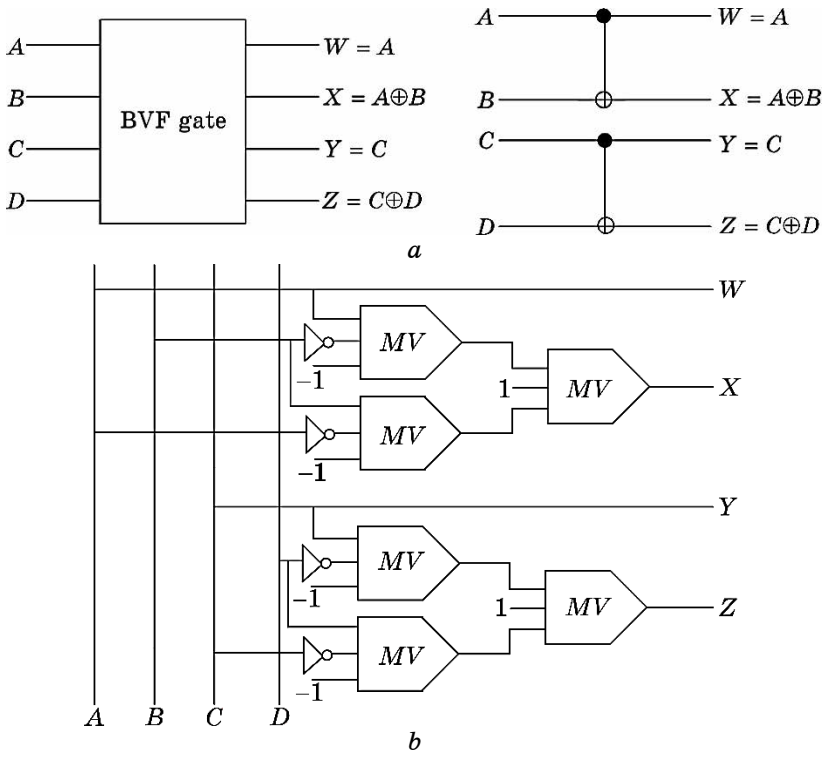

Fig. 5. Block diagram of (*a*) BVF gate; (*b*) proposed layout of BVF gate in QCA.

input vector of TR gate is stated as $I_v(A, B, C)$ and the corresponding output vector is $O_v(P, Q, R)$. The outcome is denoted as $P = A$, $Q = A \oplus B$ and $R = AB' \oplus C$. The quantum cost of TR gate can be realized from the quantum execution of Toffoli gate [38]. Using 2 NOT gates and 1 CNOT and Toffoli gate, the cost of TR gate is achieved. Therefore, the cost will be quantum cost of 1 Toffoli gate + quantum cost of 1 CNOT gate, *i.e.*, = 6.

BVF gate also identified as 4×4 double XOR reversible logic gate [39]. The input vector is defined as $I_v(A, B, C, D)$ and the output vector is $O_v(W, X, Y, Z)$. The result is expressed as $W = A$, $X = A \oplus B$, $Y = C$ and $Z = C \oplus D$ as shown in Fig. 5. This gate can be operated for the replication of the expected inputs to meet the fan out conditions, and the gate is employed to model the operand bits and the number of gates needed to copy is decreased by 50% with similar quantum effort.

A 1-bit comparator takes two 1-bit numbers, for example, A and B as inputs and generates an output specifying whether $Y_1 = AB'$, $Y_2 = A$ NOR B, and $Y_3 = A'B$ for $A > B$, $A = B$, and $A < B$, correspondingly. Figure 6 illustrates the simulated layout of proposed XNOR,

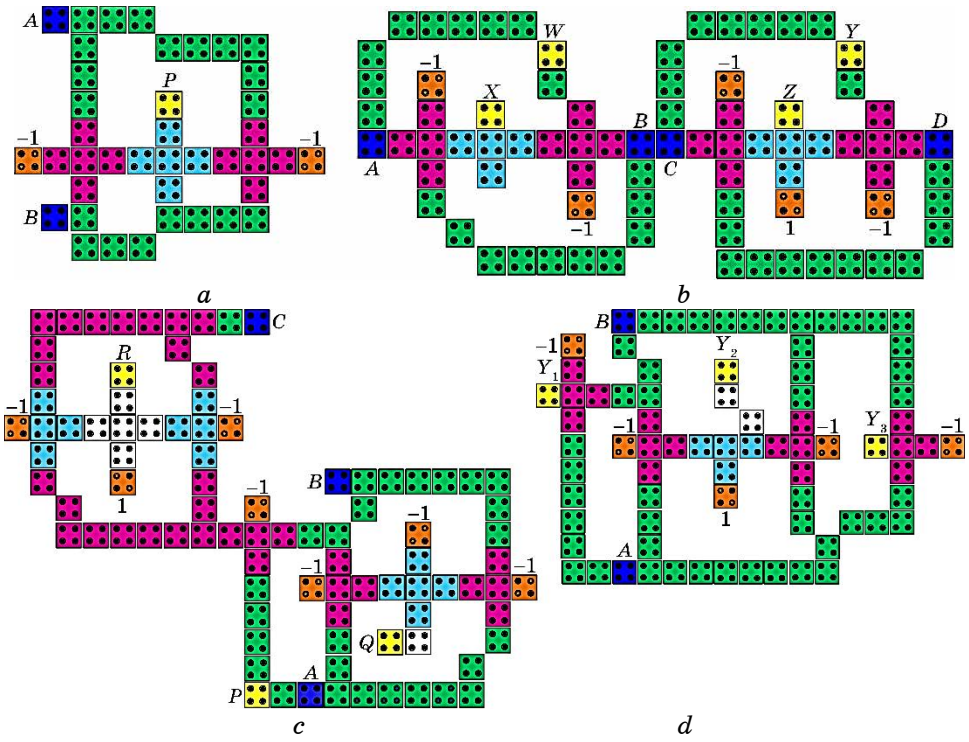

Fig. 6. QCA simulated circuit design of proposed: (*a*) XNOR gate; (*b*) BVF gate; (*c*) TR gate; (*d*) 1-bit comparator by Feynman gate.

BVF, TR, and 1-bit comparator in Feynman gate, respectively, where: in Fig. 6, *a*, *A*, *B* and *P* are the input and output cell, correspondingly; in Fig. 6, *b*, the inputs are *A*, *B*, *C*, *D* and their equivalent outputs are *W*, *X*, *Y*, and *Z*; in Fig. 6, *c*, the inputs are *A*, *B*, *C* and their corresponding outcomes are *P*, *Q*, *R*; in Fig. 6, *d*, inputs are *A*, *B* and their corresponding outputs are Y_1, Y_2, and Y_3. In circuit composition, two static polarizations $P = +1$ and $P = -1$ are operated that are occupied to shift the logic form.

4. SIMULATION-RESULTS' ANALYSIS

The design has been functionally fabricated and simulated using the QCA designer that presents some criterions in the coherence vector and bistable approximation, which are the default features in QCA designer. These parameters are exhibited in Table 2. The decisive QCA functioning design of the proposed XNOR, BVF, TR and 1-bit comparator design of Feynman gate is illustrated in Fig. 7, *a*, *b*, *c* and *d*, respectively. The first layout involves of 40 cells and cover-

TABLE 2. Parameters of bistable approximation and coherence vector.

Criterion	Value
Size of cell	20 nm
Dot diameter	5.000
Number of samples	12800
Temperature	1.00 K
Relaxation time	$1.000000e^{-15}$ s
Convergence tolerance	0.001000
Radius of effect (bistable)	65.000000 nm
Time step	$1.000000e^{-16}$ s
Relative permittivity	12.900000
Layer separation	11.500000
Radius of effect (coherence)	80.000000 nm
Clock amplitude factor	2.000000
Clock high	9.800000*e*–022
Clock low	3.800000*e*–023
Lower threshold [0]	–0.500
Upper threshold [1]	0.500
Maximum iterations per sample	100
Total simulation time	$7.000000e^{-11}$ s

ing an extent of 0.04 μm^2, the second layout involves of 79 cells and covering an extent of 0.07 μm^2, the third layout involves of 92 cells and covering an extent of 0.12 μm^2 and the comparator involves of 78 cells and covering an extent of 0.08 μm^2. It is very essential to create an operationally firm layout in QCA functions. There are certain concerns realized into account to raise the design stability. When building models in QCA, a substantial attempt should be made to maintain the wire length in a specified clocking region to a minimum. For smaller wires, it is almost certainly that all cells creating up the wire will switch effectively.

The scheme of proposed design in CMOS is organized in Fig. 8, *a*, *b* and *c*, respectively, which is performed using Microwind Lite engine, a fast-systematized EDA tool for front and back-end chip fashion into an integrated flow. Table 3 explains the complication of the proposed design respecting the number of cells, majority voters, clocking zones and covered area applied to perform the layout.

Table 4 illustrates that the proposed XNOR has improvements of 38.46% and 42.85% in terms of total cell and area respectively, relative to the design proposed in Ref. [40]. Similarly, the improvements of BVF, TR and 1-bit Feynman gate comparator are 3.66% and 30.00%, 18.58% and 40.00%, 10.36% and 3.00%, correspondingly, proposed in Refs. [41, 42].

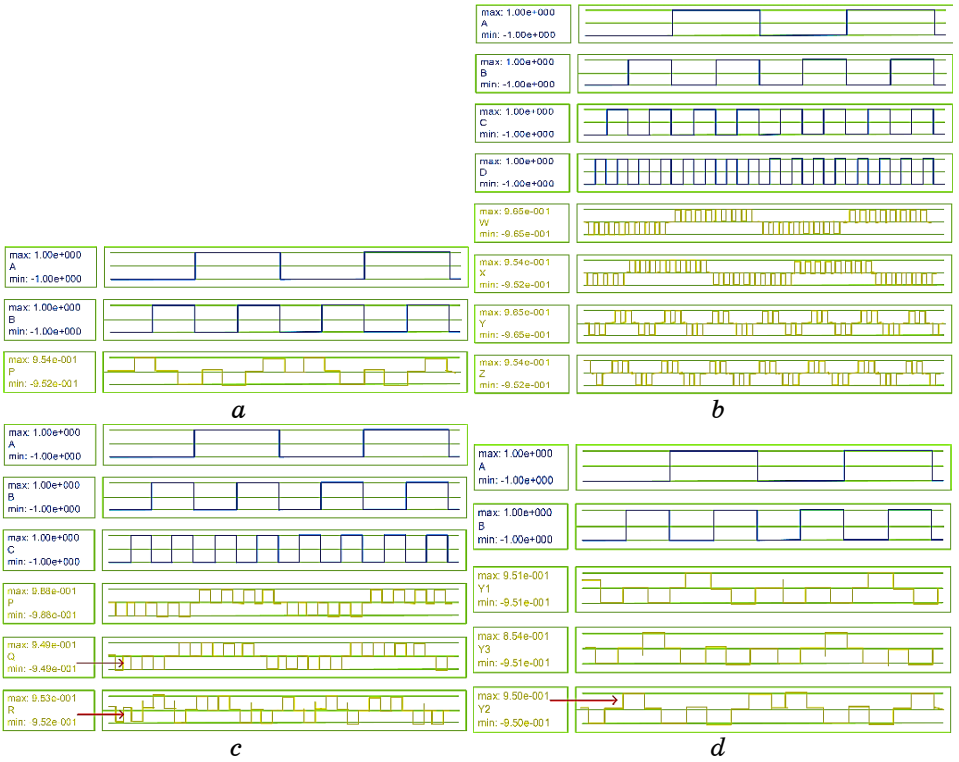

Fig. 7. QCA outcome of the proposed: (*a*) XNOR, (*b*) BVF, (*c*) TR, and (*d*) 1-bit comparator design of Feynman gate.

5. DESIGN QUANTUM COST AND POWER DISSIPATION OF THE PROPOSED CIRCUIT AND ITS QCA OUTLINE

The quantum cost of 2×2 reversible circuit is counted one, however all reversible 1×1 circuit have a quantum cost of zero [24]. Thus, the quantum cost of XNOR gate is one. BVF and TR gate have a quantum cost of two and four respectively.

The proposed 1-bit comparator in Feynman gate is organized of one Feynman gate and three reversible NOT gate, Thus, the proposed 1-bit Feynman gate comparator has a quantum cost of (1×1 + 0), *i.e.*, 1.0. The corresponding quantum costs of the proposed layouts are figured in Table 5.

The proposed XNOR design has area of 0.04 μm^2 and latency of 0.75. Therefore, the cost of the proposed QCA design is area×latency 2 = 0.04×0.752, *i.e.*, 0.022. The proposed QCA BVF circuit has an extent of 0.07 μm^2 and latency of 0.50, which reason the quantum cost of the proposed circuit is = 0.07×0.502, *i.e.*, 0.017.

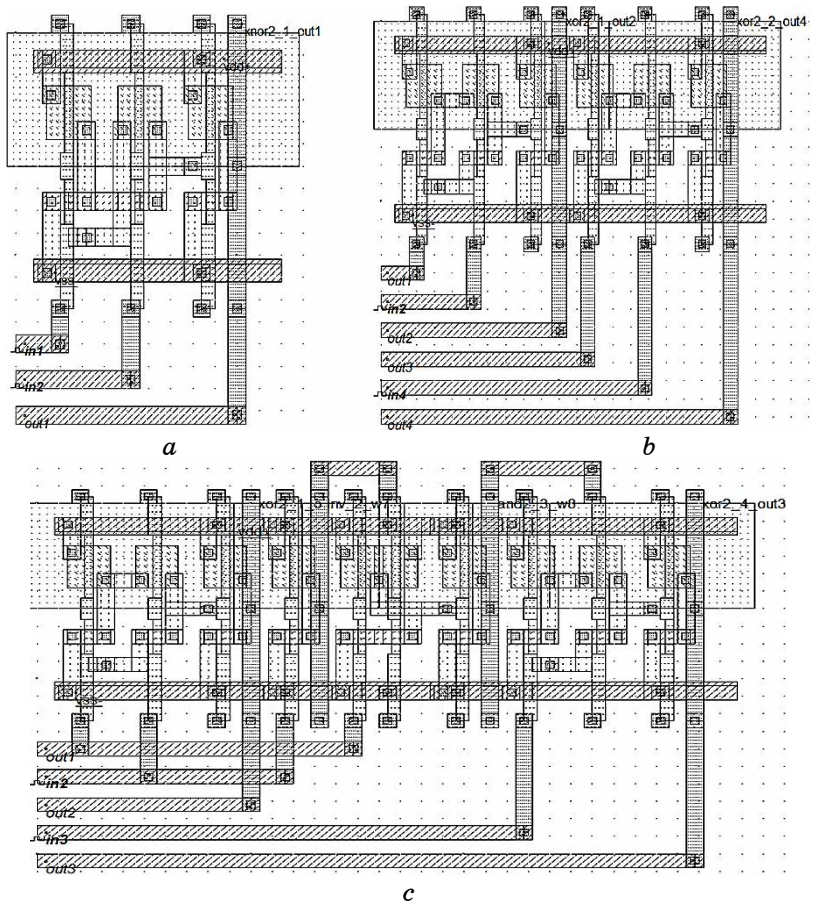

Fig. 8. Simulated circuit design in CMOS: (*a*) XNOR gate; (*b*) BVF gate; (*c*) TR gate.

Just as, the costs of other circuits are estimated, and the results are presented in Table 5. The quantum cost of XNOR gate in typical design is 1.0, however in QCA-based design, it is of 0.022. For 1-bit Feynman gate comparator, typical layout has a quantum cost of 2.0, but QCA-based layout requires a quantum cost of 0.020. Table 5 illustrates that the quantum cost of QCA-based layouts is lower than that of traditional layouts. Hence, QCA-based designs are cost effectual with corresponding to quantum cost. The relevant comparison is also illustrated in Fig. 9.

The dissipation of power by each QCA cell in a circuit is identical [43]. Therefore, in a range of connected QCA cells, the total dispelled power can be projected by adding the dispelled power of each cell within the range. The circuit power consumption is reliant on

TABLE 3. Performance criterions of proposed design.

Parameter	Cell intricacy	Clock used	Time delay	Covered area, μm^2	Area in CMOS, μm^2	Improvement (in times)
Proposed XNOR gate	40	3	0.75	0.04	21.9	548
XNOR gate [41]	65	4	1	0.07		
Proposed BVF gate	79	3	0.50	0.07	47.6	595
BVF gate [41]	82	3	0.50	0.10		
Proposed TR gate	92	4	1	0.12	71	592
TR gate [42]	113	4	1	0.20		
Proposed 1-bit Feynman gate comparator	78	3	0.50	0.08	—	
1-bit Feynman gate comparator [42]	87	4	0.50	0.11		

TABLE 4. Complexity of the proposed designs.

Proposed design	Cell area, μm^2	Area use, %	Cell improvement, %	Area improvement, %
XNOR gate	0.013	32.50	38.46	42.85
BVF gate	0.026	37.14	3.66	30.00
TR gate	0.031	25.83	18.58	40.00
1-bit Feynman gate comparator	0.026	32.50	10.36	3.00

the logic gates operated in constructing the circuit.

Applying a larger quantity of logic gates involves larger power dissipation by the circuits. The dispelled energy of the circuit is the total of the power dissipated by all the majority voters, inverters, and the range of QCA cells. The computation is achieved with the QCA power dissipation tool QCA Pro [43]. This paper, in spite of using the QCA Pro, mathematical analysis of Hamming distance-based assessment of power dissipation is applied to achieve the power dissipation of the proposed circuits. The assessment is achieved using the similar temperature (*i.e.*, $T = 2.0$ K) and the similar channelling energies (*i.e.*, $0.25E_k$, $0.75E_k$, *etc.*). It has been described [43] that, for a shift in the Hamming distance between inputs to the circuit, the energy dispelled will be differed too. In the case of the inverter, $1 \to 1$ or $0 \to 0$ input switching means Hamming distance '0', and the inverter has dispelled power of 0.8 meV at $\gamma = 0.25E_k$ and 2.7 meV at $\gamma = 0.5E_k$. For $1 \to 0$ or $0 \to 1$ input switching, Hamming distance '1' is considered for the inverter and the inverter has dispelled power of 28.4 meV at $\gamma = 0.25E_k$ and 28.6 meV at $\gamma = 0.5E_k$. A ceiling Hamming distance of '3' is measured for the

TABLE 5. Complexity of the proposed designs.

Proposed layout	Quantum cost	Area, μm^2	Latency	Quantum cost of proposed layout
XNOR gate	1	0.04	0.75	0.022
BVF gate	2	0.07	0.50	0.017
TR gate	4	0.12	1.00	0.120
1-bit Feynman gate comparator	1	0.08	0.50	0.020

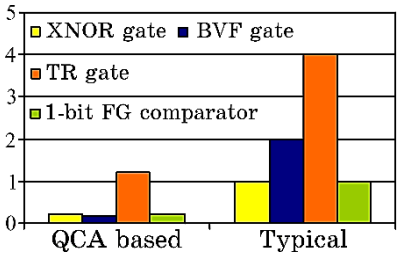

Fig. 9. Quantum cost of the proposed circuit and its QCA layout.

majority voter for $000 \rightarrow 111$ input switching that affects the ceiling dissipated energy of 41.0 meV by the majority voter at $\gamma = 0.25E_k$ and 41.2 meV at $\gamma = 0.5E_k$. Correspondingly, dissipation of power by the majority voter and inverter for several Hamming distances was testified in Refs. [44, 45]. The QCA design of the proposed XNOR consists of one inverter and three majority gates. Each of these majority voters has one stable input polarization.

Therefore, the Hamming distance for these majority voters is measured to be '2', correspondingly. For maximum energy dissipation, Hamming distance '1' is measured for each of the inverters. Applying the Hamming distances related to the input to logic gates and counting the QCA arrays perform in XNOR, the power dissipation of the proposed XNOR is analysed. The results are shown in Table 6. An equal method is applied for figuring the power dissipation by the BVF, TR and 1-bit Feynman gate comparator and the outcomes are denoted in Table 6. Table 6 illustrates that the power dissipated by the XNOR at $\gamma = 0.25E_k$ is of 79.3 meV, and at $\gamma = 1.0E_k$, it is of 94.6 meV. Similarly, for BVF gate, the dissipated power at $\gamma = 0.25E_k$ is of 260.4 meV, and at $\gamma = 1.0E_k$, it is of 295.6 meV; for TR gate, it is of 305.1 meV and 355.6 meV, correspondingly. The power dissipated by the proposed 1-bit Feynman gate comparator is of 206.7 meV when $\gamma = 0.25E_k$ and 235.6 meV when $\gamma = 1.0E_k$. Here, T is the temperature, γ stands for channelling energy, and E_k denotes the kink energy. These outcomes show that all the circuits dissipate very little heat energy. The results are also

TABLE 6. Energy dissipation by the proposed layouts.

Proposed design	$T = 2.0$ K (meV)			
	$0.25E_k$	$0.5E_k$	$0.75E_k$	$1.0E_k$
XNOR gate	79.3	82.8	88.3	94.6
BVF gate	260.4	270.8	275.2	295.6
TR gate	305.1	322.8	340.5	355.6
1-bit Feynman gate comparator	206.7	213.8	224.9	235.6

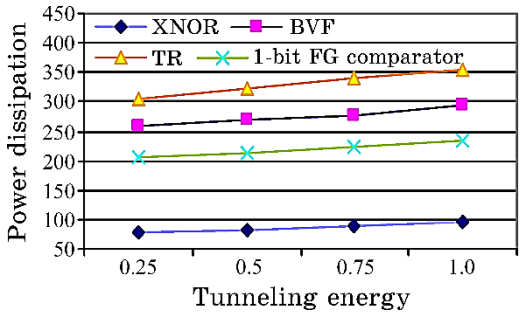

Fig. 10. Power dissipation by the proposed circuits ($T = 2.0$ K).

outlined in Fig. 10.

The average output polarization (AOP) of any cell of the QCA circuit is decreased by enhancing the temperature. The outcome of temperature on the AOP of the urged circuits is presented in Fig. 11. The AOP of the output cell P of the proposed XNOR is slowly lessened, up to a temperature of $T = 8$ K. TR gate work competently between 1 K and 4 K. Similarly, the BVF and 1-bit Feynman gate comparator circuit work proficiently between 1 K and 5 K.

To generate the AOP at separate temperatures, all the proposed designs are simulated by the QCADesigner tool [46] and the highest and lowest polarizations for each cell are observed.

For instance, at $T = 1$ K, the highest and lowest polarizations of output cell P of XNOR are of $9.54e^{-1}$ and $-9.52e^{-1}$, correspondingly. So, the AOP for cell P is of $[(9.54e^{-1})-(-9.52e^{-1})]/2 = 3.51$.

In the similar way, the AOP for separate cells of each proposed circuit at several temperatures are analysed as shown in Fig. 11.

6. CONCLUSION

QCA is an evolving nanotech where elements are micro sized and current clock speed on terahertz range. By uniting the excessive low power consumption of reversible computing and QCA, it is possible

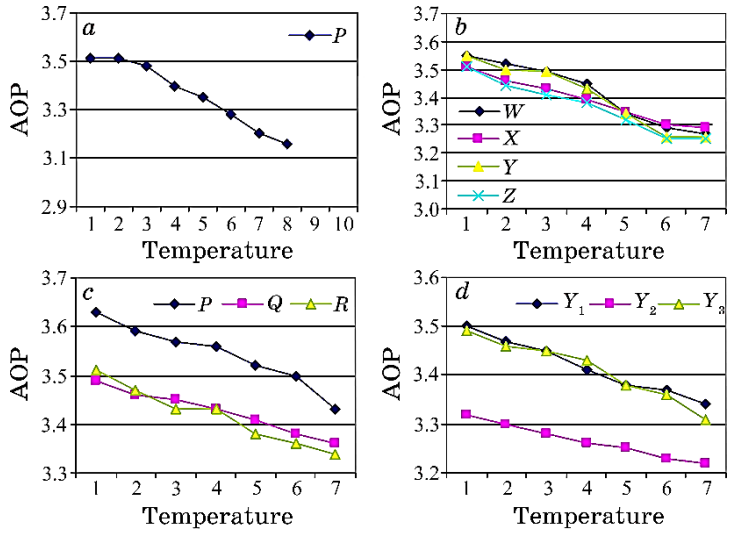

Fig. 11. Temperature effect on AOP of the proposed circuits: (*a*) XNOR, (*b*) BVF, (*c*) TR; (*d*) 1-bit Feynman gate comparator.

to design an extremely profitable logic device, which also apposite for reversible logic circuits.

This paper, a remarkable layout of XNOR, TR, BVF and 1-bit Feynman gate comparator is presented in QCA. The proposed XNOR, TR, BVF gate is 548, 592, 595 times reduced in area, correspondingly, than CMOS technology and flout multilayer wire crossing that would be extremely substantial for designing fault tolerant and compact low power expending nanomaterial.

For the first time, the power dissipation, quantum cost and constancy of the XNOR, TR, BVF and 1-bit Feynman gate comparator have been proposed in this paper.

The proposed QCA circuits exceed the existing ones in terms of cell complexity, area, and latency. The quantum cost-based assessment confirms that the proposed circuits have incredibly low quantum cost measure up to typical designs. The layouts have extremely low heat-energy dissipations, presenting that QCA nanomaterials are appropriate for applying reversible circuits.

The analysis of constancy of the proposed designs under thermal randomness exhibits the permanence of the circuits.

The assessment of simulation outcomes of the proposed circuit with theoretical significances verifies the functionality of the circuits.

The projected design can be used to achieve the nanoscopic scale reversible computing architecture in communication through low power consumption.

REFERENCES

1. J. A. Carballo, W. T. J. Chan, P. A. Gargini, A. B. Kahng, and S. Nath, *32nd International Conference on Computer Design—ICCD (19 October, 2014)*, p. 139; https://doi.org/10.1109/ICCD.2014.6974673
2. C. S. Lent, P. D. Tougaw, W. Porod, and G. H. Bernstein, *Nanotechnology*, **4**, Iss. 1: 49 (1993); https://doi.org/10.1088/0957-4484/4/1/004
3. N. Gallagher and G. Wise, *IEEE Trans. Acoust., Speech, Signal Process*, **29**, Iss. 6: 1136 (1981); https://doi.org/10.1109/TASSP.1981.1163708
4. E. Aptoula and S. Lefèvre, *Pattern Recognit.*, **40**, Iss. 11: 2914 (2007); https://doi.org/10.1016/j.patcog.2007.02.004
5. I. Grattan-Guinness, *Hist. Math.*, **31**, Iss. 2: 163 (2004); https://doi.org/10.1016/S0315-0860(03)00032-6
6. K. Michielsen and H. De Raedt, *Phys. Rep.*, **347**, Iss. 6: 461 (2001); https://doi.org/10.1016/S0370-1573(00)00106-X
7. V. Chatzis and I. Pitas, *IEEE Trans. Image Process.*, **19**, Iss. 7: 699 (2000); https://doi.org/10.1109/42.875192
8. K. Benkrid, A. Benkrid, and S. Belkacemi, *J. Syst. Archit.*, **53**, Iss. 4: 184 (2007); https://doi.org/10.1016/j.sysarc.2006.09.010
9. K. Konstantinidis, G. C. Sirakoulis, and I. Andreadis, *IEEE Trans. Syst. Man. Cybern. Part C*, **39**, Iss. 5: 520 (2009); https://doi.org/10.1109/TSMCC.2009.2020511
10. T. Cole and J. C. Lusth, *Prog. Quantum. Electron.*, **25**, Iss. 4: 165 (2001); https://doi.org/10.1016/S0079-6727(01)00007-6
11. M. Abdullah-Al-Shafi and A. N. Bahar, *5th Intl. Conf. on Informatics, Electronics & Vision (May 13, 2016, Dhaka, Bangladesh)*, p. 620; https://doi.org/10.1109/ICIEV.2016.7760076
12. P. D. Tougaw and C. S. Lent, *J. Appl. Phys.*, **75**, Iss. 3: 1818 (1994); https://doi.org/10.1063/1.356375
13. M. Abdullah-Al-Shafi and A. N. Bahar, *Cogent. Eng.*, **3**, Iss. 1: 1237864 (2016); https://doi.org/10.1080/23311916.2016.1237864
14. M. Abdullah-Al-Shafi, *Nanosistemi, Nanomateriali, Nanotehnologii*, **16**, Iss. 2: 289 (2018); http://dx.doi.org/10.15407/nnn.16.02.289
15. M. Abdullah-Al-Shafi, M. S. Islam, and A. N. Bahar, *Int. J. Comput. Appl.*, **128**, Iss. 2: 27 (2015); https://doi.org/10.5120/ijca2015906434
16. M. Abdullah-Al-Shafi, A. N. Bahar, F. Ahmad, and K. Ahmed, *Cogent. Eng.*, **4**, Iss. 1: 1349539 (2017); https://doi.org/10.1080/23311916.2017.1349539
17. M. Abdullah-Al-Shafi and A. N. Bahar, *Cogent Engineering*, **4**, Iss. 1: 1391060 (2017); https://doi.org/10.1080/23311916.2017.1391060
18. M. Abdullah-Al-Shafi and A. N. Bahar, *J. Nanoelectron. Optoelectron.*, **13**, Iss. 6: 856 (2018); https://doi.org/10.1166/jno.2018.2302
19. M. Abdullah-Al-Shafi and A. N. Bahar, *Int. Nano Lett.*, **9**, Iss. 3: 265 (2019); https://doi.org/10.1007/s40089-019-0279-1
20. M. Abdullah-Al-Shafi and A. N. Bahar, *J. Comput. Theor. Nanosci.*, **14**, Iss. 5: 2416 (2017); https://doi.org/10.1166/jctn.2017.6842
21. M. Abdullah-Al-Shafi and A. N. Bahar, *Sens. Lett.*, **17**, Iss. 7: 595 (2019); https://doi.org/10.1166/sl.2019.4117
22. M. Abdullah-Al-Shafi and A. N. Bahar, *J. Nanoelectron. Optoelectron.*, **14**, Iss. 9: 1275 (2019); https://doi.org/10.1166/jno.2019.2630
23. M. Abdullah-Al-Shafi and Z. Rahman, *Solid State Electron. Lett.*, **1**, Iss. 2: 73

(2019); https://doi.org/10.1016/j.ssel.2019.11.004
24. M. Abdullah-Al-Shafi, A. N. Bahar, M. A. Habib, M. M. R. Bhuiyan, F. Ahmad, P. Z. Ahmad, and K. Ahmed, *Ain Shams Eng. J.*, **9**, Iss. 4: 2641 (2018); https://doi.org/10.1016/j.asej.2017.05.010
25. M. T. Niemier, M. J. Kontz, and P. M. Kogge, *Proc. 37th Annual Design Automation Conference (June 5–9, 2000, Los Angeles, California, USA)*, p. 227; https://doi.org/10.1145/337292.337398
26. M. Crocker, X. S. Hu, M. Niemier, M. Yan, and G. Bernstein, *IEEE Trans. Nanotechnol.*, **7**, Iss: 3: 376 (2008); https://doi.org/10.1109/TNANO.2007.915022
27. M. Abdullah-Al-Shafi and A. N. Bahar, *Int. J. Inf. Technol. Comput. Sci.*, **10**, Iss. 10: 38 (2018); https://doi.org/10.5815/ijitcs.2018.10.05
28. Md. Abdullah-Al-Shafi, *Commun. Appl. Electron.*, **4**, Iss. 1: 20 (2016); http://dx.doi.org/10.5120/cae2016652004
29. J. L. Cardenas-Barrera, K. N. Plataniotis, and A. N. Venetsanopoulos, *Math. Probl. Eng.*, **8**, Iss. 1: 87 (2002); https://doi.org/10.1080/10241230211381
30. V. Mardiris and V. Chatzis, *J. Eng. Sci. Technol. Rev.*, **9**, Iss. 2: 25 (2016); https://doi.org/10.25103/jestr.092.05
31. R. Zhang, K. Walus, W. Wang, and G. A. Jullien, *IEEE Trans. Nanotechnol.*, **3**, Iss. 4: 443 (2004); https://doi.org/10.1109/TNANO.2004.834177
32. I. Amlani, A. O. Orlov, R. K. Kummamuru, G. H. Bernstein, C. S. Lent, and G. L. Snider, *Appl. Phys. Lett.*, **77**, Iss. 5: 738 (2000); https://doi.org/10.1063/1.127103
33. S. B. Tripathi, A. Narzary, R. Toppo, M. Goswami, and B. Sen, *J. Phys. Conf. Ser.*, **1039**, Iss. 1: 012028 (2018); https://doi.org/10.1088/1742-6596/1039/1/012028
34. M. Abdullah-Al-Shafi and R. Ziaur, *Solid State Electron. Lett.*, **1**, Iss. 2: 73 (2019); https://doi.org/10.1016/j.ssel.2019.11.004
35. S. Sheikhfaal, S. Angizi, S. Sarmadi, M. H. Moaiyeri, and S. Sayedsalehi, *Microelectron. J.*, **46**, Iss. 6: 462 (2015); https://doi.org/10.1016/j.mejo.2015.03.016
36. S. S. Ahmadpour, M. Mosleh, and S. Rasouli Heikalabad, *J. Supercomput.*, **76**, Iss. 12: 10155 (2020); https://doi.org/10.1007/s11227-020-03249-3
37. M. Abdullah-Al-Shafi, M. S. Islam, and A. N. Bahar, *Int. Nano Lett.*, **10**, Iss. 3: 177 (2020); https://doi.org/10.1007/s40089-020-00304-y
38. M. R. Hasan, R. Guest, and F. Deravi, *ACM Comput. Surv.*, **55**, Iss. 13: 1 (2023); https://doi.org/10.1145/3583135
39. M. S. Islam, M. Abdullah-Al-Shafi, and A. N. Bahar, *JOT-TT*, **3**, Iss. 2: 145 (2015); https://doi.org/10.15415/jotitt.2015.32010
40. M. S. Islam, M. Abdullah-Al-Shafi, and A. N. Bahar, *Int. J. Comput. Appl.*, **134**, Iss. 7: 1 (2016); https://doi.org/10.5120/ijca2016907711
41. A. N. Bahar, S. Waheed, and N. Hossain, *Springer Plus*, **4**, Iss. 1: 153 (2015); https://doi.org/10.1186/s40064-015-0928-4
42. R. Akter, N. Islam, and S. Waheed, *Int. J. Comput. Appl.*, **109**, Iss. 1: 41 (2015); https://doi.org/10.5120/19155-0591
43. M. Abdullah-Al-Shafi, A. N. Bahar, F. Ahmad, M. M. R. Bhuiyan, and K. Ahmed, *Data Brief.*, **11**, Iss. 1: 593 (2017); https://doi.org/10.1016/j.dib.2017.03.001
44. M. Abdullah-Al-Shafi and A. N. Bahar, *Act. Passiv. Electron. Compon.*, **2018**, Iss. 1: 1 (2018); https://doi.org/10.1155/2018/5062960
45. M. Abdullah-Al-Shafi and A. N. Bahar, *Int. J. Multimed. Ubiq. Eng.*, **11**, Iss. 8: 379 (2016); https://doi.org/10.14257/IJMUE.2016.11.8.38
46. M. Abdullah-Al-Shafi, R. H. Aneek, and A. N. Bahar, *Int. J. Grid. Distrib. Comput.*, **10**, Iss. 1: 43 (2017); https://doi.org/10.14257/ijgdc.2017.10.1.05

Наносистеми, наноматеріали, нанотехнології
Nanosistemi, Nanomateriali, Nanotehnologii
2026, т. 24, № 1, сс. 53–64
https://doi.org/10.15407/nnn.24.01.0053

PACS numbers: 03.67.-a, 03.67.Dd, 05.40.Ca, 07.05.Tp, 89.20.Bb, 89.20.Ff, 89.70.Cf

Розробка пристрою для одержання високої ентропії з фотонного шуму у криптографічних застосуваннях

Т. О. Горелікова

Запорізький національний університет,
вул. Університетська, 66,
69011 Запоріжжя, Україна

Робота стосується розробки прототипу квантового ґенератора випадкових чисел, що долає фундаментальні обмеження традиційних методів. На відміну від псевдовипадкових ґенераторів, які покладаються на обчислювальну складність, і класичних апаратних ґенераторів, схильних до зовнішніх впливів, запропонований пристрій базується на онтологічній природі випадковости мікросвіту. Джерелом ентропії є дробовий шум, що виникає внаслідок дискретної природи проходження зарядів у фотодетекторі. Такий підхід ґарантує непередбачуваність, що є основою для формування стійких криптографічних ключів і цифрових підписів. Представлений пристрій є комплексним апаратно-програмним рішенням. Ця розробка пропонує ефективне та надійне джерело ентропії для інтеґрації у сучасні системи безпеки, забезпечуючи стійкість до атак, які використовують слабкість ґенераторів випадкових чисел.

The work is concerned with the development of a prototype of a quantum random-number generator that overcomes the fundamental limitations of traditional methods. Unlike pseudo-random generators, which rely on computational complexity, and classical hardware generators, which are susceptible to external influences, the proposed device is based on the ontological nature of the randomness of the microworld. The source of entropy is fractional noise that arises from the discrete nature of the passage of charges inside the photodetector. This approach guarantees unpredictability, which is the basis for the formation of stable cryptographic keys and digital signatures. The presented device is a comprehensive hardware–software solution. This development offers an efficient and reliable source of entropy for integration into modern security systems, ensuring resistance to attacks, which exploit the weakness of random-number generators.

Ключові слова: квантовий ґенератор випадкових чисел, істинна ентропія, дробовий шум, криптографічна стійкість, фон Нейманів алґоритм,

апаратний захист інформації, системи безпеки.

Key words: quantum random-number generator, true entropy, fractional noise, cryptographic stability, von Neumann algorithm, hardware information protection, security systems.

(Отримано 2 жовтня 2025 р.)

1. ВСТУП

У сучасному цифровому світі забезпечення надійної інформаційної безпеки є одним з найбільш актуальних завдань. Зростання обсягів даних і популярности блокчейн-платформ створюють нові виклики для захисту від несанкціонованого доступу, шахрайства та кібератак. Одним з фундаментальних елементів безпечних інформаційних систем виступає ґенерація випадкових чисел, адже саме від їхньої якости залежить стійкість криптографічних алґоритмів, які, у свою чергу, є основою сучасних засобів захисту даних [1, 2].

Випадковість є необхідною для формування криптографічних ключів, одноразових паролів, цифрових підписів, а також для процедур автентифікації та верифікації. Будь-яке відхилення від істинної випадковости може мати катастрофічні наслідки. Доведено, що слабкі ґенератори випадкових чисел ставали причиною численних компрометацій криптосистем:

— компрометація RSA-ключів у чипах Infineon (2017) (через слабкий ГВЧ, що використовувався в чипах, дослідники змогли відновити приватні ключі RSA на основі відкритих);
— вразливість Debian OpenSSL (2008) (помилка в коді призвела до того, що для ґенерації ключів використовувалися передбачувані значення, що зробило їх легко зламуваними);
— компрометація Bitcoin-гаманців на Android (2013) (деякі додатки для криптовалют використовували слабкий ГВЧ, що дало змогу зловмисникам передбачити приватні ключі та викрасти кошти);
— вразливість PHP (2007) (слабка ентропія в ґенераторі випадкових чисел PHP робила сеансові ідентифікатори передбачуваними, що давало змогу викрадати сеанси користувачів на вебсайтах) [3].

Саме тому питання джерела випадковости не є другорядним; воно має першорядне значення у контексті побудови захищених систем.

Традиційно у цифрових системах використовуються псевдовипадкові ґенератори чисел (PRNG). Їхня робота базується на детермінованих алґоритмах, які з початкового значення (seed) обчис-

люють послідовності чисел, що виглядають випадковими. Популярними є алґоритми на основі лінійних конґруентних методів, зсувних реґістрів або криптографічних примітивів (наприклад, AES або SHA в режимі ґенератора). Перевагою PRNG є висока швидкодія, проте головним недоліком залишається їхня передбачуваність: знаючи початкове значення або внутрішній стан, зловмисник може відтворити всю послідовність [4].

Для підвищення рівня безпеки застосовуються криптографічно стійкі ґенератори (CSPRNG), які ускладнюють відновлення початкових умов навіть за відомої частини вихідної послідовности. Втім, їхня безпека завжди спирається на припущення про обчислювальну складність певних математичних задач. Тобто стійкість CSPRNG відносна: за умови відкриття нових алґоритмів чи розвитку швидкости обчислень такі ґенератори виявляються вразливими [5].

Іншою категорією є апаратні ґенератори випадкових чисел (HRNG), які використовують фізичні процеси як джерело ентропії. Найчастіше це — тепловий шум у резисторах, коливання електронних схем або хаотичні зміни в електромагнетних середовищах. Незважаючи на більш високу якість у порівнянні з PRNG, ці методи не позбавлені проблем:

— фізичні процеси можуть піддаватися зовнішньому впливу (наприклад, температурних змін або електромагнетних наведень);
— шумові процеси іноді мають латентні закономірності, що понижує рівень ентропії;
— складно формально довести істинну випадковість одержаних послідовностей.

Таким чином, обидва підходи, як псевдовипадкові, так і апаратні класичні ґенератори, мають істотні обмеження. У контексті високонавантажених криптографічних систем, де ціна помилки є надзвичайно високою, цього виявляється недостатньо [6].

2. КВАНТОВІ ПРОЦЕСИ ЯК ПРИРОДНЄ ДЖЕРЕЛО ВИПАДКОВОСТИ

На противагу класичним методам, квантові ґенератори випадкових чисел (QRNG) базуються на фундаментальних законах квантової механіки, які мають ймовірнісну природу. Випадковість тут не є наслідком складности чи неповноти розуміння, а виступає онтологічною характеристикою мікросвіту. Прикладами квантових процесів, що застосовуються у QRNG, є:

— фотонна поляризація: вибір напрямку поляризації окремого фотона є непередбачуваним;
— квантове тунелювання: час ймовірного переходу електрона через бар’єр не можна визначити наперед;

— дробовий шум (shot noise), який виникає внаслідок того, що носії заряду (фотони чи електрони) надходять у детектор у випадкові моменти часу;

— спонтанне випромінювання в лазерах: момент емісії фотона має квантово-ймовірнісну природу.

На відміну від теплового чи електронного шуму, ці процеси принципово не піддаються класичному передбаченню. Вони є реалізацією базових постулатів квантової теорії, і жоден алґоритм чи модель не дають змогу реконструювати їх наперед. Саме тому QRNG забезпечують істинну випадковість [7].

Вибір QRNG як базового джерела випадкових чисел у даній роботі зумовлений багатьма об'єктивними причинами. У PRNG випадковість лише емулюється, а в HRNG вона може бути спотворена шумом або зовнішніми чинниками. У QRNG випадковість ґарантована самою природою квантових явищ. Ґенерація значень на основі QRNG виключає ризик слабких значень, які виникають за недостатньої ентропії. Це критично важливо під час використання алґоритмів еліптичних кривих, де навіть невелика втрата випадковости може призвести до повного компрометування системи. На відміну від класичних джерел, QRNG не потребує статистичного моделювання для підтвердження випадковости: її ґарантують закони квантової механіки [8].

3. ПРИНЦИПИ РОБОТИ КВАНТОВОГО ҐЕНЕРАТОРА ВИПАДКОВИХ ЧИСЕЛ

Метод випадкового вибору учасників і контрольних точок базується на комбінації криптографії еліптичних кривих і ґенерації істинно випадкових чисел. QRNG у цьому контексті виступає не допоміжним, а визначальним елементом:

— він забезпечує непередбачуваність вибору учасників, що унеможливлює маніпуляції з боку окремих вузлів;

— ґарантує рівномірність розподілу під час вибору блоків, запобігаючи концентрації контролю;

— створює базу для формування ключів і підписів, стійких щодо атак на рівні як класичних, так і потенційних квантових комп'ютерів.

Вибір на користь квантового ґенератора випадкових чисел є свідомою відмовою від псевдовипадкових і класичних апаратних методів, які не відповідають сучасним вимогам щодо криптографічної безпеки. Використання QRNG уможливлює підняти рівень захищености системи на якісно новий щабель, забезпечуючи непередбачуваність і стійкість до будь-яких відомих типів атак.

Запропонований розроблений пристрій базується на використанні квантових джерел випадковости, що забезпечує якісно ви-

щий рівень непередбачуваности у порівнянні з класичними ґенераторами псевдовипадкових чисел. В основі роботи покладено явище дробового шуму (shot noise), яке виникає внаслідок дискретної природи фотонів та електронів. За падіння світлового потоку на фотодетектор процес реєстрації фотонів описується Пуассоновим розподілом, де ймовірність спостереження k фотонів за певний проміжок часу задається формулою

$$P(k;\lambda) = \lambda^k e^{-\lambda}/k!, \tag{1}$$

де λ — середня інтенсивність фотонного потоку.

У струмі, що виникає в результаті такого процесу, спостерігається шумова складова з квантовою природою, спектральна густина якої описується рівнянням

$$S_I(f) = 2qI, \tag{2}$$

де q — заряд електрона, а I — середній фотострум. Саме ця непередбачувана складова і стає основним джерелом ентропії у даному пристрої. Для того, щоб оцінити якість одержаних випадкових послідовностей, використовується Шеннонова ентропія, яка визначається як

$$H(x) = -\sum_{i=1}^{n} p_i \log_2 p_i, \tag{3}$$

де p_i — ймовірність появи відповідного символу. Ідеальний випадковий ґенератор забезпечує максимальне значення ентропії, близьке до одного біта на кожний зґенерований біт [9].

Однак фізичні джерела випадковости, зокрема фотодетектори, можуть демонструвати статистичні перекоси у бік ґенерації більшої кількости нулів чи одиниць. Для усунення цієї проблеми у пристрої був реалізований фон Нейманів алґоритм. Його суть полягає у тому, що вхідна послідовність розбивається на пари бітів, після чого відкидаються комбінації «00» і «11», тоді як «01» інтерпретується як нуль, а «10» як одиниця. Завдяки цьому зберігається лише рівноймовірна інформація, а перекіс джерела усувається. Формально процедура описується таким чином:

$$f\left(b_1, b_2\right) = \begin{cases} \varnothing, & b_1 = b_2, \\ 0, & \left(b_1, b_2\right) = (0,1), \\ 1, & \left(b_1, b_2\right) = (1,0). \end{cases} \tag{4}$$

Таким чином, навіть якщо первинний фотонний шум містить структурні відхилення, вихідна послідовність після оброблення за фон Неймановим алґоритмом набуває властивостей рівномір-

ного випадкового розподілу [10].

Розроблений ґенератор випадкових чисел базується на використанні фотонного шуму як джерела ентропії та його подальшому підсиленні за допомогою малошумних аналогових каскадів. Для практичної реалізації ґенератора було використано мікроконтролер ESP32, який виконує функції дискретизації аналогового сиґналу фотодіоди за допомогою вбудованого АЦП, його попереднього оброблення та подальшої цифрової трансформації. Зібрані біти послідовности подаються на програмну реалізацію фон Нейманового алґоритму для підвищення рівня ентропії. Такий підхід уможливлює одержати послідовності, що відповідають криптографічним вимогам до випадковости й успішно проходять перевірку за статистичними тестами стандарту NIST SP 800-22.

У структурі пристрою можна виділити три функціональні блоки: сенсорний, підсилювальний та обчислювальний. Сенсорну частину представлено фотодетектором, що працює в умовах слабкого освітлення або під впливом деякого джерела світла. Як базовий варіянт, застосовується фотодіода BPW34 у режимі зворотнього зміщення; проте для підвищення рівня шуму може бути використана лавинна фотодіода (APD), що працює у режимі пробою. Через неї тече дуже малий струм, настільки малий, що його неможливо сприйняти безпосередньо без посилення; тому у схему пристрою також додано підсилювач. Цей струм — непостійний; він складається з окремих перенесень заряду, що хаотично виникають. Електрони в напівпровіднику не рухаються як безперервний потік, а перестрибують випадково, підкоряючись ймовірнісній природі квантових процесів. Це і є дробовий шум — флюктуації (випадкові коливання), які виникають саме через дискретність електричного заряду, які неможливо передбачити або змоделювати, тому що вони відбуваються в квантовому масштабі, поза рамками класичної причинности.

Фотодіода у цій системі виконує роль не просто давача світла, а квантового джерела ентропії. Вона створює сиґнал, який абсолютно не піддається розрахунку, навіть якщо точно відомі всі параметри схеми, напруги, температури, рівня освітлення. Для підкреслення незалежности від зовнішніх чинників фотодіоду розташовано у світлонепроникній коробці. Фотодіода ґенерує темновий струм (dark current) навіть у повній темряві. Це пов’язане з тепловими коливаннями та квантовими ефектами у матеріялі, тому що сам факт проходження кожного окремого електрона крізь потенціяльний бар’єр — це процес ймовірнісний. Жодна програма, ніякий суперкомп’ютер не може заздалегідь зазначити, коли проскочить наступний електрон, і саме в цьому полягає фундаментальна непередбачуваність [11].

Джерелом світла може виступати світлодіода з низьким рівнем

власних шумів, розташована у світлонепроникному корпусі разом із фотодіодою для формування стабільного шумового каналу.

Аналоговий каскад реалізовано на операційному підсилювачі малошумного типу (наприклад MOPA2340UA). Схему побудовано за конфіґурацією неінвертувального підсилювача з великим коефіцієнтом підсилення, що забезпечує реєстрацію навіть незначних флюктуацій фотоструму. Резистор зворотнього зв'язку номіналом у 100 кОм визначає величину підсилення, тоді як паралельно ввімкнений конденсатор у 100 нФ виконує функцію обмеження високочастотної складової.

Вихід підсилювального каскаду подається на аналоговий вхід ESP32 (наприклад GPIO34), де сиґнал оцифровується вбудованим АЦП. Подальше оброблення передбачає застосування алґоритму за фон Нейманом, що усуває можливі статистичні перекоси у послідовності бітів.

Представлений різновид розробленого ґенератора випадкових чисел складається з трьох незалежних пар фотоелементів (фотодіод із відповідною підсилювальною обв'язкою), кожна з яких формує власний канал шумового сиґналу. Така архітектура дає змогу зменшити вплив локальних флюктуацій і підвищити стійкість системи: навіть якщо один канал тимчасово дає занижений рівень шуму, два інші залишаються активними, забезпечуючи ентропію. Для стабільности роботи додатково використовується допоміжна світлодіода, що створює контрольований рівень освітлення фотодіод і мінімізує ризик повної втрати сиґналу через зовнішні перешкоди. Електричну схему пристрою представлено на рис. 1.

Аналогові сиґнали з кожної пари фотоелементів надходять на входи ESP32, де перетворюються в цифровий вигляд за допомогою вбудованого АЦП. Подальше програмне оброблення передбачає поєднання даних трьох каналів у єдиний результат. Для цього використовується процедура з вибірковим застосуванням медіянного значення, яка пригнічує одиничні викиди, а також операції XOR, що забезпечують непередбачуваність вибору. Таким чином, кінцевий сиґнал містить як фізичну ентропію фотонного шуму, так і математично посилену випадковість. На рисунку 2 представлено зображення макетної плати готового прототипу пристрою, де розміщено усі описані вище компоненти.

У демонстраційному варіянті пристрою передбачено використання невеликого OLED-дисплея, який дає змогу у реальному часі виводити випадкове значення. Така функція має, насамперед, демонстраційний характер: вона дає можливість наочно показувати зміну випадкових величин і контролювати працездатність системи під час експериментів чи публічних презентацій.

Разом із тим, наявність дисплея не є обов'язковою умовою для

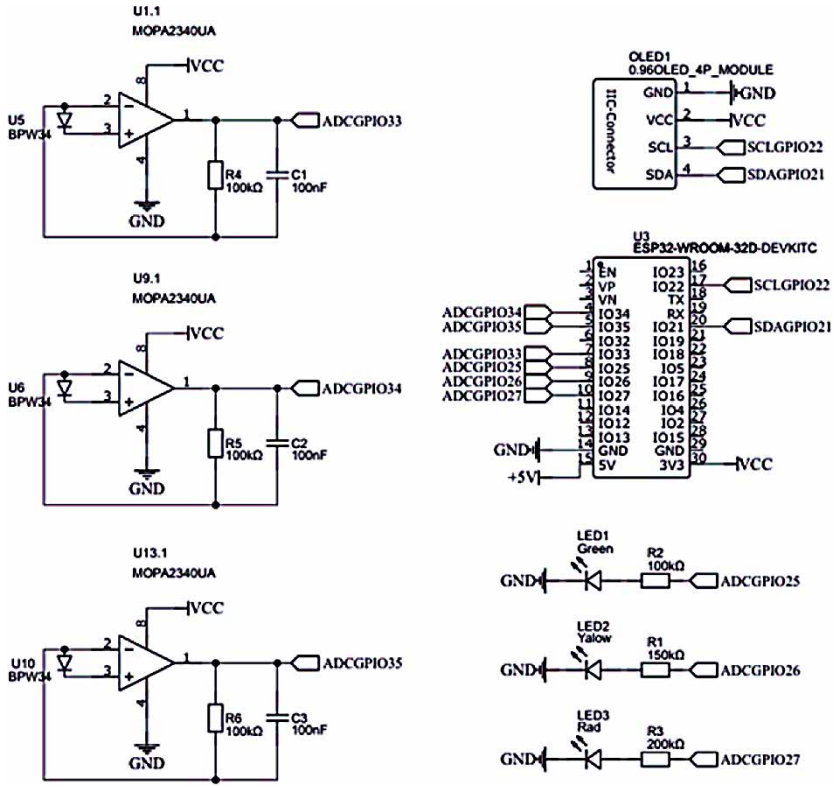

Рис. 1. Електрична схема розробленого прототипу квантового ґенератора випадкових чисел.[1]

роботи ґенератора. У практичних застосуваннях випадкові послідовності можуть безпосередньо передаватися через інтерфейс Serial (UART/USB) або ж передаватися по бездротових каналах (Wi-Fi, Bluetooth) на інші пристрої, зокрема на персональний комп'ютер, сервер або вбудовану систему, де вони будуть використані для криптографічних або статистичних задач. Такий підхід робить систему гнучкою: вона може виступати як автономний демонстраційний модуль із візуалізацією, так і як повноцінне джерело ентропії для інтеґрації у складніші апаратно-програмні комплекси. Демонстраційний варіянт пристрою представлено на фотографії (рис. 3).

4. ЕКСПЕРИМЕНТАЛЬНІ РЕЗУЛЬТАТИ Й ОЦІНКА ЕНТРОПІЇ

Для оцінки якости зґенерованих випадкових чисел було проведено статистичну аналізу вибірки з 2500 значень у діяпазоні від

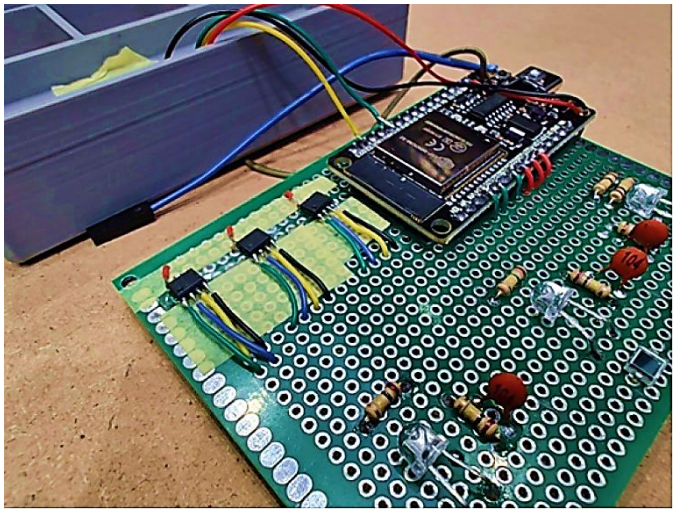

Рис. 2. Фотографія розпаяної макетної плати прототипу квантового ґенератора випадкових чисел.[2]

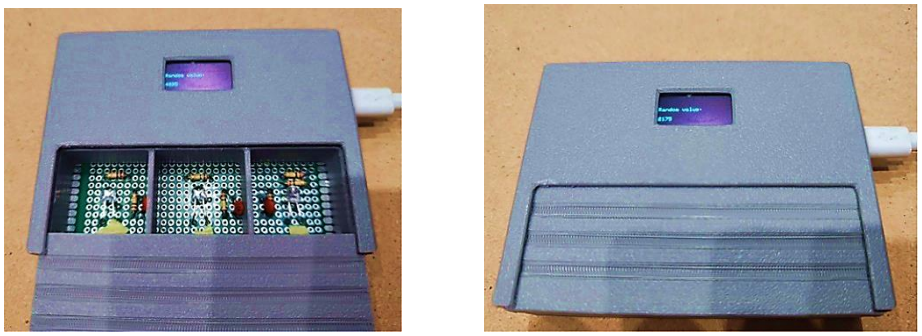

Рис. 3. Зовнішній вигляд готового демонстраційного прототипу квантового ґенератора випадкових чисел.[3]

101 до 9988. Усі числа виявилися унікальними, повтори відсутні, що свідчить про високий рівень різноманітности та відсутність очевидних артефактів у ґенерації. Середнє значення склало 4879,02, медіяна — 4619,5, а стандартний відхил — 2740,6, що добре узгоджується з очікуванням рівномірного розподілу.

Для перевірки рівномірности було виконано χ''-тест із розбиттям вибірки на десять рівних інтервалів. Одержане значення $\chi'' = 5{,}68$ із 9 ступенями свободи відповідає p-значенню приблизно у 0,77, що значно перевищує традиційний рівень значущости у 0,05. Таким чином, гіпотеза про рівномірний розподіл не відхиляється і можна стверджувати, що числа охоплюють увесь діяпа-

зон без концентрації у вузьких зонах.

Додатково було розраховано Шеннонову ентропію, яка склала $H \approx 7{,}97$ біт/символ, що є майже максимально можливим значенням для множини з 2500 рівноймовірних унікальних елементів. Це підтверджує високу ступінь невизначености та випадковости вибірки.

На рівні бітових послідовностей проведені тести на серійність, автокореляцію та стиснення не виявили статистично значимих відхилів.

Було проведено додаткові експерименти для незалежної вибірки, що дало змогу підтвердити стійкість одержаних результатів:

χ''-тест рівномірності (10 інтервалів від 1 до 9999): $\chi'' = 10{,}24$, $p = 0{,}3314$; значення $p > 0.05$ означає відсутність значних відхилів від рівномірного розподілу;

тест Колмогорова–Смирнова (нормування на [0, 1]): $KS = 0{,}070$, $p = 0{,}1663$; тест останньої цифри (χ'' для 0–9): $\chi'' = 5{,}36$, $p = 0{,}8019$;

цифри розподілені рівномірно, відсутнє упередження на рівні молодших розрядів; автокореляція (лаги 1–20): значення коливаються навколо нуля, істотних залежностей не виявлено.

Одержані результати свідчать, що вибірка пройшла ключові статистичні тести на випадковість. Серйозних закономірностей чи упереджень не виявлено. Це підтверджує, що розроблений ґенератор може використовуватися як надійне джерело ентропії для криптографічних задач та інших систем, де потрібна висока якість випадкових чисел.

5. ВИСНОВОК

У описаному пристрої поєднано фізичну непередбачуваність квантового шуму з математично обґрунтованими методами усунення перекосів і криптографічними механізмами постоброблення. Завдяки цьому досягається високий рівень ентропії за помірних апаратних витратах, що робить реалізацію на ESP32 ефективною як для наукових експериментів, так і для практичного використання у системах безпеки, блокчейн-технологіях чи Інтернеті речей.

Продемонстрований прототип квантового ґенератора випадкових чисел успішно вирішує актуальну проблему забезпечення криптографічних систем джерелом істинної випадковости, яке є невразливим до класичних методів злому чи обчислювального прогнозування. Створений пристрій є значним кроком вперед, оскільки він свідомо відходить від застарілих псевдовипадкових і класичних апаратних ґенераторів, чия стійкість є лише відносною. Натомість, у роботі інтеґровано фундаментальне квантове

явище, — шум на напівпровідниковому переході, — в архітектуру, що забезпечує непередбачуваність на атомарному рівні. Апаратне рішення поєднує багаторазове фізичне джерело ентропії (три незалежні канали фотодетекторів) із спеціялізованими аналоговими каскадами. Ця багатоканальна архітектура у поєднанні з програмною корекцією, що використовує методи усунення перекосів, дала змогу досягти максимальної якости вихідної послідовности.

Експериментальні дослідження підтвердили, що ґенератор виробляє послідовності, які відповідають вимогам щодо якости випадкових чисел. Це робить розроблений пристрій джерелом ентропії для важливих застосувань, включаючи формування ключів у блокчейн-технологіях, механізми автентифікації, а також інші системи, де ціна помилки є надзвичайно високою. Таким чином, реалізація прототипу квантового ґенератора випадкових чисел на базі ESP32 демонструє ефективний шлях щодо побудови захищених і стійких щодо майбутніх атак апаратно-програмних комплексів.

ЦИТОВАНА ЛІТЕРАТУРА–REFERENCES

1. T. O. Horelikova and S. V. Choporov, *Int. J. Comput. Appl. Math. Comput. Sci.*, **2024**: 54 (2024); https://doi.org/10.1007/ijcams.2024.54
2. T. O. Horelikova, *Proc. All-Ukrainian Sci.-Pract. Conf. Students, Postgraduates and Young Scientists 'Existential Challenges of Education, Science, Security and Health in Modern Conditions: Research by Young Scientists' (December 12, 2024, Odesa)*, **41**, p. 89 (in Ukrainian).
3. L.-Y. Deng, N. Kumar, H. H.-S. Lu, and C.-C. Yang, *Random Number Generators for Computer Simulation and Cyber Security: Design, Search, Theory, and Application* (Cham: Springer: 2025); https://doi.org/10.1007/978-3-031-76722-7
4. J.-P. Aumasson, *Serious Cryptography* (San Francisco: No Starch Press: 2024).
5. T. Lugrin, *Random Number Generator. Trends in Data Protection and Encryption Technologies* (Eds. V. Mulder, A. Mermoud, V. Lenders, and B. Tellenbach) (Cham: Springer: 2023), p. 31; https://doi.org/10.1007/978-3-031-33386-6_7
6. H. Ravichandran, D. Sen, A. Wali, T. F. Schranghamer, N. Trainor, B. Ray, and S. Das, *ACS Nano*, **17**, No. 17: 16817 (2023); https://doi.org/10.1021/acsnano.3c03581
7. D. Johnston, *Random Number Generators—Principles and Practices: A Guide for Engineers and Programmers* (Berlin: Walter de Gruyter: 2018); https://doi.org/10.1515/9781501506062
8. C. Kollmitzer, S. Schauer, S. Rass, and B. Rainer, *Quantum Random Number Generation: Theory and Practice* (Cham: Springer: 2020); https://doi.org/10.1007/978-3-319-72596-3
9. M. Orszag, *Quantum Optics: Including Noise Reduction, Trapped Ions,*

Quantum Trajectories, and Decoherence (Cham: Springer: 2024); https://doi.org/10.1007/978-3-031-54853-6
10. Douglas Cenzer and Christopher P. Porter, *Computability*, **12**, No. 1: 1 (2023); https://doi.org/10.3233/COM-210343
11. *Quantum Probability and Randomness* (Eds. A. Khrennikov and K. Svozil) (Basel: MDPI Books: 2019); https://doi.org/10.3390/books978-3-03897-715-5

Zaporizhzhya National University,
66 Universytetska Str.,
UA-69011 Zaporizhzhia, Ukraine

[1] **Fig. 1.** Electrical diagram of the developed prototype of the quantum random-number generator prototype.
[2] **Fig. 2.** Photograph of the unsoldered breadboard of the prototype of the quantum random-number generator prototype.
[3] **Fig. 3.** Appearance of the finished prototype of the quantum random-number generator.

Наносистеми, наноматеріали, нанотехнології
Nanosistemi, Nanomateriali, Nanotehnologii
2026, т. 24, № 1, сс. 65–82
https://doi.org/10.15407/nnn.24.01.065

PACS numbers: 71.35.-y, 73.21.La, 73.22.Lp, 73.63.Kv, 78.40.Fy, 78.67.Hc, 81.07.Ta

Nanolasers Based on Semiconductor Quantum Dots

S. I. Pokutnii, V. O. Mashira, and T. Yu. Gromovoy

Chuiko Institute of Surface Chemistry, N.A.S. of Ukraine,
17, Olega Mudraka Str.,
UA-03164 Kyiv, Ukraine

The minireview analyses fundamental experimental and theoretical research and applied applications of nanolasers based on semiconductor (including also perovskite) quantum dots. As shown, the development of nanolasers based on semiconductor and perovskite quantum dots is a consequence of long-term progress in the physics and chemistry of semiconductors. Due to the dimensional quantum limitation of the motion of quasiparticles (electrons and holes) in quantum dots, it becomes possible to vary the emission and absorption spectra by changing the sizes of quantum dots in the nanorange. This allowed semiconductor and perovskite quantum dots to demonstrate a high quantum yield and a narrow width of the emission spectrum. These properties of semiconductor (including also perovskite) quantum-dots' ensembles made it possible to develop a number of nanolasers with high optical characteristics. Current trends in laser-technology development are focused on environmental requirements, in particular, on the development of lead-free perovskite quantum dots to reduce toxicity. Hybridization of perovskite quantum dots allows passivation of the surface, reduction of defect density and increase of charge-carrier lifetime, which lowers the threshold of laser generation and increases the stability of the devices. Such hybrid systems demonstrate improved crystallinity, increased charge-carrier mobility and efficient charge transfer between layers that contributes to increasing quantum efficiency and expanding the emission spectrum from the visible range to the near-infrared range. This opens up new opportunities for the creation of highly efficient, stable and environmentally safe optoelectronic and laser devices of a new generation.

В мініогляді проведено аналізу фундаментальних експериментальних і теоретичних досліджень та прикладних застосувань нанолазерів на основі напівпровідникових (включаючи також перовськітних) квантових цяток. Показано, що розвиток нанолазерів на базі напівпровідникових і перовськітних квантових цяток є наслідком тривалого проґресу в фізиці та хемії напівпровідників. Завдяки розмірному квантовому обме-

женню руху квазичастинок (електронів і дірок) у квантових цятках стало можливим варіювати спектри випромінення та вбирання шляхом зміни розмірів квантових цяток у нанодіяпазоні. Це уможливило в напівпровідникових і перовськітних квантових цятках демонструвати високий квантовий вихід і вузьку ширину спектру випромінення. Ці властивості ансамблів напівпровідникових (включаючи також перовськітних) квантових цяток надали можливість розробити цілий ряд нанолазерів з високими оптичними характеристиками. Сучасні тенденції розвитку лазерних технологій орієнтовано на екологічні вимоги, зокрема на розробку безплюмбумових перовськітних квантових цяток для зменшення токсичности. Гібридизація квантових цяток перовськітів уможливлює пасивувати поверхню, зменшити густину дефектів і підвищити час життя носіїв заряду, що понижує поріг лазерної ґенерації та підвищує стабільність роботи пристроїв. Такі гібридні системи демонструють поліпшену кристалічність, підвищені рухливість носіїв заряду й ефективне перенесення заряду між шарами, що сприяє підвищенню квантової ефективности та розширенню спектру випромінення від видимого до близького інфрачервоного діяпазону. Це відкриває нові можливості для створення високоефективних, стабільних і екологічно безпечних оптоелектронних і лазерних пристроїв нового покоління.

Key words: perovskites, quantum dots, optical transitions, quantum energy levels, nanolasers.

Ключові слова: перовськіти, квантові цятки, оптичні переходи, квантові енергетичні рівні, нанолазери.

(Received 6 September, 2025; in revised form, 12 September, 2025)

1. INTRODUCTION

Nanolasers based on semiconductor (including also perovskite) quantum dots (QDs) are attracting significant attention from researchers due to the rapid advancement of nanolaser technologies driven by fundamental experimental and theoretical studies [1–20]. Their practical interest stems from their potential for creating compact photonic chips, biosensors, and single-photon sources, enabled by high photoluminescent efficiency, narrow emission bandwidth, and low lasing thresholds [20–28].

A key theoretical challenge in studying nanosystems is describing the interaction of electromagnetic fields with surface electronic states localized at the interfaces of nanosystems [11–18]. This approach requires accurately modelling interactions (Coulomb, polarization, exchange, spin–orbit, spin–spin, *etc.*) between quasiparticles (electrons, holes, and excitons) induced by electromagnetic fields at these interfaces. It is also necessary to determine the size limits of quantum objects (QDs, nanofilms, quantum wires), where the effec-

tive mass approximation remains valid [11–18].

In the 1960s and 1970s, despite the availability of advanced technologies (nuclear energy, semiconductor nanoheterostructures) and known perovskite materials, these materials were not used as the basis for devices (solar cells, LEDs, lasers) due to several objective reasons. Firstly, their unique optoelectronic properties, particularly those of organic–inorganic halide perovskites, which now drive fundamental and practical interest, were not yet discovered [12–18, 29–31]. Secondly, technologies for producing high-quality thin films and nanostructures with controlled parameters were unavailable, and synthesis methods were limited, preventing the creation of materials with the required purity and structure [30–32]. Additionally, there was a lack of theoretical understanding of charge transfer mechanisms, defects, stability, and interface interactions, which are critical for developing efficient devices [11–18]. Furthermore, there was no urgent need for new materials in solar energy or displays, as silicon, GaAs, and other semiconductors met the technological demands of that time [32, 33].

The development of nanolasers based on semiconductor (including also perovskite) QDs is the result of long-term progress in semiconductor physics and chemistry. In the 1980s and 1990s, the foundations for creating QDs—nanocrystals, which allow tuning of emission and absorption spectra by varying their size in the nanoscale range due to quantum confinement—were established. Classical QDs, such as CuCl, CdS, CdSe, ZnS, ZnSe, GaAs, and aluminium oxide, demonstrated high quantum yields and narrow spectral widths but faced limitations in stability and environmental safety [12–28, 34–51]. Concurrently, research on perovskite materials gained attention due to their unique properties, realized in solar cells: high absorption coefficients, long carrier diffusion lengths, and low defect concentrations [11–17, 52, 53]. A major breakthrough occurred with the synthesis of halide perovskite QDs with the formula $CsPbX_3$ (X = Cl, Br, I), which combined the advantages of classical QDs and perovskites—high photoluminescent efficiency (up to 90–100%), narrow spectral width (18–36 nm), a wide tuneable emission range (from blue to red), and high carrier mobility [53, 54]. Key contributions came from studies [6, 11, 15, 55], which first demonstrated the effectiveness of such QDs for nanolasers, providing low lasing thresholds and emission stability [53].

In study [11], the photoluminescent properties of $CsPbX_3$ QDs with average sizes of 10–12 nm were investigated. It was found that interband transitions between quantum-confined electronic states in these QDs exhibit giant dipole moments (on the order of 10 Debye) [12, 15, 17]. Such quantum-confined electronic states can lead to strong optical absorption in these QDs. Additionally, these

states were found to be long-lived (on the order of 30 ns), raising hopes for achieving Bose–Einstein condensation of excitons in these QDs [12, 15, 17].

Research has focused on optimizing the composition of perovskites (*e.g.*, fully inorganic $CsPbBr_3$), morphology, and surface ligands to enhance the stability and efficiency of nanolasers, as well as developing new compositions from simple nanocrystals to hybrid structures and laser arrays [51, 52, 54]. Encapsulation of materials in bilayer mesoporous SiO significantly improved moisture resistance and device durability, while the use of plasmonic nanostructures reduced lasing thresholds and expanded functionality for biophotonics [56]. Thus, the development of nanolasers based on semiconductor and perovskite QDs illustrates a rapid evolution from fundamental discoveries to practical applications in modern optoelectronic technologies [12–17, 51–54].

Following initial studies of halide perovskites, which exhibited high absorption coefficients (> 10 cm^{-1}) and long carrier diffusion lengths (up to 1 μm), their potential in laser technologies was recognized [52, 57]. The next step was the creation of $CsPbX_3$ (X = Cl, Br, I) QDs with sizes of 3–13 nm, which, due to quantum confinement, enabled precise tuning of emission spectra: blue ($CsPbCl_3$, 410–430 nm), green ($CsPbBr_3$, 510–520 nm), and red ($CsPbI_3$, 680–700 nm) [52, 57]. Subsequently, hybrid structures such as 'quantum-dot-in-perovskite' were developed, where colloidal QDs were integrated into a perovskite matrix, improving charge transfer and stability [58]. A significant breakthrough was the creation of nanolasers with ultralow lasing thresholds (*e.g.*, 1.9 W/cm^2 at 120 K for $CsPbBr_3$ QDs) and small mode volumes ($\cong 0.2\%$), enabling their integration into photonic chips [57]. Each step was accompanied by improvements in the physical parameters of materials and devices, facilitating the transition from laboratory samples to practical nanolasers with controllable properties [52, 56–58].

This minireview analyses fundamental experimental and theoretical studies and applied applications of nanolasers based on semiconductor (including also perovskite) quantum dots. As shown, their applied interest stems from their potential to create compact photonic chips, biosensors, and single-photon sources, enabled by high photoluminescent efficiency, narrow emission bandwidth, and low lasing thresholds.

2. SEMICONDUCTOR QUANTUM DOTS IN NANOLASERS

The unique optoelectronic properties of semiconductor and perovskite QDs have enabled the creation of nanolasers [17, 34, 44, 50]. QDs made of cadmium and zinc sulphides/selenides, gallium arse-

nide, and perovskites such as $CsPbBr_3$ and $CsPbI_3$ exhibit low defect densities, high carrier mobility (up to 60 $cm^2/(V{\cdot}s)$), and low Auger recombination rates [59]. The bandgap energies (E_g) of such QDs range from 1.5 to 2.6 eV, allowing experimental observation of interband transitions of charge carriers (electrons and holes) across a wide range, including near-infrared and optical spectral regions [59].

Chemically, perovskites are easily synthesized by solution methods, which simplify their application in nanolasers [59, 60]. Quantum confinement in semiconductor and perovskite QDs occurs, when the radii a of the QD become smaller than the Bohr radius of the exciton $a_{ex} = \varepsilon\hbar^2 / (m_{ex}e^2)$ ($m_{ex} = m_e m_h / (m_h + m_e)$—the reduced mass of the exciton in the QD , m_e and m_h—the effective masses of the electron and hole in the QD; ε—the dielectric constant of the QD), Bohr radius of the electron $a_e = \varepsilon\hbar^2 / (m_e e^2)$ and Bohr radius of the hole $a_h = \varepsilon\hbar^2 / (m_h e^2)$, *i.e.*, the conditions must be fulfilled [11–18] as follow:

$$a < a_e, a_h, a_{ex} . \tag{1}$$

Usually, the Bohr radii of quasiparticles a_e, a_h, a_{ex} are of the order of 2–7 nm [11–18]. We will assume that the motion of quasiparticles (electrons, holes, and excitons) in QDs can be described in the effective-mass approximation [11–18]. We will describe QDs by the model of an infinite spherical-potential well. Then, the lower energy levels of the electron $E_{n_e,l_e}(a)$ in the conduction band of QDs and the hole $E_{n_h,l_h}(a)$ in the valence band of QDs are determined by the formulas [11–18]

$$E_{n_e,l_e}(a) = \hbar^2(\varphi_{n_e,l_e})^2 / (2m_e a^2) , \tag{2}$$

$$E_{n_h,l_h}(a) = \hbar^2(\varphi_{n_h,l_h})^2 / (2m_h a^2) , \tag{3}$$

where the subscripts (n_e, l_e) and (n_h, l_h) are the principal and azimuthal quantum numbers for the electron and the hole; and $\varphi_{n,l}$ are the roots of the Bessel function, *i.e.*, $J_{l+1/2}(\varphi_{n,l}) = 0$. The expressions $E_{n_e,l_e}(a)$ (2) and $E_{n_h,l_h}(a)$ (3) correctly describe the lower quantum-dimensional energy levels of the electron and hole within the QD, if their position is much lower than the depth of the QD potential well (of the order of the band gap width E_g). In this case, the conditions are satisfied as follow:

$$E_{n_e,l_e}(a), E_{n_h,l_h}(a) \ll E_g . \tag{4}$$

Fulfilment of condition (4) also allows us to consider the motion of quasiparticles within the QD, in which the conduction band and

the valence band have a parabolic shape. To observe the energy levels of an electron (2) and a hole (3) in a QD at room temperature T_0, it is necessary that the energy distance between adjacent levels,

$$\Delta E_{e(h)}(a) \ll k_B T_0 , \tag{5}$$

was much smaller than a quantum of thermal energy $k_B T_0$ [11–18].

When conditions (1), (4) and (5) are met, as a result of interband transitions of an electron from quantum-dimensional energy levels $E_{n_e,l_e}(a)$ (2) to quantum-dimensional energy levels $E_{n_h,l_h}(a)$ (3) in a QD, emission (absorption) spectra are formed [11–18]:

$$\hbar\omega_{n,l}(a) = E_{n_e,l_e}(a) + E_{n_h,l_h}(a) + E_g , \tag{6}$$

where $\hbar\omega_{n,l}(a)$ is the quantum of light emitted during the transition. The selection rules allow only interband transitions, in which the quantum numbers $(n_e = n_h)$ and $(l_e = l_h)$ of the electron and hole are preserved. With a decrease in the radius a of the QD, the positions of the quantum-dimensional energy levels $E_{n_e,l_e}(a) \propto a^{-2}$ (2) of the electron and $E_{n_h,l_h}(a) \propto a^{-2}$ (3) of the hole shift upward, approaching the boundary of the QD potential well. As a result, the energy levels $E_{n_e,l_e}(a)$ (2) of the electron and $E_{n_h,l_h}(a)$ (3) of the hole are pushed out of the QD potential well. For instance, for the CdS QD with a radius $a \le 2$ nm, only two electron levels $(n_e = 1, l_e = 0)$, $(n_e = 1, l_e = 1)$ and two hole levels $(n_h = 1, l_h = 0)$, $(n_h = 1, l_h = 1)$ remain in the QD potential wells [17]. These interband transitions can be used in the operation of CdS QD nanolasers [17]. The decrease in the radius a of the QD also led to an increase in the effective band-gap width $(\hbar\omega_{n,l}(a) \propto a^{-2})$ of the QD [11–18, 61, 62]. Therefore, varying the parameters of nanosystems, such as the values of the effective masses of quasiparticles and the radii a of the QD, allows for the directed production of nanosystems with predetermined optical properties.

For $CsPbBr_3$-perovskite QDs, a size reduction from 8.5 to 4.1 nm causes an increase in the band gap from 2.37 to 2.5 eV, which is accompanied by a blue shift of photoluminescence [11, 61, 62]. In such QDs, an increased exciton binding energy is observed (for example, for $CsPbBr_3$ nanoplates, it can exceed 40 meV), which ensures efficient charge transfer and a longer lifetime of excited states compared to bulk crystals [11, 63, 64]. In two-dimensional perovskites, a decrease in the layer thickness leads to an increase in the effective mass of carriers and an increase in the exciton binding energy, which allows tuning the optical properties [65]. Quantum confinement also affects the rate and mechanisms of relaxation: for example, in $MAPbI_3$ QDs, multiexciton generation processes occur

in a few femtoseconds and radiative recombination in nanoseconds [66]. Due to these effects, perovskite QDs exhibit high photoluminescence quantum efficiency, narrow emission spectrum width, and the ability to tune precisely the colour of the glow through control of size and composition [61, 62]. This makes perovskites unique structures for creating efficient nanolasers, LEDs, and solar cells [11, 61–63].

Compact nanolasers based on perovskite and semiconductor QDs are a new class of miniature coherent light sources that combine ease of fabrication, a wide tuning range, and high optical characteristics. Perovskite QDs, in particular $CsPbBr_3$, allow the creation of lasers with extremely small dimensions (*e.g.*, 10×10 μm^2), narrow emission linewidth $\cong 0.1$ nm, and low losses due to the use of quasi-continuum-coupled states (quasi-BIC) [67]. Vertical cavity lasers based on $CsPbBr_3$ QDs demonstrate an ultralow generation threshold 0.39 $\mu J/cm^2$, high stability of operation (over 5 hours or $1.8\cdot10$ pulses), and the ability to operate in the femtosecond regime, which is important for portable electronics and optical communications [67, 69]. Nanolasers based on perovskite QDs provide a wide range of wavelength tuning (from blue to near-infrared ones), a narrow emission band (0.1–0.2 nm), and the possibility of flexible 3*D* patterning for integration into miniature photonic chips, displays, sensors, and biomedical devices [56, 67, 70, 71]. An important advantage of these lasers over semiconductor QD lasers is also their high stability to moisture and temperature, especially in composites with SiO or liquid crystal resonators [56, 72]. Recent developments include topological lasers based on $CsPbBr_3$ QDs, which are defect-resistant and provide single-mode generation even with miniaturization [69].

3. THEORETICAL MODEL OF AN OPTICAL NANOLASER ON HEAVY HOLE TRANSITIONS

The optical properties of quasi-0*D* structures consisting of spherical semiconductor (or dielectric) nanocrystals (NCs) (or QDs) of radius $a \cong 1–10$ nm, grown in transparent dielectric (or semiconductor) matrices, are currently being intensively studied [11–18]. Optical and nonlinear optical properties of heterophase nanosystems are determined by the energy spectrum of spatially limited electron–hole pairs (EHP) (or excitons) [11–18]. Quantum size effects have been detected in the energy spectra of electrons and excitons in such quasi-0*D* structures using optical spectroscopy [11–18].

The motion of charge carriers in NC, like in QDs, is limited in three directions. Therefore, the energy spectrum of charge carriers is discrete in NC with linear dimension of the order 1–10 nm [12,

15, 17, 34, 44, 50]. This property can be used to create optical nanolasers or optical computers [37, 44, 50]. In this context, we point out that the size (*i.e.*, radius) a of a QD should be in the range of a few nm in order to provide that the difference, *i.e.*, energy splitting $\Delta E_{e(h)}$, between electron and hole levels are of the order of a few $k_B T_0$ at the room temperature T_0. In Ref. [17], it was discussed theoretically the prospect of using semiconductor NCs for designing nanolasers.

The energy spectrum of an EHP

$$E_{n_e, l_e=0, t_h}(S) = \\ = E_g + \pi^2 n_e^2 S^{-2} Kb + S^{-1}\left(Z_{n_e,0} + P_{n_e,0} + \varepsilon_2/\varepsilon_1\right) + \omega(S, n_e)\left(t_h + 3/2\right), \tag{7}$$

in the quantum state $(n_e l_{e=0}, t_h)$; (n_e, l_e) are the principal and orbital quantum numbers of the electron, and t_h are the principal quantum number of the hole in a spherical NC with permittivity ε_2, submerged in a dielectric matrix with ε_1 such that $\varepsilon_2 >> \varepsilon_1$ was obtained in Ref. [17] within the adiabatic approximation ($m_e << m_h$, where m_e and m_h are the effective masses of an electron and a hole in the NC) using only the first-order perturbation theory in the functions of a spherical-potential well of infinite depth. Here, $t_h = 2n_r + l_h = 0, 1, \ldots$ (n_r is the hole radial quantum number and l_h is the orbital quantum number of a hole), $S = a/a_h$ is the dimensionless radius of the NC, and a_h and E_g—the Bohr radius of the hole and the band gap in an infinite semiconductor with permittivity ε_2, respectively. The energy in Eq. (1) is measured in the units of $Ry = \hbar^2/(2m_h a_h^2)$, the coefficient $K = 0.67$ accounts for the variance of the NCs with respect to the radii a [17], and the parameter $b = m_e/m_h$. The parameters $Z_{n_e,0}$ and $P_{n_e,0}$ were determined in Refs. [17]:

$$Z_{n_e,0} = 2\int_0^1 dx (1 - x^2)^{-1} \sin^2(\pi n_e x), \tag{8}$$

$$P_{n_e,0} = 2Ci(2\pi n_e) - 2\ln(2\pi n_e) - 2\delta + \varepsilon_2/\varepsilon_1 - 1, \tag{9}$$

where $Ci(y)$ is the cosine integral and $d = 0.577$—the Euler constant.

The EHP spectrum (7) was obtained for NCs whose sizes a are limited by the condition

$$a_0 << a_h << a \le a_e, \tag{10}$$

where a_e are the Bohr radius of the electron in an infinite semiconductor with permittivity ε_2, and a_0 is a characteristic length of the order of the interatomic distance. When this condition is satisfied, the polarization interaction of an electron and a hole with the sur-

face of the NC plays a large role in the potential energy of the EHP. The condition (10) also makes it possible to study the motion of an electron and a hole in the NC in the effective-mass approximation.

The last term in the EHP spectrum (7) gives the hole spectrum $\mu_{n_e,l_e=0,t_h}(S)$ in oscillator form [17]:

$$\mu_{n_e,l_e=0,t_h}(S) = P_{n_e,0}S^{-1} + \omega(S,n_e)\left(t_h + 3/2\right), \qquad (11)$$

$$\omega(S,n_e) = 2.232\left(1 + (2/3)\pi^2 n_e^2\right)^{1/2} S^{-3/2}, \qquad (12)$$

where $\omega(S,n_e)$ is the frequency of the hole-oscillator vibrations, in an adiabatic electronic potential [17]. The second term in Eq. (7) (kinetic energy of the electron), which is due to the purely spatial limitation of the quantization region, makes the main contribution to the EHP spectrum (1) obtained within the adiabatic approximation, and the last two terms, which are associated with the Coulomb and polarization of the electron and the hole with the surface of the NC, appear only as corrections.

Thus, the polarization interaction of an electron and a hole with the surface of a NC, just as the quantization of the charge carriers, contributes to the renormalization of the energy gap (8) of the NCs.

In Ref. [17], interband absorption spectra of CdS NC ($\varepsilon_2 = 9.3$) of sizes varying from 1 to 10 nm dispersed in a transparent dielectric matrix of silicate glass were investigated. The effective masses of electrons and holes in CdS were ($m_e/m_0 = 0.205$) and ($m_h/m_0 = 5$), respectively (*i.e.*, $m_e << m_h$).

In the experiment reported in Refs. [16, 34, 44, 50], an energy structure consisting of an equidistant series of levels was found in the region of transitions to the lower level of dimensional quantization of the electron ($n_e = 1$). The above structure is caused by quantization of the hole energy spectrum in the adiabatic potential of the electron.

From the comparison of formula (6) (for $n_e = 1$) with the experimental dependence of the splitting magnitude of the NC size a obtained in Refs. [17], it follows that, for NC of radii $1.5 \le a \le 3.0$ nm, the splitting $\omega(S, n_e)$ (12) is in good agreement with the experimental data [34, 44, 50] and differs from the latter only slightly ($\le 4\%$) [17].

Based on the presented results, a scheme of operation of a laser developed on the basis of CdS NCs grown in boric–silicate glass matrices was formulated [17] as follow.

1. Pumping: the hole transition from energy level $\mu_{n_e=1,l_e=0,t_h=1}(S)$ (11) to electron state ($n_e = 1, l_e = 0$) (1*s* state) (7) in conduction band with energy

$$\hbar\omega_1(S) = E_g + E_{n_e=1,l_e=0}(S) + \mu_{n_e=1,l_e=0,t_h=1}(S). \quad (13)$$

2. Creation of inverse population on the hole level ($t_h = 0$ by means of electron transition from the energy level $E_{n_e=1,l_{e=0}}(S)$ (1), with spin flip [50], to the hole energy level $\mu_{n_e=1,l_e=0,t_h=1}(S)$ (5). The energy of this transition

$$\hbar\omega_2(S) = E_g + E_{n_e=1,l_e=0}(S) + \mu_{n_e=1,l_e=0,t_h=0}(S). \quad (14)$$

3. Lasing step: transition of the hole in the valence band between equidistant levels $(t_h = 0) \rightarrow (t_h = 1)$ separated by the energy

$$\Delta\omega(S, n_e = 1) = \hbar\omega(S, n_e = 1); \quad (15)$$

for NC of the radius $a = 2$ nm, $\Delta\omega \cong 54$ meV (15) is several times greater than the thermal energy $k_B T$.

Thus, in a nanolaser on CdS NCs, the pumping energy $\hbar\omega_1 \cong 3.12$ eV (7) would correspond to visible light, and lasing at energy $\Delta\omega \cong 54$ meV (9) would occur in the infrared range.

4. APPLICATION OF NANOLASERS IN OPTICAL INTERCONNECTS

Due to their unique properties, nanolasers based on perovskite and semiconductor QDs fined a variety of applications. In each specific application (for example, optical interconnects, photonics, biophotonics), not all general properties of perovskite and semiconductor QDs are used, namely those that are critical to achieving the desired functions and efficiency of the device. Properties such as band gap width, emission wavelength, generation threshold, carrier transfer rate, and moisture stability are not just universal characteristics, but those that are specially selected and optimized for a specific field of application.

Thus, in the field of optical interconnects, nanolasers based on perovskite and semiconductor QDs are used as sources of coherent light for ultrafast data transfer between chips. The most common perovskite QDs used for this purpose are methylammonium lead bromide ($MAPbBr_3$), methylammonium lead iodide ($MAPbI_3$), and caesium lead bromide ($CsPbBr_3$). QDs often have the formula $CsPbX_3$, where X is Cl, Br or I [56, 57, 73, 74]. They are used to create integrated photonic circuits, sensors, spectroscopic systems, and optical computers. High quantum efficiency, a wide emission spectrum, and the ability to tune precisely the wavelength make these materials versatile for such photonic applications [1, 56, 74]. For example, $CsPbBr_3$ perovskite QDs embedded in a two-layer mesoporous silica

matrix demonstrate efficient two-photon excitation and moisture resistance, which allows them to be used in biophotonics and sensors. Such nanolasers are characterized by high optical quality factor, high carrier transfer rate and bright emission even in the near infrared range [56, 73]. Experiments have shown that photoelectrons and holes generated in a perovskite matrix with a significant band gap (of the order of 2.5 eV) are transferred to the QD with an efficiency of up to 80%, where intense light emission occurs [73]. Thus, nanolasers based on perovskite QDs (*e.g.*, $MAPbBr_3$, $CsPbBr_3$, $CsPbX_3$) characterized by a band gap of 1.5–2.3 eV, a radiation wavelength of 520–800 nm, an ultralow generation threshold (up to 1.9 W/cm^2), and a high optical *Q*-factor have the potential for effective integration into optical interconnects and photonic devices [57, 73–76].

5. APPLICATION OF NANOLASERS IN BIOMARKET DETECTION, SENSING AND DIAGNOSTICS

Promising nanolasers for use in biomarker detection, sensing and diagnostics are created based on perovskite QDs with the general formula ABX_3, where *A* is an organic or inorganic cation (*e.g.*, Cs^+, MA^+—methylammonium, FA^+—formamidine), *B* is a metal (usually PbI^+), *X* is a halogen (Cl^-, Br^-, I^-). Typical examples are $CsPbBr_3$, $MAPbBr_3$, and $CsPbI_3$.

The quantum dimensional effect in QDs with sizes of 2–10 nm makes it possible to tune precisely the values of the effective band gap and emission spectra by changing the particle size [12–18, 61, 75, 77]. Perovskite QDs used in nanolasers are characterized by high photoluminescence quantum efficiency (PLQY > 90%), narrow emission bandwidth ($FWHM \cong 15$–30 nm), wide wavelength tuning range (400–800 nm) and low lasing threshold ($I\_th \cong 10$–100 $\mu J/cm^2$) [61, 74, 75, 77], existence of long-lived edge-dimensional electronic states with lifetime $\tau \cong 20$–50 ns [12–18, 61, 77]. Due to high defect tolerance and ease of synthesis, such QDs demonstrate stable luminescence even without additional surface passivation [61, 75]. CdSe, InP-based QDs, as well as perovskite QDs (*e.g.*, $CsPbIX_3$, where $X = Cl$, Br, I) are used for cell biomarkers, protein and DNA sensing, and for the creation of highly sensitive biosensors [74, 77]. In biomedical applications, perovskite QDs are encapsulated in biocompatible shells (*e.g.*, SiO_2, polymers), which ensures stability in aqueous media and minimizes toxicity [61, 75]. Thus, $CsPbBr_3$@SiO QDs are used for high-resolution cell labelling and for sensing metal ions and biomolecules due to changes in luminescence intensity upon interaction with the analyte [61, 74]. In laser biosensors based on perovskite QDs, a generation threshold of < 100 $\mu J/cm^2$ is

achieved that allows them to be used for point sensing of biological objects [77]. Thus, nanolasers based on perovskite QDs (ABX_3, in particular, $CsPbBr_3$, $MAPbBr_3$) and QDs (CdSe, InP, $CsPbBr_3$), which have found application in this field combine high photoluminescence, narrow emission band, low generation threshold and the possibility of biofunctionalization, which makes them ideal for modern biomarkers, sensing and diagnostics [61,74, 75, 77].

6. APPLICATIONS IN QUANTUM AND NEUROMORPHIC TECHNOLOGIES

Nanolasers based on perovskite QDs (ABX_3, *e.g.*, $CsPbBr_3$, $CsPbI_3$) and semiconductor QDs (CdSe, InP, PbS) demonstrate unique physical properties, which makes them promising for quantum and neuromorphic technologies (systems whose architecture and operating principles are similar to the biological brain). The main physical parameters, which give them promise in such applications, are the bandgap widths (from 1.7 to 2.3 eV); photoluminescence quantum efficiency (PLQY) can exceed 90–99% even without additional passivation; emission bandwidth (*FWHM*)—15–30 nm; excited state lifetime—10–100 ns; QD sizes are of 4–12 nm (strong quantum confinement) [11, 12, 15, 17, 34, 44, 50, 61, 77].

For quantum technologies, the important properties are single-photon emission, narrow spectral line, spin control and coherence: for example, $CsPbBr_3$ QDs demonstrate emission coherence up to 80 ps, as well as the possibility of spin control through size and composition [61, 77]. In quantum computing and cryptography, such QDs are used as single-photon sources for quantum communications, as well as for multistimulus optical coding and 3*D* optical memory [61, 74, 77].

In neuromorphic technologies, hybrid structures based on $CsPbBr_3$ QDs/graphene or QDs/carbon nanotubes provide photonic synapses with energy consumption on the order of tens of attojoules, simulation of short- and long-term memory, and associative learning [61]. Promising transistors based on perovskite QDs demonstrate high carrier mobility (up to 10 $cm^2/(V{\cdot}s)$), an extended hysteresis window, and stability under multiple switching [61]. Highly confined $CsPbBr_3$ QDs with dimensions (4–8 nm) are a source of single photons for quantum computing, with high colour purity and stability [77]. Hybrid perovskite/QD structures are used for optical memory, where the information storage time can reach several hours, and recording/erasing is performed by a laser pulse [61, 77]. QDs in photonic neuromorphic sensors provide sensitivity up to 10^{-15} Joules, which allows us to recognize weak signals and simulate synaptic transmission [61].

7. PROSPECTS FOR THE DEVELOPMENT OF LASER-TECHNOLOGY RESEARCH

One of the main problems of theoretical research on nanosystems is the correct description of the interactions of nanoparticles (Coulomb, polarization, exchange, spin–orbit, spin–spin ones) with the interfaces of nanosystems (semiconductor–dielectric–metal) [12–18]. Theoretical modelling of hybrid nanosystems based on perovskite and semiconductor QDs, which takes into account quantum-dimensional effects, allows us to predict the influence of the size, shape and composition of QDs on the effective band gap, emission and absorption spectra that is key to optimizing the optoelectronic properties of materials [12–18, 78, 79]. Studies show that the interaction between nanoparticles localized above the QD surfaces in the perovskite matrix can lead to efficient energy transfer, changes in the emission and absorption spectra (*e.g.*, red and blue shifts) and even to the emergence of quantum effects such as coherence, which opens up prospects for quantum technologies [73, 78]. Hybrid structures of the 'quantum-dot-in-perovskite' type provide high quality interfaces, which contribute to efficient charge transfer and increase the stability and diffusion length of charge carriers [73, 78].

Current trends in the development of laser technologies are focused on environmental requirements, in particular, on the development of lead-free perovskites and QDs to reduce toxicity [12–18, 31, 44, 50, 79, 80]. Hybridization of perovskite QDs allows passivation of the surface, reduction of defect density and increase of charge carrier lifetime, which lowers the threshold of laser generation and increases the stability of the devices [11–17, 78, 81]. Such hybrid systems demonstrate improved crystallinity, increased charge carrier mobility and efficient charge transfer between layers, which contributes to the increase of quantum efficiency and expansion of the emission spectrum from the visible to the near infrared range [12–18, 73, 78, 81]. This opens up new opportunities for the creation of highly efficient, stable and environmentally safe optoelectronic and laser devices of a new generation [78, 79, 80].

REFERENCES

1. Ziwen Wang, Zezhong Yin, Dongze Xie, Yifei Wang, Zhenyu Yang, Fukai Shan, Jia Huang, and Dandan Hao, *ACS Photonics*, **14**, Iss. 9: 1088 (2025); https://doi.org/10.1021/acsphotonics.5c01387
2. Zhen-Bo Guo, Xiang-Mei Duan, and Jing Wang, *J. Phys. Chem. Lett.*, **16**, Iss. 34: 8657 (2025); https://doi.org/10.1021/acs.jpclett.5c02152
3. Yujie Jiao, Bing Gu, and Siying Peng, *J. Phys. Chem. Lett.*, **16**, Iss. 33: 8627 (2025); https://doi.org/10.1021/acs.jpclett.5c01663

4. Jiaying Liu, Xiaohui Liu, Jianwei Wang, Zhongyu Liu, Chenyu Zhou, Hubin Zeng, Heng Qiao, Jing Zhang, Like Huang, Ning Chen, and Yuejin Zhu, *J. Phys. Chem. Lett.*, **16**, Iss. 34: 8632 (2025); https://doi.org/10.1021/acs.jpclett.5c02129
5. Dongke Chen, Han Cai, Xiaoyu Xuan, Zhili Hu, Yang Lu, Wanlin Guo, and Zhuhua Zhang, *J. Phys. Chem. Lett.*, **16**, Iss. 32: 8165 (2025); https://doi.org/10.1021/acs.jpclett.5c01745
6. Lanfang Hou, Siyi Hu, Butian Zhang, and Shun Wang, *J. Phys. Chem. Lett.*, **16**, Iss. 32: 8290 (2025); https://doi.org/10.1021/acs.jpclett.5c01837
7. Rohit Abraham John, Yiğit Demirağ, Yevhen Shynkarenko, Yuliia Berezovska, Natacha Ohannessian, Melika Payvand, Peng Zeng, Maryna I. Bodnarchuk, Frank Krumeich, Gökhan Kara, Ivan Shorubalko, Manu V. Nair, Graham A. Cooke, Thomas Lippert, Giacomo Indiveri and Maksym V. Kovalenko, *Nature Commun.*, **13**: Article No. 2074 (2022); doi:10.1038/s41467-022-29727-1
8. Oleksandr Kolomiiets, Andriy Stelmakh, Amrutha Rajan, Sebastian Sabisch, Gabriele Rainò, Andrij Baumketner, Maksym V. Kovalenko, and Maryna I. Bodnarchuk, *ACS Nano*, **19**, Iss. 30: 9117 (2025); doi:10.1021/acsnano.5c09117
9. Arnab Ghosh, Samuel Palato, Patrick Brosseau, Rui Tao, Dmitry N. Dirin, Maksym V. Kovalenko, and Patanjali Kambhampati, *ACS Nano*, **19**, Iss. 29 7429 (2025); doi:10.1021/acsnano.5c07429
10. Yuliia Kominko, Sebastian Sabisch, Andrii Kanak, Lidiia Dubenska, Ihor Cherniukh, Matthias Klimpel, Xuqi Liu, Sergey Tsarev, Simon C. Boehme, Gebhard J. Matt, Gabriele Rainò, Maksym V. Kovalenko, and Sergii Yakunin, *ACS Nano*, **19**, Iss. 32: 7771 (2025); doi:10.1021/acsnano.5c03771
11. S. I. Pokutniĭ, *Semiconductors*, **40**: 217 (2006); doi:10.1134/S106378260602019
12. S. I. Pokutnii, *Physics of the Solid State*, **39**: 634 (1997); doi:10.1134/1.1129943
13. Sergey I. Pokutnyi, Yuri N. Kulchin, Vladimir P. Dzyuba, and Andrey V. Amosov, *Journal of Nanophotonics*, **10**, Iss. 3: 036008 (2016); https://doi.org/10.1117/1.JNP.10.036008
14. S. I. Pokutnyi, *Low Temperature Physics*, **44**: 819 (2018); https://doi.org/10.1063/1.5049165
15. S. I. Pokutnyi, *Physics of the Solid State*, **39**: 528 (1997); doi:10.1134/1.1129923
16. Viktor G. Klyuev, Denis V. Volykhin, Oleg V. Ovchinnikov, and Sergey I. Pokutnyi, *Journal of Nanophotonics*, **10**, Iss. 3: 033507 (2016); doi:10.1117/1.JNP.10.033507
17. Sergey I. Pokutnyi, *Physics Letters A*, **342**, Iss. 4: 347 (2005); https://doi.org/10.1016/j.physleta.2005.04.070
18. S. I. Pokutnyi, *Semiconductors*, **47**: 1626 (2013); doi:10.1134/S1063782613120178
19. Sandrine Ithurria and Benoit Dubertret, *J. Am. Chem. Soc.*, **130**, Iss. 49 16504 (2008); https://doi.org/10.1021/ja807724e
20. M. D. Tessier, B. Mahler, R. P. S. M. Lobo, B. Dubertret, and Al. L. Efros, *Nature Mater.*, **10**: 936 (2011); https://doi.org/10.1038/nmat3145
21. Pooja Tyagi, Sarah M. Arveson, and William A. Tisdale, *J. Phys. Chem.*

Lett., **6**, Iss. 10: 1911 (2015); https://doi.org/10.1021/acs.jpclett.5b00664
22. Daniel Sapori, Mikaël Kepenekian, Laurent Pedesseau, Claudine Katan, and Jacky Even, *Nanoscale*, **8**: 6369 (2016); https://doi.org/10.1039/C5NR07175E
23. Shalini Singh, Renu Tomar, Stephanie ten Brinck, Jonathan De Roo, Pieter Geiregat, José C. Martins, Ivan Infante, and Zeger Hens, *J. Am. Chem. Soc.*, **140**, Iss. 41: 13292 (2018); https://doi.org/10.1021/jacs.8b07566
24. A. Di Giacomo, C. Roda, A. H. Khan, and I. Moreels, *Chem. Mater.*, **32**: 9260 (2020); https://doi.org/10.1021/acs.chemmater.0c03066
25. Michael W. Swift, Alexander L. Efros, and Steven C. Erwin, *Nature Communications*, **15**: Article No. 7737 (2024); https://doi.org/10.1038/s41467-024-51842-4
26. Christian Meerbach, Remo Tietze, Sascha Voigt, Vladimir Sayevich, Volodymyr M. Dzhagan, Steven C. Erwin, Zhiya Dang, Oleksandr Selyshchev, Kristian Schneider, Dietrich R. T. Zahn, Vladimir Lesnyak, and Alexander Eychmüller, *Adv. Opt. Mater.*, **7**, Iss. 7: 1801478 (2019); https://doi.org/10.1002/adom.201801478
27. Claudine Katan, Nicolas Mercier, and Jacky Even, *Chem. Rev.*, **119**, Iss. 5: 3140 (2019); https://doi.org/10.1021/acs.chemrev.8b00417
28. Elena V. Shornikova, Dmitri R. Yakovlev, Louis Biadala, Scott A. Crooker, Vasilii V. Belykh, Mikhail V. Kochiev, Alexis Kuntzmann, Michel Nasilowski, Benoit Dubertret, and Manfred Bayer, *Nano Lett.*, **20**, Iss. 2: 1370 (2020); https://doi.org/10.1021/acs.nanolett.9b04907
29. R. Benchamekh, N. A. Gippius, J. Even, M. O. Nestoklon, J.-M. Jancu, S. Ithurria, B. Dubertret, Al. L. Efros, and P. Voisin, *Phys. Rev. B*, **89**: 035307 (2014); https://doi.org/10.1103/PhysRevB.89.035307
30. Elena V. Shornikova, Dmitri R. Yakovlev, Nikolay A. Gippius, Gang Qiang, Benoit Dubertret, Ali Hossain Khan, Alessio Di Giacomo, Iwan Moreels, and Manfred Bayer, *Nano Lett.*, **21**, Iss. 24: 10525 (2021); https://doi.org/10.1021/acs.nanolett.1c04159
31. Carlos Moure and Octavio Peña, *Progress in Solid State Chemistry*, **43**, Iss. 4: 123 (2015); https://doi.org/10.1016/J.PROGSOLIDSTCHEM.2015.09.001
32. Priyanka Roy, Aritra Ghosh, Fraser Barclay, Ayush Khare, and Erdem Cuce, *Coatings*, **12**, Iss. 8: 1089 (2022); https://doi.org/10.3390/coatings12081089
33. Jiang-Yang Shao, Dongmei Li, Jiangjian Shi, Chuang Ma, Yousheng Wang, Xiaomin Liu, Xianyuan Jiang, Mengmeng Hao, Luozheng Zhang, Chang Liu, Yiting Jiang, Zhenhan Wang, Yu-Wu Zhong, Shengzhong Frank Liu, Yao-hua Mai, Yongsheng Liu, Yixin Zhao, Zhijun Ning, Lianzhou Wang, Baomin Xu, Lei Meng, Zuqiang Bian, Ziyi Ge, Xiaowei Zhan, Jingbi You, Yongfang Li, and Qingbo Meng, *Science China Chemistry*, **66**: 10 (2022); https://doi.org/10.1007/s11426-022-1445-2
34. Alexander L. Efros and Louis E. Brus, *ACS Nano*, **15**, Iss. 4: 6192 (2021); https://doi.org/10.1021/acsnano.1c01399
35. Moritz Gramlich, Michael W. Swift, Carola Lampe, John L. Lyons, Markus Dцblinger, Alexander L. Efros, Peter C. Sercel, and Alexander S. Urban, *Adv. Sci.*, **9**, Iss. 5: 2103013 (2022); https://doi.org/10.1002/advs.202103013
36. Ali Naeem, Francesco Masia, Sotirios Christodoulou, Iwan Moreels, Paola

Borri, and Wolfgang Langbein, *Phys. Rev. B*, **91**: 121302 (2015); https://doi.org/10.1103/PhysRevB.91.121302
37. Elad Benjamin, Venkata Jayasurya Yallapragada, Daniel Amgar, Gaoling Yang, Ron Tenne, and Dan Oron, *J. Phys. Chem. Lett.*, **11**, Iss. 16: 6513 (2020); https://doi.org/10.1021/acs.jpclett.0c01628
38. Botao Ji, Eran Rabani, Alexander L. Efros, Roman Vaxenburg, Or Ashkenazi, Doron Azulay, Uri Banin, and Oded Millo, *ACS Nano*, **14**, Iss. 7: 8257 (2020); https://doi.org/10.1021/acsnano.0c01950
39. Benjamin T. Diroll and Richard D. Schaller, *J. Phys. Chem. C*, **127**, Iss. 9: 4601 (2023); https://doi.org/10.1021/acs.jpcc.2c08079
40. Alessio Di Giacomo, Carmelita Roda, Ali Hossain Khan, and Iwan Moreels, *Chem. Mater.*, **32**, Iss. 21: 9260 (2020); https://doi.org/10.1021/acs.chemmater.0c03066
41. Sotirios Christodoulou, Juan I. Climente, Josep Planelles, Rosaria Brescia, Mirko Prato, Beatriz Martín-García, Ali Hossain Khan, and Iwan Moreels, *Nano Lett.*, **18**, Iss. 10: 6248 (2018); https://doi.org/10.1021/acs.nanolett.8b02361
42. Alexander W. Achtstein, Sabrine Ayari, Sophia Helmrich, Michael T. Quick, Nina Owschimikow, Sihem Jaziri, and Ulrike Woggon, *Nanoscale*, **12**, Iss. 46: 23521 (2020); https://doi.org/10.1039/D0NR04745G
43. Benjamin T. Diroll, Corentin Dabard, Emmanuel Lhuillier, and Sandrine Ithurria, *Adv. Opt. Mater.*, **12**, Iss. 9: 2302004 (2024); https://doi.org/10.1002/adom.202302004
44. Mengxia Liu, Nuri Yazdani, Maksym Yarema, Maximilian Jansen, Vanessa Wood, and Edward H. Sargent, *Nature Electron.*, **4**: 548 (2021); https://doi.org/10.1038/s41928-021-00632-7
45. Namyoung Ahn, Clément Livache, Valerio Pinchetti, Heeyoung Jung, Ho Jin, Donghyo Hahm, Young-Shin Park, and Victor I. Klimov, *Nature*, **617**: 79 (2023); https://doi.org/10.1038/s41586-023-05855-6
46. Mickaël D. Tessier, Clémentine Javaux, Ivan Maksimovic, Vincent Loriette, and Benoit Dubertret, *ACS Nano*, **6**, Iss. 8: 6751 (2012); https://doi.org/10.1021/nn3014855
47. Mickaël D. Tessier, Louis Biadala, Cécile Bouet, Sandrine Ithurria, Benjamin Abecassis, and Benoit Dubertret, *ACS Nano*, **7**, Iss. 4: 3332 (2013); https://doi.org/10.1021/nn400833d
48. Alexander W. Achtstein, Andrei Schliwa, Anatol Prudnikau, Marya Hardzei, Mikhail V. Artemyev, Christian Thomsen, and Ulrike Woggon, *Nano Lett.*, **12**, Iss. 6: 3151 (2012); https://doi.org/10.1021/nl301071n
49. Felipe V. Antolinez, Freddy T. Rabouw, Aurelio A. Rossinelli, Jian Cui, and David J. Norris, *Nano Lett.*, **19**, Iss. 12: 8495 (2019); https://doi.org/10.1021/acs.nanolett.9b02856
50. C. Trallero-Giner, A. Debernardi, M. Cardona, E. Menéndez-Proupín, and A. I. Ekimov, *Physical Rev. B*, **57**: 4664 (1998); doi:10.1103/PhysRevB.57.4664
51. Katie Hills-Kimball, Hanjun Yang, Tong Cai, Junyu Wang, and Ou Chen, *Advanced Science*, **8**, Iss. 12: 214 (2021); https://doi.org/10.1002/advs.202100214
52. Kaiyang Wang, Shuai Wang, Shumin Xiao, and Qinghai Song, *Advanced Optical Materials*, **6**, Iss. 18: 278 (2018);

https://doi.org/10.1002/adom.201800278
53. Qi Wei, Xiaojun Li, Chao Liang, Zhipeng Zhang, Jia Guo, Guo Hong, Guichuan Xing, and Wei Huang, *Advanced Optical Materials*, **7**, Iss. 17: 80 (2019); https://doi.org/10.1002/adom.201900080
54. Aryamol Stephen, A. Biju, Sona C. P, and Jayaram Peediyekkal, *Journal of Luminescence*, **269**: 120462 (2024); https://doi.org/10.1016/j.jlumin.2024.120462
55. Loredana Protesescu, Sergii Yakunin, Maryna I. Bodnarchuk, Franziska Krieg, Riccarda Caputo, Christopher H. Hendon, Ruo Xi Yang, Aron Walsh, and Maksym V. Kovalenko, *Nano Lett.*, **15**, Iss. 6: 3692 (2015); https://doi.org/10.1021/nl5048779
56. Yu Chen, Minghuai Yu, Shuai Ye, Jun Song, and Junle Qu, *Nanoscale*, **10**, Iss. 14: 6704 (2018); https://doi.org/10.1039/c7nr08670a
57. Yu-Hung Hsieh, Bo-Wei Hsu, Kang-Ning Peng, Kuan-Wei Lee, Chih Wei Chu, Shu-Wei Chang, Hao-Wu Lin, Ta-Jen Yen, and Yu-Jung Lu, *ACS Nano*, **14**, Iss. 9: 11670 (2020); https://doi.org/10.1021/acsnano.0c04224
58. Richard T. Williams, Weronika W. Wolszczak, Xiaoheng Yan, and David L. Carroll, *ACS Nano*, **14**, Iss. 5: 5161 (2020); https://doi.org/10.1021/acsnano.0c02529
59. Lei Lei, Qi Dong, Kenan Gundogdu, and Franky So, *Advanced Functional Materials*, **31**, Iss. 16: 144 (2021); https://doi.org/10.1002/adfm.202010144
60. Haiyun Dong, Chunhuan Zhang, Xiaolong Liu, Jiannian Yao, and Yong Sheng Zhao, *Chemical Society Reviews*, **49**, Iss. 3: 951 (2020); https://doi.org/10.1039/c9cs00598f
61. Chien-Yu Huang, Hanchen Li, Ye Wu, Chun-Ho Lin, Xinwei Guan, Long Hu, Jiyun Kim, Xiaoming Zhu, Haibo Zeng, and Tom Wu, *Nano-Micro Letters*, **15**: Article No. 16 (2022); https://doi.org/10.1007/s40820-022-00983-6
62. Junhao Lin, Leyre Gomez, Chris de Weerd, Yasufumi Fujiwara, Tom Gregorkiewicz, and Kazutomo Suenaga, *Nano Letters*, **16**, Iss. 1: 7198 (2016); https://doi.org/10.1021/ACS.NANOLETT.6B03552
63. Leepsa Mishra, Ranjan Kumar Behera, Aradhana Panigrahi, Priyanka Dubey, Soumi Dutta, and Manas Kumar Sarangi, *The Journal of Physical Chemistry Letters*, **14**, Iss. 10: 2651 (2023); https://doi.org/10.1021/acs.jpclett.3c00010
64. Anja Barfüßer, Sebastian Rieger, Amrita Dey, Ahmet Tosun, Quinten A. Akkerman, Tushar Debnath, and Jochen Feldmann, *Nano Letters*, **22**, Iss. 22: 8810 (2022); https://doi.org/10.1021/acs.nanolett.2c02223
65. Mateusz Dyksik, Shuli Wang, Watcharaphol Paritmongkol, Duncan K. Maude, William A. Tisdale, Michal Baranowski, and Paulina Plochocka, *The Journal of Physical Chemistry Letters*, **12**, Iss. 6: 1638 (2021); https://doi.org/10.1021/acs.jpclett.0c03731
66. Dayton J. Vogel, Andrei Kryjevski, Talgat Inerbaev, and Dmitri S. Kilin, *The Journal of Physical Chemistry Letters*, **8**, Iss. 13: 3032 (2017); https://doi.org/10.1021/acs.jpclett.6b03048
67. Di Xing, Mu-Hsin Chen, Zhiyu Wang, Chih-Zong Deng, Ya-Lun Ho, Bo-Wei Lin, Cheng-Chieh Lin, Chun-Wei Chen, and Jean-Jacques Delaunay, *Advanced Functional Materials*, **34**, Iss. 26: 2314953 (2024); https://doi.org/10.1002/adfm.202314953
68. Chun-Ying Huang, Chen Zou, Chenyi Mao, Kathryn L. Corp, Yung-Chi Yao,

Ya-Ju Lee, Cody W. Schlenker, Alex K. Y. Jen, and Lih Y. Lin, *ACS Photonics*, **4**, Iss. 9: 2281 (2017); https://doi.org/10.1021/ACSPHOTONICS.7B00520

69. Jingyi Tian, Qi Ying Tan, Yutao Wang, Yihao Yang, Guanghui Yuan, Giorgio Adamo, and Cesare Soci, *Nature Communications*, **14**: Article No. 1433 (2022); https://doi.org/10.1038/s41467-023-36963-6
70. Lei Wang, Linghai Meng, Lan Chen, Sheng Huang, Xiangang Wu, Guang Dai, Luogen Deng, Junbo Han, Bingsuo Zou, Chunfeng Zhang, and Haizheng Zhong, *The Journal of Physical Chemistry Letters*, **10**, Iss. 12: 3248 (2019); https://doi.org/10.1021/acs.jpclett.9b00658
71. Ziyu Li, Zhiyuan Gao, Lige Liu, Kai Zhang, Rui Ma, Yue Wang, Gaoling Yang, and Kebin Shi, *Nano Letters*, **25**, Iss. 18: 7410 (2025); https://doi.org/10.1021/acs.nanolett.5c00861
72. Lihua Ye, Shaoqiang Hong, Chunguang Lu, and Qing Zhao, *Journal of Luminescence*, **277**: 120990 (2025); https://doi.org/10.1016/j.jlumin.2024.120946
73. Zhijun Ning, Xiwen Gong, Riccardo Comin, Grant Walters, Fengjia Fan, Oleksandr Voznyy, Emre Yassitepe, Andrei Buin, Sjoerd Hoogland, and Edward H. Sargent, *Nature*, **523**: 324 (2015); https://doi.org/10.1038/nature14563
74. Jifan Zou, Mengkai Li, Xiaoyu Zhang, and Weitao Zheng, *Journal of Applied Physics*, **132**: 220901 (2022); https://doi.org/10.1063/5.0126496
75. Hung-Chia Wang, Zhen Bao, Hsin-Yu Tsai, An-Cih Tang, and Ru-Shi Liu, *Small*, **14**, Iss. 1: 2433 (2018); https://doi.org/10.1002/smll.201702433
76. Lin-Jer Chen, Jia-Heng Dai, Jia-De Lin, Ting-Shan Mo, Hong-Ping Lin, Hui-Chen Yeh, Yu-Chou Chuang, Shun-An Jiang, and Chia-Rong Lee, *ACS Applied Materials & Interfaces*, **10**, Iss. 39: 33307 (2018); https://doi.org/10.1021/acsami.8b08474
77. Junzhi Ye, Deepika Gaur, Chenjia Mi, Zijian Chen, Iago Lypez Fernández, Haitao Zhao, Yitong Dong, Lakshminarayana Polavarapu, and Robert L. Z. Hoye, *Chemical Society Reviews*, **53**, Iss. 16: 8095 (2024); https://doi.org/10.1039/d4cs00077c
78. Haijie Chen, Joao M. Pina, Yi Hou, and Edward H. Sargent, *Advanced Energy Materials*, **12**, Iss. 4: 2100774 (2021); https://doi.org/10.1002/aenm.202100774
79. Jianguo Cao, Yingge Geng, Lijie Wu, Yuan Zhang, Jie Xu, Haixia Xie, and Yong Pan, *Chemistry Select.*, **10**, Iss. 17: e202501401 (2025); https://doi.org/10.1002/slct.202501401
80. Hyung Ryul You, Han Na Yu, Eon Ji Lee, Hyeon Soo Ma, Younghoon Kim, and Jongmin Choi, *Applied Physics Reviews*, **11**, Iss. 4: 041329 (2024); https://doi.org/10.1063/5.0218208
81. Jianhua Han, Songping Luo, Xuewen Yin, Yu Zhou, Hui Nan, Jianbao Li, Xin Li, Dan Oron, Heping Shen, and Hong Lin, *Small*, **14**, Iss. 31: 1801016 (2018); https://doi.org/10.1002/smll.201801016

Наносистеми, наноматеріали, нанотехнології
Nanosistemi, Nanomateriali, Nanotehnologii
2026, т. 24, № 1, сс. 83–96
https://doi.org/10.15407/nnn.24.01.0083

PACS numbers: 07.05.Tp, 42.70.Qs, 73.30.+y, 78.40.Ha, 78.67.-n, 84.60.Jt, 88.40.hj

Improving the Efficiency of Lead-Free Nanoperovskite Cells Using SCAPS-1*D* Software

Hardan T. Ghanem[1], Muaamar A. Kamil[2], and Mahmood H. Mayoof[3]

[1]*Shirqat Department,*
Salah al-Din Education Directorate, Ministry of Education,
34001 Shirqat, Iraq
[2]*College of Education for Pure Sciences,*
Department of Physics,
Tikrit University,
34001 Tikrit, Iraq
[3]*Anbar Education Directorate, Ministry of Education,*
34001 Anbar, Iraq

The OMeATP/$Cs_2AgBiBr_6$/TiO_2/FTO solar cell is studied using SCAPS-1*D* simulation, where a compound with nanoparticles with sizes ranging from 1.2 to 2.9 nm is used. Previous practical research is compared with the program, and good results are obtained that mimic the results of the practical research used. The cell is improved by increasing the work function; so, the conversion efficiency is increased from 0.31% to 1.01%. The distortion rate of the reflection layer is increased; so, the efficiency is increased from 1.01% to 1.22%. The thickness of the absorption layer is changed; so, the efficiency is increased from 1.22% to 3.91%. Then, the radiation recombination coefficient is changed. It is noticed that the cell efficiency is increased and the recombination is decreased; so, the efficiency is increased from 3.91% to 4.79%.

Сонячний елемент OMeATP/$Cs_2AgBiBr_6$/TiO_2/FTO досліджено за допомогою моделювання симулятором ємности сонячних елементів SCAPS-1*D*, де використано сполуку з наночастинками розміром від 1,2 до 2,9 нм. Попередні практичні дослідження порівняно з програмою й одержано хороші результати, що імітують результати використаних практичних досліджень. Елемент вдосконалено шляхом збільшення роботи виходу; тому ефективність перетворення збільшилася від 0,31% до 1,01%. Швидкість спотворення шару відбивання збільшено; тому ефективність збільшилася від 1,01% до 1,22%. Товщину шару вбирання змінено; тому ефективність збільшилася від 1,22% до 3,91%. Потім змінено коефіцієнт рекомбінації випромінення. Помічено, що ефективність елементу збільшилася, а рекомбінація зменшилася; тому ефективність збільшилася від 3,91% до 4,79%.

Key words: nanoperovskite, $Cs_2AgBiBr_6$, SCAPS simulation, absorption layer, distortion rate, efficiency.

Ключові слова: наноперовськіт, $Cs_2AgBiBr_6$, СЄСЕ-моделювання, вбиральний шар, швидкість спотворення, ефективність.

(Received 18 July, 2024; in revised form, 8 August, 2024)

1. INTRODUCTION

Over the past ten years, lead-halide perovskite (LHP) nanocrystals have garnered a great deal of attention because of their exceptional optical and optoelectronic qualities, which include long photocarrier diffusion lengths, low exciton binding energies, and high photoluminescence quantum yields (PL QYs) [1–3]. Over the past ten years, lead-halide perovskite (LHP) nanocrystals have garnered a great deal of attention because of their exceptional optical and optoelectronic qualities, which include long photocarrier diffusion lengths, low exciton binding energies, and high photoluminescence quantum yields (PL QYs) [4, 5]. The materials exhibit diffusion of both holes and electrons of more than approximately one micron, and the diffusion length means that these materials can operate effectively in a thin structure, and that charges can be transported in the perovskite itself over long distances [6, 7]. Recent research has indicated that the charges of perovskites always exist in the form of free electrons and holes, rather than as bound excitons, because the exciton binding energy is low enough to enable charge separation at room temperature [8]. Double perovskite materials, $Cs_2AgBiBr_6$, have been discovered, as they are layered. Absorption is suitable for the manufacture of solar cells, as it is a highly crystalline compound, which encourages energy generation [9, 10], as it is more stable because it is not affected by moisture [11]. In this research, we will take the main absorption layer, the perovskite compound $Cs_2AgBiBr_6$, which is a double layer that is free of toxicity and less affected by humidity, with a back reflection layer, OMeTAD, a matching layer, TiO_2, and FTO permeation. The theoretical work was compared with experimental work, and a great convergence in the results was revealed, to show the extent of the program sobriety, because we performed an improvement on the cell generated through the SCAPS-1*D* program.

2. NUMERICAL SIMULATION IN SCAPS

Modelling can be performed using the SCAPS program, which is a one-dimensional solar cell simulation program designed at the Uni-

versity of Ghent in Belgium to simulate traditional semiconductor crystalline materials such as CIGS, CdTe, or other materials such as SnS. The user can describe a cell consisting of a maximum of seven layers for different properties such as optical absorption, thickness, doping concentration, energy gap, *etc*. The spectral responses are determined and can be calculated in the dark and in the light as a function of temperature. This program has been developed and applied to all solar cells. It is a program is available free. The program is based on solving semiconductor equations. We begin by writing the Poisson equation, an elliptical partial differential equation, named after the French physicist Simeon Poisson, who discovered its application in universal gravity and static electricity with the equation also known by its name, the Poisson–Boltzmann equation, which regulates the relationship between electric potential and the distribution of electric charge, and in general, it has applications in quantum theory [12, 13]:

$$\nabla E = \frac{q}{\varepsilon}\left(p - n + N_D^+ - N_A^-\right). \tag{1}$$

Then, the continuity equation gives the following relationships [14]:

$$\frac{dn}{dt} = \frac{1}{q}\left(\nabla J_n + G_n - R_n\right), \tag{2}$$

$$\frac{dp}{dt} = -\frac{1}{q}\left(\nabla J_p + G_p - R_p\right). \tag{3}$$

Finally, the charge carrier equations for the diffusion and drift current density can be obtained from the following equations [15]:

$$J_n = q\left(\mu_n nE + D_n \nabla n\right), \tag{4}$$

$$J_p = q\left(\mu_p PE + D_p \nabla p\right). \tag{5}$$

To measure the quality of photovoltaic cells, fill factor (*FF*), short circuit current J_{sc}, open circuit voltage V_{oc}, and conversion efficiency η must be known, as these variables are related to each other with the following equations [15]:

$$FF = \frac{P_{\max}}{P_t} = \frac{V_{\max} I_{\max}}{V_{oc} J_{sc}}, \tag{6}$$

$$\eta = \frac{P_{\max}}{P_{in}} = \frac{V_{oc} J_{sc} FF}{P_{in}}. \tag{7}$$

The age of the minority carriers can be determined, which is the

average time required for the recombination of the minority carriers, and it is linked to the doping concentration and recombination by the following relationships [16]:

$$\eta = (\sigma V_{th} N_t)^{-1}, \tag{8}$$

$$\tau = \Delta n / R. \tag{9}$$

The saturation current equation for the diode is one of the important equations, which determines the effect of propagation length and carrier density on cell performance [12, 15]:

$$I_0 = \left[\frac{q D_n n_i^2}{L_n N_A} + \frac{q D_p n_i^2}{L_p N_D} \right]. \tag{10}$$

Likewise, quantum efficiency (QE) greatly affects the performance of the cell, whose equation can be written [16, 17] as follows:

$$QE = 1.24 R_\lambda / \lambda. \tag{11}$$

3. SOLAR CELL INSTALLATION

The OMeATP/Cs_2AgBiBr6/TiO_2/FTO solar cell consists of a FTO window layer of transparent metal oxides that has a relatively large energy gap; then, it is followed by the TiO_2 compatibility layer, which has an energy gap suitable for the gradient of the absorption layer with the penetration, and then the $Cs_2AgBiBr_6$ absorption layer, which has a relatively small energy gap and forget. It has a flat band front and silver ohmic contact with a work function 4.26 V and the cell is on a glass floor [18]. Table 1 gives the values of the program parameters. Table 2 gives the values of the defects that must be entered in the absorption layer for the SCAPS program to study the performance of the experimental cell. The temperature was 300 K. Figure 1 shows the installation of the solar cell.

To enhance the efficiency of solar cells, we must work on: compare the experimental cell with the theoretical cell; optimize the cell by changing the back-connection work function; improve the cell by changing the thickness and the impurity ratio to obtain the best cell.

4. DISCUSSION OF RESULTS

4.1. Comparing the Experimental Cell with the Theory

To simulate the performance of the solar cell, the program used must be verified and the extent of its conformity with the practical

TABLE 1. Physical parameters for all layers [19–23].

Parameters	Symbol, unit	OMeTAD	$Cs_2AgBiBr_6$	TiO_2	FTO
Thickness	W, μm	0.05	0.5	0.07	0.05
Band gap	E_g, eV	2.9	2.05	3.45	3.5
Electron affinity	χ, eV	2.2	4.19	4.2	4
Dielectric permittivity	ε_r	3.0	5.8	10	9
CB effective density of states	N_C, cm^{-3}	$2.5 \cdot 10^{18}$	$1.0 \cdot 10^{16}$	$2.2 \cdot 10^{18}$	$2.2 \cdot 10^{18}$
VB effective density of states	N_V, cm^{-3}	$2.2 \cdot 10^{18}$	$1.0 \cdot 10^{16}$	$1.8 \cdot 10^{19}$	$1.8 \cdot 10^{19}$
Electron thermal velocity	V_n, cm/s	$1.0 \cdot 10^{7}$	$1.0 \cdot 10^{7}$	$1.0 \cdot 10^{7}$	$1.0 \cdot 10^{7}$
Hole thermal velocity	V_P, cm/s	$1.0 \cdot 10^{7}$	$1.0 \cdot 10^{7}$	$1.0 \cdot 10^{7}$	$1.0 \cdot 10^{7}$
Electron mobility	μ_n, $cm^2/(V \cdot s)$	$1 \cdot 10^{-4}$	11.8	100	20
Hole mobility	μ_p, $cm^2/(V \cdot s)$	$1 \cdot 10^{-4}$	6.49	25	10
Shallow uniform donor density	N_D, $1/cm^3$	0	$1.0 \cdot 10^{19}$	$1.0 \cdot 10^{19}$	$1.0 \cdot 10^{20}$
Shallow uniform acceptor density	N_A, $1/cm^3$	$1.0 \cdot 10^{19}$	$1.0 \cdot 10^{19}$	0	0
Coefficient absorption	α, 1/cm	$1.0 \cdot 10^{5}$	$4.5 \cdot 10^{3}$	$1.0 \cdot 10^{5}$	$1.0 \cdot 10^{5}$
Radiative recombination coefficient	cm^3/s	$1.0 \cdot 10^{-9}$	$4.0 \cdot 10^{-9}$	$2.3 \cdot 10^{-9}$	$2.3 \cdot 10^{-9}$

TABLE 2. Surface defects and absorption layer defects.

Characteristics of defects	Surface defects OMeTAD/$Cs_2AgBiBr_6$	Absorption defects *p*-$Cs_2AgBiBr_6$	Surface defects $Cs_2AgBiBr_6/TiO_2$
Energy level with respect to reference, eV	1.3	0.6	1.3
Total density, N_t, cm^{-2}	$1.0 \cdot 10^{7}$	$1.0 \cdot 10^{13}$	$1.0 \cdot 10^{9}$
Capture cross section area of electrons, δ_e, cm^2	$2.3 \cdot 10^{-18}$	$1.0 \cdot 10^{-15}$	$2.3 \cdot 10^{-18}$
Capture cross section area of holes, δ_h, cm^2	$2.3 \cdot 10^{-18}$	$1.0 \cdot 10^{-15}$	$2.3 \cdot 10^{-18}$

results must be verified. We conducted a simulation of the practical research by FAN, Ping *et al.* [24] on the SCAPS program, and the results showed a great match between the practical and theoretical results, as shown in Table 3, but the match is not complete.

Among the results, it is a decrease in the filling factor, which led to a decrease in the conversion efficiency. The reason is due to the defects in the interface P-OMeATD/$Cs_2AgBiBr_6$, *p*-$Cs_2AgBiBr_6/TiO_2$ and the defects in the absorption layer *p*-$Cs_2AgBiBr_6$. With a de-

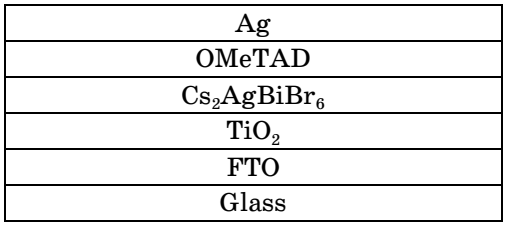

Fig. 1. Solar cell installation.

TABLE 3. Theoretical and experimental cell outputs.

Solar cell	V, V	J, mA/cm^2	FF, %	η, %
OMeATD/$Cs_2AgBiBr_6$/TiO_2/FTO (Experimental) [24]	0.87	1.24	0.65	0.70
OMeATD/$Cs_2AgBiBr_6$/TiO_2/FTO (Theoretical)	0.84	2.61	32.2	0.72

crease in N_t defects, the correspondence of the experimental work with the theory increases, due to the increase in durability. Minority carriers, which are inversely proportional to defects, as shown in Eq. (8); so, recombination will decrease, and as shown in Eq. (9), the efficiency of the theoretical cell increases over the experimental cell.

4.2. Effect of the Work Function

The layers of the solar cell consist of semiconductor materials and have a front connection and a back connection to transfer electrical power outside the cell. The front connection is between a metal and a semiconductor, and its resistance is very small compared to the resistance of the device. It is called ohmic contact because the resistance is very small [25]. Ohmic contact depends on the form Main on the relative difference between the work function of a conductor and the electronic affinity of a semiconductor material. The work function can be defined as the lowest binding energy of an electron to the surface of the metal. The front connection in the program has a flat band icon, but the back connection has a certain resistance and is called as the Schottky connection.

The Schottky connection works the opposite of the ohmic connection, as it does not allow current to flow except in one direction, that is, it resembles a one-sided p–n diode. Therefore, we notice that the concentration of carriers on the conductive side is much higher than its focus is on Semi Mosul. For the back connection, silver metal was used [26], and the work function was changed from

4.2 eV to 4.9 eV. We noticed an increase in the conversion efficiency, fill factor, and open circuit voltage. This is because for a *p*-type metal-semiconductor connection, the work function of the metal is less than the work function of the semiconductor, which leads to the flow of electrons from the conductor to the semiconductor, and increasing the work function helps to achieve quickly a state of thermal equilibrium [27].

Figure 2 shows the effect of the work function on the cell outputs. Figure 3 shows the relationship of voltage with current, and we notice an increase in efficiency and fill factor with an increase in the work function. Quantum efficiency was studied, which is the percentage of the number of carriers generated in the cell to the number of photons falling on the solar cell.

Figure 4 shows the relationship of wavelength as a function of quantum efficiency, and we notice that there is no it as affected by the change in the work function because it depends on the spectral response and wavelength [16, 17].

4.3. Effect of Acceptance on Reflection Layer

The distortion of the back reflection layer was changed from $1 \cdot 10^{19}$ cm^{-3} to $1 \cdot 10^{22}$ cm^{-3} so we noticed an increase in the conversion efficiency and filling factor, and Fig. 5 shows the change.

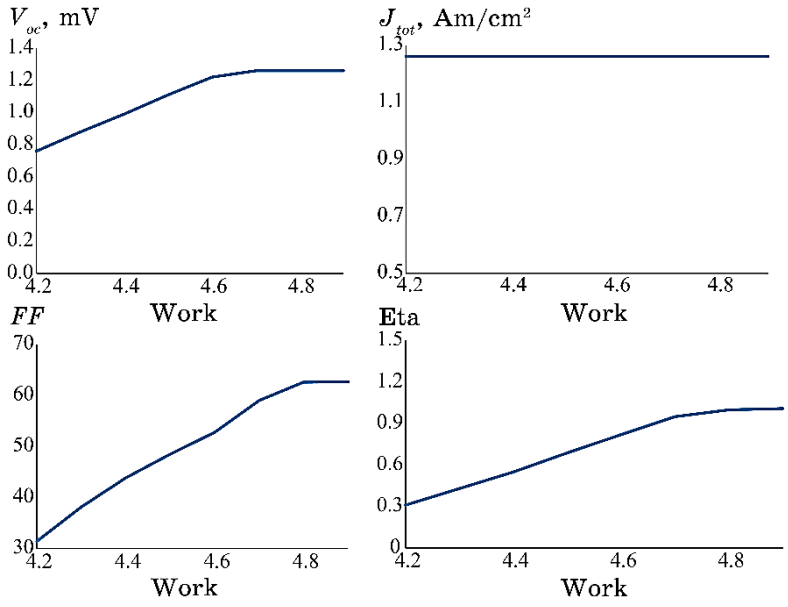

Fig. 2. Work function as a function of cell output.

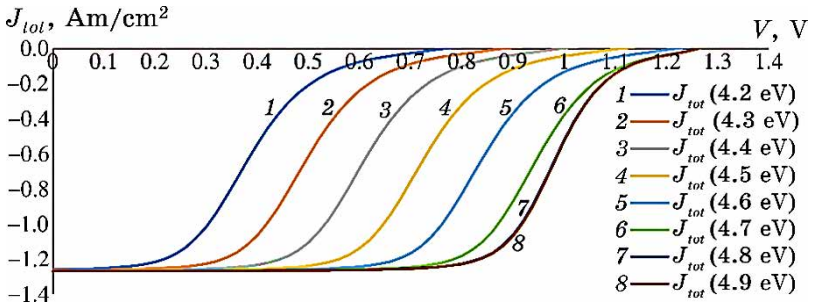

Fig. 3. Voltage as a function of current.

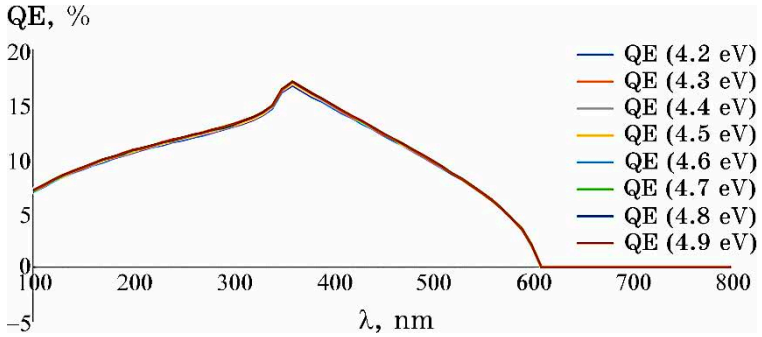

Fig. 4. Wavelength as a function of quantum efficiency.

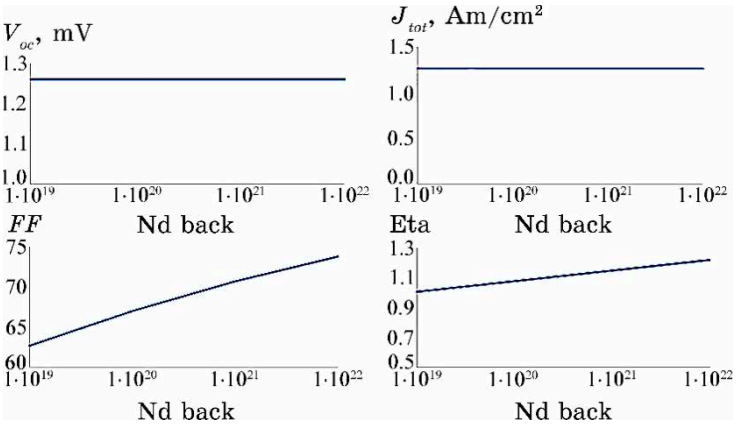

Fig. 5. Percentage of midwife defects as a function of cell output

The cell outputs increase the doping ratio, because increasing the doping ratio leads to an increase in carriers; so, the saturation current of the cell decreases, as shown in Eq. (10). Figure 6 shows the

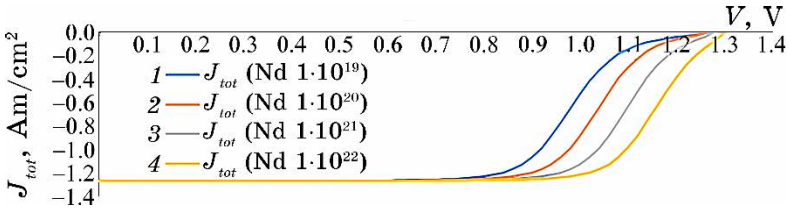

Fig. 6. Voltage as a function of current.

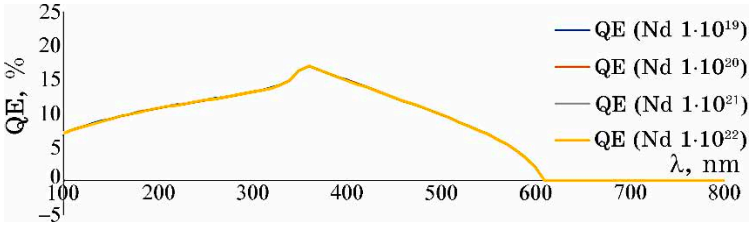

Fig. 7. Relationship of wavelength with quantum efficiency nm.

relationship of voltage with current. Figure 7 shows the relationship of wavelength with quantum efficiency, and that quantum efficiency begins at 7% at the length. The wavelength is of 100 nm and increases to 17% with the greatest amount at the wavelength of 370 nm; then, it begins to decrease gradually until it reaches zero. The reason is that the length of propagation decreases and the absorbance is at the lowest amount at high wavelengths because the efficiency is inversely proportional to the wavelength according to Eq. (11) [28].

4.4. Effect of Thickness and Radiation Recombination of the Absorption Layer

The thickness of the absorption layer was changed from 0.5 μm to 2.5 μm. We noticed an increase in the shunt efficiency and a decrease in the fill factor and short circuit current, as shown in Fig. 8. This is because increasing the thickness leads to an increase in the absorption of photons, so the generation of the electron-gap pair increases and the recombination process at the interface decreases, which leads to an increase in the optical current [29, 30].

Figure 9 shows the relationship of voltage with current.

Figure 10 shows the wavelength with quantum efficiency. Notice the increase in quantum efficiency that starts at the smallest thickness of 7% until it reaches 15% at the largest thickness, where the quantum efficiency increases and reaches the greatest amount of

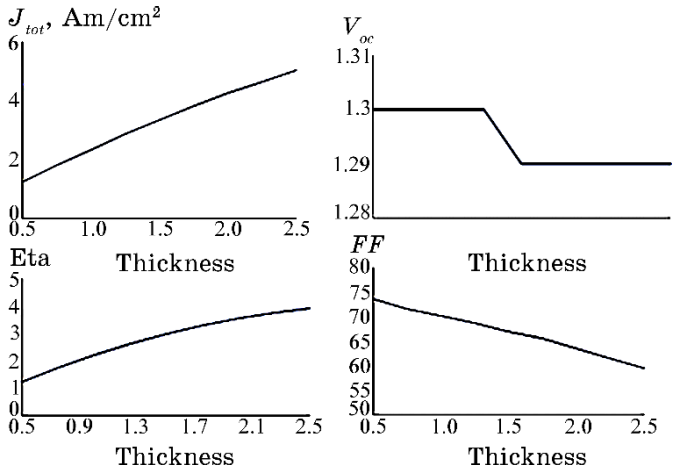

Fig. 8. Thickness as a function of cell output.

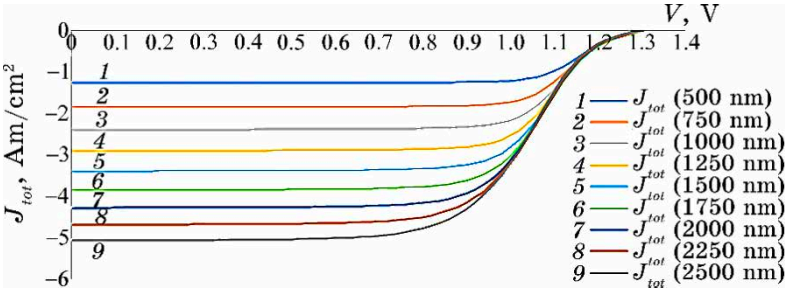

Fig. 9. Voltage as a function of current for different absorption layer thicknesses.

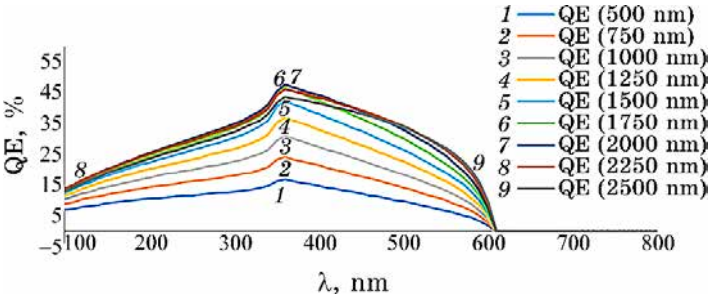

Fig. 10. Wavelength as a function of quantum efficiency for different absorption layer thicknesses.

45% at the wavelength of 370 nm; then, it begins to decrease.

Therefore, because the value of the absorption coefficient is high at short wavelengths, absorption occurs near the surface because the recombination time is short; so, the previously generated carriers are captured by the $p-n$ crystal diode [31].

Figure 11 shows the relationship of recombination with the cell output. You notice an increase in cell efficiency and fill factor whenever recombination decreases, with both current and voltage remaining constant, because the decrease in recombination increases the durability of the minority carriers, which increases the cell efficiency according to Eq. (8) and Eq. (9), due to the increase in the voltage barrier [32, 33].

Figure 12 shows the relationship of voltage with current. Figure 13 shows the relationship of wavelength with quantum efficiency. We notice a slight increase in Auger recombination, which leads to a decrease in the average life of the carriers at the surface, in addition to the formation of deposits and deformation on the surface

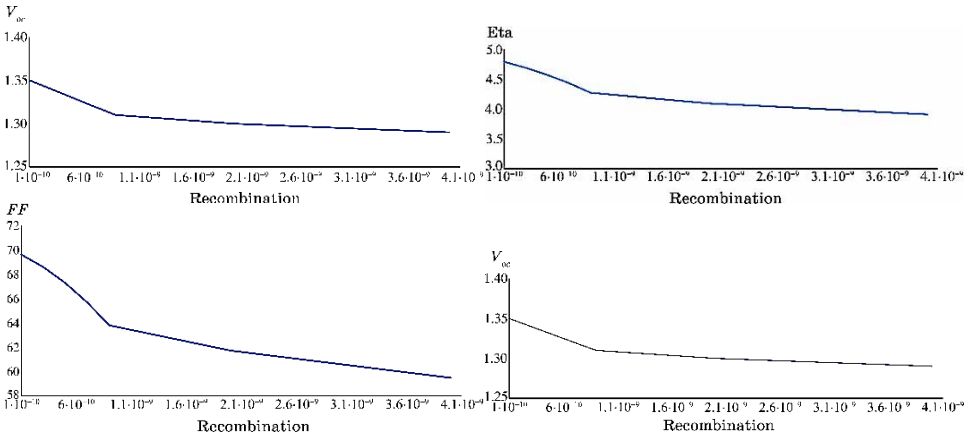

Fig. 11. Recombination as a function of cell output of the absorption layer.

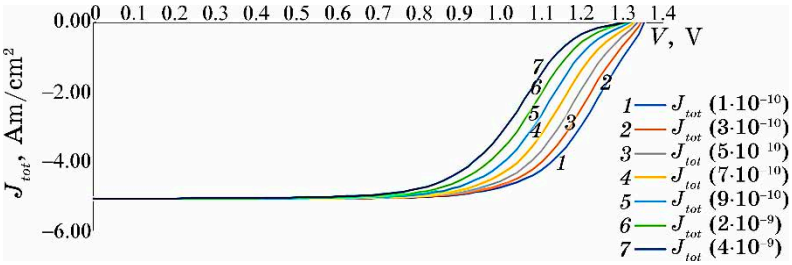

Fig. 12. Voltage as a function of current for different recombination values of the absorber layer.

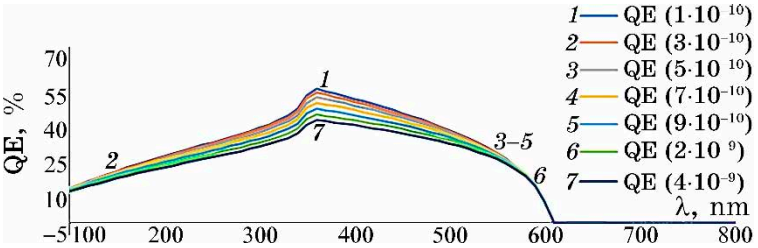

Fig. 13. Wavelength as a function of quantum efficiency for different recombination values of the absorption layer.

TABLE 4. Meaning of the symbols used in the research.

Mean of Symbol	Symbol	Mean of Symbol	Symbol
Open circuit voltage	V_{oc}	Electric filed	E
Conversion efficiency	η	charge	q
Maximum power	$P_{\max}$	Holes constriction	P
Actual power	P_t	Electron constriction	n
Input power	P_{in}	Acceptance consternation	N_A^-
Time of minority carriers	τ	Electron current density	J_n
Defects concentration	N_t	Holes current density	J_p
Heat velocity	V_{th}	Electron generation rate	G_n
Conductivity	σ	holes generation rate	G_p
Various concentrations of minority carriers	Δn	The rate of electron recombination	R_n
saturation current	I_0	The rate of holes recombination	R_p
The propagation length of electrons	L_e	Electron diffusion constant	D_n
The propagation length of holes	L_p	Holes diffusion constant	D_p
Electron concentration of pure semiconductor	n_i^2	Electron mobility	μ_n
Quantitative efficiency	QE	Holes mobility	μ_p
Spectral acceptance	R_λ	Fill factor	FF
Wave length	λ	Short circuit current	J_{sc}

[34]. Quantum efficiency is zero at long wavelength because no light can be absorbed below the forbidden energy gap.

5. CONCLUSIONS

The OMeATP/$Cs_2AgBiBr_6$/TiO_2/FTO cell was simulated using the SCAPS program and compared with an experimental cell. A very

large convergence was found between theoretical and experimental. The cell was also improved by increasing the work function. It was noted that increasing the distortion of the back reflection layer increases the performance of the cell to return photons to the cell. The thickness of the absorption layer has a significant impact on the performance of the cell. We noticed that increasing the thickness increases the efficiency of the cell due to increasing the absorption coefficient, and decreasing recombination increases the cell efficiency because recombination reduces the generation of the electron-gap pair.

REFERENCES

1. Zhenyang Liu, Hanjun Yang, Junyu Wang, Yucheng Yuan, Katie Hills-Kimball, Tong Cai, Ping Wang, Aiwei Tang, and Ou Chen, *Nano Letters*, **21**, Iss. 4: 1620 (2021); https://doi.org/10.1021/acs.nanolett.0c04148
2. Masataka Higashiwaki, Kohei Sasaki, Akito Kuramata, Takekazu Masui, and Shigenobu Yamakoshi, *phys. status solidi (a)*, **211**, No. 1: 21 (2014); https://doi.org/10.1002/pssa.201330197
3. Miao He, Qing Zeng, and Lijuan Ye, *Crystals*, **13**, No. 10: 1434 (2023); https://doi.org/10.3390/cryst13101434
4. Xing Chen, Kewei Liu, Zhenzhong Zhang, Chunrui Wang, Binghui Li, Haifeng Zhao, Dongxu Zhao, and Dezhen Shen, *ACS Appl. Mater. Inter.*, **8**, Iss. 6: 4185 (2016); https://doi.org/10.1021/acsami.5b11956
5. Sudheer Kumar, and R. Singh, *phys. status solidi (RRL)*, **7**, Iss. 10: 781 (2013); https://doi.org/10.1002/pssr.201307253
6. D. Y. Guo, Z. P. Wu, Y. H. An, P. G. Li, P. C. Wang, X. L. Chu, X. C. Guo, Y. S. Zhi, M. Lei, L. H. Li, and W. H. Tang, *Appl. Phys. Lett.*, **106**, No. 6: 042105 (2015); https://doi.org/10.1063/1.4907174
7. R. H. Al-Saqa, and I. K. Jassim, *Journal of Nanomaterials & Biostructures*, **18**, No. 1: 165 (2022); doi:10.15251/DJNB.2023.181.165
8. Rikiya Suzuki, Shinji Nakagomi, Yoshihiro Kokubun, Naoki Arai and Shigeo Ohira, *Appl. Phys. Lett.*, **94**, No. 22: 222102 (2009); https://doi.org/10.1063/1.3147197
9. K. Sasaki, M. Higashiwaki, A. Kuramata, T. Masui, and S. Yamakoshi, *IEEE Electron. Device Lett.*, **34**, No. 4: 493 (2013); https://doi.org10.1109/LED.2013.2244057
10. Masataka Higashiwaki, *AAPPS Bull.*, **32**: 3 (2022); https://doi.org/10.1007/s43673-021-00033-0
11. Kohei Sasaki, Masataka Higashiwaki, Akito Kuramata, Takekazu Masui, and Shigenobu Yamakoshi, *J. Cryst. Growth*, **378**: 591 (2013); https://doi.org/10.1016/j.jcrysgro.2013.02.015
12. O. M. Bordun, B. O. Bordun, I. Yo. Kukharskyy, and I. I. Medvid, *J. Appl. Spectrosc.*, **86**, No. 6: 1010 (2020); https://doi.org/10.1007/s10812-020-00932-4
13. Ashwin Kumar Saikumar, Shraddha Dhanraj Nehate, and Kalpathy B Sundaram, *ECS J. of Solid State Science and Technol.*, **8**, No. 7: Q3064 (2019); https://doi.org/10.1149/2.0141907jss
14. Lingyi Kong, Jin Ma, Caina Luan, Wei Mi, and Yu Lv, *Thin Solid Films*, **520**,

No. 13: 4270 (2012); https://doi.org/10.1016/j.tsf.2012.02.027
15. O. M. Bordun, B. O. Bordun, I. I. Medvid, and I. Yo. Kukharskyy, *Acta Physica Polonica A*, **133**, No. 4: 910 (2018); https://doi.org/10.12693/APhysPolA.133.910
16. K. H. Choi and H. C. Kang, *Materials Letters*, **123**: 160 (2014); https://doi.org/10.1016/j.matlet.2014.03.038
17. C. B. Willingham, J. M. Wahl, P. K. Hogan, L. C. Kupferberg, T. Y. Wong, and A. M. De, *Proc. SPIE*, **5078**: 179 (2003); https://doi.org/10.1117/12.500986
18. T. Igarashi, M. Ihara, T. Kusunoki, K. Ohno, T. Isobe, and M. Senna, *Appl. Phys. Lett.*, **76**, No. 12: 1549 (2000); https://doi.org/10.1063/1.1260921
19. O. M. Bordun, I. M. Bordun, and S. S. Novosad, *J. Appl. Spectr.*, **62**, No. 6: 1060 (1995); https://doi.org/10.1007/BF02606760
20. K. Wasa, M. Kitabatake, and H. Adachi, *Thin Film Materials Technology: Sputtering of Compound Materials* (New York: Springer–William Andrew Inc Publishing: 2004).
21. O. M. Bordun, B. O. Bordun, I. J. Kukharskyy, I. I. Medvid, O. Ya. Mylyo, M. V. Partyka, and D. S. Leonov, *Nanosistemi, Nanomateriali, Nanotehnologii*, **17**, Iss. 1: 123 (2019); https://doi.org/10.15407/nnn.17.01.123
22. Carl V. Thompson, *Sol. State Phys.*, **55**: 269 (2001); https://doi.org/10.1016/S0081-1947(01)80006-0
23. Carl V. Thompson, *J. Appl. Phys.*, **58**: 763 (1985); https://doi.org/10.1063/1.336194
24. O. M. Bordun, B. O. Bordun, I. Yo. Kukharskyy, I. I. Medvid, I. I. Polovynko, Zh. Ya. Tsapovska, and D. S. Leonov, *Nanosistemi, Nanomateriali, Nanotehnologii*, **19**, Iss. 1: 159 (2021); https://doi.org/10.15407/nnn.19.01.159
25. J. E. Palmer, C. V. Thompson, and Henry L. Smith, *J. Appl. Phys.*, **62**, No. 6: 2492 (1987); https://dx.doi.org/10.1063/1.339460
26. O. M. Bordun, I. O. Bordun, I. M. Kofliuk, I. Yo. Kukharskyy, I. I. Medvid, Zh. Ya. Tsapovska, and D. S. Leonov, *Nanosistemi, Nanomateriali, Nanotehnologii*, **20**, Iss. 1: 91 (2021); https://doi.org/10.15407/nnn.20.01.091
27. Tejaswini Sahoo and Paresh Kale, *Advanced Materials Interfaces*, **8**, Iss. 23: 2100649 (2021); https://doi.org/10.1002/admi.202100649
28. Sophie de Reguardati, Juri Pahapill, Alexander Mikhailov, Yuriy Stepanenko, and Aleksander Rebane, *Optics Express*, **24**, Iss. 8: 9053 (2016); https://doi.org/10.1364/OE.24.009053
29. Amrita Masurkar and Ioannis Kymissis, *Applied Physics Reviews*, **2**, Iss. 3: (2015); https://doi.org/10.1063/1.4926767
30. Mahmood M. Saleh, Hamadi Khemakhem, Ismel K. Jassim, and Read Hashim Al-Saqa, *Ochrona przed Korozją*, **67**, Nr. 1: 9 (2024); doi:10.15199/40.2024.1.2
31. Henry Kressel, *Semiconductors and Semimetals*, **16**: 1 (1981); https://doi.org/10.1016/S0080-8784(08)60128-3
32. Mehdi Leilaeioun and Zachary C. Holman, *Journal of Applied Physics*, **120**, Iss. 12: 123111 (2016); https://doi.org/10.1063/1.4962511
33. Raed Hashim Al-Saqa, Ismail Kalil Jassim, and Mohammad Mahmood Uonis, *Ochrona przed Korozją*, **66**, Nr. 8: 243 (2023); doi:10.15199/40.2023.8.3
34. Richard Haight, *Surface Science Reports*, **21**, Iss. 8: 275 (1995); https://doi.org/10.1016/0167-5729(95)00002-X

Наносистеми, наноматеріали, нанотехнології
Nanosistemi, Nanomateriali, Nanotehnologii
2026, т. 24, № 1, сс. 97–103
https://doi.org/10.15407/nnn.24.01.0097

PACS numbers: 42.70.Qs, 72.40.+w, 78.40.Fy, 78.67.-n, 84.60.Jt, 88.40.hj

Solar-Cell Properties of Porous Silicon/Cadmium Telluride Junction

M. Al-Hadidi[1], Z. B. Ibraheem[2], Rana Z. A. Al-fayih[1,2], and M. M. Uonis[1]

[1]*College of Science,*
Department of New and Renewable Energy,
Mosul University,
Mosul, Iraq
[2]*College of Science,*
Department of Physics,
Mosul University,
Mosul, Iraq

PSi–CdTe junction is prepared using spray pyrolysis and photoelectrochemical etching methods; the deposition method of thin CdTe films is performed at 90°C; thin CdTe films are completely crystalline with energy gap of 2.4 eV. The grain sizes are investigated using SEM and x-ray spectroscopy; both measurement techniques show that the grain sizes are within the nanoscale. The junction show I–V characteristics similar to the diode in both forward and reverse bias; the junction also show solar-cell characteristics with fill factor of 0.594.

Перехід PSi–CdTe одержано методами розпорошувальної піролізи та фотоелектрохемічного щавлення; метод осадження тонких плівок CdTe виконано за температури у 90°C; тонкі плівки CdTe є повністю кристалічними із забороненою енергетичною зоною у 2,4 еВ. Розміри зерен досліджено за допомогою сканівної електронної мікроскопії та рентґенівської спектроскопії; обидва методи міряння показують, що розміри зерен знаходяться в наномасштабі. Перехід демонструє вольт-амперні характеристики, подібні до діоди, як у прямому, так і у зворотньому зміщенні; перехід також демонструє характеристики сонячного елемента з коефіцієнтом заповнення у 0,594.

Key words: porous silicon, cadmium telluride, thin films, semiconductors, optical properties of semiconducting thin films, diode characteristics, solar-cell characteristics.

Ключові слова: поруватий кремній, телурид Кадмію, тонкі плівки, напівпровідники, оптичні властивості напівпровідникових тонких плівок,

характеристики діоди, характеристики сонячних елементів.

(Received 7 September, 2024; in revised form, 8 October, 2024)

1. INTRODUCTION

Cadmium telluride CdTe is one of the II–VI group semiconductors; cadmium telluride has unique properties, which enable it to enter into many applications, including gamma-ray detection [1], fuel cells [2], photocatalytic hydrogen production [3], sensors [4, 5], laser materials [6], and solar panels [7]. It is a *p*-type semiconductor and can be converted to *n*-type by heat treatment [8], has a band-to-band energy gap of about 1.4–1.5 eV [9–12], high absorption coefficient of 10^4 cm^{-1} [13, 14]. Cadmium telluride can be deposited *via* different easy methods including chemical bath deposition [15–17], flash evaporation [18], close spaced sublimation [19], spray method [20], thermal evaporation [21, 22], and electrodeposition [23].

In our work, thin CdTe films have been deposited on porous silicon to fabricate PSi–CdTe solar cell; the optical, structural, and electrical properties were measured for thin CdTe films and PSi–CdTe junction.

2. EXPERIMENTAL METHOD

n-type silicon wafer was used as a substrate to construct PSi–CdTe solar cell. The silicon wafer was etched to obtain the porous silicon using photoelectrochemical-etching technique; the method was performed with etching current of 15 mA/cm^2, etching period of 10 min with 18 wt.% HF and ethanol (99.9%) (1:1) aqueous solution [24].

Tellurium oxide TeO_2 was dissolved in 25 ml distilled water in-

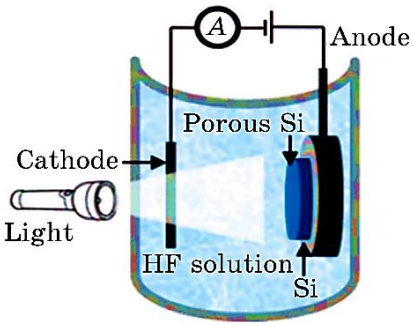

Fig. 1. Experimental setup for the fabrication of porous silicon by electrochemical etching of silicon wafers [25].

cluded 5 ml HCl, while $ZnCl_2$ was dissolved in 25 ml of distilled water; both solutions were mixed for 1 hr at 90°C using magnetic stirrer. Finally, the deposition of the mixture was performed using spray-pyrolysis method with deposition temperature of 100°C, 20 sprays, nozzle distance of 30 cm, and air pressure of 7.5 kg/cm^2.

3. RESULTS AND DISCUSSION

Thin films of CdTe on porous silicon were deposited; the optical, structural, and electrical properties of the CdTe film and the junction have been discovered.

The film show a high transmittance, which increases with wavelength, where the maximum transmittance was of 97.3. The absorbance spectrum has a peak at wavelength of 540 nm, which belong to the CdTe nanotubes (Fig. 2).

The energy gap of the cadmium-telluride films was calculated using Scherrer equation; it was of about 2.4 eV (Fig. 3).

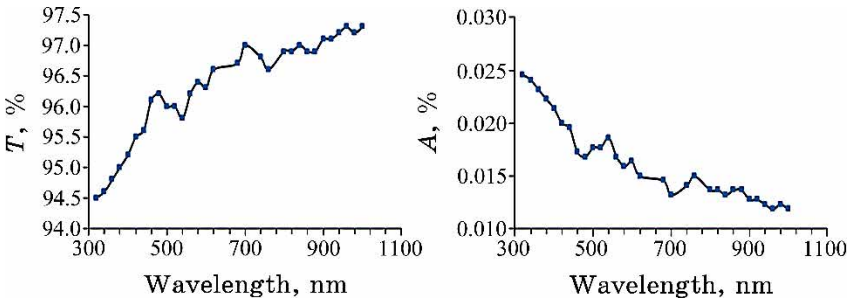

Fig. 2. The transmittance and absorbance of thin CdTe films.

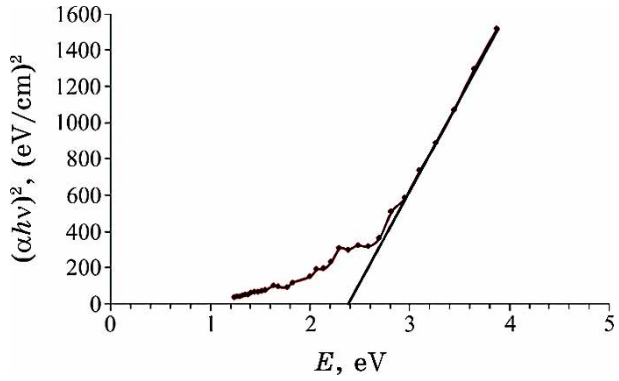

Fig. 3. Energy gap of thin CdTe films.

Field-emission scanning electron microscope has been used in the examining of thin CdTe films (Fig. 2); the images show the for-

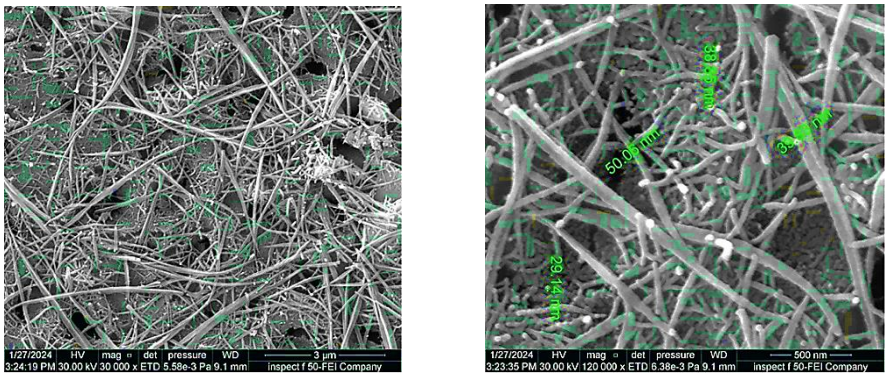

a *b*

Fig. 4. FE–SEM images of thin CdTe films on porous silicon substrate: (*a*) magnification ×30000, (*b*) magnification ×120000.

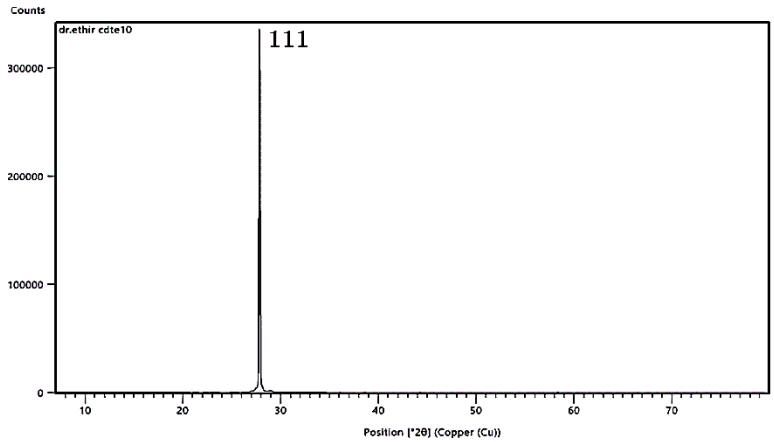

Fig. 5. XRD spectrum of thin CdTe films on porous silicon substrate.

TABLE 1. The average grain size of thin CdTe film.

2-theta, θ	*FWHM* [2Th.]	*D*, nm	Average grain size, nm
27.0091	0.4489	18.20207032	
27.7446	0.5628	14.54100846	
27.832	0.0858	95.39885917	37.07802849
27.9339	0.1667	49.1123415	
28.8395	1.0083	8.135862994	

mation of the CdTe nanotube in different orientations and diameters; the average nanotube diameters was of about 39.47 nm.

XRD spectrum of the CdTe shows that the film was completely crystalline, where a single significant peak appear at $2\theta = 27.82°$ with the (111) orientation. The average grain size was calculated using Scherrer equation; it was equal to 37.07802849 nm (Fig. 5 and Table 1); this result agrees with the FE–SEM image.

The electrical properties of PSi–CdTe junction were investigated; the junction show I–V characteristics similar to diode characteristics in both forward and reverse bias as shown in Fig. 6. PSi–CdTe junction also show solar-cell characteristics with short circuit current density of 9.362 mA/cm^2, open circuit voltage of 0.730 V, fill factor of 0.594, and efficiency of 4.061% (see Fig. 7 and Table 2).

4. CONCLUSIONS

Thin films of CdTe have been deposited *via* spray-pyrolysis method

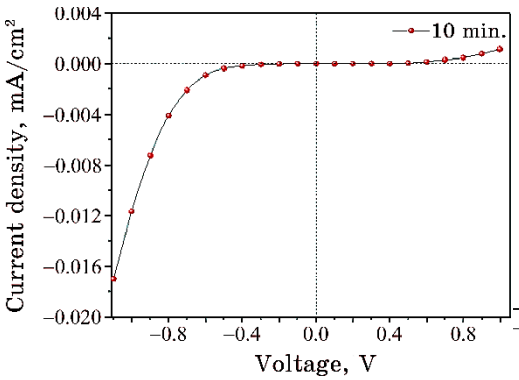

Fig. 6. I–V diode characteristics of PSi–CdTe junction.

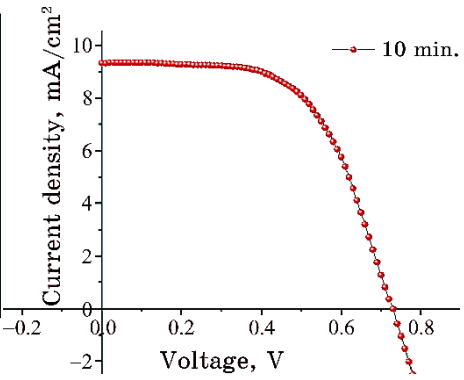

Fig. 7. Solar-cell characteristics of PSi–CdTe junction.

TABLE 2. Solar-cell parameters' values of PSi–CdTe junction.

Area	cm^2	10 min
P_{in}	mW/cm^2	100
J_{sc}	mA/cm^2	9.362
V_{oc}	V	0.730
$J_{\max}$	mA/cm^2	8.122
$V_{\max}$	V	0.500
FF		0.594
PCE	%	4.061

on porous silicon, which has already been prepared using photoelectrochemical etching technique. The energy gap of thin CdTe films was of 2.4 eV. The grain sizes were measured using SEM images and x-ray spectrum; they were of about 39.47 nm and 37.07 nm, respectively. The x-ray spectrum shows also that the film was completely crystalline. The PSi–CdTe junction show diode and solar-cell characteristics with fill factor of 0.594 and efficiency of 4.061%.

ACKNOWLEDGMENTS

We would like to thank our college and university for the assistance they provided in completing our research.

REFERENCES

1. S. C. Ray and K. Mallick, *International Journal of Chemical Engineering and Applications*, **4**, Iss. 4: 183 (2013); doi:10.7763/IJCEA.2013.V4.290
2. X. Ai, S. Yan, Y. Chen, S. Chen, Y. Jiang, X. Song, and X. Wu, *Journal of Luminescence*, **252**: 119372 (2022); https://doi.org/10.1016/j.jlumin.2022.119372
3. Z. Fan, W. Weng, J. Zhou, D. Gu, and W. Xiao, *Journal of Energy Chemistry*, **58**: 415 (2021); https://doi.org/10.1016/j.jechem.2020.10.049
4. Azqa F. Butt, M. Azhar, Hassan Yousaf, K. M. Batoo, Dilbar Khan, M. Noman, Mujeeb U. Chaudhry, Shahzad Naseem, and Saira Riaz, **10**, Iss. 3: 24492 (2024); https://doi.org/10.1016/j.heliyon.2024.e24492
5. A. U. Yimamu, M. A. Afrassa, B. F. Dejene, O. K. Echendu, K. G. Tshabalala, J. J. Terblans, and S. J. Motloung, *Materials Research Express*, **10**, No. 5: 056403 (2023); doi:10.1088/2053-1591/acd322
6. Subhash Chander, A. Purohit, C. Lal, and M. S. Dhaka, *Materials Chemistry and Physics*, **185**: 202 (2017); https://doi.org/10.1016/j.matchemphys.2016.10.024
7. H. I. Salim, V. Patel, A. Abbas, J. M. Walls, and I. M. Dharmadasa, *Journal of Materials Science: Materials in Electronics*, **26**: 3119 (2015); https://doi.org/10.1007/s10854-015-2805-x
8. Antonio Arce-Plaza, Fernando Sánchez-Rodriguez, Maykel Courel-Piedrahita, Osvaldo Vigil Galán, Viviana Hernandez-Calderon, Sergio Ramirez-Velasco, and Mauricio Ortega Lypez, *Coatings and Thin-Film Technologies*: *CdTe Thin Films: Deposition Techniques and Applications* (Eds. Jaime Andres Perez-Taborda and Alba G. Avila Bernal) (Intechopen: 2018), p. 131; doi:10.5772/intechopen.79578
9. B. A. Ahmed, I. H.Shallal, and F. I. Mustafa Al-Attar, *Journal of Physics: Conference Series*, **1032**, No. 1: 012022 (2018); doi:10.1088/1742-6596/1032/1/012022
10. G. S. Sanyal, A. Mondal, K. C. Mandal, B. Ghosh, H. Saha, and M. K. Mukherjee, *Solar Energy Materials*, **20**, Iss. 5–6: 395 (1990); https://doi.org/10.1016/0165-1633(90)90031-U
11. A. Bosio, G. Rosa, and N. Romeo, *Solar Energy*, **175**: 31 (2018);

doi:10.1016/j.solener.2018.01.018
12. D. G. Diso, T. S. Bichi, M. A. Y. Hotoro, I. A. Faragai, and A. O. Musa, *Bayero Journal of Pure and Applied Sciences*, **8**, Iss. 2: 58 (2015); doi:10.4314/bajopas.v8i2.11
13. R. S. Kapadnis, S. B. Bansode, A. T. Supekar, P. K. Bhujbal, S. S. Kale, S. R. Jadkar, and H. M. Pathan, *ES Energy & Environment*, **10**: 3 (2020); https://dx.doi.org/10.30919/esee8c706
14. Kazi Sajedur Rahman, Muhammad Najib Harif, Hasrul Nisham Rosly, Mohamad Ibrahim Bin Kamaruzzaman, Md. Akhtaruzzaman, Mohammad Alghoul, Halina Misran, and Nowshad Amin, *Results in Physics*, **14**: 102371 (2019); https://doi.org/10.1016/j.rinp.2019.102371
15. M. Mahendar, A. K. Chaudhary, Ganesh Damarla, and Vinay Gupta, *2019 Workshop on Recent Advances in Photonics (WRAP) (13–14 December, 2019)* (Guwahati, India: IEEE: 2019); doi:10.1109/WRAP47485.2019.9013662
16. M. Soliman, A. B. Kashyout, M. Shabana, and M. Elgamal, *Renewable Energy*, **23**, Iss. 3–4: 471 (2001); https://doi.org/10.1016/S0960-1481(00)00153-1
17. S. Surabhi, S. Rajpal, and S. R. Kumar, *Materials Today: Proceedings*, **44**: 1463 (2021); https://doi.org/10.1016/j.matpr.2020.11.635
18. S. H. Ibraheem, *Journal of the College of Basic Education*, **21**, Iss. 88: 117 (2015); https://doi.org/10.35950/cbej.v21i88.9957
19. Todd A. Schneider, Jason A. Vaughn, Kenneth H. Wright, and Brandon S. Phillips, *IEEE 42nd Photovoltaic Specialist Conference (PVSC) (14–19 June, 2015, New Orleans, LA, USA)*; doi:10.1109/PVSC.2015.7355909
20. V. M. Nikale, S. S. Shinde, C. H. Bhosale, and K. Y. Rajpure, *Journal of Semiconductors*, **32**, Iss. 3: 033001 (2011); doi:10.1088/1674-4926/32/3/033001
21. S. A. Fadaam, M. H. Mustafa, A. H. Abd AlRazaK, and A. A. Shihab, *Energy Procedia*, **157**: 635 (2019); https://doi.org/10.1016/j.egypro.2018.11.229
22. H. M. Ali and M. H. Mustafa, *Chalcogenide Letters*, **20**, Iss. 6: 431 (2023); https://doi.org/10.15251/CL.2023.206.431
23. A. U. Yimamu, M. A. Afrassa, B. F. Dejene, O. K. Echendu, K. G. Tshabalala, J. J. Terblans, and S. J. Motloung, *Materials Research Express*, **10**, Iss. 5: 056403 (2023); https://doi.org/10.1016/j.rinp.2019.102371
24. I. A. Younus, A. M. Ezzat, and M. M. Uonis, *Nanocomposites*, **6**, Iss. 4: 165 (2020); doi:10.1080/20550324.2020.1865712
25. Gonzalo Recio-Sánchez, Ramyn J. Peláez, and Raúl J. Martín-Palma, *Porous Silicon: An Attractive Material for Biomedical Uses. Inorganic Frameworks as Smart Nanomedicines* (William Andrew Publishing: 2018), Ch. 3, p. 93–135; https://doi.org/10.1016/B978-0-12-813661-4.00003-1

Наносистеми, наноматеріали, нанотехнології
Nanosistemi, Nanomateriali, Nanotehnologii
2026, т. 24, № 1, сс. 105–113
https://doi.org/10.15407/nnn.24.01.0105

PACS numbers: 68.37.Hk, 73.61.Ga, 78.20.Ci, 78.66.Hf, 78.67.Bf, 78.67.Pt

Structural, Optical, and Electrical Properties of Nano-Zinc Sulphide at 250°C

Sabah S. Hamdi

College of Computer Science and Mathematics,
Physics Department,
Tikrit University,
34001 Tikrit, Iraq

The thin films of zinc sulphide (ZnS) with nanograins are produced on (glass) substrates at 250°C using the spray-pyrolysis deposition technique (SPDT). The films have a polycrystalline cubic structure with preferred orientation along (111) direction of growth. The optical characteristics of the thin ZnS film indicate a direct optical energy gap of 3.320 eV. The film displays a thickness of 250.25 nm with grain sizes ranging from 9.76 nm to 11.46 nm. For approximate values, the measurements are done with the use of a computer simulation tool 'Hebal Optic'. It is also observed for all the films that there is an inverse proportional change in resistance to temperature and that the formed films have two activation energies.

Тонкі плівки сульфіду Цинку (ZnS) з нанозернами було одержано на скляних підкладинках за 250°C за допомогою методу осадження розпорошувальною піролізою. Плівки мали полікристалічну кубічну структуру з переважною орієнтацією вздовж напрямку росту (111). Оптичні характеристики тонкої плівки ZnS вказували на ширину прямої оптичної забороненої енергетичної зони у 3,320 еВ. Плівка мала товщину у 250,25 нм із розмірами зерен від 9,76 нм до 11,46 нм. Для одержання приблизних значень міряння виконувалися за допомогою засобу комп'ютерного моделювання «Hebal Optic». Також було відзначено, що для всіх плівок є обернено пропорційна зміна опору з температурою та що утворені плівки мають дві енергії активації.

Key words: software 'Hebal Optic', nano-ZnS, thiourea, energy gap, spray-pyrolysis deposition technique.

Ключові слова: програмні засоби «Hebal Optic», нано-ZnS, тіосечовина, заборонена енергетична зона, метод розпорошувальної піролізи.

(Received 6 July, 2024; in revised form, 17 September, 2024)

1. INTRODUCTION

Zinc sulphide (ZnS), also referred to as sphalerite, is a chemical compound having the chemical formula ZnS. Its name suggests a lack of similarity with other minerals. ZnS is a transparent, semiconducting, and yellow salt. The dissolution of ZnS is limited because to its low sublimation; hence, it is soluble in acids but not in water. Additionally, it exhibits low toxicity [1]. Because of its broad energy gap, ZnS is an excellent material for luminescence, which may be achieved in the almost visible range with appropriate grafting. ZnS is now considered as one of the best materials for diodes among multi-buffer layers. Compared with CdSe or CdS, benefits of the ZnS include its environmentally safe handling and nontoxic, and moreover, its ability to provide better lattice matching to CIGS absorbers with energy gaps ranging from 1.30 to 1050 eV, when compared to CdS, which transmits photons with higher energy and boosts light absorption in the absorber layer [2]. ZnS has many applications according to the physical and chemical properties for it, including field effect transistors. ZnS has two phase compositions: one is the cubic zinc blende phase, the most appropriate phase at 300 K, which may transform into the hexagonal phase, upon heating to 1298 K under atmospheric pressure; while, the other compound belongs to the wurtzite-type phase of hexagonal system, which is the most preferred phase for its optical optimum, ZnS is consistently utilized in blue light-emitting lasers' diodes, and antireflective and corrosion coatings. It is always used to create television and x-ray screens [3].

2. EXPERIMENTAL PART

Nanosize thin ZnS films are produced using an aqueous solution of zinc nitrate (a white powdered material, which is dissolved more rapidly in water than in other liquids, with a molecular weight of 297.364 g/mole and a purity of 99.96%) and thiourea (C.S. $(NH_2)_2$). The colure is a white powder rapidly soluble in water. An initial solution, weighing 76.614 g/mole and having a purity of 98%, was obtained by dissolving 1.480 g of zinc nitrate in 0.1 L of distilled water at room temperature. A second solvent, with a concentration of 0.01 M, was also made at room temperature. The solvent were mixed using a magnetic mixer to dissolve completely thiourea (0.076 g) in 100 mL of distilled water. The solvent was placed on a

magnetic mixer for 10 minutes until homogenous and free of plankton. The two solvent were then mixed in an equal volume ratio (1:1); for getting a homogeneous solution, the solution was stirred with a magnetic stirrer for an additional 10 minutes.

Thin ZnS films are formed, when the solution is deposited onto a glass substrate using a chemical decomposition process. Thermochemical spraying technology was chosen to appropriate for creating oxide and sulphate materials and is inexpensive according to the cheap cost of the equipment required to generate these films. The film can be created by combining two components or by combining materials with various melting points. The film is formed using normal conditions. The prepared solution is applied to the glass substrate at 250°C; the average distance from the sprayer (nozzle) to the glass substrate is of 28 cm, as a larger distance would cause the material to evaporate before reaching the substrate.

The glass substrate with a thickness of 0.1 cm is covered with a thin layer. The properties of the resulting film can be affected by the presence of impurities; so, the glass substrate is thoroughly cleaned before spraying. The substrate is cleaned after cutting it into small squares of 2.5 cm×2.5 cm. To remove plankton, the substrate is first rinsed with water. The substrate is then incubated in a glass flask with 99.99%-pure acetone for 10 minutes. The substrate is then incubated in another container with 99%-pure ethanol for 10 minutes. Finally, to remove any residual acetone and ethanol, the substrate (glass) was put in a flask containing only distilled water and let to stand for 15 minutes; to clean the glass lens, the glass substrate is finally wiped dry with a cloth. At 250°C, a thin layer of ZnS was deposited on the glass substrate.

3. RESULTS AND DISCUSSION

3.1. Structure

ZnS was prepared on a substrate (glass) at 250°C; then, it was annealed at 300°C for 30 min. XRD data showed that the system was cubic with (111) being the main growth direction. In Figure 1, angle $2\theta \cong 27.55°$, 47.87°, 56.39° corresponds to (220), (311) and (111) in sequence [4, 5]. The peak positions of ZnS in XRD were compared with ICDD 00-001-0792 and the structural characteristics of the standard peaks (Table 1).

Table 1 shows how close they are to each other. In addition, we observed that with increasing base temperature, the peak intensity of the ZnS nanocrystal-size film increased and the full width at half-maximum (*FWHM*) curve decreased. This supports the increase in the percentage of crystallization, as the increase in peak height

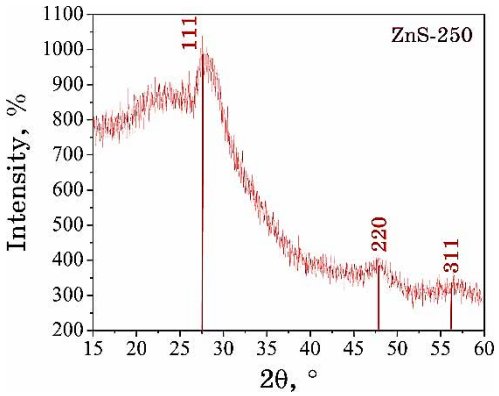

Fig. 1. XRD for ZnS at substrate temperature of 250°C.

TABLE 1. Structural parameters of ZnS at 250°C.

Sample	2θ	*hkl*	d_{hkl}, Å	*FWHM*	*D*, nm
ZnS-250°C	27.55	(111)	3.12	0.8659	9.87
	47.87	(220)	1.91	0.8755	9.76
	56.39	(311)	1.63	0.7456	11.46

Fig. 2. FE-SEM for thin ZnS-250°C film.

indicates a decrease in crystal defects and an increase in crystallization [6]. The average grain size of ZnS was within the range of 9.76 nm–11.46 nm, when computed using Eq. (1):

$$D_{ave} = \frac{0.9}{\beta \cos\theta} \tag{1}$$

($\lambda = 1.5406$ Å is x-ray wavelength (K_α-line); β is XRD 'full width at half-maximum' [in radians]; θ is Bragg's diffraction angle) [7].

When observing the morphology of the film surface using a scanning electron microscope (FE-SEM), as in Fig. 2, the ZnS-250°C film consists of orderly arranged nanosheets, which adhere to each other. This is the result of increasing heat to stimulate grain growth and alignment. As can be seen in Fig. 2, the particles have this shape, which is related to Refs. [4–6]. The thickness of the film was calculated using a computer simulation tool called 'Hebal Optic'. Based on the permeability value, the film thickness was determined to be approximately of 250.25 nm. The film was found to have a thickness of 250.25 nm.

3.2. Optical Properties

To calculate the absorption coefficients, we used equation

$$\alpha h\nu = \beta\left(h\nu - E_g\right)^r \tag{2}$$

(β is a constant, α is the absorption coefficient, $h\nu$ represents the energy of photon, E_g is optical energy gap, and $r = 1/2$ is allowed direct transition) and Fig. 3, which depicts the absorption spectrum ($A = \log(T/d)$, d is thickness of the sample, T is transmission) as a function of wavelength. The findings indicated that, when the substrate temperature increases, the generated thin-film absorbency improves, indicating enhanced crystallization (increase in crystal size).

Figure 4 depicts how the absorption coefficient varies with incident photon energy. The results indicated that the absorption coefficient of thin ZnS films developed on a glass substrate increased with photon energy. The maximum absorption was seen at 320 nm,

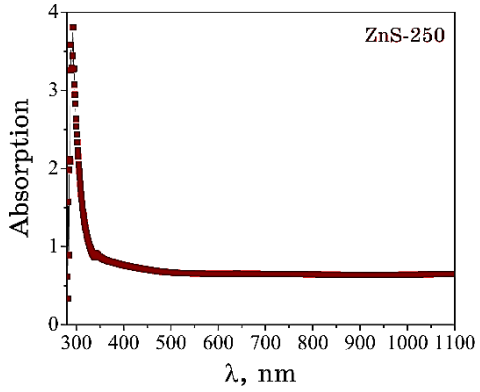

Fig. 3. The absorption of thin ZnS-250°C films.

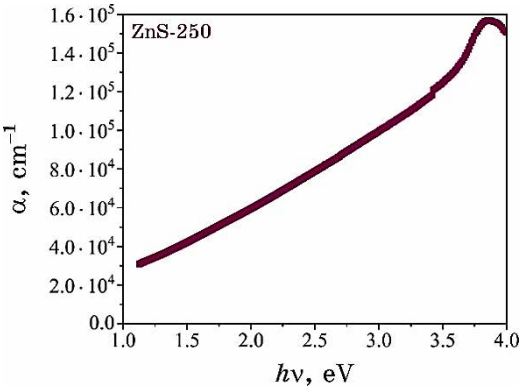

Fig. 4. The absorption coefficient of thin ZnS-250°C films.

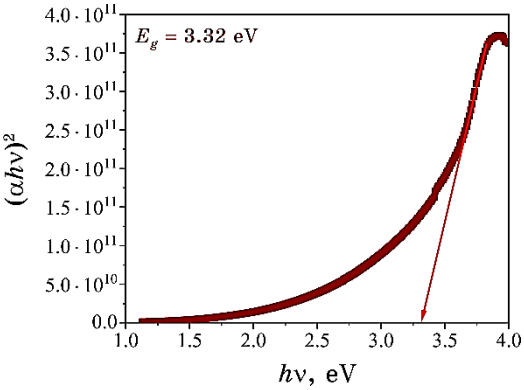

Fig. 5. Tauc plot for thin ZnS-250°C films.

with the highest values occurring at high photon energy ranging from 4 to 4.3 eV. This indicates that the absorption occurs within this specific frequency range, which encompasses the optical absorption edge.

The probability of electronic transitions occurring between the conduction and valence bands aligns with the results of empirical investigations [8, 9, 10]. The difference between the valence and conduction bands was calculated using the energy-gap value, which may be used to evaluate a material's electrical, thermal, and electronic properties. Equation (2) [11] demonstrates the application of the Tauc equation in computing the direct energy gap. Given that the transitions are permitted to be of the direct kind, characterized by a value of ($r = 1/2$), draw the link for tangent $(\alpha h\nu)^2$ and the incident photons' energy, then extend the curve straight portion to determine the point, where it crosses (where $(\alpha h\nu)^2 = 0$), represent

the optical energy gap.

In Figure 5, the band gap of the films was observed for ZnS; it has an optical energy gap of 3.32 eV at 250°C, which is nearly in line with the findings of Refs. [12, 13].

3.3. Electrical Properties

Figure 6 illustrates the link between inverse temperature and conductivity. The conductivity increases, when temperature increases from 40°C to 180°C, indicating that the layers are semiconductors. With increasing temperature, conductivity increases, while activation energy decreases. The underlying cause could be large particle sizes and excellent crystallization. Grain-boundary scattering has a general effect on charge-carrier mobility and film crystallinity. In our situation, grain expansion caused by the charge-carrier transport mechanism reduced grain-boundary scattering [14, 15]. To evaluate electrical conductivity, we use the given equation:

$$\sigma = \sigma_0 \exp\left(-\frac{E_a}{k_B T}\right) \tag{3}$$

(σ_0 is temperature-independent constant, E_a is activation energy for conduction, k_B is Boltzmann's constant, and here, T is a temperature [K]).

The conductivity and activation energy are shown in Table 2.

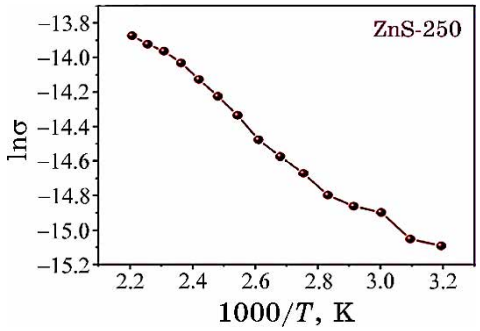

Fig. 6. Energy gap from electrical conductivity of ZnS-250°C films.

TABLE 2. The activation energy and optical energy gap.

Sample	E_{a1} (313–363 K)	E_{a2} (363–453 K)	E_a
ZnS-250°C	0.903 eV	1.833 eV	3.32 eV

Energy gap can be computed using the linear relationship, as illustrated in Fig. 6.

For the thin ZnS films, the presence of two linked zones is the reason for the alteration in the conduction mechanism. The temperature in the first zone is low (313–363 K), whereas the second zone is greater (363–453 K) [16].

4. CONCLUSION

The thin ZnS films were formed on a glass substrate using spray-pyrolysis deposition technique. The x-ray diffraction (XRD) study of this thin film revealed a 'full width at half maximum' (*FWHM*) value of 0.141°. This indicates that the crystallinity of the films can be enhanced by increasing the temperatures of the glass substrate. It was also shown that all films had a cubic crystal structure with a favourite (111) orientation. An increase in substrate temperature resulted in enhanced crystalline quality of the films, accompanied by a growth in grain sizes of thin film from 9.760 nm to 11.460 nm. A comprehensive analysis of the morphological, optical, and structural characteristics of the films was carried out using the computer program 'Hebal Optic' of simulation. The findings indicated an energy gap of 3.32 eV as well as nanoscale branching dendritic formations. As a result, it has semiconductor properties, which are important in electronic devices and solar cell manufacture.

ACKNOWLEDGEMENTS

Authors would like to thank the University of Tikrit, College of Education, Physics Department, management and staff for the support during the experimental-work stage.

REFERENCES

1. N. Imam and M. B. Mohamed, *Superlattices and Microstructures*, **73**: 203 (2014); https://doi.org/10.1016/j.spmi.2014.05.026
2. W. K. Bae, J. Kwak, J. W. Park, K. Char, C. Lee, and S. Lee, *Advanced Materials*, **21**, No. 17: 1690 (2009); https://doi.org/10.1002/adma.200801908
3. Hanaa I. Mohammed, Iman H. Khdayer, and Iqbal S. Naji, *AIP Conference Proceedings*, **2372**, No. 1: 090005 (2021); https://doi.org/10.1063/5.0068737
4. Jiaguo Huang and Kanyi Pu, *Chem. Int. Ed. Engl.*, **59**: 11717 (2020); https://doi.org/10.1002/anie.202001783
5. W. Daranfed, M. S. Aida, A. Hafdallah, and H. Lekiket, *Thin Solid Films*,

518, Iss. 4: 10821084 (2009); https://doi.org/10.1016/j.tsf.2009.03.227
6. J. Ady, S. F. Umroati, S. Meliana, S. D. A. Ariska, and D. I. Rudyardjo, *Nanosistemi, Nanomateriali, Nanotehnologii*, **19**, Iss. 3: 585 (2021); https://doi.org/10.15407/nnn.19.03.585
7. A. Ateş, M. Kundakçı, A. Astam, and M. Yıldırım, *Physica E: Low-dimensional Systems and Nanostructures*, **40**, Iss. 8: 2709 (2008); https://doi.org/10.1016/j.physe.2007.12.010
8. S. Ilican, Y. Caglar, M. Caglar, and F. Yakuphanoglu, *Physica E: Low-dimensional Systems and Nanostructures*, **35**, Iss. 1: 131 (2006); https://doi.org/10.1016/j.physe.2006.07.009
9. Z. Zhao, M. Liu, K. Yang, C. Xu, Y. Guan, X. Ma, and F. Zhang, *Advanced Functional Materials*, **31**, Iss. 43: 2106009 (2021); https://doi.org/10.1002/adfm.202106009
10. N. P. Huse, A. S. Dive, K. P. Guttu, and R. Sharma, *Mater. Sci. Semicond. Proc.*, **67**: 62 (2017); https://doi.org/10.1016/j.mssp.2017.05.010
11. K. Priya, V. K. Ashith, G. K. Roa, and G. Sanjeev, *Ceramics. International*, **43**: 10487 (2017); https://doi.org/10.1016/j.ceramint.2017.05.094
12. M. C. Lopez, J. P. Espinos, F. Martin, D. Leinen, and J. R. Ramos-Barrado, *Journal of Crystal Growth*, **285**, Iss. 1–2: 66 (2005); https://doi.org/10.1016/j.jcrysgro.2005.07.050
13. S. Mondal, S. Bhattacharyya and P. Mitra, *Pramana*, **80**, Iss. 2: 315 (2013); https://doi.org/10.1007/s12043-012-0463-6
14. C. F. Niedik, C. Freye, F. Jenau, D. Haring, G. Schroder, and J. Bittmann, *2016 IEEE International Conference on Dielectrics (ICD)*, **2**: 1114 (2016); https://doi.org/10.1109/ICD.2016.7547814
15. X. Huang, N. Hu, L. Zhang, L. Wei, H. Wei, and Y. Zhang, *Synthetic Metals*, **185**: 25 (2013); https://doi.org/10.1016/j.synthmet.2013.09.034
16. H. Wu, J. Yu, G. Yao, Z. Li, W. Zou, X. Li, and Z. Tang, *Sensors and Actuators. B: Chemical*, **369**: 132195 (2022); https://doi.org/10.1016/j.snb.2015.01.070

Наносистеми, наноматеріали, нанотехнології
Nanosistemi, Nanomateriali, Nanotehnologii
2026, т. 24, № 1, сс. 115–122
https://doi.org/10.15407/nnn.24.01.0115

PACS numbers: 61.05.cp, 78.30.Hv, 78.55.Hx, 78.67.Bf, 81.07.Bc, 81.70.Pg

Preparing of Sb:SrF_2 Nanoparticles and Studying Their Structural and Luminescence Properties

Ahmad Khoudro[1], Mufid Diab[2], and Omar Al-Aboush[1]

[1]*Department of Physics,*
Faculty of Science,
Tishreen University,
Latakia, Syria
[2]*Department of Physics,*
Faculty of Science,
AL-Baath University,
Homs, Syria

In this research, strontium fluoride doped with antimony in different proportions is prepared using solid-state method. The prepared compounds are characterized using XRD, FT-IR and photoluminescence techniques. As found, the prepared compounds crystallize according to the cubic pattern with nanosize grains and have a clear fluorescence property.

У цьому дослідженні фторид Стронцію, леґований Стибієм у різних пропорціях, був одержаний твердофазним методом. Одержані сполуки було охарактеризовано за допомогою методів рентґенівської дифракції (XRD), інфрачервоної спектроскопії на основі Фур'є-перетвору (FT-IR) та фотолюмінесценції. Було виявлено, що одержані сполуки кристалізуються у кубічну структуру із нанорозмірними зернами, а також мають чітку флюоресцентну властивість.

Key words: strontium fluoride, doping, SrF_2:Sb, photoluminescence.

Ключові слова: фторид Стронцію, леґування, SrF_2:Sb, фотолюмінесценція.

(Received 14 November, 2024; in revised form, 22 November, 2024)

1. INTRODUCTION

Since the first Nd:YAG laser ceramic was reported by Ikesue *et al.* in 1995 [1], transparent polycrystalline ceramics have found increased interest over the last few years. The majority of transpar-

ent ceramics researches focus on oxide materials like $Nd_{3x}Y_{3-3x}Al_5O_{12}$ (Nd:YAG), however, fluoride materials are very attractive and promising materials for laser applications [2–5]. Among the fluoride compounds, strontium fluoride (SrF_2) is an attractive material. Because of its excellent optical properties, *e.g.*, the high transmission in the infrared and ultraviolet spectral range 0.13–11 μm, the low refractive index nDj1.439 and 589 nm, and the extremely low solubility in water 120 mg L1, SrF_2 is an ideal material for optical applications and is often used as a coating material for high-quality optical windows, prisms and lenses to reduce reflection and to increase transmission. Furthermore, as the isotype of CaF_2, SrF_2 has gained great interest as a laser material when doped with rare-earth ions [6–8].

For example, thanks to its broad emission bands, Yb:SrF_2 single crystal is a promising gain medium in tuneable laser and ultra-short pulse laser generator [9, 10]. With their superior optical and chemical properties, SrF_2 ceramics are highly suitable for a wide range of industrial and scientific applications such as laser technology, scintillators, photolithographic processing and specialized window production. However, few works have been done on the preparation of SrF_2 transparent ceramics. Basiev *et al.* reported laser operation of rare-earth doped ceramics of Nd:SrF_2 and its solid solutions fabricated by a hot-forming method [11]. However, it is deformation of single crystals and lacks for advantages of ceramics such as much superior mechanical property, lower temperatures than single crystal growth process.

In this study, we have focused on preparation of SrF_2 nanopowders doped with Sb.

2. EXPERIMENTAL

2.1. Preparation of Sb:SrF_2 Nanoparticles

The solid-state method was used to prepare SrF_2:Sb 0.0, 0.1, 0.15, 0.2, 0.25, 0.3 wt.% as follow accurately weighed in the required proportions and thoroughly mixed and ground using an agate slurry and pestle to convert into very fine powders. Acetone was used to help the solid compounds mix during the sample preparation process in relatively small quantities. The previous materials were ground and mixed with an agate mortar to ensure obtaining a homogeneous mixture after adding an amount of acetone in order to improve the homogeneous mixing process for it for about 15 minutes until the acetone dried. This process was repeated three consecutive times for each of the samples. After that, the resulting mixture was dried by heating it to a temperature of 100°C for a pe-

riod of time sufficient to ensure the removal of moisture. The samples were annealed at 350°C for 4 hours, after which the samples were gradually cooled in the heating oven to room temperature at a rate of 1°C/min.

2.2. Characterization

The crystallite structure and size of the synthesized nanoparticle samples were calculated using an x-ray powder diffractometer (XRD) (Philips-PW-1840) with a CoK_α radiation of 1.789 Å in a 2θ range of 20–80°. While the analysis of the chemical composition was carried out using Fourier transformation infrared (FT-IR model: Jasco Spectrum 4100 FT-IR) spectroscopy. The luminescence properties were studied using UV-Vis Spectroscopy.

3. RESULTS AND DISCUSSION

3.1. DTA Analysis

The DTA curve shown in Fig. 1, demonstrate the thermal behaviour of the system as it was scanned within a temperature range 0–1000°C. The ratio of 0.25 was chosen to study the thermal changes.

The DTA diagram shows exothermic effects. The first exothermic effect at 288°C indicates the entry of antimony into the crystal structure of strontium fluoride. The second exothermic effect at

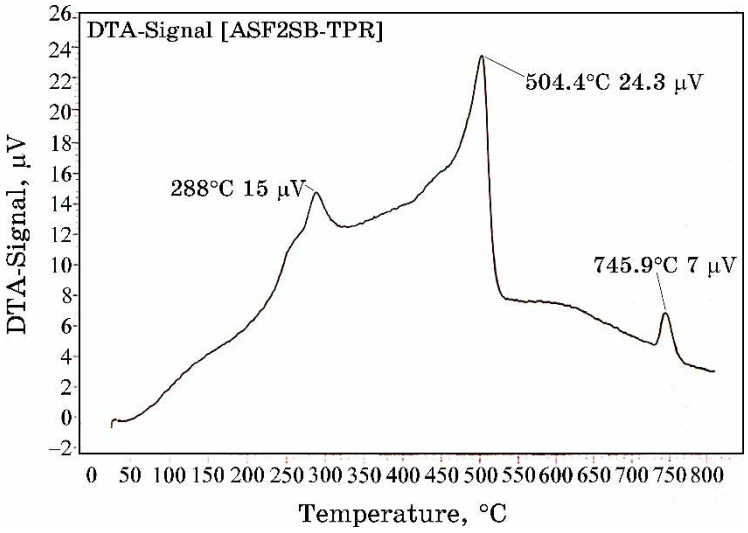

Fig. 1. DTA of SrF_2:Sb (0.25 wt.%).

504.4°C indicates the formation of antimony pentoxide Sb_2O_5. The third exothermic effect at 745.9°C indicates the formation of strontium oxide.

3.2. XRD Analysis

Figure 2 shows x-ray diagrams of strontium fluoride compound doped with antimony in different proportions. These diagrams are consistent with the reference card (SrF_2: 96-900-9044) for pure strontium fluoride with some displacement, indicating a clear change in the dimensions of the primary lattice cell as a result of the entry of antimony into the structure of strontium fluoride. The diagram SrF_2:0.3Sb shows a significant change in the structure in accordance with the reference card and this is explained by the formation of antimony pentoxide.

The average crystallite size was calculated using Scherrer's equation, which is expressed as follows [14]:

$$D = \frac{K\lambda}{\beta \cos\theta}, \tag{1}$$

where K is Scherrer's constant ($K = 0.89$ assuming spherical parti-

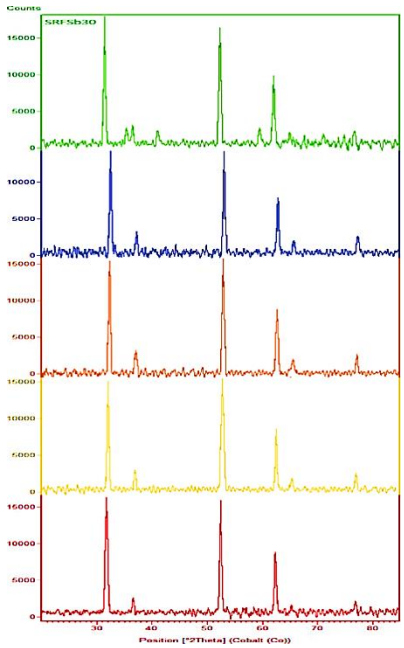

Fig. 2. XRD patterns of SrF_2:Sb nanoparticles.

cles), λ is the x-ray wavelength, β is the peak width at half maximum (*FWHM*), and θ is the Bragg's diffraction angle. The average crystal size was of 7.778 nm for SrF_2:0.25Sb.

3.4. FT-IR Spectroscopy

The FT-IR spectrum of SrF_2:Sb nanoparticles is presented in Fig. 3.

By comparing the infrared spectra of the compounds prepared

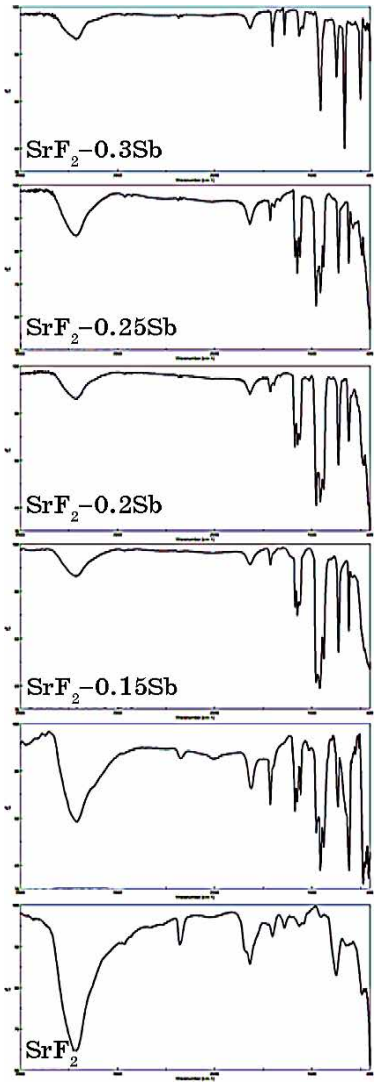

Fig. 3. FT-IR spectra of synthesized SrF_2:Sb nanoparticles.

with different proportions of antimony, it was found that new absorption bands appeared that were different from the absorption bands of the pure strontium fluoride compound. These bands appear at 469, 615, 728, 876, 953, 1115, 1147, 1172 cm^{-1}. These bands may be due to the vibration of the bonds according to the vibrational patterns: Sr–Sb–Sr, Sb–Sr–Sb, Sr–Sb–F, Sb–Sr–F, Sb–F–Sb, and F–Sb–F. This is evidence of the occurrence of a bond between the antimony atoms and the strontium fluoride, which confirms the entry of these atoms into the crystal structure of the compound.

As for the doping ratio (0.3), it was observed in the resulting spectrum that the previously formed bands disappeared, indicating the dissociation of antimony from strontium fluoride and the appearance of new absorption bands at wave numbers 414, 447 cm^{-1}

TABLE. The emission wavelength and the calculated energy gap.

	Wavelength	Energy gap
excitation	200	6.18
emission	310	3.99
emission	340	3.64
emission	355.4	3.48
emission	420	2.94
emission	451	2.74
emission	473	2.61
emission	495	2.50

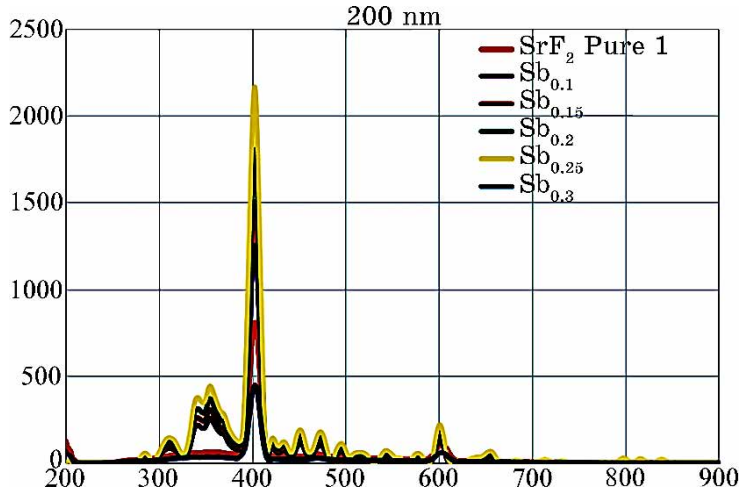

Fig. 4. Luminescence spectrum of SrF_2:Sb nanoparticles at 200 nm excitation wavelength.

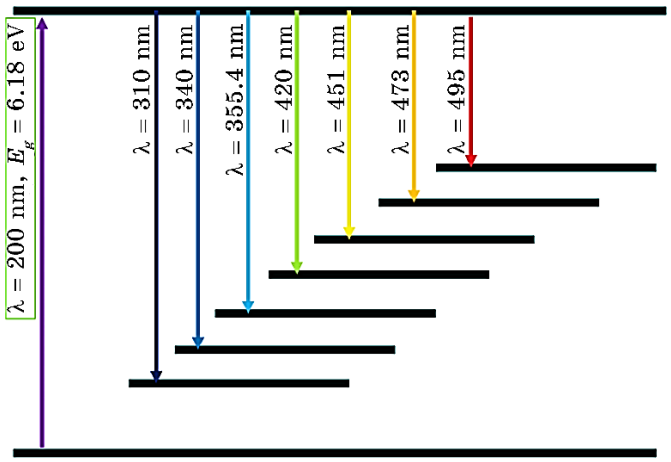

Fig. 5. The electronic transitions in the SrF_2:Sb.

due to the bonds Sb–O–Sb, O–Sb–O, and this is evidence of the formation of antimony oxide (Sb_2O_3).

3.3. The Luminescence Properties

The luminescence of the samples was measured using a UV-Vis spectroscopy, where the samples were excited at different wavelengths and the emission spectrum of these samples was recorded (Table).

Figure 4 shows the luminescence spectrum of the prepared samples with different doping ratios at 200 nm excitation wavelength.

These electronic transitions can be represented by the following diagram shown in Fig. 5.

CONCLUSION

SrF_2:Sb nanoparticles were successfully synthesized using soled state method. The resulting compounds were characterized using XRD techniques, which confirmed the size of nanoparticles, and IR spectroscopy. The photoluminescence was studied and have a clear fluorescence property.

REFERENCES

1. A. Ikesue, T. Kinoshita, K. Kamata, and K.J. Yoshida, *J. Am. Ceram. Soc.*, **78**, Iss. 4: 1033 (1995); https://doi.org/10.1111/j.1151-

2916.1995.tb08433.x
2. S. J. Pearton, D. P. Norton, K. Ip, Y. W. Heo, and T. Steiner, *Prog. Mater. Sci*, **50**, Iss. 3: 293 (2005); https://doi.org/10.1016/j.pmatsci.2004.04.001
3. S. Faÿ, L. Feitknecht, R. Schlüchter, U. Kroll, E. Vallat-Sauvain, and A. Shah, *Sol. Energy Mater. Sol. Cells*, **90**, Iss. 18–19: 2960 (2006); https://doi.org/10.1016/j.solmat.2006.06.003
4. W. Minrui, J. Wang, W. Chen, Y. Cui, and L. Wang, *Mater. Chem. Phys.*, **97**, Iss. 2–3: 219 (2006); https://doi.org/10.1016/j.matchemphys.2005.07.072
5. L. Su-Shia, J. Huang, and D. Lii, *Mater. Chem. Phys*, **90**, Iss. 1: 22 (2005); https://doi.org/10.1016/j.matchemphys.2004.08.040
6. M. Kaur, S. Bhattacharya, M. Roy, S. K. Deshpande, P. Sharma, S. K. Gupta, and J. V. Yakhmi, *Appl. Phys*, **A87**: 91 (2007); https://doi.org/10.1007/s00339-006-3858-8
7. Y. Ishikawa, Y. Shimizu, T. Sasaki, and N. Koshizaki, *J. Colloid. Interface Sci*, **300**, Iss. 2: 612(2006); https://doi.org/10.1016/j.jcis.2006.04.005
8. V. V. Pokropivny and M. M. Kasumov, *Tech. Phys. Lett.*, **33**: 44 (2007); https://doi.org/10.1134/S1063785007010129
9. G. P. Zhu, C. X. Xu, X. F. Wu, Y. Yang, X. W. Sun, and Y. P. Cui, *J. Electron. Mater.*, **36**: 494 (2007); https://doi.org/10.1007/s11664-006-0068-2
10. W. T. Yao, S. H. Yu, Y. Zhou, J. Jiang, Q. S. Wu, L. Zhang, and J. Jiang, *J. Phys. Chem. B*, **109**, Iss. 29: 14011 (2005); https://doi.org/10.1021/jp0517605
11. C. H. Loa, T. T. Tsung, and H. M. Lin, *J. Alloys Compd*, **434–435**: 659 (2007); https://doi.org/10.1016/j.jallcom.2006.08.217
12. J. K. Lung, J. C. Huang, D. C. Tien, C. Y. Liao, K. H. Tseng, T. T. Tsung, W. S. Kao, T. H. Tsai, C. S. Jwo, H. M. Lin, and L. Stobinski, *J. Alloys Compd*, **434–435**: 655(2007); https://doi.org/10.1016/j.jallcom.2006.08.213
13. A. A. Ashkarran, A. I. Zad, M. M. Ahadian, and S. A. Ardakani, *Nanotechnology*, **19**, Iss. 19: 195709 (2008); https://doi.org/10.1088/0957-4484/19/19/195709
14. J. Al-Ebraheem, M. N. Alkhoder, and R. H. Tulaimat, *Heliyon*, **10**, Iss. 2: 24652 (2024); https://doi.org/10.1016/j.heliyon.2024.e24652

Наносистеми, наноматеріали, нанотехнології
Nanosistemi, Nanomateriali, Nanotehnologii
2026, т. 24, № 1, сс. 123–139
https://doi.org/10.15407/nnn.24.01.0123

PACS numbers: 64.75.Ef, 64.75.Jk, 64.75.Nx, 81.30.Dz, 81.30.Mh, 82.33.Pt, 82.60.Lf

Prediction of the Thermodynamic Stability and Limits of Isomorphous Substitutions in Solid Solutions $Y_{1-x}Ln_xPO_4$, Where Ln = Gd–Lu, Sc

E. I. Get'man[1], O. Yu. Mariichak[1], L. I. Ardanova[2], and S. V. Radio[1]

[1]*Vasyl' Stus Donetsk National University,*
21, 600-Richchia Str.,
UA-21021 Vinnytsia, Ukraine
[2]*Minnesota State University,*
228, Wiecking Center,
56001 Mankato, Minnesota, USA

Using V. S. Urusov's crystal-energy theory of isomorphous miscibility, the mixing energies (interaction parameters), critical decomposition (stability) temperatures, and limits of isomorphous substitutions are calculated, as well as the thermodynamic stability regions of zircon-type orthophosphate solid solutions with the composition $Y_{1-x}Ln_xPO_4$, where Ln—lanthanides or Sc. The contributions to the mixing energy arising from differences in the sizes of the substitutional structural units and from differences in the nature of the chemical bonding of the system components are characterized. A thermodynamic-stability diagram of solid solutions and the corresponding decomposition domes are presented, enabling graphical prediction of the decomposition temperatures of solid solutions for given substitution limits, or the equilibrium substitution limits for a given temperature and thermodynamic-stability region. The results do not contradict the experimental data reported in the literature. They may be helpful in the search for compositions of mixed matrices and activators for new luminescent, laser, and other materials based on $Y_{1-x}Ln_xPO_4$ (Ln = Gd–Lu, Sc) solid solutions, including nanomaterials.

З використанням кристалоенергетичної теорії ізоморфної змішуваности В. С. Урусова розраховано енергії змішання (параметри взаємодії), критичні температури розпаду (стабільности), границі ізоморфних заміщень, а також визначено області термодинамічної стабільности твердих розчинів ортофосфатів зі структурою циркону складу $Y_{1-x}Ln_xPO_4$, де Ln — лантаноїди або Sc. Охарактеризовано внески в енергію змішання, зумовлені відмінностями у розмірах заміщуваних структурних одиниць, а також у характері хемічного зв'язку компонентів систем.

Подано діяграму термодинамічної стабільности твердих розчинів і куполи їхнього розпаду, що дає змогу графічно прогнозувати температури розпаду твердих розчинів за заданими границями заміщення або рівноважні границі заміщення за заданої температури та області термодинамічної стабільности. Результати роботи не суперечать експериментальним літературним даним і можуть бути корисними під час пошуку складів змішаних матриць та активаторів нових люмінесцентних, лазерних та інших матеріялів на основі твердих розчинів $Y_{1-x}Ln_xPO_4$ (Ln = Gd–Lu, Sc), у тому числі й наноматеріялів.

Key words: solid solutions, lanthanides, yttrium, scandium, orthophosphates, isomorphous substitutions, mixing energy, thermodynamic stability, substitution limits.

Ключові слова: тверді розчини, лантаноїди, Ітрій, Скандій, ортофосфати, ізоморфні заміщення, енергія змішання, термодинамічна стабільність, границі заміщень.

(Received 11 August, 2025; in revised form, 18 August, 2025)

1. INTRODUCTION

Solid solutions based on rare-earth element (REE) orthophosphates are promising materials with excellent luminescent properties and high thermal and radiation stability. They are used as scintillation detectors, phosphors for radiography and plasma panels, materials for radioactive waste storage [1], laser media, protective coatings, cements, high-temperature ion exchangers [2], light-emitting diodes, solar panels, thermal barrier coatings, and in optical thermometry [3].

In addition, in recent years, REE orthophosphate-based nanomaterials have begun to find medical applications. Nanocrystals of yttrium orthophosphate (YPO_4) doped with Dy^{3+} ions at various concentrations are considered promising for use in laser-induced hyperthermia of cancerous tumours. The local temperature of nanoparticle powders increases linearly with increasing laser power and Dy^{3+} concentration, enabling high heating and cooling rates. This allows for precise control of the exposure time and minimal doses of laser irradiation on patients [4].

UV phosphors emitting in the 200–280 nm range are of particular interest for medical applications due to their pronounced bactericidal properties, resulting from the coincidence of their emission wavelengths with the range of maximum DNA sensitivity of microorganisms to UV irradiation. Moreover, ultraviolet radiation effectively destroys surface cancer cells without damaging deeper tissues [5]. REE orthophosphates are also employed in drug delivery sys-

tems and as fluorescent labels for visualizing biomolecules and cellular structures [6].

Initially, materials based on individual orthophosphates were used. Later, it was found that 'double' orthophosphates containing two or more rare-earth elements (REEs) in the host lattice are more effective. For example, very high intensity under ultraviolet excitation was observed for the solid solution $Gd_{0.5}Y_{0.5}PO_4:Tb^{3+}$, which exhibits a twofold increase in luminescence intensity compared to $YPO_4:Tb^{3+}$ [6].

The choice of yttrium orthophosphate as one of the components in the $Y_{1-x}Ln_xPO_4$ systems is because, along with gadolinium and lutetium compounds, it is most commonly used as a host matrix for mixed orthophosphates. In addition, it is isostructural with the orthophosphates of REEs, and the crystal ionic radius of yttrium (1.159 Å) differs only slightly from the radii of other REE ions (from 1.193 Å for Gd^{3+} to 1.117 Å for Lu^{3+}) [7]. Therefore, a continuous series of solid solutions between the components is possible in most of the previously described systems (see, *e.g.*, Refs. [1–3, 5, 6, 8–11]). In some works (*e.g.*, Refs. [4, 12, 13]), only individual fragments of continuous solid solution series were synthesized, as substitution limits were not reported.

At the same time, to the best of our knowledge, there is no literature data on $Y_{1-x}Ln_xPO_4$ systems (Ln = Gd–Lu, and Sc) with limited solid solution series. However, it is known [14–16] that, in general, continuous solid solution series should decompose upon cooling samples synthesized at high temperatures, forming limited composition ranges based on the system components.

The choice of YPO_4-based systems for the present study was also motivated by the absence of intrinsic luminescence in YPO_4 crystals down to 5 K [17].

Considering the above, before synthesizing solid solutions and studying the 'composition–property' relationships, it is desirable to know the limits of isomorphous substitutions and their thermodynamic stability under synthesis, intended use, and even storage conditions. Knowledge of the thermodynamic stability regions of solid solutions is essential for controlling their properties and ensuring their reproducibility over time and under varying temperatures.

Experimental determination of substitution limits and stability regions of solid solutions synthesized by the 'annealing and quenching' method using x-ray diffraction analysis (XRD) is complicated by the difficulty of achieving equilibrium at low temperatures due to the low diffusion rate in the solid phase, as well as by the possibility of partial decomposition upon cooling from high temperatures.

In addition, XRD may be of limited informativeness when the components are isostructural with very close sizes of the substituting structural units, as in the case of the $Y_{1-x}Dy_xPO_4$ system [4], in the case of spinodal decomposition of the solid solution [14–16], or when the studied samples are of nanoscale size, due to broadening and overlapping of x-ray reflections.

A lack of data on the limits of isomorphous substitutions and the stability regions of solid solutions forces researchers to select matrix and dopant compositions either by analogy with closely related systems or through a 'trial and error' approach. Such a method is often accompanied by excessive consumption of costly reagents and a significant increase in the time required for research. In this regard, it is advisable to use experimental methods and computational approaches that allow for a preliminary assessment of the stability of solid solutions and the substitution ranges, thus avoiding the mentioned limitations.

An example of such a rational approach can be found in studies [3, 5], where, in selecting the synthesis conditions for compounds in the $Y_{1-x}Sc_xPO_4$ system, the authors used calculation results for this system presented in Ref. [18].

It should be noted that nanoscale orthophosphates exhibit enhanced practically relevant properties due to their larger specific surface area. This is related to the fact that structural units located at the surface differ in coordination numbers from those inside the bulk, and this difference becomes more pronounced as the particle size decreases, leading to modifications of the material properties. As reported in Ref. [19], the conventional concepts of surface energy developed for macroparticles remain applicable to nanoparticles larger than 10 nm.

At the same time, it is known that in nanocrystalline materials with particle diameters above 6 nm, the volume of the surface layer remains smaller than that of the crystal interior [20]. Furthermore, according to Ref. [20], the structural characteristics of solid solutions do not depend on the particle size, at least within the range of 6-to-40–80 nm.

Based on the above considerations, the present work aimed to predict the thermodynamic stability and the limits of isomorphous substitutions in zircon-type orthophosphates of the composition $Y_{1-x}Ln_xPO_4$, where Ln = Gd–Lu, Sc. In this study, the calculated mixing energies (Q_{mix}), substitution limits (x), and critical decomposition temperatures (T_{cr}), obtained regarding the key energetic contributions (size-related, Q_R, and bond-ionicity contribution, Q_ε), provide a framework both for assessing the stability of $Y_{1-x}Ln_xPO_4$, including their nanoscale forms, and for selecting the optimal conditions for their synthesis.

2. INITIAL DATA AND CALCULATION METHOD

Within the Urusov's crystal-energy theory of isomorphous substitutions, the main challenge in determining the limits of isomorphous substitutions is finding the mixing energy. In the quasi-chemical approach, this corresponds to the interchange energy, and in the theory of subregular solid solutions, it corresponds to the interaction parameter [14–16]. Within the approximation of regular solid solutions, the critical (maximum) decomposition temperatures T_{cr} are calculated using Eq. (1) [14]:

$$T_{cr} = Q_{mix}/(2k_B N), \quad (1)$$

where Q_{mix} is the mixing energy, k_B is the Boltzmann's constant, and N is Avogadro's number.

In the considered systems, the relative differences in interatomic distances 'cation–tetrahedral anion' are significantly less than 0.1 (ranging from 0.0003 to 0.0411; Table 1). Therefore, according to Ref. [14], the calculation of solid-solution decomposition temperatures can be performed in the regular-solution approximation using

TABLE 1. Selected initial data, calculated mixing energies, and critical decomposition temperatures of solid solutions $Y_{1-x}Ln_xPO_4$, Ln = Gd–Lu, and Sc.

Ln	R, Å	$\Delta R/R_1 = (R_{Ln} - R_1)/R_1$	Q_R, kJ/mole	χ_{Ln}	$\chi(PO_4^{3-}) - \chi(Ln^{3+})$	ε_{Ln}	Δ_ε	Q_ε, kJ/mole	Q_{mix}, kJ/mole	T_{cr}, K
Gd	3.561	0.0177	4.250	1.386	2.314	0.712	0.010	0.618	4.868	291
Tb	3.537	0.0108	1.582	1.410	2.290	0.708	0.014	1.212	2.794	167
Dy	3.526	0.0077	0.804	1.426	2.274	0.705	0.017	1.787	2.591	155
Ho	3.512	0.0037	0.186	1.433	2.267	0.703	0.019	2.233	2.419	144
Er	3.498	0.0003	0.001	1.438	2.262	0.702	0.020	2.474	2.475	148
Tm	3.490	0.0026	0.092	1.455	2.245	0.695	0.027	4.521	4.613	275
Yb	3.480	0.0054	0.395	1.479	2.221	0.692	0.030	5.597	5.992	358
Lu	3.467	0.0092	1.148	1.431	2.269	0.704	0.018	2.023	3.171	189
Sc	3.361	0.0411	22.869	1.415	2.285	0.707	0.015	1.449	24.318	1452
Y	3.499	—	—	1.340	2.360	0.722	—	—	—	—

Becker's equation (Eq. (2)) [21]:

$$-\frac{1-2x}{\ln\dfrac{1}{1-x}} = \frac{R_g T_d}{Q_{mix}}, \qquad (2)$$

where x is the mole fraction of the dissolved component, R_g is the universal gas constant, and T_d is the solid-solution decomposition temperature. In both equations, R_g and Q_{mix} are expressed in calories [14].

Since the system components are isostructural, the mixing energy Q_{mix} was calculated using Urusov's equation (Eq. (3)), representing it as the sum of two contributions caused by differences in the degree of ionicity of the chemical bond in the system components (Q_ε) and the sizes of the substituting structural units (Q_R) [14–16]:

$$Q_{mix} = Q_\varepsilon + Q_R = \frac{1390 m z_m z_x \alpha(\Delta\varepsilon)^2}{2R} + C m n z_m z_x \left(\frac{\Delta R}{R_1}\right)^2 \text{ [kJ/mole]}, \qquad (3)$$

where $m = 2$—the number of different structural units in the system components in the pseudo-binary approximation of the zircon structure; $z_m = z_x = 3$—the charge magnitudes of the substituting and common structural units in the components; $\alpha = 1.723$—the reduced Madelung's constant calculated using Templeton's formula [22]; $C = 113$ kJ—an empirical value depending on compressibility and other crystal characteristics taken from Ref. [14]; $n = 6$—the coordination number of the substituting structural unit in the pseudo-binary approximation of the structure; R—interatomic distances 'cation–tetrahedral anion' Ln–PO_4 in the system components taken from Ref. [23]; ΔR and $\Delta R/R_1$—the difference and relative difference of interatomic distances 'cation–tetrahedral anion'; R_1—the interatomic distance in the system component with the smaller cation radius; $\Delta\varepsilon$—the difference in the degree of ionicity of the chemical bond in the system components.

The degrees of ionicity ε of the chemical bonds in the REE phosphate systems were determined based on the difference in electronegativities $\chi(Ln^{3+})$ of the cations [24] and the PO_4^{3-} anion. The electronegativity of the PO_4^{3-} anion was taken as 3.7 according to Batsanov [25].

3. RESULTS OF CALCULATIONS AND DISCUSSION

3.1. Mixing Energies of Solid Solutions

Some initial data and calculation results of the contributions Q_R,

caused by differences in the sizes of substituting structural units in the system components, to the total mixing energy Q_{mix}, are presented in Table 1 and Fig. 1, *a*.

As seen from the presented data, with increasing REE atomic number, the contributions Q_R, caused by differences in the sizes of substituting structural units, change smoothly. They decrease significantly from 4.250 to 0.001 kJ/mole along the series of solid solutions from $Y_{1-x}Gd_xPO_4$ to $Y_{1-x}Er_xPO_4$ and then increase to 1.148 kJ/mole in the series from $Y_{1-x}Er_xPO_4$ to $Y_{1-x}Lu_xPO_4$.

In the case of the $Y_{1-x}Sc_xPO_4$ system, the contribution Q_R is significantly larger (22.869 kJ/mole) because the crystal ionic radius of scandium is much smaller than those for the REEs [7], resulting in a larger size parameter $\Delta R/R_1$ for $Y_{1-x}Sc_xPO_4$, accordingly.

The smooth (regular) variation of Q_R values is apparently because the size parameter $\Delta R/R_1$ was calculated based on sufficiently accurate interatomic distances. The minimal values of Q_R in the middle of the dependence result from minimal differences in interatomic distances between the orthophosphate ions Y^{3+} (3.499 Å) and Ho^{3+} (3.512 Å), Er^{3+} (3.498 Å), and Tm^{3+} (3.490 Å).

The contributions caused by differences in the degree of ionicity of the chemical bond in the system components, Q_ε, to the total mixing energies Q_{mix} increase with the atomic number of the rare-earth element (REE) from Gd to Yb, rising from 0.618 to 5.597 kJ/mole, and then sharply decrease to 2.023 kJ/mole in the case of lutetium orthophosphate (Table 1, Fig. 1, *b*). This behaviour is due

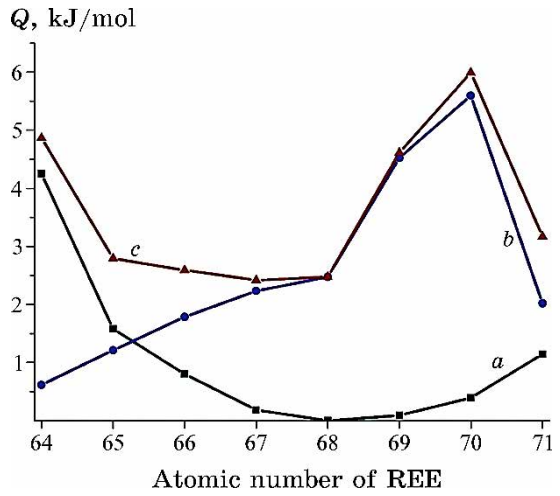

Fig. 1. Dependences of the contributions Q_R (curve *a*) and Q_ε (curve *b*) to the total mixing energies Q_{mix} (curve *c*) of solid solutions $Y_{1-x}Ln_xPO_4$, Ln = Gd–Lu, Sc, on the atomic numbers of the rare-earth elements.

to symbiotic changes both in the differences in ionicity degrees of the chemical bonds among the system components and in the electronegativities of the REEs.

The latter is explained by the fact that in the REE series, when moving from Tb to Yb, one electron is added to the 4*f*-sublevel of the REE with each step. In contrast, the transition from Yb to Lu does not add an electron to the 4*f*-sublevel but instead places it in the 5*d*-sublevel.

Overall, for REE orthophosphates from Dy to Lu, the total mixing energy Q_{mix} is mainly determined by contributions associated with differences in the degree of ionicity of the chemical bond Q_{ε}, while for Gd and Tb orthophosphates, the contributions due to differences in the sizes of substituting structural units Q_R dominate.

3.2. Substitution Limits and Thermodynamic Stability Regions

The decomposition temperatures T_d for limited solid-solution series were calculated using Eq. (2) for given substitution limits: $x = 0.01$, 0.03, 0.09, and 0.20 (Table 2). Based on the calculated decomposition temperatures (T_d) and critical decomposition temperatures (T_{cr}), their dependences on the atomic numbers of the REEs were plotted (Fig. 2).

These dependencies allow graphical determination, for limited solid solution series, of the equilibrium substitution limits x at given decomposition temperatures, or the decomposition temperatures at given substitution limits, for the orthophosphate systems ranging from Gd to Lu.

The intersection points of an isotherm drawn at the given decomposition temperature with a vertical line drawn from the REE atomic number enable estimating the composition interval within which the substitution limit lies. Interpolation along this vertical segment between the two closest curves then gives the substitution limit itself [26, 27]. The substitution limit can be refined by constructing, for a specific system, the dependence of the calculated decomposition temperatures (from Becker's equation) on the given composition, *i.e.*, by plotting the decomposition domes.

The calculated critical decomposition temperatures of the continuous solid solution series for the systems under consideration (Table 1, Fig. 2, *e*) are of 144–358 K for REEs orthophosphates and 1452 K for scandium orthophosphate. These values allow one to determine the temperature range for a continuous solid solution series. Thus, at $T > T_{cr}$ (curve *e*), the unlimited solid solutions are thermodynamically stable over the entire concentration range $0 \le x \le 1$. At $T < T_{cr}$, the unlimited solid solutions are unstable and may decompose into phases with limited solubility, if the diffusion rate and

TABLE 2. Decomposition temperatures (T_d [K]) of limited solid-solution series in the $Y_{1-x}Ln_xPO_4$ systems for substitution limits: $x = 0.01$, 0.03, 0.09, and 0.20.

Ln	Decomposition temperatures T_d [K] for substitution limit x			
	0.01	0.03	0.09	0.20
Gd	124	157	206	251
Tb	71	90	119	144
Dy	66	84	110	134
Ho	62	78	102	125
Er	53	80	105	128
Tm	117	149	195	238
Yb	153	193	254	310
Lu	81	102	134	164

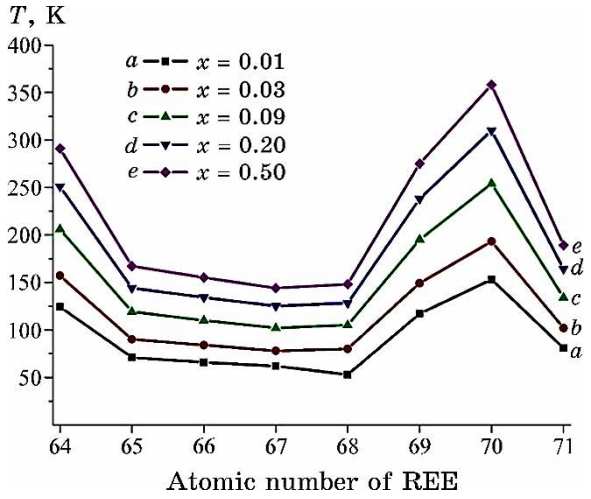

Fig. 2. Dependences of the calculated decomposition temperatures of solid solutions in the $Y_{1-x}Ln_xPO_4$ system on the REE numbers (thermodynamic stability diagram) for substitution limits $x = 0.01$ (*a*), $x = 0.03$ (*b*), $x = 0.09$ (*c*), $x = 0.20$ (*d*), and $x = 0.50$ (*e*).

time are sufficient for their formation.

It should be noted that the solid solutions in the $Y_{1-x}Ln_xPO_4$ systems have very low critical decomposition temperatures, with most of them even below room temperature. Consequently, they will remain stable over a wide temperature range from the critical temperatures up to the melting points of the system components, which exceed 2400 K [28]. This fact may indicate an advantage of materials based on continuous solid-solution series of yttrium orthophos-

phate with the composition $Y_{1-x}Ln_xPO_4$ in terms of property stability and reproducibility compared to similar materials based on solid solutions of other orthophosphates, such as scandium orthophosphate $Sc_{1-x}Ln_xPO_4$, whose critical temperatures range from 810 to 2880 K [18]. Moreover, materials based on continuous solid-solution series of the $Y_{1-x}Ln_xPO_4$ system may find preferential use in the production of nanomaterials by the sol–gel or low-temperature hydrothermal method, since nanomaterials are usually synthesized at low temperatures.

For all $Y_{1-x}Ln_xPO_4$ systems, where Ln = Gd–Lu, and Sc, the decomposition temperatures were calculated in the composition range $1.0 > x > 0$ with a step of $x = 0.05$, and decomposition domes were plotted (Figs. 3, 4). From these data, with greater accuracy than in Fig. 2, one can graphically determine the decomposition temperature for a given substitution limit, the substitution limit for a given temperature, and the regions of thermodynamic stability of the solid solutions. Above the peaks of the decomposition domes, continuous solid-solution series will be stable; below the peaks but above the dome lines, two limited solubility regions will exist; below

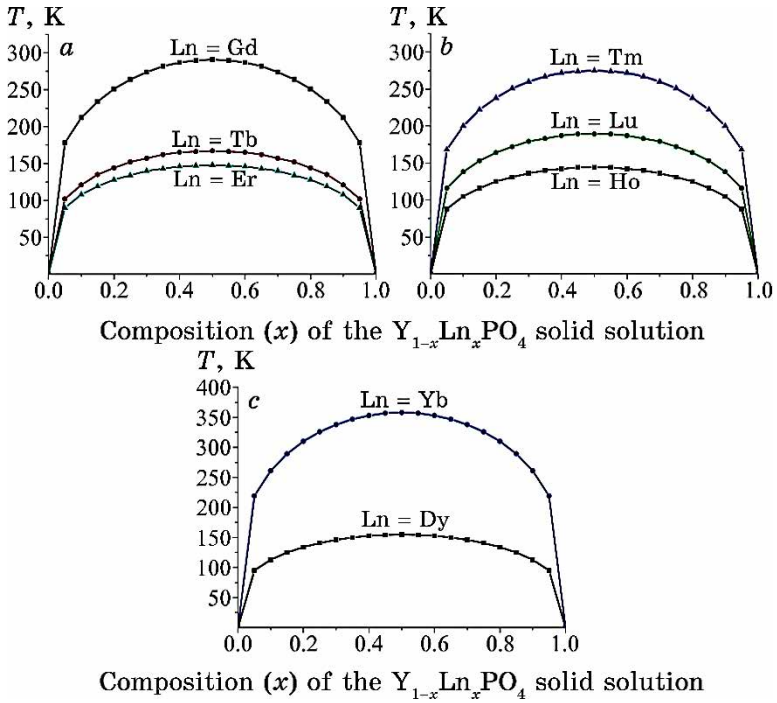

Fig. 3. Decomposition domes of solid solutions in the $Y_{1-x}Ln_xPO_4$ systems: (*a*) Ln = Gd, Tb, Er; (*b*) Ln = Ho, Tm, Lu; (*c*) Ln = Dy, Yb.

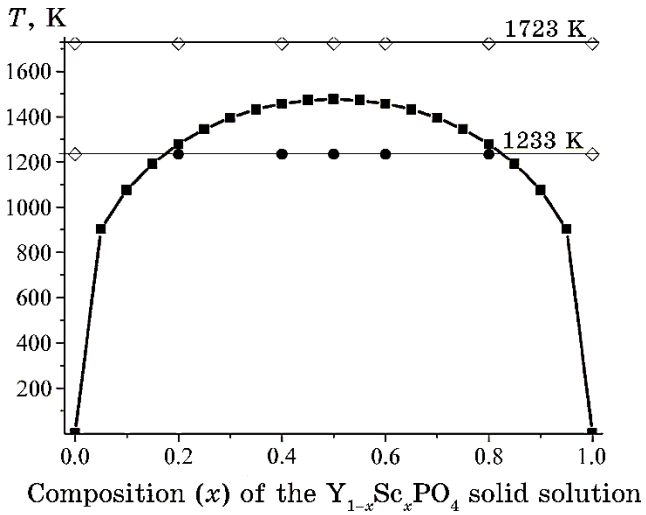

Fig. 4. Decomposition dome of the $Y_{1-x}Sc_xPO_4$ solid solution (■) and experimental data on synthesis temperatures for samples at 1233 K [3] and 1723 K [3, 5] (single-phase ◇ and multiphase ● samples).

the dome lines, mixtures of two solid solutions based on each component of the systems will be present.

4. COMPARISON OF CALCULATION RESULTS WITH LITERATURE DATA

Since the size parameters $\Delta R/R_1$ for the substitution of yttrium by scandium (Table 1), or scandium by yttrium [18], are less than 0.1 and equal, the solid solutions in the $Y_{1-x}Sc_xPO_4$ [3, 5] and $Sc_xY_{1-x}PO_4$ [11] systems can be considered within the regular solution approximation [14], and the calculated critical decomposition temperatures for both solid solutions will be practically identical.

To our knowledge, there is no literature on the critical decomposition temperatures, thermodynamic stability, or substitution limits for the $Y_{1-x}Ln_xPO_4$ solid solution systems with limited component solubility. Of course, this complicates the assessment of the reliability of the performed calculations.

However, there are reports on the synthesis temperatures of specific solid-solution compositions (Table 3). As seen from the data in Table 3, in most of the cited works (12 out of 13), the synthesis temperatures exceed the calculated critical decomposition temperatures, above which a continuous series of solid solutions exists in these systems. This indicates that the calculation results do not contradict the experimental literature data in the sense that synthe-

TABLE 3. Comparison of calculated T_{cr} results with synthesis temperatures from experimental studies*.

Composition, Ref.	x or %	Synthesis method	Synthesis temperature, K	T_{cr}, K
$Y_{1-x}Lu_xPO_4$ [2]	0.0, 0.25, 0.50, 0.75, 1.00	Precipitation from aqueous solutions	293–383; 773	189
$Y_{1-x}Sc_xPO_4$:0.5 mol.% Eu^{3+} [3]	0, 0.2, 0.4, 0.5, 0.6, 0.8, 1,0	Sol–gel method + annealing	1233 + 1723	1452
$Y_{1-x}Dy_xPO_4$ [4]	0.01, 0.05, 0.475	Sol–gel method with microwave–hydrothermal (MW–HT) treatment	473	155
$Y_{1-x}Sc_xPO_4$ [5]	0, 0.01, 0.05, 0.10, 0.2, 0.4, 0.5, 0.6, 0.8, 1.0	Solid-state method	1723	1452
$(Gd_xY_{1-x})_{1-y}PO_4$:yTb^{3+} (y = 0 or 0.15) [6]	0, 0.25, 0.5, 1.0	Solvothermal method	433 + 1023 + + 1273	291
$Y_{0.95(1-x)}Yb_{0.95x}Er_{0.05}PO_4$ [8]	0, 0.3, 0.5, 0.7, 1.0	MW–HT	473	358
$Y_{1-x}Yb_xPO_4$ [9]	$0 < x < 1$	Solid-state method	1473	358
YPO_4 doped with Tm^{3+} (0.1, 0.3, 0.5, 1 mol.%)/Yb^{3+} (10 mol.%) [10]	0.001, 0.003, 0.005, 0.01 (for Tm^{3+}); 0.10 (for Yb^{3+})	Co-precipitation from aqueous solution followed by annealing	333, 1073	275 (for Tm^{3+}); 358 (for Yb^{3+})
$Sc_xY_{1-x}PO_4$:0.5 мол.% Eu^{3+} [11]	0, 0.2, 0.4, 0.5, 0.6, 0.8, or 1.0	Sol–gel method + annealing	1373	1450
$Y_{1-x}Dy_xPO_4$ [12]	0.005–0.1	Flux growth technique	1673–1073	155
$Y_{1-x}PO_4$:xYb^{3+} [13]	0–0.1	Low-temperature hydrothermal method	473	358

Notes: *1. References [2, 6] provide synthesis and subsequent annealing temperatures of nanomaterials aimed at eliminating defects that, according to Refs. [29–31], are typically present in nanomaterials obtained at low temperatures. 2. References [3, 11] list only the annealing temperatures after synthesis by the sol–gel method. 3. References [4, 12, 13] do not specify substitution limits; it is possible that fragments of continuous series of solid solutions were synthesized.

sis was carried out within the thermodynamic-stability regions of solid solutions predicted by us.

At the same time, the synthesis of zircon-type solid-solution samples in the $Y_{1-x}Sc_xPO_4$:0.5 mol.% Eu^{3+} [3] and $Sc_xY_{1-x}PO_4$:0.5 mol.% Eu^{3+} [11] systems have been described, carried out by annealing mixtures of the components at 1233 and 1373 K, respectively. Under these conditions, according to XRD data, continuous solid-solution series were formed, as reported in those studies. However, in the luminescence spectra, which, according to the authors of Ref. [3], are more sensitive than XRD, additional bands were observed, indicating the multiphase nature of the synthesized samples. This agreed with our previously calculated [18] critical decomposition temperature for these solid solutions (1450 K), according to which, at 1233 and 1373 K, a continuous solid-solution series should not form (Fig. 4). Therefore, considering the critical decomposition temperature reported by us in Ref. [18], the authors of Refs. [3, 5] annealed $Y_{1-x}Sc_xPO_4$:0.5 mol.% Eu^{3+} samples at 1723 K, obtaining a continuous solid-solution series (Table 3, Fig. 4).

It should be noted that the orthophosphates $Y_{1-x}Lu_xPO_4 \cdot nH_2O$ ($x = 0.0$, 0.25, 0.50, 0.75, and 1.00) obtained in Ref. [2] at 293–383 K were nanosized (particle size of 5–10 nm); after calcination at 773 K, the particle size increased to 10–20 nm, and after calcination at 1373 K, it further increased to 40–80 nm.

The $Y_{1-x}Dy_xPO_4$ samples synthesized in Ref. [4] exhibited a high degree of crystallinity, with average particle sizes determined by transmission electron microscopy of 40 ± 15 nm for $x = 0.01$, 65 ± 22 nm for $x = 0.475$, and 125 ± 45 nm for $x = 1$.

The $GdPO_4$ powders obtained in Ref. [6] consisted of nanowires with lengths of 600 nm–3 μm and diameters of 20–70 nm; for $Gd_{0.75}Y_{0.25}PO_4$, the nanorods of 100–600 nm in length and 40–80 nm in diameter were observed, whereas, for $Gd_{0.5}Y_{0.5}PO_4$, the nanorods were of 100–400 nm in length and 50–100 nm in diameter. In contrast, YPO_4 powders displayed a rice-grain-like morphology, with particle sizes of 60–100 nm. Analysis of the data in Ref. [6] clearly shows that the amount of Y substituting for Gd in the $GdPO_4$ matrix affects the length-to-diameter ratio of the nanorods' morphology.

The particle sizes of $Y_{0.95(1-x)}Yb_{0.95x}Er_{0.05}PO_4$ ($x = 0$, 0.3, 0.5, 0.7, and 1) obtained in Ref. [8], as estimated from transmission electron microscopy images, ranged from 20 to 45 nm.

The average particle size of YPO_4 doped with Tm^{3+} (0.3 mol.%) and Yb^{3+} (10 mol.%) was approximately of 140 nm [10]. At the same time, the average crystallite sizes of YPO_4 doped with Tm^{3+} (0.1, 0.3, 0.5, and 1 mol.%) at a fixed Yb^{3+} concentration (10 mol.%) were 23, 22, 21, and 22 nm, respectively [10].

According to TEM data, $Y_{1-x}Yb_xPO_4$ particles ($x = 0$–0.1) exhibited a leaf-like nanomorphology with particle sizes of about 80 nm in

length and of about 16 nm in width [13].

Thus, comparison of the calculated critical decomposition temperatures with the synthesis data (Table 3) shows that the compositions obtained by sol–gel, hydrothermal, or microwave methods at 293–473 K [2, 4, 6, 8, 10, 13] are formed under conditions in which surface effects of nanoscale particles may significantly influence thermodynamic stability. At the same time, the calculated T_{cr} values for these systems are lower than the synthesis temperatures that confirms the applicability of the crystal-energy theory of isomorphous miscibility for predicting the conditions of nanoparticle formation. Therefore, the proposed computational approach optimizes the synthesis conditions, including those of nanocrystalline forms obtained at relatively low temperatures.

4. CONCLUSIONS

1. It has been shown that in the $Y_{1-x}Ln_xPO_4$ systems, the Q_ε contributions to the mixing energies Q_{mix} increase with the atomic number of the rare-earth element (REE) in the series of systems involving orthophosphates from Gd to Yb and, in most cases, determine the total values of the mixing energies (in 6 out of 8 systems, except for those involving Gd and Tb orthophosphates).
2. It has been established that the Q_R contributions to the mixing energy decrease in the Gd–Er series from 4.250 to 0.001 kJ/mole, and then increase to 1.148 kJ/mole in the Er–Lu series. Such variations in Q_ε and Q_R lead to nearly identical values for the total mixing energies and the critical decomposition temperatures of solid solutions in systems involving Tb, Dy, Ho, and Er orthophosphates.
3. A thermodynamic stability diagram for the $Y_{1-x}Ln_xPO_4$ (Ln = Gd–Lu) systems and decomposition domes for the $Y_{1-x}Ln_xPO_4$ (Ln = Gd–Lu, and Sc) systems are presented, enabling graphical prediction of solid-solution decomposition temperatures for given substitution limits, equilibrium substitution limits for a given temperature, and thermodynamic stability regions.
4. It has been established that most $Y_{1-x}Ln_xPO_4$ systems have critical decomposition temperatures either much lower than room temperature (systems $Y_{1-x}Tb_xPO_4$, $Y_{1-x}Dy_xPO_4$, $Y_{1-x}Ho_xPO_4$, $Y_{1-x}Er_xPO_4$, and $Y_{1-x}Lu_xPO_4$) or, within the calculation error, close to room temperature ($Y_{1-x}Gd_xPO_4$, $Y_{1-x}Tm_xPO_4$, and $Y_{1-x}Yb_xPO_4$). Therefore, they may be promising to produce nanomaterials, as the latter are synthesized at comparatively low temperatures.
5. Due to the extensive temperature range of thermodynamic stability (of about 2000 K), materials based on yttrium orthophosphate solid solutions $Y_{1-x}Ln_xPO_4$ may surpass materials based on solid

solutions of other REE orthophosphates in terms of stability of properties and reproducibility.

6. It has been shown that the calculation results do not contradict the experimental literature data in the sense that the synthesis of solid solutions in the $Y_{1-x}Ln_xPO_4$ systems in [2–6, 8–10, 12, 13] was carried out within the thermodynamic stability regions predicted by us. In addition, our calculated critical decomposition temperature for $Y_{1-x}Sc_xPO_4$, as well as the previously reported value for $Sc_{1-x}Y_xPO_4$ [18], agree with the results of Refs. [3, 5] concerning the choice of synthesis conditions for $Y_{1-x}Sc_xPO_4$.
7. Since the critical decomposition temperatures, substitution limits, and regions of thermodynamic stability of solid solutions are derived from the mixing energy Q_{mix}, which in the systems considered is governed primarily by differences in the interatomic distances of the components, and given that these distances have been shown in Ref. [20] to be independent of nanoparticle size in the range of 6-to-40–80 nm, the quantitative theory of isomorphous miscibility can be confidently applied for predicting isomorphous substitutions in particles larger than 6 nm.

ACKNOWLEDGMENTS

This research was carried out with the support of the Ministry of Education and Science of Ukraine within the framework of the priority areas of scientific development of the accredited research direction ‘Natural and Mathematical Sciences’ at Vasyl’ Stus Donetsk National University.

REFERENCES

1. V. S. Levushkina, D. A. Spassky, E. M. Aleksanyan, M. G. Brik, M. S. Tretyakova, B. I. Zadneprovski, and A. N. Belsky, *J. Lumin.*, **171**: 33 (2016); https://doi.org/10.1016/j.jlumin.2015.10.074
2. A. V. Osipov, L. P. Mezentseva, I. A. Drozdova, S. K. Kuchaeva, V. L. Ugolkov, and V. V. Gusarov, *Glass Phys. Chem.*, **33**, No. 2: 169 (2007); https://doi.org/10.1134/S1087659607020125
3. V. S. Voznyak-Levushkina, A. A. Arapova, D. A. Spassky, I. V. Nikiforov, and B. I. Zadneprovski, *Phys. Solid State*, **64**, No. 11: 567 (2022); https://doi.org/10.1134/S1063783422110130
4. Yu. V. Orlovskii, A. S. Vanetsev, I. D. Romanishkin, A. V. Ryabova, K. K. Pukhov, A. E. Baranchikov, E. V. Samsonova, K. Keevend, I. Sildos, and V. B. Loschenov, *Opt. Mater. Express*, **5**, No. 5: 1230 (2015); https://doi.org/10.1364/OME.5.001230
5. D. Spassky, A. Vasil’ev, V. Nagirnyi, I. Kudryavtseva, D. Deyneko, I. Nikiforov, I. Kondratyev, and B. Zadneprovski, *Materials*, **15**, No. 19: 6844 (2022); https://doi.org/10.3390/ma15196844

6. A. G. Hernández, D. Boyer, A. Potdevin, G. Chadeyron, A. G. Murillo, F. de J. C. Romo, and R. Mahiou, *Opt. Mater.*, **73**: 350 (2017); https://doi.org/10.1016/j.optmat.2017.08.034
7. R. D. Shannon, *Acta Crystallogr. Sect. A*, **A32**, No. 5: 751 (1976); https://doi.org/10.1107/S0567739476001551
8. S. A. Khrushchalina, P. A. Ryabochkina, V. M. Kyashkin, A. S. Vanetsev, O. M. Gaitko, and N. Yu. Tabachkova, *JETP Lett.*, **103**, No. 5: 302 (2016); https://doi.org/10.1134/S0021364016050064
9. O. Ya. Manashirov, A. N. Georgobiani, V. B. Gutan, E. M. Zvereva, and A. N. Lobanov, *Inorg. Mater.*, **47**, No. 12: 1384 (2011); https://doi.org/10.1134/S0020168511110124
10. H. Thakur, A. K. Gathania, S. Kachhap, S. K. Singh, and R. K. Singh, *J. Lumin.*, **254**, Pt. A: 119513 (2023); https://doi.org/10.1016/j.jlumin.2022.119513
11. D. Spassky, V. Voznyak-Levushkina, A. Arapova, B. Zadneprovski, K. Chernenko, and V. Nagirnyi, *Symmetry*, **12**, No. 6: 946 (2020); https://doi.org/10.3390/sym12060946
12. R. Faoro, F. Moglia, M. Tonelli, and E. Cavalli, *Physics Proc.*, **2**, No. 2: 345 (2009); https://doi.org/10.1016/j.phpro.2009.07.018
13. G. Wang, L. Gao, H. Zhu, and W. Zhou, *Front. Mater. Sci.*, **10**, No. 2: 197 (2016); https://doi.org/10.1007/s11706-016-0340-1
14. V. S. Urusov, *Teoriya Izomorfnoi Smesimosti* [The Theory of Isomorphous Miscibility] (Moskva: Nauka: 1977) (in Russian).
15. V. S. Urusov, *Fortschr. Mineral.*, **52**: 141 (1975).
16. V. S. Urusov, *Bulletin de la Société Française de Minéralogie et de Cristallographie*, **97**: 217 (1974); https://www.persee.fr/doc/bulmi_0037-9328_1974_act_97_2_6883
17. V. S. Levushkina, *Lyuminestsentnyye i Strukturnyye Svoistva Smeshannykh Kristallofosforov na Osnove Slozhnykh Oksidov* [Luminescent and Structural Properties of Mixed Crystal Phosphors Based on Complex Oxides] (Disser. for Degree Cand. Phys.-Math. Sci.) (Moskva: MSU: 2016) (in Russian); https://istina.ipmnet.ru/download/28937563/1uiTpO:H-EY-8zVYEzmDTCZfEKgNk8tBXdEO5Evd9jhyf8iFhs/
18. E. I. Get'man, S. V. Radio, and L. I. Ardanova, *Inorg. Mater.*, **54**, No. 6: 596 (2018); https://doi.org/10.1134/S0020168518060031
19. C. P. Poole Jr. and F. J. Owens, *Introduction to Nanotechnology* (John Wiley&Sons: 2003).
20. A. I. Grabchenko, L. I. Pupanj, L. L. Tovazhnyansky, *Vvedenie v Nanotekhnologii: Tekst Lektsiy* [Introduction to Nanotechnology: Lecture Notes] (Kharkiv: National Technical University «KhPI»: 2012) (in Russian).
21. R. Becker, *Z. Metallkunde*, **29**: 245 (1937) (in German).
22. D. H. Templeton, *J. Chem. Phys.*, **21**, No. 11: 2097 (1953); https://doi.org/10.1063/1.1698788
23. E. I. Get'man, *Izomorfnyye Zameshcheniya v Vol'framatnykh i Molibdatnykh Sistemakh* [Isomorphic Substitutions in Tungstate and Molybdate Systems] (Novosibirsk: Nauka: 1985) (in Russian).
24. K. Li and D. Xue, *J. Phys. Chem. A*, **110**, No. 39: 11332 (2006); https://doi.org/10.1021/jp062886k
25. S. S. Batsanov, *Strukturnaya Khimiya. Fakty i Zavisimosti* [Structural Chemistry. Facts and Dependences] (Moskva: Dialog-MGU: 2000) (in Russian).

26. E. I. Get'man and S. V. Radio, *Inorg. Mater.*, **53**, No. 7: 718 (2017). https://doi.org/10.1134/S0020168517070044
27. E. I. Get'man, S. V. Radio, L. B. Ignatova, and L. I. Ardanova, *Russ. J. Inorg. Chem.*, **64**, No. 1: 118 (2019); https://doi.org/10.1134/S0036023619010091
28. L. A. Boatner, *Rev. Mineral. Geochem.*, **48**, No. 1: 87 (2002); https://doi.org/10.2138/rmg.2002.48.4
29. R. Calderyn-Villajos, C. Zaldo, and C. Cascales, *Physics Proc.*, **8**: 109 (2010); https://doi.org/10.1016/j.phpro.2010.10.020
30. K. Lenczewska, M. Ptak, V. Boiko, K. Ledwa, and D. Hreniak, *J. Alloys Compd.*, **860**: 158393 (2021); https://doi.org/10.1016/j.jallcom.2020.158393
31. O. Savchuk, J. J. C. Marti, C. Cascales, P. Haro-Gonzalez, F. Sanz-Rodríguez, M. Aguilo, and F. Diaz, *Nanomaterials*, **10**, No. 5: 993 (2020); https://doi.org/10.3390/nano10050993

Наносистеми, наноматеріали, нанотехнології
Nanosistemi, Nanomateriali, Nanotehnologii
2026, т. 24, № 1, сс. 141–163
https://doi.org/10.15407/nnn.24.01.0141

PACS numbers: 61.05.cp, 68.37.Hk, 68.43.Mn, 68.43.Pq, 68.47.Pe, 81.05.uj, 83.80.Mc

Study of Meloxicam Adsorption on Prepared Activated Nanocarbon from Pinecones: Thermodynamics and Kinetics

Lubna A. Al-Siqillee and Noha Mohammad Yahya

College of Education for Girls,
Department of Chemistry,
University of Mosul,
Mosul, Iraq

This research involves the preparation of activated nanocarbon using pinecones obtained from the forestry of the city of Mosul, Iraq. The prepared carbon is observed as nanoparticles with a particle size of 16.08 nm measured by a scanning electron microscope and a BET-theory surface area of 1.9719 nm^2. The iodine number of 1147 mg/g^{-1} and x-ray diffraction spectrum of the prepared activated carbon are also evaluated. The adsorption of meloxicam onto prepared activated carbon is studied in aqueous solutions. Freundlich and Langmuir isotherms are applied; the Freundlich model is more relevant to the practical data for the studied system due to the significant results of high $R^2 = 0.9968$ values compared to Langmuir's $R^2 = 0.9915$. The study of adsorption thermodynamically at equilibrium has shown that the adsorption process is spontaneous, as indicated by the negative value of Gibbs free energy (ΔG^0) and the low value of the entropy after the adsorption process (negative ΔS^0). Moreover, the type of adsorption refers to physical absorption ($\Delta H = -33.090$ kJ/mole) due to the force controlling the bond between the drug and the surface of carbon, which indicates adsorption as a heat-releasing process. Pseudo-first-order, pseudo-second-order, and intraparticle molecular diffusion are studied. The kinetic results show that the adsorption process at equilibrium follows the equation of a pseudo-second-order reaction, while interaction and molecular diffusion are not the only mechanisms dominating the adsorption process.

Це дослідження включало приготування активованого нановуглецю з використанням соснових шишок, отриманих з лісництва міста Мосул, Ірак. Підготовлене вугілля спостерігалося у вигляді наночастинок з розміром частинок у 16,08 нм, виміряним за допомогою сканувального електронного мікроскопа, та площею поверхні за Брунером, Емметом і Теллером (БЕТ-теорією) у 1,9719 $нм^2$. Також були оцінені йодне число 1147 $мг/г^{-1}$ та спектер рентґенівської дифракції підготовленого активованого вугілля. Адсорбцію мелоксикаму на підготовленому активова-

ному вугіллі вивчали у водних розчинах. Були застосовані ізотерми за Фрейндліхом і Ленґмюром; Фрейндліхів модель був більш релевантним для практичних даних стосовно досліджуваної системи завдяки значним результатам із високими значеннями $R^2 = 0{,}9968$ порівняно з $R^2 = 0{,}9915$ за Ленґмюром. Термодинамічне дослідження адсорбції в рівновазі показало, що процес адсорбції є спонтанним, на що вказує неґативне значення Ґіббсової вільної енергії (ΔG^0) та низьке значення ентропії після процесу адсорбції (неґативне ΔS^0). Більше того, тип адсорбції відноситься до фізичної абсорбції ($\Delta H = -33{,}090$ кДж/моль) через силу, яка контролює зв'язок між препаратом і поверхнею вуглецю, що вказує на те, що адсорбція є процесом виділення тепла. Була досліджена псевдопершого порядку, псевдодругого порядку та внутрішньочастинкова молекулярна дифузія. Кінетичні результати показують, що процес адсорбції в рівновазі відповідає рівнянню реакції псевдодругого порядку, хоча взаємодія та молекулярна дифузія є не єдиними механізмами, що домінують у процесі адсорбції.

Key words: pinecone, nanocarbon, surface area, Freundlich and Langmuir isotherms, adsorption, meloxicam, activated carbon.

Ключові слова: соснова шишка, нановуглець, площа поверхні, Фрейндліхові та Ленґмюрові ізотерми, адсорбція, мелоксикам, активоване вугілля.

(Received 25 July, 2024; in revised form, 5 September, 2024)

1. INTRODUCTION

The major problems of environmental pollution are one of the biggest facing the modern world and the most widespread due to industrial progress, which has caused an increase in the world's population. Industry is considered one of the biggest pollutants in the environment. Chemicals, or their biological decomposition products, are among the pollutants that affect the water ecosystem because they contain harmful chemical groups. Recently, pharmaceutical products have increased in their application, depending on their widespread use. As a result, large amounts of pharmaceutical products are discharged as waste materials, which cause the main environmental pollutants in liquids to be wasted due to their toxicity [1].

It is also considered an antibiotic-resistant pathogen. The classification of non-steroidal anti-inflammatory drugs (NSAIDs) represents one of the most important groups of pollutants due to their widespread use, as these medicines treat diseases that affect humans and animals in terms of their analgesic effect [2], anti-inflammatory effect, and antipyretic effect. In addition, NSAIDs belong to the OTC group of medications; without a prescription, they are the most common drugs observed in aqueous wastewater

because of their characteristics in terms of their hydrophobicity and stability [3].

NSAIDs can remain in the aqueous phases and can also exist at a surface concentration of up to 1 μg/L of water molecules [4]. The most common wastewater contamination is from homes, hospitals, clinics, or production plants. Medicine has prolonged exposure and caused bioaccumulation, which leads to chronic effects of toxicity that may include growth patterns, metabolism, and reproductive problems. The removal of NSAIDs has been applied in several ways, such as photocatalytic degradation [5, 6], microextraction [7], oxidation [8], biodegradation [9], chlorination [10], biofiltration [11], electrochemical oxidation [12] and an adsorption using activated carbon from different sources.

Meloxicam (MLX) is a member of NSAIDs has been observed in waste water in despite of its poor water solubility, its more soluble in alkaline solution at pH of 10.7 up to 19.9 mg/mL in recent study three type of activated carbon were synthesized and applied as sorbent for MLX removed sorbent for MLX removed from aqueous solution [1].

The aim of this study is to synthesized activated carbon from pinecone to be used for the removal of MLX from aqueous solution. This study includes the determination of adsorption efficiency and capacity of MLX in terms of isotherms, kinetics and thermodynamics at equilibrium.

Freundlich Isotherm. The Freundlich equation is one of the well-known isotherm models that can be successfully applied to single-component systems. This model assumes that the surface of the adsorbent is not homogeneous due to the irregularity of the potential energy on it as a result of the adsorption sites having varying levels of energy, the strength of the linear relationship can be expressed through the value of the correlation coefficient R^2, as this value is used to evaluate the extent, to which experimental data for adsorption can be represented by this isotherm. The linear model can be expressed as follows:

$$\log q_e = \log K_f + n^{-1} \log C_e, \tag{1}$$

where K_f and n represent Freundlich isotherm constants, the value of q_e represents the amount of adsorbed material per gram of adsorbent, which is known as the adsorption capacity (at equilibrium) (mg/g), while C_e represents the concentration of the remaining material, which is the non-adsorbed at equilibrium (mg/L). When drawing the relationship between $\log q_e$ *versus* $\log C_e$, it gives a straight line with a slope equal to $1/n$, which represents a measure of the intensity of adsorption, and a cross section equal to $\log K_f$,

which is a function of the adsorption capacity, whereas the value of n indicates the best value for obtaining the adsorbent feature and the degree of non-openness to the adsorbent feature layer, where, when it is only limited between 1–10, this means that adsorption is good and preferred; however, when the value of n is less than one, this adsorption is preferred and not preferable. When $n = 1$, this adsorption is linear, whereas when $n < 1$, the adsorption is chemical, and when $n > 1$, there is physical adsorption [13].

Langmuir Isotherm. This model assumes that molecules adsorb on a specific number of openings (pores) located on a specific weight of the adsorbent surface, which are energetically equivalent and each hole can hold only one adsorbed molecule, the molecules adsorbed on the adsorbent surface do not interfere with each other or with other attacking molecules present in the solutions. Therefore, a single layer of adsorbed molecules is formed on the adsorbent surface. According to this model, the adsorption phenomenon is rapid in the beginning and then reaches a state of equilibrium after the relative rate of speed equals due to the attachment of molecules on the surface of the adsorbent and the rate of their return to the solution [14]. According to this model, the amount of adsorbed material is proportional to the part exposed to the adsorption phenomenon, while the amount of returning particles is proportional to the covered part of the surface, this model can be expressed as follows:

$$C_e/q_e = 1/Q_{\max} + C_e/(bQ_{\max}), \tag{2}$$

where b is the Langmuir isotherm constant and indicates the strength of the drugs' attachment to the surface of the adsorbent material, while the value of $Q_{\max}$ represents the maximum theoretical capacity for adsorption of the adsorbent material (milligrams of adsorbent per gram of adsorbent material), while the values of C_e and q_e are the remaining concentration and adsorption capacity at equilibrium, respectively [15].

Kinetic Study. In order to obtain accurate information that explains the mechanism of adsorption and the kinetic forces affecting it, kinetic models were studied on the studied drug as follows.

The first description of the kinetic data for adsorption was by Lagergren, and that was through the pseudo-first-order equation, which is considered the first equation used to describe the speed rate of adsorption, based on its capacity, and then it was used by many researchers [16, 17]. The pseudo-first-order equation can be expressed as follows:

$$\ln(q_e - q_t) = \ln q_e - k_1 t. \tag{3}$$

In order for this model to apply to practical data for adsorption,

by plotting the relationship between $\ln(q_e - q_t)$ *versus* time t, it must give a linear relationship and a match must be obtained between the calculated and practical adsorption capacity value.

This model is also used to describe the kinetics of adsorption, as this model explains how the rate of speed depends on the adsorption capacity of the solid adsorbent and not on the concentration of the adsorbent. Unlike the other kinetic models, it predicts the behaviour of adsorption along the time period of adsorption, this is consistent with an adsorption mechanism that includes a step that determines the rate of speed, which may include countervailing forces through the sharing or exchange of electrons between the solution and the adsorbent, where the pseudo-second-order equation can be expressed as follows:

$$t/q_t = 1/\{k_2(q_e)^2\} + (1/q_e)t. \quad (4)$$

In order for this model to apply to practical adsorption data, by plotting the relationship between t/q_t *versus* time t, it must give a linear relationship, and a match must be obtained between the calculated and practical adsorption capacity value [16, 17]. It is also possible to use the adsorption rate constant k_2 to find the value of the initial pseudo-second-order adsorption speed (h) through Eq. (5):

$$h = k_2(q_{\text{ecal.}})^2. \quad (5)$$

The overall rate of adsorption will be determined by the slowest step, which may be diffusion from the outer boundaries of the liquid to the adsorbent surface, or the implicit molecular diffusion within the pores of the adsorbent material. The rate of adsorption speed on the active sites is assumed to be fast, and one of the important things that must be found and determined is the potential rate of speed specific to the adsorption mechanism. If the implicit molecular diffusion is the controlling factor, depending on the reaction rate, the process of removing adsorbed materials changes with the square root of time. As a result, it is possible to calculate the rate of adsorption speed by calculating the adsorption capacity of the adsorbent as a function of the square root of time, as the implicit molecular diffusion model can be represented by Eq. (6) [18]:

$$q_t = K_{diff}t^{1/2} + C; \quad (6)$$

K_{diff} ($\text{mg}\cdot\text{g}^{-1}\cdot\text{min}^{-1/2}$) represents the velocity rate constant for implicit molecular diffusion, while C ($\text{mg}\cdot\text{g}^{-1}$) is the value of the cross-section, and the value of K_{diff} can be found from the slope of the straight line.

2. EXPERIMENTAL METHOD

2.1. Instruments

Ultraviolet–Visible Spectrophotometer, double beam type (model 1800-UV) supplied by Shimadzu company, Japan. pH meter (Jenway 3510 model) was used for pH measurement. Scanning electron microscopy (SEM) was used to study the morphology. Oven and muffle furnace were used for drying and carbonization purposes, respectively. Water bath shaker of Type ST402 from Jwrio Tech. of Korean origin centrifuge used to isolate samples; the Hermle (LDZ4-2MEDICAL Low SPEED CENTERFUGE) type is of German origin and equipped by HERME LABORTECHNIK, SEM scanning device of MIRA3LMU model. The measurements were conducted at the University of Tabriz in Iran.

2.2. Chemical Materials

All chemical used, including hydrochloric acid (0.1M), potassium carbonate and distilled water supplied by BDH-Fluke company, thiosulphate, starch, iodine, meloxicam (MLX) 4-hydroxy-2-methyl-N-(5-methyl2-thiazolyl)-2H-1.2-benzothiazine-3-carboxamide-1,1-dioxide (Fig. 1) were supplied from Sammara drug company, Iraq. All solvents and reactants were at analytical grade.

Synthesized activated carbon (SAC), a new type of charcoal, was prepared using pine cone by cutting them, washing several times, drying under atmosphere air, and then, drying using oven at a temperature of 105–110°C for 48 hours, then, carry out the initial carbonization process by heating the powder at temperature of 450°C for 1:15 hour, then, the charcoal is cooled at room temperature, and for the purpose of performing the final carbonization, it is heated the charcoal powder using muffle furnace after mixing it with (K_2CO_3) in ratio of (1:1) by weight of (K_2CO_3:charcoal) to a degree of temperature of 750°C for one hour. Then, the mixture was cooled and washed with distilled water several times until the pH of

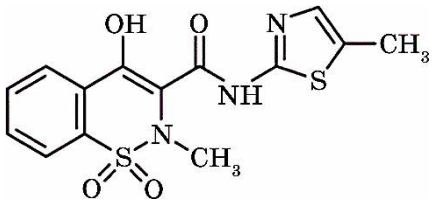

Fig. 1. Structural formula of meloxicam.

the washing water was equal to 7. Then, it was treated with a solution of 5% hydrochloric acid and heated for two hours. Then, it is cooled to laboratory temperature and washed until the acidity of the wash water reaches = 7. The prepared activated charcoal was dried well, then, mechanically crushed, and molecular sieves were used to isolate it and preserved in sealed containers for subsequent study.

2.3. Adsorption

Many factors may be affected on the adsorption efficiency and adsorption capacity like the amount of activated carbon, initial concentration of MLX, contact time, temperature and pH were studied to investigate the optimum condition of these parameters.
Determination of the Iodine Number of SAC. The adsorption of iodine was reported in a simplest test for determination of surface area of a synthesized activated carbon (SAC), which correlated to the volume of pores. Iodine number was considered as the amount of iodine solution per 0.25 mg of activated carbon placed in 250 mL of conical flask, then, added 5 mL of cone HCl and boiling for 30 sec. After cooled, the sowing 25 mL of iodine solution (0.1 N) were added and shaken for 10 min. The suppurated was filtrated; 5 mL of filtrate was calibrated with sodium thiosulphate (0.1 N) using addition of two drops of starch. Iodine number (1. N) was calculated as

$$IN = \frac{5\left(10C_1 - 1.2C_2V_2\right)126.93D}{m}, \tag{7}$$

where C_1 [mole·L^{-1}] refers to the concentration of standard iodine solution; C_2 [mole·L^{-1}] represents the concentration; V_2 [mL] volume of burette; m [gm] weight of coal; D is the correction factor.

2.4. Determination of the Amount of Adsorbent

Both the adsorption efficiency and capacity are used to express the amount of the adsorbed substance, by estimating the remaining amount of the substance in the solution. Since the drug that was studied is not coloured, the spectroscopic method in the (UV) region, which falls in the lower range 362 nm, was calculated. The amount of adsorbed material is determined by the difference between the initial concentration and the remaining concentration in the solution. The calibration curve was adopted to find these concentrations. The adsorbed material, adsorption efficiency, and adsorption capacity were found using Eq. (8), (9):

$$A = \varepsilon bCl, \tag{8}$$

$$q_e = (C_i - C_e)V_L/m\,, \tag{9}$$

$$\text{Adsorption [\%]} = \{(C_i - C_e)/C_i\} \cdot 100\,, \tag{10}$$

where A represents the absorption, ε is the absorption coefficient, b is length of the light path for visible rays, C is the concentration, l represents the cell width ($l = 1$ cm), C_i represents the initial concentration, C_e represents the remaining concentration, $(C_e - C_i)$ represents the adsorbed concentration, which is symbolized by C_{ads}, while q_e represents the adsorption capacity, as for V_l is the volume of the drug solution in [litres], and m is the weight of the adsorbed material [g]. All concentrations are in [mg/L].

2.5. The Use of the Batch Method

All studies have been completed on the influence of factors on the adsorption process and its kinetic studies, which include applying the study in a one-shot method by changing some variables and fixing others, as follows.

Solutions of different concentrations of the drug were prepared in tightly sealed conical glass flasks under the same conditions. Then, quantities of adsorbent material prepared activated carbon were added to it, and it was shaken continuously at specific times and at a rate of shaking (100 revolutions/minute) using a water bath shaker after with temperature controller [19].

3. RESULTS AND DISCUSSION

3.1. Adsorbent Material

The surface of the material was characterized using an experimental study with Debye–Scherrer Eq. (11) [20]:

$$D = k\lambda/(\beta\cos\theta), \tag{11}$$

where D—the size of minutes in aggregate unit, k—Debye's constant equal to 0.94, λ—the total wavelength of 1.5406 Å copper, β—the total width at the maximum opening of the apex. The full width at half-maximum $FWHM$ is measured in the degree unit [deg.] and converted to the unit [rad]), as the $FWHM$ value is set by π/180, and θ is the diffraction angle in [deg.] (Fig. 2).

The x-ray spectrum notes the presence of several bands, each band indicating a specific phase. The bands located at the location ($2\theta = 23°$) and ($2\theta = 43°$) belong to the (100) and (002) phases, respectively, which confirm the natural porous structure of activated

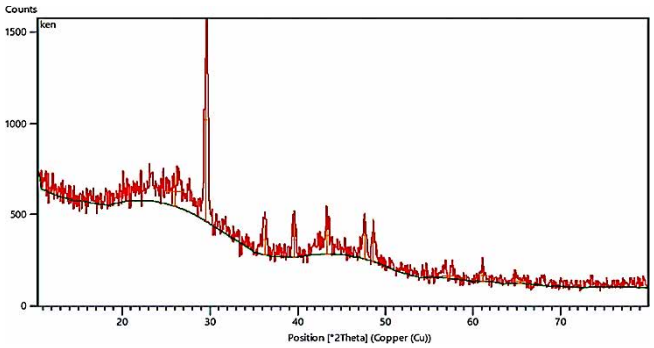

Fig. 2. X-ray diffraction (XRD) spectrum of prepared activated charcoal.

carbon. In addition, the presence of this broad band in the spectrum of activated carbon indicates that the carbon has a high surface area, and these results were consistent with the values of the surface area and the microscopic image of the scanning electron device, which showed that activated carbon possesses structural porosity [21].

From the high-field scanning electron microscope images shown at different magnification powers, the carbon surface has porous as it contained a large number of pores in different shapes and sizes. It was also noted that there were white crystals on the surface of the activated carbon, which play an essential role in the process of removing pollutants from the liquid phase, as shown in Fig. 3.

3.2. Determine the Maximum Wavelength and Calibration Curve

The maximum wavelength λ_{max} was determined at the highest absorption of the solution prepared from the drug under study, by recording the absorption spectrum of the drug solution with an appropriate concentration, through which the highest wavelength of the drug solution was determined. Different concentrations of drug solution were prepared from stock solution 1000 ppm, then, the absorption of the solution at those concentrations was detected to plot the relationship between the absorption with the corresponding concentrations by applying the Beer–Lambert law. It was found that the λ_{max} value of MLX is of 362 nm, as shown in Fig. 4.

3.3. The Effect of Adsorbent Weight

This study was conducted for a series of solutions of 25 mL with concentrations of the drug meloxicam at 35 ppm with different

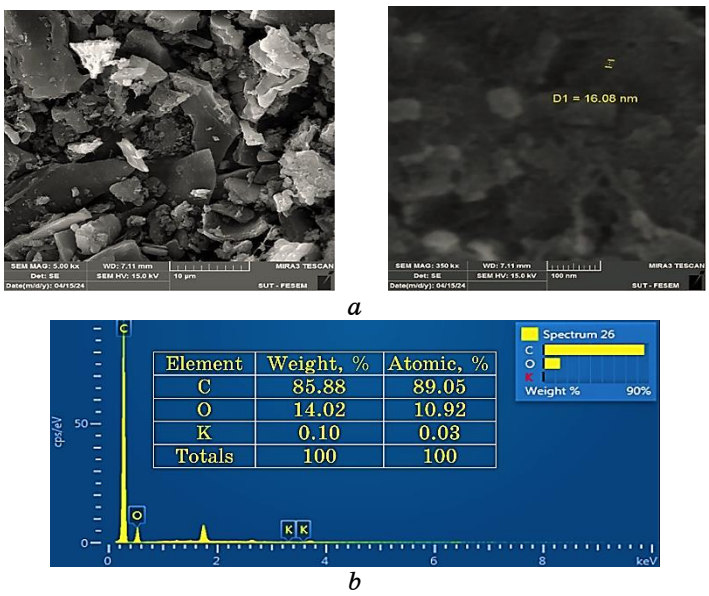

Fig. 3. *a*—SEM; *b*—XRD shapes of the surface of prepared carbon (SAC).

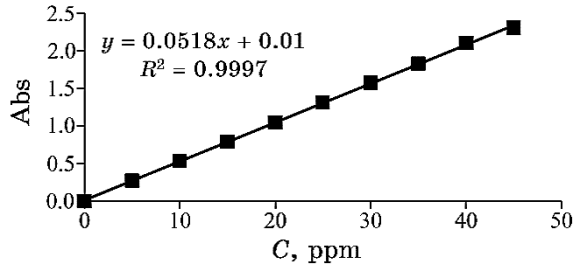

Fig. 4. Calibration curve for the MLX.

weights of activated charcoal prepared to obtain the required removal ranging from 0.01 g to 0.12 g. After shaking these solutions for a period of 60 minutes, the solutions were separated and the absorption was measured and calculated. The concentrations of the remaining materials were then estimated, and the adsorption capacity and percentage of adsorption were estimated based on Eq. (1) and Eq. (2), respectively. Studying the effect of the amount of adsorbent material is considered very important because it has a significant impact on the adsorption process, and those weights mentioned were adopted in our current study [22], as in the following Table 1.

The adsorption capacity decreases with an increase in the weight of the adsorbent, accompanied by an increase in the percentage of

TABLE 1. Effect of the amount of adsorbent in the efficiency and capacity of adsorption for 60 min. at 25°C; shaking speed of 100 rpm; a concentration of 35 ppm of 25 mL of MLX drug solution.

Type of adsorbent	C_i, mg/L	Quantity of adsorbent, g	C_e, mg/L	%	q_e, mg/L
SAC	35	0.01	21.467	38.665	33.832
		0.02	20.405	41.699	18.243
		0.04	13.320	61.941	13.549
		0.06	9.131	73.910	10.778
		0.08	6.833	80.474	8.801
		0.1	4.305	87.699	7.673
		0.12	2.278	93.491	6.817

TABLE 2. The effect of concentration in the efficiency and capacity of adsorption for 60 min.; the amount of adsorbent is of 0.12 g at 25°C; shaking speed of 100 rpm of 25 mL of MLX solution.

Type of adsorbent	C_i, mg/L	C_e, mg/L	%	q_e, mg/g
SAC	15	0.424	97.168	3.036
	20	0.965	95.173	3.965
	25	1.312	94.749	4.934
	30	2.007	93.307	5.831
	35	2.277	93.491	6.817
	40	4.729	88.175	7.347
	45	6.196	86.229	8.083
	50	7.760	84.478	8.798
	55	9.961	81.888	9.383

adsorption. This can be explained by the fact that increasing the amount of adsorbent increases the number of empty effective adsorption sites [23], which leads to a decrease in the adsorption capacity when a specific number of drug molecules are adsorbed using fixed concentrations of meloxicam, and at the same time the percentage of adsorption increases. With the increase in the amount of adsorbent material, this is due to the easily attachment between the drug molecules and the sites eligible for adsorption on the surface of the adsorbent material.

3.4. The Effect of Initial Concentration

The results obtained with studying the effect of the initial concen-

tration are shown in Table 2.

The results in Table 2 is a sequential adsorption reduction with increasing concentration and for all adsorbed materials, because increasing concentrations at the beginning of adsorption lead to an increase in the number of available molecules over time as they compete among molecule by molecule in association to achieve distinction of sites, and the continuity remaining on the surface of the adsorbent was with a constant quantity that is likely to be used with increasing the concentration leading to the occurrence of a larger amount of adsorbent in the solutions. Thus, an increase in the remaining amount in the solutions is greater with increasing concentrations in working on an effective rate of adsorption (an effective rate of adsorption), while the safety of adsorption increases with increasing concentrations due to the increase in concentrations. In the adsorbent material, small quantities are recorded [24].

3.5. Effect of Contact Time

The effects of contact time shown in Table 3.

These results obtained in the Table 3 regarding the effect of contact time indicate that the adsorption process in the beginning, from the first minutes, is very fast, and then it begins to slow down gradually until the adsorption is reached to a state of equilibrium, since the adsorption process takes place after the equilibrium occurs, it remains approximately constant, since the adsorption process reaches the speed, at which the molecules of the adsorbent (drug) bond to the surface of the adsorbent, equal to the speed of the return of other molecules from the adsorbent surface to the solution. This is called as the state of equilibrium. It has been found

TABLE 3. Effect of contact time in the efficiency and capacity of adsorption at 25°C; the amount of charcoal prepared of 0.12 g; an initial concentration of 35 ppm for MLX solution.

Type of adsorbent	Time, min.	C_e, mg/L	%	q_t, mg/g
SAC	10	8.977	74.351	5.421
	20	8.745	75.013	5.469
	30	7.568	78.378	5.715
	40	5.927	83.066	6.056
	50	4.730	86.486	6.306
	60	2.277	93.491	6.817
	70	2.239	93.601	6.825
	80	2.239	93.601	6.825

that all materials under study have reached to equilibrium in a time ranging between 60–70 min.; this variation in the speed of adsorption occurs due to the abundance of empty active sites that are found on the surface of the adsorbent material, which qualifies it to bind to the adsorbent material at the beginning of the adsorption process, in addition to the fact that the concentration of the adsorbent material at the beginning of adsorption is high, which easily accomplishes the process of transferring the molecules of the adsorbent material (meloxicam) to the surface of the adsorbent material (SAC), and with the passage of time it will decrease at the effective eligible sites for adsorption, and with it, the competition between the drug molecules to bind to these eligible sites will increase, resulting in a decrease in the acceleration of the adsorption process until the system reaches a state of equilibrium [25].

3.6. Effect of Temperature

The effect of temperature on the adsorption of drugs adsorbed on the surface of activated charcoal was studied over a specific range of temperatures ranging from 288–338 K, as the effect of temperature is considered one of the important studies for calculating the thermodynamic functions ΔS^0, ΔH^0, and ΔG^0. This study was conducted at fixed concentrations of the drug and fixing all other variables, including the amount of adsorbent and the natural acid value of meloxicam, and using a fixed volume of the drug solution 25 mL and a constant shaking speed of 100 revolutions/minute. Table 4 shows the results obtained.

According to the results listed in Table 4, an increase in temperature leads to a decrease in the adsorption efficiency (percentage) and the adsorption capacity in all materials under study. This means that increasing the temperature will lead to an increase in the process of the return of the molecules of the adsorbed material

TABLE 4. Effect of temperature in the efficiency and capacity of adsorption using the amount of adsorbent 0.12 g; an initial concentration of 35 ppm; a time of 70 minutes.

Type of adsorbent	Temperature, K	C_e, mg/L	%	q_e, mg/g
SAC	288	1.428	95.918	6.994
	298	2.239	93.601	6.825
	308	3.861	88.968	6.487
	318	5.250	84.997	6.197
	328	7.297	79.150	5.771
	338	8.146	76.723	5.594

from the surface of the adsorbent to the solution. This is as a result of the breaking of the bonding forces between the adsorbent material and the adsorbent surface, and this indicates that the adsorption process is heat-emitting, which clearly indicates the physical nature of adsorption in the carefully studied system, and that this statement is completely consistent with the rule of Chatelier [26].

3.7. pH Effect

The results obtained of studying the effect of acid function are shown in Table 5.

The natural acid function of drugs is shown with the symbol (*), which is indicated on the number of the natural acid function for each drug shown, and from Table 5. It has been observed that the adsorption efficiency and adsorption capacity decrease clearly when moving with the acid function from the acidic medium to the neutral medium and then the basic medium. It is concluded that the process adsorption may occur in acidic and basic functions. It is known that the surface of activated carbon is dominated by a negative charge and a small amount of positive charge. In the acidic medium, the proton atoms dominate the solution, which is equivalent to the positive charge on the surface. However, in the basic medium, it is dominated by the negative charge, as these charges are equivalent to the positive charge in the drug compound, thus hindering its movement. It reduces the adsorption efficiency [27].

3.8. Calculating Thermodynamic Parameters

Thermodynamic functions are among the important variables that give a distinct interpretation when studying the adsorption process.

TABLE 5. Effect of acid function in the efficiency and capacity of adsorption at a time of 70 min.; an initial concentration of 35 ppm at 25°C; the amount of adsorbent material is of 0.12 g; a shaking speed of 100 rpm of 25 mL of MLX solution.

Type of adsorbent	pH	C_e, mg/L	C_{ads}, mg/L	%	q_e, mg/g
SAC	13	1.525	33.474	95.642	6.973
	12*	2.239	32.760	93.601	6.825
	11	3.513	31.486	89.961	6.559
	10	4.710	30.289	86.541	6.310
	9	5.463	29.536	84.390	6.153
	8	6.911	28.088	80.253	5.851

They explain the nature of the system studied, as well as the type of forces that control it and the course of the adsorption process. In addition, they can give an idea of the type of molecular interactions that can occur during the adsorption process, which have a major role in determining its competence. The heat of adsorption can be found from the Van't Hoff equation, which represents the relationship between temperature and the equilibrium constant:

$$K_c = K_0 e^{-\Delta H/RT}, \tag{12}$$

where ΔH represents the heat of adsorption, K represents the equilibrium constant for adsorption, while K_0 represents a constant value.

Taking ln for both sides, we get the following form:

$$\ln K_c = \ln K_0 \cdot \{-\Delta H/(RT)\}, \tag{13}$$

The value of ΔH can be found by drawing the relationship between ln$K$ *versus* the reciprocal of temperature $1/T$, which gives a straight line with a slope equal to $(-\Delta H/R)$, and by knowing the value of the equilibrium constant for adsorption, which can be found from the ratio between concentration of the adsorbed material remaining in the solution:

$$K_c = C_{ads}[\text{mg/L}]/C_e[\text{mg/L}]. \tag{14}$$

It is possible to find the value of ΔH and then find the other thermodynamic functions ΔS^0, ΔG^0 through the following equations:

$$\Delta G^0 = -RT\ln K_c, \tag{15}$$

$$\Delta G^0 = \Delta H - T\Delta S^0, \tag{16}$$

$$\Delta S^0 = (\Delta H - \Delta G^0)/T. \tag{17}$$

The value of ΔG^0 represents the change in the standard free energy at any stage of adsorption, while ΔG^0 represents the zero value and the free energy, when the equilibrium process is constant. Therefore, the value of ΔS^0 was found, which represents the state of the system at any stage of adsorption stages [28].

As for the figure that represents the linear relationship resulting from plotting ln$K$ *versus* $1/T$ by applying the Van't Hoff Eq. (12), it is shown in Fig. 5 and Table 6.

The values of the equilibrium constants K_c decrease with increasing temperature for a single drug, which agrees with what was previously found, as the efficiency of adsorption decreases with in-

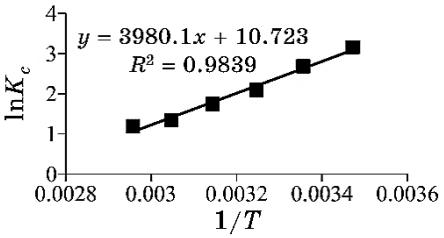

Fig. 5. The relationship between $\ln K_c$ *versus* $1/T$ to calculate the thermodynamic functions for drug adsorption.

TABLE 6. Equilibrium constants and thermodynamic functions at equilibrium.

Type of adsorbent	Temperature, K	K_c	ΔG, kJ·mole^{-1}	ΔH, kJ·mole^{-1}	ΔS, J·mole^{-1}·K^{-1}
SAC	288	23.5	–7.559	–33.090	–88.605
	298	14.629	–6.647		–88.735
	308	8.065	–5.345		–90.081
	318	5.665	–4.585		–89.638
	328	3.796	–3.637		–89.794
	338	3.296	–3.351		–87.984

creasing temperature, which indicates that the forces responsible for the adsorption process are physical forces, as the increase in temperature leads to its breakdown. Then, the adsorbed molecules return to the solution.

The value of the enthalpy change ΔH that was calculated over a range of temperatures, in which Van't Hoff assumed that the value of (ΔH) is constant over a certain range of temperatures, was all of a negative sign, which indicates that the adsorption process is heat emitting. While their values indicate the type and nature of the forces responsible for the adsorption process, they are of a physical nature, as all their obtained values are less than 40 kJ·mole^{-1}, which is within the energy range of physical bonds [25]. Most of the forces in which drugs bind to the adsorbent surface (carbon) are of the type of hydrogen bonding forces, whose energy ranges 5–15 kJ/mole.

The negative values of ΔS^0 give an indication of the state of regularity in the system studied. What is worth noting is that the strength of the interference and the preference for adsorption to occur over extortion and the fact that its values are within a certain range and are close at all temperatures, this supports that the system is of a physical nature, and that the role of entropy change

is limited. In influencing the progress of the adsorption process, these results are supported by the values of the change in free energy ΔS^0, as their values indicate a decrease in the spontaneity of adsorption with the increase in temperature.

3.9. ADSORPTION ISOTHERMS

3.9.1. Freundlich Isotherm

When applying Eq. (1) for this isotherm to the practical data for adsorption, by drawing the graphical relationship between $\log q_e$ *versus* $\log C_e$, and through it, the values of the Freundlich constants K_f, n were calculated from the slope n and the cross-section K_f of the straight line in order, as shown in Fig. 6 and Table 7.

As observed, the results listed in Table 7 showed that the Freundlich isotherm equation applied to the data for the adsorption system was fitted based on the data of correlation coefficient value $R^2 = 0.9968$, so that isotherm Freundlich is more applicable to describe the adsorption of MLX. Therefore, the adsorption followed a multilayer model as a heterogeneous surface indicated by n value of 3.203, which is between 1 and 10. Moreover, the adsorption process is higher than desorption process for the value of K_f, which has a relationship with the adsorption coupling, with energy value and a factor that depends on the nature of both the adsorbent and the adsorbent [30].

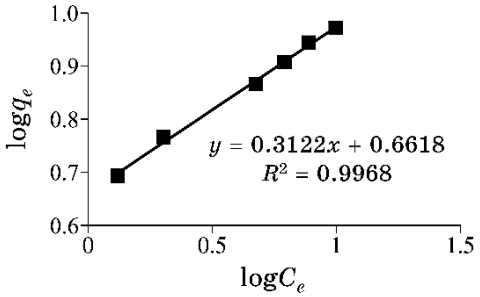

Fig. 6. Application of Freundlich isotherm to practical data for adsorption of the studied drug.

TABLE 7. Freundlich constants K_F, n and correlation coefficient R^2 obtained by applying them to practical adsorption data.

Type of adsorbent	Drug	n	K_f	R^2
SAC	meloxicam	3.203	4.589	0.9968

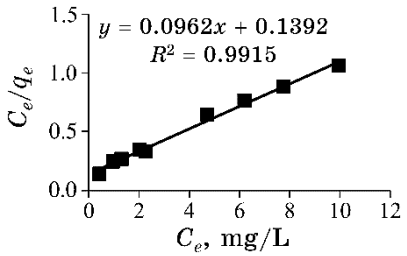

Fig. 7. Application of the Langmuir isotherm to experimental drug adsorption data.

TABLE 8. Langmuir constants b, Q_{max} and the correlation coefficient R^2 obtained by applying them to practical adsorption data.

Type of adsorbent	Drug	Q_{max}, mg/g	K_L, L/mg	R^2
SAC	meloxicam	10.395	0.691	0.9915

3.9.2. Langmuir Isotherm

This isotherm is the most common and applied to practical adsorption data. Through it, information is obtained that shows the extent of the ability of the adsorbent material to absorb molecules of the adsorbent material, which is represented by the maximum theoretical adsorption capacity Q_{max} [mg/g], which is supposed to be in the form of a single layer on the surface. The strength of its connection is also expressed by the Langmuir constant K_L [L/mg].

The practical results of the adsorption of the drugs, which were chosen to complete this study, were applied to the surface of the adsorbent materials at equilibrium using the mathematical equation of the Langmuir isotherm, Eq. (2), by drawing the graphical relationship between C_e/q_e *versus* C_e, and the Langmuir constants Q_{max} and K_L were calculated from the slope and cross-section of that straight line, as shown in Fig. 7 and Table 8.

3.10. KINETICS STUDY

3.10.1. Pseudo-First Order Equation

The pseudo-first order equation model, Eq. (3), was applied by drawing the relationship between $\ln(q_e - q_t)$ *versus* t (the time per minute) to obtain a linear relationship with the magnitude of its slope k_1 and its intercept $\ln q_e$ and through it, values of q_e and k_1 can be found. The shape and results obtained are shown in Fig. 8 and

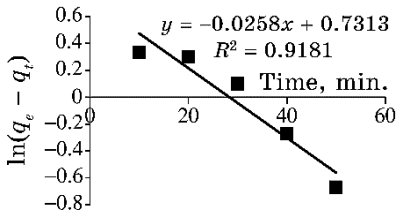

Fig. 8. Pseudo-first order model to experimental drug adsorption data.

TABLE 9. Practical and theoretical pseudo-first-order rate constants, adsorption capacity, and the correlation coefficient obtained by applying them to practical adsorption data.

Type of adsorbent	Drug	$q_{e(exp)}$, mg/g	$q_{e(calc.)}$, mg/g	K_1, min.$^{-1}$	R^2
SAC	meloxicam	6.825	2.077	0.0258	0.9181

listed in Table 9.

3.10.2. Pseudo-Second Order Equation

When applying the pseudo-second order model to practical adsorption data by plotting the relationship between t/q_t *versus* time t as Eq. (4), it is also possible to use the adsorption rate constant k_2 to find the value of the initial pseudo-second-order adsorption speed h through Eq. (5). The shape and results obtained are shown in Fig. 9 and listed in Table 10.

3.10.3. Intraparticle Diffusion Model

The intraparticle diffusion model was applied to the practical data for adsorption by applying Eq. (6) by plotting the relationship between the value of q_t *versus* the square root of time. The value of C gives evidence of the thickness of the outer layer of the solution boundaries and its effect, as a high value of C indicates this class as having a greater influence. The shape and results obtained are shown in Fig. 10 and listed in Table 11.

According to the results presented in Table 11 and from the shapes shown in Fig. 10, the implicit molecular diffusion mechanism will be the only mechanism that guides the adsorption process, only when the relationship between q_t *versus* $t^{1/2}$ is blinded by a straight line passing through the original point, and since this does not happen, it is inferred that the process of implicit molecular diffusion plays an important role in the process of removing the drug

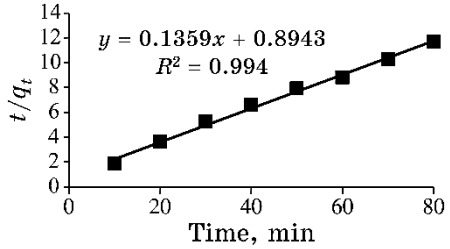

Fig. 9. Application of the pseudo-second order model to experimental drug adsorption data.

TABLE 10. Rate constant of practical and theoretical pseudo-second order adsorption capacity and correlation coefficient obtained by applying them to practical adsorption data.

Type of adsorbent	Drug	$q_{e(exp)}$, mg/g	$q_{e(calc.)}$, mg/g	K_2, g·mg^1·min.$^{-1}$	h, mg·g^{-1}·min^{-1}	R^2
SAC	meloxicam	6.825	7.358	0.0206	0.962	0.994

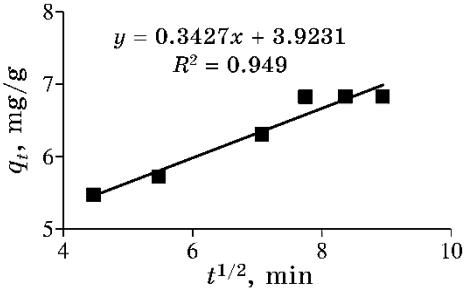

Fig. 10. Application of the intraparticle molecular diffusion model to practical drug adsorption data.

TABLE 11. Intramolecular diffusion constants and correlation coefficient obtained from their application to practical adsorption data.

Type of adsorbent	Drug	C_i, mg/L	K_{diff}, mg·g^{-1}·min$^{-1/2}$	C, mg·g^{-1}	R^2
SAC	meloxicam	35	0.3427	3.9231	0.949

from its aqueous solutions using activated carbon.

With the experimental results, it suggested that not the only mechanism controlling the drug adsorption as shown previously. The results listed in Table 11 have shown that an increase in drug concentration leads to increase, in the force for adsorption, in the

drug diffusion rate K_{diff}. It has been observed that increasing of the drug concentration leads to an increase in the thickness of the boundary layer between the carbon surface and the drug molecules [31].

4. CONCLUSIONS

As concluded, a novel activated nanocarbon was prepared from pinecone and then characterized. The nanoparticles of activated carbon were applied to study the adsorption of MLX from its aqueous solution. The optimum condition of the adsorption process was evaluated, such as the amount of adsorbent in SAC of 0.12 g with the initial concentration of MLX of 15–35 mg/L for 60 minutes of contact time at equilibrium for alkaline medium at 288–338 K, and the adsorption was found to be an exothermic process. The experimental process of adsorption was evaluated using the Langmuir and Freundlich isotherms to detect the type of adsorption. Based on the correlation ($R^2 = 0.996$), the Freundlich model has a significant pattern compared to other models, which were fitted to the experimental data. Hence, the adsorption process is suggested to be a heterogeneous, multilayer process. Kinetically, the adsorption process is followed by a pseudo-second-order reaction.

ACKNOWLEDGEMENTS

Authors would like to thank the University of Mosul, College of Education for Girls, Chemistry Department, management and staff for all the support during the experimental work stage.

REFERENCES

1. Masoumeh Mohammadnejad and Alieh Moeinipour, *Analytical and Bioanalytical Chemistry Research*, **11**, Iss. 1: 77 (2024); https://doi.org/10.22036/abcr.2023.409114.1962
2. S. H. Huo, H. Y. An, J. Yu, X. F. Mao, Z. Zhang, L. Bai, and P. X. Zhou, *Journal of Chromatography A*, **1517**: 18 (2017); https://doi.org/10.1016/j.chroma.2017.08.039
3. Y. Bian, N. Xiong, and G. Zhu, *Processes*, **6**, Iss. 8: 122 (2018); https://doi.org/10.3390/pr6080122
4. J. R. de Andrade, M. F. Oliveira, M. G. da Silva, and M. G. Vieira, *Industrial & Engineering Chemistry Research*, **57**, Iss. 9: 3103 (2018); https://doi.org/10.1021/acs.iecr.7b05137
5. S. Pap, M. A. Taggart, L. Shearer, Y. Li, S. Radovic, and M. T. Sekulic, *Chemosphere*, **264**: 128439 (2021); https://doi.org/10.1016/j.chemosphere.2020.128439

6. S. Banerjee and F. Maric, *European Journal of Physiotherapy*, **25**, Iss. 1: 51 (2023); https://doi.org/10.1080/21679169.2021.1976272
7. H. Lord and J. Pawliszyn, *Journal of Chromatography A*, **902**, Iss. 1: 17 (2000); https://doi.org/10.1016/S0021-9673(00)00836-0
8. G. R. Wallwork, *Reports on Progress in Physics*, **39**, Iss. 5: 401 (1976); doi:10.1088/0034-4885/39/5/001
9. A. Sivan, *Current Opinion in Biotechnology*, **22**, Iss. 3: 422 (2011); https://doi.org/10.1016/j.copbio.2011.01.013
10. C. Noutsopoulos, E. Koumaki, D. Mamais, M. C. Nika, A. A. Bletsou, and N. S. Thomaidis, *Chemosphere*, **119**: S109 (2015); https://doi.org/10.1016/j.chemosphere.2014.04.107
11. A. Binelli, S. Magni, C. Soave, F. Marazzi, E. Zuccato, S. Castiglioni, M. Parolini, and V. Mezzanotte, *Ecological Engineering*, **71**: 710 (2014); https://doi.org/10.1016/j.ecoleng.2014.08.004
12. R. F. B. De Souza, L. S. Parreira, D. C. Rascio, J. C. M. Silva, E. Teixeira-Neto, M. L. Calegaro, E. V. Spinace, A. O. Neto, and M. C. Santos, *Journal of Power Sources*, **195**, Iss. 6: 1589 (2010); http://dx.doi.org/10.1016/j.jpowsour.2009.09.065
13. A. L. Myers and P. A. Monson, *Adsorption*, **20**: 591 (2014); https://doi.org/10.1007/s10450-014-9604-1
14. E. A. Al-hyali, T. Ra'ed, and N. H. Saleem, *Samarra Journal of Pure and Applied Science*, **3**, Iss. 4: 41 (2021); https://doi.org/10.54153/sjpas.2021.v3i4.292
15. J. Wang and X. Guo, *Chemosphere*, **258**: 127279 (2020); https://doi.org/10.1016/j.chemosphere.2020.127279
16. Fadirah Fadzail, Masitah Hasan, and Zulfakar Mokhtar, *IOP Conf. Ser.: Earth Environ. Sci.*, **646**, No. 1: 012031 (2012); doi:10.1088/1755-1315/646/1/012031
17. A. M. Ali, R. Alsaqa, and N. S. Sultan, *International Journal of Thermodynamics*, **25**, Iss. 2: 33 (2022); https://doi.org/10.5541/ijot.1003950
18. K. Chinoune, K. Bentaleb, Z. Bouberka, A. Nadim, and U. Maschke, *Applied Clay Science*, **123**: 64 (2016); https://doi.org/10.1016/j.clay.2016.01.006
19. C. Nanthamathee and P. Dechatiwongse, *Materials Chemistry and Physics*, **258**: 123924 (2021); https://doi.org/10.1016/j.matchemphys.2020.123924
20. D. Mohammadyani, S. A. Hosseini, and S. K. Sadrnezhaad, *International Journal of Modern Physics: Conference Series*, **5**: 270 (2012); https://doi.org/10.1142/S2010194512002127
21. Q. M. Abdulhamid, E. T. Al-Tikrity, A. B. Fadhil, and P. J. Foot, *Journal of Analytical and Applied Pyrolysis*, **173**: 106072 (2023); https://doi.org/10.1016/j.jaap.2023.106072
22. H. Tun and C. C. Chen, *Adsorption*, **27**, Iss. 6: 979 (2021); https://doi.org/10.1007/s10450-020-00296-3
23. R. S. Abdul Hamza, I. Oreibi, and M. A. Habeeb, *Nanosistemi, Nanomateriali, Nanotehnologii*, **22**, Iss. 2: 379 (2024); https://doi.org/10.15407/nnn.22.02.379
24. K. Y. Foo and B. H. Hameed, *Chemical Engineering Journal*, **166**, Iss. 2: 792 (2011); https://doi.org/10.1016/j.cej.2010.11.019
25. M. Abdulkarim, I. L. Ibrahim, M. Mohammed, and M. Musah, *Fudma Journal of Sciences*, **8**, Iss. 3: 409 (2024); https://doi.org/10.33003/fjs-2024-

0803-2567
26. Y. Ngernyen, D. Petsri, K. Sribanthao, K. Kongpennit, P. Pinijnam, R. Pedsakul, and A. J. Hunt, *RSC Advances*, **13**, Iss. 21: 14712 (2023); https://doi.org/10.1039/D3RA01949G
27. S. F. Fatima, R. Sabouni, G. Husseini, V. Paul, H. Gomaa, and R. Radha, *Nanomaterials*, **14**, Iss. 13: 1081 (2024); https://doi.org/10.3390/nano14131081
28. S. Sivalingam and S. Sen, *Environ. Sci. Pollut. Res.*, **26**: 34693 (2019); https://doi.org/10.1007/s11356-018-3664-9
29. K. A. AL-Memary, E. A. Al-Hyali, and H. T. A. S. Toohi, *Research Journal of Pharmacy and Technology*, **12**, Iss. 3: 1206 (2019); http://dx.doi.org/10.5958/0974-360X.2019.00201.4
30. L. Z. Zhang and L. Wang, *Applied Thermal Engineering*, **19**, Iss. 2: 195 (1999); https://doi.org/10.1016/S1359-4311(98)00023-4
31. E. A. S. Al-Hyali, K. A. O. AL-Memary, and T. AL-Sayd, *Journal of Education and Science*, **29**, No. 1: 233 (2020); doi:10.33899/edusj.2020.164375

Наносистеми, наноматеріали, нанотехнології
Nanosistemi, Nanomateriali, Nanotehnologii
2026, т. 24, № 1, сс. 165–174
https://doi.org/10.15407/nnn.24.01.0165

PACS numbers: 61.05.cp, 68.37.Vj, 75.50-y, 81.30.Mh

Preparation and Investigation of Structural Properties of Nano-Spinel Ferrite by Co-Precipitation Method

Leal Abdullah Hamza and Sameer H. Al-Nesrawy

College of Education for Pure Science,
Department of Physics,
University of Babylon,
Hilla, Iraq

The co-precipitation method is used in this study to prepare and characterize the structural properties of two types of ferrites: zinc–nickel ferrite Zn–Ni Fe_2O_4 and zinc–chromium ferrite Zn–Cr Fe_2O_4. These ferrites are separated into two parts: one without sintering and the other after sintering at 1100°C for 3 hours to facilitate further crystallization. The ferrites are investigated by x-ray diffraction (XRD) to confirm Zn–Cr-, Zn–Ni-nanoferrite samples without sintering and sintered at 1100°C. These are attributed to the face-centred cubic (f.c.c.) spinel phase, and the Debye–Scherrer equation is used to determine the average crystallite sizes of the prepared samples, which are found to be equal to 7.05 nm for Zn–Cr-ferrite nanoparticles without sintering and 64.67 nm Zn–Cr-ferrite nanoparticles sintered at 1100°C. Being equal 46.86 nm Zn–Ni-ferrite nanoparticle without sintering and 57.41 nm for the Zn–Ni-ferrite nanoparticle sintered at 1100°C, it is shown that these materials are of nanoscale. The composition of the ferrite has better crystallization. That is sintering at that temperature has led to an increase in the degree of crystallization and a decrease in the crystal defects formed in the ferrites during preparation. The field-emission scanning electron microscope (FE–SEM) is used to examine Zn–Cr-, Zn–Ni-nanoferrite samples without sintering and sintered at 1100°C. The pores separating the particles are eliminated during the sintering process that produces strong bonds in the agglomeration form.

У цьому дослідженні використано метод спільного осадження для одержання та характеризації структурних властивостей двох типів феритів: цинк-ніклевого фериту Zn–Ni Fe_2O_4 та цинк-хромового фериту Zn–Cr Fe_2O_4. Ферити розділено на дві частини: одну без спікання, а іншу після спікання за 1100°C впродовж 3 годин для полегшення подальшої кристалізації. Ферити досліджено за допомогою рентґенівської дифракції для підтвердження зразків наноферитів Zn–Cr, Zn–Ni без спікання

та спечених за 1100°C. Це пояснюється гранецентрованою кубічною шпінельною фазою, і для визначення середніх розмірів кристалітів підготовлених зразків було використано рівняння Дебая–Шеррера, яке дорівнюють 7,05 нм для наночастинок фериту Zn–Cr без спікання та 64,67 нм для наночастинок фериту Zn–Cr, спечених за 1100°C. Дорівнюючи 46,86 нм для наночастинок фериту Zn–Ni без спікання та 57,41 нм для наночастинок фериту Zn–Ni, спечених за 1100°C, ці розміри показують наномасштабність цих матеріялів. Склад фериту має ліпшу кристалізацію, тобто спікання за цієї температури приводить до збільшення ступеня кристалізації та зменшення кристалічних дефектів, що утворюються у феритах під час приготування. Для дослідження зразків наноферитів Zn–Cr, Zn–Ni без спікання та спечених за 1100°C було використано сканувальний електронний мікроскоп з польовою емісією. Пори, що розділяють частинки, були усунені під час процесу спікання, що привело до утворення міцних зв'язків у формі аґломерації.

Key words: co-precipitation, ferrite, nanoparticles, spinel, field-emission scanning electron microscopy, x-ray diffraction.

Ключові слова: співосадження, ферит, наночастинки, шпінель, сканувальна електронна мікроскопія з польовою емісією, рентґенівська дифракція.

(Received 15 September, 2024; in revised form, 17 September, 2024)

1. INTRODUCTION

In science research, magnetic nanoparticle systems have generated great interest, especially in physics and related fields. Owing to their many and significant characteristics, recent advanced research has shifted to the synthesis of metallic oxide nanoparticles, where a pressing need has arisen to produce materials known as nanomaterials-materials with a large surface area relative to their size [1]. Magnetic drug targets, magnetic resonance imaging for medical diagnosis, recording materials and catalysts, environments, and more are just a few of the numerous applications for magnetic nanoparticles [2]. Over time, ferrites have continued to garner interest. Because ferrites are stable, reasonably priced, and have a broad range of technological applications, they cannot be replaced by any other magnetic material [3].

Ceramic materials known as ferrites are created by chemically adding one or more metals to iron oxides (Fe_2O_4). Ferrites are mixtures of two metallic oxides, which can include any bivalent element, such as barium (Ba), zinc (Zn), nickel (Ni), manganese (Mn), or zinc oxide. Ferrites have exceptional magnetic and electrical properties [4]. Based on their structural characteristics, ferrites are divided into two groups: cubic and hexagonal. Soft ferrites are an-

other name for cubic ferrites.

These cubic ferrites are further classified into two types: spinel ferrite and garnet ferrite. Hexagonal ferrites are also known as hexaferrites and are hard ferrites because it is tough to magnetize and demagnetize them. They are also known as permanent [5]. Applications for hard ferrites include microwave absorbing systems, refrigerators, loudspeakers, washing machines, TVs, communication systems, switch-mode power supplies, and high-frequency applications. However, soft ferries have a wide range of uses in the electronic industry, including the development of transformer cores, high-frequency inductors, and microwave components, due to their good magnetic field conductivity [6].

Soft chemical techniques like hydrothermal synthesis, sol–gel, and co-precipitation can be used to create ferrite particles at the nanoscale [7]. Because co-precipitation does not require high pressure or temperature and because impure materials are removed through filtration and washing, it is an appropriate chemical method for synthesizing nanoparticles [8]. The benefits of the co-precipitation method include high yield, high purity of product, and ease of use [9]. From a physical perspective, the co-precipitation process is driven by three main mechanisms: Surface adsorption: Ions in solution with the opposing charge can be drawn to the precipitate's surface charge. Inclusion: The analyte can high frequency be incorporated non-isomorphically (solid solution) or isomorphically (mixed crystal) to replace an ion in the precipitate's crystal structure. Additionally, Ions are physically engulfed in the precipitate before they can diffuse or disperse, known as occlusion [10].

2. EXPERIMENTAL

Synthesis of the ferrite nanoparticles was done by co-precipitation in two parts: part one, was mixed thoroughly 8.11 gm ferric chloride $FeCl_3$, 11.9 gm chrome nitrate $Cr(NO_3)\cdot 9H_2O$ and 14.85 gm zinc nitrate $Zn(NO_3)_2$ and part two, 8.11 gm ferric chloride $FeCl_3$, 14.54 gm nickel nitrate $Ni(NO_3)_2$ and 14.85 gm zinc nitrate $Zn(NO_3)_2$ as starting materials, each starting material was weighted separately and add 100 ml of distilled water and then mixed all these cationic solutions while stirring to complete dissolution. A sufficient amount of the NaOH solution is made at a concentration of 2M. After that, a thin stream of NaOH solution is added to the cationic solution while stirring and heating the mixture until precipitation happens. To finish the reaction, the precipitate is heated to a temperature of 50°C while still in its alkaline state. After another hour of stirring to allow the particles to age, the precipitated particles are filtered and repeatedly cleaned before being dried for an hour at 150 degrees Cel-

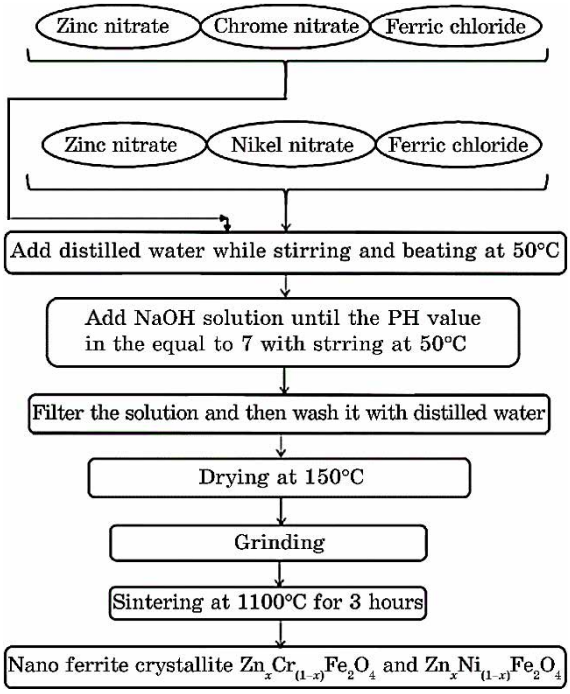

Fig. 1. Preparation steps of nanoferrite crystallite.

sius.

After that, the co-precipitated ferrite agglomerates were ground into extremely fine particles for a few minutes using an agate mortar and pestle. These particles are finally sintering at 1100 degrees Celsius to continue crystallizing. The primary steps used in the preparation are schematically represented in Fig. 1.

3. RESULTS AND DISCUSSION

3.1 XRD Analysis and Particle Size Calculation

Figures 2, 3 show the XRD pattern of the Zn–Cr Fe_2O_4 nanoparticle prepared using co-precipitation technique.

Figure 2 the sample without sintered, the appearance of some phases shows the part of the oxides of raw materials at $\theta = 29.3$, 31.9, 38.9, 47.9 because the Zn–Cr ferrite phase isn't grown yet, at $\theta = 35.1$ which there is a partial phase grown of Zn–Cr ferrite.

Figure 3 sintered at 1100°C for 3 hours, x-ray diffraction pattern shows fully the growth of crystalline Zn–Cr ferrites phases. Different peaks appear on the XRD pattern, namely, $2\theta = 30.09$, 35.42,

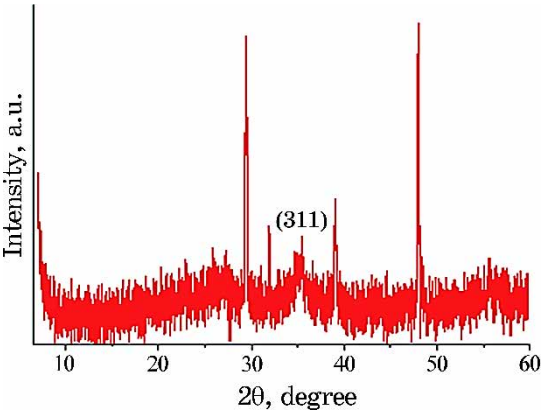

Fig. 2. The XRD pattern of the Zn–Cr ferrite nanoparticle without sintered.

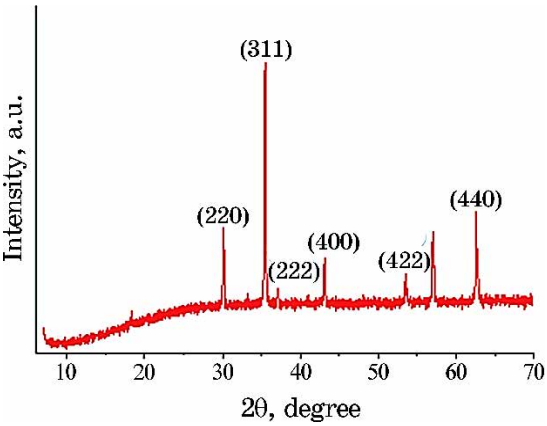

Fig. 3. The XRD pattern of the Zn–Cr ferrite nanoparticle sintered at 1100°C.

37.05, 43.05, 53.39, and 62.51 degrees, which are attributed to (220), (311), (222), (400), (422), (511) and (440) planes, respectively. The pattern of Zn–Cr ferrite nanoparticles is compatible with (JCPDS card numbers 84-0314 and 89-1012). Verification of the face-centred cubic spinel phase (FCC) [11]. The Debye-Scherer's equation has been used to determine the average crystallite size:

$$D = 0.9\lambda/(\beta\cos\theta_\beta), \quad (1)$$

where λ is the incident x-ray radiation wavelength 1.54056 Å, β is the peak's full width at half maximum (radian), and (θ_β) is the XRD

TABLE 1. The XRD result obtained for the Zn–Cr ferrite nanoparticle without sintered.

Component	2θ, degree	*hkl*	*FWHM*, β, degree	*d*, Å	Crystallite size, nm	Average crystallite size, nm
Zn–Cr·Fe_2O_4	35.13	311	1.2343	2.56683	7.054478	7.054478

TABLE 2. The XRD result obtained for the Zn–Cr ferrite nanoparticle sintered at 1100°C.

Component	2θ, degree	*hkl*	*FWHM*, β, degree	*d*, Å	Crystallite size, nm	Average crystallite size, nm
Zn–Cr·Fe_2O_4	30.09	220	0.1511	2.96835	56.88784	64.67817408
	35.42	311	0.1448	2.53081	60.18393	
	37.05	222	0.1278	2.42308	68.50793	
	43.05	400	0.1329	2.09797	67.15018	
	53.39	422	0.1328	1.71284	69.98047	
	62.51	440	0.1486	1.4834	65.35871	

peak's Bragg diffraction angle (degree) [12]. Tables 1 and 2 provide the assignments of different reflections as well as a detailed analysis of the XRD.

Figures 4 and 5 show the XRD pattern of the Zn–Ni Fe_2O_4 nanoparticle prepared too using the co-precipitation technique.

Figure 4 shows the diffraction pattern of ferrite without sintered and Fig. 5 shows the X-ray diffraction pattern of the same nanoferrite using sintering at a temperature of 1100°C for 3 hours. When comparing these patterns, Fig. 4 shows that the dominant direction (311) also remains for the sintered ferrite, with its intensity increasing with sintering at the expense of other peaks. This indicates the presence of some levels that are preferred for the growth of crystalline directions, and the intensity of this peak increases accordingly, which confirms that the ferrite composition has better crystallization. That is, sintering at that temperature has led to an increase in the degree of crystallization and a decrease in the crystalline defects formed in the ferrite during preparation, which indicates that sintering leads to a rise in crystalline regularity.

The diffraction patterns match the spinel ferrite standard pattern (ICDD no. 00-022-1012) fairly well. At diffraction angles (2θ) of 29.9, 35.3, 36.9, 42.8, 53.1, 56.6, 62.2, 70.5, 73.5, and 74.5 degrees, they are clearly defined and comprise robust reflection peaks that are attributed to the (220), (311), (222), (400), (422), (511), (440), (620), (533), and (622) planes, respectively. By taking into

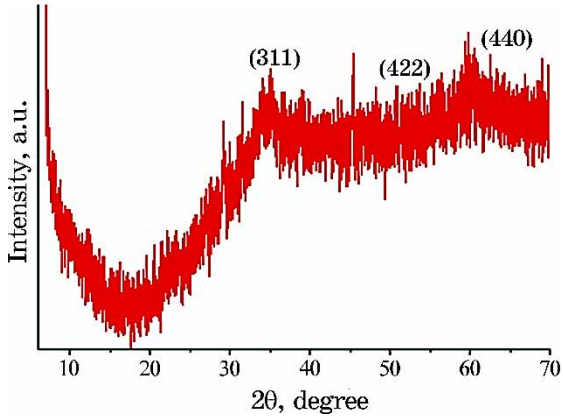

Fig. 4. The XRD pattern of the Zn–Ni ferrite nanoparticle without sintered.

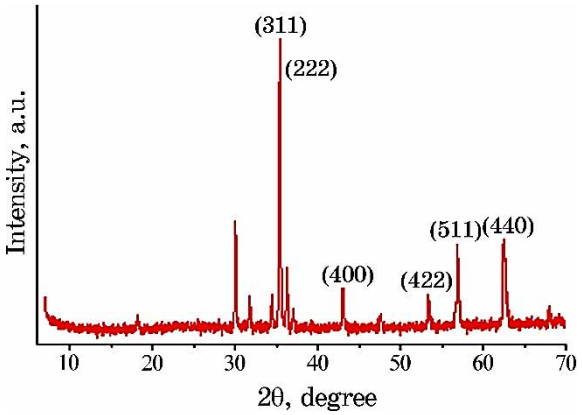

Fig. 5. The XRD pattern of the Zn–Ni ferrite nanoparticle sintered at 1100°C.

account the strongest diffraction peaks in XRD spectra, the crystal size of the ferrite samples was ascertained [13]. In this study, the crystal size of the tested sample was determined. The crystal size of the ferrite samples was ascertained by taking into account the strongest diffraction peaks in XRD spectra using Scherrer's formula, as indicated in Eq. (1). Tables 3, 4 are a summary of the crystallite size D calculation.

3.2. Field-Emission–Scanning Electron Microscopy (FE–SEM)

FE–SEM was used to examine Zn–Cr Nano ferrite samples without

TABLE 3. The XRD result obtained for the Zn–Ni ferrite nanoparticle without sintered.

Component	2θ, degree	*hkl*	*FWHM*, degree	*d*, Å	Crystallite size, nm	Average crystallite size, nm
Zn–Ni·Fe_2O_4	35.3	311	0.9323	3.06377	9.199623	46.86716588
	53.1	422	6.0734	2.56683	1.43285	
	62.2	440	0.0692	2.0012	129.969	

TABLE 4. The XRD result obtained for the Zn–Ni ferrite nanoparticle sintered at 1100°C.

Component	2θ, degree	*hkl*	*FWHM*, degree	*d*, Å	Crystallite size, nm	Average crystallite size, nm
Zn–Ni Fe_2O_4	35.3609	311	0.1554	2.53632	56.0663222	57.41132041
	36.2246	222	0.1321	2.4778	66.1159439	
	42.9799	400	0.1687	2.1027	52.8816646	
	53.3301	422	0.1692	1.71645	54.8963699	
	56.5681	511	0.1313	1.62564	71.7883791	
	62.4414	440	0.2272	1.4861	42.7192428	

sintered and sintered at 1100°C for 3 hours.

Figure 6, *a*, *b* depicts a typical FE–SEM image. The FE–SEM image *b* is nearly uniform and agglomerated grains are observed [11]. Particle aggregation takes place in the nanometer range, as seen in FE–SEM image *b*. As seen in image a, the pores separating the particles were eliminated during the sintering process, which produced strong bonds in the agglomeration form. The limited grain size of the particle is determined by the interplay between porosity and the grain boundary. Through this investigation, it was found that when the particles were sintered at 1100°C, their average grain size decreased.

Figure 7, *a*, *b* shows FE–SEM pictures of Zn–Ni Fe_2O_4 NPs. The FE–SEM images of the zinc-nickel ferrite without sintered and sintered at 1100°C for 3 hours.

Figure 7, *a* without sintered shows irregular, non-symmetrical particles. For the Zn–Ni ferrite sample sintered at 1100°C, Fig. 7, *b* the agglomeration shows uniform particles [14]. The FE–SEM image shows that the agglomeration of Zn–Ni ferrite that sintered at 1100°C nanoparticle is relatively higher when compared to that of the without sintered nanoparticles because of the effect of the capping agent on modifying crystal sizes.

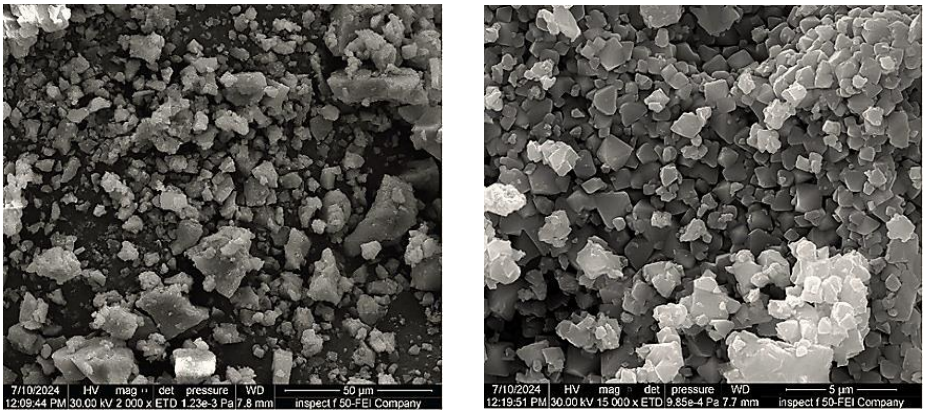

a *b*

Fig. 6. FE–SEM images for Zn–Cr ferrite: (*a*) without sintered; (*b*) sintered at 1100°C.

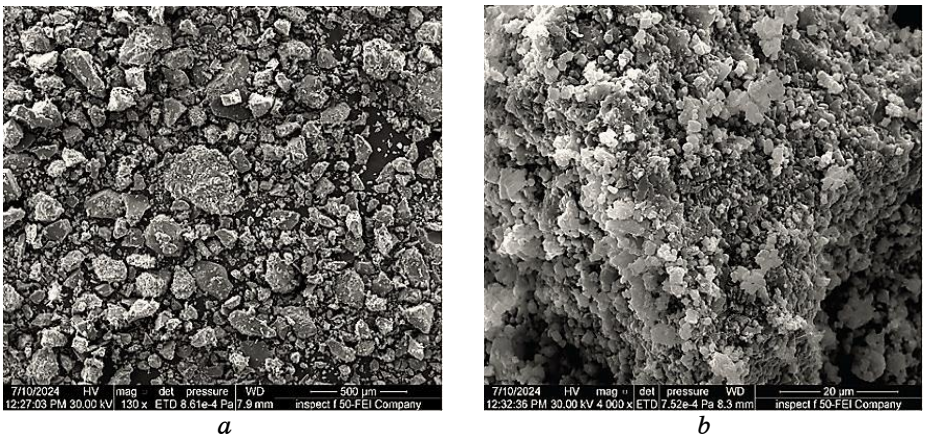

a *b*

Fig. 7. FE–SEM images for Zn–Ni ferrite: (*a*) without sintered; (*b*) sintered at 1100°C.

4. CONCLUSION

In conclusion, this study found the following:
1. the powders obtained by co-precipitated presented the formation of Zn–Cr ferrite and Zn–Ni ferrite crystalline phase;
2. the powders' crystallinity and crystallite size increased with sintered at 1100°C for 3 hours in the spinel lattice Zn–Cr ferrite and Zn–Ni ferrite;
3. all the compositions studied here by means of the XRD and FE–SEM showed the formation of soft nanoparticles' agglomerates.

REFERENCES

1. W. A. Shatti, Z. M. A. Abbas, and Z. T. Khodair, *Journal of Ovonic Research*, **18**, No. 4: 473 (2022); https://doi.org/10.15251/JOR.2022.184.473
2. P. L. Hariani, M. Faizal, Ridwan, Marsi, and D. Setiabudidaya, *International Journal of Environmental Science and Development*, **4**, No. 3: 336 (2013); https://doi.org/10.7763/IJESD.2013.V4.366
3. S. V. Soni, C. L. Khobragade, R. K. Khatarkar, and U. V. Rathod, *Archives of Physics Research*, **5**, No. 6: 49 (2014).
4. A. Vedrtnam, K. Kalauni, S. Dubey, and A. Kumar, *AIMS Materials Science*, **7**, No. 6: 800 (2020); https://doi.org/10.3934/matersci.2020.6.800
5. A. Sharma, H. Mahajan, I. Mohammed, S.K. Godara, S. Sinha, and A. K. Srivastava, *Materials Performance and Characterization*, **12**, No. 1: 64 (2023); https://doi.org/10.1520/MPC20220084
6. P. Thakur, S. Taneja, D. Chahar, N. Bhalla, and A. Thakur, *Ceramics International*, **46**, No. 10: 15740 (2020); https://doi.org/10.1016/j.ceramint.2020.03.287
7. B. P. Rao, A. M. Kumar, K. H. Rao, Y. L. N. Murthy, O. F. Caltun, I. Dumitru, and L. Spinu, *Journal of Optoelectronics and Advanced Materials*, **8**, No. 5: 1703 (2006).
8. S. Tazikeh, A. Akbari, A. Talebi, and E. Talebi, *Materials Science—Poland*, **32**, No. 1: 98 (2014); https://doi.org/10.2478/s13536-013-0164-y
9. D. D. Kulkarni, V. R. Joshi, S. N. Shetty, S. B. Patel, and M. S. Khalfe, *IJARSCT*, **2**: 2581 (2022); https://doi.org/10.48175/IJARSCT-3467
10. N. Bader, A. A. Benkhayal, and B. Zimmermann, *Int. J. Chem. Sci.*, **12**, No. 2: 519 (2014).
11. R. R. Powar, V. D. Phadtare, V. G. Parale, S. Pathak, P. B. Piste, and D. N. Zambare, *Journal of the Korean Ceramic Society*, **56**, No. 5: 474 (2019); https://doi.org/10.4191/kcers.2019.56.5.06
12. A. J. Mohammed and S. H. Al-Nesrawy, *Neuro Quantology*, **20**: 251 (2022); https://doi.org/10.14704/nq.2022.20.3.NQ22087
13. M. Suwan, N. Sangwong, and S. Supothina, *Ceramics–Silikaty*, **64**, No. 2: 172 (2020); https://doi.org/10.13168/cs.2020.0006
14. W. R. M. Alsuiai, B. S. Yadav, A. K. Singh, and V. Singh, *Webology*, **19**, No. 2: 2258 (2022).

Наносистеми, наноматеріали, нанотехнології
Nanosistemi, Nanomateriali, Nanotehnologii
2026, т. 24, № 1, сс. 175–187
https://doi.org/10.15407/nnn.24.01.0175

PACS numbers: 61.72.Mm, 61.72.uj, 68.35.Ct, 68.37.Hk, 68.37.Ps, 68.55.J-, 81.15.Cd

Influence of Mn^2 and Tb^3 Activators on the Surface Morphology of GaN Thin Films

O. M. Bordun[1], I. I. Medvid[1], I. Yo. Kukharskyy[1], I. O. Bordun[1], I. M. Kofliuk[1], O. Y. Mylyo[1], V. O. Maksymiv[1], D. S. Leonov[2], and M. V. Protsak[1]

[1]*Ivan Franko National University of Lviv,*
50, Drahomanov Str.,
UA-79005 Lviv, Ukraine
[2]*Technical Centre, N.A.S. of Ukraine,*
13, Pokrovska Str.,
UA-04070 Kyiv, Ukraine

The study investigates the influence of transition (Mn) and rare-earth (Tb) dopants on the surface morphology of as-deposited GaN thin films. GaN, GaN:Mn, and GaN:Tb thin films are obtained by radio frequency (RF) ion-plasma sputtering in a nitrogen atmosphere on single-crystal Si substrates. Surface morphology studies performed using atomic force microscopy (AFM) show that the addition of Mn promotes an increase in the average grain diameter from 85 nm to 166 nm and is accompanied by a decrease in the root-mean-square roughness from 6.4 nm to 4.8 nm. An analysis of crystallite-size distributions by diameter, area, and volume is carried out, and it is suggested that anomalous secondary grain growth occurs during the RF-sputtering process, when Mn impurity is added. The addition of Tb impurity leads to an even greater increase in grain size, which is attributed to the large ionic radius of the Tb^{3+} ion and the generation of significant mechanical stresses.

У роботі проведено дослідження впливу домішок перехідних (Mn) і рідкісноземельних (Tb) елементів на морфологію поверхні свіжонанесених тонких плівок GaN. Тонкі плівки GaN, GaN:Mn і GaN:Tb одержано методом високочастотного йонно-плазмового розпорошення в атмосфері азоту на монокристалічних підкладинках Si. Дослідження морфології поверхні тонких плівок методом атомно-силової мікроскопії показали, що додавання Mn сприяє зростанню середнього діяметра зерен з 85 до 166 нм і супроводжується пониженням середньоквадратичної шерсткости від 6,4 до 4,8 нм. Проведено аналізу розподілів кристалітів за діяметром, площею й об'ємом і запропоновано, що у процесі ВЧ-

напорошення відбувається аномальний ріст вторинних зерен за додавання домішки Mn. З додаванням домішки Tb спостерігається ще більше зростання розмірів зерен, що пов'язується з великим йонним радіюсом йона Tb^{3+} і створенням сильних механічних напружень.

Key words: thin films, GaN, doping, manganese, terbium, RF sputtering, surface morphology, atomic force microscopy.

Ключові слова: тонкі плівки, GaN, леґування, Манґан, Тербій, ВЧ-розпорошення, морфологія поверхні, атомно-силова мікроскопія.

(Received 16 February, 2026)

1. INTRODUCTION

In recent years, gallium nitride (GaN) has been extensively studied by many researchers due to its widespread use in optoelectronic devices, lasers, and photodetectors [1–7]. In particular, the luminescent properties of both pure and doped GaN are widely studied, which allows for a significant expansion of the functional capabilities of this material [8–13]. In addition, GaN is widely used in power electronics [14] and is the preferred semiconductor for power converters in automotive electronics and the power supply industry [15].

Gallium nitride is an important material in the development of efficient light-emitting diodes (LEDs) [16, 17] and micro-light-emitting diodes (μLEDs) with green and blue emission, designed for integration into display systems [18]. The application of this material is not limited to these areas, as researchers have developed and tested a light-controlled artificial synapse based on gallium nitride (GaN), capable of mimicking the learning and memory processes of the human brain for the creation of ultrafast and energy-efficient neuromorphic computing systems [19].

For the practical application of semiconductor thin films in optoelectronics and instrument engineering, their morphological characteristics are quite important, since they affect the efficiency of devices created on their basis. In general, the issue of the physical properties of thin films is complicated by the fact that their structure is often far from perfect. Obtaining the required, stable, and reproducible properties of polycrystalline films is limited due to the presence of grain boundaries. The physical properties of polycrystalline thin films depend significantly not only on the characteristics of the material, but also on the energy levels that arise due to the presence of grain boundaries. It is clear that these levels are determined by the size of the crystallites that form thin films. This has led to the investigation of the surface morphology of GaN, GaN:Mn, and GaN:Tb thin films using atomic force microscopy

(AFM) and scanning electron microscopy (SEM). The thin-film samples were obtained by RF ion-plasma sputtering, which is optimal for producing homogeneous semiconductor and dielectric films [20].

2. EXPERIMENTAL TECHNIQUE

GaN, GaN:Mn, and GaN:Tb thin films with thicknesses of 0.3–0.8 μm were obtained by RF ion-plasma sputtering on monocrystalline Si substrates. RF ion-plasma sputtering was carried out in a nitrogen atmosphere in a system using a magnetic field of external solenoids for compression and additional ionization of the plasma column. The concentration of Mn^{2+} and Tb^{3+} activators was 1 mol.%. The structure and phase composition of the obtained films were investigated by x-ray diffraction analysis (Shimadzu XDR-600). The characteristic diffraction patterns of the thin films were presented previously in our work [21].

Elemental analysis of the studied samples at several points on the surface of the thin films was performed using an OXFORD INCA Energy 350 energy-dispersive spectrometer.

The surface morphologies of GaN and GaN:Mn thin films were studied using an atomic force microscope (AFM) 'INTEGRA TS-150'. Surface images of the thin films were recorded in semi-contact mode (tapping mode) in air. A silicon cantilever of the NSG10 series with a resonance frequency of 323 kHz and a stiffness of 24 N/m was used. In addition, a scanning electron microscope (JSM-7200F, Jeol) operated at an accelerating voltage of 7 kV was also employed to investigate the surface morphology of GaN, GaN:Mn, and GaN:Tb thin films.

3. RESULTS AND DISCUSSION

AFM images of the surface morphology of as-deposited GaN and GaN:Mn thin films obtained by RF ion-plasma sputtering on Si substrates are shown in Fig. 1.

For areas of identical size (5×5 μm) on the AFM surface morphology images of the studied samples, a number of standard parameters were calculated: root-mean-square roughness, average roughness, average grain diameter, average grain area and volume, grain height with maximum number of grains, coefficient of kurtosis and surface skewness. The characteristic surface roughness parameters and grain size characteristics of as-deposited GaN and GaN:Mn thin films obtained by RF ion-plasma sputtering on Si substrates are presented in Table. As can be seen from the obtained results, Mn doping significantly affects the surface roughness and grain size of

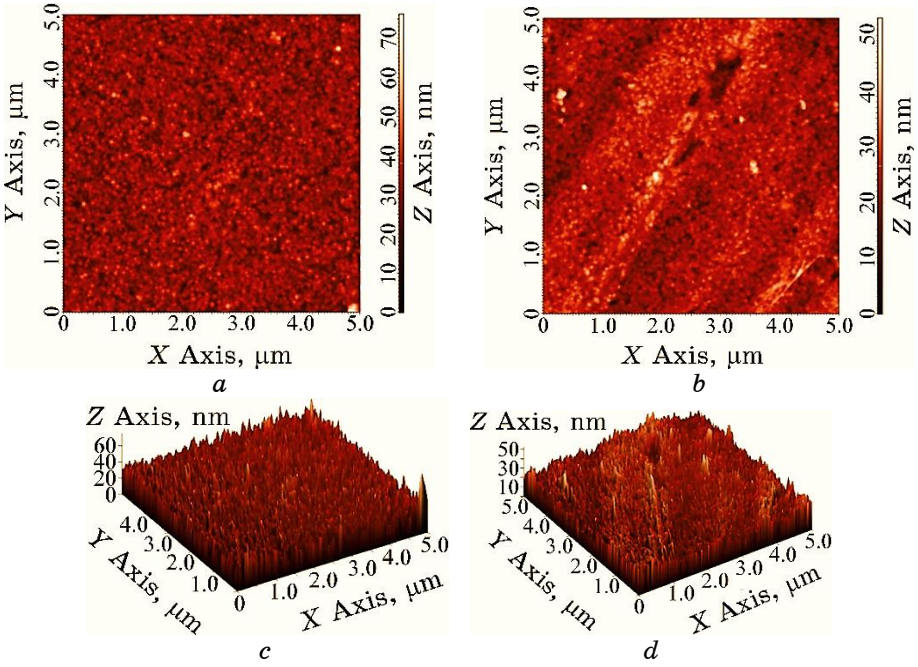

Fig. 1. AFM images of the surface morphology of as-deposited GaN (*a*, *c*) and GaN:Mn (*b*, *d*) thin films obtained by RF sputtering on Si substrates. Images *a* and *b* are two-dimensional; *c* and *d* are three-dimensional.

TABLE. Surface roughness and crystalline grain parameters of GaN and GaN:Mn thin films.

Parameter	GaN	GaN:Mn
Average grain diameter D, nm	85	166
Root mean square roughness S_q, nm	6.4	4.8
Average roughness S_a, nm	5.1	3.8
Grain height with maximum number of grains Z, nm	29	23
Average grain area S, nm^2	2660	7750
Average grain volume V, nm^3	8240	23700
Coefficient of kurtosis S_{ka}	3.7	4.0
Surface skewness S_{sk}	0.08	0.20

GaN thin films.

Analysis of the AFM images (Fig. 1), as well as the surface roughness and crystalline grain parameters (Table) of GaN and GaN:Mn thin films, shows that the grain sizes of as-deposited GaN:Mn thin films obtained by RF ion-plasma sputtering on Si sub-

strates are significantly larger compared to those of pure GaN samples. For example, the average grain diameter of GaN:Mn thin films is almost twice that of GaN films. At the same time, for GaN:Mn thin films, a decrease in both the root-mean-square and the average arithmetic surface roughness parameters by nearly 1.3 times is observed compared to the corresponding values for GaN thin films.

The increase in crystalline grain size, in particular the increase in the average grain diameter, area, and volume, along with the simultaneous decrease in parameters such as root-mean-square and average-arithmetic surface roughness, indicates a complication of the surface structure of the thin films. The S_q/S_a ratio for GaN and GaN:Mn thin films is 1.25 and 1.26, respectively, which corresponds to a normal distribution of grain heights forming the sample surface [22].

Comparison of the histograms of grain height distribution (Fig. 2) shows that Mn doping influences the formation of the surface morphology of GaN thin films obtained by RF ion-plasma sputtering on Si substrates and leads to a reduction in grain heights compared to undoped samples. The results obtained show that GaN:Mn thin films are characterized by horizontal grain growth parallel to the substrate surface.

The S_q/S_a ratio values and the grain height distribution histograms (Fig. 2) confirm that coarse structural defects are not typical for GaN and GaN:Mn thin films, *i.e.*, there are no extreme peaks on the sample surface. To evaluate further the effect of Mn impurity on the surface morphology of GaN thin films, we analyse the surface skewness (S_{sk}) and coefficient of kurtosis (S_{ka}) parameters, which are sensitive to the presence of isolated deep valleys or high peaks [23]. For both types of films, the value of $S_{sk} > 0$, and for the

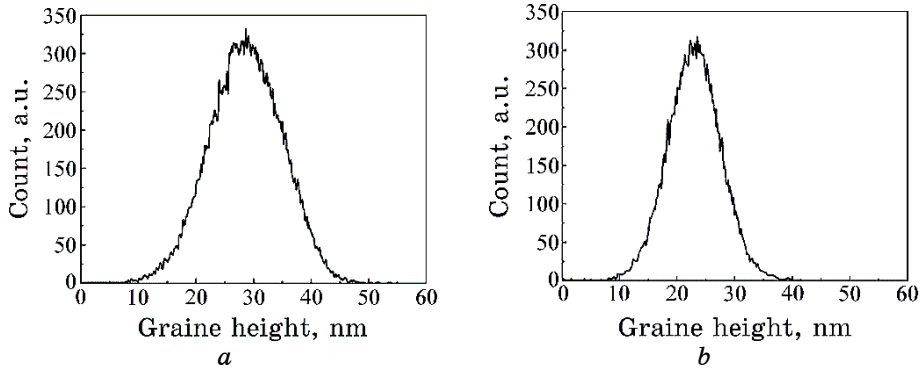

Fig. 2. Grain height distribution on AFM images of as-deposited GaN (*a*) and GaN:Mn (*b*) thin films obtained by RF sputtering on Si substrates.

as-deposited GaN thin film, the value is 0.08, while for the as-deposited GaN:Mn film, this value is 2.5 times higher and amounts to 0.20. The surface morphology of both undoped and Mn-doped GaN thin films are characterized by a large number of protruding peaks above the valleys. For pure as-deposited GaN thin films, an almost symmetrical grain height distribution is observed, which is consistent with the S_q/S_a ratio data and the analysis of height histograms, while in the as-deposited Mn-doped GaN films, the surface is formed with a larger number of protruding peaks (crystallites). The S_{ka} value for as-deposited GaN and GaN:Mn thin films is greater than 3, indicating that the surfaces of both samples contain a significant number of pronounced peaks.

Various factors can influence the formation of the surface morphology of thin films, such as the methods of production and the thermal treatment process of thin films, in which both the annealing temperature and the annealing atmosphere in which the thermal treatment process takes place play significant roles. The type of substrate and the presence of buffer sublayers have different effects on the formation of the surface morphology of the samples. In work [24] investigated the influence of $MgAl_2O_4$, AlN, and ZnO buffer layers on the crystallite size in GaN thin films and found that the smallest crystallite sizes and highest mechanical stresses are characteristic of GaN thin films deposited on quartz substrates with a $MgAl_2O_4$ buffer layer. In Ref. [25], the evolution of the surface morphology of GaN films grown by molecular beam epitaxy on Si(111) substrates using AFM was studied as a function of layer thickness, and two different models of morphology formation behaviour depending on the GaN layer thickness were identified. In Ref. [26], the structural, morphological, and magnetic properties of GaN:Tb and AlGaN:Tb films obtained by ion implantation of Tb^+ into *c*-oriented (0001) GaN and AlGaN films followed by thermal annealing were investigated. The effect of impurities and annealing on changes in surface morphology was studied using AFM, and it was shown that the annealing process effectively repairs crystal defects and reduces surface roughness caused by the ion activator.

To better understand the formation of the surface morphology of as-deposited GaN and GaN:Mn thin films obtained by RF ion-plasma sputtering on Si substrates, we analyse the grain size distributions that form the surface of the studied samples. The characteristic grain diameter size distributions of GaN and GaN:Mn thin films are shown in Fig. 3.

In a comprehensive review [27], it is noted that polycrystalline thin films with thicknesses up to 1 μm often exhibit 2*D*-like structures in which most grain boundaries are perpendicular to the film surface. Perpendicular grain growth to the surface is also charac-

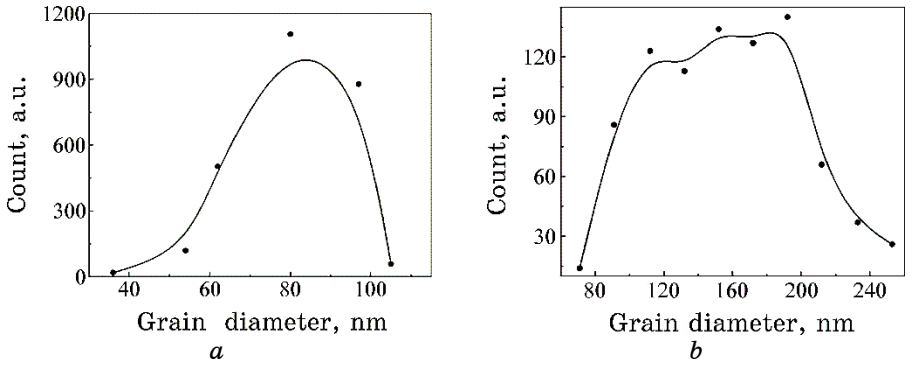

Fig. 3. Grain diameter size distribution and the calculated fitted diameter distribution from AFM images of as-deposited GaN (*a*) and GaN:Mn (*b*) thin films obtained by RF sputtering on Si substrates.

teristic of our GaN films. For most materials analysed in Ref. [27], films are formed from non-equilibrium grains with sizes smaller than the film thickness and form two-dimensional structures only after annealing. In general, the grain sizes in polycrystalline films are lognormally distributed. In a number of cases, further grain growth occurs due to 'abnormal' growth or the preferential growth of several grains, which usually have specific crystallographic orientation relationships with respect to the substrate surface plane. Our results indicate that such a situation is most likely characteristic of the GaN:Mn films we obtained. When the number of growing grains leads to the formation of a grain 'matrix' beyond static boundaries, a bimodal grain size distribution develops and is referred to as secondary grain growth [28]. Grains that grow abnormally often exhibit a limited or uniform texture. The growth of secondary grains in thin films typically involves evolution in the distribution of grain textures as well as evolution in the distribution of grains by size.

Our results for the grain diameter size distribution in GaN and GaN:Mn thin films obtained by RF ion-plasma sputtering (Fig. 3) indicate that for GaN films deposited on Si substrates, a unimodal diameter distribution with a peak at approximately 80 nm is observed (Fig. 3, *a*). A more complex diameter distribution is formed when GaN:Mn thin films are deposited (Fig. 3, *b*). For these films, three local maxima appear in the diameter distribution at approximately 112, 152, and 192 nm, indicating the appearance of a trimodal diameter distribution. The diameter distributions (Fig. 3) and the average diameter sizes values (Table) indicate that during the deposition process of GaN films, the addition of Mn impurity leads to a change in surface energy and promotes the 'coalescence' of

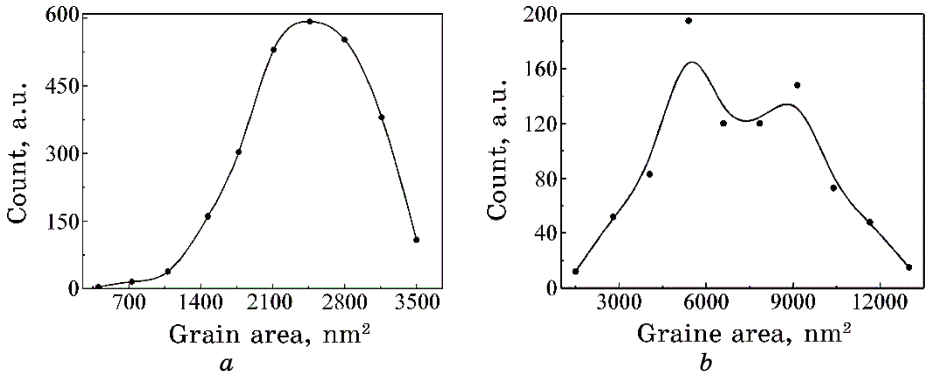

Fig. 4. Grain area size distribution and the calculated fitted area distribution from AFM images of GaN (*a*) and GaN:Mn (*b*) thin films obtained by RF sputtering on Si substrates.

grains into larger formations during film growth. In these films, secondary and tertiary grain growth was observed during the RF sputtering process.

The grain area distribution for sputtered GaN thin films deposited on Si substrates is also characterized by a normal distribution, whereas for as-deposited GaN:Mn thin films on Si substrates, the distribution has a more complex shape, exhibiting two maxima that indicate a bimodal grain area distribution (Fig. 4).

For a more detailed analysis, let us consider the grain volume distribution in GaN and GaN:Mn thin films obtained by RF ion-plasma sputtering on Si substrates. The characteristic grain volume size distributions of GaN and GaN:Mn thin films are shown in Fig. 5.

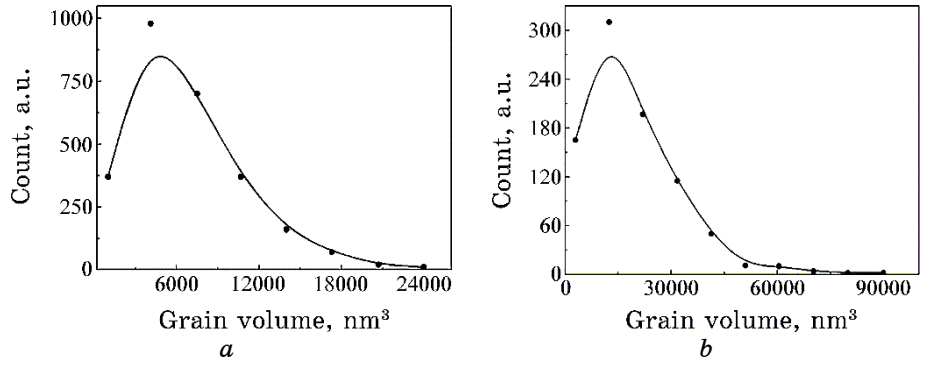

Fig. 5. Grain volume size distribution and the calculated fitted volume distribution from AFM images of GaN (*a*) and GaN:Mn (*b*) thin films obtained by RF sputtering on Si substrates.

As shown in Fig. 5, the grain volume distribution for the GaN and GaN:Mn thin films deposited on Si substrates is fairly well described by a lognormal law. Such behaviour is typical for grain diameter distributions in polycrystalline films [29]. The results of the grain volume distributions are in good agreement with the previously discussed ratio of the root-mean-square surface roughness to the average arithmetic roughness, as well as with the grain height histograms forming the surface of the studied samples, and are described by a normal statistical distribution.

For GaN:Mn thin films obtained by RF sputtering on Si substrates, the grain size distributions, specifically, by diameter and area, exhibit a more complex behaviour. This can be explained by the formation of non-equilibrium grains on the Si substrate upon the addition of Mn dopant, which changes the film growth mechanism compared to undoped films.

To understand better the AFM surface morphology results of GaN and GaN:Mn thin films, Fig. 6 presents an AFM image of the Si substrate surface onto which the studied samples were deposited.

The AFM image in Fig. 6 shows the surface of the Si substrate, which is characterized by linear traces of mechanical polishing and isolated local protrusions, without signs of morphology formation typical for the surface of films deposited on this substrate.

The surface morphology results of GaN and GaN:Mn thin films obtained by AFM are in good agreement with the results recorded using SEM. Figure 7 shows SEM images of the surface morphology of GaN, GaN:Mn, and GaN:Tb thin films.

The SEM results (Fig. 7) correlate well with the AFM data for GaN and GaN:Mn thin films. The as-deposited undoped GaN thin film is characterized by a fine-grained structure (Fig. 7, *a*), which is confirmed by the smaller average grain sizes determined from the AFM images (Fig. 1 and Table). The SEM images of the surface of GaN:Mn and GaN:Tb samples indicate a significant influence of the impurity and its type on the formation of the film surface morphology. The introduction of Mn impurity leads to an increase in grain size, as evidenced by the increase in their average diameter, area, and volume from AFM data, accompanied by a decrease in surface roughness parameters S_a and S_q (Fig. 1 and Table). In the GaN crystal lattice, Mn atoms relatively easily replace Ga atoms, since the ionic radius of Mn^{2+} (0.66 Å) is close to the ionic radius of Ga^{3+} (0.62 Å) [30]. The grain boundaries in GaN:Mn thin films become more distinct, and the grain peaks appear flatter. In the case of Tb doping, the films exhibit an even larger grain structure, indicating a change in the nucleation and crystallite growth mechanisms. It is likely that the large ionic radius of terbium Tb^{3+} (0.92 Å) [31] creates such strong stresses that the film begins to grow more uneven-

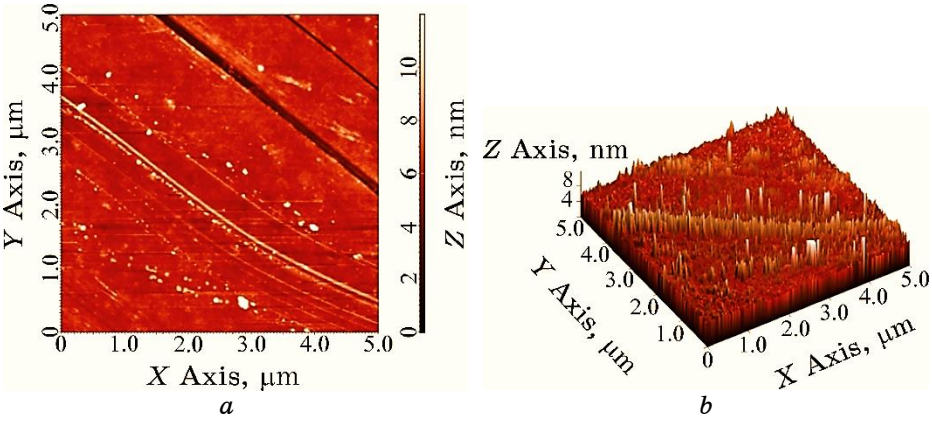

Fig. 6. 2*D* (*a*) and 3*D* (*b*) AFM images of the surface morphology of the Si substrate.

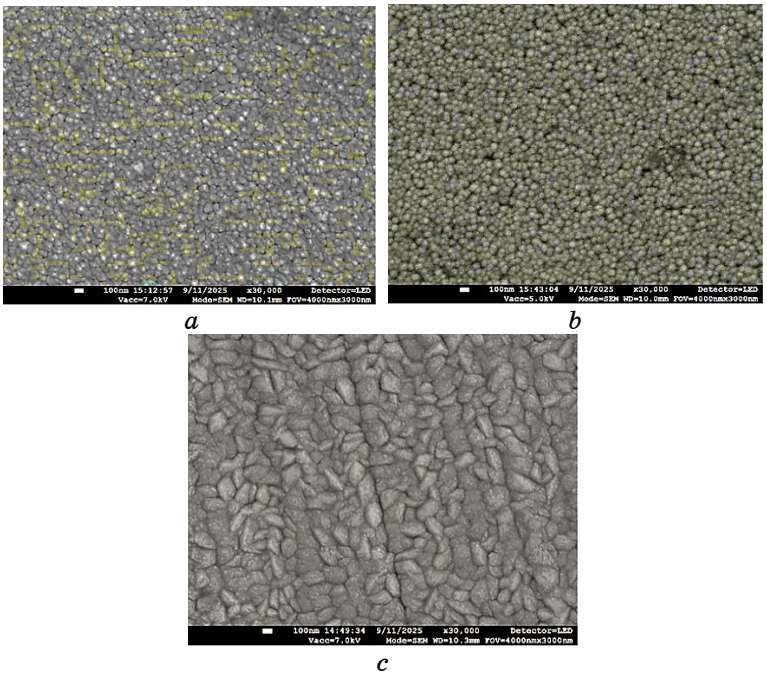

Fig. 7. SEM images of the surface morphology of as-deposited GaN (*a*), GaN:Mn (*b*), and GaN:Tb (*c*) thin films obtained by RF sputtering on Si substrates.

ly with large grain sizes.

The obtained results indicate that transition and rare-earth ele-

ment impurities significantly influence the formation of the surface structure of GaN films.

4. CONCLUSIONS

It has been established that RF ion-plasma sputtering onto single-crystal Si substrates results in the formation of GaN and GaN:Mn thin films composed of nanometer-sized grains. Based on AFM images, it was shown that the average grain diameter is 85 nm for GaN thin films and increases to 166 nm for GaN:Mn films. It was found that for GaN:Mn thin films, the root-mean-square and average-arithmetic surface roughness values are 4.8 and 3.8, respectively, which are 1.3 times lower than the corresponding values for the as-deposited GaN film. Based on the analysis of the grain diameter size distributions, it is shown that GaN films exhibit a unimodal distribution, whereas GaN:Mn films follow a trimodal distribution. Based on the analysis of the grain diameter size distributions, it is proposed that secondary and tertiary grain growth processes occur during the RF sputtering process. Based on the analysis of the grain volume distribution results, it is shown that, in both cases, the grain volume distribution follows a lognormal law. Comparison of AFM and SEM results showed that the surface morphology depends on the type of impurity, and the introduction of Tb^{3+} with a larger ionic radius (0.92 Å) leads to significant structural stresses and the formation of a pronounced coarse-grained structure.

REFERENCES

1. Chunyu Zhao, Swee Tiam Tan, and Hilmi Volkan Demir, *Semicond. Sci. Technol.*, **40**: 073001 (2025); https://doi.org/10.1088/1361-6641/ade81f
2. K. Murakawa, Y. Kawaguchi, M. Usagawa, Y. Tanabe, T. Yokoyama, M. Tonomura, Y. Aoki, K. Takeuchi, and T. Kamikawa, *Optics Express*, **33**, No. 3: 4100 (2025); https://doi.org/10.1364/OE.542386
3. Toshihiko Fukamachi, Junichi Nishinaka, Koichi Naniwae, Shuichi Usuda, Haruki Fukai, Akihiko Sugitani, Masahiro Uemukai, Tomoyuki Tanikawa, and Ryuji Katayama, *Japanese Journal of Applied Physics*, **64**: 022001 (2025); https://doi.org/10.35848/1347-4065/ada903
4. A. Dubey, R. Mishra, Yu-H. Hsieh, Ch.-W. Cheng, B.-H. Wu, L.-J. Chen, S. Gwo, and T.-J. Yen, *Adv. Sci.*, **7**: 2002274 (2020); doi:10.1002/advs.202002274
5. E. Yilmaz, H. Wang, E. Doganci, M. Feng, Q. Sun, A. Mutale, A. Kahraman, U. Gurer, O. Yilmaz, A. Sadigov, F. Ahmadov, and E. Budak, *IEEE Transactions on Electron Devices*, **72**, No. 4: 1993 (2025); doi:10.1109/TED.2025.3539636
6. J. Zhang, L. Deng, S. Xia, C. Guo, K. Liu, L. Chen, W. Liu, H. Xiao, Zh. Yang, W. Guo, and J. Ye, *Semicond. Sci. Technol.*, **39**: 073001 (2024);

https://doi.org/10.1088/1361-6641/ad5100
7. Zitong Fan, *IOP Conf. Series: Materials Science and Engineering*, **738**: 012006 (2020); doi:10.1088/1757-899X/738/1/012006
8. H. J. Lozykowski, W. M. Jadwisienczak, and I. Brown, *Materials Science and Engineering: B*, **81**, Iss. 1–3: 140 (2001); https://doi.org/10.1016/S0921-5107(00)00697-8
9. J. Laski, J. H. Tao, K. Mishra, D. Hamby, M. Raukas, K. Klinedinst, J. McKittrick, J. B. Talbot, N. Perea-Lopez, and G. Hirata, *ECS Transactions*, **16**, No. 31: 123 (2009); https://doi.org/10.1149/1.3112647
10. M. Stachowicz, A. Kozanecki, C.-G. Ma, M. G. Brik, J. Y. Lin, Hx. Jiang, and J. M. Zavada, *Optical Materials*, **37**: 165 (2014); http://dx.doi.org/10.1016/j.optmat.2014.05.018
11. Or H. Chaulker, Yury Turkulets, and Ilan Shalish, *Scientific Reports*, **15**: 18773 (2025); https://doi.org/10.1038/s41598-025-97446-w
12. Wenxuan Wu, Yangye Pan, Xiaodong Gao, Xiaodan Wang, Sida Wei, Jiahao Sun, Xionghui Zeng, Shunan Zheng, and Ke Xu, *J. Phys. D: Appl. Phys.*, **58**: 135101 (2025); https://doi.org/10.1088/1361-6463/ada8bb
13. Michael Alexander Reshchikov, Benjamin McEwen, and Shadi Shahedipour-Sandvik, *phys. status solidi (b)*, **262**: 2400656 (2025); doi:10.1002/pssb.202400656
14. Y. Xiong, M. Sadek, and R. Chu, *Semicond. Sci. Technol.*, **40**: 033002 (2025); https://doi.org/10.1088/1361-6641/adb32d
15. H. Amano, Y. Baines, E. Beam, Matteo Borga, T. Bouchet, Paul R. Chalker, M. Charles, Kevin J. Chen, Nadim Chowdhury, Rongming Chu, Carlo De Santi, Maria Merlyne De Souza, Stefaan Decoutere, L. Di Cioccio, Bernd Eckardt, Takashi Egawa, P. Fay, Joseph J. Freedsman, L. Guido, Oliver Häberlen, Geoff Haynes, Thomas Heckel, Dilini Hemakumara, Peter Houston, Jie Hu, Mengyuan Hua, Qingyun Huang, Alex Huang, Sheng Jiang, H. Kawai, Dan Kinzer, Martin Kuball, Ashwani Kumar, Kean Boon Lee, Xu Li, Denis Marcon, Martin März, R. McCarthy, Gaudenzio Meneghesso, Matteo Meneghini, E. Morvan, A. Nakajima, E. M. S. Narayanan, Stephen Oliver, Tomás Palacios, Daniel Piedra, M. Plissonnier, R. Reddy, Min Sun, Iain Thayne, A. Torres, Nicola Trivellin, V. Unni, Michael J. Uren, Marleen Van Hove, David J. Wallis, J. Wang, J. Xie, S. Yagi, Shu Yang, C. Youtsey, Ruiyang Yu, Enrico Zanoni, Stefan Zeltner, and Yuhao Zhang, *J. Phys. D: Appl. Phys.*, **51**: 163001 (2018); https://doi.org/10.1088/1361-6463/aaaf9d
16. C. Braun, L. Mereacre, Z. Chen, and A. Slabon, *Scientific Reports*, **12**: 2503 (2022); https://doi.org/10.1038/s41598-022-06148-0
17. Heesoo Kim, Anh Thi Dieu Nguyen, Beomjun Kim, Hyerin Jo, Imasda Rahmatulloh, Hyobin Yoo, Hongseok Oh, Aziz Ahmed, Hyeonjun Beak, and Kunook Chung, *NPG Asia Materials*, **17**: 13 (2025); https://doi.org/10.1038/s41427-025-00594-8
18. Mandar A. Kulkarni, Hyesu Ryu, Sohyeon Park, Tae Kyoung Kim, Sangjin Min, Seung Hyun Shin, Hamza Thaalbi, Fawad Tariq, Sang Hyun Lee, Ho Won Jang, Joon Seop Kwak, Dong-Soo Shin, Pyoung Gug Kim, Sang-Wan Ryu, *Adv. Optical Mater.*, **13**: 2500271 (2025); doi:10.1002/adom.202500271
19. Xiaoqin Yang, Jiawen Lu, Luyu Zhao, Xiaorui Han, Zhongwei Bai, Peiwen Quan, Liangshuai Xie, Liang Li, Haoxuan Sun, Mark Hermann Rummeli,

Bingcheng Luo, and Hong Gu, *Adv. Photonics Res.*, **6**: 2400146 (2025); doi:10.1002/adpr.202400146
20. K. Wasa, M. Kitabatake, and H. Adachi, *Thin Film Materials Technology: Sputtering of Compound Materials* (New York: Springer–William Andrew Inc Publishing: 2004).
21. O. M. Bordun, I. Yo. Kukharskyy, M. V. Protsak, I. I. Medvid, I. M. Kofliuk, Zh. Ya. Tsapovska, and D. S. Leonov, *Nanosistemi, Nanomateriali, Nanotehnologii*, **22**, Iss. 2: 287 (2024); https://doi.org/10.15407/nnn.22.02.287
22. B. Rajesh Kumar and T. Subba Rao, *Digest Journal of Nanomaterials and Biostructures*, **7**, No. 4: 1881 (2012); https://storage.imrpress.com/IMR/DJNB/7/4/1881_RajeshKumar.pdf
23. E. S. Gadelmawla, M. M. Koura, T. M. A. Maksoud, I. M. Elewa, and H. H. Soliman, *Journal of Materials Processing Technology*, **123**, Iss. 1: 133 (2002); https://doi.org/10.1016/S0924-0136(02)00060-2
24. O. M. Bordun, I. Yo. Kukharskyy, M. V. Protsak, I. I. Medvid, I. O. Bordun, I. M. Kofliuk, I. S. Kuz, A. I. Tyslyuk, R. V. Pavlius, and D. S. Leonov, *Nanosistemi, Nanomateriali, Nanotehnologii*, **23**, Iss. 3: 771 (2025); https://doi.org/10.15407/nnn.23.03.0771
25. S. Vézian, F. Natali, F. Semond, and J. Massies, *Physical Review B*, **69**: 125329 (2004); doi:10.1103/PhysRevB.69.125329
26. X. Gao, C. Liu, C. Yin, D. Tao, C. Yang, and B. Man, *Materials Science and Engineering B*, **178**: 349(2013); http://dx.doi.org/10.1016/j.mseb.2012.12.005
27. C. V. Thompson, *Sol. State Phys.*, **55**: 269 (2001); https://doi.org/10.1016/S0081-1947(01)80006-0
28. C. V. Thompson, *J. Appl. Phys.*, **58**: 763 (1985); https://doi.org/10.1063/1.336194
29. J. E. Palmer, C. V. Thompson, and Henry I. Smith, *J. Appl. Phys.*, **62**, No. 6: 2492 (1987); http://dx.doi.org/10.1063/1.339460
30. Yoon Shon Hae Kwon, Deuk Young Kim, and Xiangjun Fan Won Kang, *Jpn. J. Appl. Phys.*, **40**: 5304 (2001); https://doi.org/10.1143/JJAP.40.5304
31. Natalie T. Rice, Ivan A. Popov, Dominic R. Russo, John Bacsa, Enrique R. Batista, Ping Yang, Joshua Telser, and Henry S. La Pierre, *J. Am. Chem. Soc.*, **141**, No. 33: 1 (2019); doi:10.1021/jacs.9b06622

Наносистеми, наноматеріали, нанотехнології
Nanosistemi, Nanomateriali, Nanotehnologii
2026, т. 24, № 1, сс. 189–200
https://doi.org/10.15407/nnn.24.01.0189

PACS numbers: 68.37.Hk, 68.37.Vj, 68.55.A-, 78.20.Ci, 78.40.Fy, 78.67.-n, 81.15.Rs

Study of the Optical and Structural Properties of Cadmium-Oxide Thin Films Prepared Using Chemical Spray Pyrolysis Technique

Mohammed S. Sinjar and Mushtaq Abed Al-Jubbori

College of Education for Pure Sciences,
Department of Physics,
University of Mosul,
41001 Mosul, Iraq

Cadmium oxide (CdO) thin films are synthesized by the chemical spray pyrolysis method on glass. The thin-film substrates are prepared at varying temperatures: 400°C, 450°C, 500°C. The samples are examined using a double beam spectrometer UV–Vis; the absorbance and reflectance spectra of the produced films are measured over a range of wavelengths 310–910 nm in order to study the optical properties of these films. As discovered, the absorbance varies with wavelength. Specifically, we observe that the absorbance behaves in the opposite direction of the transmittance, peaking at 350 nm, after which the absorbance spectrum starts to decay exponentially until the absorbance hits its lowest value at the 700 nm wavelength. The results reveal absorbance spectrum achieving its maximum value at 400°C and lowest value at 500°C. As also observed, the value of the spectrum remains consistent within the range of 700–910 nm; the evaluated energy band gap increases from 2.33 eV to 2.41 eV with the increase of substrate temperature. Furthermore, the results for the optical constants such as the refractive index, extinction coefficient, and absorption coefficient decrease with substrate temperature.

Тонкі плівки оксиду Кадмію (CdO) було синтезовано методом хемічної розпорошувальної струминної піролізи на склі. Тонкоплівкові підкладинки було підготовлено за різних температур: 400°C, 450°C, 500°C. Зразки було досліджено за допомогою двопроменевого UV–Vis-спектрометра; спектри вбирання та відбивання одержаних плівок було виміряно в діяпазоні довжин хвиль 310–910 нм задля вивчення оптичних властивостей цих плівок. Було виявлено, що вбирання змінюється з довжиною хвилі. Зокрема, ми спостерігаємо, що вбирання поводиться протилежним чином щодо пропускання, досягаючи піку при 350 нм, після чого спектер вбирання починає експоненційно спадати, поки вбирання не досягне свого найнижчого значення за довжини хвилі у

700 нм. Результати показали, що спектер вбирання досяг свого максимального значення при 400°C, а найнижчого значення — при 500°C; також було відзначено, що значення спектру залишається стабільним у діяпазоні 700–910 нм, а оцінена ширина забороненої зони збільшується з 2,33 еВ до 2,41 еВ зі збільшенням температури підкладинки. Крім того, результати стосовно оптичних констант, таких як показник заломлення, коефіцієнт екстинкції та коефіцієнт вбирання, зменшуються з температурою підкладинки.

Key words: cadmium oxide, chemical spray pyrolysis, energy gap, absorbance spectrum.

Ключові слова: оксид Кадмію, хемічна розпорошувальна струминна піроліза, заборонена енергетична зона, спектер вбирання.

(Received 30 September, 2024; in revised form, 18 October, 2024)

1. INTRODUCTION

Recent years have seen a significant increase in interest in transparent conducting oxides (TCO) thin films due to their distinct chemical and physical characteristics that set them apart from bulk materials and individual atoms. Because of its uses in optoelectronic devices like solar cells, phototransistors and diodes, transparent electrodes, and gas sensors, researchers have turned their attention to cadmium oxide (CdO) in recent years [1].

Large energy band gaps (bulk CdO is an *n*-type broad band gap semiconductor with a direct band gap of 2.3 eV and an indirect band gap of 1.36 eV), a high transmission coefficient in the visible spectral domain, and remarkable luminescence characteristics are just a few of the materials' many appealing qualities that make CdO thin films appealing.

Over the past decade, numerous techniques have been employed to prepare CdO thin films, including spray pyrolysis [2], oxidation of cadmium films [3], metal organic chemical vapour deposition (MOCVD) [4], sol–gel [5], sputtering [6], vacuum evaporation [7], and reactive pulsed laser deposition [8]. These techniques have all been studied for their electrical and optical properties. It was demonstrated through experimentation that these characteristics are highly dependent on the deposition circumstances and film structure. The size and form of the particles, in addition to deviations from the ideal CdO stoichiometry, determine the intensity of the optical and electrical effects of CdO.

The primary impacts of UV irradiation on thin films are alterations in their thickness, chemical composition, and structure, which result in changes to their electrical and optical properties, accord-

ing to several recent researches [9–12]. When silicon oxide thin films were exposed to airborne UV light, Bradford *et al.* [11, 12] noticed changes in the films' optical characteristics and explained these changes as the result of an increase in oxygen molecules or atoms in the deposited films. Electrons are excited by UV light and move from the valence to the conduction band, creating holes in the process. Redox interactions with the surface species can be started by the photogenerated electron–hole pairs that move to its surface [10, 13, 14]. When TiO_2 films are subjected to UV irradiation, two distinct and independent processes take place, according to Fernández–Rodríguez *et al.* [10]: changes in the contact angle. These alterations mostly impact the film surfaces, and the majority of the material is probably going to undergo oxygen incorporation and rearrangement. We are curious as to whether these changes brought about by UV irradiation might also have an impact on its other characteristics. This research aims to examine how UV irradiation affects the optical characteristics and structure of CdO thin films.

CdO films can be grown using a variety of methods, including thermal evaporation [5], sputtering [6], pulsed laser deposition [7], molecular beam epitaxy [8], spray pyrolysis [4], and metal organic chemical vapour deposition (MOCVD) [9, 10]. However, despite its great promise, the formation of films thinner than 100 nm of this material has not been well studied, that is, to the best of our knowledge, and no results have been found in the literature as of yet. The paucity of reports may be explained by the challenges in regulating the growth parameters to promote lateral development when growing into substrates [11], where flat surfaces with varying growth rates are essential.

However, because of their unique nucleation characteristics and the lack of a substantial number of nucleation sites on the substrate, some research on the growth of this material reveals the challenges in obtaining high densities of isolated nanoparticles of CdO on substrates [12]. Some growth restrictions on flat thin layers with good crystalline quality may also stem from this challenge.

2. EXPERIMENTAL DETAILS

2.1. Sample Preparation

The process of preparing CdO solution is done using cadmium acetate [$(CH_3COO)_2Cd_2H_2O$] [M.W. = 266.53 gm/m]. It is a white powder of American origin provided by (SIGMA CHEMICAL CO). To prepare a solution with a concentration of 0.1 M at room temperature, 2.6653 gm is dissolved using a sensitive four-level electronic balance of cadmium acetate to be dissolved in 100 mL of distilled water and the

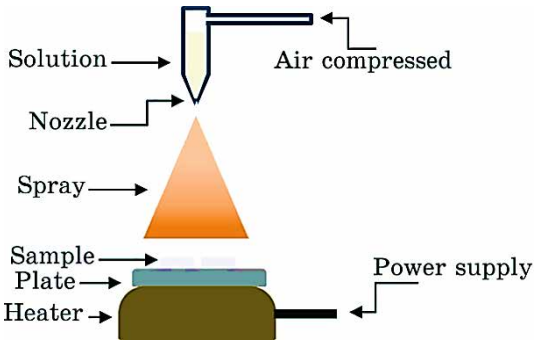

Fig. 1. Experimental setup of the spray pyrolysis technique.

two materials are mixed well using a magnetic stirrer at a temperature of 40°C for 10 min to ensure the homogeneity of the solution, which results in a colourless solution like water. Then, the solution is filtered through filter paper to obtain a clear solution without any sediments or possible impurities. Square glass slides with dimensions of 2.5 cm and an area of 6.25 cm^2 are used, where they are cleaned well in three stages to ensure obtaining completely clean slides. These three stages begin by cleaning them using running water with soap solution for 3 min to remove traditional dirt, then immersing them in acetone and placing them in the ultrasonic device for 15 min, and finally washing them with distilled water and then drying them using hot air for 120 sec.

The prepared substrates are placed on the surface of an electric heater to obtain the required temperature as shown in Fig. 1. The deposition time is set at 10 sec at a rate of 20 sprays with a 3 min pause between each two sprays. The vertical distance between the nozzle of the spray device and the glass substrate is 30 cm and the temperature of the substrates is fixed at 400, 450, and 500°C and a total of 20 sprays for each temperature. The air pressure is set at 2 bars. The details of the spraying process are mentioned in Table.

3. RESULTS AND DISCUSSIONS

3.1. The Optical Absorption Analysis

The interaction of light with CdO thin films was studied to learn more about the optical properties. We used UV–Vis spectroscopy (Shimadzu UV-1800) to characterize the optical properties of CdO thin films at a scanning rate of 400 nm/min and the absorption spectra were obtained from 190–1100 nm). When light interacts with the thin film, an optical absorption process occurs against the

TABLE. Parameters for the spray deposition of the films.

Spray parameters	Optimum value/item
$(CH_3COO)_2Cd_2H_2O$ solution concentration	0.1 M
Nozzle	Glass
Nozzle–substrate distance	30 cm
Solvent	Distilled water
Carrier gas	Compressed air
Pressure	2 bar
Solution flowrate	5 mL/min
Substrate temperature	400, 450, 500°C

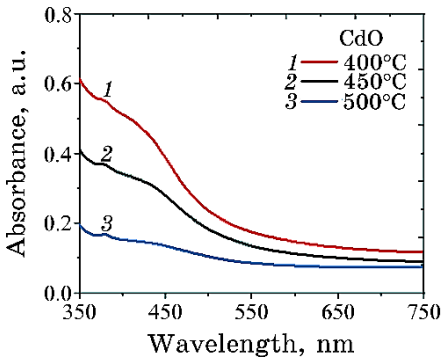

Fig. 2. UV–Vis absorbance curves of CdO films as a function of substrate temperature.

wavelength spectra of the thin films deposited at different temperatures of the glass substrates on which they were deposited. Figure 2 shows a decrease in absorption with increasing temperature. The spectra also showed a clear decrease in absorption at long wavelengths, indicating the presence of direct optical transition in the thin films, as well as a shift to red with increasing temperatures of the glass substrates. High temperatures can affect structural properties such as crystallinity, grain size, and defect density, which in turn affect the optical behaviour of the material.

The surface plasmon resonance (SPR) peak of CdO thin films on glass was observed at 350 nm. The peak shape is due to the light scattering caused by the CdO thin films and the peak position due to the absence of agglomeration in the nanoparticles deposited on the glass and the interactions between CdO particles and different substrates. It is worth noting that the UV–Vis spectrum of CdO nanoparticles on glass substrate shows only the SPR peak corresponding to the in-plane dipole. Crystallization is enhanced at higher temperatures during the

growth of the thin film better, the density of defects such as grains and dislocations decreases and, as a result, the light absorption by these defects decreases. This in turn leads to a decrease in the overall absorption. Higher temperatures can also facilitate the growth of smoother film surfaces by enhancing the mobility and diffusion of nanoparticles on the surface. Reducing the surface roughness reduces light scattering and increases the light transmission through the film. This also leads to a decrease in absorption. The colour of the CdO film changes from light brown to dark brown with increasing temperature of the glass substrates.

The incident photon energy as well as the properties of the material itself have an impact on a materials' absorption coefficient. According to Beer's law, the transmission (T) and reflection (R) spectra are related to the absorption coefficient [12]:

$$\alpha = \frac{1}{d}\log\left[\frac{(1-R)^2}{2T} + \frac{(1-R)^2}{\sqrt{2T^2+R^2}}\right], \tag{1}$$

where d is the thickness of the sample. The absorption coefficient (α) at the wavelength of maximum absorption decreases with the increased substrate temperatures of CdO thin films as shown in Fig. 3.

An important factor affecting a materials' optical and electronic properties is the optical band gap $E_g^{opt.}$. The optical band gap of the CdO thin films was determined using the Tauc plot and calculated by fitting the equation to the data of Ref. [13]:

$$(\alpha h\nu)^{1/2} = k\left(h\nu - E_g^{opt.}\right), \tag{2}$$

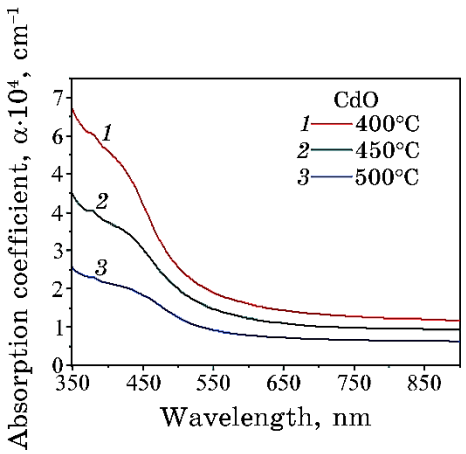

Fig. 3. Absorption coefficient of CdO thin films as a function of wavelength with difference substrate temperatures.

where r is a number that indicates the type of electronic transition that causes the absorption and takes values of 1/2 or 2/3 for direct transitions and 2 or 3 for indirect ones, depending on whether the transition is allowed or forbidden, respectively. $h\nu$ is the photon energy; α is the absorption coefficient, and B is a constant of effective mass. Figure 4 presents the optical energy gap increasing with increasing substrate temperatures.

The refractive index (n) describes how a beam propagates through a transparent medium. The optical parameters of the samples can be used to determine the refractive index using the following relationship [14]:

$$n = \left(\frac{1+R}{1-R}\right) + \sqrt{\frac{4R}{(1-R)^2} - K^2}\,. \tag{3}$$

Reflectivity (R) is calculated from absorption and transmission spectra using the law of conservation of energy [$R = 1 - T - A$]. On the other hand, the extinction coefficient (K) depends on the absorption coefficient and wavelength of the incident beam and is given by [15]

$$K = \frac{\alpha\lambda}{4\pi}\,. \tag{4}$$

The refractive index and the extinction coefficient against wavelength are given in Eq. (3) and Eq. (4). It can be seen that n and K of CdO thin films decreases with increasing substrate temperatures, and, in the visible region, when thin films are deposited onto a sub-

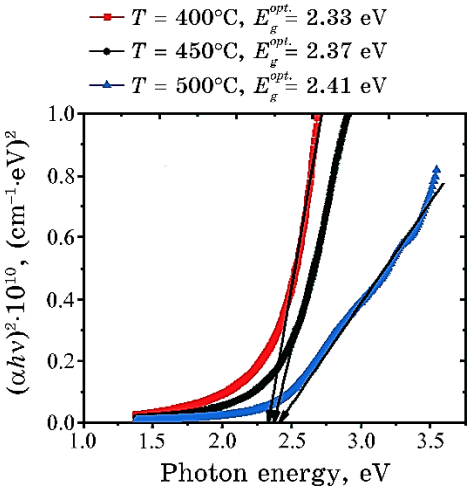

Fig. 4. Optical band gap values for prepared CdO thin films for different substrate temperatures.

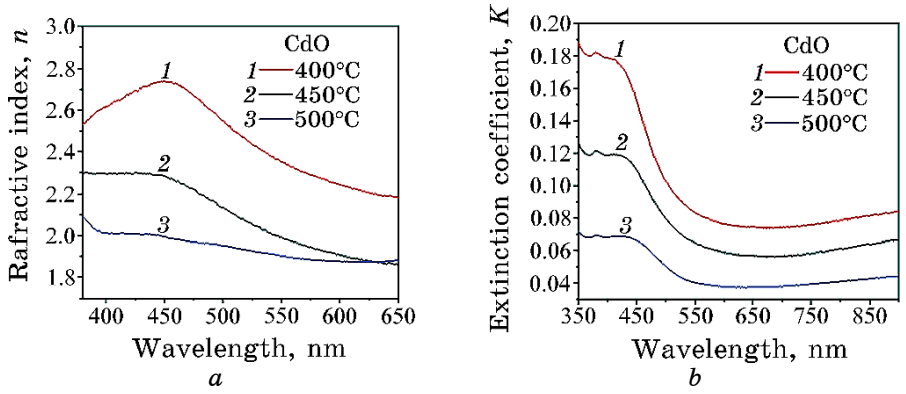

Fig. 5. Refractive index (*a*) and extinction coefficient (*b*) as a function of wavelength for CdO thin films for different substrate temperature.

strate at higher temperatures, they tend to have improved crystallinity and reduced defects. In the case of CdO thin films, increasing the substrate temperature can lead to better crystallization and larger grain sizes, which can result in reduced light scattering and absorption. This, in turn, leads to a decrease in both the refractive index and extinction coefficient as displayed in Fig. 5.

The complex dielectric constant caused by photon interactions with medium charges is commonly referred to as polarization. Using Maxwell's relations, evaluation the real (ε_r) and imaginary (ε_i) parts of the dielectric constant can be calculated for optical wavelengths based on optical constants. The refractive index and extinction coefficient are connected to the real and imaginary of the dielectric constant through the following relationships [16]:

$$\varepsilon_r = n^2 - K^2, \ \varepsilon_i = 2nK. \tag{5}$$

The real and imaginary dielectric constants of CdO thin films decrease with increasing substrate temperatures and in the visible region as are plotted in Fig. 6. Nanoparticles size in CdO thin films can be affected by increasing the substrate temperature. The materials' dielectric properties are impacted by changes in bandgap and carrier concentration, as, especially in the visible range. Consequently, the real and imaginary dielectric constants decrease.

The optical conductivity CdO thin films can be determined using the correlation between the absorption coefficient and the refractive index [16]:

$$\sigma_{opt.} = \frac{\alpha nc}{4\pi}, \tag{6}$$

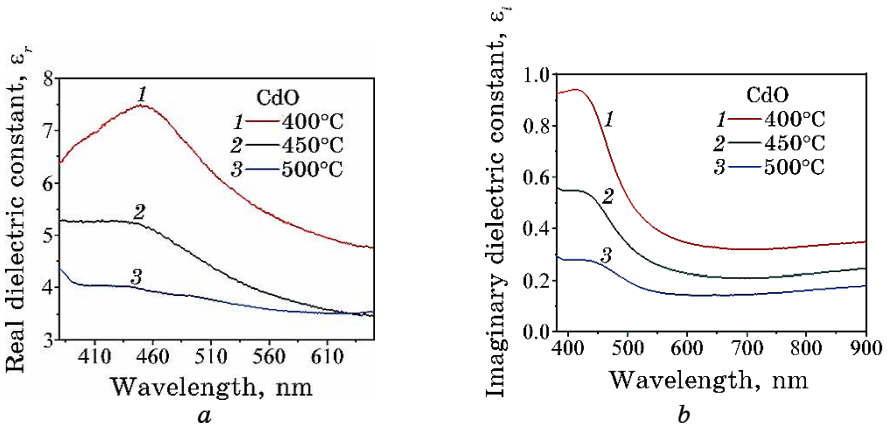

Fig. 6. Real dielectric constants (*a*) and imaginary dielectric constants (*b*) as functions of wavelength for CdO thin films for different substrate temperature.

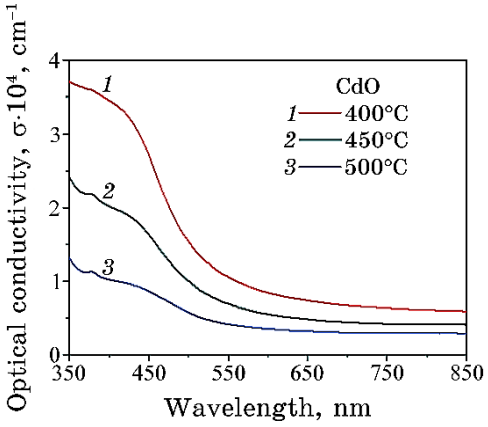

Fig. 7. Optical conductivity as a function of wavelength for CdO thin films for different substrate temperature.

where c is the speed of light in a vacuum. The decrease in optical conductivity can be attributed to decrease for absorption coefficient and the refractive index with increasing the substrate temperature, as shown in Fig. 7.

3.2. Field Emission–Scanning Electron Microscopy (FE–SEM) Results

Utilizing the FE–SEM analysis at a 200k× magnification, it possible to analyse the morphology and particle size distribution of CdO thin

films for different substrate temperature.

With increasing substrate temperature, the nanoparticles of CdO become larger due to the heightened kinetic energy of the particles, rendering them more susceptible to diffusion and coalescence, leading to the formation of larger particles. Consequently, a denser and less porous membrane is formed, exhibiting greater cohesion. More-

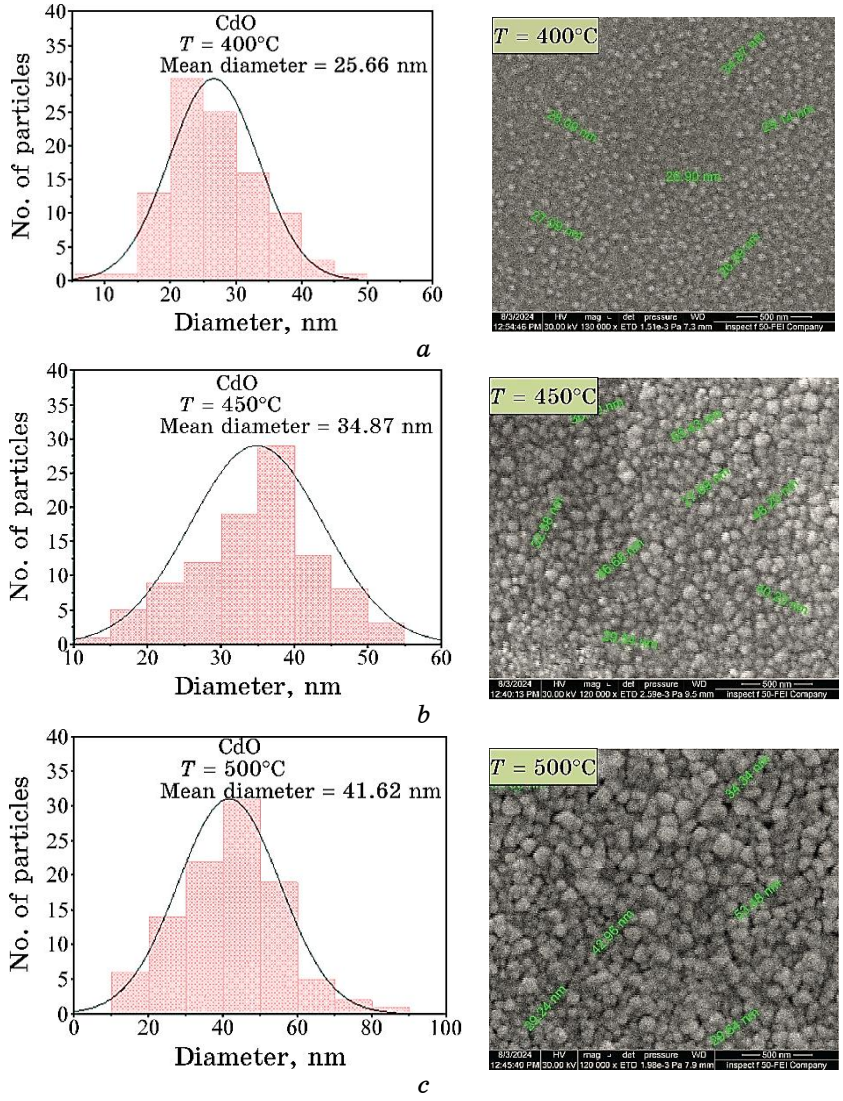

Fig. 8. FE–SEM micrographs of CdO thin films for different substrate temperature and the particle size distribution for (*a*) 400°C, (*b*) 450°C, and (*c*) 500°C.

over, the shape of the membrane particles is also affected, as the particles tend to become more spherical with increasing substrate temperature. This is because of the increasing in temperature reduces the surface tension on the membrane particles, allowing them to adopt a more stable shape.

The FE–SEM images in Fig. 8 clearly show that CdO-nanoparticles' diameters with a size range of 25, 34, and 41 nm for 400, 450, and 500°C, respectively. Finally, the FE–SEM results are in good agreement with the results of UV–Vis analysis.

4. CONCLUSIONS

Cadmium oxide thin films can be easily and low-cost produced by chemical spray pyrolysis technique. The optical properties show that the optical constants such as refractive index, extinction coefficient, dielectric constants and optical conductivity decreases with increasing substrate temperature. In addition, the surface morphology of CdO thin films is a sphere-like shape and diameters increasing with substrate temperature. The average particles size range of 25, 34 and 41 nm for 400, 450, and 500°C, respectively.

ACKNOWLEDGEMENTS

The authors would like to express their warmest thanks to the University of Mosul, College of Education for Pure Science, Department of Physics for supporting this work.

REFERENCES

1. Yoon-Heung Tak, Ki-Beom Kim, Hyoung-Guen Park, Kwang-Ho Lee, and Jong-Ram Lee, *Thin Solid Films*, **411**, Iss. 1: 12 (2002); https://doi.org/10.1016/S0040-6090(02)00165-7
2. Seval Aksoy, Yasemin Caglar, Saliha Ilican, and Mujdat Caglar, *Int. J. Hydrogen Energy*, **34**, Iss. 12: 5191 (2009); https://doi.org/10.1016/j.ijhydene.2008.09.057
3. C. Danţuş, G. G. Rusu, M. Dobromir, and M. Rusu, *Appl. Surf. Sci.*, **255**, Iss. 5: 2665 (2008); https://doi.org/10.1016/j.apsusc.2008.07.176
4. Antonino Gulino and Giovanni Tabbi, *Appl. Surf. Sci.*, **245**, Iss. 1–4: 322 (2005); https://doi.org/10.1016/j.apsusc.2004.10.026
5. D. M. Carballeda-Galicia, R. Castanedo-Pérez, O. Jiménez-Sandoval, S. Jiménez-Sandoval, G. Torres-Delgado, and C. I. Zúciga-Romero, *Thin Solid Films*, **371**, Iss. 1–2: 105 (2000); https://doi.org/10.1016/S0040-6090(00)00987-1
6. Qiang Zhou, Zhenguo Ji, BinBin Hu, Chen Chen, Lina Zhao, Chao Wang, *Mater. Lett.*, **61**, Iss. 2: 531 (2007); https://doi.org/10.1016/j.matlet.2006.05.004
7. A. A. Dakhel and F. Z. Henari, *Cryst. Res. Technol.*, **38**, Iss. 11: 979 (2003);

https://doi.org/10.1002/crat.200310124
8. Raid A. Ismail, Bassam G. Rasheed, Evan T. Salm, and Mukram Al-Hadethy, *J. Mater. Sci.: Mater. Electron.*, **18**: 1027 (2007); https://doi.org/10.1007/s10854-007-9129-4
9. Khalaf Ajaj, Abdullah M. Ali, and Mushtaq Abed Al-Jubbori, *Nanosistemi, Nanomateriali, Nanotehnologii*, **22**, Iss. 1: 209 (2024); https://doi.org/10.15407/nnn.22.01.209
10. M. Fernández-Rodríguez, V. J. Rico, A. R. González-Elipe, and A. Álvarez-Herrero, *phys. stat. sol. (c)*, **5**: 1164 (2008); https://doi.org/10.1002/pssc.200777790
11. A. P. Bradford, G. Hass, M. McFarland, and E. Ritter, *Appl. Opt.*, **4**, Iss. 8: 971 (1965); https://doi.org/10.1364/AO.4.000971
12. Alan P. Bradford and Georg Hass, *J. Opt. Soc. Am.*, **53**: 1096 (1963); https://doi.org/10.1364/JOSA.53.001096
13. Yunxia Wang, Hongling Wang, and Fengyuan Yan, *Surf. Interface Anal.*, **41**, Iss. 5: 399 (2009); https://doi.org/10.1002/sia.3039
14. Kenichi Katsumata, Akira Nakajima, Tadashi Shiota, Naoya Yoshida, Toshiya Watanabe, Yoshikazu Kameshima, and Kiyoshi Okada, *J. PhotoChem. Photobiol. A*, **180**, Iss. 1–2: 75 (2006); https://doi.org/10.1016/j.jphotochem.2005.09.023
15. M. Zaien, N. M. Ahmed, and Z. Hassan, *Mater. Lett.*, **105**: 84 (2013); https://doi.org/10.1016/j.matlet.2013.04.070
16. Q. Zhou, Z. Ji, B. Hu, C. Chen, L. Zhao, and C. Wang, *Mater. Lett.*, **61**: 531 (2007); http://dx.doi.org/10.1016/j.matlet.2006.05.004
17. B. J. Zheng, J. S. Lian, L. Zhao, and Q. Jiang, *Vacuum*, **85**, Iss. 9: 861 (2011); http://dx.doi.org/10.1016/j.vacuum.2011.01.002
18. A. B. M. A. Ashrafi, H. Kumano, I. Suemune, Y. W. Ok, and T. Y. Seong, *J. Cryst. Growth*, **237–239**: 518 (2002); http://dx.doi.org/10.1016/S0022-0248(01)01956-X
19. L. C. S. Murthy and K. S. R. K. Rao, *Bull. Mater. Sci.*, **22**: 953 (1999); https://doi.org/10.1007/BF02745685
20. J. Zúniga-Pérez, C. Martínez-Tomás, and V. Munoz-Sanjosé, *physica status solidi (c)*, **2**, Iss. 3: 1233 (2005); http://dx.doi.org/10.1002/pssc.200460672
21. D. Lamb and S. J. C. Irvine, *Thin Solid Films*, **518**, Iss. 4: 1222 (2009); https://doi.org/10.1016/j.tsf.2009.05.067
22. Y. J. Chen, Y. Y. Shih, C. H. Ho, J. H. Du, and Y. P. Fu, *Ceram. Int.*, **36**, Iss. 1: 69 (2010); http://dx.doi.org/10.1016/j.ceramint.2009.06.018
23. Sreekumar Rajappan Achary, Said Agouram, Juan F. Sánchez-Royo, M. Carmen Martínez-Tomás, and Vicente Mucoz-Sanjosé, *RSC Adv.*, **4**, Iss. 44: 23137 (2014); http://dx.doi.org/10.1039/c4ra01818d
24. Isha Saini, Jyoti Rozra, Navneet Chandak, Sanjeev Aggarwal, Pawan K. Sharma, and Annu Sharma, *Materials Chemistry and Physics*, **139**, Iss. 2–3: 802 (2013); https://doi.org/10.1016/j.matchemphys.2013.02.035
25. J. Tauc, R. Grigorvici, and A. Vancu, *physica status solidi (b)*, **15**, Iss. 2: 627 (1966); https://doi.org/10.1002/pssb.19660150224
26. M. Rashidian and D. Dorranain, *J. Theor. Appl. Phys.*, **8**: Article No. 121 (2014); https://doi.org/10.1007/s40094-014-0121-0
27. A. Kurt, *Turkish Journal of Chemistry*, **34**, Iss. 1: 67 (2010); https://doi.org/10.3906/kim-0903-29
28. Dinesh Babu K, Philominathan P, and Murali K, *Optik*, **186**, Iss. 3: 350 (2019); https://doi.org/10.1016/j.ijleo.2019.03.048

Наносистеми, наноматеріали, нанотехнології
Nanosistemi, Nanomateriali, Nanotehnologii
2026, т. 24, № 1, сс. 201–209
https://doi.org/10.15407/nnn.24.01.0201

PACS numbers: 78.20.Ci, 78.40.Fy, 78.66.-w, 79.20.Eb, 81.20.Fw, 81.40.Tv, 81.70.Fy

Synthesis and Characterization of Cadmium-Oxide Thin Films Prepared by Sol–Gel Spin Coating Method

Mohammed Al-Badrani, Yasir Yahya Kassim, and Mutaz Salih Hasan Aljuboori

College of Education for Pure Sciences,
Department of Physics,
University of Mosul,
41001 Mosul, Iraq

In this work, cadmium-oxide films are prepared using the spin-coating technique. The study is focused on clarifying the effect of changing the thickness of the film on the optical properties of cadmium-oxide films deposited on 1.5×2 cm^2 glass substrates at a temperature of 400°C. The behaviour of the visible and ultraviolet absorption spectra of cadmium-oxide films are also studied as functions of wavelength. These results show that the intensity of absorption increases with increasing membrane thickness; this indicates an increase in the concentration of the membrane material. Some optical constants are also studied, such as the index of refraction and the real and imaginary dielectric constants, in addition to the extinction coefficient and electrical conductivity. As found, their values change with increasing film thickness. Through the absorption spectrum, the optical energy gap is calculated, and it is found that there is a slight change with increasing film thickness, as its value decreases from 2.22 eV to 2.20 eV, when the film thickness increases from 143 nm to 368 nm.

У цій роботі плівки оксиду Кадмію було одержано нанесенням покриття методом центрифуґування. Дослідження зосереджено на з'ясуванні впливу зміни товщини плівки на оптичні властивості плівок оксиду Кадмію, нанесених на скляні підкладинки площею 1,5×2 $см^2$ за температури у 400°C. Також досліджено поведінку спектрів видимого й ультрафіолетового вбирання плівок оксиду Кадмію як функцій довжини хвилі. Ці результати показують, що інтенсивність вбирання зростає зі збільшенням товщини мембрани, що вказує на збільшення концентрації матеріялу мембрани. Також досліджено деякі оптичні константи, такі як показник заломлення та дійсна й уявна діелектричні константи, на додаток до коефіцієнта екстинкції й електропровідности. Було виявлено, що всі їхні значення змінюються зі збільшенням товщини плівки. За допомогою спектру вбирання було розраховано ширину оп-

тичної забороненої зони та виявлено, що спостерігається незначна зміна зі збільшенням товщини плівки, оскільки її значення зменшується з 2,22 еВ до 2,20 еВ, коли товщина плівки збільшується від 143 нм до 368 нм.

Key words: cadmium oxide, spin coating, energy gap, absorbance spectrum.

Ключові слова: оксид Кадмію, одержані методом центрифуґування покриття, заборонена енергетична зона, спектер вбирання.

(Received 28 November 2024)

1. INTRODUCTION

In recent years, there has been a notable surge in interest in transparent conducting oxides (TCO) thin films, attributed to their unique chemical and physical properties that differentiate them from bulk materials and individual atoms [1].

Cadmium oxide (CdO), characterized by a direct optical band gap ranging from 2.2 eV to 2.7 eV and exhibiting *n*-type conductivity, is frequently employed in applications including spintronics, transparent electronics, optoelectronics, and sensors. Cadmium oxide (CdO) is a commonly favoured material for applications such as photodiodes, gas sensors, solar cells, and anti-reflective coatings [2–4]. Cadmium oxide (CdO) is regarded as a potential material for photovoltaic applications owing to its elevated electrical conductivity and optical transmittance in the visible spectrum. CdO thin films are produced using various deposition processes, including pulsed-laser deposition (PLD) and spray pyrolysis, chemical bath deposition, hydrothermal synthesis, and magnetron sputtering. In comparison to these approaches, the sol–gel process is effective for creating metal oxide coatings as it achieves a homogeneous structure and can be maintained under the management of each phase necessitates uncomplicated apparatus and is applicable at reduced temperatures. The sol–gel spin-coating technique involves the solutions formulated for the films and is applied to a substrate, which is subsequently spun at varying velocities and durations. The solution is applied to this base to create a film [5]. The spin-coating process allows for the straightforward diversification of required films, modifying parameters including film thickness, rotation speed, and rotation duration, number of coatings, solution volume, and annealing temperature. This approach is favoured because of its cost-effectiveness and rapid manufacturing capabilities [6]. As discovered, the thermal treatment of CdO thin films after deposition at different annealing temperatures reveals significant modifications in their opti-

cal and structural characteristics [7].

This work aims to prepare thin films of cadmium oxide using the sol–gel spin-coating technique, to study their optical properties, and to demonstrate the effect of film thickness and temperature on those properties.

2. EXPERIMENTAL DETAILS

2.1. Preparation of the Solution

The solution was prepared by dissolving 1.33 gm of aqueous cadmium acetate [$(CH_3COO)_2Cd_2H_2O$)] in 10 mL of 2-Methoxyethanol and stirring it with a magnetic stirrer for 20 min at room temperature. After that, the temperature of the solution is raised to 70°C. Then, ethanolamine (MONO) is added dropwise to the solution. This process takes 120 min in order to obtain a homogeneous, transparent and colourless solution. The temperature of the final solution is reduced to room temperature, then, filtered using filter paper, and then, left for 24 hours.

2.2. Preparation of Glass Substrates

A glass substrate with dimensions 1.5×2 cm was prepared. These substrates are cleaned by first washing them with water for 3 min, then, they are immersed in a solution (distilled water + acetone) with 20% acetone. The substrates and the solution are placed in the ultrasound machine for 15 min at room temperature. The slides are cleaned then with distilled water for 3 min and dried then using hot

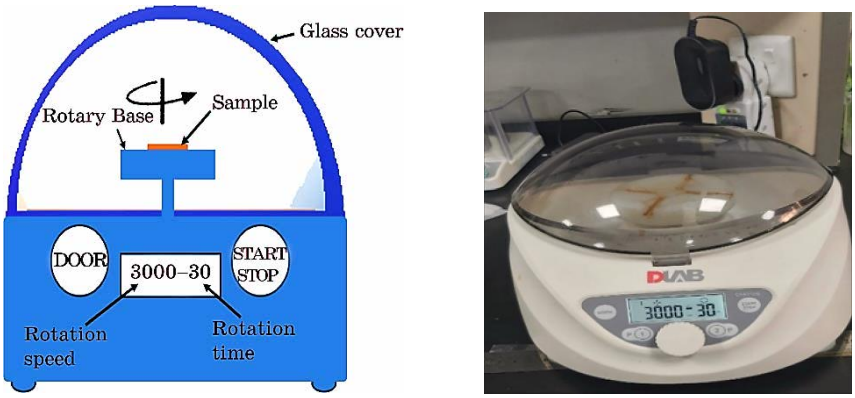

Fig. 1. (*a*) Device diagram for spin coating; (*b*) photo of spin coating.

air for 1 minute. Sample weights are measured using a very sensitive four-stage balance.

2.3. Deposition Process

The sol–gel solution is coated on glass substrates using a device spin coating as shown in Fig. 1. The parameter used was of 3000 rev/min for 30 s. The samples are then dried using an electric heater at a temperature of 200°C for 15 minutes to get rid of solvents and organic contamination. The thin films are then annealed in an oven at temperatures of 400–500°C. Finally, the weights of the samples are measured after the deposition process in order to calculate the thickness of the film prepared by the gravimetric method.

3. RESULTS AND DISCUSSIONS

3.1. The Optical Absorption Analysis

The interaction of light with CdO thin films was studied to learn more about the optical properties. We used a UV–Visible spectrometer (Shimadzu UV-1800) to characterize the optical properties of CdO thin films; the absorption spectra from 190 nm to 1100 nm were obtained. When light interacts with the thin film, an optical absorption process occurs against the wavelength spectra of the thin films deposited at an annealing temperature of 400°C. Figure 2 shows an increase in absorption with increasing film thickness. The spectra also showed a clear increase in absorption, indicating the presence of a direct optical transition in the thin films, as well as a red shift with increasing thickness of the deposited films. High

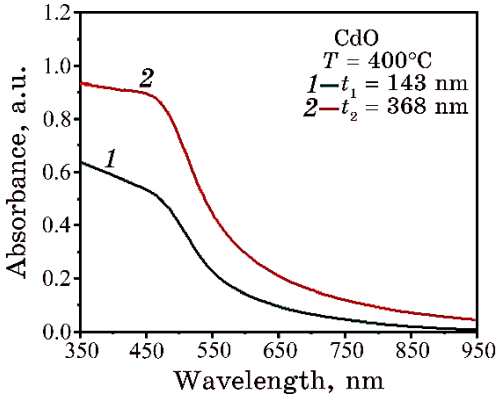

Fig. 2. UV–Vis absorbance curves for CdO films with different thickness.

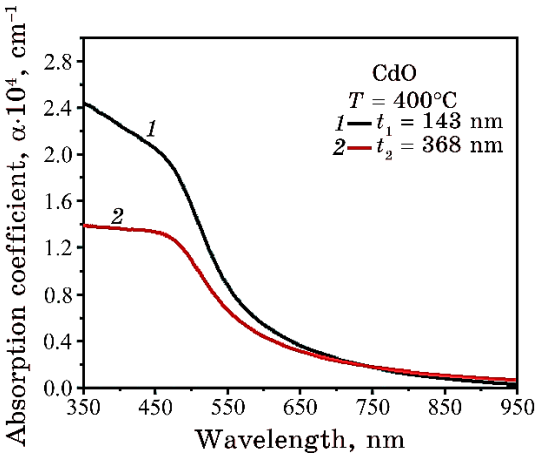

Fig. 3. Absorption coefficient of CdO thin films with difference of film thickness as a function of wavelength.

temperatures in the annealing process can affect structural properties such as crystallinity, grain size, and defect density, which in turn affects the optical behaviour of the material. The surface plasmon resonance (SPR) peak of CdO thin films on glass was observed at 350 nm. The peak shape is due to the light pooling caused by the CdO thin films and the peak position due to the agglomeration of nanoparticles deposited on glass and the interactions between CdO particles and different substrates. It is worth noting that the UV–Vis spectrum of CdO nanoparticles on glass substrate shows only the SPR peak corresponding to the in-plane dipole. Crystallization is enhanced at higher temperatures during thin film growth better, the density of defects such as grains and dislocations decreases and, as a result, the light absorption increases. This in turn leads to the increase in the overall absorption.

The incident photon energy (as well as the properties of the material itself) has an impact on a materials' absorption coefficient. According to Beer's law, the transmission (T) and reflection (R) spectra are related to the absorption coefficient [8]:

$$\alpha = \frac{1}{d}\log\left[\frac{(1-R)^2}{2T} + \frac{(1-R)^2}{\sqrt{2T^2+R^2}}\right], \qquad (1)$$

where d is the thickness of the sample. The absorption coefficient (α) at the wavelength of maximum absorption decreases with increasing membrane thickness of CdO thin films as shown in Fig. 3.

An important factor affecting the materials' optical and electronic properties is the optical band gap $E_g^{opt.}$. The optical band gap of

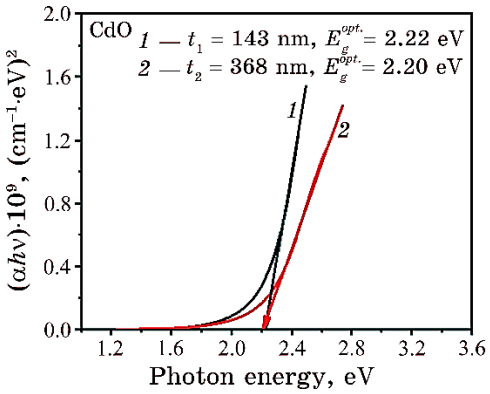

Fig. 4. Optical band gap values of CdO thin films prepared for two different thicknesses.

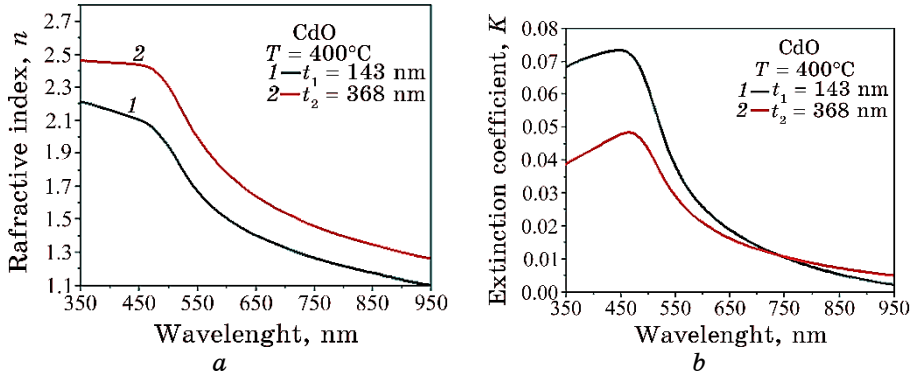

a *b*

Fig. 5. Refractive index (*a*) and extinction coefficient (*b*) as functions of wavelength for CdO thin films with different thicknesses.

the CdO thin films was determined using the Tauc plot and calculated by fitting the equation to the data of Ref. [9]:

$$(\alpha h\nu)^{1/r} = B\left(h\nu - E_g^{opt.}\right), \qquad (2)$$

where r is a number that indicates the type of electronic transition that causes the absorption and takes values of 1/2 or 2/3 for direct transitions and 2 or 3 for indirect ones, depending on whether the transition is allowed or forbidden, respectively. $h\nu$ is the photon energy; α is the absorption coefficient, and B is a constant of effective mass. Figure 4 presents the optical energy gap decreasing with increasing film thickness.

The refractive index (n) describes how a beam propagates through

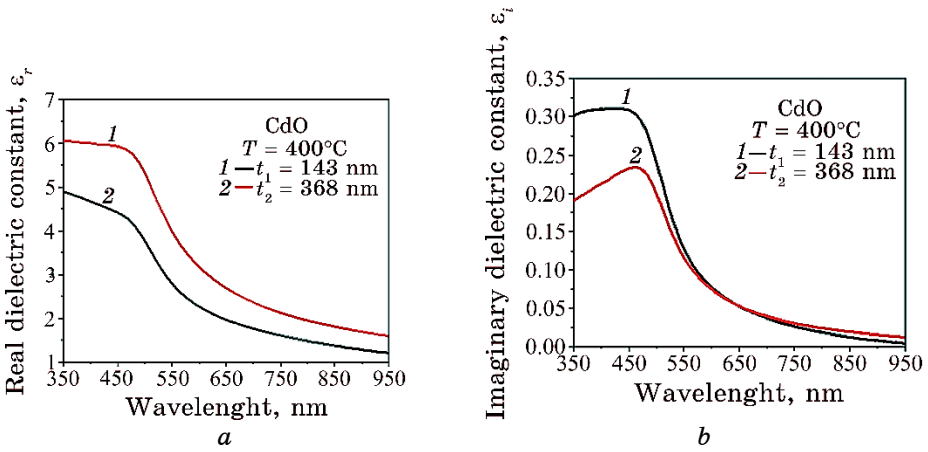

Fig. 6. Real dielectric constants (*a*) and imaginary dielectric constants (*b*) as functions of wavelength for CdO thin films with different thickness.

a transparent medium. The optical parameters of the samples can be used to determine the refractive index using the following relationship [10]:

$$n = \frac{1+R}{1-R} + \sqrt{\frac{4R}{(1-R)^2} - K^2}\,. \tag{3}$$

Reflectivity (R) is calculated from absorption and transmission spectra using the law of conservation of energy ($R = 1 - T - A$). On the other hand, the extinction coefficient (K) depends on the absorption coefficient and wavelength of the incident beam and is given by [11]

$$K = \frac{\alpha\lambda}{4\pi}. \tag{4}$$

The refractive index and extinction coefficient *versus* wavelength are given in Eq. (3) and Eq. (4). It can be seen that the extinction coefficient (K) of CdO thin films decreases and the refractive index (n) increases with increasing film thickness and in the visible region. Increased thickness can result in better crystallinity and larger grain sizes, which can result in reduced light scattering and absorption [12]. This in turn leads to an increase in the refractive index and a decrease in extinction coefficient as shown in Fig. 5.

The complex dielectric constant caused by photon interactions with medium charges is commonly referred to as polarization. Using Maxwell's relations, evaluation of the real (ε_r) and imaginary (ε_i) parts of the dielectric constant can be calculated for optical wave-

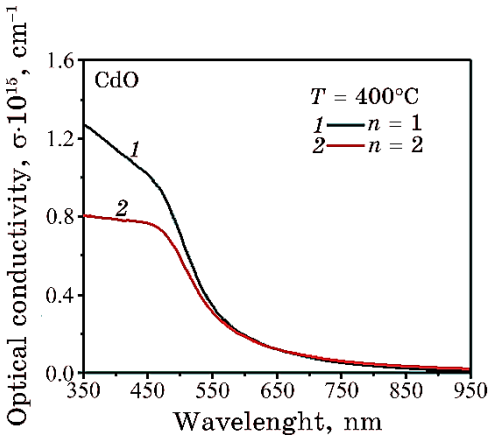

Fig. 7. Optical conductivity as a function of wavelength for CdO thin films for different thickness.

lengths based on optical constants. The refractive index and extinction coefficient are connected to the real and imaginary parts of the dielectric constant through the following relationships [13]:

$$\varepsilon_r = n^2 - K^2 , \ \varepsilon_i = 2nK . \tag{5}$$

It can be seen from Fig. 6 that the real dielectric constant increases, while the amount of the imaginary dielectric constant decreases with the increase in membrane thickness.

The optical conductivity of CdO thin films can be determined using the correlation between the absorption coefficient and the refractive index [12]:

$$\sigma_{opt.} = \frac{\alpha nc}{4\pi} , \tag{6}$$

where c is the speed of light in a vacuum. The decrease in optical conductivity can be attributed to decrease for absorption coefficient and the refractive index with increasing the substrate temperature, as shown in Fig. 7.

4. CONCLUSIONS

It was shown through this research that the thickness of the film has a direct effect on the optical properties of cadmium-oxide films. It was found that the absorption increases with increasing film thickness (t), and this indicates the occurrence of the crystal growth process. By analysing the absorbance spectrum using a UV–

Vis device, it was found that the refractive index, the real dielectric constant, and the optical conductivity increase with increasing film thickness, but that both the extinction coefficient and the imaginary dielectric constant decrease with increasing film thickness. It was also found that the optical energy gap decreases slightly from 2.22 eV to 2.20 eV with increasing film thickness from 143 nm to 368 nm.

ACKNOWLEDGEMENTS

The authors would like to express their warmest thanks to the University of Mosul, College of Education for Pure Science, Department of Physics for supporting this work.

REFERENCES

1. M. Abed Al-Jubbori, Omar Ayed, and Kh. Ajaj, *Radiation Physics and Chemistry*, **226**: 112190 (2025); https://doi.org/10.1016/j.radphyschem.2024.112190
2. M. Soylu and H. S. Kader, *J. Electron. Mater.*, **45**, No. 11: 5756 (2016); https://doi.org/10.1007/s11664-016-4819-4
3. J. K. Rajput, T. K. Pathak, V. Kumar, and L. P. Purohit, *Appl. Surf. Sci.*, **409**: 8 (2017); https://doi.org/10.1016/j.apsusc.2017.03.019
4. M. Ramamurthy, M. Balaji, and P. Thirunavukkarasu, *Optik*, **127**, No. 8: 3809 (2016); https://doi.org/10.1016/j.ijleo.2016.01.031
5. N. Kati, *Mater. Sci. Pol.*, **37**, No. 1: 136 (2019); https://doi.org/10.2478/msp-2018-0104
6. S. Park, C. H. Kim, W. J. Lee, S. Sung, and M. H. Yoon, *Mater. Sci. Eng. R Rep.*, **114**: 1 (2017); https://doi.org/10.1016/j.mser.2017.01.003
7. J. K. Rajput, T. K. Pathak, V. Kumar, H. C. Swart, and L. P. Purohit, *Phys. B: Condensed Matter*, **535**: 314 (2018); https://doi.org/10.1016/j.physb.2017.08.014
8. R. P. Madden, L. R. Canfield, and G. Hass, *J. Opt. Soc. Am.*, **53**: 620 (1963); https://doi.org/10.1364/JOSA.53.000620
9. Yunxia Wang, Hongling Wang, and Fengyuan Yan, *Surf. Interface Anal.*, **41**: 399 (2009).
10. M. Fernández-Rodríguez, V. J. Rico, A. R. González-Elipe, and A. Álvarez-Herrero, *phys. stat. sol. (c)*, **5**: 1164 (2008); https://doi.org/10.1002/pssc.200777790
11. A. P. Bradford, G. Hass, M. McFarland, E. Ritter, A. P. Bradford, G. Hass, and M. McFarland, *Appl. Opt.*, **4**: 971 (1965); https://doi.org/10.1364/AO.4.000971
12. Khalaf Ajaj, Mushtaq Abed Al-Jubbori, and Abdullah M. Ali, *Radiation Physics and Chemistry*, **216**: 111384 (2024); https://doi.org/10.1016/j.radphyschem.2023.111384
13. Q. Zhou, Z. Ji, B. Hu, C. Chen, L. Zhao, and C. Wang, *Mater. Lett.*, **61**, No. 2: 531 (2007); http://dx.doi.org/10.1016/j.matlet.2006.05.004

Наносистеми, наноматеріали, нанотехнології
Nanosistemi, Nanomateriali, Nanotehnologii
2026, т. 24, № 1, сс. 211–224
https://doi.org/10.15407/nnn.24.01.0211

PACS numbers: 07.07.Df, 78.20.Ci, 78.66.Li, 79.20.Ds, 81.15.Fg, 81.16.Mk, 87.85.fk

Synthesis and Characterization of Nano-CdO:SnO_2 Thin Film for Gas-Sensing Applications

Huda Saadi Ali[1] and Zuheer N. Majeed[2]

[1]*College of Energy and Environmental Sciences,*
Department of Renewable Energy,
Al-Karkh University of Science,
Baghdad, Iraq
[2]*College of Education for Women,*
Kirkuk University,
Kirkuk, Iraq

Motivated by the utility of gas-sensing technology, investigations of thin films of the tin oxide-doped cadmium oxide (CdO:SnO_2) of nanograin size in the range between 10.3 nm and 18.3 nm have been undertaken applying different characterization methods. CdO films doped with nano-SnO_2 contents in the range of 1–3% were deposited on soda lime glass (SLG) substrates at room temperature by pulsed laser deposition (PLD) and succeeded by annealing for 60 min at a temperature of 400°C. The dominant phase for these films shows a hexagonal crystal structure, which is the metastable phase of the doped CdO. Tauc's relation is used for determining the energy band gap (E_g) regarding doped CdO thin films over the photon energy range of 300 nm to 800 nm. A rise in SnO_2 concentrations is accompanied by a reduction in optical transmittance. The Hall effect measurement demonstrates the *n*-type conductivity of our produced films. When the SnO_2 content is of $\cong 0.01$ and the operating temperature is of 300°C, the maximum attainable sensitivity of CdO:SnO_2 mixed films toward nitrogen dioxide (NO_2) gas is achieved in terms of sensing characteristics. The outcomes demonstrate that, with a recovery time of 60 seconds and a response time of 25 seconds, the maximum sensitivity is equivalent to 78.05%. From room temperature to 300°C, the resistance to NO_2 gas is reduced linearly with operating temperature.

Мотивовані корисністю технології газового зондування, дослідження тонких плівок оксиду Кадмію, леґованого оксидом Стануму (CdO:SnO_2), з нанорозміром зерен у діяпазоні від 10,3 нм до 18,3 нм були проведені з використанням різних методів характеризації. Леґовані плівки CdO із вмістом наночастинок SnO_2 у діяпазоні 1–3% були осаджені на підкладинках зі скла з натронного вапна за кімнатної температури методом

імпульсного лазерного осадження з подальшим відпалом упродовж 60 хвилин за температури у 400°C. Домінувальна фаза для цих плівок має гексагональну кристалічну структуру, яка є метастабільною фазою й леґованого CdO. Таукове співвідношення було використано для визначення ширини забороненої зони (E_g) для леґованих тонких плівок CdO в діяпазоні енергій фотонів від 300 нм до 800 нм. Збільшення концентрації SnO_2 супроводжується пониженням оптичного пропускання. Мірян Голлового ефекту демонструє n-тип провідности виготовлених плівок. Коли вміст SnO_2 становить $\cong 0{,}01$, а робоча температура — 300°C, досягається максимально досяжна чутливість змішаних плівок CdO:SnO_2 щодо газоподібного діоксиду Нітроґену (NO_2) з точки зору характеристик чутливости. Результати показують, що за часу відновлення у 60 секунд і часу відгуку у 25 секунд максимальна чутливість еквівалентна 78,05%. Від кімнатної температури до 300°C стійкість щодо газоподібного NO_2 лінійно зменшується з робочою температурою.

Key words: transparent metal oxide, nanothin film, pulse laser deposition, CdO, SnO_2, gas-sensing application.

Ключові слова: прозорий оксид металу, нанотонка плівка, імпульсне лазерне осадження, CdO, SnO_2, застосування в газовій сенсориці.

(Received 26 September, 2024; in revised form, 20 November, 2024)

1. INTRODUCTION

Metal peroxides are interesting since they could be employed as sensors [1], catalysts [2], sources of oxygen in organic synthesis [3], and precursors for metal-oxides' synthesis [4–6]. There are numerous ways to make metal peroxides [6], such as the direct route reaction of oxygen with metal in air (or ammonia) as well as in liquid, the reaction regarding a metal salt with hydrogen peroxide, typically in basic solution, the thermal decomposition of the superoxide, and the electrochemical route. Unfortunately, the majority of currently used techniques have some drawbacks. These include hazardous and complex fabrication processes, costly and difficult-to-find precursors, and poorly crystallized or even impure final products. The automotive industry as well as environmental research in both outdoor and indoor settings, like greenhouse gas monitoring, are only two of the many uses for gas-sensing technologies [1–6].

People are currently aware of the environmental damage caused by industrial emissions. One of such waste gases, NO_2, was linked to an increased risk of developing respiratory diseases in people, including pulmonary edema and asthma, and has raised concerns about environmental pollution on a global scale [7]. Yet, human beings cannot survive in an environment with 3 ppm NO_2 for more than 8 hrs, according to the Health and Safety Rule Alarm [8].

Lately, researchers and industry have become more interested in gas-sensing technology as a common application for intelligent devices. Researchers were exploring a range of options to improve gas-sensing performance because of the limitations and wide range of applications of numerous gas-sensing technologies. Numerous elements, including selectivity, sensitivity, response time, cost, and size, must be taken into account in order to evaluate the effectiveness of gas-sensing systems. A repeatable and stable gas signal throughout time should be shown by gas sensors as well, but structural alterations, composition, appropriate doping materials, and application of the right surface treatment all affect stability [9].

Techniques for gas sensing include liquid chromatography, gas chromatography, electrochemical sensors, acoustic sensors, optical sensors, and chemical resistance sensors. Some of these techniques, for instance, gas and liquid chromatography, and acoustic sensors have limitations of high cost, low sensitivity, slow response, and difficulty in downsizing [10–16]. On the other hand, gas sensors depend on chemical resistance of such polymers, carbon nanotubes, and metal oxide-based sensors have been used to minimize the size of a powerful and cheap device. Among these three types, metal oxides are the most popular type due to their brilliant properties [17–20].

Transparent conducting metal oxides (TCO), like tin oxide (SnO_2), indium oxide (InO), cadmium oxide (CdO), and zinc oxide (ZnO), have been investigated intensively in the last decade. CdO has attracted greater attention than other potential TCO due to its various advantages such as high carrier concentrations and moderate electron mobility [21]. These properties of CdO thin films facilitate its inclusion in different applications such as photodiodes, transparent electrodes, solar cells, and gas sensors [22]. CdO thin films crystallize as a cubic crystal system, and the dominant phase for CdO films exhibits the rock-salt crystal structure, which is the stable phase of CdO [23, 24], but it can also crystallize in metastable phases such as zinc blende, wurtzite, CsCl, and NiAs crystal structure [25]. Polycrystalline CdO thin films could be deposited through various methods, such as metal-oxide chemical vapour deposition (MOCVD), direct current sputtering (DCS) and radio-frequency sputtering (RFS), spray pyrolysis, chemical bath, and pulsed laser deposition (PLD). However, to deposit stoichiometric and tin-doped CdO, PLD is considered as the preferred method [25].

This work aims to find a correlation between the optical, structural, and electrical properties regarding doped CdO thin films with different SnO_2 contents. It is also an attempt to optimize the SnO_2 content for the best sensing ability using crystal structure, grain size, transmission, band gap, carrier concentration, mobility, and sensing characteristics for NO_2 sensing applications.

2. EXPERIMENTAL WORK

Samples were prepared using high-purity cadmium oxide (CdO) powder (99.99%) that was doped with tin oxide (SnO_2) of 99.8%. Samples weighing 3 gm, one of them pure CdO and three samples doped with SnO_2 with impurity percentages of 2, 4, 6% were weighed with a sensitive electronic balance with four decimal places after sorting from. The mixing technique has been utilized for obtaining high homogeneity between the pure CdO granules and the samples doped with SnO_2, where the powders were ground using a ceramic mortar for half an hour; then, the ground powders were placed in plastic boxes containing three balls with a diameter of 0.50 cm. After that, each box was placed inside an English type mixer (Spex) for ten minutes, and then, the mixed powders were compressed with a pressure force of 6 Tons in a special mould (steel stainless) with a diameter of 1.2 cm and a thickness of 0.3 cm for a period of 5 minutes using an American-made hydraulic press manufactured by Across International, as shown in Fig. 1.

To produce CdO tablets before and after doping, we used glass slides as substrates for film growth after cutting them into smaller pieces. To ensure their cleanliness, such glass slides are precleaned through ethanol and distilled water. Subsequently, the glass slides undergo ultrasonic cleaning. Sedimentation system consists of two parts as follow.

1. Laser System. The pulsed Nd:YAG laser manufactured by the company DIAMON-288 pattern EPLS System with a wavelength of 1064 nm, as can be seen in Fig. 2, was used in the process of depositing the prepared patterns on glass bases. The system consists of a power supply and a control system. Using a computer and an internal cooling system, the path of the laser beams is fixed on the target manually, as the laser used has the following specifications: laser energy of 100–1000 mJ (energy used is of 600 mJ); frequency 6–1 Hz (frequency used is of 6 Hz); laser wavelength $\lambda = 1064$ nm; duration of each pulse = 10 nsec and a number of 100 pulses at room temperature, as the incident laser rays create an angle of 45° with the surface of the target. Cooling method for the device: it is by manually circulating the device hot water with cold water through a tank located inside the device.

2. Sediment Chamber. It is a cylindrical chamber with a diameter of 30 cm and a height of 40 cm made of quartz. The film deposition process takes place in it, using a pulsed laser at high discharge, and it is designed to contain a gate for the gas to escape upon discharge and for viewing the laser rays.

The process of deposition of samples prepared from CdO discs before and after doping with SnO_2 took place inside the vacuum

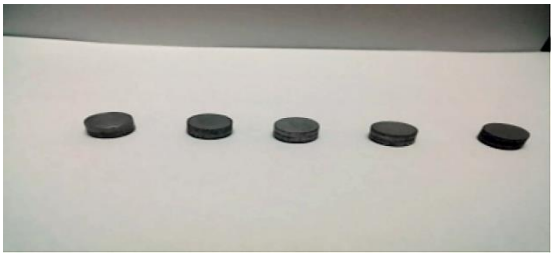

Fig. 1. Shape of the samples.

Fig. 2. The Nd:YAG pulsed laser instrument.

chamber of the laser system and under a vacuum pressure of 10^{-2} hPa. The deposition process includes basic steps, which are the interaction regarding pulsed laser beams with target, which is a compressed powder disk. Subsequently, the prepared thin films were annealed at a temperature of 400°C.

At room temperature, the experiments have been carried out with CuK_α radiation source ($\lambda = 1.5414$ Å) at 2θ-values ranging between 20 and 80 for recording the XRD data. An accelerating voltage of 30 kV and emission current of 20 mA were used in the experiment. UV–Vis spectrophotometry (UV-265 Shimadzu) was used to examine the optical characteristics of CdO:SnO_2 thin films inside the wavelength range of 300–1100 nm. A test of a gas sensor with a bias voltage of 6 V has been carried out at various sensing temperatures. With the use of aluminium electrodes for each measurement, Hall coefficient was determined utilizing a four-probe approach. Through introducing a magnetic field perpendicular to the membrane surface, Hall effect has been computed. Additionally, the Hall probability (μ_H) of electrical conductivity (σ) and the concentration of charge carriers (p) have been ascertained. Furthermore, the test was run under a bias voltage of 6 V specifically for NO_2 gas and at multiple sensing temperatures for the gas sensor measurement.

3. RESULTS AND DISCUSSION

3.1. The Crystal Structure: X-Ray Diffraction Analysis

The x-ray diffraction results of all mixed CdO:SnO_2 thin films deposited on glass substrates through PLD method and annealed at 400°C are illustrated in Fig. 3. The observed peaks include (110), (104), (111), (101), (220), (200), (311), and (222). The dominant plane is (111), which is attributed to its stability. The samples consist of a film comprising a mixture of the cubic structure of cadmium oxide and the polycrystalline structure of tin oxide with a tetrahedral arrangement [26, 27]. It can be observed that increasing the weight ratio results in an increase in the intensity regarding thin films.

Additionally, there is a reduction in full width at half maximum (*FWHM*) from 0.704 nm to 0.4257 nm in the (111) direction, indicating that the crystallite size increases from 11.8 nm to 18.3 nm for the thin film (Table) [28].

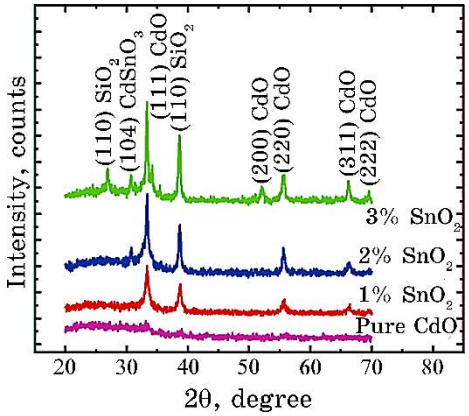

Fig. 3. XRD patterns of pure CdO and nanocomposite $CdO_{1-x}SnO_{2(x)}$.

TABLE. XRD parameters for CdO:SnO_2 thin films.

Sample	2θ, degree	*FWHM*, degree	$d_{hkl\ exp}$, Å	Grain size, nm	*hkl*
Pure	33.1539	0.8048	2.6999	10.3	(111)
1%	33.3551	0.7042	2.6841	11.8	(111)
2%	33.4054	0.5784	2.6802	14.3	(111)
3%	33.3551	0.4527	2.6841	18.3	(111)

3.2. Optical Properties

3.2.1. Transmission (T)

Figure 4 presents the optical transmittance spectra of CdO:SnO_2 thin films within wavelengths ranging from 300 nm to 800 nm and with SnO_2 contents of 0.01%, 0.02%, and 0.03%. It could be indicated that the transmittance is gradually increased with the increase in wavelength, albeit at a small rate. However, for wavelengths below 400 nm, a sharp decrease in transmittance is observed that is associated to the absorption edge in the corresponding wavelength region [29].

In the visible region, the transmittance spectrum shows a gradual increase, reaching a maximum transparency of approximately 77% in the near-infrared (NIR) region. This behaviour reflects the nature of the film. It could be attributed to an increase in oxygen content in the material or the scattering of photons by crystal defects [30]. Overall, optical transmittance decreases with an increase in SnO_2 content.

3.2.2. Optical Energy Band Gap

A critical optical constant used in fabrication of many electrical devices, depending on semiconductor physics, is the energy band gap, which is specified as the energy needed to transfer an electron from valence band maxima to the conduction band minima. The relationship (1) could be used to compute the energy gap value (E_g) [31]:

$$\alpha h\nu = A\left(h\nu - E_g\right)^r, \tag{1}$$

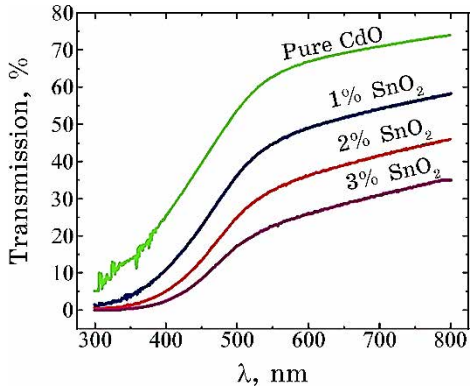

Fig. 4. Transmission of CdO thin films with different SnO_2 contents as a function of the wavelength.

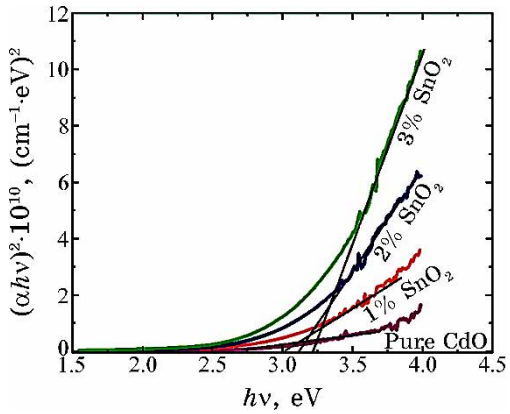

Fig. 5. Energy gap of CdO thin films with different SnO_2 contents.

in which α represents the absorption coefficient, ν represents the photon energy, A represents a constant, and r is an exponential index with a value of 1/2. By squaring Eq. (1), we obtain the following equation:

$$(\alpha h\nu)^2 = A^2(h\nu - E_g)\,. \tag{2}$$

Doping results in decreased energy-gap values, especially at higher weight ratios (Fig. 5). The energy gap is impacted by the increased doping ratios because they cause new localized states to form inside the band gap and tail states to form close to the band edges [32].

3.3. Electrical Properties: Hall Effect

Several electrical characteristics of the prepared samples are ascertained by means of the Hall-effect measurement. For nanocomposite films, carrier concentration, μ_H, conductivity, mobility, and the majority charge-carrier types are examined [33].

The electrical conductivity of a material is influenced by the concentration and mobility of the carriers, both of which are affected by temperature and impurities.

Figure 6 shows that the increase in the SnO_2 contents from 0.01 to 0.03 results in an increase in carrier concentration of the prepared thin films from $1.50 \cdot 10^{15}$ to $1.89 \cdot 10^{15}$ cm^{-3}. On the other hand, the behaviour of carrier mobility shows the opposite trend, where the increase of the SnO_2 content reduces the value of the carrier mobility from $\cong 2000$ to 800 $cm^2/(V \cdot sec)$, as depicted in Fig. 6. Results are in good agreement with Ocak *et al.* [29].

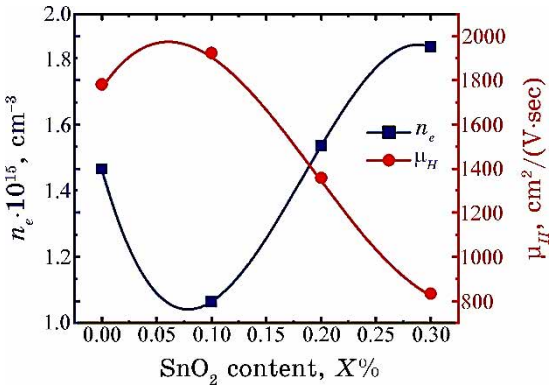

Fig. 6. Variation of n_e and μ_H with different weight ratio for CdO:SnO_2.

3.4. Gas-Sensing Properties

Two factors affect the sensors' response: the rate, at which gas molecules diffuse to the surface, and the kinetics of chemical processes taking place outside the grains. The varying rates of such processes set a limit on the sensor response at different temperatures. The maximum sensor response is achieved at intermediate temperatures, when the rates of both processes equalize. According to this process, the sensor response peaks for each gas at a particular temperature [34].

Figure 7, *a*–*d*, *e*–*h*, *i*–*l*, *m*–*p* illustrates the variation of resistance with time for the films at different operating temperatures in the case, when exposed to NO_2 gas. Gas-on period is indicated by the red arrow, while the gas-off period is shown by the green arrow. It is well known that NO_2 gas is oxidative in nature. The resistance to NO_2 gas exhibits a linear decrease with increasing temperature within the range of room temperature to 300°C.

The sensitivity regarding the sensor to NO_2 gas exhibits a linear increase with temperature within the range of room temperature to 300°C. This relationship is illustrated in Fig. 8. The maximum sensitivity of prepared CdO:SnO_2 thin films towards nitrogen dioxide (NO_2) gas is achieved, when the SnO_2 content is of 0.01. This optimal operating condition occurs at a temperature of 300°C. At this point, the maximum sensitivity reaches 78.05%. The recovery time of the sensor is of 60 seconds and response time is of 25 seconds.

When a reducing or oxidizing gas is introduced, a gas-sensor response time is the amount of time, which the sensor takes to achieve 90% of its minimum or maximum conductance value. Comparably, recovery time is the amount of time needed for the sensor to stabilize within 10% of its original baseline following the stop-

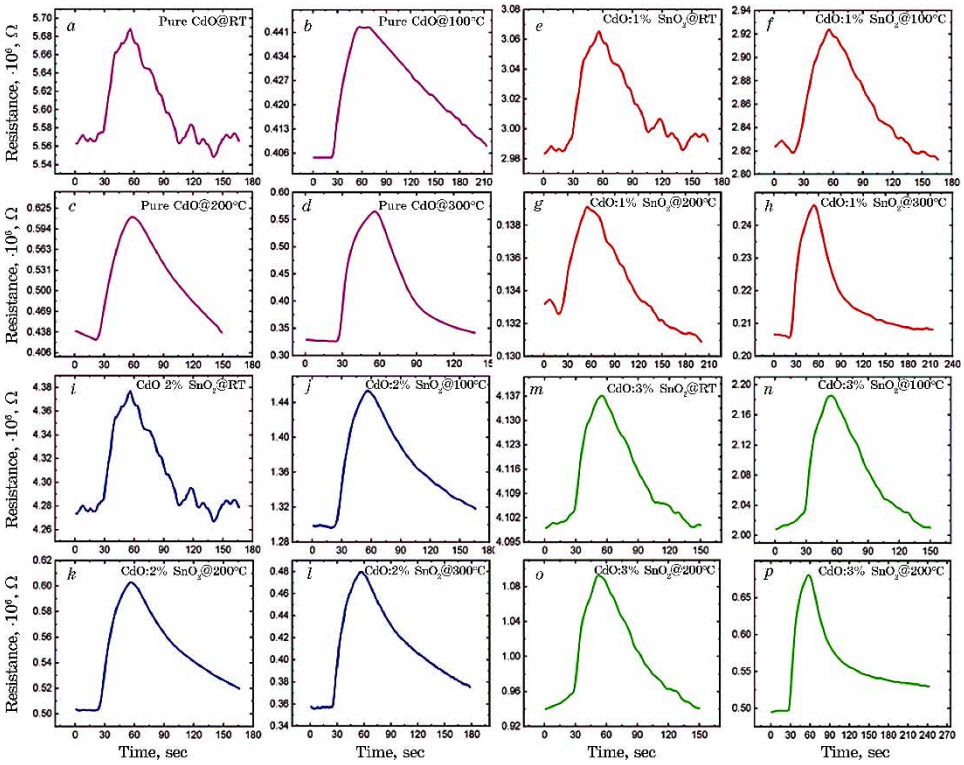

Fig. 7. Resistance variation: (*a*, *b*, *c*, *d*) for pure CdO, (*e*, *f*, *g*, *h*) for CdO:1% SnO_2, (*i*, *j*, *k*, *l*) for CdO:2% SnO_2, and (*m*, *n*, *o*, *p*) for CdO:3% SnO_2 thin films with different operating temperatures for NO_2 gas.

ping of the reducing or oxidizing gas flow [35, 36].

Figures 9 and 10 depict the relation between recovery time and response time at different operating temperatures and etching times for pure CdO and its combinations with 1%, 2%, and 3% SnO_2 (CdO:SnO_2). It is observed that the response time is fast (of approximately 20 seconds), while the recovery time is also fast (of approximately 40 seconds).

4. CONCLUSIONS

Using the PLD approach, nano-CdO:SnO_2 thin films of different compositions have been successfully formed on glass substrates. The films with the CdO:SnO_2 compositions have a polycrystalline structure, as shown by XRD analysis. As the weight ratio of SnO_2 rises, the energy gap shrinks, suggesting a trend towards lower energy levels. Thin films demonstrated the behaviour of an *n*-type charge

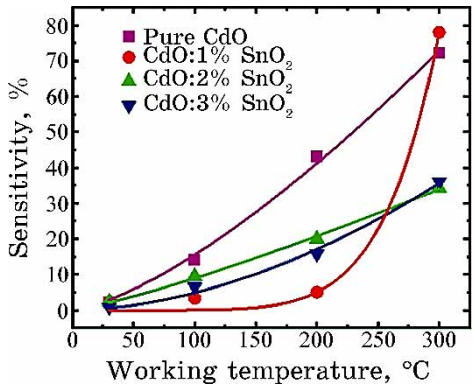

Fig. 8. Sensitivity of CdO:SnO_2 thin film towards NO_2 gas under various temperatures with different SnO_2 contents measured under various operating temperature.

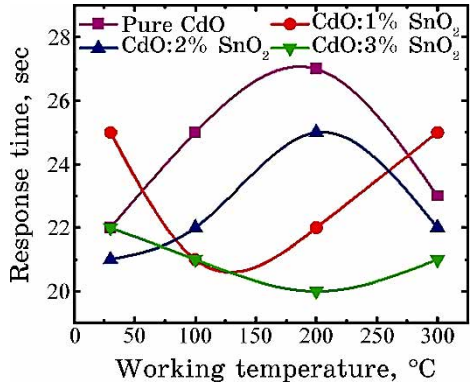

Fig. 9. Response time of CdO:SnO_2 thin films towards NO_2 gas with different SnO_2 contents measured under various operating temperature.

carrier. There appears to be an inverse link between temperature and resistance since the resistance to nitrogen dioxide reduces linearly with rising temperature. With the exception of one particular instance, the sensor sensitivity to NO_2 gas rises linearly with temperature, suggesting a positive association between the both magnitudes. Both pure CdO and mixed CdO:SnO_2 films show high resistivity at high temperatures in the case, when measuring NO_2 gas with the gas sensor, indicating lower sensitivity to NO_2 gas.

AUTHORS' NOTE

The manuscript authors affirm that they have no conflicting inter-

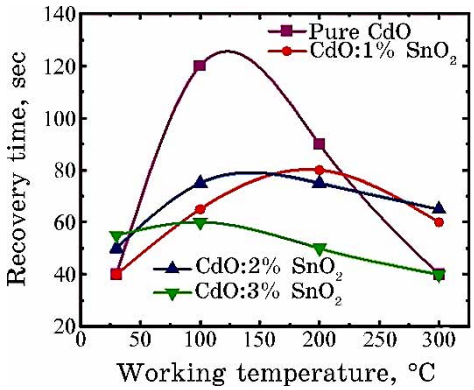

Fig. 10. Recovery time of CdO:SnO_2 thin films towards NO_2 gas with different SnO_2 contents measured under various operating temperature.

ests with publishing this work. The manuscript writers attest to its lack of plagiarism.

REFERENCES

1. M. Hulko, I. Hospach, N. Krasteva, and G. Nelles, *Sensors*, **11**, No. 6: 5968 (2011); https://doi.org/10.3390/s110605968
2. D. Lazik, S. Ebert, M. Leuthold, J. Hagenau, H. Geistlinger, *Sensors*, **9**, No. 2: 756 (2009); https://doi.org/10.3390/s90200756
3. G. F. Fine, L. M. Cavanagh, A. Afonja and R. Binions, *Sensors*, **10**, No. 6: 5469 (2010); https://doi.org/10.3390/s100605469
4. J. Zhang, J. Q. Hu, F. R. Zhu, H. Gong, and S. J. O'Shea, *Sensors*, **3**, No. 10: 404 (2003); https://doi.org/10.3390/s31000404
5. I. C. Chen, S. S. Lin, T. J. Lin, C. L. Hsu, T. J. Hsueh, and T. Y Shieh, *Sensors*, **10**, No. 4: 3057 (2010); https://doi.org/10.3390/s100403057
6. G. Coulby, A. Clear, O. Jones, and A. Godfrey, *International Journal of Environmental Research and Public Health*, **17**, No. 11: 3995 (2020); doi:10.3390/ijerph17113995
7. P. Biswas, C. Zhang, Y. Chen, Z. Liu, S. Vaziri, W. Zhou, and Y. Sun, *Biosensors*, **11**, No. 9: 326 (2021); https://doi.org/10.3390/bios11090326
8. Y. H. Navale, S. T. Navale, M. A. Chougule, N. S. Ramgir, and V. B. Patil, *Journal of Materials Science: Materials in Electronics*, **32**, No. 7: 18178 (2021); https://doi.org/10.1007/s10854-021-06360-0
9. X. Liu, S. Cheng, H. Liu, S. Hu, D. Zhang, and H. Ning, *Sensors*, **12**, No. 7: 9635 (2012); https://doi.org/10.3390/s120709635
10. P. Biswas, C. Zhang, Y. Chen, Z. Liu, S. Vaziri, W. Zhou, and Y. Sun, *Biosensors*, **11**, No. 9: 326 (2021); https://doi.org/10.3390/bios11090326
11. S. Zampolli, I. Elmi, G. C. Cardinali, L. Masini, F. Bonafè, and F. Zardi, *Sensors and Actuators B: Chemical*, **305**, No. 8: 1274 (2020); https://doi.org/10.1016/j.snb.2019.127444
12. M. I. A. Asri, M. N. Hasan, M. R. A. Fuaad, Y. M. Yunos, and

M. S. M. Ali, *IEEE Sensors Journal*, **2**, No. 17: 18381 (2021); https://doi.org/10.1109/JSEN.2021.3091854
13. H. Xu, P. Wu, C. Zhu, A. Elbaz, and Z. Z. Gu, *Journal of Materials Chemistry C*, **1**, No. 38: 6087 (2013); https://doi.org/10.1039/C3TC30722K
14. R. Yu, Y. Chen, L. Shui, and L. Xiao, *Sensors*, **20**, No. 10: 2996 (2020); https://doi.org/10.3390/s20102996
15. M. Aazi, M. Kudinova, D. Kinet, J. L. Auguste, S. Delépine-Lesoille, P. Mégret, and G. Humbert, *Journal of Physics: Photonics*, **2**, No. 1: 014005 (2019); https://doi.org/10.1088/2515-7647/ab5cec
16. J. Li, H. Yan, H. Dang, and F. Meng, *Optics & Laser Technology*, **135**: 106658 (2021); https://doi.org/10.1016/j.optlastec.2020.106658
17. Y. Zhang, C. Wang, L. Zhao, F. Liu, X. Sun, X. Hu, and G. Lu, *Sensors and Actuators B: Chemical*, **334**: 129514 (2021); https://doi.org/10.1016/j.snb.2021.129514
18. H. Wang, Y. Luo, B. Liu, L. Gao, and G. Duan, *Sensors and Actuators B: Chemical*, **338**: 129806 (2021); https://doi.org/10.1016/j.snb.2021.129806
19. M. Wang, Y. Zhu, Q. Luo, C. Ge, G. Liu, G. Qiao, and E. G. Kim, *Applied Surface Science*, **566**: 150750 (2021); https://doi.org/10.1016/j.apsusc.2021.150750
20. Y. Wang, Y. Cui, X. Meng, Z. Zhang, and J. Cao, *Surfaces and Interfaces*, **24**: 10110 (2021); https://doi.org/10.1016/j.surfin.2021.101110
21. K. Karthik, S. Dhanuskodi, C. Gobinath, and S. Sivaramakrishnan, *Spectrochimica Acta Part A: Molecular and Biomolecular Spectroscopy*, **139**: 7 (2015); https://doi.org/10.1016/j.saa.2014.11.079
22. J. K. Rajput, T. K. Pathak, V. Kumar, H. C. Swart, and L. P. Purohit, *Physica B: Condensed Matter*, **535**: 314 (2018); https://doi.org/10.1016/j.physb.2017.08.014
23. J. C. Boettger, *International Journal of Quantum Chemistry*, **107**, No. 15: 2988 (2007); https://doi.org/10.1002/qua.21350
24. H. P. Singh and B. Dayal, *Solid State Communications*, **7**, No. 10: 725 (1969); https://doi.org/10.1016/0038-1098(69)90651-6
25. Joseph A. Spencer, Alyssa L. Mock, Alan G. Jacobs, Mathias Schubert, Yuhao Zhang, and Marko J. Tadjer, *Applied Physics Reviews*, **9**, No. 1: 2113 (2022); doi:10.1063/5.0078037
26. K. A. Jasim, T. J. ALwan, K. H. Mahdi, and H. L. Mansour, *Turkish Journal of Physics*, **37**, No. 2: 237 (2013); doi:10.3906/fiz-1203-16
27. E. Sirotin and M. Shaskolskaya, *Fundamentals of Crystal Physics* (Moskva: Mir: 1982) (in Russian).
28. R. A. Al-Ansari, H. Q. Khaleel, J. H. Awadh, G. H. Mohammed, and I. R. Swadi, *DJPS*, **13**, No. 4: 91 (2017); http://dx.doi.org/10.24237/djps.1304.318E
29. Y. S. Ocak, D. Batibay, and S. Baturay, *Journal of Materials Science: Materials in Electronics,* **29**, No. 20: 17425 (2018); https://doi.org/10.1007/s10854-018-9841-2
30. S. Dugan, M. M. Koç, and B. Coşkun, *Journal of Molecular Structure*, **1202**: 127235 (2020); https://doi.org/10.1016/j.molstruc.2019.127235
31. R. A. Moqbel, M. A. Gondal, T. F. Qahtan, and M. A. Dastageer, *International Journal of Energy Research*, **42**, No. 4: 1487 (2018); https://doi.org/10.1002/er.3935

32. Y. Lin, W. J. Wang, J. Cai, M. Ying, R. Zhao, M. Li, and N. Ce-Wen, *Phys. Rev. B*, **73**: 193308 (2006); https://doi.org/10.1103/PhysRevB.73.193308
33. J. J. Shea, *IEEE Electrical Insulation Magazine*, **21**, No. 4: 57 (2005); https://doi.org/10.1109/MEI.2005.1490003
34. A. A. Yousif and M. H. Hasan, *J. Biosens. Bioelectron*, **6**, No. 4: 254 (2015); https://doi.10.4172/2155-6210.1000192
35. A. Sreedhar, M. Hari Prasad Reddy, S. Uthanna, and J. F. Pierson, *International Scholarly Research Notices*, **1**: 527341 (2013); https://doi.org/10.1155/2013/527341
36. J. A. Dirksen, K. Duval, and T. A. Ring, *Sensors and Actuators B: Chemical*, **80**, No. 2: 125 (2001); https://doi.org/10.1016/S0925-4005(01)00898

Наносистеми, наноматеріали, нанотехнології
Nanosistemi, Nanomateriali, Nanotehnologii
2026, т. 24, № 1, сс. 225–240
https://doi.org/10.15407/nnn.24.01.0225

PACS numbers: 68.37.Hk, 68.37.Vj, 78.20.Ci, 78.40.Ha, 78.67.Uh, 81.07.Gf, 81.15.Gh

Effect of Aluminium Doping on the Characteristics of One-Dimensional Zinc-Oxide Nanowires Grown by Atmospheric Pressure Chemical Vapour Deposition

Zahra Mohammed Saeed[1], Samir Mahmmod Ahmad[2], and Yasir Hussein Mohammed[3]

[1]*Polytechnic College Mosul,*
Department of Electrical Techniques,
Northern Technical University,
41002 Mosul, Iraq
[2]*College of Science,*
Department of Physics,
University of Mosul,
41002 Mosul, Iraq
[3]*College of Education for Pure Science,*
Department of Physics,
University of Mosul,
41002 Mosul, Iraq

The atmospheric-pressure chemical vapour deposition (APCVD) technique is used to grow ZnO nanowires (NWs) on glass substrates. The effect of different doping ratios (0, 2, 4, and 6 wt.%) of aluminium on the structure, morphological and optical properties of the ZnO:Al nanowires is studied. The optical, structural, and morphological results were evaluated using ultraviolet–visible (UV–Vis) spectroscopy, x-ray diffraction (XRD), and field emission scanning electron microscopy (FE–SEM) with energy dispersive x-ray (EDX) spectroscopy. Optical results indicate that, with the increase of aluminium doping, the interatomic distance in the crystal lattice is decreased, and the energy gap is shifted to redshift. The doping with aluminium improves the crystallinity of the network. Morphological observations indicate that, when measuring the diameters of ZnO nanowires, the diameter of the aluminium-doped ZnO nanowires increases with increasing doping ratio. The surface of the ZnO nanowires also contains Al atoms, and EDX spectroscopy supports this finding. Our current research may serve the development of future nanooptical devices.

Для вирощування нанодротів (НД) ZnO на скляних підкладинках було використано метод хемічного осадження з парової фази (APCVD) за ат-

мосферного тиску. Було досліджено вплив різних ступенів леґування (0, 2, 4, 6 мас.%) алюмінієм на структурні, морфологічні й оптичні властивості нанодротів ZnO:Al. Оптичні, структурні та морфологічні результати оцінювали за допомогою ультрафіолетової й оптичної (UV–Vis) спектроскопії, рентґенівської дифракції (XRD) та польової емісійної сканувальної електронної мікроскопії (FE–SEM) з енергодисперсійною рентґенівською (EDX) спектроскопією. Оптичні результати показали, що зі збільшенням леґування алюмінієм міжатомова віддаль у кристалічній ґратниці зменшується, а енергетична щілина зміщується в бік довших хвиль. Леґування алюмінієм поліпшило кристалічність структурної мережі. Морфологічні спостереження показали, що з мірянням діяметрів нанодротів ZnO діяметер леґованих алюмінієм нанодротів ZnO збільшувався зі збільшенням ступеня леґування. Поверхня нанодротів ZnO також містила атоми Al, а EDX-спектроскопія підтвердила цей висновок. Наші поточні дослідження можуть сприяти розробці майбутніх нанооптичних пристроїв.

Key words: atmospheric-pressure chemical vapour deposition, ZnO nanowires, band gap, doping with Al, vapour–solid process.

Ключові слова: хемічне осадження з парової фази за атмосферного тиску, ZnO нанодроти, заборонена зона, Al-леґування, парофазний процес.

(Received 15 August, 2024; in revised form, 30 September, 2025)

1. INTRODUCTION

ZnO strong exciton-binding energy of 60 meV at room temperature, wide band gap of 3.37 eV, strong radiation tolerance, high thermal conductivity, high electron mobility, and high breakdown electric-field strength are appropriate for optoelectronics, laser technology, and electronics applications [1, 2]. There are various structural arrangements of ZnO nanomaterials [3] such as nanotubes [4], nanowires (NWs) [5], nanobelts [6], nanorods [7], nanoribbons [8], and nanocables [9]. Numerous ZnO nanowires distinguish from the rest of the configurations with the large surface-to-volume ratio, which gives a large active area, the high electron mobility, and transparency, are worthy for the electron-transport layer, which is beneficial for UV lasers [10], light-emitting diodes [11], solar cells [12], nanogenerators [13], gas sensors [14], photodetectors [15], and photocatalysts [16].

Aluminium (Al) is a cheap and abundant element; hence, Al:ZnO could be a good replacement for indium–tin oxide films, which are commonly used in solar energy systems [17]. It has been believed that adding dopants Ga, In, Li, Cu, Al, *etc.* is one of the easiest ways to control the nanostructures produced by chemical vapour deposition [18]. It should be mentioned that the band-gap energy of

ZnO is lowered by Cd, Ti, and Al, but raised by Li and Mg, for example [19]. Increasing ZnO electrical conductivity is the primary objective of Al doping. The doping concentration primarily dictates where the Al atom is located inside the ZnO lattice; at concentrations below 2%, it occupies the Zn site, while, at concentrations above 2%, it occupies the interstitial site. The concentration of free carriers increases, when Al^{3+} is used in place of Zn^{2+} [20].

Previous research investigated the effects of Al doping on properties of ZnO nanowires; however, a detailed analysis is still required to ascertain the effects of Al-doping concentration on ZnO [21–23]. Many deposition methods like sputtering [24], pulsed laser deposition [25], chemical vapour deposition, spray pyrolysis [26], and sol–gel processing [27] ways have been adduced to produce Al:ZnO nanowires. The method used in this paper, the chemical vapour deposition (CVD) method, for growing ZnO NWs does not require complex equipment or high vacuum and can be adapted to many practical variations. Its flexibility, thus, allows for many composition and location changes during deposition. This results in high-quality materials, *i.e.*, with excellent homogeneity and purity of the fabricated material, step coverage, and adhesion, high productivity, *etc.* [28]. In this work, pure ZnO and Al:ZnO nanostructures were produced *via* the chemical vapour deposition approach. It examined the relationship between Al concentration and both the growth of morphology and the tuning of the optical band gap. It was demonstrated that the evolution of surface form and optical properties was related to the Al content in the Al:ZnO nanostructures.

2. EXPERIMENTAL DETAILS

Initially, the glass substrates of 10×10 mm was ultrasonically cleaned in acetone, ethanol, and deionized water (D_I) for ten minutes in each solution to eliminate impurities. Then, high-purity zinc acetate dihydrate 99.97% $Zn(CH_3COO)_2{\cdot}2H_2O$ was used to produce zinc vapour, while aluminium nitrate $Al(No_3)_3{\cdot}9H_2O$ was used to dope aluminium with 0, 2, 4, and 6 wt.% for 1*D* ZnO NWs growth *via* a dual-zone APCVD method at growth temperature of 600°C. Growing low-dimensional nanomaterials *via* vapour-transport deposition within the horizontal tube furnace are widely used [29]. A thorough explanation of the APCVD system was provided in another place [30].

The temperature of growth was raised by 10°C/min. The substrate and activator were weighed according to the weight ratios listed in Table 1 and placed in an alumina boat (5 cm) away from the flat steel substrate holder; after inserting them into the deposi-

TABLE 1. The proportions of doping.

Fixed weight	Fixed ratio	Weight of doping material	Weight of base material	The mixture weight remains constant
Zn acetate, g	Percentage	Al nitrate, g $\equiv x$	Zn acetate, g $\equiv (1-x)$	Total, g
0.8	0%	0.016	0.784	0.8
0.8	2%	0.032	0.764	0.8
0.8	4%	0.048	0.752	0.8
0.8	6%	0.064	0.736	0.8

tion reactor, the quartz tube was tightly closed to prevent any leakage out of the system. 1*D* ZnO NWs were synthesized for 10 min at evaporation temperature of 600°C using O_2 gas applied at a flow rate of 25 cm^3/min. The temperature of growth was raised by 10°C/min. To regulate precisely the flow rate, a mass flow controller (MFC) was used.

Then, without an oxygen atmosphere, the samples were annealed for three hours at a constant temperature of 600°C. Every other parameter related to the growth was maintained at a constant level and closely monitored. Finally, after the annealing time was over and the furnace was switched off, and once it gradually cooled down to room temperature, the samples were taken out from the reactor and analysed. It should be noticed that the substrates darkened (took on a brown tinge). A UV–Vis spectroscopy (UV-1800 Shimadzu, Japan) was utilized to measure the optical transmittance (*T*) and absorbance (*Abs*) spectra of the grown materials ZnO NWs/glass in the 360–1000 nm wavelength range, with bare glass serving as a reference. Using an x-ray diffractometer (Malvern PANalytical-Aeris) with CuK_α ($\lambda = 1.5406$ Å) radiation operating at 40 kV and 30 mA, the orientation and crystal structure of the grown samples (ZnO NWs/glass) were confirmed. The samples were scanned in the range of 25–75° with an angle step size of 0.011°. FE–SEM equipped with EDX spectroscopy was inviting to obtain surface and cross-sectional images and settle the chemical composition of the grown samples.

3. RESULTS AND DISCUSSION

UV–Vis spectroscopy is a direct approach to studying the optical characteristics and band structure of semiconductor materials. The optical transmittance (*T*) and absorption (*Abs*) spectra of ZnO NWs fabricated on glass substrates with different impurity ratios are

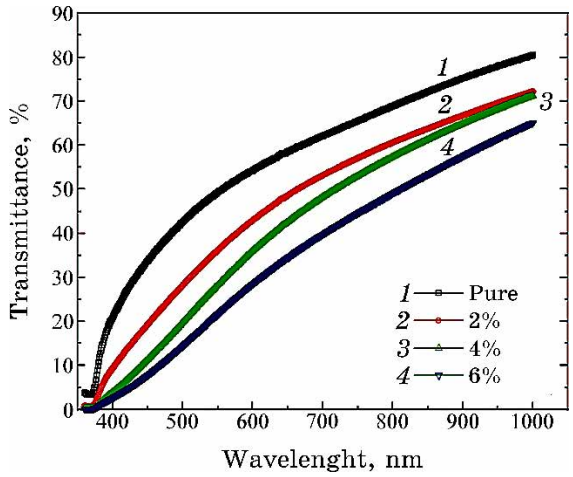

Fig. 1. Optical transmittance spectra of ZnO NWs prepared with different doping ratios.

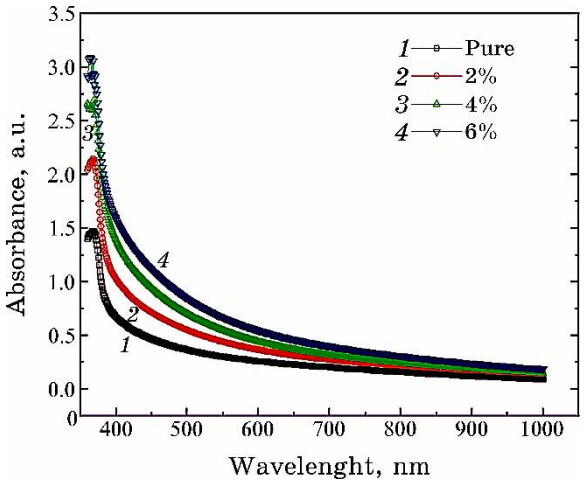

Fig. 2. Optical absorption spectra of ZnO NWs prepared with different doping ratios.

shown in Figs. 1, 2, respectively. These spectra show that the materials have low optical T in the visible range (400–700 nm). It was found that, as the impurity ratios grow from 0 to 6 wt.%, the transmittance values decrease, the absorption values increase, and the fundamental absorption edge shifts toward lower energies, or longer wavelengths. This may be due to the donor levels increasing near the conduction band [31].

Moreover, a decline in transmittance from 80% to 60% has been

noted in the visible region of the spectrum with a small transmittance in the ultraviolet region known as the absorption. As the aluminium-doping ratio increased, the absorption likewise increased from 1.5 to almost 3.5, and it is well known that this is one of the factors used to calculate several optical constants, including optical energy [32]. This indicates that the doping caused actual donor levels to form within the energy gap and close to the absorption edge. These donor levels then absorb low-energy photons, resulting in a noticeable increase in the absorption-coefficient values. Consequently, this allowed us to select the proper activation ratio, or the necessary sample to block the necessary portion of the solar spectrum in the context of solar cell manufacturing, for instance [33].

The absorption-coefficient values (α) for all prepared formulations were obtained using the Beer–Lambert law [34] according to the following equation:

$$\alpha\ [\mathrm{cm}^{-1}] = -\ln(T)/t\,, \tag{1}$$

where t is the thickness; the samples had a thickness of approximately 541 nm.

The optical energy gap of the prepared samples was calculated using Tauc's relation according to the following equation [35]:

$$\alpha h\nu = A\left(h\nu - E_g\right)^n, \tag{2}$$

where h is Planck's constant, ν is the frequency of the incident light photon, and A is a constant that depends on the values of the effective mass of the charge carriers; n depends on the nature of the prevailing optical transitions.

Figure 3 shows the α spectra of ZnO NWs grown on glass substrates with different impurity ratios. As shown in Fig. 3, the α of NWs in the UV region increased from $\cong 1.3 \cdot 10^5$ cm^{-1} to $\cong 6.0 \cdot 10^4$ cm^{-1} with the increase of impurity ratio. This behaviour can be attributed to the difference in impurity ratios.

Figure 4 shows the relationship between $(\alpha h\nu)^2$ and $h\nu$ for ZnO NWs doped with different doping ratios (0–6 wt.%), where they decreased optical energy gap $E_g = h\nu$ from 3.2 eV to 3.1 eV with increasing doping ratios, respectively. We also notice from Fig. 4 that the optical absorption edge showed a redshift. The decrease in the energy gap of the prepared samples with increasing doping ratio can be observed in Table 2 and Fig. 4, and can be attributed to the Burstein–Moss shift [36].

Thus, for ZnO NWs made on glass substrates (see Fig. 5), the development of different intensities of the (002) plane was ascribed to the crystallite-size variation and lattice-strain effects on the struc-

tural-parameters' current values.

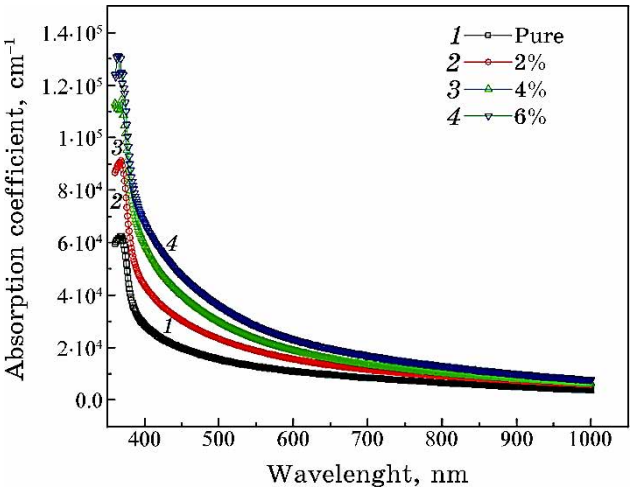

Fig. 3. Suggested malfunction spectra of ZnO NWs prepared with different doping ratios as the wavelength functions.

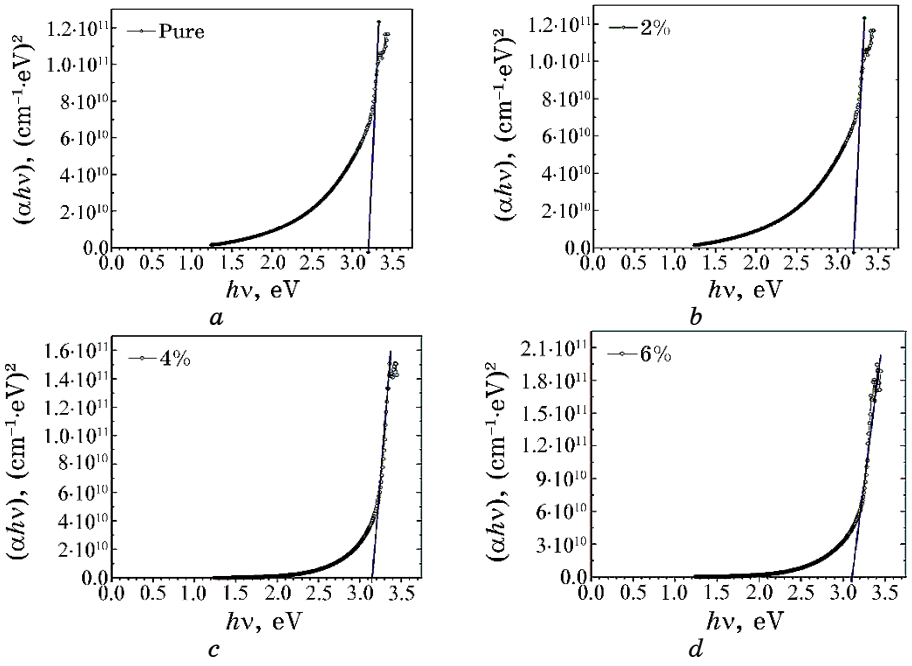

Fig. 4. The relationship between $(\alpha h\nu)^2$ and $h\nu$ for ZnO NWs prepared with different doping ratios.

TABLE 2. Experimental results of ZnO NWs synthesized on glass substrates with different doping ratios.

Doping rate, wt.%	E_g, eV	*FWHM*, degree	2θ, degree	*D*, nm	δ, nm^{-2}	ε, a.u.	*d*, nm	Lattice parameters	
								$a_{(100)}$, Å	$c_{(002)}$, Å
Pure	3.2	0.16398	34.4484	53.0	3.56E-04	0.002308	0.260138	3.2481	5.2027
2%	3.15	0.14381	34.4502	60.4	2.74E-04	0.002024	0.260125	3.2448	5.2025
4%	3.13	0.1595	34.4447	54.5	3.37E-04	0.002245	0.260166	3.2470	5.2033
6%	3.1	0.1552	34.4646	56.0	3.19E-04	0.002183	0.260020	3.2459	5.2003

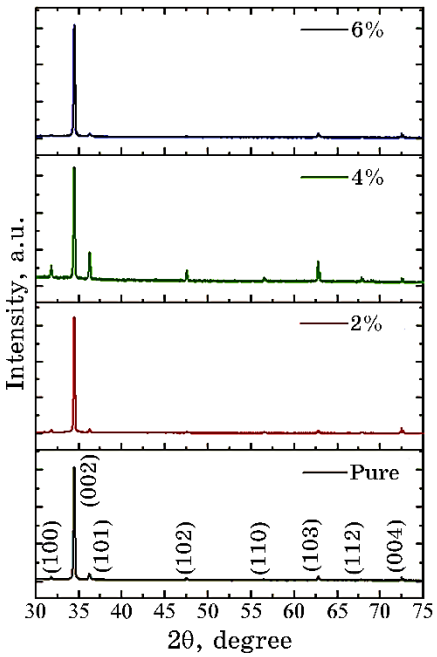

Fig. 5. XRD patterns of ZnO NWs prepared on glass substrates with different doping ratios.

Figure 5 shows that each peak can be matched with the standard pattern (JCPDS 36-1451). Each sample has a highly-crystalline wurtzite structure. The diffraction intensity of the ZnO NWs was significantly higher than that of the other axes, indicating that the NWs grew in line with the *c*-axis [37], which is because ZnO has the lowest surface free energy. In the 002 plane, no diffraction peaks of ZnO:Al NWs were observed in the XRD spectra, indicating that all samples had a preferential orientation of the *c*-axis perpendicular to the substrate surface. The intensity of the (002) peak of the ZnO:Al NWs is similar to that of the pure ZnO sample [38].

From the XRD patterns, the structural parameters including crystallite-size ratio (D), dislocation density (δ), lattice conformation (ε), interplanar distance (d), and lattice constants (a and c) of ZnO NWs were calculated using following equations [30]:

$$D = 0.94\lambda/(\beta\cos\theta)\,, \tag{3}$$

$$\delta = D^{-2}\,, \tag{4}$$

$$\varepsilon = \beta/(4\tan\theta)\,, \tag{5}$$

$$d = \lambda/(2\sin\theta)\,, \tag{6}$$

$$\frac{1}{d^2_{(hkl)}} = \frac{4}{3}\frac{h^2 + hk + k^2}{a^2} + \frac{l^2}{c^2}, \tag{7}$$

where the x-ray wavelength, Bragg's angle, Miller's indices of the crystal plane, and *FWHM* of the diffraction peak in radians are represented by the variables, λ, θ, *hkl*, and β, respectively. Table 2 contains a tabulation of all the calculated values.

The values of the structural parameters of the grown nanofibers differ slightly from those in previous studies [39, 40]. This divergence indicates that the values of the structural parameters were determined by the synthesis process and reaction parameters. We note that the increase in the crystal size in Table 2 and Fig. 5 with the increase in the doping ratio indicates an increase in the degree of crystallization of these samples after doping [41]. The crystal size of the samples prepared with different doping ratios was calculated based on the values of the (002) plane angle, which are ap-

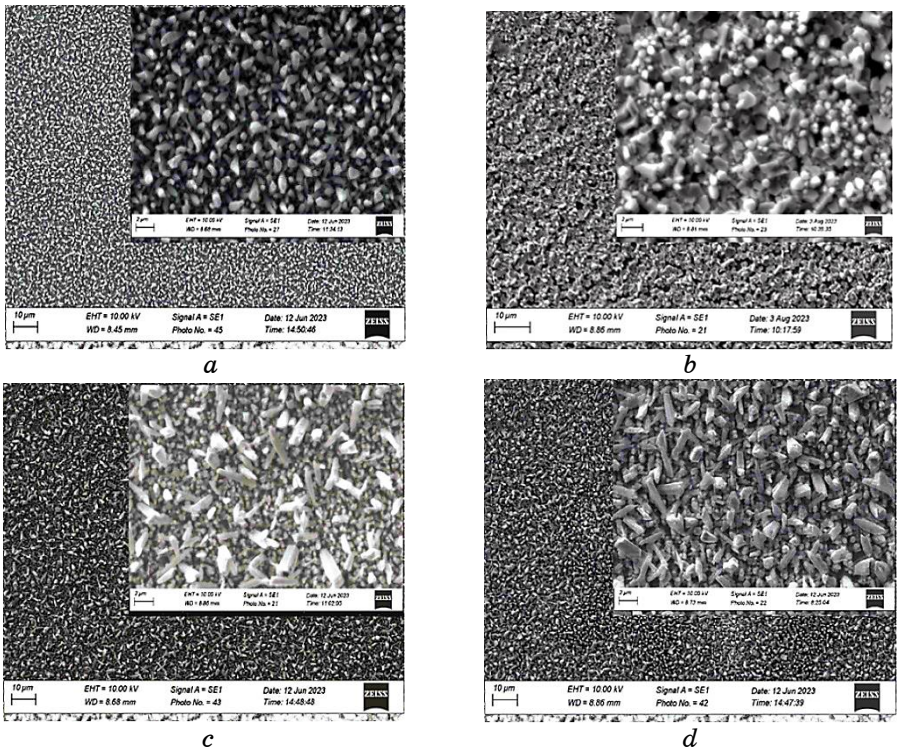

Fig. 6. SEM images of ZnO NWs grown with different doping ratios (*a*—0 wt.%, *b*—2 wt.%, *c*—4 wt.%, *d*—6 wt.%) on glass. The insets in *a*–*d* show a high-magnification top view of the grown ZnO NWs.

proximately equal to 34°, and the values were within the nanoscale. Table 2 shows samples prepared with a 2%-doping ratio, which has a low value of δ. This behaviour indicates a low defect rate in these samples [42].

Figure 6, *a*–*d* shows the FE–SEM images of the samples doped with aluminium with different ratios, where increasing the impurity content to 6% inhibited the growth process towards the *c*-axis, which has the lowest surface energy, indicating that the growth direction became more likely lateral (horizontal), leading to an increase in the diameter of the nanowires [43].

Using ImageJ 1.47v software, the average diameter ($D_{Avg.}$) of the grown nanowires was calculated from, at least, thirty measurements in FE–SEM images (see Fig. 6, *a*–*d*).

Figure 7 shows the distribution of the average diameters of the nanowires after the aluminium-doping process at different ratios (0, 2, 4, 6 wt.%); different diameters of ZnO NWs were obtained on

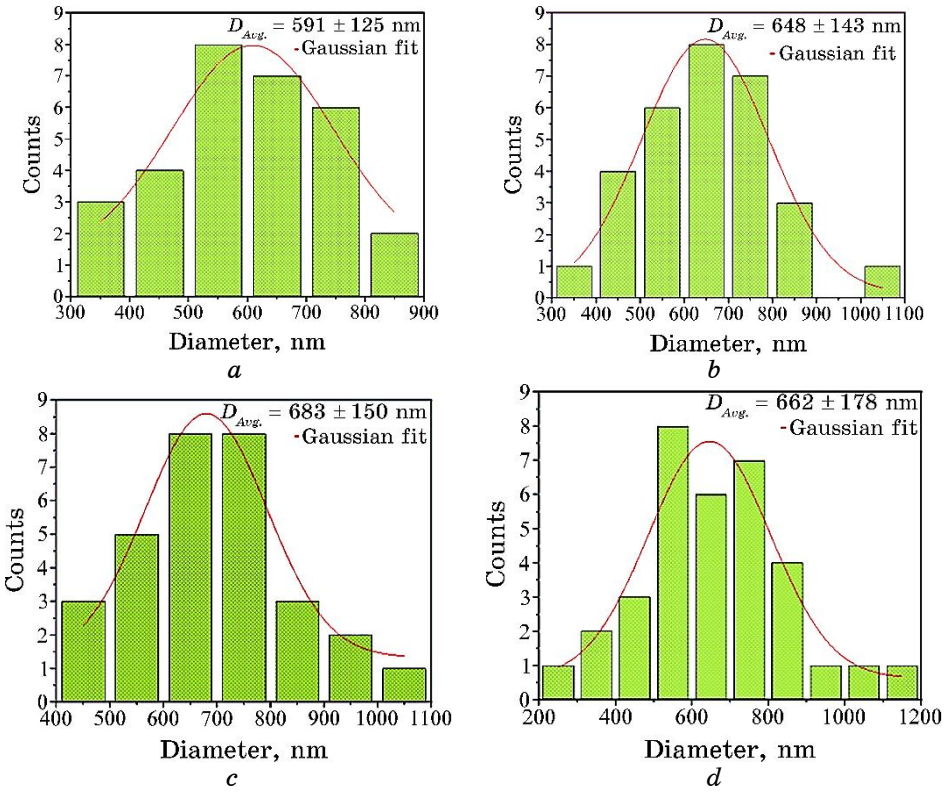

Fig. 7. Diameters' distribution for ZnO NWs prepared at different doping ratios: *a*—0%, *b*—2%, *c*—4%, and *d*—6%.

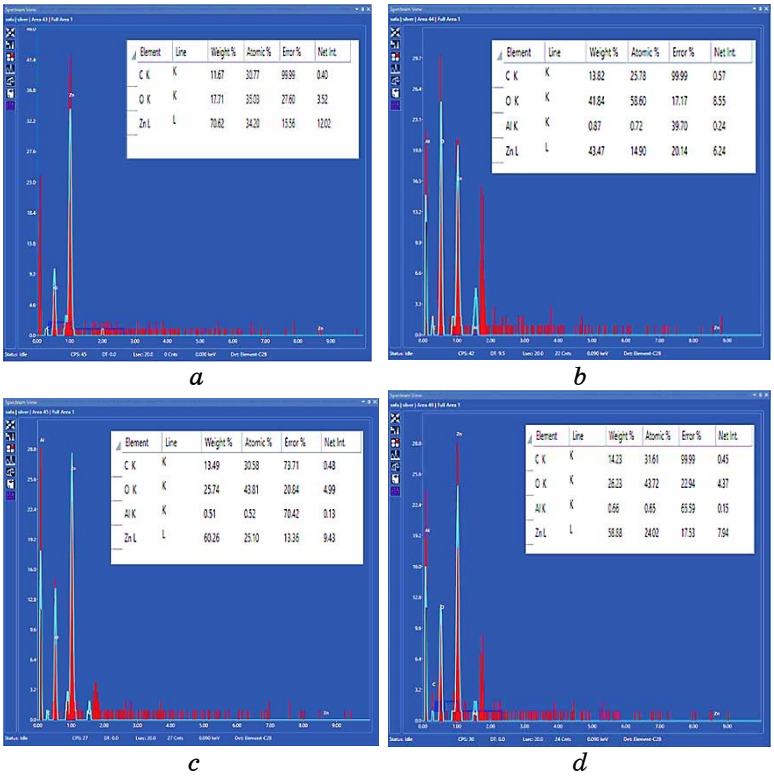

Fig. 8. EDX spectra of ZnO NWs prepared on glass substrates with different doping ratios.

glass substrates, and the average diameter increased from 591 ± 125 nm to 662 ± 178 nm as the doping ratio increases.

The growing-samples' diameters' distribution was fitted with a Gaussian distribution and shown as a solid red line in each histogram with the $D_{Avg.}$ serving as the peak position.

EDX analysis was performed as shown in Fig. 8 to evaluate the nanochemical composition of the samples grown on glass substrates, where the presence of carbon (C), oxygen (O), zinc (Zn), and aluminium (Al) elements was confirmed. EDX spectra clearly showed the doping material through this analysis, as its percentage increased significantly with increasing doping. This demonstrates that Al is integrated into the ZnO NWs [44].

4. CONCLUSION

ZnO NWs were successfully prepared on glass substrates using the

APCVD technique. The effect of changing the aluminium-impurity ratio on the physical properties of the synthesized samples was determined. Optical measurements revealed that the doped nanostructures resulted in decreased transmittance and increased absorption. This could be because the donor levels rise near the conduction band, and the absorption edge shifts to lower energies, which increases the probability of photon absorption. XRD results confirmed the synthesis of ZnO NWs with a hexagonal structure and a preferential orientation along the (002) lattice plane. FE–SEM images revealed the growth of ZnO NWs on glass substrates with different diameters, where the diameter of the nanowires increased with increasing the aluminium-doping ratio. EDX analysis confirmed the high purity of the synthesized samples. In addition, quantitative surface EDX results revealed that the zinc content with aluminium content was suitable for the doping ratios. Therefore, it was demonstrated that the addition of aluminium in different ratios plays a key role in improving the nanostructure properties and increasing the crystallinity of ZnO, using APCVD technique. Finally, our results demonstrate the potential of APCVD as a viable method for producing pure and doped ZnO nanowires.

ACKNOWLEDGMENTS

The authors acknowledge the support provided by the Iraqi Ministry of Higher Education and Scientific Research, as well as the University of Mosul for providing some financial assistance and for monitoring the status of the research.

REFERENCES

1. A. Shah, M. Ahmad, Rahmanuddin, Shakil Khan, Uzma Aziz, Zahid Ali, Afzal Khan, and A. Mahmood, *Applied Physics A*, **125**: Article No. 713 (2019); https://doi.org/10.1007/s00339-019-3005-y
2. R. Yousefi, *Doped ZnO Nanostructures: Growth Properties and Applications* (Eds. A. Umar) (American Scientific Publishers: 2011), vol. **2**, ch. 14, p. 1; doi:10.1039/C2JM15548F
3. R. S. Rai and V. Bajpai, *Adv. Nano Res.*, **11**, No. 1: 37 (2021); doi:10.12989/anr.2021.11.1.037
4. C. N. R. Rao, B. C. Satishkumar, A. Govindaraj, and Manashi Nath, *Nanotubes. ChemPhysChem*, **22**, Iss. 2: 78 (2001); https://doi.org/10.1002/1439-7641(20010216)2:2<78::AID-CPHC78>3.0.CO;2-7
5. S. Bagga, J. Akhtar, and S. Mishra, *AIP Conference Proceedings*, **1989**, No. 1: 020004 (2018); https://doi.org/10.1063/1.5047680
6. W. Z. Wang, B. Q. Zeng, J. Yang, B. Poudel, J. Y. Huang, M. J. Naughton, and Z. Ren, *Advanced Materials*, **18**, Iss. 24: 3275 (2006); https://doi.org/10.1002/adma.200601274

7. Bai Shouli, Chen Liangyuan, Li Dianqing, Yang Wensheng, Yang Pengcheng, Liu Zhiyong, Chen Aifan, and Chung Chiun Liu, *Sensors and Actuators B: Chemical*, **146**, Iss. 1: 129 (2010); https://doi.org/10.1016/j.snb.2010.02.011
8. Zhou Gui, Jian Liu, Zhengzhou Wang, Lei Song, Yuan Hu, Weicheng Fan, and Daoyong Chen, *The Journal of Physical Chemistry B*, **109**, Iss. 3: 1113 (2005); https://doi.org/10.1021/jp047088d
9. J. Q. Hu, Q. Li, X. Meng, C. Lee, and S. Lee, *Chemistry of Materials*, **15**, No. 1: 305 (2002); https://doi.org/10.1021/cm020649y
10. A. T. Ali, W. Maryam, Y. W. Huang, H. C. Hsu, N. M. Ahmed, N. Zainal, H. Abu Hassan, and M. A. Dheyab, *Journal of the Optical Society of America B*, **38**, No. 9: C69 (2021); https://doi.org/10.1364/JOSAB.427132
11. Oleg Lupan, Thierry Pauporté, Tangui Le Bahers, Bruno Viana, and Ilaria Ciofini, *Advanced Functional Materials*, **21**, Iss. 18: 3564 (2011); https://doi.org/10.1002/adfm.201100258
12. Yun-Ming Sung, Fang-Chi Hsu, and Yang-Fang Chen, *Solar Energy Materials and Solar Cells*, **125**: 239 (2014); https://doi.org/10.1016/j.solmat.2014.03.014
13. Te-Hua Fang and Shao-Hui Kang, *Current Nanoscience*, **6**, No. 5: 505 (2010); https://doi.org/10.2174/157341310797574961
14. Sang Kyoo Lim, Seong Hui Hong, Sung-Ho Hwang, Won Mi Choi, Soonhyun Kim, Hyunwoong Park, and Min Gi Jeong, *Journal of Materials Science & Technology*, **31**, Iss. 6: 639 (2015); https://doi.org/10.1016/j.jmst.2014.12.004
15. Jitesh Agrawal, Tejendra Dixit, I. A. Palani, and Vipul Singh, *IEEE Sensors Letters*, **3**, Iss. 9: 9900134 (2019); https://doi.org/10.1109/LSENS.2019.2938638
16. Pierre Gaffuri, Tatjana Dedova, Estelle Appert, Mati Danilson, Adrien Baillard, Odette Chaix-Pluchery, Frank Güell, Ilona Oja-Acik, and Vincent Consonni, *Applied Surface Science*, **582**: 152323 (2022); https://doi.org/10.1016/j.apsusc.2021.152323
17. Frank Maldonado and Arvids Stashans, *Journal of Physics and Chemistry of Solids*, **71**, Iss. 5: 784 (2010); https://doi.org/10.1016/j.jpcs.2010.02.001
18. Soaram Kim, Giwoong Nam, Hyunggil Park, Hyunsik Yoon, Sang-Heon Lee, Jin Soo Kim, Do Yeob Kim, Sung-O Kim, and Jae-Young Leem, *Bulletin of the Korean Chemical Society*, **34**, No. 4: 1205 (2013); https://doi.org/10.5012/bkcs.2013.34.4.1205
19. Ziling Peng, Dan Wu, Wei Wang, Fatang Tan, Xinyun Wang, Jianguo Chen, and Xueliang Qiao, *Powder Technology*, **315**: 73 (2017); https://doi.org/10.1016/j.powtec.2017.03.052
20. A. Nakrela, N. Benramdane, A. Bouzidi, Z. Kebbab, M. Medles, and C. Mathieu, *Results in Physics*, **6**: 133 (2016); https://doi.org/10.1016/j.rinp.2016.01.010
21. T. Holloway, R. Mundle, H. Dondapati, R. B. Konda, M. Bahoura, and A. K. Pradhan, *Proc. SPIE 8344. Nanosensors, Biosensors, and Info-Tech Sensors and Systems 2012 (30 March, 2012)*, **8344A**; https://doi.org/10.1117/12.914482
22. Sining Yun, Juneyoung Lee, Jahyun Yang, and Sangwoo Lim, *Physica B: Condensed Matter*, **405**, Iss. 1: 413 (2010);

https://doi.org/10.1016/j.physb.2009.08.297
23. Hua Zheng, Rong-Jun Zhang, Da-Hai Li, Xin Chen, Song-You Wang, Yu-Xiang Zheng, Meng-Jiao Li, Zhi-Gao Hu, Ning Dai, and Liang-Yao Chen, *Nanoscale Research Letters*, **13**: Article No. 149 (2018); https://doi.org/10.1186/s11671-018-2563-9
24. D. H. Zhang, Z. Y. Xue, and Q. P. Wang, *Journal of Physics D: Applied Physics*, **35**, Iss. 21: 2837 (2002); https://doi.org/10.1088/0022-3727/35/21/321
25. Jae Hyoung Choi, Hitoshi Tabata, and Tomoji Kawai, *Journal of Crystal Growth*, **226**, Iss. 4: 493 (2001); https://doi.org/10.1016/S0022-0248(01)01388-4
26. D. F. Paraguay, M. Miki-Yoshida, J. Morales, J. Solis, and W. Estrada L., *Thin Solid Films*, **373**, Nos. 1–2: 137 (2000); https://doi.org/10.1016/S0040-6090(00)01120-2
27. Jin Zhang and Wenxiu Que, *Solar Energy Materials and Solar Cells*, **94**, Iss. 12: 2181 (2010); https://doi.org/10.1016/j.solmat.2010.07.009
28. Mariana Fraga and Rodrigo Pessoa, *Micromachines*, **11**, No. 9: 799 (2020); https://doi.org/10.3390/mi11090799
29. Hong Jin Fan, Bodo Fuhrmann, Roland Scholz, Cameliu Himcinschi, Andreas Berger, Hartmut Leipner, Armin Dadgar, Alois Krost, Silke Christiansen, and Ulrich Gösele, *Nanotechnology*, **17**, No. 11: S231 (2006); doi:10.1088/0957-4484/17/11/S02
30. Iman Amer Ahmad and Yasir Hussein Mohammed, *Micro and Nanostructures*, **181**: 207628 (2023); https://doi.org/10.1016/j.micrna.2023.207628
31. Ilyass Jellal, Hassan Ahmoum, Yassine Khaaissa, Khalid Nouneh, Mourad Boughrara, Mounir Fahoume, Siddheshwar Chopra, and Jamal Naja, *Applied Physics A*, **125**: Article No. 650 (2019); https://doi.org/10.1007/s00339-019-2947-4
32. S. Ilican, Y. Caglar, and M. Caglar, *Journal of Optoelectronics and Advanced Materials*, **10**, No. 10: 2578 (2008); https://joam.inoe.ro/articles/preparation-and-characterization-of-zno-thin-films-deposited-by-sol-gel-spin-coating-method/fulltext
33. S. Kasap and P. Capper, *Springer Handbook of Electronic and Photonic Materials* (Eds. S. Kasap and P. Capper) (Springer International Publishing AG: 2017), vol. **1**, ch. 4, p. 723–1095; doi:10.10071978-3-319-48933-9
34. N. Yahya, *Carbon and Oxide Nanostructures* (Eds. N. Yahya) (New York–Berlin–Heidelberg: Springer: 2011), vol. **5**, ch. 3, p. 263–280; https://doi.org/10.1007/978-3-642-14673-2
35. S. Kasap, and P. Capper, *Springer Handbook of Electronic and Photonic Materials* (Eds. S. Kasap and P. Capper) (Springer International Publishing AG: 2017), vol. **1**, ch. 4, p. 723–1095; doi:10.10071978-3-319-48933-9
36. Haixia Chen, Jijun Ding, Wenge Guo, Feng Shi, and Yingfeng Li, *Applied Surface Science*, **258**, Iss. 24: 9913 (2012); https://doi.org/10.1016/j.apsusc.2012.06.050
37. L. D. Tang, B. Wang, J. G. Qi, S. J. Peng, and J. Z. Wang, *Materials Research Innovations*, **19**, Iss. 9: S9-6 (2015); https://doi.org/10.1179/1432891715Z.0000000001904
38. Y. Geng, L. Guo, S. S. Xu, Q. Q. Sun, S. J. Ding, H. L. Lu, and D. W. Zhang, *The Journal of Physical Chemistry C*, **115**, No. 25: 12317 (2011); https://doi.org/10.1021/jp2023567

39. Carina Hedrich, Stefanie Haugg, Leutrim Pacarizi, Kaline P. Furlan, Robert H. Blick, and Robert Zierold, *Coatings*, **91**, Iss. 1: 698 (2019); https://doi.org/10.3390/coatings9110698
40. S. Paiman, T. H. Ling, M. Husham, and S. Sagadevan, *Results in Physics*, **17**: 103185 (2020); https://doi.org/10.1016/j.rinp.2020.103185
41. L. Chabane, N. Zebbar, M. L. Zeggar, M. Aida, M. Kechouane, and M. Trari, *Materials Science in Semiconductor Processing*, **40**: 840 (2015); https://doi.org/10.1016/j.mssp.2015.07.080
42. T. Srinivasulu, K. Saritha, and K. T. Ramakrishna Reddy, *Modern Electronic Materials*, **3**, Iss. 2: 76 (2017); https://doi.org/10.1016/j.moem.2017.07.001
43. Mohammad R. Alenezi, Simon J. Henley, Neil G. Emerson, and S. Ravi P. Silva, *Nanoscale*, **6**, Iss. 1: 235 (2014); https://doi.org/10.1039/C3NR04519F
44. Gregor Zimmermann, Martin Lange, Bingqiang Cao, Michael Lorenz, and Marius Grundmann, *physica status solidi (RRL)–Rapid Research Letters*, **4**, Nos. 3–4: 82 (2010); https://doi.org/10.1002/pssr.201004015

Наносистеми, наноматеріали, нанотехнології
Nanosistemi, Nanomateriali, Nanotehnologii
2026, т. 24, № 1, сс. 241–247
https://doi.org/10.15407/nnn.24.01.0241

PACS numbers: 61.05.cp, 78.20.Ci, 78.30.Hv, 78.40.Ha, 78.67.Bf, 81.16.Fg

Degradation of Methylene Blue Using ZnO Nanoparticles Prepared by Biochemical Synthesis

Mohammad Nour Ahmad Alkhoder

Department of Chemistry,
Homs University,
Homs, Syria

In this paper, ZnO nanoparticles are synthesized by biosynthesis method using aloe vera gel/leaf aqueous extract. The obtained nanoparticles are characterized using IR and XRD. The IR results show the absorption band of Zn–O at 498 cm^{-1}, while the powder XRD pattern confirms the hexagonal wurtzite-type structure with particles' size of 35.01 nm. ZnO nanoparticles are used as catalysts for degradation of methylene blue using hydrogen peroxide as an oxidant. The catalytic activity is calculated.

У цій роботі наночастинки ZnO було синтезовано методом біосинтези з використанням водного екстракту ґелю/листя алое вера. Одержані наночастинки було охарактеризовано за допомогою ІЧ- і рентґенівської дифракційної спектроскопії. Результати ІЧ-спектроскопії показують смугу вбирання Zn–O при 498 $см^{-1}$, тоді як порошкова рентґенівська дифрактограма підтверджує гексагональну структуру типу вюртциту з розміром частинок у 35,01 нм. Наночастинки ZnO було використано як каталізатори для деґрадації метиленового синього із застосуванням перекису водню як окиснювача. Було розраховано каталітичну активність.

Key words: ZnO nanoparticles, plant extract, aloe vera gel, methylene blue degradation.

Ключові слова: наночастинки ZnO, рослинний екстракт, ґель алое вера, деґрадація метиленового синього.

(Received 27 August, 2024)

1. INTRODUCTION

Metal oxides, mainly ZnO, have attracted attention for environmen-

tal remediation [1–3]. Residual dye contents in textile wastewater have complex aromatic structures that are difficult to degrade by a biological treatment. Therefore, over the last few decades, considerable attention has been paid to decomposing these textile waste dyes by improving the properties of metal oxides, mainly ZnO, by preparing nanoparticles (NPs). Several methods have been developed for their synthesis including physical, chemical and biological methods [4–7].

The use of plant extracts in the synthesis techniques make the use of moderately pollutant free chemicals to synthesize nanomaterials and increase the use of eco-friendly solvents such as water. Green chemistry seeks reducing pollution at the source [8]. Green chemistry encompasses all aspects and types of chemical processes that reduce negative impacts to human health and the environment. This principle focuses on choosing reagents that encounters the least risk and generate only benevolent by products. Though physical and chemical methods are trendier for the synthesis of NPs, the biogenic fabrication is a better choice due to eco-friendliness. Because of the need of environmental friendly NPs, researchers are using green methods for the synthesis of various NPs for pharmaceutical applications [9–12].

The biological approaches of using microorganisms and plants or plant extracts for the synthesis of NPs have been suggested as valuable alternatives to chemical methods. Several biological systems including bacteria, fungi and yeast have been used in synthesis of nanoparticles. Nanoparticles, due to their smaller size and large surface, exhibit remarkable novel properties and methodical applications in the field of biotechnology, sensors, medical, catalysis, optical devices, DNA labelling, drug delivery, and they are rewardingly treated as a bridge between bulk material and atomic and molecular structures.

It is well known that ZnO is an important metal oxide semiconductor. ZnO NPs have found fabulous applications in biomolecular detection, diagnostics, and microelectronics [13–16].

The aim of this study is to prepare ZnO NPs using a green chemical method and examine the catalytic properties of the ZnO nanocomposites for methylene blue (MB) oxidation.

2. MATERIALS AND METHODS

2.1. Materials

($Zn(CH_3COO)_2$ 99%), (NaOH 99.5%) were supplied from Riedel de Haen. These chemicals were utilized in the synthesis of the samples using distilled water.

2.2. Preparation of ZnO Nanoparticles

Aqueous zinc acetate solution 50 mL of 0.02 M was prepared and added to the aqueous leaf extract of aloe vera 100 mL of 50% because of better size distribution of ZnO NPs at room temperature. The resulting mixture was stirred for 20 min. Then, sodium hydroxide solution 8 mL of 3.0 M NaOH was added drop wise to increase the pH to 12. The resulting pale creamy mixture was then stirred (2 h). The white precipitate was collected by filtration; it was washed with distilled water and with ethanol (96%) to remove the impurities. The resulting white powder of ZnO NPs was dried in a vacuum oven (at 80°C during 2 h). Then, the product was calcinated at 700°C during 3 h. The yield of the ZnO NPs was of 99%.

2.3. Characterization

The crystallite structure and size of the synthesized nanoparticles' samples were calculated using an x-ray powder diffractometer (XRD) (Philips-PW-1840) with a CuK_α radiation of 1.5418 Å in a 2θ range of 20–80°, while the analysis of the chemical composition was carried out using Fourier transformation infrared red (FT–IR) model: Jasco Spectrum 4100 FT–IR spectroscopy.

2.4. Catalytic Degradation Experiments

The degradation experiments were performed in the glass bottle 250 mL containing 100 mL of MB solution. In details, a certain amount of catalyst 0.1 gr was added to the MB solution 64 mg/L under stirring for 1 h in the dark. 10 mL of H_2O_2 solution 30% v/v was added.

The ultraviolet–visible (UV–Vis) absorbance of supernatant was determined at wavelength of 665 nm (for MB).

The catalytic activity (Ca, %) of MB was calculated by Eq. (1):

$$Ca = \left[(A_0 - A_e)/A_0\right] \cdot 100\%, \quad (1)$$

where A_0 and A_e are the initial and equilibrium absorptions of MB, respectively.

3. RESULTS AND DISCUSSION

3.1. FT–IR Spectroscopy

The FT–IR spectra of ZnO nanoparticles are presented in Fig. 1. All FT–IR spectra results, which were observed in the range of 400–

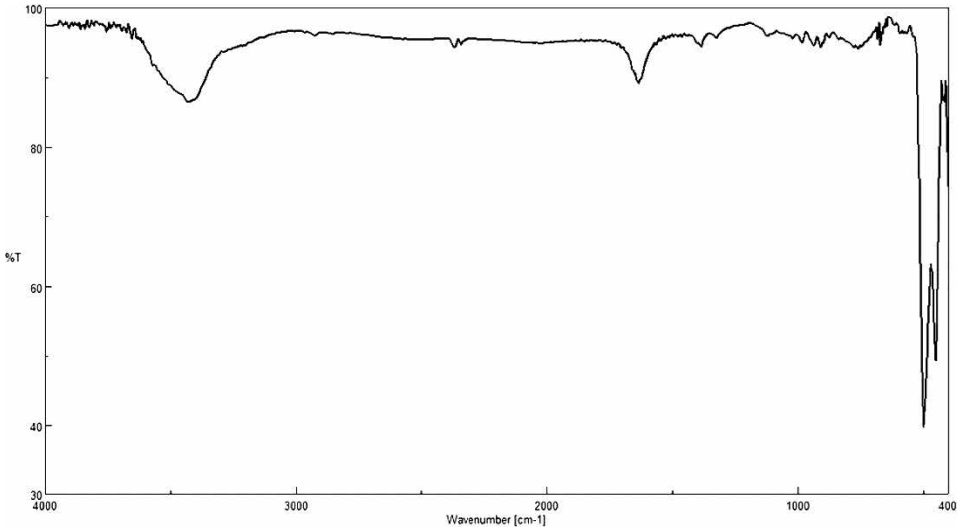

Fig. 1. FT–IR spectra of synthesized ZnO NPs.

TABLE. The absorption bands wave number of the FT–IR spectra of ZnO NPs.

Wave number, cm^{-1}	Bond type
3425	O–H (stretching)
1634	H–O–H (bending)
498	Zn–O (stretching)
450	Zn–O–Zn (stretching)

4000 cm^{-1} at room temperature, are arranged in Table. The most important absorption bands in the spectra are at 450 cm^{-1}, 498 cm^{-1} and belong to Zn–O, Zn–O–Zn, respectively.

3.2. XRD Analysis

The XRD pattern for the prepared ZnO nanoparticles *via* biochemical method was shown in Fig. 2. The phase of the samples has a hexagonal structure. The calculated unit cell parameters ($a = b = 3.242$ Å, $c = 5.188$ Å) with a good agreement with the values reported in the JCPDS file # 96-210-7060.

Figure 3 shows the lattice cells of prepared metal ferrite.

The average crystallite size was calculated using Scherrer's equation, which is expressed as follows [17]:

$$D = K\lambda/(\beta \cos\theta) , \qquad (2)$$

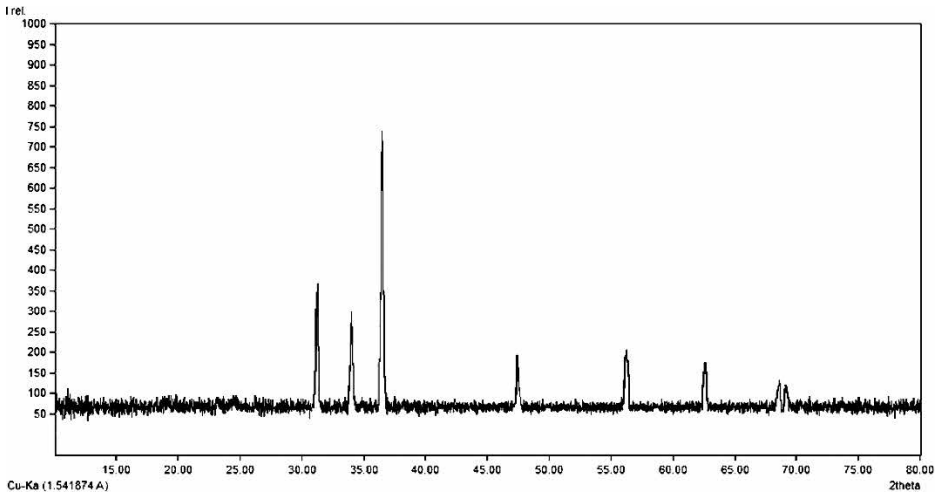

Fig. 2. XRD patterns of ZnO NPs.

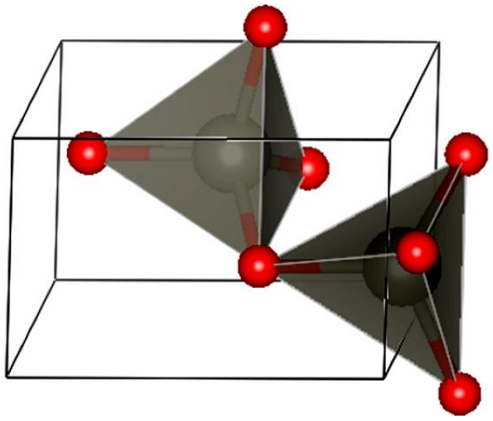

Fig. 3. Lattice cells of ZnO NPs.

where K is Scherrer's constant ($K = 0.89$ assuming spherical particles), λ is the x-ray wavelength, β is the peak width at half maximum (FWHM), and θ is the Bragg's diffraction angle. The average crystal size was of 35.01 nm.

3.3. The Catalytic Activity

The catalytic activity of ZnO NPs prepared by the biochemical method was studied through the methylene blue oxidation reaction using hydrogen peroxide. Figure 4 shows the absorption spectra of

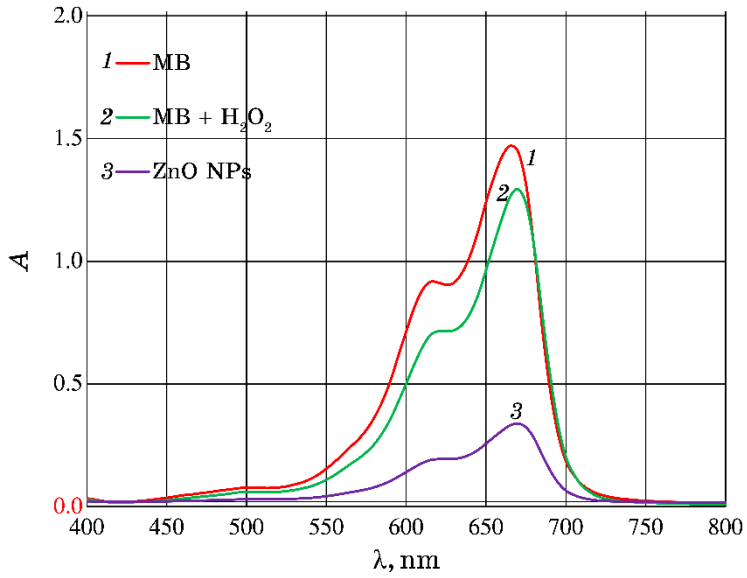

Fig. 4. UV–Vis spectra of MB with and without ZnO NPs.

methylene blue with and without ZnO after 30 min of reaction time. The catalytic activity was calculated by means of Eq. (1).

As can be seen from the previous results, the catalytic activity reached to 88.7%.

4. CONCLUSION

ZnO NPs was successfully synthesized using biochemical method. The resulting compounds were characterized using XRD techniques, which confirmed the size of nanoparticles, and IR spectroscopy. The catalytic activity was studied, and it was found that the ZnO NPs have a high catalytic activity.

REFERENCES

1. Jesty Thomas and Minjoong Yoon, *Appl. Catal. B*, **111–112**: 502 (2012); https://doi.org/10.1016/j.apcatb.2011.10.039
2. Gonghu Li, Shannon Ciston, Zoran V. Saponjic, Le Chen, Nada M. Dimitrijevic, Tijana Rajh, and Kimberly A. Gray, *J. Catal.*, **253**, Iss. 1: 105 (2008); https://doi.org/10.1016/j.jcat.2007.10.014
3. Haihan Chen, Charith E. Nanayakkara, and Vicki H. Grassian, *Chem. Rev.*, **112**, Iss. 1: 5919 (2012); https://doi.org/10.1021/cr3002092
4. Natalia Zotova, Felicity J. Roberts, Geoffrey H. Kelsall, Alan S. Jessiman, Klaus Hellgardt, and King Kuok (Mimi) Hii, *Green Chem.*, **14**, Iss. 1: 226

(2012); https://doi.org/10.1039/C1GC16118K
5. Xiaobo Chen and Samuel S. Mao, *Chem. Rev.*, **107**, Iss. 7: 2891 (2007); https://doi.org/10.1021/cr0500535
6. Shafeer Kalathil, Mohammad Mansoob Khan, Arghya Narayan Banerjee, Jintae Lee, and Moo Hwan Cho, *Journal of Nanoparticle Research*, **14**, Iss. 8: 1051 (2012); https://doi.org/10.1007/s11051-012-1051-x
7. Kevin Kдhler, Marie C. Holz, Markus Rohe, Andre C. van Veen, and Martin Muhler, *J. Catal.*, **299**: 162 (2013); https://doi.org/10.1016/j.jcat.2012.12.001
8. Bala Subramaniam, Richard K. Helling, and Claudia J. Bode, *ACS Sustain Chem. Eng.*, **4**, Iss. 11: 5859 (2016); https://doi.org/10.1021/acssuschemeng.6b01571
9. Akl M. Awwad, Nida M. Salem, and Amany O. Abdeen, *Nanoscience and Nanotechnology*, **2**, Iss. 6: 164 (2013); https://doi.org/10.5923/j.nn.20120206.03
10. Sunandan Baruah, Sudarson Sekhar Sinha, Barnali Ghosh, Samir Kumar Pal, A. K. Raychaudhuri, and Joydeep Dutta, *J. Appl. Phys.*, **105**, Iss. 7: 074308 (2009); https://doi.org/10.1063/1.3100221
11. Roberta Brayner, Roselyne Ferrari-Iliou, Nicolas Brivois, Shakib Djediat, Marc F. Benedetti, and Fernand Fiévet, *Nano Lett.*, **6**, Iss. 4: 866 (2006); https://doi.org/10.1021/nl052326h
12. Sanaz Alamdari, Morteza Sasani Ghamsari, Chan Lee, Wooje Han, Hyung-Ho Park, Majid Jafar Tafreshi, Hosein Afarideh, and Mohammad Hosein Majles Ara, *Applied Sciences*, **10**, Iss. 10: 3620 (2020); https://doi.org/10.3390/app10103620
13. J. Sawai, *J. Microbiol Methods*, **54**, Iss. 2: 177 (2003); https://doi.org/10.1016/S0167-7012(03)00037-X
14. Y. Liu, L. He, A. Mustapha, H. Li, Z. Q. Hu, and M. Lin, *J. Appl. Microbiol.*, **107**, Iss. 4: 1193 (2009); https://doi.org/10.1111/j.1365-2672.2009.04303.x
15. N. Jones, B. Ray, K. T. Ranjit, and A. C. Manna, *FEMS Microbiol. Lett.*, **279**, Iss. 1: 71 (2008); https://doi.org/10.1111/j.1574-6968.2007.01012.x
16. J.-J. Hwang and T.-W. Ma, *Mater. Chem. Phys.*, **136**, Iss. 2–3: 613 (2012); https://doi.org/10.1016/j.matchemphys.2012.07.034
17. J. Suliman Al Ebraheem, M. N. Ahmad Alkhoder, and R. H. Tulaimat, *Heliyon*, **10**, Iss. 2: 24652 (2024); https://doi.org/10.1016/j.heliyon.2024.e24652

Наносистеми, наноматеріали, нанотехнології
Nanosistemi, Nanomateriali, Nanotehnologii
2026, т. 24, № 1, сс. 249–265
https://doi.org/10.15407/nnn.24.01.0249

PACS numbers: 07.07.Vx, 68.37.Hk, 68.37.Vj, 68.55.J-, 72.80.Tm, 78.20.Ci, 78.67.Sc

The Effect of Increasing ZnO Nanomaterial in PVA–ZnO Nanocomposites and Investigating Some of Their Properties for Utilization as Humidity Sensor

Ameen Alwan Mohaimeed[1,2] and Maher Hassan Rasheed[3]

[1]*College of Sciences,*
Medical Physics Department,
Al-Mustaqbal University,
51001 Babil, Iraq
[2]*Directorate of Education Babylon,*
Ministry of Education,
Homs, Iraq
College of Basic Education,
[3]*Department of Science,*
University of Babylon,
Hilla, Iraq

This research is aimed to prepare PVA with ratios of 0.2, 0.4, and 0.6 wt.% by the casting method and with a thickness of 270±5 μm. The morphological characteristics are examined *via* FE–SEM and FT–IR, and the results show that the composites have a homogeneous and granular structure and that ZnO is well distributed within the polymer. The reason for the increased movement of charges is the action of a grid of nanomaterials inserted into the polymer. FT–IR analysis reveals absorption peaks at 3251.3 cm^{-1} and 2812 cm^{-1} due to the O–H bond, which indicates the presence of polyvinyl alcohol. The absorbance of the prepared composites increases with increasing nanomaterials' concentration, reaching 93% at 6 wt.%. In addition, the energy gap decreases with increasing nanomaterial concentration to 2.87–2.73 eV, and all optical parameters α, n, k, ε_r, and ε_i increase with increasing nanomaterials' concentration. For all the samples, the dielectric constant decreases as the frequency increases and increases with increasing nanomaterials' concentration within the polymer. A decrease in the effect of charge polarization is the main factor of the dielectric loss of the PVA–ZnO nanocomposite; at the same time, increasing the concentration of nanomaterials leads to an increase in the dielectric loss. An increase in the frequency of the electric field and an increase in the concentration of nanomaterials increase the electrical conductivity. The humidity sensor shows almost no humidity hysteresis, and its resistance decreases with increasing humidity and zinc-oxide concentration.

This makes these films useful for electronic applications and light filters, and they can be also used as ultraviolet detectors and humidity sensors.

Це дослідження має на меті приготування полівінілового спирту (ПВС) зі співвідношенням компонентів 0,2, 0,4 та 0,6 мас.% методом лиття та товщиною у 270±5 мкм. Морфологічні характеристики досліджено за допомогою емісійної (автоелектронної) сканувальної електронної мікроскопії та інфрачервоної спектроскопії на основі Фур'є-перетвору; результати показали, що композити мають однорідну та зернисту структуру, а ZnO добре розподілений у полімері. Причиною посиленого руху зарядів є дія сітки наноматеріялів, вставлених у полімер. Аналіза даних інфрачервоної спектроскопії на основі Фур'є-перетвору виявила піки вбирання в околі 3251,3 $см^{-1}$ і 2812 $см^{-1}$, зумовлені зв'язком O–H, що вказує на наявність полівінілового спирту. Вбирання одержаних композитів збільшується зі збільшенням концентрації наноматеріялів, досягнувши 93% за 6 мас.%. Крім того, заборонена енергетична зона зменшується зі збільшенням концентрації наноматеріялів до 2,87–2,73 еВ, а всі оптичні параметри α, n, k, ε_r і ε_i збільшуються зі збільшенням концентрації наноматеріялів. Для всіх зразків діелектрична проникність зменшується зі збільшенням частоти та збільшується зі збільшенням концентрації наноматеріялів у полімері. Зменшення впливу поляризації заряду є основним чинником діелектричних втрат нанокомпозиту ПВС–ZnO; водночас збільшення концентрації наноматеріялів призводить до збільшення діелектричних втрат. Підвищення частоти електричного поля та збільшення концентрації наноматеріялів підвищують електропровідність. Датчик вологости майже не демонструє гістерези вологости, а його опір зменшується з підвищенням вологости та концентрації оксиду Цинку. Це робить зазначені плівки корисними для електронних застосувань і світлофільтрів, а також їх можна використовувати як ультрафіолетові детектори та датчики вологости.

Key words: PVA–ZnO nanocomposites, a.c. electrical properties, morphological properties, zinc oxide, humidity sensor.

Ключові слова: нанокомпозити полівініловий спирт–ZnO, електричні властивості на змінному струмі, морфологічні властивості, оксид Цинку, датчик вологости.

(Received 5 August, 2024)

1. INTRODUCTION

Composite materials are composed of two or more phases that are different from one another both chemically and physically [1]. These amazing materials, sometimes referred to as nanocomposites, are an integral part of contemporary materials due to their many advantages, which include low weight, resistance to corrosion, high fatigue strength, and simple assembly [2]. When creating compos-

ites, reinforcing material is often added in a continuous phase called the matrix or binder [3]. Strengthening and enhancing overall properties are frequently achieved by incorporating dispersed phases into the matrix, which may be an engineered material such as a metal, polymer, or ceramic [4].

Nanocomposites do not differ from traditional materials in terms of the filling and matrix, but traditionally, they use, for example, glass or carbon fibres [5], while nanocomposites use a filling made of nanomaterial such as gold, silver, and silicon [2]. The composite depends upon three factors: the matrix, the reinforcement, and the adherence of the matrix to the reinforcement [6], compatibility and the ability to dissolve in water. In addition, hydrogels can be formed by physical and chemical methods [7]. Polyvinyl alcohol (PVA) has features that have made it the focus of researchers' attention due to its strong storage and insulating ability and its optical and electrical properties depending on the activator [8, 9]. PVA, with the formula $(C_2H_4O)_n$, is frequently used in various contexts, with semiconductors being one of the most prevalent [10]. The semiconductor zinc oxide (ZnO) has a large exciton binding energy of 60 meV at ambient temperature and relatively wide band-gap energy of 3.37 eV [11].

For use in medicine and the environment, ZnO is also biocompatible, biodegradable, and biosafe [11, 12]. The energy gap of ZnO is wide, making it one of the most promising semiconductor materials for optical applications in the ultraviolet spectral range [13]. The process of doping polymers and forming a matrix is beneficial for the formation of nanocomposites, and as a result, the structural and other physical properties increase [14], the fabrication of polymer-based nanocomposites for investment in electronic and optical applications and solar cells [15, 16]. This work investigated the morphological, electrical, and optical properties of PVA–ZnO nanocomposites *via* FE–SEM, optical microscopy, and FT–IR spectroscopy. This research aims to create PVA–ZnO nanocomposites and analyze their electrical and optical properties, as well as some structural aspects, with the intention of employing them as humidity sensors.

2. COMPUTATIONAL DETAILS

This section concentrates on the procedural aspects of employing the casting process to produce and examine PVA–ZnO. 25 ml of distilled water was used to dissolve 1 g of PVA, and after the polymer was completely dissolved, a percentage of 0, 2, 4 and 6 wt.% ZnO were added. Then, the nanomaterial was dispersed with an ultrasonic device. After that, the mixture was poured into dishes to a thickness of 270 ± 5 μm. After one week, these films were measured.

Zinc oxide (ZnO): Zhengzhou Dongyao Nano Materials Co., Ltd., is a Chinese company, from which this powder was obtained. Its features include a high purity of 99.99%, a white colour, a density of 5.606 g/cm^3, and a nanoparticle size of 50 nm.

The molecular weight of the utilized polyvinyl alcohol (PVA) ranged from 26.200 to 30.400 g/mol. China's Shanghai Kaidu Industrial Development Co., Ltd. is the manufacturer of PVA.

The optical properties of the films, such as the absorbance (A), absorbance coefficient (α), real dielectric constant (ε_r), imaginary dielectric constant (ε_i), refractive index (n), extinction coefficient (k) and band gab (E_g), were evaluated *via* several measurements. These measurements were conducted using a spectrophotometer equipped with two laser beams Shimadzu, UV-1800 A0, Japan across the spectrum range of 200 nm to 1100 nm. The structural characteristics of the PVA–ZnO films were investigated by Fourier transform infrared (FT–IR) spectroscopy in the range of 500–4000 cm^{-1} and FE–SEM, and the results were analyzed. Additionally, the electrical properties of the a.c. films were examined and analyzed.

Understanding a material's optical constants in great detail across a broad range of wavelengths is necessary for its use in optical applications and the creation of reflective coatings [17]. The optical characteristics of all materials may be correlated with their electrical, electronic band, and atomic structures [18]. The Beer–Lambert equation is the equation, by which the optical absorption coefficient can be described [19]:

$$\alpha = \frac{2.303A}{t}. \tag{1}$$

The logarithmic relationship between the incident intensity I_0 and the reflected I_A is known as the absorbance A [20]:

$$A = -\log T_r = \log\left(\frac{I_0}{I_A}\right). \tag{2}$$

Optical constants of the optical properties of films, such as the complex dielectric constant (with parts ε_r, ε_i), extinction coefficient (k), and index of refraction (n), can be described as follow [21]:

$$k = \frac{\alpha\lambda}{4\pi}, \tag{3}$$

$$n = \frac{1 + R_{1/2\,0}}{1 - R_{1/2\,0}}. \tag{4}$$

Through these two equations, complex dielectric constants can be

calculated as follow [22]:

$$\varepsilon_r = n^2 - k^2, \tag{5}$$

$$\varepsilon_i = 2nk. \tag{6}$$

The optical energy gap can be determined from that region as shown in the following relationship [23]:

$$\alpha h\nu = \beta\left(h\nu - E_g\right)^r. \tag{7}$$

The presence of free ions in the polymer increases its electrical conductivity:

$$\sigma_v = \frac{1}{\rho_v} = \frac{L}{R_V A_r}. \tag{8}$$

Using the Debye equation, the dielectric constant can be calculated:

$$\varepsilon = \varepsilon' - i\varepsilon'', \tag{9}$$

where ε'' represents the dielectric loss [24].

3. RESULTS AND DISCUSSION

3.1. Optical Properties

Figure 1 shows the absorption for samples with a thickness of 270 ± 5 μm. The absorption in the ultraviolet region is high and begins to decrease at a wavelength of 400 nm. Additionally, with increasing concentrations of the ZnO nanomaterial, the absorption decreases even with increasing wavelength, and the absorbance reaches 93% at 6 wt.% [25]. The absorption coefficient can be calculated from Eq. (1). Figure 2 shows that with increasing energy, the absorption coefficient increases, and the type of electronic transitions can be determined. This increase is due to an increase in the concentration of ZnO, which leads to electronic crossing between the partial orbitals with the help of phonons, and the electronic momentum is preserved [8, 26]. It is possible to draw a tangent slope for all the films, which shows the energy gap *versus* the photon energy. The results also showed that by increasing the concentration of nanomaterials ZnO, the energy gap decreases, which explains the narrowing of the crossing region from the valence band to the conduction band and the increase in the movement of electrons [27].

Figure 3 shows that the energy gap decreased as 2.87, 2.83, 2.79,

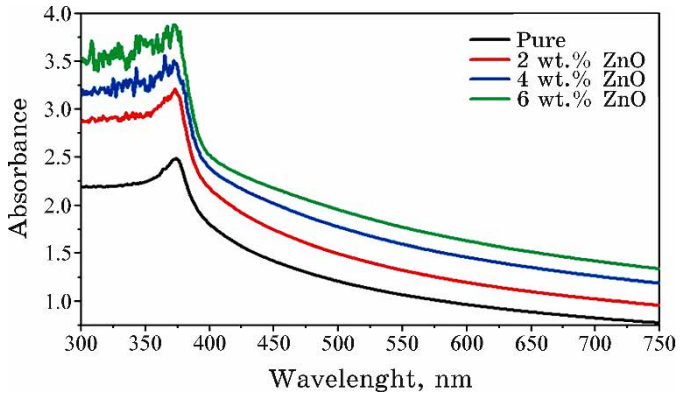

Fig. 1. Absorbance *versus* wavelength for the PVA–ZnO nanocomposites.

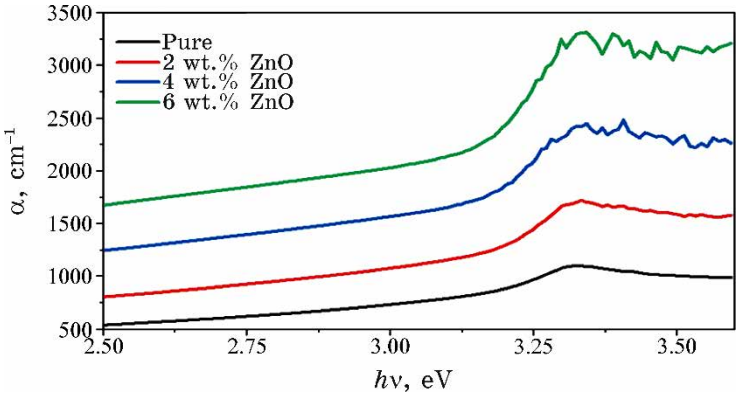

Fig. 2. The photon energy ($h\nu$) and absorption coefficient (α) for ZnO at various concentrations in PVA.

and 2.73 eV; the reason for this decrease is the creation of local bands due to the increase in the amount of the nanomaterial ZnO in the polymer.

This nanocomposite can be used as a humidity sensor. These nanocomposites are also used in optical applications [27, 28].

An increase in the concentration of nanomaterials ZnO increased the extinction coefficient, as shown in Fig. 4; since this nanocomposite contains polyvinyl alcohol, the unsaturated carbonyl group attached to ethylene will show a peak in all samples close to 400 nm [8, 19, 21, 29]. Because of the link between them, the extinction-coefficient curve behaviour of the nanocomposites is comparable to the absorption coefficient (see Eq. (3)) [16]. Furthermore, a sharp increase in the extinction coefficient occurred at the absorption edge. These results could be ascribed to both increased absorbance

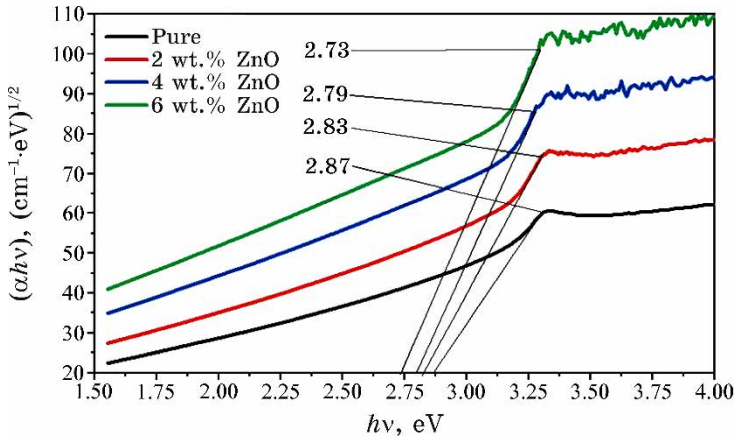

Fig. 3. Optical energy gap for $(\alpha h\nu)^{1/2}$ *versus* the photon energy ($h\nu$) for PVA with different concentrations of ZnO.

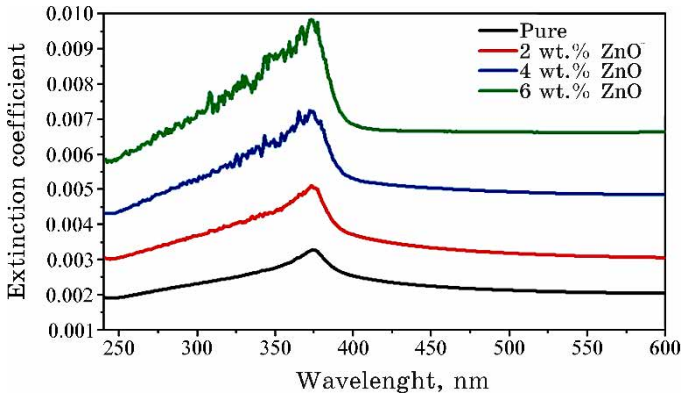

Fig. 4. Extinction coefficient *versus* wavelength for the PVA–ZnO nanocomposites.

because of the transmission phase and increased scattering due to the increase; this finding matches the morphological characteristics of the FE–SEM images [30, 31].

Figure 5 shows that when the concentration of nanomaterials (ZnO) increases, so does the refractive index. The optical energy gap and reflectivity of the films are responsible. The packing density and orientation are related to variations in the n value [32].

The amount, by which a substance slows the speed of light, is proportional to its real component. The imaginary fraction, ε_i, shows how a dielectric absorbs energy from an electric field through dipole motion. As a result of k_0^2 being less than n^2 according to

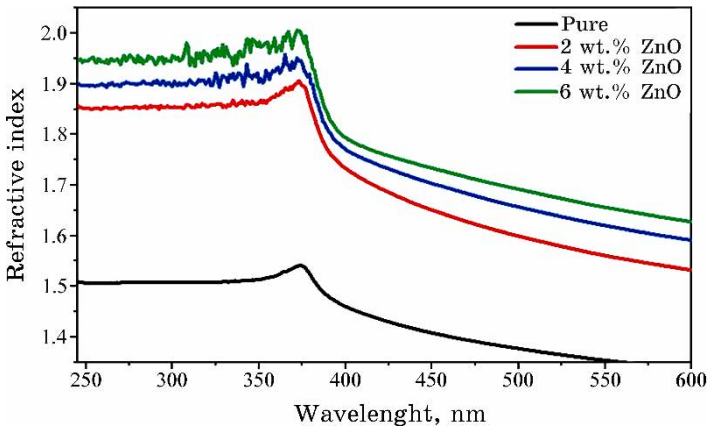

Fig. 5. Refractive index *versus* wavelength for the PVA–ZnO nanocomposites.

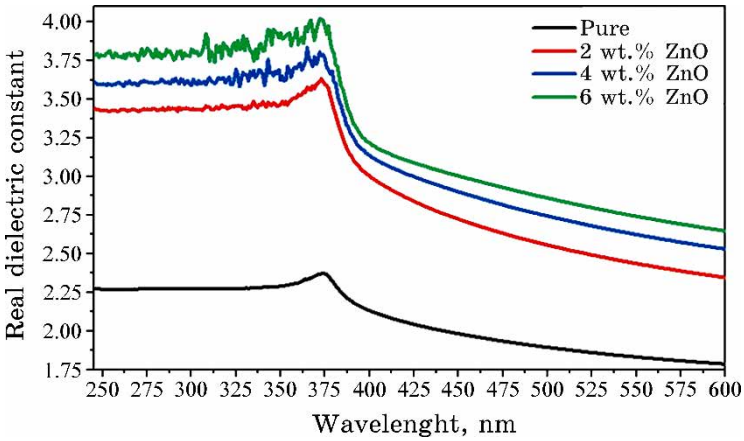

Fig. 6. Real dielectric properties *versus* wavelength for the PVA–ZnO nanocomposites.

Eq. (5), the behaviour of ε_r in Fig. 6 is comparable to the refractive index performance. However, ε_i depends mostly on the value of the extinction coefficient (k_0) according to Eq. (6) [33].

3.2. A.C. Electrical Conductivity

Using Eq. (9), the dielectric constant (ε') of the PVA–ZnO nanocomposites was determined.

Figure 8 shows the dielectric constant of the PVA–ZnO nanocomposites as a function of the frequency. The dielectric constant de-

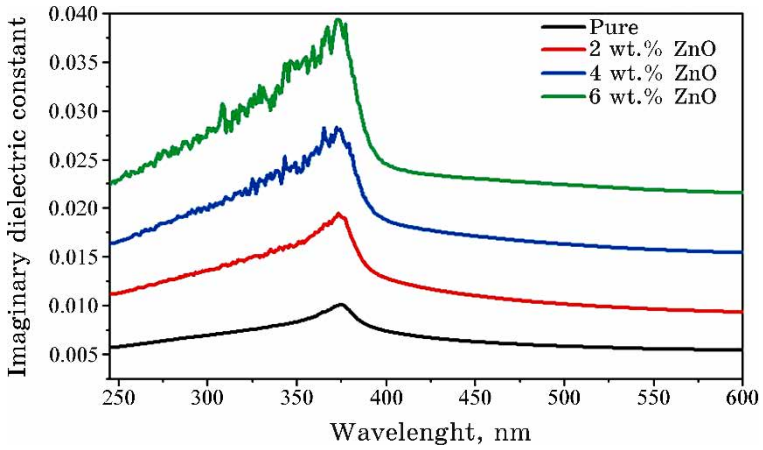

Fig. 7. Imaginary dielectric constant *versus* wavelength for the PVA–ZnO nanocomposites.

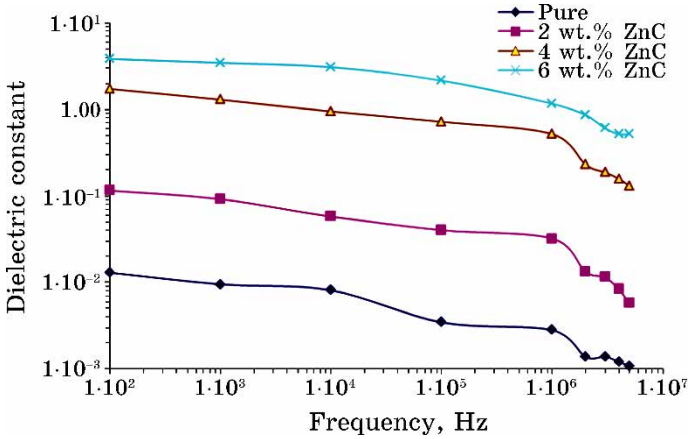

Fig. 8. Dielectric constant *versus* frequency at standard room temperature for the PVA–ZnO nanocomposites.

creases with increasing frequency in all the samples. This phenomenon can be attributed to the dipoles in the nanocomposites turning in the direction of the applied electric field and the reduction of space charges or interfacial polarization to overall polarization [34].

Figure 9 illustrates how the dielectric constant of the PVA–ZnO nanocomposites varies with the number of nanoparticles present at $f = 100$ Hz. This indicates that the dielectric constant of the PVA–ZnO nanocomposites increases as the amount of ZnO nanoparticles increases. It is noted that all nanocomposite samples increase with increasing nanoparticle loading. Interfacial polarization within the

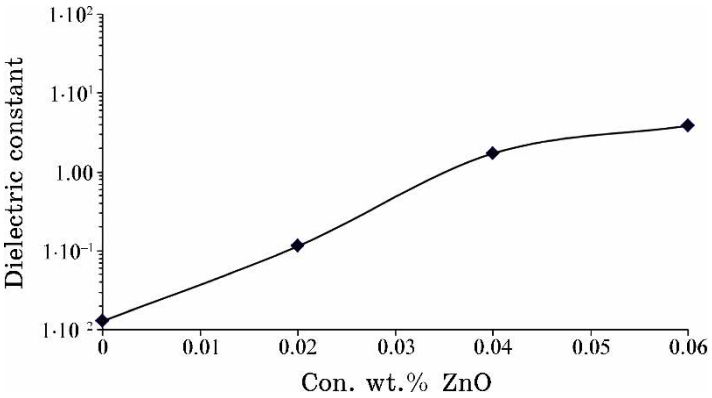

Fig. 9. Impact of ZnO-nanoparticles' content on the dielectric constant of PVA–ZnO nanocomposites at 100 Hz.

nanocomposites in an applied field with an alternating electric field and an increase in charge carriers could be used to characterize these processes [35]. This indicates that the produced nanocomposites have low or low energy loss, making them appropriate for use in pressure sensors and nanoelectronics applications.

The dielectric loss (ε'') was calculated from Eq. (9).

Figure 10 shows the dielectric loss for the PVA–ZnO nanocomposites as a function of frequency. As the frequency increases, the dielectric loss of the PVA–ZnO nanocomposites decreases, which is caused by a decrease in the influence of space charge polarization. The dielectric loss is highest at low frequencies and decreases as the frequency increases. This is because the electric dipoles have adequate time to align with the electric field before changing direction [36].

The effect of ZnO concentration on the dielectric loss of PVA polymer at $f = 100$ Hz is shown in Fig. 11. An increase in the number of nanoparticles causes a rise in the dielectric loss, which is explained by an increase in the number of charge carriers [37]. Clusters are formed when the number of nanoparticles in the nanocomposites is minimal, but when the concentration is high, up to 6 wt.%, they combine to form networks. The dielectric loss of the nanocomposites increases as the amount of ZnO NPs increases, as illustrated in the figures. As the amount of ZnO NPs in the polymer (PVA) increases, so does its dielectric loss, which is explained by the increase in charge carriers for the nanocomposites [38].

To measure the a.c. electrical conductivity of the nanocomposites, Eq. (8) was used. Nanoparticles produce a route network inside the nanocomposite at high concentrations of nanoparticles 6 wt.% for the PVA polymer.

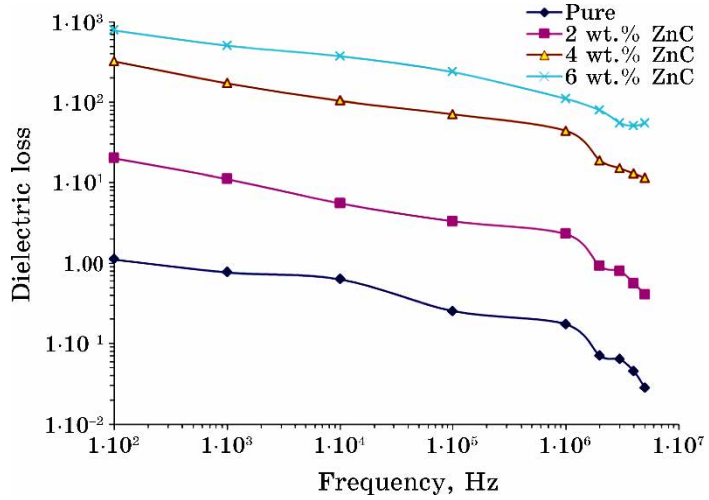

Fig. 10. Dielectric loss *versus* frequency at standard room temperature for the PVA–ZnO nanocomposites.

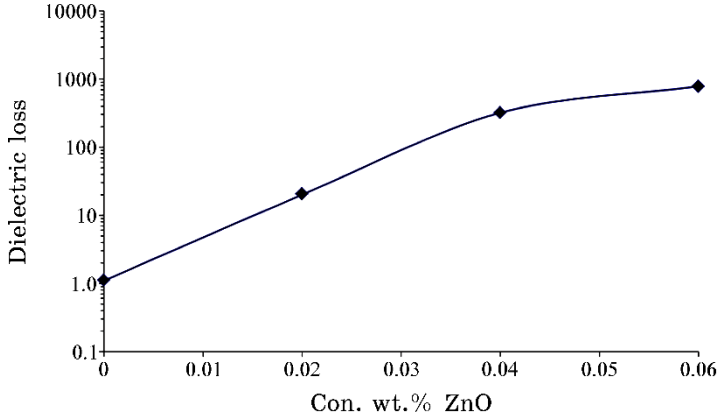

Fig. 11. Effect of ZnO NPs on the dielectric loss of the PVA–ZnO nanocomposites at 100 Hz.

Figure 12 displays the fluctuation in the electrical conductivity of the PVA–ZnO nanocomposites with frequency. As demonstrated in the figures, the electrical conductivity increases as the electric field frequency increases for all the prepared nanocomposites. This behaviour is caused by the hopping process, which moves charge carriers, and space charge polarization, which occurs at low frequencies. For PVA–ZnO nanocomposites, the electrical conductivity increases with increasing frequency due to the enhanced mobility of charge carriers in the high-frequency region [39]. Figure 13 shows

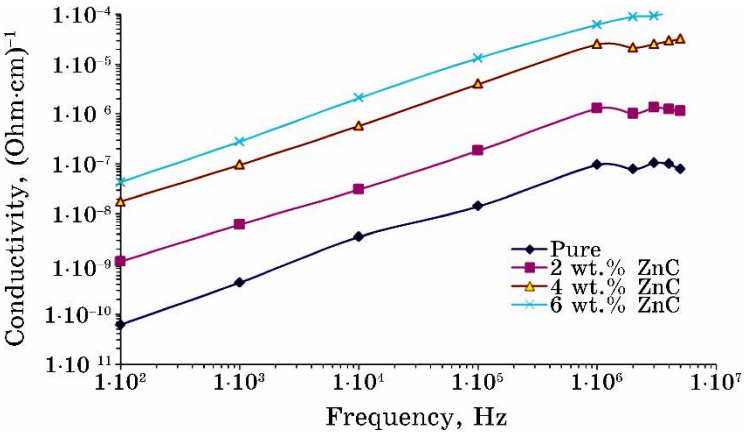

Fig. 12. Electrical conductivity *versus* frequency for the PVA–ZnO nanocomposites.

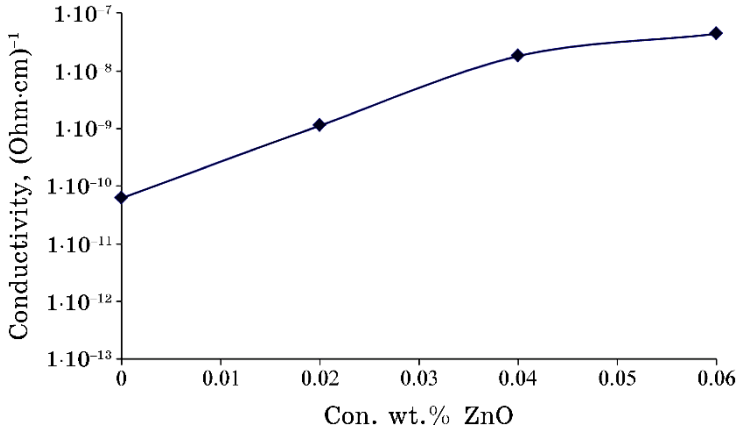

Fig. 13. Effect of ZnO-NPs' filling on the electrical conductivity of nanocomposites at 100 Hz.

how ZnO nanoparticles affect the electrical conductivity of the PVA polymer at 100 Hz. According to the figures, as the concentration of ZnO nanoparticles increased. Because of the composition of the dopant nanoparticles, which gradually reduce the resistance of the nanocomposites and increase the electrical conductivity, the increase in electrical conductivity with increasing ZnO nanoparticle content is attributed to an increase in the number of charge carriers. This finding aligns with the findings of previous studies [40, 41].

Figure 14 shows the measured values of the humidity sensor. The humidity and temperature were maintained at room temperature.

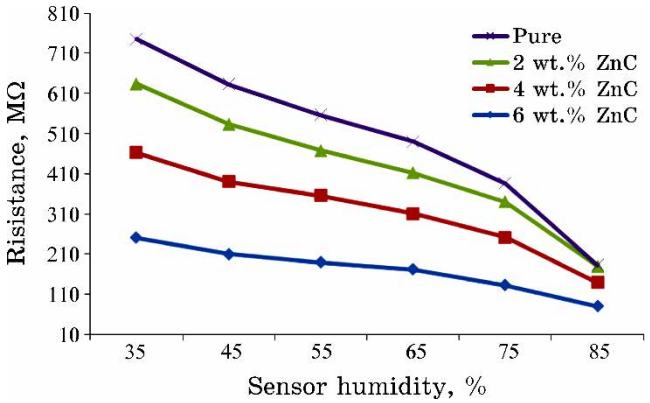

Fig. 14. Relationships between the sensor resistance and humidity.

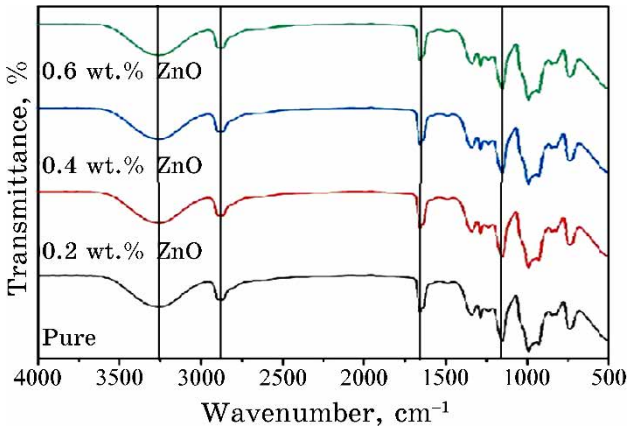

Fig. 15. FT–IR spectrum of the PVA–ZnO nanocomposites.

According to the experimental findings, the humidity sensor exhibited nearly no humidity hysteresis, and its resistance decreased as humidity increased [42]. An increase in the zinc-oxide concentration decreased the resistance level with increasing humidity [43].

3.3. Morphological Properties

The purpose of the FE–SEM examination was to clarify the density and distribution of the nanoparticles in the manufactured polymeric film, as the images showed a homogeneous distribution of ZnO within the polymer. The image also showed that the ZnO nanoparticles appeared to have been coated with the polymeric material (PVA), as shown in Fig. 15 [8]. Increasing the number of ZnO molecules rep-

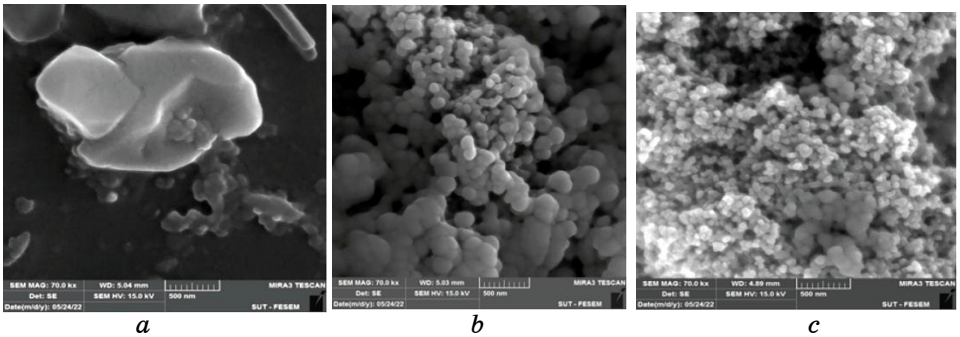

a *b* *c*

Fig. 16. FE–SEM images of (*a*) PVA, (*b*) PVA/0.2 wt.% ZnO, and (*c*) PVA/0.6 wt.% ZnO.

resented in a network in the polymer matrix increases the conductivity due to its ability to accelerate electron motion, which is the main reason for the reduction in the E_g [44].

Other nanomaterials, such as graphene, can be used [45–46].

Figure 16 shows the FT–IR spectrum of the PVA/ZnO nanocomposites; the O–H bond is responsible for the absorption peak observed at 3251.3 cm^{-1} and 2812 cm^{-1}, which indicates the presence of PVA and indicates its identity; these two peaks are attributed to the PVA polymer, which is an aliphatic compound. It traps water from the air, which is typical in humidity sensor applications [8]. The vibration peaks that appeared at 1625.03 cm^{-1} and 1154 cm^{-1} indicate weak Zn–O and ZnO_2 bonds. When ZnO nanomaterials were added to the polymer at various concentrations, some changes were observed in the vibration peaks, and no peak creep was observed. This means that the reaction is physical [7, 8].

4. CONCLUSION

The results showed that the prepared films are homogeneous, and the diffusion of the nanomaterial within the polymer is good, which, in turn, enables the electrons to move more freely. FTIR analyses revealed the highest absorption at 3251.3 cm^{-1} and 2812 cm^{-1} due to the O–H bond, which indicates the presence of PVA. It traps water from the air, which is typical in humidity sensor applications. Additionally, in the UV region, as the number of nanomaterials increases, the energy gap decreases to between 2.87 eV and 2.73 eV, and all the optical constants increase with increasing nanomaterial concentration. Therefore, they can be used as detectors in the UV region. As the frequency and concentration of nanomaterials increase, the dielectric constant, dielectric loss, and

AC electrical conductivity increase.

ACKNOWLEDGMENTS

The authors gratefully acknowledge the technical support provided by Al-Mustaqbal University, University of Babylon, and the Applied Sciences Department, University of Technology, Baghdad, Iraq.

REFERENCES

1. Shehu Sa'ad Abdullahi, Rania Edrees Adam Mohammad, Ahmad Hussaini Jagaba, Haruna Musa, and Abdullahi Haruna Birniwa, *Case Studies in Chemical and Environmental Engineering*, **9**: 100570 (2023); https://doi.org/10.1016/j.cscee.2023.100570
2. Gaurav Choudhary, Jyoti Dhariwal, Moumita Saha, Shruti Trivedi, Manoj K. Banjare, Rahul Kanaoujiya, and Kamalakanta Behera, *Environmental Science and Pollution Research*, **31**, Iss. 7: 10296 (2024); https://doi.org/10.1007/s11356-023-25468-w
3. Sheng Dai, Mengchao Cui, Jiahui Li, and Meng Zhang, *Coatings*, **14**, Iss. 7: 822 (2024); https://doi.org/10.3390/coatings14070822
4. Tawfik A. Saleh, Prakash Parthasarathy, and Muhammad Irfan, *Trends in Environmental Analytical Chemistry*, **24**: e00067 (2019); https://doi.org/10.1016/j.teac.2019.e00067
5. O. Anthony Ogunmefun, B. Lawrence Bayode, T. Jamiru, Peter A. Olubambi, *Journal of Alloys and Compounds*, **960**: 170407 (2023); https://doi.org/10.1016/j.jallcom.2023.170407
6. Aditya Prakash Kanth and Aditya Krushang Soni, *Journal of Cultural Heritage*, **59**: 120 (2023); https://doi.org/10.1016/j.culher.2022.11.010
7. Haifa Mohammed Alghamdi and A. Rajeh, *J. Inorg. Organomet. Polym.*, **32**: 1935 (2022); https://doi.org/10.1007/s10904-022-02322-z
8. Ameen Alwan Mohaimeed and Bahaa H. Rabee, *Opt. Quant Electron.*, **55**: 254 (2023); https://doi.org/10.1007/s11082-022-04523-9
9. Dominic Byrne, Geert Boeije, Ian Croft, Gerd Hьttmann, Gerard Luijkx, Frank Meier, Yash Parulekar, and Gerard Stijntjes, *Tenside Surfactants Deterg.*, **58**, No. 2: 88 (2021); https://doi.org/10.1515/tsd-2020-2326
10. Behnam Eslami, Ismaeil Ghasemi, and Masoud Esfandeh, *Polymers*, **15**, Iss. 14: 3063 (2023); https://doi.org/10.3390/polym15143063
11. Niyaz M. Sadiq, Shujahadeen B. Aziz, and Mohd F. Z. Kadir, *Gels*, **8**, Iss. 3: 153 (2022); https://doi.org/10.3390/gels8030153
12. A. M. Schwan, S. Chwatal, C. Hendler, D. Kopp, J. M. Lackner, R. Kaindl, M. Tscherner, M. Zirkl, P. Angerer, B. Friessnegger, S. Augl, D. Heim, A. Hinterer, M. Stummer, and W. Waldhauser, *Applied Nanoscience*, **13**, Iss. 9: 6421 (2023); https://doi.org/10.1007/s13204-023-02936-w
13. Shaheer Ahmed Khan, Zakaria Mohd Zain, Mohammad Mansoor, M. M. Hasan Mahfuz, Ataur Rahman, Mir Akmam Noor Rashid, and Mohammad Salman Rais, *Materials Today: Proceedings*, **2100**, No. 1: 020045 (2019); https://doi.org/10.1016/j.matpr.2021.05.197

14. Roberto Ambrosio, Amanda Carrillo, Maria L. Mota, Karla de la Torre, Richard Torrealba, Mario Moreno, Hector Vazquez, Javier Flores, and Israel Vivaldo, *Polymers*, **10**, Iss. 12: 1370 (2018); https://doi.org/10.3390/polym10121370
15. Kesong Hu, Dhaval D. Kulkarni, Ikjun Choi, and Vladimir V. Tsukruk, *Progress in Polymer Science*, **39**, Iss. 11: 1934 (2014); https://doi.org/10.1016/j.progpolymsci.2014.03.001
16. Yumnam Bonney Singh, Dipankar Biswas, Rittwick Mondal, Saikat Chattopadhyay, Anindya Sundar Das, Debabrata Mandal, Soumyajyoti Kabi, and Loitongbam Surajkumar Singh, *Materials Today, Communications*, **38**: 108002 (2024); https://doi.org/10.1016/j.mtcomm.2023.108002
17. Dileep Chekkaramkodi, Liya Jacob, Muhammed Shebeeb C, Rehan Umer, and Haider Butt, *Additive Manufacturing*, **86**: 104189 (2024); https://doi.org/10.1016/j.addma.2024.104189
18. Ammar Qasem, Mohamed S. Mostafa, H. A. Yakout, Mona Mahmoud, and E. R. Shaaban, *Opt. Laser Technol.*, **148**: 107770 (2022); https://doi.org/10.1016/j.optlastec.2021.107770
19. Ameen Alwan Mohaimeed and Bahaa H. Rabee, *Annals of Agri-Bio Research*, **27**, Iss. 2: 222 (2022); https://www.researchgate.net/profile/Ameen-Mohaimeed-2/publication/365301579_Influence_of_Natural_Crocus_Dye_on_Morphological_and_Optical_Properties_of_PVATiO_2_Nanocomposite_Prepared_by_the_Spin_Coater_Method/links/636e13832f4bca7fd05054ab/Influence-of-Natural-Crocus-Dye-on-Morphological-and-Optical-Properties-of-PVA-TiO-2-Nanocomposite-Prepared-by-the-Spin-Coater-Method.pdf
20. Torki A. Zughaibi, *Sustainable Chemistry and Pharmacy*, **39**: 101566 (2024); https://doi.org/10.1016/j.scp.2024.101566
21. Ameen Alwan Mohaimeed and Bahaa H. Rabee, *Annals of Biology*, **39**, Iss. 1: 108 (2023); https://agribioj.com/wp-content/uploads/2019/11/108-111.pdf
22. Hui Tang, Changjin Yang, Li Qin, Lei Liang, Yuxin Lei, Peng Jia, Yongyi Chen, Yubing Wang, Yue Song, Cheng Qiu, Chuantao Zheng, Xin Li, Dabing Li, and Lijun Wang, *Sensors*, **23**, Iss. 17: 7326 (2023); https://doi.org/10.3390/s23177326
23. Ravi Kumar, Rajiv Kumar, Anil Arya, Pawan K. Sharma and Annu Sharma, *Braz. J. Phys.*, **52**, Iss. 5: 1 (2022); https://doi.org/10.1007/s13538-022-01170-z
24. C. R. Mariappan and G. Govindaraj, *Mater. Sci. Eng. B*, **94**: 82 (2002); https://doi.org/10.1016/S0921-5107(02)00083-1
25. C. Ravi Dhas, R. Venkatesh, R. Sivakumar, A. Moses Ezhil Raj, and C. Sanjeeviraja, *Opt. Mater.*, **72**: 717 (2017); https://doi.org/10.1016/j.optmat.2017.07.026
26. Mohamed Oubaha, Salem Elmaghrum, Robert Copperwhite, Brian Corcoran, Colette McDonagh, and Arnaud Gorin, *Opt. Mater.*, **34**: 1366 (2012); https://doi.org/10.1016/j.optmat.2012.02.023
27. Y. Al-Hadeethi, M. I. Sayyed, and Y. S. Rammah, *Ceram. Int.*, **45**, No. 16: 20724 (2019); https://doi.org/10.1016/j.ceramint.2019.07.056
28. Hyuk-Joon Youn, Tomohiro Sogabe, Clive A. Randall, Tom R. Shrout, and Michael T. Lanagan, *J. Am. Ceram. Soc.*, **84**, No. 11: 2557 (2001); https://doi.org/10.1111/j.1151-2916.2001.tb01053.x
29. Raghvendra Singh Yadav and Ivo Kuřitka, *Advances in Colloid and Interface*

Science, **326**: 103137 (2024); https://doi.org/10.1016/j.cis.2024.103137
30. Sze-Mun Lam, Jin-Chung Sin, Ahmad Zuhairi Abdullah and Abdul Rahman Mohamed, *Water Air Soil Pollut.*, **224**: 1 (2013); https://doi.org/10.1007/s11270-013-1565-6
31. Doaa Domyati, *Optical Materials*, **152**: 115479 (2024); https://doi.org/10.1016/j.optmat.2024.115479
32. R. Syafinar, N. Gomesh, M. Irwanto, M. Fareq, and Y. M. Irwan, *Energy Proc.*, **79**: 799 (2015); https://doi.org/10.1016/j.egypro.2015.11.569
33. Mohanad H. Meteab, Ahmed Hashim and Bahaa H. Rabee, *Opt. Quantum Electron.*, **55**: 187 (2023); https://doi.org/10.1007/s11082-022-04447-4
34. P. Lokanatha Reddy, Kalim Deshmukh, K. Chidambaram, Mohammad M. Nazeer Ali, Kishor Kumar Sadasivuni, Y. Ravi Kumar, R. Lakshmipathy, and S. K. Khadheer Pasha, *J. Mater. Sci. Mater. Electron.*, **30**, Iss. 4: 4676 (2019); https://doi.org/10.1007/s10854-019-00761-y
35. L. H. Gaabour, *AIP Adv.*, **11**, Iss. 10: 105120 (2021); https://doi.org/10.1063/5.0062445
36. Chainarong Srivabut, Thanate Ratanawilai, and Salim Hiziroglu, *Journal of Material Cycles and Waste Management*, **23**, Iss. 4: 1503 (2021); https://doi.org/10.1007/s10163-021-01230-7
37. S. Ju, M. Chen, H. Zhang, and Z. Zhang, *Express Polym. Lett.*, **8**, Iss. 9: 682 (2014); doi:10.3144/expresspolymlett.2014.71
38. Xingyi Huang, Shen Wang, Ming Zhu, Ke Yang, Pingkai Jiang, Yoshio Bando, Dmitri Golberg, and Chunyi Zhi, *Nanotechnology*, **26**, Iss. 1: 015705 (2014); doi:10.1088/0957-4484/26/1/015705
39. H. Shivashankar, Kevin Amith Mathias, Pavankumar R. Sondar, M. H. Shrishail, and S. M. Kulkarni, *J. Mater. Sci. Mater. Electron.*, **32**, Iss. 20: 28674 (2021); https://doi.org/10.1007/s10854-021-07242-1
40. Roshini Gunasekaran and Julie Charles, *Polymer-Plastics Technology and Materials*, **63**, Iss. 6: 716 (2024); https://doi.org/10.1080/25740881.2024.2302539
41. Monika Barala, Jyoti Jaglan, Devendra Mohan, Sujata Sanghi, and Parveen Sharma, *Brazilian Journal of Physics*, **53**, Iss. 1: 29 (2023); https://doi.org/10.1007/s13538-022-01234-0
42. Ming-Zhi Yang, Ching-Liang Dai, and Wei-Yi Lin, *Sensors*, **11**: 8143 (2011); https://doi.org/10.3390/s110808143
43. Peng Li, Shuguo Yu, and Hongyan Zhang, *Sensors*, **21**, Iss. 3: 857 (2021); https://doi.org/10.3390/s21030857
44. M. M. Abdelhamied, A. Atta, A. M. Abdelreheem, A. T. M. Farag, and M. A. El Sherbiny, *Inorgan. Chem. Commun.*, **133**: 108926 (2021); https://doi.org/10.1016/j.inoche.2021.108926
45. Salah Abdul Mahdi Khudair and Ameen Alwan Mohaimeed, *Neuro Quantol.*, **18**, Iss. 9: 87 (2020); doi:10.14704/nq.2020.18.9.NQ20221
46. Ammar Abd Ali Najm, Saif M. Alshrefi, Zaid L. Hadi, Ehssan Al-Bermany, and Ameen Alwan Mohaimeed, *Silicon*, **16**: 4227 (2024); https://doi.org/10.1007/s12633-024-02997-8

Наносистеми, наноматеріали, нанотехнології
Nanosistemi, Nanomateriali, Nanotehnologii
2026, т. 24, № 1, сс. 267–280
https://doi.org/10.15407/nnn.24.01.0267

PACS numbers: 68.55.J-, 72.80.Tm, 77.22.Gm, 78.20.Ci, 78.66.Sq, 78.67.Bf, 78.67.Sc

Fabrication and Exploring the Morphological, Optical, and Dielectric Properties of PVA/MgO/Fe_2O_3 Nanocomposites for Nanoelectronics Applications

Ahmed Hashim[1], Aseel Hadi[2], and M. H. Abbas[1]

[1]*College of Education for Pure Sciences,*
Department of Physics,
University of Babylon,
Hillah, Iraq
[2]*College of Materials Engineering,*
Department of Ceramic and Building Materials,
University of Babylon,
Hillah, Iraq

The PVA/MgO/Fe_2O_3 nanocomposites' films are fabricated in the present work to utilize in different nanoelectronics applications. The morphological, optical, and dielectric properties of PVA/MgO/Fe_2O_3 nanocomposites are studied. The results show that the MgO/Fe_2O_3 nanoparticles (NPs) have good distribution inside the polymer matrix. The absorbance of PVA is increased, while the transmittance and energy gap are decreased with rising in the MgO/Fe_2O_3-NPs' content. The dielectric properties (dielectric constant, dielectric loss, and electrical conductivity) are enhanced with increasing MgO/Fe_2O_3-NPs' content. The final results confirm that the PVA/MgO/Fe_2O_3 nanocomposites can be useful for different nanoelectronics applications.

У цій роботі було виготовлено плівки нанокомпозитів полівініловий спирт (ПВС)/MgO/Fe_2O_3 для використання у різних наноелектронних застосуваннях. Були досліджені морфологічні, оптичні та діелектричні властивості нанокомпозитів ПВС/MgO/Fe_2O_3. Результати показали, що наночастинки MgO/Fe_2O_3 мають хороший розподіл всередині полімерної матриці. Вбирання ПВС збільшувалося, тоді як пропускання та ширина забороненої зони зменшувалися зі збільшенням вмісту наночастинок MgO/Fe_2O_3. Діелектричні властивості (діелектрична проникність, діелектричні втрати й електропровідність) поліпшувалися зі збільшенням вмісту наночастинок MgO/Fe_2O_3. Остаточні результати підтвердили, що нанокомпозити ПВС/MgO/Fe_2O_3 можуть бути корисними для різних застосувань наноелектроніки.

Key words: PVA, MgO/Fe_2O_3, nanocomposites, optical properties, dielectric constant,

Ключові слова: полівініловий спирт, MgO/Fe_2O_3, нанокомпозити, оптичні властивості, діелектрична проникність.

(Received 10 March, 2024)

1. INTRODUCTION

Organic–inorganic hybrid optical materials are extremely valuable from a technological perspective. Hybrid compositions with remarkable properties may emerge once the relationships between the properties of inorganic elements and polymer matrices are clarified. Polymeric nanocomposites, because of their interesting properties, are also a significant class in the field of applied materials science technology. Polymer composites display a variety of fascinating optical features, including a high/low refractive index, tailored absorption/emission spectra, and strong optical nonlinearities. Hybrids are eligible for potential optoelectronic applications because they possess such rare properties [1–4].

Polymer nanocomposites are one of the most important materials in the academic and industrial areas, and are produced by dispersing nanofillers with one or more dimensions at nanoscale into the polymeric matrix. Recently, researchers have been attracted to polymer nanocomposites over conventional microcomposites due to their wide applications in electromechanical systems and their large interfacial area per unit volume of the dispersion medium [5].

Polyvinyl alcohol (PVA) anions are suitable bridging ligands for constructing network coordination polymers. PVA is a semicrystalline polymer and its crystalline index depends on the synthetic process and physical ageing. It has gained increasing attention in the biomedical field due to bioinertness [6]. Metal-oxide nanoparticles (NPs) production has received a lot of interest over the last two decades. Plethoras of ways have also been developed to prepare nanoparticles. Magnesium oxide (MgO) was chosen for this study because of its several features, including high purity, nontoxicity, and odorlessness. They also have a high hardness and a high melting point [7].

Fe_2O_3 NPs have special properties like good electron mobility, magnetic ability, and a 2.2 eV optical energy-band gap, which are useful for optoelectronic applications. Fe_2O_3 NPs have potential applications in the fields of medicine, life sciences and computer technology like magnetic resonance imaging (MRI), drug carriers in delivery, gene carriers in gene therapy, nanofertilizers, non-

fungicides, nanopesticides, nanofood, food packing, nanocoating, nanosensors, nanoscale memory, nanowires, spintronics, *etc*. They can be used as filters in sunscreens, biosensors [8]. The nanocomposites were investigated to employ in various fields included sensors [9–15], optical fields [16–25], antibacterial [26–34], energy storage [35–43], radiation shielding and bioenvironmental [44–48], electronics and optoelectronics [49–63]. This paper aims to prepare of PVA/MgO/Fe_2O_3 nanocomposites to employ in various photonics and optics applications.

2. MATERIALS AND METHODS

Films of PVA/MgO/Fe_2O_3 nanocomposites were fabricated using casting process with different contents of MgO/Fe_2O_3 NPs are 2.5% and 5% with concentration 50% MgO: 50% Fe_2O_3.

The optical properties of PVA/MgO/Fe_2O_3 nanocomposites were tested using the double beam spectrophotometer (Shimadzu, UV-1800Å) at wavelength from 340 nm to 740 nm.

The dielectric properties of PVA/MgO/Fe_2O_3 nanocomposites were examined at frequency range (100 Hz–$2 \cdot 10^6$ Hz) by LCR meter (HIOKI 3532-50 LCR HI TESTER). The absorption coefficient α is given [64] by

$$\alpha = 2.303A/t, \tag{1}$$

where A is the absorbance and t is the film thickness.

The energy gap is calculated [65] by

$$\alpha h\nu = C\left(h\nu - E_g\right)^r, \tag{2}$$

where C is the constant; $h\nu$ is the energy of photon; E_g is the energy gap, and $r = 2$ and 3 for allowed and forbidden indirect transitions, respectively.

The dielectric constant ε' is defined [66] by

$$\varepsilon' = C_p/C_0, \tag{3}$$

wherever C_p is the matter capacitance and C_0 is the vacuum capacitance.

Dielectric loss ε'' is determined [67] by

$$\varepsilon'' = \varepsilon' D, \tag{4}$$

where D is the dispersion factor. The A.C. electrical conductivity is given [68] by

$$\sigma_{A.C.} = 2\pi f \varepsilon' D \varepsilon_0, \quad (5)$$

3. RESULTS AND DISCUSSION

The performances of absorbance and transmittance for PVA/MgO/Fe_2O_3 nanocomposites with wavelength are demonstrated in Figs. 1, 2, respectively. As represented in these figures, the PVA/MgO/Fe_2O_3 nanocomposites have high absorbance with low transmittance at UV region because the high photons energies at these spectra. The absorbance decreases and transmittance increases with increasing wavelength. Also, the absorbance of PVA raises,

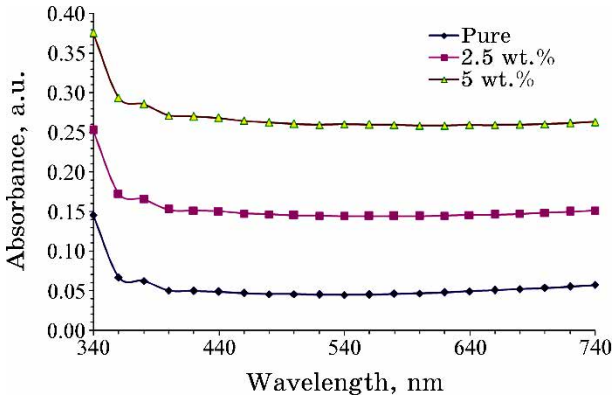

Fig. 1. Performance of absorbance for the PVA/MgO/Fe_2O_3 nanocomposites with wavelength.

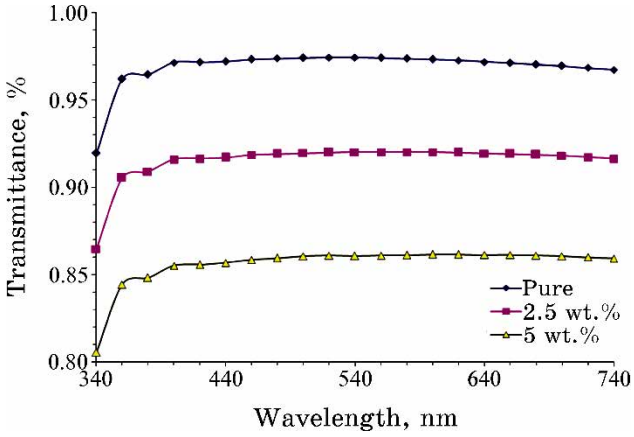

Fig. 2. Variation of transmittance for the PVA/MgO/Fe_2O_3 nanocomposites with wavelength.

while the transmittance reduces with increasing MgO/Fe_2O_3-NPs' content, which is related to increase of charge carriers density, as shown in Fig. 3, which are absorb or scat the photons [69–83].

The energy gaps for $PVA/MgO/Fe_2O_3$ nanocomposites of allowed and forbidden indirect transitions are shown in Figs. 4 and 5, respectively. The energy gaps of PVA are reduced with rising MgO/Fe_2O_3-NPs' content; this is related to the creation of complexes of charge transfer in the polymer matrix. These charges transfer complexes rise the electric conduction by generating extra charges, this effect in a decrease of the energy gap. With increasing MgO/Fe_2O_3 content, the dopant molecules begin bridging the gap separating the two localized levels and reduce the potential barrier between them, thereby create easily the charge carrier transfer between localized levels [84–97].

The variations of dielectric constant and dielectric loss for $PVA/MgO/Fe_2O_3$ nanocomposites with frequency are confirmed in Figs. 6, 7, respectively. As shown in these figures, the dielectric constant and dielectric loss are decreased with increasing frequency.

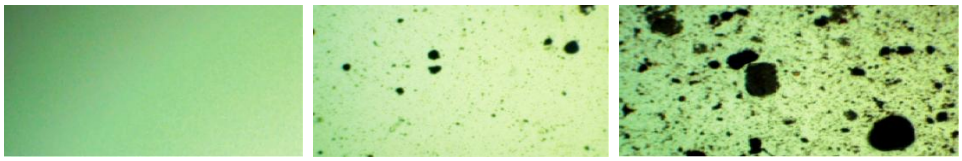

Fig. 3. Optical microscopic images for the $PVA/MgO/Fe_2O_3$ nanocomposites (×10): *a*—pure; *b*—2.5 wt.% MgO/Fe_2O_3 NPs, *c*—5 wt.% MgO/Fe_2O_3 NPs.

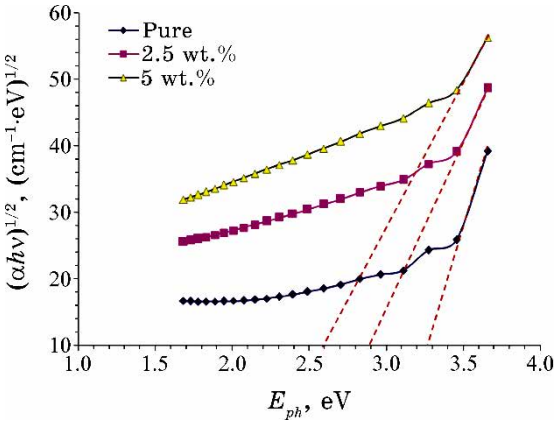

Fig. 4. Energy gap for the $PVA/MgO/Fe_2O_3$ eV nanocomposites of allowed indirect transition.

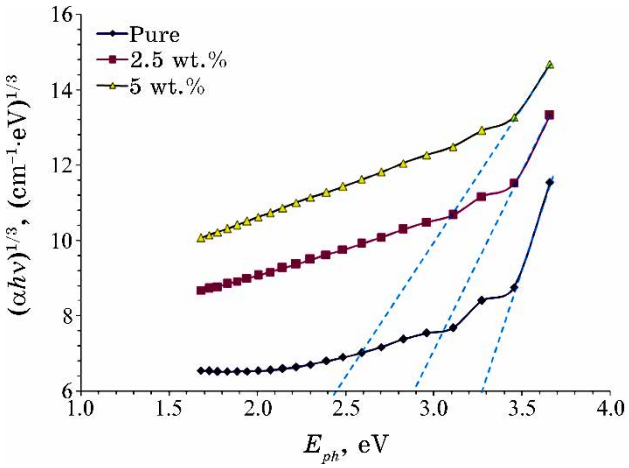

Fig. 5. Energy gap for the PVA/MgO/Fe_2O_3 nanocomposites of forbidden indirect transition.

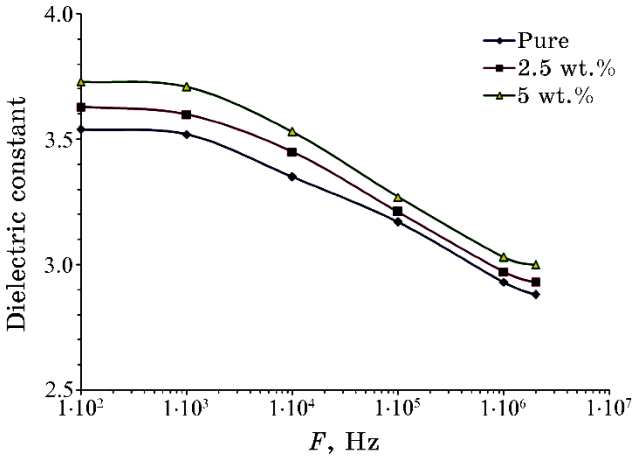

Fig. 6. Variation of dielectric constant for the PVA/MgO/Fe_2O_3 nanocomposites with frequency.

For low frequency, the polymer molecules obtain enough time to orient themselves according to the applied field. With rising frequency, the molecules are not getting sufficient time to orient themselves according to the direction of the electrical field. Therefore, the overall polarization effect decreases and, consequently, the value of dielectric constant decreases too as it is directly proportional to the amount of polarization. At elevated frequencies as the polarization decreases the dielectric loss and dissipation factor, also decreased, as sufficient time is not provided to the polymer chain to

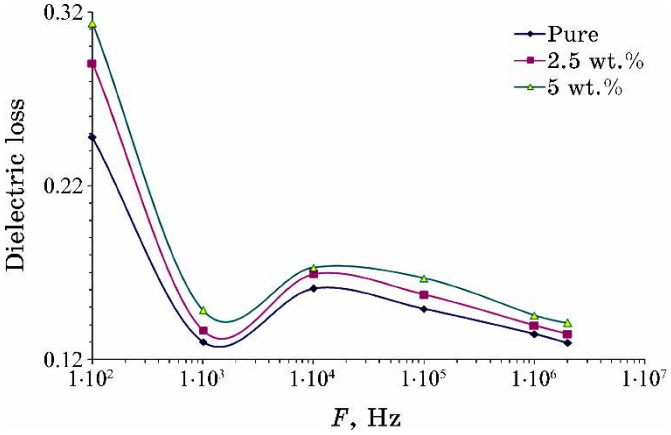

Fig. 7. Variation of dielectric loss for the PVA/MgO/Fe_2O_3 nanocomposites with frequency.

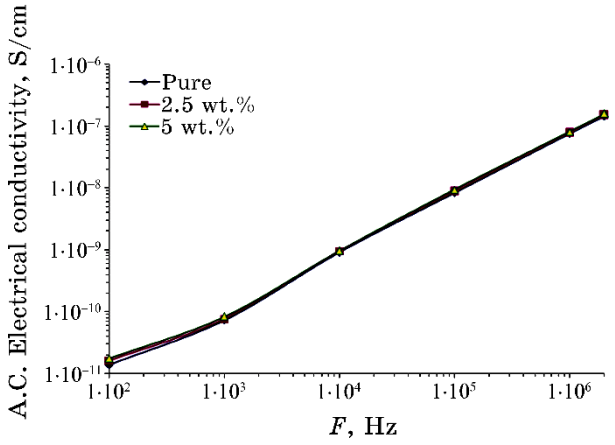

Fig. 8. Variation of electrical conductivity for the PVA/MgO/Fe_2O_3 nanocomposites with frequency.

generate phase angle. Thus, at high frequencies the contribution of orientational or dipole polarization vanishes and the effect is only for electronic polarization, which is instantaneous. The dielectric constant and dielectric loss are increased with increasing contents of nanoparticles, which is due to increase in charge-carriers' numbers [98–116].

The variation of electrical conductivity for PVA/MgO/Fe_2O_3 nanocomposites with frequency is represented in Fig. 8. The electrical conductivity rises with increasing nanoparticles contents and frequency. The increase of electrical conductivity with increasing

nanoparticles contents related to raise in the charges carriers numbers. The frequency-dependent conductivity is caused by the hopping of electrons in the localized states near the Fermi level and also attributed to the charge-carriers' excitation to the levels in the conduction band [117–127].

4. CONCLUSIONS

The current work included fabrication of PVA/MgO/Fe_2O_3-nanocomposites' films to exploit in various nanoelectronics fields. The morphological, optical, and dielectric properties of PVA/MgO/Fe_2O_3 nanocomposites were studied. The results showed that the absorbance of PVA was increased while the transmittance and energy gap were decreased with rising in the MgO/Fe_2O_3-NPs' content. The dielectric properties were enhanced with increasing MgO/Fe_2O_3-NPs' content. The final results confirmed that the PVA/MgO/Fe_2O_3 nanocomposites can be useful for various nanoelectronics applications.

REFERENCES

1. A.M. El-Naggar, Z. K. Heiba, A. M. Kamal, O. H. Abd-Elkader, and M. B. Mohamed, *Polymers*, 15: 1(2023); https://doi.org/10.3390/polym15092091
2. A. G. Hadi, Z. Al-Ramadhan, and A. Hashim, *Nanosistemi, Nanomateriali, Nanotehnologii*, **20**, Iss. 2: 535 (2022); https://doi.org/10.15407/nnn.20.02.535
3. O. B. Fadil and A. Hashim, *Nanosistemi, Nanomateriali, Nanotehnologii*, **21**, Iss. 1: 153 (2023); https://doi.org/10.15407/nnn.21.01.153
4. W. O. Obaid and A. Hashim, *Nanosistemi, Nanomateriali, Nanotehnologii*, **21**, Iss. 1: 163 (2023); https://doi.org/10.15407/nnn.21.01.163
5. D. A. Nasrallah and M. A. Ibrahim, *Journal of Polymer Research*, **29**: 1 (2022); https://doi.org/10.1007/s10965-022-02943-5
6. T. A. Hanafy, *Journal of Applied Physics*, **112**: 1 (2012).
7. B. Bharati, B. T. Vijaykumar, N. Ramabai, and S. Basavaraj, *Materials Today: Proceedings*, **92**: 1640 (2023); https://doi.org/10.1016/j.matpr.2023.06.116
8. J. S. Goud and N. Narsimlu, *Indian Journal of Chemical Technology*, **29**: 737 (2022); doi:10.56042/ijct.v29i6
9. H. Ahmed and A. Hashim, *International Journal of Scientific & Technology Research*, **8**, Iss. 11: 1014 (2019).
10. B. Mohammed, H. Ahmed, and A. Hashim, *Nanosistemi, Nanomateriali, Nanotehnologii*, **20**, Iss. 1: 187 (2022); https://doi.org/10.15407/nnn.20.01.187
11. Huda Abdul Jalil Hussien, Raheem G. Kadhim, and Ahmed Hashim, *J. of Physics: Conf. Series*, **1818**: 012119 (2021); doi:10.1088/1742-

6596/1818/1/012119
12. Huda Abdul Jalil Hussien, Raheem G. Kadhim, and Ahmed Hashim, *J. of Physics: Conf. Series*, **1818**: 012186 (2021); doi:10.1088/1742-6596/1818/1/012186
13. Huda Abdul Jalil Hussien, Raheem G. Kadhim, and Ahmed Hashim, *J. of Physics: Conf. Series*, **1818**: 012187 (2021); doi:10.1088/1742-6596/1818/1/012187
14. A. G. Hadi, Z. Al-Ramadhan, and A. Hashim, *Nanosistemi, Nanomateriali, Nanotehnologii*, **19**, Iss. 4: 865 (2021); https://doi.org/10.15407/nnn.19.04.865
15. A. Hashim and Z. S. Hamad, *Nanosistemi, Nanomateriali, Nanotehnologii*, **19**, Iss. 4: 893 (2021); https://doi.org/10.15407/nnn.19.04.893
16. H. Ahmed and A. Hashim, *Silicon*, **14**: 6637 (2022); https://doi.org/10.1007/s12633-021-01449-x
17. H. Ahmed and A. Hashim, *Silicon*, **13**: 4331(2021); https://doi.org/10.1007/s12633-020-00723-8
18. H. Ahmed and A. Hashim, *Transactions on Electrical and Electronic Materials*, **22**: 335 (2021); https://doi.org/10.1007/s42341-020-00244-6
19. N. AH. Al-Aaraji, A. Hashim, A. Hadi, and H. M. Abduljalil, *Silicon*, **14**: 10037 (2022); https://doi.org/10.1007/s12633-022-01730-7
20. H. Ahmed and A. Hashim, *Opt. Quant. Electron.*, **55**: 1 (2023); https://doi.org/10.1007/s11082-022-04273-8
21. W. O. Obaid and A. Hashim, *Silicon*, **14**: 11199 (2022); https://doi.org/10.1007/s12633-022-01854-w
22. O. B. Fadil and A. Hashim, *Silicon*, **14**: 9845 (2022); https://doi.org/10.1007/s12633-022-01728-1
23. H. Ahmed and A. Hashim, *Silicon,* **15**: 2339 (2023); https://doi.org/10.1007/s12633-022-02173-w
24. H. B. Hassan, H. M. Abduljalil, and A. Hashim, *Nanosistemi, Nanomateriali, Nanotehnologii*, **20**, Iss. 4: 941 (2022); https://doi.org/10.15407/nnn.20.04.941
25. H. A. Jawad and A. Hashim, *Nanosistemi, Nanomateriali, Nanotehnologii*, **20**, Iss. 4: 963 (2022); https://doi.org/10.15407/nnn.20.04.963
26. A. Hashim, I. R. Agool, and K. J. Kadhim, *Journal of Bionanoscience*, **12**, No. 5: 608 (2018); doi:10.1166/jbns.2018.1580
27. A. Hazim, A. Hashim, and H. M. Abduljalil, *International Journal of Emerging Trends in Engineering Research*, **7**, No. 8: 68 (2019); https://doi.org/10.30534/ijeter/2019/01782019
28. A. Hazim, H. M. Abduljalil, and A. Hashim, *International Journal of Emerging Trends in Engineering Research*, **7**, No. 8: 104 (2019); https://doi.org/10.30534/ijeter/2019/04782019
29. O. B. Fadil and A. Hashim, *Nanosistemi, Nanomateriali, Nanotehnologii*, **20**, Iss. 4: 1029 (2022); https://doi.org/10.15407/nnn.20.04.1029
30. W. O. Obaid and A. Hashim, *Nanosistemi, Nanomateriali, Nanotehnologii*, **20**, Iss. 4: 1009 (2022); https://doi.org/10.15407/nnn.20.04.1009
31. M. H. Meteab, A. Hashim, and B. H. Rabee, *Nanosistemi, Nanomateriali, Nanotehnologii*, **21**, Iss. 1: 199 (2023); https://doi.org/10.15407/nnn.21.01.199
32. M. H. Meteab, A. Hashim, and B. H. Rabee, *Nanosistemi, Nanomateriali,*

Nanotehnologii, **21**, Iss. 2: 451 (2023); https://doi.org/10.15407/nnn.21.02.451
33. H. B. Hassan, A. Hashim, and H. M. Abduljalil, *Nanosistemi, Nanomateriali, Nanotehnologii*, **20**, Iss. 3: 815 (2022); https://doi.org/10.15407/nnn.20.03.815
34. H. B. Hassan, A. Hashim, and H. M. Abduljalil, *Nanosistemi, Nanomateriali, Nanotehnologii*, **20**, Iss. 3: 821 (2022); https://doi.org/10.15407/nnn.20.03.821
35. A. S. Shareef, F. Lafta R., A. Hadi, and A. Hashim, *International Journal of Scientific & Technology Research*, **8**, Iss. 11: 1041 (2019).
36. A. Hadi, A. Hashim, and D. Hassan, *Bulletin of Electrical Engineering and Informatics*, **9**, No. 1: 83 (2020); doi:10.11591/eei.v9i1.1323
37. H. Ahmed and A. Hashim, *Nanosistemi, Nanomateriali, Nanotehnologii*, **20**, Iss. 4: 951 (2022); https://doi.org/10.15407/nnn.20.04.951
38. F. L. Rashid, A. Hadi, A. A. Abid, and A. Hashim, *International Journal of Advances in Applied Sciences*, **8**, No. 2: 154 (2019) doi:10.11591/ijaas.v8i2.pp154-156
39. M. H. Rasheed, A. Hashim, and F. L. Rashid, *Nanosistemi, Nanomateriali, Nanotehnologii*, **19**, Iss. 2: 374 (2021); https://doi.org/10.15407/nnn.19.02.347
40. A. Hashim, F. L. Rashid, N. AH. Al-Aaraji, and B. H. Rabee, *East European Journal of Physics*, **1**: 173 (2023); doi:10.26565/2312-4334-2023-1-21
41. F. L. Rashid, A. Hashim, N. AH. Al-Aaraji, and A. Hadi, *East European Journal of Physics*, **1**: 177 (2023); doi:10.26565/2312-4334-2023-1-22
42. F. L. Rashid, A. Hashim, M. H. Abbas, and A. Hadi, *East European Journal of Physics*, **1**: 181 (2023); doi:10.26565/2312-4334-2023-1-23
43. A. Hashim, F. L. Rashid, M. H. Abbas, and B. H. Rabee, *East European journal of physics*, **1**: 185 (2023); doi:10.26565/2312-4334-2023-1-24
44. A. Hashim and N. Hamid, *Journal of Bionanoscience*, **12**, No. 6: 788 (2018); doi:10.1166/jbns.2018.1591
45. A. Hashim and Z. S. Hamad, *Journal of Bionanoscience*, **12**, No. 4: 504 (2018); doi:10.1166/jbns.2018.1561
46. B. Abbas and A. Hashim, *International Journal of Emerging Trends in Engineering Research*, **7**, No. 8: 131 (2019); https://doi.org/10.30534/ijeter/2019/06782019
47. K. H. H. Al-Attiyah, A. Hashim, and S. F. Obaid, *Journal of Bionanoscience*, **12**: 200 (2018); doi:10.1166/jbns.2018.1526
48. H. A. J. Hussien, A. Hadi, and A. Hashim, *Nanosistemi, Nanomateriali, Nanotehnologii*, **20**, Iss. 4: 1001 (2022); https://doi.org/10.15407/nnn.20.04.1001
49. H. Ahmed and A. Hashim, *Silicon*, **14**: 4907 (2022); https://doi.org/10.1007/s12633-021-01258-2
50. H. Ahmed and A. Hashim, *Trans. Electr. Electron. Mater.*, **23**: 237 (2022); https://doi.org/10.1007/s42341-021-00340-1
51. H. Ahmed and A. Hashim, *Silicon*, **14**: 7025 (2021); https://doi.org/10.1007/s12633-021-01465-x
52. H. Ahmed and A. Hashim, *Opt. Quant. Electron.*, **55**: 280 (2023); https://doi.org/10.1007/s11082-022-04528-4
53. B. Mohammed, H. Ahmed, and A. Hashim, *Nanosistemi, Nanomateriali,*

Nanotehnologii, **21**, Iss. 1: 113 (2023); https://doi.org/10.15407/nnn.21.01.113
54. H. Ahmed and A. Hashim, *Physics and Chemistry of Solid State*, **23**, No. 1: 67 (2022); doi:10.15330/pcss.23.1.67-71
55. H. B. Hassan, H. M. Abduljalil, and A. Hashim, *Physics and Chemistry of Solid State*, **23**, No. 3: 454 (2022); doi:10.15330/pcss.23.3.454-460
56. H. Ahmed and A. Hashim, *Nanosistemi, Nanomateriali, Nanotehnologii*, **19**, Iss. 4: 841 (2021); https://doi.org/10.15407/nnn.19.04.841
57. Huda Bukheet Hassan, Hayder M. Abduljalil, and Ahmed Hashim, *AIP Conference Proceedings* , **2591**: 040008 (2023); https://doi.org/10.1063/5.0119838
58. N. AH. Al-Aaraji, A. Hashim, H. M. Abduljalil, and A. Hadi, *Optical and Quantum Electronics*, **55**: 743 (2023); https://doi.org/10.1007/s11082-023-05048-5
59. H. B. Hassan, H. M. Abduljalil, and A. Hashim, *Nanosistemi, Nanomateriali, Nanotehnologii*, **21**, Iss. 2: 289 (2023); https://doi.org/10.15407/nnn.21.02.289
60. H. Ahmed and A. Hashim, *Silicon*, **15**: 83 (2023); https://doi.org/10.1007/s12633-022-01978-z
61. F. S. Jaber, A. Hashim, and H. M. Abduljalil, *Silicon*, **15**: 71 (2023); https://doi.org/10.1007/s12633-022-02000-2
62. H. Ahmed and A. Hashim, *Optical and Quantum Electronics*, **54**: 403 (2022); https://doi.org/10.1007/s11082-022-03784-8
63. H. Ahmed and A. Hashim, *Silicon*, **14**: 4079 (2022); https://doi.org/10.1007/s12633-021-01186-1
64. A. A. A. Ahmed, A. M. Al-Hussam, A. M. Abdulwahab, and A. N. A. A. Ahmed, *AIMS Mater. Sci.*, **5**, Iss. 3: 1 (2018); doi:10.3934/matersci.2018.3.533
65. T. A.-Baset, M. Elzayat, and S. Mahrous, *Int. J. of Polym. Sci.*, **2016**: Article ID 1707018 (2016); http://dx.doi.org/10.1155/2016/1707018
66. Sarir Uddin, Naheed Akhtar, Sumbal Bibi, Abid Zaman, Asad Ali Khaled Althubeiti, Hussein Alrobei, and Muhammad Mushtaq, *Materials*, **14**: 5430 (2021); https://doi.org/10.3390/ma14185430
67. T. A. Abdel-Baset and A. Hassen, *Physica B*, **499**: 24 (2016); http://dx.doi.org/10.1016/j.physb.2016.07.002
68. H. M. Alhusaiki-Alghamdi, *Results in Physics*, **24**: 104125 (2021); https://doi.org/10.1016/j.rinp.2021.104125
69. A. Hashim, E. H. Abdullah, F. L. Rashid, and A. Hadi, *Nanosistemi, Nanomateriali, Nanotehnologii*, **19**, Iss. 3: 697 (2021); https://doi.org/10.15407/nnn.19.03.697
70. M. Sajjad and A. Hashim, *Nanosistemi, Nanomateriali, Nanotehnologii*, **19**, Iss. 4: 831 (2021); https://doi.org/10.15407/nnn.19.04.831
71. A. Hashim, *Nanosistemi, Nanomateriali, Nanotehnologii*, **19**, Iss. 3: 647 (2021); https://doi.org/10.15407/nnn.19.03.647
72. M. K. Mohammed, E. H. Abdullah, D. Hassan, and A. Hashim, *Revue des Composites et des Matériaux Avancés–Journal of Composite and Advanced Materials*, **32**, No. 6: 305 (2022); https://doi.org/10.18280/rcma.320606
73. Y. Y. Mijbil and A. Hashim, *Nanosistemi, Nanomateriali, Nanotehnologii*, **20**, Iss. 2: 497 (2022); https://doi.org/10.15407/nnn.20.02.497

74. M. H. Rasheed, A. K. Abbas, F. Rashid, and A. Hashim, *Nanosistemi, Nanomateriali, Nanotehnologii*, **20**, Iss. 3: 761 (2022); https://doi.org/10.15407/nnn.20.03.761
75. Ahmed Hashim, Aseel Hadi, and M. H. Abbas, *Silicon*, **15**: 6431 (2023); https://doi.org/10.1007/s12633-023-02529-w
76. A. Hashim, A. Hadi, and N. A. H. Al-Aaraji, *Optical and Quantum Electronics*, **55**: 716 (2023); https://doi.org/10.1007/s11082-023-04994-4
77. A. Hashim, B. Mohammed, A. Hadi, and H. Ibrahim, *Journal of Inorganic and Organometallic Polymers and Materials*, **34**: 611 (2024); https://doi.org/10.1007/s10904-023-02846-y
78. H. B. Hassan, A. Hashim, and H. M. Abduljalil, *Optical and Quantum Electronics*, **55**: 556 (2023); https://doi.org/10.1007/s11082-023-04830-9
79. H. K. Jaafar, A. Hashim, and B. H. Rabee, *Optical and Quantum Electronics*, **55**: 989 (2023); https://doi.org/10.1007/s11082-023-05208-7
80. Ahmed Hashim, Saif M. Alshrefi, Hussein H. Abed, and Aseel Hadi, *Journal of Inorganic and Organometallic Polymers and Materials*, **34**: 703 (2024); https://doi.org/10.1007/s10904-023-02866-8
81. Hiba Kamil Jaafar, Ahmed Hashim and Bahaa H. Rabee, *Silicon*, **16**: 603 (2024); https://doi.org/10.1007/s12633-023-02706-x
82. H. A. J. Hussien, R. G. Kadhim, and A. Hashim, *Optical and Quantum Electronics,* **54**: 704 (2022); https://doi.org/10.1007/s11082-022-04094-9
83. Z. K. Heiba, M. B. Mohamed, and S. I. Ahmed, *Alexandria Engineering Journal*, **61**, Iss. 5: 3375 (2022); https://doi.org/10.1016/j.aej.2021.08.051
84. H. B. Hassan, A. Hashim, and H. M. Abduljalil, *Polymer Bulletin*, **80**: 9059 (2023); https://doi.org/10.1007/s00289-022-04502-w
85. H. A. J. Hussien, R. G. Kadhim, and A. Hashim, *Optical and Quantum Electronics*, **53**: 501 (2021); https://doi.org/10.1007/s11082-021-03157-7
86. H. A. J. Hussien, R. G. Kadhim, and A. Hashim, *Polymer Bulletin*, **79**: 5219 (2022); https://doi.org/10.1007/s00289-021-03778-8
87. Ahmed Hashim, *Opt. Quant. Electron.*, **53**: Article No. 478 (2021); https://doi.org/10.1007/s11082-021-03100-w
88. Ghaith Ahmed and Ahmed Hashim, *Silicon*, **15**: 7085 (2023); https://doi.org/10.1007/s12633-023-02572-7
89. A. Hazim, A. Hashim, and H. M. Abduljalil, *Egypt. J. Chem.*, **64**, No. 1: 359 (2021); doi:10.21608/EJCHEM.2019.18513.2144
90. A.F. Kadhim and A. Hashim, *Opt. Quant. Electron.*, **55**: 432 (2023); https://doi.org/10.1007/s11082-023-04699-8
91. L. H. Gaabour, *Optics and Photonics Journal*, **10**: 197 (2020); doi:10.4236/opj.2020.108021
92. M. H. Meteab, A. Hashim, and B. H. Rabee, *Opt. Quant. Electron.*, **55**: 187 (2023); https://doi.org/10.1007/s11082-022-04447-4
93. A. Hazim, A. Hashim, and H. M. Abduljalil, *Nanosistemi, Nanomateriali, Nanotehnologii*, **18**, Iss. 4: 983 (2020); https://doi.org/10.15407/nnn.18.04.983
94. A. Hashim and Z. S. Hamad, *Nanosistemi, Nanomateriali, Nanotehnologii*, **18**, Iss. 4: 969 (2020); https://doi.org/10.15407/nnn.18.04.969
95. Ahmed Hashim, Aseel Hadi, Hamed Ibrahim, and Farhan Lafta Rashid, *Journal of Inorganic and Organometallic Polymers and Materials*, **34**: 1678 (2024); https://doi.org/10.1007/s10904-023-02908-1

96. Ahmed Kareem, Ahmed Hashim, and Huda Bukheet Hassan, *Silicon*, **16**: 2827 (2024); https://doi.org/10.1007/s12633-024-02891-3
97. Huda Abdul Jalil Hussien and Ahmed Hashim, *J. Inorg. Organomet. Polym.*, **34**: 2716 (2024); https://doi.org/10.1007/s10904-024-03007-5
98. M. Singhi and M. Fahim, *International Journal of Scientific Research*, **3**, Iss. 11: 45 (2014).
99. Z. S. Hamad and A. Hashim, *Nanosistemi, Nanomateriali, Nanotehnologii*, **20**, Iss. 1: 159 (2022); https://doi.org/10.15407/nnn.20.01.159
100. A. Hashim and Z. S. Hamad, *Nanosistemi, Nanomateriali, Nanotehnologii*, **20**, Iss. 1: 165 (2022); https://doi.org/10.15407/nnn.20.01.165
101. A. Hashim and A. Jassim, *Nanosistemi, Nanomateriali, Nanotehnologii*, **20**, Iss. 1: 177 (2022); https://doi.org/10.15407/nnn.20.01.177
102. A. Hashim and Z. S. Hamad, *Nanosistemi, Nanomateriali, Nanotehnologii*, **20**, Iss. 2: 507 (2022); https://doi.org/10.15407/nnn.20.02.507
103. Batool Mohammed, Hind Ahmed, and Ahmed Hashim, *Journal of Physics: Conference Series*, **1879**: 032110 (2021); doi:10.1088/1742-6596/1879/3/032110
104. D. Hassan and A. H. Ah-Yasari, *Bulletin of Electrical Engineering and Informatics*, **8**, Iss. 1: 52 (2019); doi:10.11591/eei.v8i1.1019
105. D. Hassan and A. Hashim, *Bulletin of Electrical Engineering and Informatics*, **7**, Iss. 4: 547 (2018); doi:10.11591/eei.v7i4.969
106. Ahmed Hashim, M. H. Abbas, Noor Al-Huda Al-Aaraji, and Aseel Hadi, *J. Inorg. Organomet. Polym.*, **33**: 1 (2023); https://doi.org/10.1007/s10904-022-02485-9
107. A. Hashim, M. H. Abbas, N. AH. Al-Aaraji, and A. Hadi, *Silicon*, **15**: 1283 (2023); https://doi.org/10.1007/s12633-022-02104-9
108. M. H. Meteab, A. Hashim, and B. H. Rabee, *Silicon*, **15**: 1609 (2023); https://doi.org/10.1007/s12633-022-02114-7
109. N. Al-Huda Al-Aaraji, A. Hashim, A. Hadi, and H. M. Abduljalil, *Silicon*, **14**: 4699 (2022); https://doi.org/10.1007/s12633-021-01265-3
110. M. H. Meteab, A. Hashim, and B. H. Rabee, *Silicon*, **15**: 251 (2023); https://doi.org/10.1007/s12633-022-02020-y
111. A. Hashim, A. Hadi, and M. H. Abbas, *Opt. Quant. Electron.*, **55**: 642 (2023); https://doi.org/10.1007/s11082-023-04929-z
112. Huda Abdul Jalil Hussien and Ahmed Hashim, *J. Inorg. Organomet. Polym.*, **33**: 2331 (2023); https://doi.org/10.1007/s10904-023-02688-8
113. Ahmed Hashim, Aseel Hadi, Noor Al-Huda Al-Aaraji, and Farhan Lafta Rashid, *Silicon*, **15**: 5725 (2023); https://doi.org/10.1007/s12633-023-02471-x
114. Arshad Fadhil Kadhim and Ahmed Hashim, *Silicon*, **15**: 4613 (2023); https://doi.org/10.1007/s12633-023-02381-y
115. H. A. Jawad and A. Hashim, *Nanosistemi, Nanomateriali, Nanotehnologii*, **21**, Iss. 1: 133 (2023); https://doi.org/10.15407/nnn.21.01.133
116. B. Hussien, A. K. Algidsawi, and A. Hashim, *Australian Journal of Basic and Applied Sciences*, **5**, No. 7: 933 (2011).
117. A. G. Hadi, Z. Al-Ramadhan, and A. Hashim, *J. of Physics: Conf. Series*, **1879**: 032109 (2021); doi:10.1088/1742-6596/1879/3/032109
118. A. Hashim and Q. Hadi, *Nanosistemi, Nanomateriali, Nanotehnologii*, **19**, Iss. 4: 873 (2021); https://doi.org/10.15407/nnn.19.04.873

119. A. Hashim and A. Jassim, *Nanosistemi, Nanomateriali, Nanotehnologii*, **19**, Iss. 4: 883 (2021); https://doi.org/10.15407/nnn.19.04.883
120. W. O. Obaid and A. Hashim, *AIP Conference Proceedings*, **2591**: 040039 (2023); https://doi.org/10.1063/5.0120116
121. O. B. Fadil and A. Hashim, *AIP Conference Proceedings*, **2591**: 040031 (2023); https://doi.org/10.1063/5.0120171
122. A. Hashim, A. Hadi, and N. A. H. Al-Aaraji, *Nanosistemi, Nanomateriali, Nanotehnologii*, **21**, Iss. 3: 553 (2023); https://doi.org/10.15407/nnn.21.03.553
123. A. Hashim, A. Hadi, and N. A. H. Al-Aaraji, *Nanosistemi, Nanomateriali, Nanotehnologii*, **21**, Iss. 3: 545 (2023); https://doi.org/10.15407/nnn.21.03.545
124. A. Hashim, A. Hadi, M. H. Abbas, *Nanosistemi, Nanomateriali, Nanotehnologii*, **21**, Iss. 3: 505 (2023); https://doi.org/10.15407/nnn.21.03.505
125. A. Hashim, A. Hadi, and N. A. H. Al-Aaraji, *Nanosistemi, Nanomateriali, Nanotehnologii*, **21**, No. 3: 527 (2023); https://doi.org/10.15407/nnn.21.03.527
126. Ghaith Ahmed and Ahmed Hashim, *Silicon*, **15**: 3977 (2023); https://doi.org/10.1007/s12633-023-02322-9
127. Ann Mary K. Aippunny, Sajna M. Shamsudeen, Prakashan Valparambil, Siby Mathew, and Unnikrishnan N. Vishwambharan, *J. Appl. Polym. Sci.*, **133**, Iss. 25: 43568 (2016); doi:10.1002/APP.43568

Наносистеми, наноматеріали, нанотехнології
Nanosistemi, Nanomateriali, Nanotehnologii
2026, т. 24, № 1, сс. 281–291
https://doi.org/10.15407/nnn.24.01.0281

PACS numbers: 68.37.Hk, 68.37.Vj, 78.20.Ci, 78.67.Sc, 81.05.Qk, 81.07.Pr, 82.35.Np

Fabrication and Characterization of PVA–PEG–SiO_2–NiO Nanocomposites for Modern Applications

Waleed Khalid Kadhim[1] and Majeed Ali Habeeb[2]

[1]*Directorate of Education Babylon,*
Ministry of Education,
34001 Hillah, Iraq
[2]*College of Education for Pure Sciences,*
Department of Physics,
University of Babylon,
34001 Hillah, Iraq

The purpose of this work is to create new nanocomposite films using polyvinyl alcohol (PVA) and polyethylene glycol (PEG) with nanostructures of silicon dioxide (SiO_2) and nickel oxide (NiO) for use in challenges involving gamma-rays as shields. The nanocomposites indicate favourable characteristics for gamma ray shielding, including lightweight, good flexibility, large attenuation coefficients, and cost-efficiency. The structural properties and surface morphological changes of the nanocomposite are analysed using an optical microscope. Scanning electron microscopy displays multiple coherent and consistently dispersed, randomly scattered clusters or pieces. The created nanocomposites are evaluated to see how well they can block gamma-radiation. According to the experimental results, the PVA–PEG–SiO_2–NiO-nanocomposite films reveal substantial attenuation coefficients, when subjected to gamma rays. This nanocomposite has potential as a material for gamma-ray shielding and elastic uses.

Метою цієї роботи є створення нових нанокомпозитних плівок з використанням полівінілового спирту (ПВС) та поліетиленгліколю (ПЕГ) з наноструктурами діоксиду Силіцію (SiO_2) та оксиду Ніклю (NiO) для використання в завданнях, пов'язаних з гама-променюванням, як екрани. Нанокомпозити демонструють сприятливі характеристики для екранування гама-випромінення, включаючи легку вагу, добру гнучкість, великі коефіцієнти ослаблення й економічну ефективність. Структурні властивості та морфологічні зміни поверхні нанокомпозиту було проаналізовано за допомогою оптичного мікроскопа. Сканувальна електронна мікроскопія показує численні когерентні та послідовно розподілені, хаотично розкидані кластери або фраґменти. Створені нанокомпозити було оцінено, щоб побачити, наскільки добре вони можуть

блокувати гама-випромінення. Згідно з експериментальними результатами, нанокомпозитні плівки ПВС–ПЕГ–SiO_2–NiO демонструють значні коефіцієнти ослаблення гама-променів. Цей нанокомпозит має потенціал як матеріял для екранування гама-випромінення та використання в еластичних матеріялах.

Key words: PVA/PEG nanocomposites, SiO_2–NiO nanoparticles, scanning electron microscopy, gamma rays.

Ключові слова: нанокомпозити PVA/PEG, наночастинки SiO_2–NiO, сканувальна електронна мікроскопія, гама-променювання.

(Received 25 April, 2024)

1. INTRODUCTION

Nowadays, polymeric materials are among the most widely utilized materials because of their low cost, simplicity of production, good norms, and frequent excellent performance. It is well known that the majority of polymeric materials are insulators and that the electrical and electronic industries have long used these materials. Polymeric materials have long been utilized as an auxiliary material, but due to their advantageous properties, they are now considered a fundamental material for usage in the electrical and electronic sectors [1, 2].

A polymer mixture is created by combining two or more polymers to form a novel material with different physical characteristics. There are five main types of polymer blends, including thermoplastics, thermosetting blends. A lot of interest has been focused on polymer mixing as a simple and affordable method of producing scalable polymeric materials for industrial use [3]. Put another way, the characteristics of the mixes may be adjusted based on their intended use by carefully selecting the polymer materials [4, 5].

One kind of material with special qualities is called a polymer nanocomposite (PNC). When nanoparticles or nanofillers are dispersed throughout a polymer matrix, the result is a polymer nanocomposite (PNC). To enhance the material's high-quality qualities, at least one dimension of an organic polymer matrix is filled with metallic particles [6, 7]. Modern polymers called PNCs can be utilized in place of more conventional packed polymers. Among these attributes are the greatly improved characteristics of nanocomposites due to their filler dispersion in comparison to pure polymers. Heightened conductivity, thermal stability, and tensile strength combined with decreased flammability. Additionally, the addition of nanoparticles to polymer composites produced a new class of composite materials with enhanced and distinctive characteristics. Exam-

ples of these are spheroids, fibres, and platelets [8, 9].

Polyvinyl alcohol, or PVA, is a polymer that exhibits remarkable qualities, including its capacity to produce hydrogels by chemical or physical means, as well as its non-toxicity, biocompatibility, water solubility, and non-carcinogenic nature [10, 11]. PVA is suitably flexible and has a high sufficient tensile strength. Ranges of low molecular chemicals, the majority of which include polar groups, are often used to plasticize PVA in order to increase its deformability [12, 13]. Another manmade polymer that is dissolved in water and has a wide molecular weight band is polyethylene glycol (PEG). Because of its elastic chain, combining it with rigid polymers to generate new materials with certain properties is a good alternative [14, 15]. Polyethylene glycol (PEG) is a polyether molecule that is used in a variety of scientific sectors and businesses because of its unique physicochemical properties [16].

Silicon oxide (SiO_2) or silica is a most common in nature as quartz. It has many forms, but all forms of silica are identical in chemical composition, but with different atomic arrangements. All forms of silica are odourless solids composed of silicon and oxygen atoms [17]. Among its many exceptional qualities are low expansion factor, rigidity, and thermal stability. Nanosilica is also known as nano-silicon dioxide (SiO_2). Researchers from all around the world are interested in composites made of silicon dioxide at the nanoscale [18, 19]. Among the many nanomaterials, which are accessible, nickel oxide (NiO) nanoparticles have attracted a lot of interest primarily due to their exceptional stability and superior optical, electrical, magnetic, and catalytic characteristics. Their numerous uses, such as in gas detectors, electrochromic parts, rechargeable batteries, dye-sensitive solar cells, solar energy absorbers, and magnetic cameras [20, 21].

NiO nanoparticles (NPs) are essential for preserving the quality of the environment because they can efficiently remove both organic and inorganic contaminants [22]. The potential harm that gamma rays can do to human health makes the study of shielding against gamma radiation an exciting field of research. To block γ-rays, varieties of materials were used, such as glass and concrete. Recycled thermoplastics and inorganic nanofillers were combined to create nanocomposites with the desired γ-radiation and x-ray attenuation capabilities [23]. With the growing use of radioactive materials in industry and medicine, shielding is essential to safeguarding people and equipment [24].

2. MATERIALS AND METHODS

In order to make a more homogeneous solution, PVA/PEG was com-

bined in 45 mL of distilled water using a magnetic stirrer at 70°C for 50 minutes. This process produced nanocomposites. The casting procedure was utilized to generate films of nanocomposites with different weight percentages 0, 2, 4, 6, and 8 wt.% of silicon dioxide (SiO_2)–nickel oxide (NiO) NPs. The homogeneous solution was placed in a petri dish and left to dry for 6 days at room temperature. It was then extracted and cut into parts. The following measurements were performed on the resulting PVA–PEG–SiO_2–NiO nanocomposites: A 20× magnification Olympus system Nikon-73346 optical microscope equipped with a microscopic photographic camera was employed. The structural features of nanocomposites were investigated using field emission scanning electron microscopy (FE–SEM) (Model/Inspect TM F50-DETAILS ≅ 1.2 nm at 10 kV; pressure 3.11e-3 par; country—Holland). PVA–PEG–SiO_2–NiO nanocomposites under study were used to attenuate gamma rays for different concentrations of SiO_2–NiO nanoparticles with different volume fractions, applying nanocomposites as a gamma-ray shield .The samples were placed parallel in front of a gamma-ray source Cs-137.5 mci, at a distance of 3 cm. Utilizing Geiger counter measurements of transmitted gamma ray fluxes *via* PVA–PEG–SiO_2–NiO NCs nanocomposites, the linear attenuation coefficients were computed.

Based on the thicknesses of the films, the linear attenuation coefficients (μ) may be obtained using the following equation [25, 26]:

$$N = N_0 e^{-\mu x}. \quad (1)$$

Here, μ—the attenuation coefficient of gamma radiation, and the number of radiation particles, designated as N_0, measured during a certain time frame in the absence of an absorber. Furthermore, when a sample of thickness x is added, the research looks at the number of particles, N, found throughout the same time period.

3. RESULTS AND DISCUSSIONS

3.1. Optical Microscopy for PVA–PEG–SiO_2–NiO NCs

Photographs of PVA–PEG–SiO_2–NiO nanocomposites taken at a power of 20×magnification are displayed cross-sectionally in Fig. 1. A clear distinction is made between SiO_2–NiO nanoparticles and PVA–PEG mixture in nanocomposites. The clearly visible interconnected network of SiO_2–NiO nanoparticles forming paths connected to each other within the nanocomposite samples resembles sponge bonding. It indicates that the nanoparticles spread in the matrix of the polymer mixture in a regular manner in all directions, filling

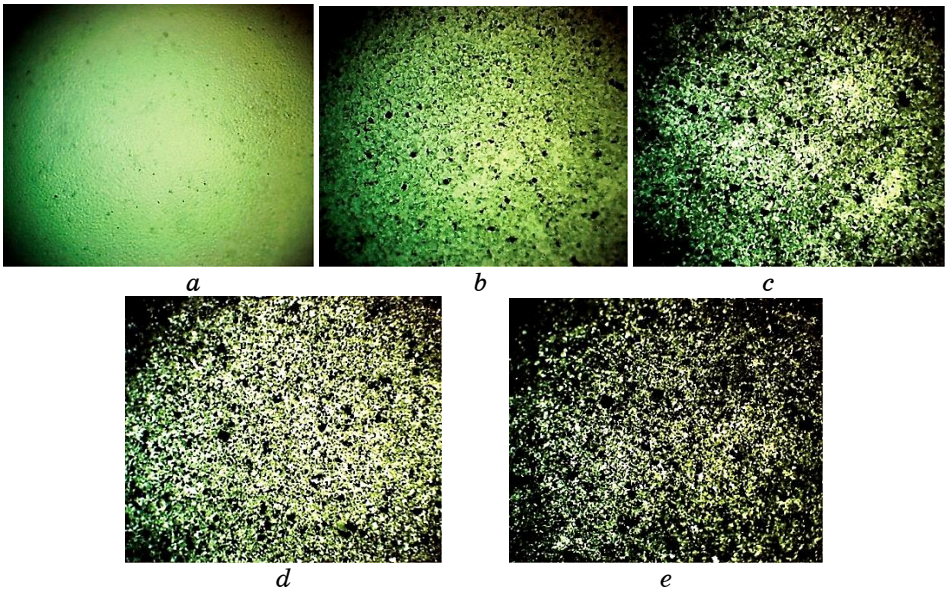

Fig. 1. Photomicrographs ×20 for PVA–PEG–SiO_2–NiO NCs: *a*—for pure PVA–PEG; *b*—for 2 wt.% SiO_2/NiO; *c*—for 4 wt.% SiO_2/NiO; *d*—for 6 wt.% SiO_2/NiO; *e*—for 8 wt.% SiO_2/NiO.

all the voids inside the polymer. Based on the microscopic images in Fig. 1, the proportions of the nanoparticles can be distinguished. The continuous network in the shapes *b*, *c*, *d*, and *e* increases the movement of charge carriers, and thus changes the properties of the nanocomposite [27, 28].

3.2. Scanning Electron Microscopy (SEM) Measurements of PVA–PEG–SiO_2–NiO NCs

A scanning electron microscope is used to look at the distribution of nanocomposites particles in the matrix of polymers and to assess the overall effect of the quantity of SiO_2/NiO NPs. A SEM image of the pure blend surface for films composed of PVA–PEG–SiO_2–NiO NCs is shown in Fig. 2. The films were placed sequentially with different concentrations of SiO_2/NiO nanoparticles. Image (*a*) in Fig. 2 for the polymer mix appears to be clear, linked, and to have a constant form, revealing a somewhat smooth surface [29, 30]. As the ratio of SiO_2/NiO nanoparticles increases, the surface morphology of the polymer mixtures PVA/PEG in Fig. 2, *b*, *c*, *d*, and *e* varies. Furthermore, the surface of nanocomposites films exhibits a large number of equally distributed, widely varying elliptical particle ag-

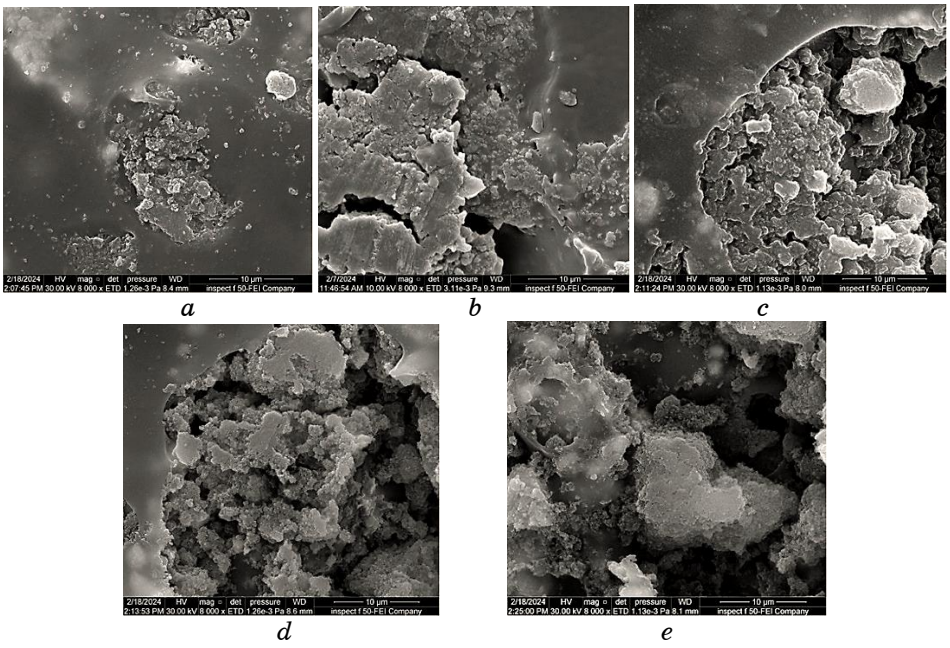

Fig. 2. SEM images of PVA–PEG–SiO_2–NiO NCs: *a*—PVA–PEG; *b*—2 wt.% SiO_2–NiO; *c*—4 wt.% SiO_2–NiO; *d*—6 wt.% SiO_2–NiO; *e*—8 wt.% SiO_2–NiO.

gregates or pieces, which could indicate a uniform growth process [31, 32]. As the nanoparticle ratio in polymer blends increases, surface form evolves. When the concentrations of SiO_2/NiO NCs increase, the grains agglomerate and converge, and more aggregates or fragments are randomly distributed on the upper surface of the nanoparticles [33–36], as shown in Fig. 2, *e*.

3.3. Application of PVA–PEG–SiO_2–NiO NCs for Gamma-Ray Shielding

The percentages of silicon dioxide/nickel oxide SiO_2–NiO nanoparticles are positively correlated with the natural logarithm of the ratio of N to N_0 for polymer mixtures PVA/PEG, as demonstrated in Fig. 3. Table presents the values, which were achieved. The fluctuation of gamma-radiation attenuation coefficients for PVA/PEG polymer mixes as a function of SiO_2–NiO-nanoparticles' ratios is displayed in Fig. 4. The PVA/PEG-polymer blends exhibited promising radiation absorption capabilities. As SiO_2–NiO-nanoparticles' concentration increases; so, the attenuation coefficients do. This is so because the substance used to make shielding materials is PNC, by

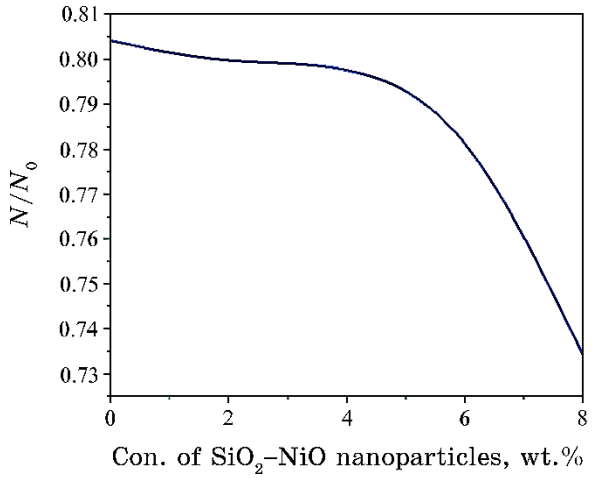

Fig. 3. Variability of N/N_0 for PVA/PEG-polymer blends with varying SiO_2–NiO-NPs' ratios.

TABLE. Values of N/N_0, $\ln(N/N_0)$, and μ [cm^{-1}] for PVA–PEG–SiO_2–NiO PNC.

Content of SiO_2–NiO nanoparticles, wt.%	N/N_0	$\ln(N/N_0)$	μ, cm^{-1}
0	0.804	0.2180	0.002704
2	0.799	0.2234	0.001357
4	0.797	0.2261	0.010378
6	0.781	0.2469	0.031016
8	0.734	0.3089	0.038618

which gamma rays can be reflected, scattered, or absorbed [37, 38].

The gamma-radiation attenuation coefficient numbers for PNC are as high as 0.03861 cm^{-1}. When compared, the results of polymer PNC and concrete indicated a great deal of similarities, as seen in the figure below. Because of the polymer nanocomposite increased mobility, lack of electrical conductivity, and ability to prevent neutron escape, it demonstrated better characteristics than concrete [39–41]. Furthermore, growing $\ln(N/N_0)$ of the PVA/PEG mixture is observed in Fig. 5 along with rising SiO_2–NiO-NPs' concentrations [42, 43]. Table shows N/N_0, $\ln(N/N_0)$, and μ [cm^{-1}] values for PVA–PEG–SiO_2–NiO PNC.

4. CONCLUSIONS

In the present investigation, the casting solution method of production was used for manufacturing plastic nanocomposite films.

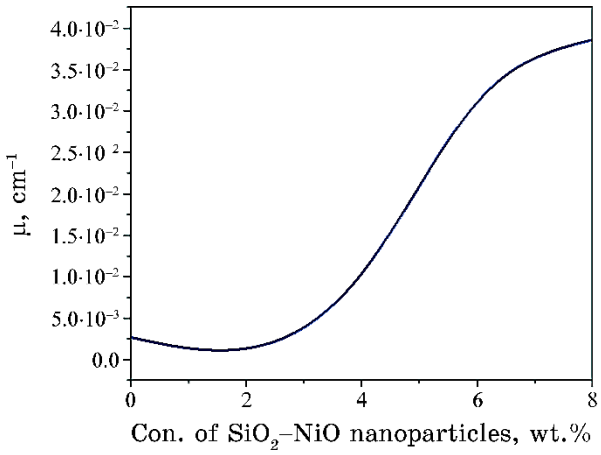

Fig. 4. Variability of μ [cm^{-1}] for PVA/PEG-polymer blends with varying SiO_2–NiO-NPs' ratios.

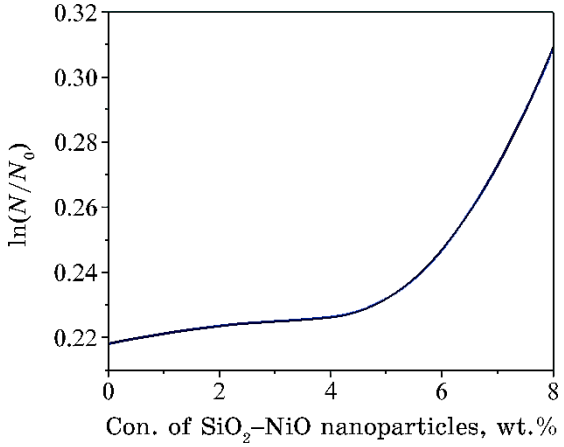

Fig. 5. Variability of $\ln(N/N_0)$ for PVA/PEG-polymer blends with varying SiO_2–NiO-NPs' ratios.

The film consists of a mixture of PVA/PEG as the basic matrix and SiO_2–NiO nanoparticles added in variable proportions. The optical-microscope photographs illustrate that the SiO_2–NiO additions were dispersed uniformly, and the nanoparticles organized into a consecutive network inside the polymer mixture. SEM examination was performed on the top surface of the PVA–PEG–SiO_2–NiO-NCs' films to examine the surface morphology. The findings point to the existence of several aggregates or pieces, which were dispersed randomly over the surface. Eventually, when the amount of SiO_2–NiO

nanoparticles increases, the attenuation coefficient for gamma radiation climbs as well. The results of the investigation display that the PVA–PEG–SiO_2–NiO-nanocomposite films exhibit good gamma-ray shielding features, when employed as a lead-free material. This implies that it may be a good substitute for traditional shielding materials in the field of nuclear medicine.

REFERENCES

1. A. A. ElBellihi, W. A. Bayoumy, E. M. Masoud, and M. A. Mousa, *Bulletin of the Korean Chemical Society*, **33**, No. 9: 2949 (2012); https://doi.org/10.5012/bkcs.2012.33.9.2949
2. M. A. Habeeb, *European Journal of Scientific Research*, **57**, No. 3: 478 (2011).
3. R. Tintu, K. Saurav, K. Sulakshna, V. P. N. Nampoori, P. Radhakrishnan, and S. Thomas, *J. Nan. Oxide Glas.*, **2**, No. 4: 167 (2010).
4. M. A. Habeeb and Z. S. Jaber, *East European Journal of Physics*, **4**: 176 (2022); doi:10.26565/2312-4334-2022-4-18
5. S. M. Mahdi and M. A. Habeeb, *Optical and Quantum Electronics*, **54**, Iss. 12: 854 (2022); https://doi.org/10.1007/s11082-022-04267-6
6. Q. M. Jebur, A. Hashim, and M. A. Habeeb, *Egyptian Journal of Chemistry*, **63**: 719 (2020); https://dx.doi.org/10.21608/ejchem.2019.14847.1900
7. S. Ganeshan, P. Ramasundari, A. Elangovan, G. Arivazhagan, and R. Vijayalakshmi, *Int. J. Sci. Res. Phys. Appl. Sci.*, **5**, No. 6: 5 (2017); https://doi.org/10.26438/ijsrpas/v5i6.58
8. A. H. Hadi and M. A. Habeeb, *Journal of Mechanical Engineering Research and Developments*, **44**, No. 3: 265 (2021); https://jmerd.net/03-2021-265-274/
9. N. Hayder, M.A. Habeeb, and A. Hashim, *Egyptian Journal of Chemistry*, **63**: 577 (2020); doi:10.21608/ejchem.2019.14646.1887
10. S. M. Mahdi and M. A. Habeeb, *Polymer Bulletin*, **80**, No. 12: 12741 (2023); https://doi.org/10.1007/s00289-023-04676-x
11. M. A. Habeeb, A. Hashim, and N. Hayder, *Egyptian Journal of Chemistry*, **63**: 709 (2020); https://dx.doi.org/10.21608/ejchem.2019.13333.1832
12. A. Hashim, M. A. Habeeb, and Q. M. Jebur, *Egyptian Journal of Chemistry*, **63**: 735 (2020); https://dx.doi.org/10.21608/ejchem.2019.14849.1901
13. S. M. Mahdi and M. A. Habeeb, *Physics and Chemistry of Solid State*, **23**, No. 4: 785 (2022); doi:10.15330/pcss.23.4.785-792
14. Nawras Karim Al-Sharifi and Majeed Ali Habeeb, *Silicon*, **15**: 4979 (2023); https://doi.org/10.1007/s12633-023-02418-2
15. M. A. Habeeb and W. S. Mahdi, *International Journal of Emerging Trends in Engineering Research*, **7**, No. 9: 247 (2019); doi:10.30534/ijeter/2019/06792019
16. M. A. Habeeb and R. S. Abdul Hamza, *Journal of Bionanoscience*, **12**, No. 3: 328 (2018); https://doi.org/10.1166/jbns.2018.1535
17. A. Hashim, A. J. Kadham Algidsawi, H. Ahmed, A. Hadi, M. A. Habeeb, *Nanosistemi, Nanomateriali, Nanotehnologii*, **19**, Iss. 2: 353 (2021); https://doi.org/10.15407/nnn.19.02.353

18. M. A. Habeeb, A. Hashim, and N. Hayder, *Egyptian Journal of Chemistry*, **63**: 697 (2020); https://dx.doi.org/10.21608/ejchem.2019.12439.1774
19. M. A. Habeeb and W. K. Kadhim, *Journal of Engineering and Applied Sciences*, **9**, No. 4: 109 (2014); doi:10.36478/jeasci.2014.109.113
20. Alaa Abass Mohammed and Majeed Ali Habeeb, *Silicon*, **15**: 5163 (2023); https://doi.org/10.1007/s12633-023-02426-2
21. A. H. Hadi and M. A. Habeeb, *Journal of Physics: Conference Series*, **1973**, Iss. 1: 012063 (2021); doi:10.1088/1742-6596/1973/1/012063
22. A. Hashim, A. J. Kadham, A. Hadi, and M. A. Habeeb, *Nanosistemi, Nanomateriali, Nanotehnologii*, **19**, Iss. 2: 327 (2021); https://doi.org/10.15407/nnn.19.02.327
23. S. M. Mahdi and M. A. Habeeb, *Digest Journal of Nanomaterials and Biostructures*, **17**, No. 3: 941 (2022); https://doi.org/10.15251/DJNB.2022.173.941
24. A. Hashim, A. J. Kadham Algidsawi, H. Ahmed, A. Hadi, and M. A. Habeeb, *Nanosistemi, Nanomateriali, Nanotehnologii*, **19**, Iss. 1: 91 (2021); https://doi.org/10.15407/nnn.19.01.091
25. M. A. Habeeb, *Journal of Engineering and Applied Sciences*, **9**, No. 4: 102 (2014); doi:10.36478/jeasci.2014.102.108
26. Q. M. Jebur, A. Hashim, and M. A. Habeeb, *Egyptian Journal of Chemistry*, **63**, No. 2: 611 (2020); https://dx.doi.org/10.21608/ejchem.2019.10197.1669
27. O. E. Gouda, S. F. Mahmoud, A. A. El-Gendy, and A. S. Haiba, *Indonesian Journal of Electrical Engineering*, **12**, No. 12: 7987 (2014).
28. M. A. Habeeb and A. H. Mohammed, *Optical and Quantum Electronics*, **55**, Iss. 9: 791 (2023); https://doi.org/10.1007/s11082-023-05061-8
29. M. H. Dwech, M. A. Habeeb, and A. H. Mohammed, *Ukr. J. Phys.*, **67**, No. 10: 757 (2022); https://doi.org/10.15407/ujpe67.10.757
30. R. S. Abdul Hamza and M. A. Habeeb, *Optical and Quantum Electronics*, **55**, Iss. 8: 705 (2023); https://doi.org/10.1007/s11082-023-04995-3
31. A. J. Kadham Algidsawi, A. Hashim, A. Hadi, M. A. Habeeb, and H. H. Abed, *Physics and Chemistry of Solid State*, **23**, No. 2: 353 (2022); https://doi.org/10.15330/pcss.23.2.353-360
32. M. A. Habeeb and W. H. Rahdi, *Optical and Quantum Electronics*, **55**, Iss. 4: 334 (2023); https://doi.org/10.1007/s11082-023-04639-6
33. H. N. Chandrakala, B. Ramaraj, Shivakumaraiah, G. M. Madhu, and Siddaramaiah, *Journal of Alloys and Compounds*, **551**: 531 (2013); https://doi.org/10.1016/j.jallcom.2012.10.188
34. A. Hashim and M. A. Habeeb, *Journal of Bionanoscience*, **12**, No. 5: 660 (2018); https://doi.org/10.1166/jbns.2018.1578
35. A. J. K. Algidsawi, A. Hashim, A. Hadi, and M. A. Habeeb, *Semiconductor Physics, Quantum Electronics and Optoelectronics*, **24**, No. 4: 472 (2021); https://doi.org/10.15407/spqeo24.04.472
36. J. Selvi, S. S. Mahalakshmi, and V. Parthasarathy, *J. Inorg. Organomet. Polym. Mater*, **27**: 1918 (2017); https://doi.org/10.1007/s10904-017-0662-1
37. N. K. Al-Sharifi and M. A. Habeeb, *East European Journal of Physics*, **2**: 341 (2023); doi:10.26565/2312-4334-2023-2-40
38. C. Uma Devi, A. K. Sharma, and V. V. R. N. Rao, *Materials Letters*, **56**, Iss. 3: 167 (2002); https://doi.org/10.1016/S0167-577X(02)00434-2

39. Nhiem Tran, Aparna Mir, Dhriti Mallik, Arvind Sinha, Suprabha Nayar, and Thomas J Webster, *Int. J. Nanomedicine*, **5**: 277 (2010); doi:10.2147/ijn.s9220
40. Z. S. Jaber, M. A. Habeeb, and W. H. Radi, *East European Journal of Physics*, **2**: 228 (2023); doi:10.26565/2312-4334-2023-2-25
41. M. A. Habeeb, and R. S. A. Hamza, *Indonesian Journal of Electrical Engineering and Informatics*, **6**, No. 4: 428 (2018); doi:10.11591/ijeei.v6i1.511
42. A. A. Mohammed and M. A. Habeeb, *East European Journal of Physics*, **2**: 157 (2023); doi:10.26565/2312-4334-2023-2-15
43. S. M. Mahdi and M. A. Habeeb, *AIMS Materials Science*, **10**, No. 2: 288 (2023); doi:10.3934/matersci.2023015

Наносистеми, наноматеріали, нанотехнології
Nanosistemi, Nanomateriali, Nanotehnologii
2026, т. 24, № 1, сс. 293–299
https://doi.org/10.15407/nnn.24.01.0293

PACS numbers: 78.20.Ci, 78.67.Sc, 81.05.Qk, 81.07.Pr, 81.40.Tv, 81.70.Fy, 82.35.Np

Synthesis of PEO/Si_3N_4–CeO_2-Nanocomposites' Films for Radiation Shielding

Ahmed Kareem, Ahmed Hashim, and Huda Bukheet Hassan

College of Education for Pure Sciences,
Department of Physics,
University of Babylon,
34001 Hillah, Iraq

Films of PEO/Si_3N_4–CeO_2 nanocomposites (NCs) are fabricated by casting method with different contents of PEO-polymer matrix and Si_3N_4–CeO_2 nanoparticles (NPs). The PEO/Si_3N_4–CeO_2 NCs are examined for gamma ray shielding. The results show that the PEO/Si_3N_4–CeO_2 NCs have the high attenuation coefficients for gamma rays. The attenuation coefficients increase with the increase of the Si_3N_4–CeO_2-NPs' concentration.

Плівки нанокомпозитів поліетилен оксид (ПЕО)/Si_3N_4–CeO_2 було виготовлено методом лиття з різним вмістом полімерної матриці ПЕО та наночастинок Si_3N_4–CeO_2. Нанокомпозити ПЕО/Si_3N_4–CeO_2 було досліджено стосовно екранування гама-променів. Результати показали, що нанокомпозити ПЕО/Si_3N_4–CeO_2 мають високі коефіцієнти ослаблення гама-променів. Коефіцієнти ослаблення підвищуються зі збільшенням концентрації наночастинок Si_3N_4–CeO_2.

Key words: PEO, CeO_2, Si_3N_4, nanocomposites, radiation shielding.

Ключові слова: поліетилен оксид, CeO_2, Si_3N_4, нанокомпозити, радіаційний захист.

(Received 10 March, 2024)

1. INTRODUCTION

Polymer nanocomposites (PNCs) contain typically one or more nanoparticles (NPs) components within the polymer matrix [1]. The enhancement of the properties with the addition of nanoparticles can be achieved due to different factors; one of the most important of them is a corresponding interfacial interaction between the

nanoparticles and the matrix with good dispersion of particles within the matrix [2]. Polymer nanocomposite materials are of great scientific and technological interest due to their unique mechanical, electronic, and optical properties [3]. The important properties of polymer nanocomposites cause a wide range of applications in various technologies such as advanced materials and goods, sensors, energy devices, and medicines [4]. Polyethylene oxide (PEO) is known as semi-crystalline, water-soluble, non-ionic, biodegradable and biocompatible polymer of considerable industrial significance, which finds applications in many different branches of industry [5], such as cosmetology (personal lubricants, emulsions, skin creams), pharmaceutical products, gene therapy, *etc.* [6].

Si_3N_4 nanoparticles exhibit high potential for the reinforcement of polymers. Si_3N_4 is a ceramic material with high strength and toughness. It has been used in many industrial applications, such as cutting tools, high temperature automobile components, springs, bearings and engine components. Si_3N_4 nanoparticles have also been used for enhancing the thermal conductivity of polyethylene composites and the wear resistance of polymer materials [7]. Cerium oxides have recently attracted much interest due to their unique properties, which make them suitable for various applications [8]. Cerium oxide (CeO_2) is a typical rare-earth element oxide [9]. Commercially, CeO_2 has numerous applications including fuel cells (as summarized by (EPA, 2009)), coatings, polishing agent (for glass mirrors, electronic wafers, precision optics, ophthalmic lenses, television tubes, plate glass) and petroleum refining (cracking catalysts). CeO_2 is applied in a variety of consumer products including semiconductors and as an additive in cigarettes. CeO_2 nanoparticles are predominantly employed as diesel-fuel additive [10]. There are many studies on properties of nanocomposites like optical properties [11–19] and electrical properties [20–31] to apply for radiation shielding [32, 33]. The present work aims to fabrication of PEO/Si_3N_4–CeO_2 nanocomposites for radiation shielding.

2. MATERIALS AND METHODS

The silicon nitride (Si_3N_4, 15–30 nm, purity 99.9%) and cerium dioxide (CeO_2, 99.97, 50 nm) nanopowders were obtained from US Research Nanomaterials, Inc. The PEO/Si_3N_4–CeO_2 nanocomposites (NCs) were prepared by casting method. The 1 g of the poly(ethylene oxide) (PEO) was dissolved in 60 ml of distilled water, and then the solution was thoroughly mixed for one hour with a magnetic stirrer. The nanoparticles (NPs), namely, from 50% Si_3N_4 and 50% CeO_2, are added to the PEO solution with contents of 1.9%, 3.8%, 5.7%, and 7.6%. The nanocomposites were casted in a

template, namely, a Petri dish measuring 10 cm in diameter. The PEO/Si_3N_4–CeO_2 nanocomposite films were tested by using the optical microscope (supplied from Olympus name (ToupView) type (Nikon-73346)) with magnification ×10.

The attenuation of radiation is characterized by relationship [34] $N = N_0 e^{-\mu x}$, where N_0 is the number of particles of radiation counted during a certain time duration without any absorber; μ is the attenuation coefficient of gamma radiation, and N is the number counted during the same time, with a thickness of sample x.

3. RESULTS AND DISCUSSION

Figure 1 indicates microscopic images of PEO/Si_3N_4–CeO_2 nanocom-

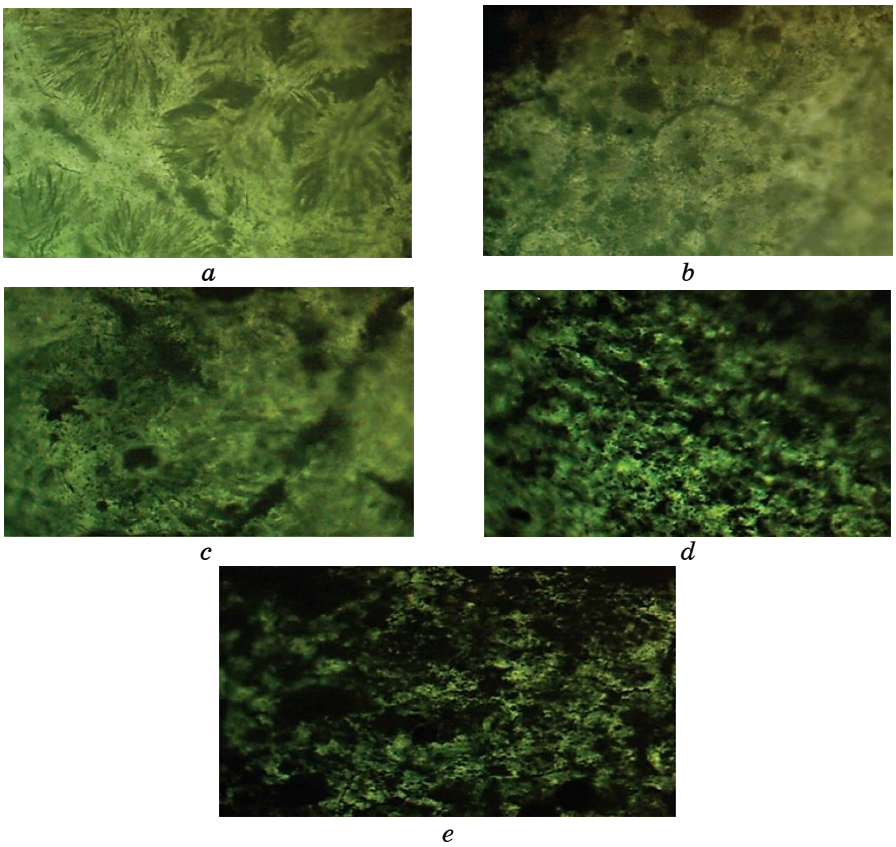

Fig. 1. Photomicrographs (×10) for PEO/Si_3N_4–CeO_2 NCs: (*a*) for PEO pure; (*b*) 1.9 wt.% Si_3N_4–CeO_2 NPs; (*c*) 3.8 wt.% Si_3N_4–CeO_2 NPs; (*d*) 5.7 wt.% Si_3N_4–CeO_2 NPs, and (*e*) 7.6 wt.% Si_3N_4–CeO_2 NPs.

posite at magnification power ×10. This figure shows that the Si_3N_4–CeO_2 nanoparticles are aggregated as clusters at low concentrations. When increasing the concentration of nanoparticles, the nanoparticles form a paths' network inside the polymer matrix [35–46].

Figure 2 shows the variation of (N/N_0) for PEO with different

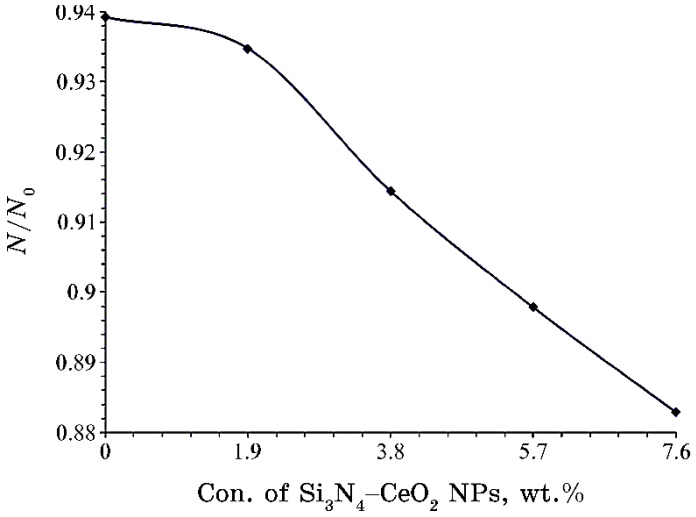

Fig. 2. Variation of N/N_0 for PEO with different concentrations of Si_3N_4–CeO_2 nanoparticles.

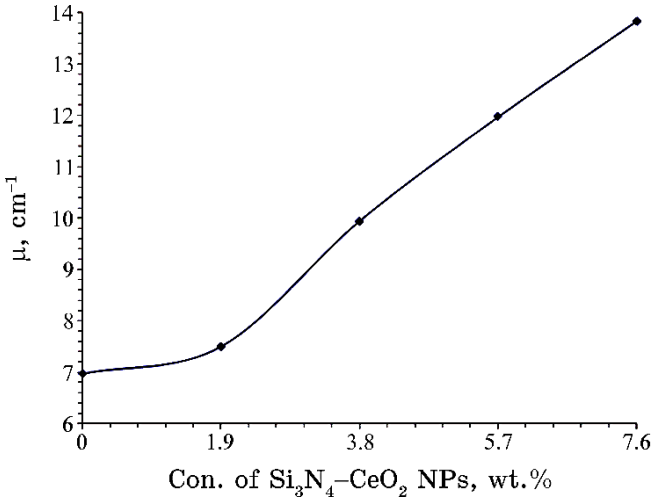

Fig. 3. Variation of attenuation coefficient of gamma radiation for PEO as a function of Si_3N_4–CeO_2-nanoparticles' concentration.

concentrations of Si_3N_4–CeO_2 nanoparticles. The transmission radiation decreases with the increasing of the concentrations of Si_3N_4–CeO_2 nanoparticles that is attributed to the increase of the attenuation radiation [47].

Figure 3 shows the variation of attenuation coefficients of gamma radiation for PEO as a function of Si_3N_4–CeO_2-nanoparticles' concentration. The attenuation coefficients increase with the increase of nanoparticles' concentration; this is due to the absorption or reflection of gamma radiation by shielding nanocomposite materials [48–50].

4. CONCLUSIONS

This work included the fabrication of PEO/Si_3N_4–CeO_2-nanocomposite films with various concentrations of polymer matrix and nanoparticles. The gamma-ray shielding application for PEO/Si_3N_4–CeO_2 nanocomposites was tested. (Incidentally, the results indicated that the PS/SiO_2–$SrTiO_3$ nanocomposites have the high attenuation coefficients of gamma rays.) The attenuation coefficients were rising with the increase of Si_3N_4–CeO_2-nanoparticles' concentration.

REFERENCES

1. S. K. Kumar, B. C. Benicewicz, R. A. Vaia, and K. I. Winey, *Macromolecules*, **50**, No. 3:714 (2017); doi:10.1021/acs.macromol.6b02330
2. A. I. Abdelamir, E. Al-Bermany, and F. S. Hashim, *J. Phys. Conf. Ser.*, **1294**, No. 2: 022029 (2019); doi:10.1088/1742-6596/1294/2/022029
3. T. S. Soliman and S. A. Vshivkov, *J. Non. Cryst. Solids*, **519**: 119452 (2019); doi:10.1016/j.jnoncrysol.2019.05.028
4. M. A. Ashraf, W. Peng, Y. Zare, and K. Y. Rhee, *Nanoscale Res. Lett.*, **13**, No. 1: 214 (2018); doi:10.1186/s11671-018-2624-0
5. M. Jakić, N. S. Vrandečić, and M. Erceg, *J. Therm. Anal. Calorim.*, **127**, No. 1: 663 (2017); doi:10.1007/s10973-016-5768-0
6. M. A. Jawad, A. J. Kadhim, and S. Y. Hasan, *Int. J. Pharm. Qual. Assur.*, **12**, No. 3: 187 (2021); doi:10.25258/ijpqa.12.3.4
7. W. Hao, W. Yang, H. Cai, and Y. Huang, *Polym. Test.*, **29**, No. 4: 527 (2010); doi:10.1016/j.polymertesting.2010.03.004
8. P. Patsalas, S. Logothetidis, L. Sygellou, and S. Kennou, *Phys. Rev. B*, **68**, No. 3: 035104 (2003); doi:10.1103/PhysRevB.68.035104
9. R. Liu, X. Liu, H. Yang, H. Jie, T. Li, K. Lyu, and S. P. Shah, *Polymers*, **14**, No. 17: 3573 (2022); doi:10.3390/polym14173573
10. F. R. Cassee, E. C. Van Balen, C. Singh, D. Green, H. Muijser, J. Weinstein, and K. Dreher, *Crit. Rev. Toxicol.*, **41**, No. 3: 213 (2011); doi:10.3109/10408444.2010.529105
11. A. Hashim, E. H. Abdullah, F. L. Rashid, and A. Hadi, *Nanosistemi, Nano-*

materiali, Nanotehnologii, **19**, Iss. 3: 697 (2021); https://doi.org/10.15407/nnn.19.03.697
12. M. Sajjad and A. Hashim, *Nanosistemi, Nanomateriali, Nanotehnologii*, **19**, Iss. 4: 831 (2021); https://doi.org/10.15407/nnn.19.04.831
13. A. Hashim, *Nanosistemi, Nanomateriali, Nanotehnologii*, **19**, Iss. 3: 647 (2021); https://doi.org/10.15407/nnn.19.03.647
14. M. K. Mohammed, E. H. Abdullah, D. Hassan, and A. Hashim, *Revue des Composites et des Matériaux Avancés–Journal of Composite and Advanced Materials*, **32**, No. 6: 305 (2022); https://doi.org/10.18280/rcma.320606
15. Y. Y. Mijbil and A. Hashim, *Nanosistemi, Nanomateriali, Nanotehnologii*, **20**, No. 2: 497 (2022); https://doi.org/10.15407/nnn.20.02.497
16. M. H. Rasheed, A. K. Abbas, F. Rashid, and A. Hashim, *Nanosistemi, Nanomateriali, Nanotehnologii*, **20**, Iss. 3: 761(2022); https://doi.org/10.15407/nnn.20.03.761
17. Ahmed Hashim, Aseel Hadi, and M. H. Abbas, *Silicon*, **15**: 6431 (2023); https://doi.org/10.1007/s12633-023-02529-w
18. A. Hashim, A. Hadi, and N. A. H. Al-Aaraji, *Optical and Quantum Electronics*, **55**: 716 (2023); https://doi.org/10.1007/s11082-023-04994-4
19. Ahmed Hashim, Batool Mohammed, Aseel Hadi, and Hamed Ibrahim, *Journal of Inorganic and Organometallic Polymers and Materials*, **34**: 611 (2024); https://doi.org/10.1007/s10904-023-02846-y
20. Z. S. Hamad and A. Hashim, *Nanosistemi, Nanomateriali, Nanotehnologii*, **20**, Iss. 1: 159 (2022); https://doi.org/10.15407/nnn.20.01.159
21. A. Hashim and Z. S. Hamad, *Nanosistemi, Nanomateriali, Nanotehnologii*, **20**, Iss. 1: 165 (2022); https://doi.org/10.15407/nnn.20.01.165
22. A. Hashim and A. Jassim, *Nanosistemi, Nanomateriali, Nanotehnologii*, **20**, Iss. 1: 177 (2022); https://doi.org/10.15407/nnn.20.01.177
23. A. Hashim and Z. S. Hamad, *Nanosistemi, Nanomateriali, Nanotehnologii*, **20**, Iss. 2: 507 (2022); https://doi.org/10.15407/nnn.20.02.507
24. B. Mohammed, H. Ahmed and A. Hashim, *Journal of Physics: Conference Series*, **1879**: 1 (2021); doi:10.1088/1742-6596/1879/3/032110
25. D. Hassan and A. H. Ah-Yasari, *Bulletin of Electrical Engineering and Informatics*, **8**, Iss. 1: 52 (2019); doi:10.11591/eei.v8i1.1019
26. D. Hassan and A. Hashim, *Bulletin of Electrical Engineering and Informatics*, **7**, Iss. 4: 547 (2018); doi:10.11591/eei.v7i4.969
27. A. Hashim, M. H. Abbas, N. AH. Al-Aaraji, and A. Hadi, *J. Inorg. Organomet. Polym.*, **33**: 1 (2023); https://doi.org/10.1007/s10904-022-02485-9
28. A. Hashim, M. H. Abbas, N. AH. Al-Aaraji, and A. Hadi, *Silicon*, **15**: 1283 (2023); https://doi.org/10.1007/s12633-022-02104-9
29. M. H. Meteab, A. Hashim, and B. H. Rabee, *Silicon*, **15**: 1609 (2023); https://doi.org/10.1007/s12633-022-02114-7
30. M. H. Meteab, A. Hashim, and B. H. Rabee, *Silicon*, **15**: 251 (2023); https://doi.org/10.1007/s12633-022-02020-y
31. A. Hashim, A. Hadi, and M. H. Abbas, *Opt. Quant. Electron.*, **55**: 642 (2023); https://doi.org/10.1007/s11082-023-04929-z
32. B. Abbas and A. Hashim, *International Journal of Emerging Trends in Engineering Research*, **7**, No. 8: 131 (2019); https://doi.org/10.30534/ijeter/2019/06782019
33. K. H. H. Al-Attiyah, A. Hashim, and S. F. Obaid, *Journal of Bion-*

anoscience, **12**: 200 (2018); doi:10.1166/jbns.2018.1526
34. L. M. Chaudhari and R. Nathuram, *Bulg. J. Phys.*, **37**, No. 1: 232 (2010).
35. A. Hashim and A. Jassim, *Nanosistemi, Nanomateriali, Nanotehnologii*, **19**, Iss. 4: 883 (2021); doi:10.15407/nnn.19.04.883
36. H. K. Jaafar, A. Hashim, and B. H. Rabee, *Optical and Quantum Electronics*, **55**: 989 (2023); https://doi.org/10.1007/s11082-023-05208-7
37. Ahmed Hashim, Saif M. Alshrefi, Hussein H. Abed, and Aseel Hadi, *Journal of Inorganic and Organometallic Polymers and Materials*, **34**: 703 (2024); https://doi.org/10.1007/s10904-023-02866-8
38. Hiba Kamil Jaafar, Ahmed Hashim and Bahaa H. Rabee, **16**: 603 (2024); https://doi.org/10.1007/s12633-023-02706-x
39. H. A. J. Hussien, R. G. Kadhim, and A. Hashim, *Optical and Quantum Electronics*, **54**: 704 (2022); https://doi.org/10.1007/s11082-022-04094-9
40. H. B. Hassan, A. Hashim, and H. M. Abduljalil, *Polymer Bulletin*, **80**: 9059 (2023); https://doi.org/10.1007/s00289-022-04502-w
41. H. A. J. Hussien, R. G. Kadhim, and A. Hashim, *Optical and Quantum Electronics*, **53**: 501 (2021); https://doi.org/10.1007/s11082-021-03157-7
42. H. A. J. Hussien, R. G. Kadhim, and A. Hashim, *Polymer Bulletin*, **79**: 5219 (2022); https://doi.org/10.1007/s00289-021-03778-8
43. Ghaith Ahmed and Ahmed Hashim, *Silicon*, **15**: 7085 (2023); https://doi.org/10.1007/s12633-023-02572-7
44. A. Hazim, A. Hashim, and H. M. Abduljalil, *Egypt. J. Chem.*, **64**, No. 1: 359 (2021); doi:10.21608/EJCHEM.2019.18513.2144
45. A. F. Kadhim and A. Hashim, *Opt. Quant. Electron.*, **55**: 432 (2023); https://doi.org/10.1007/s11082-023-04699-8
46. M. H. Meteab, A. Hashim, and B. H. Rabee, *Opt. Quant. Electron.*, **55**: 187 (2023); https://doi.org/10.1007/s11082-022-04447-4
47. I. R. Agool, K. J. Kadhim, and A. Hashim, *Int. J. Plast. Technol.*, **21**, No. 2: 444 (2017); doi:10.1007/s12588-017-9196-1
48. A. Hashim and Z. S. Hamad, *Journal of Bionanoscience*, **12**, No. 4: 488 (2018); doi:10.1166/jbns.2018.1551
50. A. Hashim, I. R. Agool, and K. J. Kadhim, *J. Mater. Sci. Mater. Electron.*, **29**, No. 12: 10369 (2018); doi:10.1007/s10854-018-9095-z
51. Ahmed Hashim and Zinah Sattar Hamad, *Journal of Bionanoscience*, **12**, No. 4: 504 (2018); doi:10.1166/jbns.2018.1561

Наносистеми, наноматеріали, нанотехнології
Nanosistemi, Nanomateriali, Nanotehnologii
2026, т. 24, № 1, сс. 301–316
https://doi.org/10.15407/nnn.24.01.0301

PACS numbers: 42.25.Dd, 42.30.Ms, 81.07.Bc, 83.80.Lz, 87.85.gf, 87.85.Pq, 87.85.Rs

Laser Speckle Analysis of Blood Coagulation: Overview and Prospects for Use in Military Medicine

Viktor Borovskyi and Mykola Bogomolov

National Technical University of Ukraine
'Igor Sikorsky Kyiv Polytechnic Institute',
37, Beresteiskyi Ave.,
UA-03056 Kyiv, Ukraine

The article discusses a promising technology for assessing the blood-coagulation system, namely, laser speckle analysis (LSA), with an emphasis on the use of optical nanostructured components to improve the quality of diagnostics. A review of the physical foundations of the method, modern scientific research and comparison with traditional viscoelastic haemostatic assays TEG, ROTEM, ClotPro is carried out. Particular attention is paid to the role of nanotechnological solutions (anti-reflective nanocoatings of the 'moth-eye' type, plasmon Ag, Si nanoparticles and silver nanofilms with a thickness of 40–80 nm) in the formation of a stable, high-contrast speckle pattern. The mechanisms of reducing parasitic reflections, increasing light transmission and amplification of the local light signal due to the effects of the local and surface plasmon resonances are described. As shown, the introduction of such nanostructures into the configuration of the LSA sensor can improve significantly the signal-to-noise ratio, increase the spatial resolution and accuracy of the assessment of the microdynamics of formed blood elements. The potential of portable implementation of LSA with nanoreinforced optical elements for the field and military medicine Role 2, Role 3 is highlighted, where the applicability of conventional coagulation devices is limited. The proposed approach combines optical diagnostics and nanotechnology methods, which open up new opportunities for the creation of a new generation of mobile biomedical sensors. This work emphasizes not only the technological novelty of LSA, but also its direct clinical value for increasing the effectiveness of treatment in conditions of emergency and military medicine.

У статті йдеться про перспективну технологію оцінки системи згортання крові, — лазерну спекл-аналізу (LSA), — з акцентом на застосування оптичних наноструктурованих компонентів для підвищення якости діягностики. Проведено огляд фізичних основ методу, сучасних наукових досліджень і порівняння з традиційними високоеластичними гемо-

статичними системами TEG, ROTEM, ClotPro. Особливу увагу приділено ролі нанотехнологічних рішень (антивідблискувальних нанопокриттів типу ‘moth-eye’, плазмонних наночастинок Ag, Si і срібних наноплівок товщиною у 40–80 нм) у формуванні стабільного, висококонтрастного спекл-патерну. Описано механізми пониження вторинних відбивань, підвищення світлопропускання та посилення локального світлового сиґналу за рахунок ефектів локального та поверхневого плазмонних резонансів. Показано, що впровадження таких наноструктур у конфіґурацію LSA-сенсора може значно поліпшити співвідношення сиґнал/шум, підвищити просторову роздільчу здатність і точність оцінки мікродинаміки формених елементів крові. Підкреслено потенціял портативної реалізації LSA з нанопосиленими оптичними елементами для польової та військової медицини Role 2, Role 3, де можливості використання класичних коаґуляційних пристроїв є обмеженими. Запропонований підхід поєднує оптичну діягностику та методи нанотехнологій, що відкриває нові можливості для створення нового покоління мобільних біомедичних сенсорів. Ця робота підкреслює не лише технологічну новизну LSA, але й її безпосередню клінічну цінність для підвищення ефективности лікування в умовах екстреної та військової медицини.

Key words: laser speckle analysis, fibre-optic light guides, blood coagulation, nanocoatings, optical diagnostics, military medicine.

Ключові слова: лазерна спекл-аналіза, волоконно-оптичні світловоди, згортання крові, нанопокриття, оптична діягностика, військова медицина.

(Received 10 August, 2025; in revised form, 15 September, 2025)

1. INTRODUCTION

High-quality monitoring of blood clotting is critically important in various clinical and emergency situations, in particular, during surgical interventions, injuries, in ICU, and in combat conditions [1–5]. Rapid detection of coagulopathy or hypercoagulation allows the timely use of blood products, haemostatic drugs or anticoagulants, which directly affects the quality of medical care [6–9].

Classic laboratory tests such as prothrombin time (PT), activated partial thromboplastin time (aPTT), and fibrinogen levels provide limited insight into the dynamic process of clot formation. Instead, viscoelastic haemostatic (VHA) methods, including thromboelastography (TEG), rotational thromboelastometry (ROTEM), and ClotPro, provide real-time assessment of coagulation kinetics, clot strength, and lysis process [10]. These systems have become the gold standard in cardiac surgery, traumatology, and liver transplantation [11–13]. However, their widespread use is limited by technical complexity, high cost, the need for trained personnel and sensitivity to mechanical stability, which limit applicability in field

or combat conditions [14].

In recent years, optical methods, in particular, laser speckle analysis (LSA), have attracted attention as a promising alternative for non-contact and operative assessment of blood clotting [15]. By capturing dynamic changes in the speckle structure that occur when coherent laser radiation interacts with a blood sample, LSA allows indirectly assessing the process of clot formation without physical contact or moving parts [7]. Such properties make the method especially interesting for creating compact, reliable, using fibre-optic LEDs, and potentially suitable for use in the field [16].

In the context of the full-scale war of the Russian Federation against Ukraine, the need for rapid and portable medical diagnostics has increased significantly. Stabilization points, UGS, and frontline medical units operate in resource-constrained environments where traditional thromboelastography systems often cannot be installed [10]. Compact an optical diagnostic method capable of assessing blood clotting without stringent installation requirements could significantly improve the effectiveness of care in such conditions.

The purpose of the review is to summarize the current state of research in the field of laser speckle analysis for monitoring blood coagulation, analyse its correlation with standard thromboelastography, highlight the advantages and limitations of the method, review the use of nanoreinforced optical elements, as well as the prospects for its implementation in military and field medicine.

2. OVERVIEW OF THROMBOELASTOGRAPHY

Thromboelastography is a method of visualizing and quantifying blood clotting processes in real time. It allows you to trace all stages of clot formation from initiation to fibrinolysis based on changes in the mechanical properties of a blood sample.

The classical thromboelastograph (TEG) and its modern analogues (ROTEM and ClotPro) use a viscoelastic analysis model. The principle of operation is to measure the force that is transmitted between a rotating or oscillating element (bowl or stem) and a clot that forms in a test tube with a blood sample [17].

The main parameters that the thromboelastograph fixes:

— *R* (Reaction Time)—the time before the onset of coagulation (thrombin activation);

— *K* (Kinetics)—the time until certain clot strength is reached;

— α angle (Alpha angle)—the rate of formation of the fibrin framework;

— MA (Maximum Amplitude)—the maximum strength of the clot, which characterizes platelet and fibrin function;

— LY30 or ML (Lysis)—the degree of fibrinolysis 30 min after reaching MA.

ROTEM and ClotPro use similar parameters, but with their own terminology, for example, CT (Clotting Time), CFT (Clot Formation Time), MCF (Maximum Clot Firmness), LI30/ML.

Due to its high information content, thromboelastography is widely used in cardiac surgery, traumatology, obstetrics and resuscitation. The method allows you to reduce the use of blood components, optimize anticoagulant therapy and prevent thrombotic complications [18, 19].

At the same time, the use of the above systems in the field is complicated due to their need for stable horizontal placement, the absence of vibrations, temperature sensitivity, as well as the high cost and need for personnel training. This opens up the prospect for the development of alternative methods, in particular optical ones, such as laser speckle analysis [10].

3. THEORETICAL FOUNDATIONS OF SPECKLE ANALYSIS

Laser speckle analysis (LSA) is based on an optical phenomenon that occurs, when a heterogeneous medium is illuminated by coherent laser radiation [20, 21].

Because of the interaction of the beam with microscopic structures (for example, blood cells or plasma components), a characteristic interference pattern is formed on the surface of the sample, namely, a speckle structure. It has a random appearance, but changes in time in response to micromovements, diffusion of particles or changes in the rheological properties of the medium [16].

In dynamic analysis, which is used to study blood coagulation, a change in the intensity or contrast of the speckle structure over time is recorded [21]. In the initial stages of coagulation, when the cells are still moving in the plasma, there is a high variability in intensity. As the fibrin clot forms and the particles lose mobility, the variability decreases, and the speckle pattern stabilizes.

The laser radiation passes through the blood sample, after which a speckle pattern is formed, which is recorded by the camera through the optical system and in a short period of time (Fig. 2) [22].

One of the key parameters is speckle contrast, which can be calculated from the standard deviation of pixel intensity in a specific time or space window. A decrease in contrast indicates an increase in the mobility of particles, while its increase indicates the stabilization of the structure, *i.e.*, the formation of a clot [14].

Other analysis techniques include constructing temporal autocorrelation functions, estimating average phase shift, detecting optical vortices, or statistical changes in image texture. All these ap-

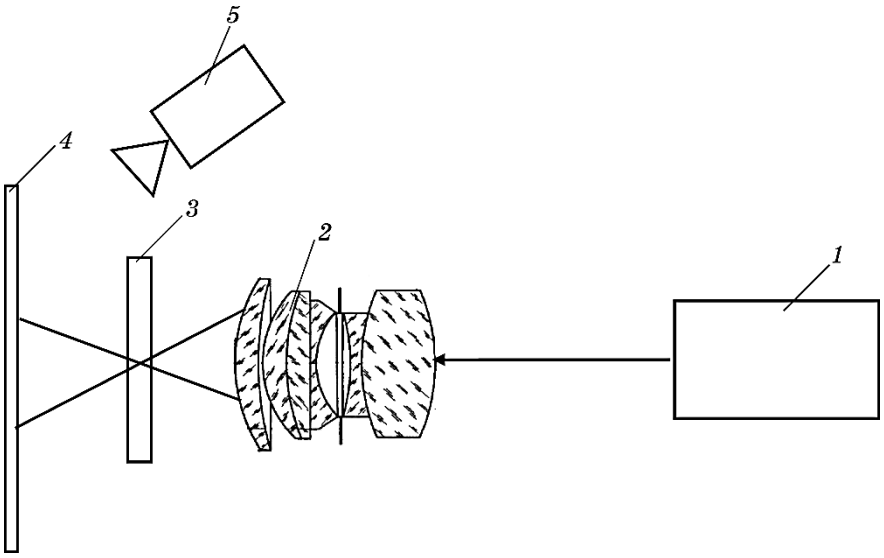

Fig. 1. Structural diagram of a laboratory setup for recording speckle images [22]: *1*—He–Ne laser; *2*—lens; *3*—blood sample; *4*—recording screen; *5*—camera.

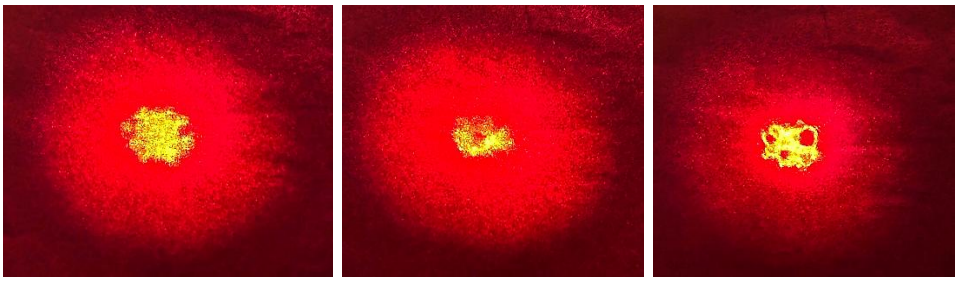

Fig. 2. Control speckle image.

proaches are aimed at obtaining information about the micromovements of blood cells, which change in the process of coagulation.

Thus, the LSA provides an indirect but informative assessment of the stages of blood clotting without physical contact with the specimen. The technique is characterized by high sensitivity, does not require markers or reagents and can be implemented on compact fibre-optic LEDs [23, 24].

The following sections discuss examples of studies, in which LSA has been used to assess blood coagulation, in particular, compared to thromboelastography systems.

4. REVIEW OF STUDIES ON THE USE OF LSA TO ASSESS BLOOD CLOTTING

Over the past decade, a number of studies have been conducted that have demonstrated the effectiveness of laser speckle analysis (LSA) in assessing blood-clotting parameters. One of the first large-scale studies in which a system based on LSA was developed to measure the viscoelastic properties of blood during coagulation. The authors showed that the indicators obtained using this method show a high correlation with the data of traditional mechanical rheometry [21].

Further research [25] proposed alternative ways to analyse speckle patterns, including the detection of optical vortices, which allowed for improved temporal resolution and accuracy in determining the moment of clot formation. In this work, a comparison was also made with the parameters of the thromboelastograph, which confirmed the clinical relevance of the technique.

Other studies have adapted the LSA to the conditions for assessing coagulation in gel-like media, demonstrating the wide versatility of the approach and the possibility of modifying the method to meet the needs of medical diagnostics.

All of the above-mentioned papers highlight the potential of LSA as a non-contact, fast, and cost-effective alternative to traditional coagulology methods. Although clinical use is still in the prototype phase and *in vitro* studies, the availability of comparative data with thromboelastography suggests significant prospects for use in resource-limited settings, including Role 2, Role 3 medical care for the wounded [1].

5. COMPARATIVE ANALYSIS OF LSA AND TEG/ROTEM/ClotPro

Comparison between laser speckle analysis (LSA) and traditional highly-elastic methods for assessing blood coagulation (TEG, ROTEM, ClotPro) allows us to determine the advantages and limitations of each of the approaches, as well as the potential of LSA in clinical applications, as shown in Table 1 below [1, 6, 7, 25].

Main parameters for comparison are as follow.

Despite the fact that thromboelastography is a recognized clinical standard, its use in difficult conditions (combat, field, mobile hospitals, *etc.*) is significantly complicated due to sensitivity to tilt, vibration and the need for consumables. LSA can be implemented as an alternative in the form of a compact, non-contact device that allows you to obtain quickly information about the state of haemostasis even under minimal laboratory conditions.

In Table 2 [21, 26–28] below, there is a comparing the quantitative indicators obtained by traditional thromboelastography tech-

TABLE 1. Comparative analysis of LSA and TEG/ROTEM/ClotPro.

Setting	Thromboelastography (TEG/ROTEM/ClotPro)	Laser speckle analysis (LSA)
Onset of clotting	R/CT	Speckle variability reduction time
Rate of clot formation	K, α/CFT, α	Contrast change gradient
Maximum clot strength	MA/MCF	Speckle field stability and intensity
Fibrinolysis	LY30/ML	Secondary increase in variability (experimental)
Contact of the sample with the instrument	Need	Not required
The need for reagents	Yes (*e.g.*, activators)	No
Research time	30–60 min	5–20 min (depending on implementation)
Field use	Limited	Possible (with proper implementation)

TABLE 2. Comparison of quantitative indicators of TEG, ClotPro and LSA.

Setting	TEG/ClotPro (average)	LSA (similar indicator)
R, min	5–8	5–7 (Contrast stabilization start)
MA, mm	55–70	Variation index = 0.75–0.90
Clot formation time	≅ 10 min	≅ 8 min
Viscosity (indirectly)	—	Speckle rheology (LSR scale 0–1)

niques (TEG, ClotPro) and the corresponding parameters, which are evaluated by laser speckle analysis (LSA), according to literature sources.

At the same time, the LSA does not yet have full clinical validation and requires further research, in particular using various coagulation profiles, *in vivo* testing, as well as the development of data interpretation standards. Despite this, the already available experimental comparisons demonstrate a high degree of correlation between optical performance and results obtained with TEG/ROTEM.

To visualize the main differences between classical thromboelastography methods and laser speckle analysis of comparison in the context of use in clinical and military practice, the following is a comparative in Table 3 [1–4, 6, 15, 19, 21].

TABLE 3. Comparison of application possibilities in the clinical and military practices of TEG, ROTEM, ClotPro and LSA.

Setting	Thromboelastography (TEG/ROTEM/ClotPro)	Laser Speckle Analysis (LSA)
Method type	Mechanical–optical	Optical (based on coherent scattering)
Contact	Pin	Contactless
The need for reagents	Reagents are needed	No reagents
Time to get the result	10–60 min	2–10 min
Mobility	Stationary device	Portable, POC option possible
Vibration sensitivity	High (requires a stable surface)	Low (can be adapted)
Possibility of field use	Low	High

In this way, LSA not only complements classical methods, but also has the potential to replace them in specific situations where classical equipment is unavailable, less practical or too difficult to use.

6. PROSPECT FOR USE IN THE FIELD

Assessing blood clotting in resource-limited settings, especially in field or combat situations, requires technologies that are as autonomous, fast, and easy to use as possible. In such conditions, traditional thromboelastography systems are often unusable due to limitations in mobility, the need for calibration, reagents, constant power supply, and stable horizontal installation.

Laser speckle analysis (LSA) has a number of features, which determine its peculiarity for use in the field:

— contactless (it reduces the risks of contamination, simplifies maintenance and allows integration into sealed modules);

— no need for reagents (it allows you to reduce costs and minimize logistics dependencies);

— compactness and energy efficiency (the technology can be implemented on the base of portable lasers and CMOS cameras);

— rapid analysis provides results within 5–20 minutes, which is critical with a mass admission of patients);

— possibility of installation in mobile laboratories or medical platforms (ambulances, stabilization points, field surgical hospitals, *etc.*).

In the context of the war in Ukraine, such decisions are especially relevant. Domestic stabilization points often operate with

minimal equipment, in the field or in rooms without a stable power supply. LSA devices can be implemented as portable diagnostic modules for the initial assessment of the coagulation status of victims, which will allow timely decisions on transfusion, the use of anticoagulants or referral to the hospital.

The minimum requirements for laboratory diagnostics vary significantly depending on the level of the medical unit. Coagulation tests PT, aPTT, INR are included in the mandatory list only for Role 3 units, while for Role 2 such tests are not provided as mandatory [1]. This creates a potential clinical risk, since urgent surgical interventions are often performed at the Role 2 level in conditions of limited laboratory infrastructure, which makes it impossible to detect coagulopathy in time. Lack of access to coagulogram results can delay critical decisions about blood transfusion, fibrinogen administration, or anti-shock measures [6, 29].

In this context, portable technologies, such as laser speckle analysis (LSA) or thromboelastography (TEG/ROTEM), can significantly enhance the diagnostic capabilities of Role 2 [30]. Due to autonomy, high speed of obtaining results 5–15 minutes and the absence of the need for reagents, such methods are able to provide a prompt assessment of haemostasis even in unstable conditions [31]. This makes them particularly suitable for Damage Control Resuscitation (DCR) scenarios, which, according to modern military doctrine, are actively implemented at the Role 2 level. LSA can act not only as an alternative to classical laboratory coagulation, but also provide continuous monitoring of the state of coagulation before, during and after surgery, which significantly increases the chances of survival in patients with polystructural injury.

Most patients admitted to the Role 2 level have combined and combined combat injuries accompanied by massive bleeding. According to clinical studies, acute traumatic coagulopathy (ATC) can occur already at the prehospital stage (for in 25–35% of seriously injured patients [32]). In such situations, delay in identifying blood-clotting disorders significantly worsens the prognosis and can lead to unjustified blood loss, hypothermia and fatal complications. As stated in the updated European guidelines for the treatment of bleeding, the use of POC methods for monitoring haemostasis can significantly reduce the time to clinical decision-making compared to traditional laboratory tests [33]. If such technologies are integrated into the Role 2 structure, it is possible to achieve more effective coagulopathy control, which corresponds to modern principles of management of seriously injured patients in the war zone.

In the context of optical diagnostics, it is also worth noting that physical and chemical environmental factors affect the biosynthetic activity of microalgae specifically for each species. For example,

may either stimulate or inhibit the synthesis of metabolites, including lipids, carotenoids, chlorophylls, proteins and carbohydrates. In addition, the spectrum and intensity of light, as well as the duration and frequency of exposure to ultrasound, UV and α-radiation, are able to alter the metabolic pathways of microalgae, which demonstrates the breadth of possibilities for the influence of physical factors on cellular processes, which is consistent with the mechanisms that underlie laser speckle analysis.

7. NANOCOATING OF OPTICAL COMPONENTS TO IMPROVE SPECKLE IMAGE QUALITY

In a configuration where laser radiation is directed at an angle of 45° directly at the sample, and the reflected signal is recorded through the lens, optical transparency and the purity of the optical path play a key role in the formation of a high-quality image [34, 35]. Under the conditions of laser speckle analysis, even minor parasitic not required on the lens or objective surfaces can cause interference noise, a decrease in contrast and errors in the analysis of particle dynamics [36].

Nanoscale particles, especially metallic particles, are essential for increasing the sensitivity of laser speckle analysis due to the phenomenon of local surface plasmon resonance (LSPR) [37, 38]. Under the action of coherent laser light, electrons on the surface of the nanoparticle oscillate synchronously, which greatly enhances the scattering and absorption of light under resonant conditions. This effect produces brighter, more sensitive speckle signals, allowing detection of cell movements or aggregation even with fewer particles or aggregation of cells or protein structures into the bloodstream [28, 39].

One of the most promising solutions is the use of nanostructured anti-reflective (AR) coatings. The *moth-eye coating* mimics the structure of the eyes of nocturnal insects and creates a gradient refractive index at the air–glass interface, which significantly reduces reflection in a wide spectral range even at angular incidence of light [40]. Such nanocoatings reduce reflection from the surface to $< 0.5\%$ and increase light transmission up to 99% in the wavelength range of 400–900 nm [20, 41].

Unlike traditional multilayer AR coatings, which are effective mainly at normal beam incidence, *moth-eye* nanotextures remain effective at oblique angles, which is especially important when observing a sample at an angle of 45° [25].

Another approach is to use coatings with plasmonic nanoparticles (*e.g.*, Ag or Si), which not only reduce reflection but can also amplify the local light signal through the surface plasmon resonance. These

effects allow not only to muffle background noise, but also to increase the amplitude of the speckle signal and image detail [25, 41].

Studies show that such nanocomposites significantly improve the signal-to-noise ratio in optical imaging systems, in particular by reducing scattering and interference artefacts [20].

Nanocoatings also have a positive effect on optical clarity and spatial resolution, as the reduction of spurious reflections allows weak signals to be recorded without additional noise. Combined with high-quality lenses, this provides better focal stability, speckle structure clarity, and a more accurate analysis of microdynamics in the blood sample.

To implement these approaches, methods of nanolithography, ion etching, self-assembly technologies, or nanoparticle sputtering can be used. Most commercial optical manufacturers already offer AR lenses with nanotextures, including Edmund Optics, Thorlabs, Jenoptik, and others.

8. PHYSICAL MECHANISMS OF THE EFFECT OF NANOPARTICLES ON LSA SENSITIVITY

One of the important factors in increasing the sensitivity of LSA is the use of nanoscale structures, whose size is commensurate with the wavelength of coherent laser radiation in the range of 400–900 nm [38]. It is at this scale that the phenomena of localized surface plasmon resonance (LSPR) and surface plasmon resonance (SPR) occur [36]. When coherent light interacts with silver, gold, or silicon nanoparticles, electrons on their surface begin to oscillate synchronously with the electromagnetic field, resulting in a significant increase in the local electric field near the nanoparticles, the formation of ‘hot spots’, and a sharp increase in the intensity of light scattering and absorption [35]. As a result, even minimal changes in the blood microstructure during the initial stages of coagulation become available for registration, which directly increases the sensitivity of the sensor.

Work in the field of biosensors confirms that the nanosize of particles itself allows recording the smallest changes in the refractive index of the medium, which is impossible for classical macroscopic optical elements. The use of nanoparticles in the near-infrared range provides an increase in refractometric sensitivity along with better control of spectral selectivity, which opens up prospects for high-precision biomedical sensors [42]. For LSA, this means that the system is able to record microdynamic changes in the movement of cells and proteins even before the appearance of a macroscopic clot, that is, those that precede the formation of the fibrin scaffold.

Another important mechanism is a sharp increase in the scattering and absorption of light by nanoparticles. For example, it has been shown that scattering from a gold nanoparticle with a diameter of 80 nm can be 10^5 times stronger than fluorescence and 10^{12} orders of magnitude more intense than the Raman signal [42]. For the practical side of LSA, this means that, even when using low-power diode lasers, a sufficiently intense speckle signal is formed, which allows reducing power consumption, simplify the optical circuit and reduce the dimensions of the device. Accordingly, the amplified signal allows you to use compact CMOS cameras without losing the quality of measurements.

The effect of nanocoatings on the signal-to-noise ratio in the system is no less important. Even minor parasitic reflections from the surfaces of lenses or lenses can lead to interference noise, which reduces the accuracy of speckle analysis. The use of anti-reflective nanocoatings of *the moth-eye type* can reduce the reflection coefficient to $< 0.5\%$ and increase light transmission to almost 99% [43], which ensures the formation of a pure speckle pattern, suitable for further digital processing and creates the prerequisites for a more accurate assessment of cell micromovements. The additional application of plasmonic nanoparticles integrated into the coating allows not only to dampen unwanted reflections, but also to amplify the useful signal thanks to LSPR [23, 44, 45].

An important role in the formation of a qualitative speckle pattern is also played by the coherence of the radiation source. Adjusting the degree of partial coherence can optimize the signal-to-noise ratio in nanoparticle imaging. For LSAs, this approach allows you to reduce the impact of static interference noise and artefacts, while remaining highly sensitive to dynamic changes in the sample. Considering this factor in the design of portable sensors makes them less demanding on ideal operating conditions, which is especially important for military medicine.

The combination of the above-mentioned physical mechanisms makes it possible to create compact and at the same time highly sensitive sensors. Signal amplification at the level of nanostructures reduces the requirements for laser power and camera sensitivity, reduces the number of optical components and simplifies the design of the system, which opens the way for the development of Point-of-Care devices suitable for use in mobile laboratories, stabilization points and field hospitals.

9. NANOCOATING OF CUVETTES: USING SILVER NANOFILM TO RECORD SPECKLE STRUCTURES WITH REFLECTED LIGHT

Laser speckle analysis involves the use of coherent radiation passing

through the sample, but, when using a heated table (so that the blood sample does not dry out), recording the reflected speckle pattern becomes less effective. To obtain a clear and stable image, it is best to have a thin silver nanocoating at the bottom of the cuvette where the blood sample is stored.

The precipitated silver nanofilm with a thickness of 40–80 nm creates an optically active surface that reflects laser radiation with a high coefficient, while allowing the phenomena of local plasmon resonance (LSPR) and surface plasmon resonance (SPR) to be realized at the silver–biological fluid interface. This makes it possible to increase the sensitivity of speckle analysis to micromovements of blood cells or changes in rheological properties during coagulation [46].

Such solutions are widely applied in PPR microscopy, biosensors and laser optical backscatter systems. Silver nanofilms with a thickness of $\cong 50$ nm offer the highest sensitivity to changes in the refractive index of the medium compared to other metals, in particular, gold.

The morphology and thickness of the silver layer has a great influence on the reflective properties and interference effects that form the structure speckle. Samidir Im Nanofilms (≤ 100 nm) gives the best-distributed display for recording speckle pattern [45, 47].

9. CONCLUSIONS

Laser speckle analysis (LSA) has established itself as a promising optical diagnostic tool for assessing blood clotting. Compared to traditional thromboelastography systems TEG, ROTEM, ClotPro, this method has a number of advantages: contactlessness, no need for reagents, the possibility of portable implementation and the speed of obtaining results.

Available studies confirm a high correlation between the indicators obtained with the help of LSA and the parameters of standard coagulological devices. Although the method is still at the stage of laboratory validation, it has significant potential for use in extreme conditions, in particular, in field hospitals, stabilization points, and during emergencies.

Further research should be aimed at standardizing the technique, developing software for signal processing and creating full-fledged prototypes for clinical use. In the future, LSA can become an integral part of mobile diagnosis of haemostasis, especially in conditions of war or disasters, where the speed of decision-making saves lives.

The use of nanocoatings on optical elements, in particular, lenses and lenses, in speckle imaging systems reduces noise levels, im-

proves contrast and image detail, which is critical for the correct analysis of coagulation processes in biological samples.

The integration of silver nanofilm as a reflective element into the optical circuit of the speckle analyser allows:
— to increase optical contrast;
— to enhance the dynamics of the speckle signal;
— to react sensitively to structural and viscous changes in the blood sample during coagulation.

This solution is a full-fledged element of the nanotechnological design of the system, taking into account the scale, application methods (*e*-beam evaporation, sputtering) and nanostructural surface properties.

REFERENCES

1. NATO Standardization Office, *AMedP-8.5: Minimum Requirements for Medical Laboratory Support to Deployed Operations* (STANAG 2571, Ed. A Ver. 2) (2020); https://www.coemed.org/files/stanags/03_AMEDP/AMedP-8.5_EDA_V2_E_2571.pdf
2. W. Z. Martini, *J. Trauma*, **67**, No. 1: 202 (2009); https://doi.org/10.1097/TA.0b013e3181a602a7
3. D. R. Spahn, B. Bouillon, V. Cerny, T. J. Coats, J. Duranteau, E. Fernández-Mondéjar, D. Filipescu, B. J. Hunt, R. Komadina, G. Nardi, E. Neugebauer, Y. Ozier, L. Riddez, A. Schultz, J.-L. Vincent, and R. Rossaint, *Crit. Care*, **17**, No. 2: R76 (2013); https://doi.org/10.1186/cc12685
4. H. Schöchl, M. Maegele, C. Solomon, K. Görlinger, and W. Voelckel, *Scand. J. Trauma Resusc. Emerg. Med.*, **20**, No. 1: 15 (2012); https://doi.org/10.1186/1757-7241-20-15
5. A. G. Burton and K. E. Jandrey, *Vet. Clin. North Am. Small Anim. Pract.*, **50**, No. 6: 1397 (2020); https://doi.org/10.1016/j.cvsm.2020.08.001
6. R. Rossaint, B. Bouillon, V. Cerny, T. J. Coats, J. Duranteau, E. Fernández-Mondéjar, D. Filipescu, B. J. Hunt, R. Komadina, G. Nardi, E. A. M. Neugebauer, Y. Ozier, L. Riddez, A. Schultz, J.-L. Vincent, and D. R. Spahn, *Crit. Care*, **20**: 100 (2016); https://doi.org/10.1186/s13054-016-1265-x
7. L. Makyeyeva, O. Frolov, and O. Aliyeva, *Innovative Biosystems and Bioengineering*, **9**, No. 1: 13 (2025); https://doi.org/10.20535/ibb.2025.9.1.310092
8. A. Sokol, D. Grekov, G. Yemets, A. Galkin, N. Shchotkina, A. Dovghaliuk, O. Telehuzova, N. Rudenko, O. Romaniuk, and I. Yemets, *Biopolym. Cell*, **36**: 392 (2020); http://dx.doi.org/10.7124/bc.000A3C
9. S. O. Bychkov and O. O. Martyniv, *The Journal of V. N. Karazin Kharkiv National University. Series Medicine*, **33**, No. 3 (54): 310 (2025); https://doi.org/10.26565/2313-6693-2025-54-01
10. Klaus Görlinger, Antonio Pérez-Ferrer, Daniel Dirkmann, Fuat Saner, Marc Maegele, Ángel Augusto Pérez Calatayud, and Tae-Yop Kim, *Korean J. Anesthesiol.*, **72**, No. 4: 297 (2019); https://doi.org/10.4097/kja.19169

11. P. Bodnar, A. Bedeniuk, T. Bodnar, L. Bodnar, and B. Verveha, *Eastern Ukrainian Medical Journal*, **13**, No. 1: 14 (2025); https://doi.org/10.21272/eumj.2025;13(1):14-27
12. O. Salekh, *The Odessa Medical Journal*, No. 2: 27 (2025); https://doi.org/10.32782/2226-2008-2025-2-4
13. F. Hladkykh, *Otsinka Vplyvu Kondytsionovanogo Seredovyshcha Mezenkhimalnykh Stovburovykh Klityn ta Krioehkstraktiv Biolohichnykh Tkanyn na Proyavy Tsytolitychnoho Syndromu pry Ehksperymentalnomu Autoimunnomu Hepatyti* [Evaluation of the Influence of Conditioned Medium of Mesenchymal Stem Cells and Cryoextracts of Biological Tissues on the Manifestation of Cytolytic Syndrome in Experimental Autoimmune Hepatitis], *The Odessa Medical Journal*, **6**: 45 (2024) (in Ukrainian); https://doi.org/10.32782/2226-2008-2024-6-8
14. U. Haque, M. H. Bukhari, N. Fiedler, S. Wang, O. Korzh, J. Espinoza, M. Ahmad, I. Holovanova, T. Chumachenko, O. Marchak, D. Chumachenko, O. Ulvi, I. Sikder, H. Hubenko, and E. S. Barrett, *JAMA Health Forum*, **5**, No. 5: e240901 (2024); https://doi.org/10.1001/jamahealthforum.2024.0901
15. Z. Hajjarian and S. K. Nadkarni, *J. Biomed. Opt.*, **25**, No. 5: 1–19 (2020); https://doi.org/10.1117/1.JBO.25.5.050801
16. M. F. Mahmood, *Innov. Biosyst. Bioeng.*, **8**, No. 2: 53 (2024); https://doi.org/10.20535/ibb.2024.8.2.298201
17. G. N. Jackson, K. J. Ashpole, and S. M. Yentis, *Anaesthesia*, **64**, No. 2: 212 (2009); https://doi.org/10.1111/j.1365-2044.2008.05752.x
18. M. Maegele, R. Lefering, N. Yucel, T. Tjardes, D. Rixen, T. Paffrath, C. Simanski, E. Neugebauer, and B. Bouillon, *Injury*, **38**, No. 3: 298 (2007); https://doi.org/10.1016/j.injury.2006.10.003
19. K. Görlinger, D. Dirkmann, and A. A. Hanke, *Curr. Opin. Anaesthesiol.*, **26**, No. 2: 230 (2013); https://doi.org/10.1097/ACO.0b013e32835ddca6
20. S. J. Wilson and M. C. Hutley, *Optica Acta: International Journal of Optics*, **29**, No. 7: 993 (1982); https://doi.org/10.1080/713820946
21. M. M. Tripathi, Z. Hajjarian, and S. K. Nadkarni, *Biomed. Opt. Express*, **5**, No. 3: 817 (2014); https://doi.org/10.1364/BOE.5.000817
22. A. Baykova, M. Bohomolov, S. Vovyanko, and V. Borovskyi, *Porivnyalnyi Analiz Metodiv Spekl-Vizualizatsii ta Mikroskopii dlya Doslidzhennya Zrazkiv Krovi* [Comparative Analysis of Speckle Imaging and Microscopy Methods for Blood Sample Research], *Biomed. Eng. Technol.*, **16**: 31 (2024) (in Ukrainian); https://doi.org/10.20535/.2024.16.317945
23. A. V. Saúde, F. S. De Menezes, P. L. S. Freitas, G. F. Rabelo, and R. A. Braga, *J. Opt. Soc. Am. A*, **29**, No. 8: 1648 (2012); https://doi.org/10.1364/josaa.29.001648
24. M. F. Bogomolov, V. V. Shlikov, and S. I. Vovyanko, *Komp'yuterna Obrobka Speklinterferohram dlya Optychnoho Diahnostuvannya Biolohichnykh Mikroob'iektiv* [Computer Processing of Speckle Interferograms for Optical Diagnostics of Biological Microobjects], *Biomed. Eng. Technol.*, **6**: 99 (2021) (in Ukrainian); https://doi.org/10.20535/2617-8974.2021.6.244563
25. J. Liu, H. He, D. Xiao, S. Yin, W. Ji, S. Jiang, D. Luo, B. Wang, and Y. Liu, *Materials*, **11**, No. 10: 1833 (2018); https://doi.org/10.3390/ma11101833
26. J. Gong, Y. Zhang, H. Zhang, Qi Li, G. Ren, W. Lu, and Jing Wang, *Micromachines*, **22**, No. 13: 4793 (2022); https://doi.org/10.3390/s22134793

27. J. Hartmann, D. Hermelin, and J. H. Levy, *Res. Pract. Thromb. Haemost.*, **7**, No. 1: 100031 (2023); https://doi.org/10.1016/j.rpth.2022.100031
28. S. Song, S. Choi, S. Ryu, S. Kim, T. Kim, J. Shin, H.-I. Jung, and C. Joo, *Biosens. Bioelectron.*, **117**: 385 (2018); https://doi.org/10.1016/j.bios.2018.06.024
29. D. S. Kauvar and C. E. Wade, *Crit. Care*, **9**, No. S5: S1 (2005); https://doi.org/10.1186/cc3779
30. M. Draijer, E. Hondebrink, T. Leeuwen, and W. Steenbergen, *Lasers Med. Sci.*, **24**, No. 4: 639 (2008); https://doi.org/10.1007/s10103-008-0626-3
31. G. Han, J. Lu, X. Dong, D. Li, J. Yuan, Q. Yang, H. Wang, R. Chen, Y. Wu, J. Wang, and X. Min, *Infrared Phys. Technol.*, **142**: 105512 (2024); https://doi.org/10.1016/j.infrared.2024.105512
32. R. Gaiser, *Best Pract. Res. Clin. Anaesthesiol.*, **26**, No. 1: 69 (2012); https://doi.org/10.1016/j.bpa.2012.01.001
33. A. Yu. Popov, N. A. Popova, A. V. Tyurin, and V. Grimblatov, *Proceedings of SPIE (Conference on Mechanisms for Low-Light Therapy VIII)*, **8569**: 85690C (2013); https://doi.org/10.1117/12.2002128
34. A. Nadort, K. Kalkman, T. G. Van Leeuwen, and D. J. Faber, *Sci. Rep.*, **6**, No. 1: 25258 (2016); https://doi.org/10.1038/srep25258
35. M. A. Toderi, B. D. Riquelme, and G. E. Galizzi, *Opt. Eng.*, **61**, No. 12: 124101 (2022); https://doi.org/10.1117/1.oe.61.12.124101
36. L. Markwalder, R. Gush, F. Khan, C. E. Murdoch, and N. Krstajić, *iScience*, **27**, No. 3: 109077 (2024); https://doi.org/10.1016/j.isci.2024.109077
37. J. Liu, H. He, D. Xiao, S. Yin, W. Ji, S. Jiang, D. Luo, B. Wang, and Y. Liu, *Materials*, **11**, No. 10: 1833 (2018); https://doi.org/10.3390/ma11101833
38. J. Dybas, F. C. Alcicek, A. Wajda, M. Kaczmarska, A. Zimna, K. Bulat, A. Blat, T. Stepanenko, T. Mohaissen, E. Szczesny-Malysiak, D. Perez-Guaita, B. R. Wood, and K. M. Marzec, *TrAC Trends Anal. Chem.*, **146**: 116481 (2021); https://doi.org/10.1016/j.trac.2021.116481
39. H. Ye, Y. Liu, L. Zhan, Y. Liu, and Z. Qin, *Theranostics*, **10**: 4359 (2020); https://doi.org/10.7150/thno.44298
40. J. W. Goodman, *Speckle Phenomena in Optics: Theory and Applications* (Bellingham, WA: SPIE Press: 2020); https://doi.org/10.1117/3.2548484
41. K. V. Baryshnikova, M. I. Petrov, V. E. Babicheva, and P. A. Belov, *arXiv*:1508.06578 (2015); https://doi.org/10.48550/arXiv.1508.06578
42. P. S. S. dos Santos, J. M. M. M. de Almeida, I. Pastoriza-Santos, and L. C. C. Coelho, *Sensors*, **21**, No. 6: 2111 (2021); https://doi.org/10.3390/s21062111
43. E. A. Savchenko and E. N. Velichko, *Opt. Spectrosc.*, **128**: 998 (2020); https://doi.org/10.1134/s0030400x2007019x
44. D. Li, Y. Zhang, and B. Chen, *J. Innov. Opt. Health Sci.*, **13**, No. 2: 20500042 (2020); https://doi.org/10.1142/s1793545820500042
45. S. J. Wilson and M. C. Hutley, *Opt. Acta*, **29**: 993 (1982); https://doi.org/10.1080/713820946
46. B. Lee, B. Park, D. Kim, C. Jung, J. H. Park, J.-H. Park, Y. E. Lee, M. G. Shin, M.-G. Kim, N. E. Yu, J. H. Kim, and K. Kim, *Nat. Commun.*, **16**: 3377 (2025); https://doi.org/10.1038/s41467-025-58663-z
47. S. K. Gahlaut, A. Pathak, and B. D. Gupta, *Biosensors*, **12**, No. 9: 713 (2022); https://doi.org/10.3390/bios12090713

Наносистеми, наноматеріали, нанотехнології
Nanosistemi, Nanomateriali, Nanotehnologii
2026, т. 24, № 1, сс. 317–326
https://doi.org/10.15407/nnn.24.01.0317

PACS numbers: 64.75.Jk, 66.30.Pa, 68.37.Yz, 81.05.Bx, 81.16.Pr, 81.65.Kn, 81.65.Lp

Effect of Nanogold Layer on the Aluminizing Process of Superalloy BV-18 and Its Resistance to Hot Corrosion

M. M. Mahmood, M. A. Hamood, and S. M. Ahmed

Department of Physics,
The University of Mosul,
Mosul, Iraq

Nanolayer of gold is obtained by the method of physical vapour deposition as a thermal barrier on a nickel-base superalloy. The effect of this layer on the aluminizing process and the efficiency for hot-corrosion resistance is studied by comparing two sets of samples: the first set, which is contained of the gold layer, while the second set is aluminized without this layer. The aluminizing process is carried out for both sets, using the pack-cementation method at a temperature of 1000°C. The samples coated with nanogold show a different behaviour from those samples, which are aluminized only, where the use of nanogold oxide improves the alloy ability to withstand hot-corrosion conditions.

Наношар золота було одержано методом фізичного осадження з парової фази як тепловий бар'єр на ніклевому суперстопі. Вплив цього шару на процес алюмінування й ефективність стійкости до гарячої корозії було досліджено шляхом порівняння двох наборів зразків: перший набір містив шар золота, а другий набір був алюмінований без цього шару. Процес алюмінування проводився для обох наборів методом пакувальної цементації за температури у 1000°C. Зразки, покриті нанозолотом, демонстрували іншу поведінку, ніж ті, що були лише алюміновані, де використання нанооксиду Ауруму поліпшило здатність стопу витримувати умови гарячої корозії.

Key words: diffusion coating, hot corrosion, nanogold, pack cementation, surface engineering.

Ключові слова: дифузійне покриття, гаряча корозія, нанозолото, тверда цементація, інженерія поверхні.

(Received 26 August, 2024; in revised form, 8 September, 2024)

1. INTRODUCTION

Diffusion coatings were developed firstly and are used primarily to enrich the surface of the superalloy with aluminium. These coatings proved very successful and in the early to mid-1960s, this coating technique was applied to turbine blades made of nickel alloys [1–3]. There are a number of methods of forming aluminide coatings such as slurry spraying followed by high temperature diffusion, electrolysis and pack cementation. Of all these methods, pack cementation is the one widely used, as it is inexpensive and ideally suited for coating small components [4–6]. Despite the mentioned features, the diffusion of Ni from the superalloy and that of Al from the overlay causes, however, structural changes capable of causing spall off of the protecting layer [7]. Diffusion barrier coating systems have excellent mechanical properties (creep and fatigue), improving alloy substrate performance, and enhance the anti-exfoliation properties of YSZ in thermal barrier coatings (TBC) in addition to providing excellent oxidation resistance [8]. Adding a layer of yttrium oxide (Y_2O_3) to the alloy Fe–30 Cr before the aluminizing process improves its resistance to oxidation, as the yttrium oxide layer acts as a diffusion barrier that prevents the spread of aluminium from the coating layer into the alloy and preventing the spread of the alloy elements outward. The concentration of the element yttrium has an effect on the properties of the coating resulting from the aluminizing process, small amounts of it act as nucleation sites that impede the growth of granules, while adding large amounts of it leads to delaying the phase transformation $\theta\text{-}Al_2O_3 \rightarrow \alpha\text{-}Al_2O_3$ [9]. The diffusion barrier may partially prevent the interdiffusion of the alloy elements, thus improving the oxidation resistance of thermal barrier coatings (TBCs), where the content of aluminium and chromium was higher, while the rest of the alloy elements were lower in the mixture coating material for the sample with the diffusion barrier compared to the one without the barrier [10]. In this research, adding a nanogold layer as a thermal barrier to a nickel-based alloy and study the effect of that layer on the aluminizing process and efficiency of hot corrosion for the BV-18 nickel-based superalloy. The resulting coatings were analysed quantitatively and qualitatively for both types of coating using x-ray spectroscopy (XRD), (SEM), and (EDX) techniques to determine the compounds that make up the coating and their phases.

2. EXPERIMENTAL METHODS

2.1. Materials

In this study, the superalloy BV-18 is used, which is one of the

blades of turbine engines used in gas stations to generate electrical power; its quantitative and qualitative specifications are shown in Table 1.

2.2. Coating Processes

In this study, two types of coating techniques are used.

2.2.1. Pack Cementation

Aluminizing is performed in a tube furnace under vacuum, which is maintained throughout the process (heating, holding, and cooling).

The cementation process was carried out for all prepared samples and for the superalloy BV-18 using a mixture of aluminium powder 30% as the coating material, aluminium oxide (alumina) 66% as a material that helps prevent agglomeration of the mixture, and ammonium chloride powder. With a percentage of 4% as an activating material, the mixture is placed after good mixing inside the pod gradually, while placing the samples to be coated in it. The pod is closed and placed inside a vacuum oven according to Fig. 1.

The temperature of the oven is set at the required degree 1000°C. Cementing takes place for a period of 6 hours, and after the completion of the coating process, the samples are cooled inside the oven until the temperature (of 200°C) reaches, while continuing to operate the vacuum device. Then, the samples are taken out, cleaned, then weighed and stored well until tests are conducted on them.

TABLE 1. Composition [wt.%] of superalloy BV-18 used in the experiments.

Element	Ni	Cr	Ti	Co	Mo	Al	C	Si	S
wt.%	balance	17.85	4.15	5.31	2.28	10.53	8.79	4.99	3.57

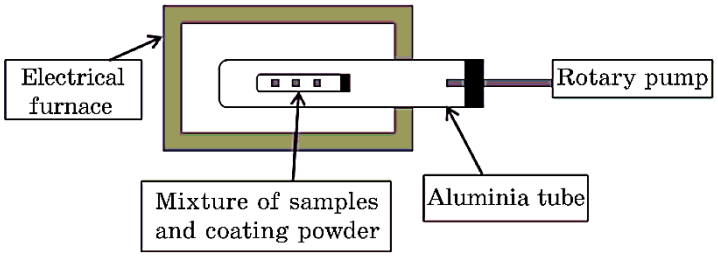

Fig. 1. Schematic drawing of the coating system.

Fig. 2. Q150R ES device used to deposit nanogold layer.

TABLE 2. Composition [wt.%] of the coated superalloy BV-18.

Type of coating	Element	Al	Ni	Co	Cr	Au	Si	Mo
Single aluminizing	wt.%	21.21	25.52	16.08	8.18	Non	0.42	0.66
Nanogold	wt.%	24.00	12.62	3.01	2.32	1.99	0.76	0.00

2.2.2. Nanogold Layer Coating

There are different techniques for fixing the diffusion barrier material on the surface of the sample, including chemical evaporation (CVD) or physical (PVD) coating, laser coating, and others. In this study, the sputtering coating technique was used. This method is one of the physical evaporation (PVD) methods and is a widely used technique. To deposit thin films, a nanogold layer was deposited on some samples of the alloy BV-18 targeted in our study using a device (Q150R ES), the image of which is shown in Fig. 2. Sputter target/disc style 57 mm×0.1 mm thick gold.

3. RESULTS AND DISCUSSION

3.1. Surface Morphology

The results were obtained after aluminizing the superalloy BV-18 with pack-cementation process through a single aluminizing process and aluminizing in the presence of the nanogold at a temperature of 1000°C and for time period of 6 h. For each processing mode, single set of parameter was used: high temperature with high Al activity (HTHA).

The results of the analysis of the scanning electron microscopy (SEM) shown in Fig. 3 for the two types of coatings showed a homogeneous spread of aluminium.

From spectroscopic analysis of the EDS (Figs. 4, 5), there are

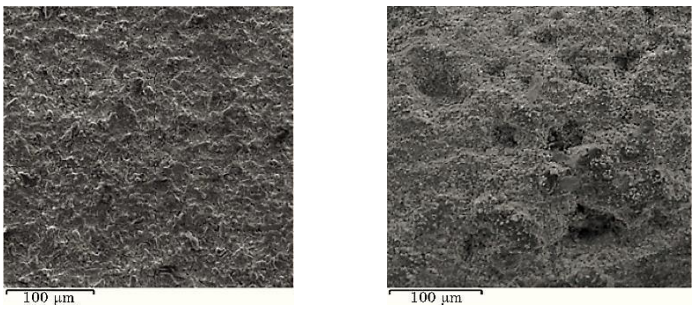

a *b*

Fig. 3. Surface morphology of aluminizing with: *a*—single aluminizing; *b*—nanogold.

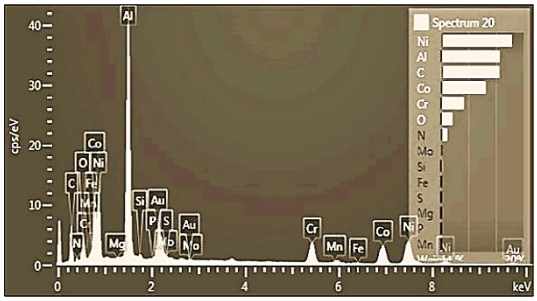

Fig. 4. EDS for aluminizing coating for single aluminizing of BV-18 superalloy at 1000°C for 6 h.

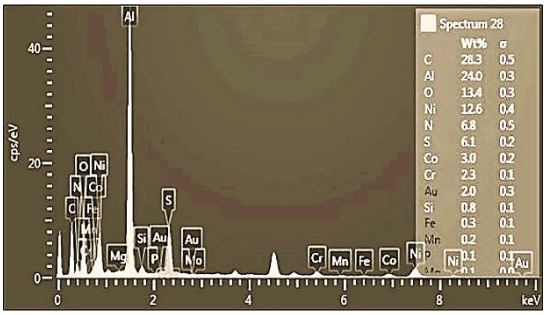

Fig. 5. EDS for aluminizing coating in the presence of nanogold layer for BV-18 superalloy at 1000°C for 6 h.

many peaks for the elements, including aluminium, nickel and cobalt, and the highest intensity of these peaks is the element aluminium, which represents the basic element for the coating layer.

This is what appeared in the data of Table 3 for quantitative and

TABLE 3. Average mass gain and average thickness of aluminized samples by single aluminizing and nanogold for BV-18 superalloy for 6 h at 1000°C.

Type of coating	Av. thickness of coating, μm	Mass gain, mg/cm^2
Single aluminizing	350	48.63
Nanogold	358	40.57

TABLE 4. The phases are possible to form in single aluminizing coating.

Ref. Code	Compound Name	Chemical Formula
03-065-0672	Aluminium Cobalt	AlCo
00-002-1261	Aluminium Nickel	AlNi
00-002-1239	Aluminium Chromium	$AlCr_2$
00-021-0008	Aluminium Nickel	$AlNi_3$
00-038-1026	Aluminium Chromium	$Al_{86}Cr_{14}$
03-065-3454	Aluminium Nickel	Al_3Ni_2
03-065-7336	Aluminium Chromium	$Al_{0.983}Cr_{0.017}$
03-065-8530	Aluminium Molybdenum	$AlMo_3$
00-042-1467	Cobalt Oxide	Co_3O_4
00-032-0285	Chromium Oxide	CrO_3

TABLE 5. The phases are possible to form in aluminizing process in presence of nanogold layer.

Ref. Code	Compound Name	Chemical Formula
03-065-8473	Aluminium Gold	Al_2Au
01-075-1865	Aluminium Oxide	Al_2O_3
00-029-0021	Aluminium Cobalt	AlCo
00-002-1261	Aluminium Nickel	AlNi
00-047-1410	Aluminium Titanium	$AlTi_2$
01-089-3697	Gold	Au

qualitative analysis by the scanning electron device (EDS).

The percentage of aluminium and nickel is shown in Table 5. This supports the analysis of XRD spectrum in obtaining the intermediate compounds of nickel–aluminium, as well as obtaining some intermediate compounds of cobalt–aluminium, with a weight ratio [wt.%] of cobalt.

3.2. Optical Microscopy Examination

The samples that were coated with single aluminium using the pack-

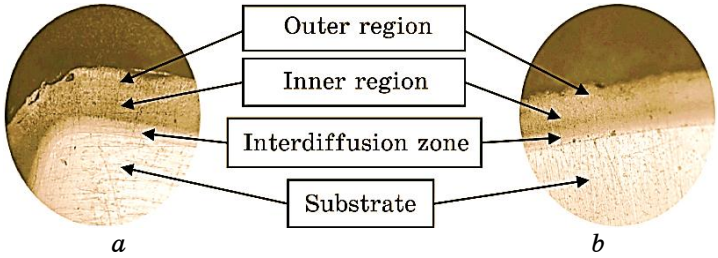

Fig. 6. Microstructure of the samples coated with two types of aluminizing coatings: (*a*) single aluminizing; (*b*) nanogold at temperature of 1000°C for 6 h.

cementations method showed the appearance of three areas of coating: the outer layer, the inner region and, interdiffusion zone, which is a narrow area free of deposits. The cross-section of the samples was photographed as shown in Fig. 6 for two types of coatings (*a*—single aluminizing; *b*—nanogold). The thickness of coating with single aluminizing and nanogold with mass gain value are shown in Table 3.

The microscopic examination of the coating after 6 h showed the presence of two regions, the outer region containing dark structures, which may be secondary phases, and the inner region having light-coloured structures, somewhat narrow and a little thick at the bottom, *i.e.*, the interdiffusion zone. This is known as the diffusive exchange zone. It is also noted that the microscopic structure of the resulting coatings is characterized by the presence of more than one phase in the coating layer, and the outer coating layer consists of phases rich in aluminium.

3.3. XRD Analysis

It must be remembered that the alloy used in the research is nickel-based, and its coating with aluminium leads to the formation of one of the phases of intermediate compounds nickel–aluminium, and this has already happened. The results of XRD analysis revealed many complications in terms of the number of resulting phases, but they confirmed the formation of the aluminium-rich phase Ni–Al and Ni_2Al_3 are mainly in the coatings produced after 6 hours this is consistent with what was stated in Ref. [11] for high temperature–high activity aluminize coating.

The results of the x-ray diffraction analysis of the coated sample for a period of 6 hours, as was shown from the diffraction model in Fig. 7, the appearance of peaks by returning to the phase diagrams for both systems nickel–aluminium and aluminium–gold. In Figures

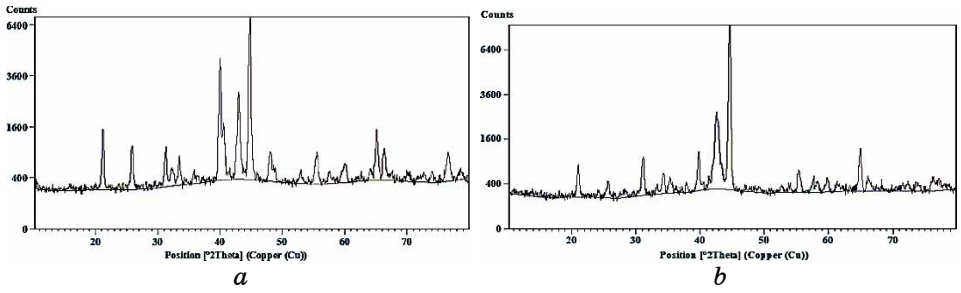

Fig. 7. X-ray diffraction plot of a sample coated with: (*a*) single aluminizing; (*b*) nanogold at 1000°C for 6 hours.

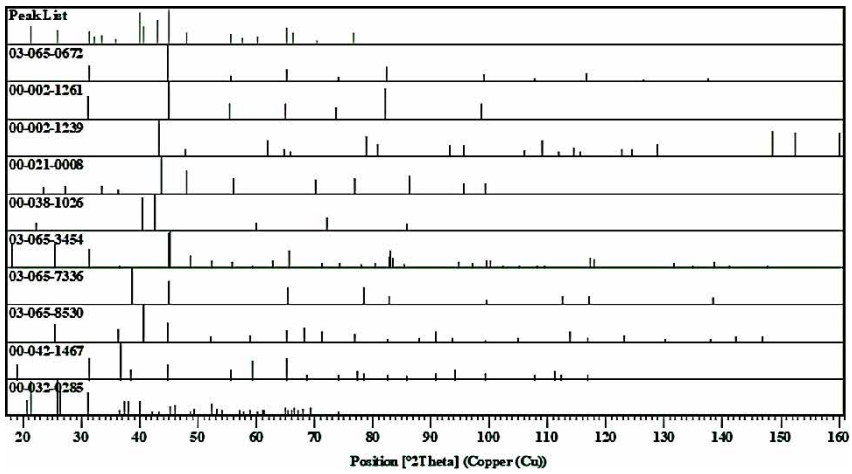

Fig. 8. Comparison of the results of X-ray analysis that are formed in a single aluminizing coating for BV-18 superalloy at 1000°C for 6 h with those stored in the X'Pert High Score Plus program.

8 and 9, we find that the phases are possible to form at this temperature. Tables 4 and 5 show the phases, which are possible to form in single aluminizing and with nanogold layer.

3.4. Hot-Corrosion Test

This test was conducted with the aim of identifying the resistance of the single aluminized sample compared to the aluminized sample in presence of nanogold layer for hot corrosion conditions, and the test results have been shown by studying (the change of mass with time) in salt vapour at 900°C. As shown in Fig. 10, the sample aluminized with single aluminizing suffered some decreasing in mass in the first

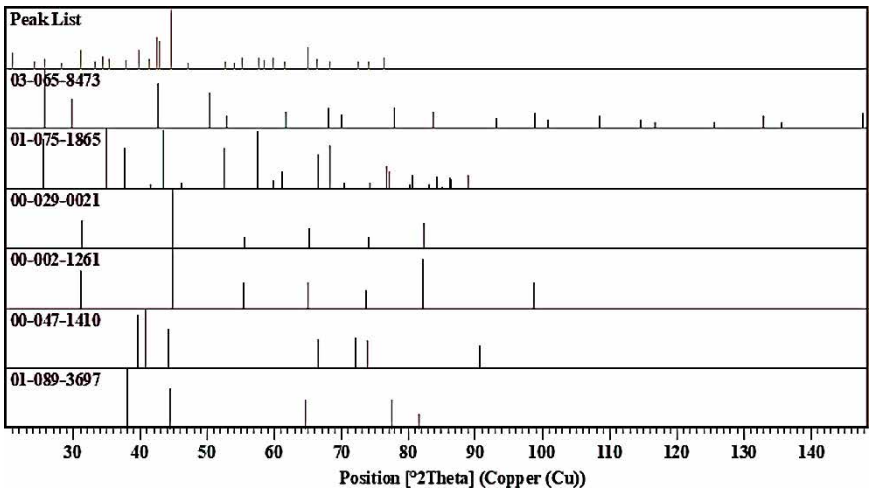

Fig. 9. Comparison of the results of x-ray analysis, which are obtained for the aluminizing coating in the presence of nanogold layer for BV-18 superalloy at 1000°C for 6 h, with those stored in the X'Pert High Score Plus program.

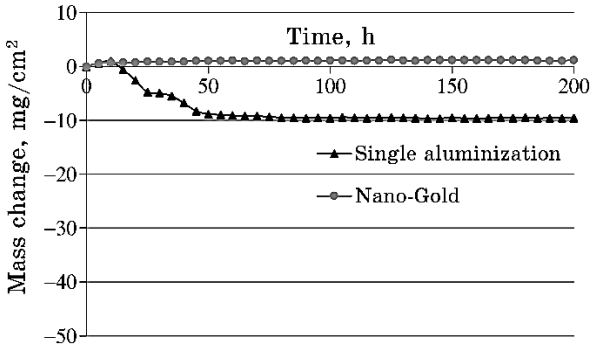

Fig. 10. Cyclic oxidation kinetics of single aluminizing coating and in presence of nanogold layer in salt vapour at 900°C.

50 hours of exposure, while stability in mass was observed with alloy that coated with nanogold layer before aluminizing process.

4. CONCLUSIONS

In this research, the effect of adding nanogold layer as a thermal barrier on (aluminizing process and resisting hot corrosion) was studied. It is indicated from the (Microscopic, XRD, SEM-EDS) analysis that inward diffusion of Al and outward diffusion of Co,

Ni and Cr have led to the formation of multilayer with different phases, the addition of nanogold produce some different phases such as Al_2Au and stable alumina phase (Ref. Code 01-075-1865), namely, α-Al_2O_3. By monitoring the weight loss and the data obtained from the kinetics of oxidation, it was shown that the coating in the presence of nanogold has the best resistance to hot corrosion and had less change in mass during the test compared to single aluminized, and the protective oxidation scale α-Al_2O_3 has very good adhesion and stability during exposure time. Overall, for the above, this thermal barrier is considered with a high efficiency in resisting the harsh operating conditions of engineering equipment.

ACKNOWLEDGMENTS

We would like to express our heartfelt gratitude to the University of Mosul/College of Science and to Dr. Mohammad M. Uonis (Department of Physics, College of Science, Mosul University, Mosul, Iraq), for their unwavering assistance throughout the research process.

REFERENCES

1. S. Bose, *High Temperature Coatings* (Elsevier Science: 2017).
2. G. W. Goward and L. W. Cannon, *J. Eng. Gas Turbines Power*, **110**, Iss. 1: 150 (1988); https://doi:10.1115/1.3240078
3. J. R. Nicholls, *JOM*, **52**, Iss. 1: 28 (2000); https://doi:10.1007/s11837-000-0112-2
4. R. Sivakumar and B. L. Mordike, *Surface and Coating Technology*, **37**, Iss. 2: 139 (1989).
5. M. O. Cojocaru, M. Branzei, and L. N. Druga, *Materials*, **15**, Iss. 15: 5453 (2022); https://doi:10.3390/ma15155453
6. R. Bianco and R. A. Rapp, *Pack Cementation Diffusion Coatings BT–Metallurgical and Ceramic Protective Coatings* (Ed. K. H. Stern) (Netherlands: Springer: 1996), p. 236; https://doi:10.1007/978-94-009-1501-5_9
7. M. Uunonen, P. Kaski, P. Henttu, and P. Kettunen, *Diffusion Barriers for the Superalloy Blades of Gas Turbines- Steels and Materials for Power Plants* (Eds. P. Neumann, D. Allen, and E. Teuckhoff) (Weinheim: Wiley-VCH: 2000), p. 332; https://doi.org/10.1002/3527606181.ch58
8. T. Narita, Y. Kato, T. Narita, and M. Ara, *High Temp. Corros. Mater.*, **100**, Iss. 5: 399 (2023); https://doi:10.1007/s11085-023-10203-0
9. C. Houngninou, S. Chevalier, and J. P. Larpin, *Appl. Surf. Sci.*, **236**, Iss. 1: 256 (2004); https://doi.org/10.1016/j.apsusc.2004.04.026
10. Z. Xu, L. He, R. Mu, X. Zhong, and X. Cao, *Vacuum*, **82**, Iss. 11: 1251 (2008); https://doi.org/10.1016/j.vacuum.2008.03.057
11. E. Pauletti and A. S. C. M. d'Oliveira, *J. Vac. Sci. Technol. A*, **36**, Iss. 4: 41504 (2018); https://doi:10.1116/1.5026272

Наукове видання

НАНОСИСТЕМИ, НАНОМАТЕРІАЛИ, НАНОТЕХНОЛОГІЇ

ЗБІРНИК НАУКОВИХ ПРАЦЬ

ТОМ 24

випуск 1

(2026)

Підписано до друку 31.03.2026. Формат 70×100/16.
Папір офсетний. Друк різографічний.
Ум. друк. арк. 27,95. Обл.-вид. арк. 25,71.
Наклад 53 прим. Зам. № 1

Поліграфічно-розмножувальна дільниця РВВ ІМФ ім. Г. В. Курдюмова НАН України
бульв. Акад. Вернадського, 36; 03142 Київ, Україна

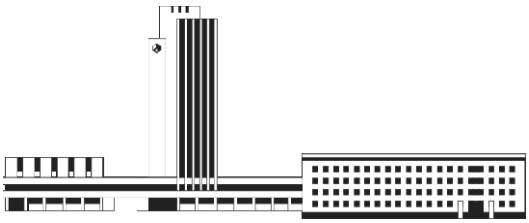

НАЦІОНАЛЬНА АКАДЕМІЯ НАУК УКРАЇНИ

Засновник: Інститут металофізики ім. Г. В. Курдюмова НАН України
Видавець: Інститут металофізики ім. Г. В. Курдюмова НАН України

Передплатний індекс 94919 ISSN 1816-5230

Інформація про передплату на збірник наукових праць
«НАНОСИСТЕМИ, НАНОМАТЕРІАЛИ, НАНОТЕХНОЛОГІЇ»

Редакція щоквартального збірника наукових праць «НАНОСИСТЕМИ, НАНОМАТЕРІАЛИ, НАНОТЕХНОЛОГІЇ» (CODEN: NNNAAT; ISSN (Print): 1816-5230, ISSN (Online): 2617-3794) повідомляє читачів про передплату (що починається з поточного кварталу випуску). Цей збірник входить за індексом **94919** до «Каталогу видань України». Рекомендуємо оформити передплату:
1) через ТОВ **«ПресЦентр Київ»** / LLC **'PresCentr Kyiv'** / (01019 Київ, Україна, а/с 185; тел. / факс: +380 44 5361180 / +380 44 5361175; e-mails: podpiska1@prescentr.kiev.ua, market7@prescentr.kiev.ua, ksl1@prescentr.kiev.ua) чи то через Internet:
Наносистеми, наноматеріали, нанотехнології (prescentr.kiev.ua) (Product Code: 14724);
2) через передплатну аґенцію «Меркурій» / Subscription agency 'Mercury' (49000 Дніпро, Слобожанський проспект, буд. 10, корп. 2, кв. 51; 03056 Київ, вул. Вадима Гетьмана, буд. 27, оф. 74; тел.: +380 93 3935740 / +380 44 2210557; e-mails: podpiska@mercury.net.ua, l.podbereznaja.mercury@gmail.com);
3) безпосереднім перерахуванням від **390 грн.** за один примірник випуску до **1560 грн.** за один том (4 випуски у рік):
«ОТРИМУВАЧУ»: Інститут металофізики ім. Г. В. Курдюмова НАН України
на розрахунковий рахунок № UA058201720313291001201001901 в банку ГУДКСУ в м. Києві
Код банку: 820172
Код єдиного державного реєстру підприємств і організацій України (ЄДРПОУ): 05417331
Для «ПОСТАЧАЛЬНИКА» — Інституту металофізики ім. Г. В. Курдюмова НАН України
Свідоцтво платника податку на додану вартість (ПДВ) № 36283185, індивідуальний податковий номер (ІПН) 054173326066
Код призначення платежу: 25010100
ПРИЗНАЧЕННЯ ПЛАТЕЖУ: за збірник «Наносистеми, наноматеріали, нанотехнології» для РВВ ІМФ НАНУ
ПІДСТАВА: передоплата 100%

INFORMATION FOR FOREIGN SUBSCRIBERS

Editorial Board of a Quarterly Collected Scientific Transactions 'Nanosistemi, Nanomateriali, Nanotehnologii' (CODEN: NNNAAT; ISSN (Print): 1816-5230, ISSN (Online): 2617-3794) advertises the subscription on an annual basis. Orders should be placed through one of the methods described below. Besides 1) the subscription *via* the LLC **'PresCentr Kyiv'** / **«ПресЦентр Київ»** (with address: UA-01019 Kyiv, Ukraine, P.B. 185; tel. / fax: +380 44 5361180 / +380 44 5361175; e-mails: podpiska1@prescentr.kiev.ua, market7@prescentr.kiev.ua, ksl1@prescentr.kiev.ua) or *via* Internet:
Наносистеми, наноматеріали, нанотехнології (prescentr.kiev.ua) (Product Code: 14724),
as well as besides 2) the subscription *via* Subscription agency 'Mercury' / «Меркурій» (with juridical address: UA-49000 Dnipro, Slobozhansky Ave., Bldg. 10/2, apt. 51; postal address in Kyiv: UA-03056 Kyiv, Vadym Hetman Str., Bldg. 27, off. 74; tel.: +380 93 3935740 / +380 44 2210557, e-mails: podpiska@mercury.net.ua, l.podbereznaja.mercury@gmail.com),
3) the Editorial Board will take orders sent directly to the Editorial Board. To obtain our collected scientific transactions, the persons and institutions interested in this title should made the definite payment sent, according to the order, to the account of the Publisher—G. V. Kurdyumov Institute for Metal Physics of the N.A.S. of Ukraine.
The periodical frequency is 4 issues per year. The annual subscription rate for 'Nanosistemi, Nanomateriali, Nanotehnologii' is **160 USD** (or **148 EUR**), including airmail postage, packing and handling charges. All other-currency payments should be made using the current conversion rate set by the Publisher (subscribers should contact the Editorial Board).
Subscription is valid after obtaining by the Editorial Board of banker's order. Banker's order should be sent to the address:
G. V. Kurdyumov Institute for Metal Physics, N.A.S. of Ukraine,
currency account No. UA603223130000025308000000067, MFO 322313,
in the Kyiv's Branch of JSC 'The State Export-Import Bank of Ukraine' (Public Joint Stock Company 'Ukreximbank') (11^{b} Bulvarno-Kudryavska Str., UA-04053 Kyiv, Ukraine)
simultaneously with written notice providing the Editorial Board with a copy of banker's order for subscription and detailed address for mailing.
Prepayment is 100%.
Address of the Editorial Board: G. V. Kurdyumov Institute for Metal Physics, N.A.S. of Ukraine, 36 Academician Vernadsky Blvd., UA-03142 Kyiv, Ukraine.
E-mail: tatar@imp.kiev.ua (with subject beginning by word 'NNN')
Fax: +380 44 4242561. Phone: +380 44 4241221, +380 44 4249042.
After receiving of banker's order, the Editorial Board will send the guarantee letter to the subscriber's address for mailing the journal for a corresponding term.
The Editorial Board of this journal hopes for effective co-operation with its present and future readers and requests to promote the maximum information about its contents to persons and organizations concerned.

Індекс 94919